

# Neutrino Physics with JUNO

Fengpeng An<sup>1</sup>, Guangpeng An<sup>2</sup>, Qi An<sup>3</sup>, Vito Antonelli<sup>4</sup>, Eric Baussan<sup>5</sup>, John Beacom<sup>6</sup>, Leonid Bezrukov<sup>7</sup>, Simon Blyth<sup>8</sup>, Riccardo Brugnera<sup>9</sup>, Margherita Buizza Avanzini<sup>10</sup>, Jose Busto<sup>11</sup>, Anatael Cabrera<sup>12</sup>, Hao Cai<sup>13</sup>, Xiao Cai<sup>2</sup>, Antonio Cammi<sup>14,15</sup>, Guofu Cao<sup>2</sup>, Jun Cao<sup>\*2</sup>, Yun Chang<sup>16</sup>, Shaomin Chen<sup>17</sup>, Shenjian Chen<sup>18</sup>, Yixue Chen<sup>19</sup>, Davide Chiesa<sup>14,20</sup>, Massimiliano Clemenza<sup>14,20</sup>, Barbara Clerbaux<sup>21</sup>, Janet Conrad<sup>22</sup>, Davide D'Angelo<sup>4</sup>, Hervé De Kerret<sup>12</sup>, Zhi Deng<sup>17</sup>, Ziyang Deng<sup>2</sup>, Yayun Ding<sup>2</sup>, Zelimir Djurcic<sup>23</sup>, Damien Dornic<sup>11</sup>, Marcos Dracos<sup>5</sup>, Olivier Drapier<sup>10</sup>, Stefano Dusini<sup>24</sup>, Stephen Dye<sup>25</sup>, Timo Enqvist<sup>26</sup>, Donghua Fan<sup>27</sup>, Jian Fang<sup>2</sup>, Laurent Favart<sup>21</sup>, Richard Ford<sup>4</sup>, Marianne Göger-Neff<sup>28</sup>, Haonan Gan<sup>29</sup>, Alberto Garfagnini<sup>9</sup>, Marco Giammarchi<sup>4</sup>, Maxim Gonchar<sup>30</sup>, Guanghua Gong<sup>17</sup>, Hui Gong<sup>17</sup>, Michel Gonin<sup>10</sup>, Marco Grassi<sup>2</sup>, Christian Grewing<sup>31</sup>, Mengyun Guan<sup>2</sup>, Vic Guarino<sup>23</sup>, Gang Guo<sup>32</sup>, Wanlei Guo<sup>2</sup>, Xin-Heng Guo<sup>33</sup>, Caren Hagner<sup>34</sup>, Ran Han<sup>19</sup>, Miao He<sup>2</sup>, Yuekun Heng<sup>2</sup>, Yee Hsiung<sup>8</sup>, Jun Hu<sup>2</sup>, Shouyang Hu<sup>35</sup>, Tao Hu<sup>2</sup>, Hanxiong Huang<sup>35</sup>, Xingtao Huang<sup>36</sup>, Lei Huo<sup>37</sup>, Ara Ioannisian<sup>38</sup>, Manfred Jeitler<sup>39</sup>, Xiangdong Ji<sup>40</sup>, Xiaoshan Jiang<sup>2</sup>, Cécile Jollet<sup>5</sup>, Li Kang<sup>41</sup>, Michael Karagounis<sup>31</sup>, Narine Kazarian<sup>38</sup>, Zinovy Krumshteyn<sup>30</sup>, Andre Kruth<sup>31</sup>, Pasi Kuusiniemi<sup>26</sup>, Tobias Lachenmaier<sup>42</sup>, Rupert Leitner<sup>43</sup>, Chao Li<sup>36</sup>, Jiaying Li<sup>44</sup>, Weidong Li<sup>2</sup>, Weiguo Li<sup>2</sup>, Xiaomei Li<sup>35</sup>, Xiaonan Li<sup>2</sup>, Yi Li<sup>41</sup>, Yufeng Li<sup>2</sup>, Zhi-Bing Li<sup>45</sup>, Hao Liang<sup>3</sup>, Guey-Lin Lin<sup>46</sup>, Tao Lin<sup>2</sup>, Yen-Hsun Lin<sup>46</sup>, Jiajie Ling<sup>47,45</sup>, Ivano Lippi<sup>24</sup>, Dawei Liu<sup>48</sup>, Hongbang Liu<sup>49</sup>, Hu Liu<sup>45</sup>, Jianglai Liu<sup>32</sup>, Jianli Liu<sup>37</sup>, Jinchang Liu<sup>2</sup>, Qian Liu<sup>50</sup>, Shubin Liu<sup>3</sup>, Shulin Liu<sup>2</sup>, Paolo Lombardi<sup>4</sup>, Yongbing Long<sup>27</sup>, Haoqi Lu<sup>2</sup>, Jiashu Lu<sup>2</sup>, Jingbin Lu<sup>51</sup>, Junguang Lu<sup>2</sup>, Bayarto Lubsandorzhev<sup>7</sup>, Livia Ludhova<sup>4</sup>, Shu Luo<sup>52</sup>, Vladimir Lyashuk<sup>7</sup>, Randolph Möllenber<sup>28</sup>, Xubo Ma<sup>19</sup>, Fabio Mantovani<sup>53</sup>, Yajun Mao<sup>54</sup>, Stefano M. Mari<sup>55</sup>, William F. McDonough<sup>56</sup>, Guang Meng<sup>24</sup>, Anselmo Mereaglia<sup>5</sup>, Emanuela Meroni<sup>4</sup>, Mauro Mezzetto<sup>24</sup>, Lino Miramonti<sup>4</sup>, Thomas Mueller<sup>10</sup>, Dmitry Naumov<sup>30</sup>, Lothar Oberauer<sup>28</sup>, Juan Pedro Ochoa-Ricoux<sup>57</sup>, Alexander Olshevskiy<sup>30</sup>, Fausto Ortica<sup>58</sup>, Alessandro Paoloni<sup>59</sup>, Haiping Peng<sup>3</sup>, Jen-Chieh Peng<sup>†47</sup>, Ezio Previtali<sup>14</sup>, Ming Qi<sup>18</sup>, Sen Qian<sup>2</sup>, Xin Qian<sup>60</sup>, Yongzhong Qian<sup>61,32</sup>, Zhonghua Qin<sup>2</sup>, Georg Raffelt<sup>62</sup>, Gioacchino Ranucci<sup>4</sup>, Barbara Ricci<sup>53</sup>, Markus Robens<sup>31</sup>, Aldo Romani<sup>58</sup>, Xiangdong Ruan<sup>49</sup>, Xichao Ruan<sup>35</sup>, Giuseppe Salamanna<sup>55</sup>, Mike Shaevitz<sup>63</sup>, Valery Sinev<sup>7</sup>, Chiara Sirignano<sup>9</sup>, Monica Sisti<sup>14,20</sup>, Oleg Smirnov<sup>30</sup>, Michael Soiron<sup>64</sup>, Achim Stahl<sup>64</sup>, Luca Stanco<sup>24</sup>, Jochen Steinmann<sup>64</sup>, Xilei Sun<sup>2</sup>, Yongjie Sun<sup>3</sup>, Dmitriy Taichenachev<sup>30</sup>, Jian Tang<sup>45</sup>, Igor Tkachev<sup>7</sup>, Wladyslaw Trzaska<sup>65</sup>, Stefan van Waasen<sup>31</sup>, Cristina Volpe<sup>12</sup>, Vit Vorobel<sup>43</sup>, Lucia Votano<sup>59</sup>, Chung-Hsiang Wang<sup>16</sup>, Guoli Wang<sup>37</sup>, Hao Wang<sup>32</sup>, Meng Wang<sup>36</sup>, Ruiguang Wang<sup>2</sup>, Siguang Wang<sup>54</sup>, Wei Wang<sup>45</sup>, Yi Wang<sup>17</sup>, Yi Wang<sup>27</sup>, Yifang Wang<sup>2</sup>, Zhe Wang<sup>17</sup>, Zheng Wang<sup>2</sup>, Zhigang Wang<sup>2</sup>, Zhimin Wang<sup>2</sup>, Wei Wei<sup>2</sup>, Liangjian Wen<sup>2</sup>, Christopher Wiebusch<sup>64</sup>, Björn Wonsak<sup>34</sup>, Qun Wu<sup>36</sup>, Claudia-Elisabeth Wulz<sup>39</sup>, Michael Wurm<sup>66</sup>, Yufei Xi<sup>29</sup>, Dongmei Xia<sup>44</sup>, Yuguang Xie<sup>2</sup>, Zhi-zhong Xing<sup>†2</sup>, Jilei Xu<sup>2</sup>, Baojun Yan<sup>2</sup>, Changgen Yang<sup>2</sup>, Chaowen Yang<sup>67</sup>, Guang Yang<sup>23</sup>, Lei Yang<sup>41</sup>, Yifan Yang<sup>21</sup>, Yu Yao<sup>31</sup>, Ugur Yegin<sup>31</sup>, Frédéric Yermia<sup>68</sup>, Zhengyun You<sup>45</sup>, Boxiang Yu<sup>2</sup>, Chunxu Yu<sup>69</sup>, Zeyuan Yu<sup>2</sup>, Sandra Zavatarelli<sup>70</sup>, Liang Zhan<sup>2</sup>, Chao Zhang<sup>60</sup>, Hong-Hao Zhang<sup>45</sup>,

Jiawen Zhang<sup>2</sup>, Jingbo Zhang<sup>37</sup>, Qingmin Zhang<sup>71</sup>, Yu-Mei Zhang<sup>45</sup>, Zhenyu Zhang<sup>13</sup>,  
Zhenghua Zhao<sup>2</sup>, Yangheng Zheng<sup>50</sup>, Weili Zhong<sup>2</sup>, Guorong Zhou<sup>27</sup>, Jing Zhou<sup>35</sup>,  
Li Zhou<sup>2</sup>, Rong Zhou<sup>67</sup>, Shun Zhou<sup>2</sup>, Wenxiong Zhou<sup>44</sup>, Xiang Zhou<sup>13</sup>, Yeling Zhou<sup>2</sup>,  
Yufeng Zhou<sup>72</sup>, and Jiaheng Zou<sup>2</sup>

<sup>1</sup>*East China University of Science and Technology, Shanghai, China*

<sup>2</sup>*Institute of High Energy Physics, Beijing, China*

<sup>3</sup>*University of Science and Technology of China, Hefei, China*

<sup>4</sup>*INFN Sezione di Milano and Dipartimento di Fisica dell'Università di Milano, Milan, Italy*

<sup>5</sup>*Institut Pluridisciplinaire Hubert Curien, Université de Strasbourg, CNRS/IN2P3, Strasbourg, France*

<sup>6</sup>*Department of Physics and Department of Astronomy, Ohio State University, Columbus, OH, USA*

<sup>7</sup>*Institute for Nuclear Research of the Russian Academy of Sciences, Moscow, Russia*

<sup>8</sup>*Department of Physics, National Taiwan University, Taipei, Taiwan, China*

<sup>9</sup>*Dipartimento di Fisica e Astronomia dell'Università di Padova and INFN Sezione di Padova, Padova, Italy*

<sup>10</sup>*Leprince-Ringuet Laboratory Ecole Polytechnique, Palaiseau Cedex, France*

<sup>11</sup>*Centre de Physique des Particules de Marseille, Marseille, France*

<sup>12</sup>*Astro-Particle Physics Laboratory, CNRS/CEA/Paris7/Observatoire de Paris, Paris, France*

<sup>13</sup>*Wuhan University, Wuhan, China*

<sup>14</sup>*INFN Sezione Milano Bicocca, Milan, Italy*

<sup>15</sup>*Politecnico di Milano, Department of Energy, CeSNEF (Enrico Fermi Center for Nuclear Studies), Milan, Italy*

<sup>16</sup>*National United University, Miao-Li, Taiwan, China*

<sup>17</sup>*Tsinghua University, Beijing, China*

<sup>18</sup>*Nanjing University, Nanjing, China*

<sup>19</sup>*North China Electric Power University, Beijing, China*

<sup>20</sup>*Department of Physics, University of Milano Bicocca, Milan, Italy*

<sup>21</sup>*Université Libre de Bruxelles, Brussels, Belgium*

<sup>22</sup>*Massachusetts Institute of Technology, Cambridge, MA, USA*

<sup>23</sup>*Argonne National Laboratory, Argonne, IL, USA*

<sup>24</sup>*INFN Sezione di Padova, Padova, Italy*

<sup>25</sup>*Department of Physics and Astronomy, University of Hawaii, Honolulu, HI, USA*

<sup>26</sup>*Oulu Southern Institute, University of Oulu, Pyhasalmi, Finland*

<sup>27</sup>*Wuyi University, Jiangmen, China*

<sup>28</sup>*Technical University of Munich, Garching, Germany*

<sup>29</sup>*Institute of Hydrogeology and Environmental Geology, Chinese Academy of Geological Sciences, Shijiazhuang, China*

<sup>30</sup>*Joint Institute for Nuclear Research, Dubna, Russia*

<sup>31</sup>*Forschungszentrum Jülich GmbH, Central Institute of Engineering, Electronics and Analytics - Electronic Systems (ZEA-2), Jülich, Germany*

<sup>32</sup>*Shanghai Jiao Tong University, Shanghai, China*

<sup>33</sup>*Beijing Normal University, Beijing, China*

- <sup>34</sup>*Institute of Experimental Physics, University of Hamburg, Hamburg, Germany*
- <sup>35</sup>*China Institute of Atomic Energy, Beijing, China*
- <sup>36</sup>*Shandong University, Jinan, China*
- <sup>37</sup>*Harbin Institute of Technology, Harbin, China*
- <sup>38</sup>*Yerevan Physics Institute, Yerevan, Armenia*
- <sup>39</sup>*Institute of High Energy Physics, Vienna, Austria*
- <sup>40</sup>*Department of Physics, University of Maryland, College Park, MD, USA*
- <sup>41</sup>*Dongguan University of Technology, Dongguan, China*
- <sup>42</sup>*Eberhard Karls Universität Tübingen, Physikalisches Institut, Tübingen, Germany*
- <sup>43</sup>*Charles University, Faculty of Mathematics and Physics, Prague, Czech Republic*
- <sup>44</sup>*Chongqing University, Chongqing, China*
- <sup>45</sup>*Sun Yat-Sen University, Guangzhou, China*
- <sup>46</sup>*Institute of Physics National Chiao-Tung University, Hsinchu, Taiwan, China*
- <sup>47</sup>*Department of Physics, University of Illinois at Urbana-Champaign, Urbana, IL, USA*
- <sup>48</sup>*Department of Physics, University of Houston, Houston, TX, USA*
- <sup>49</sup>*Guangxi University, Nanning, China*
- <sup>50</sup>*University of Chinese Academy of Sciences, Beijing, China*
- <sup>51</sup>*Jilin University, Changchun, China*
- <sup>52</sup>*Xiamen University, Xiamen, China*
- <sup>53</sup>*Department of Physics and Earth Science, University of Ferrara and INFN Sezione di Ferrara, Ferrara, Italy*
- <sup>54</sup>*School of Physics, Peking University, Beijing, China*
- <sup>55</sup>*University of Roma Tre and INFN Sezione Roma Tre, Roma, Italy*
- <sup>56</sup>*Department of Geology, University of Maryland, College Park, MD, USA*
- <sup>57</sup>*Instituto de Física, Pontificia Universidad Católica de Chile, Santiago, Chile*
- <sup>58</sup>*INFN and University of Perugia - Department of Chemistry, Biology and Biotechnology, Perugia, Italy*
- <sup>59</sup>*Laboratori Nazionali di Frascati dell'INFN, Roma, Italy*
- <sup>60</sup>*Brookhaven National Laboratory, Upton, NY, USA*
- <sup>61</sup>*School of Physics and Astronomy, University of Minnesota, Minneapolis, MN, USA*
- <sup>62</sup>*Max Planck Institute for Physics (Werner Heisenberg Institute), Munich, Germany*
- <sup>63</sup>*Columbia University, New York, NY, USA*
- <sup>64</sup>*III. Physikalisches Institut B, RWTH Aachen University, Aachen, Germany*
- <sup>65</sup>*Department of Physics, University of Jyväskylä, Jyväskylä, Finland*
- <sup>66</sup>*Institute of Physics and EC PRISMA, Johannes-Gutenberg University Mainz, Mainz, Germany*
- <sup>67</sup>*Sichuan University, Chengdu, China*
- <sup>68</sup>*SUBATECH, CNRS/IN2P3, Université de Nantes, Ecole des Mines de Nantes, Nantes, France*
- <sup>69</sup>*Nankai University, Tianjin, China*
- <sup>70</sup>*INFN Sezione di Genova, Genova, Italy*
- <sup>71</sup>*Xi'an Jiaotong University, Xi'an, China*
- <sup>72</sup>*Institute of Theoretical Physics, Beijing, China*

---

\*Co-editor, Email: caoj@ihep.ac.cn  
†Co-editor, Email: jcpeng@illinois.edu  
‡Co-editor, Email: xingzz@ihep.ac.cn

## Abstract

The Jiangmen Underground Neutrino Observatory (JUNO), a 20 kton multi-purpose underground liquid scintillator detector, was proposed with the determination of the neutrino mass hierarchy as a primary physics goal. The excellent energy resolution and the large fiducial volume anticipated for the JUNO detector offer exciting opportunities for addressing many important topics in neutrino and astro-particle physics. In this document, we present the physics motivations and the anticipated performance of the JUNO detector for various proposed measurements.

Following an introduction summarizing the current status and open issues in neutrino physics, we discuss how the detection of antineutrinos generated by a cluster of nuclear power plants allows the determination of the neutrino mass hierarchy at a  $3\text{-}4\sigma$  significance with six years of running of JUNO. The measurement of antineutrino spectrum with excellent energy resolution will also lead to the precise determination of the neutrino oscillation parameters  $\sin^2 \theta_{12}$ ,  $\Delta m_{21}^2$ , and  $|\Delta m_{ee}^2|$  to an accuracy of better than 1%, which will play a crucial role in the future unitarity test of the MNSP matrix.

The JUNO detector is capable of observing not only antineutrinos from the power plants, but also neutrinos/antineutrinos from terrestrial and extra-terrestrial sources, including supernova burst neutrinos, diffuse supernova neutrino background, geoneutrinos, atmospheric neutrinos, and solar neutrinos. As a result of JUNO's large size, excellent energy resolution, and vertex reconstruction capability, interesting new data on these topics can be collected. For example, a neutrino burst from a typical core-collapse supernova at a distance of 10 kpc would lead to  $\sim 5000$  inverse-beta-decay events and  $\sim 2000$  all-flavor neutrino-proton elastic scattering events in JUNO, which are of crucial importance for understanding the mechanism of supernova explosion and for exploring novel phenomena such as collective neutrino oscillations. Detection of neutrinos from all past core-collapse supernova explosions in the visible universe with JUNO would further provide valuable information on the cosmic star-formation rate and the average core-collapse neutrino energy spectrum. Antineutrinos originating from the radioactive decay of Uranium and Thorium in the Earth can be detected in JUNO with a rate of  $\sim 400$  events per year, significantly improving the statistics of existing geoneutrino event samples. Atmospheric neutrino events collected in JUNO can provide independent inputs for determining the mass hierarchy and the octant of the  $\theta_{23}$  mixing angle. Detection of the  ${}^7\text{Be}$  and  ${}^8\text{B}$  solar neutrino events at JUNO would shed new light on the solar metallicity problem and examine the transition region between the vacuum and matter dominated neutrino oscillations.

Regarding light sterile neutrino topics, sterile neutrinos with  $10^{-5} \text{ eV}^2 < \Delta m_{41}^2 < 10^{-2} \text{ eV}^2$  and a sufficiently large mixing angle  $\theta_{14}$  could be identified through a precise measurement of the reactor antineutrino energy spectrum. Meanwhile, JUNO can also provide us excellent opportunities to test the eV-scale sterile neutrino hypothesis, using either the radioactive neutrino sources or a cyclotron-produced neutrino beam.

The JUNO detector is also sensitive to several other beyond-the-standard-model physics. Examples include the search for proton decay via the  $p \rightarrow K^+ + \bar{\nu}$  decay channel, search for neutrinos resulting from dark-matter annihilation in the Sun, search for violation of Lorentz invariance via the sidereal modulation of the reactor neutrino event rate, and search for the effects of non-standard interactions.

The proposed construction of the JUNO detector will provide a unique facility to address many outstanding crucial questions in particle and astrophysics in a timely and cost-effective fashion. It holds the great potential for further advancing our quest to understanding the fundamental properties of neutrinos, one of the building blocks of our Universe.

# Contents

<b>1</b>	<b>Introduction</b>	<b>20</b>
1.1	Neutrino Oscillations in a Nutshell . . . . .	20
1.1.1	Flavor mixing and neutrino oscillation probabilities . . . . .	20
1.1.2	Known and unknown neutrino oscillation parameters . . . . .	22
1.2	Open Issues of Massive Neutrinos . . . . .	23
1.2.1	The nature of neutrinos and their mass spectrum . . . . .	23
1.2.2	Lepton flavor mixing pattern and CP violation . . . . .	25
1.2.3	Extra neutrino species and unitarity tests . . . . .	27
1.3	JUNO Experiment . . . . .	28
1.3.1	Experimental site . . . . .	29
1.3.2	JUNO Detector . . . . .	30
<b>2</b>	<b>Identifying the Neutrino Mass Hierarchy</b>	<b>33</b>
2.1	Introduction and motivation . . . . .	33
2.2	Signal and Background . . . . .	38
2.2.1	Reactor neutrino signal . . . . .	38
2.2.2	Background estimation . . . . .	40
2.3	The MH Sensitivity . . . . .	42
2.3.1	Basic Setup and Definition . . . . .	42
2.3.2	Baseline Optimization . . . . .	43
2.3.3	Requirement on the Energy Resolution . . . . .	44
2.3.4	Statistical Interpretation . . . . .	46
2.4	Systematics . . . . .	48
2.4.1	Reactor related uncertainties . . . . .	48
2.4.2	Detector related uncertainties . . . . .	49
2.4.3	Background related uncertainties . . . . .	52
2.4.4	Systematics summary . . . . .	52
2.5	MH Sensitivity with Precision $ \Delta m_{ee}^2 $ and $ \Delta m_{\mu\mu}^2 $ Measurements . . . . .	53
2.6	Conclusions . . . . .	53
<b>3</b>	<b>Precision Measurements of Neutrinos</b>	<b>55</b>
3.1	Introduction and motivation . . . . .	55
3.2	Precision measurements of oscillation parameters . . . . .	58
3.3	Tests of the standard three-neutrino paradigm . . . . .	63
3.4	Conclusions . . . . .	66
<b>4</b>	<b>Supernova Burst Neutrinos</b>	<b>68</b>
4.1	Core-collapse supernovae: What, where and when? . . . . .	68
4.2	Neutrino signature of core collapse . . . . .	70
4.2.1	Neutrino-driven explosion . . . . .	70
4.2.2	Three-phase neutrino signal . . . . .	72
4.3	Detection channels in JUNO . . . . .	74
4.3.1	Time-integrated event rates . . . . .	74
4.3.2	Elastic neutrino-proton scattering . . . . .	76
4.3.3	Backgrounds . . . . .	79
4.3.4	Data acquisition . . . . .	80

4.4	Implications for astrophysics . . . . .	81
4.4.1	Pre-supernova neutrinos . . . . .	82
4.4.2	Locating the supernova . . . . .	83
4.4.3	Coincidence with gravitational waves . . . . .	84
4.4.4	SN nucleosynthesis . . . . .	84
4.5	Implications for particle physics . . . . .	85
4.5.1	Bound on neutrino masses . . . . .	85
4.5.2	Impact of mass ordering . . . . .	87
4.5.3	Collective neutrino oscillations . . . . .	88
4.5.4	Constraining new physics . . . . .	89
4.6	Summary . . . . .	89
<b>5</b>	<b>Diffuse Supernova Neutrino Background (DSNB)</b>	<b>90</b>
5.1	Motivation and Opportunities . . . . .	90
5.2	Parametric DSNB flux spectrum . . . . .	91
5.3	Signal and background sources in JUNO . . . . .	93
5.4	Expected sensitivity . . . . .	95
5.5	Outlook on further studies . . . . .	97
5.6	Conclusions . . . . .	97
<b>6</b>	<b>Solar Neutrinos</b>	<b>100</b>
6.1	History of solar neutrino experiments . . . . .	100
6.2	Relevant open questions in solar neutrino physics . . . . .	101
6.3	Motivation of solar neutrino measurements at JUNO . . . . .	102
6.4	Measurement of low energy solar neutrinos at JUNO . . . . .	104
6.5	Measurement of $^8\text{B}$ solar neutrinos at JUNO . . . . .	107
6.6	Conclusions . . . . .	110
<b>7</b>	<b>Atmospheric Neutrinos</b>	<b>111</b>
7.1	Introduction . . . . .	111
7.2	Atmospheric Neutrino Oscillations . . . . .	111
7.3	Detector Performance . . . . .	115
7.3.1	Monte Carlo Simulation . . . . .	115
7.3.2	Reconstruction Potential . . . . .	116
7.3.3	Event Selection and Classification . . . . .	118
7.3.4	Identification of $\nu_\mu$ , $\bar{\nu}_\mu$ , $\nu_e$ , and $\bar{\nu}_e$ for the CP-Violation analysis . . . . .	121
7.4	Atmospheric Neutrino Analysis . . . . .	122
7.4.1	The $\chi^2$ Function . . . . .	122
7.4.2	Neutrino Mass Hierarchy . . . . .	122
7.4.3	Atmospheric Mixing Angle $\theta_{23}$ . . . . .	124
7.4.4	CP Phase $\delta$ . . . . .	125
7.4.5	Summary . . . . .	126
<b>8</b>	<b>Geoneutrinos</b>	<b>128</b>
8.1	Introduction . . . . .	128
8.2	Expected geoneutrino signal . . . . .	129
8.3	The local geology study around JUNO . . . . .	131
8.4	Detecting geoneutrino signal . . . . .	134

8.5	Reactor antineutrino background . . . . .	135
8.6	Non antineutrino background . . . . .	137
8.7	JUNO potential in measuring geoneutrinos . . . . .	138
8.7.1	Geoneutrino signal assuming chondritic mass Th/U ratio . . . . .	139
8.7.2	Potential to measure Th/U ratio . . . . .	142
8.8	Directionality measurement . . . . .	144
8.9	Conclusions . . . . .	147
<b>9</b>	<b>Sterile Neutrinos</b>	<b>149</b>
9.1	Introduction . . . . .	149
9.2	Indications of eV-scale sterile neutrinos . . . . .	150
9.3	Requirements for future measurements . . . . .	151
9.4	JUNO potential for light sterile neutrino searches . . . . .	152
9.4.1	Sensitivity using an antineutrino source at the detector center . . . . .	153
9.4.2	Sensitivity with the antineutrino sources outside the detector . . . . .	154
9.5	Sensitivity of a cyclotron-driven $^8\text{Li}$ source (IsoDAR) . . . . .	156
9.6	Sensitivity with reactor antineutrino oscillations . . . . .	159
9.7	Conclusion . . . . .	161
<b>10</b>	<b>Nucleon Decays</b>	<b>162</b>
10.1	A brief overview of nucleon decays . . . . .	162
10.2	Detection principle in liquid scintillator . . . . .	163
10.3	Signal selection and efficiency . . . . .	165
10.4	Background estimation . . . . .	166
10.5	Sensitivity . . . . .	167
<b>11</b>	<b>Neutrinos from Dark Matter</b>	<b>168</b>
11.1	Introduction . . . . .	168
11.2	The neutrino flux from DM annihilation in the Sun . . . . .	169
11.3	The sensitivities of the JUNO detector . . . . .	170
11.4	Summary . . . . .	173
<b>12</b>	<b>Exotic Searches with Neutrinos</b>	<b>175</b>
12.1	Non-standard Interactions . . . . .	175
12.2	Lorentz Invariance Violation . . . . .	181
12.3	Discussions . . . . .	185
<b>13</b>	<b>Appendix</b>	<b>187</b>
13.1	Reactor Neutrinos . . . . .	187
13.1.1	Introduction . . . . .	187
13.1.2	Neutrino flux per fission . . . . .	187
13.1.3	Reactor Power and Fuel Evolution . . . . .	188
13.1.4	Antineutrino Spectrum and Uncertainties . . . . .	189
13.1.5	Model Independent Prediction of the Antineutrino Spectrum . . . . .	192
13.2	Monte Carlo Simulation and Reconstruction . . . . .	192
13.2.1	Monte Carlo Simulation . . . . .	192
13.2.2	Reconstruction and performance . . . . .	194
13.3	Antineutrino Detection in JUNO . . . . .	196



13.4	Backgrounds in JUNO . . . . .	197
13.4.1	Cosmic Muons at JUNO experimental site . . . . .	197
13.4.2	Neutrons . . . . .	198
13.4.3	Cosmogenic Isotopes . . . . .	198
13.4.4	Natural Radioactivity . . . . .	199

## List of Figures

1-1	A schematic illustration of the “flavor hierarchy” and “flavor desert” in the fermion mass spectrum at the electroweak scale [38]. Here the neutrino masses are assumed to have a normal ordering. . . . .	24
1-2	An illustration of the correlation between $\Sigma_\nu$ and $ \langle m \rangle_{ee} $ (left panel) and that between $\Sigma_\nu$ and $\langle m \rangle_e$ (right panel) by using the $3\sigma$ inputs as given in Table 1.1. Here the red (blue) region corresponds to the normal (inverted) neutrino mass ordering. . . . .	26
1-3	Location of the JUNO site. The distances to the nearby Yangjiang NPP and Tais-han NPP are both 53 km. Daya Bay NPP is 215 km away. Huizhou and Lufeng NPPs have not been approved yet. Three metropolises, Hong Kong, Shenzhen, and Guangzhou, are also shown. . . . .	29
1-4	A schematic view of the JUNO detector. . . . .	31
2-1	Illustration for the patterns of normal and inverted neutrino mass hierarchies. . . . .	34
2-2	Values of the effective Majorana mass $ m_{\beta\beta} $ as a function of the lightest neutrino mass in the normal (NS, with $m_{\min} = m_1$ ) and inverted (IS, with $m_{\min} = m_3$ ) neutrino mass spectra after the measurement of non-zero $\theta_{13}$ . The plot is taken from [89]. . . . .	35
2-3	The current constraints and forecast sensitivity of cosmology to the neutrino mass in relation to MH [93]. In the case of an inverted MH in the upper curve, future combined cosmological constraints would have a very high-precision detection, with $1\sigma$ error shown as the blue band. In the case of a normal MH in the lower curve, future cosmology would detect the lowest $\sum m_\nu$ at a level of $\sim 4\sigma$ . . . . .	35
2-4	(left panel) The effective mass-squared difference shift $\Delta m_\phi^2$ [79] as a function of baseline (y-axis) and visible prompt energy $E_{\text{vis}} \simeq E_\nu - 0.8 \text{ MeV}$ (x-axis). The legend of color code is shown in the right bar, which represents the size of $\Delta m_\phi^2$ in $\text{eV}^2$ . The solid, dashed, and dotted lines represent three choices of detector energy resolution with 2.8%, 5.0%, and 7.0% at 1 MeV, respectively. The purple solid line represents the approximate boundary of degenerate mass-squared difference. (right panel) The relative shape difference [65,66] of the reactor antineutrino flux for different neutrino MHs. . . . .	36
2-5	The Fourier cosine transform (FCT) (left panel) and Fourier sine transform (FST) (right panel) of the reactor antineutrino energy spectrum. The solid and dashed lines are for the normal MH and the inverted MH, respectively. . . . .	37
2-6	The observable $\bar{\nu}_e$ spectrum (red line) is a product of the antineutrino flux from reactor and the cross section of inverse beta decay (blue line). The contributions of four fission isotopes to the antineutrino flux are shown for a typical pressurized water reactor. The steps involved in the detection are schematically drawn on the top of the figure [108]. . . . .	39
2-7	The MH discrimination ability as the function of the baseline (left panel) and function of the baseline difference of two reactors (right panel). . . . .	43
2-8	The comparison of the MH sensitivity for the ideal and actual distributions of the reactor cores. The real distribution gives a degradation of $\Delta\chi_{\text{MH}}^2 \simeq 5$ . . . . .	44
2-9	The iso- $\Delta\chi_{\text{MH}}^2$ contour plot as the function of the event statistics (luminosity) and the energy resolution, where the vertical dash-dotted line stands for the nominal running of six years with 80% signal efficiency. . . . .	45
2-10	The $T$ distribution function for the JUNO nominal setup of six year running. . . . .	47
2-11	Two classes of typical examples for the residual non-linear functions in our simulation. . . . .	49

2-12	$\Delta\chi^2$ distribution as functions of the free parameters $ \Delta m_{ee}^2 $ , where the normal MH is assumed, and the plus (left) and minus (right) signs of the non-linearity curves in Fig 2-11 are implemented, respectively. The dashed and dotted lines are for the cases with reduced sizes of the non-linearity. . . . .	50
2-13	The non-linearity models with the largest effects of mimicking between the normal MH and inverted MH. . . . .	50
2-14	Effects of two classes of energy non-linearity models [with plus (left) and minus (right) signs] in determination of the MH with the self-calibration effect, where the normal MH is assumed. . . . .	51
2-15	Spectra for the antineutrino signal and five kinds of main backgrounds, including the accidental, ${}^8\text{He}/{}^9\text{Li}$ , fast neutron, and ${}^{13}\text{C}(\alpha, n){}^{16}\text{O}$ and geo-neutrinos. . . . .	52
2-16	the reactor-only (dashed) and combined (solid) distributions of the $\Delta\chi^2$ function in Eq. (2.9) and Eq. (2.23), where a 1% (left panel) or 1.5% (right panel) relative error of $\Delta m_{\mu\mu}^2$ is assumed and the CP-violating phase ( $\delta$ ) is assigned to be $90^\circ/270^\circ$ ( $\cos\delta = 0$ ) for illustration. The black and red lines are for the true (normal) and false (inverted) neutrino MH, respectively. . . . .	54
3-1	The expected prompt energy spectrum of JUNO with a nominal luminosity for six years of data taking with a 20 kt detector and 36 $\text{GW}_{th}$ reactor power (a total of 100k IBD events). A $3\%/\sqrt{E}$ energy resolution is assumed. . . . .	56
3-2	The main properties of the effective mass $ m_{ee} $ as a function of the smallest neutrino mass [121]. Here $m$ denotes the common mass for the quasi-degenerate region and $t_{ij} = \tan\theta_{ij}$ , $s_{ij} = \sin\theta_{ij}$ , $c_{ij} = \cos\theta_{ij}$ . Furthermore, $\Delta m_A^2$ and $\Delta m_\odot^2$ stands for the atmospheric mass-squared difference and the solar mass-squared difference, respectively. . . . .	57
3-3	The observed neutrino events over the non-oscillation predictions as functions of $L_{\text{eff}}$ (the effective baseline) over $E$ (the neutrino energy) for Super-K [128] atmospheric neutrino oscillations (top), KamLAND [129] reactor antineutrino oscillations (middle) and Daya Bay [130] reactor antineutrino oscillations (bottom). They correspond to three different modes of effective two-flavor oscillations controlled by $(\Delta m_{32}^2, \sin^2 2\theta_{23})$ , $(\Delta m_{21}^2, \sin^2 2\theta_{12})$ and $(\Delta m_{31}^2, \sin^2 2\theta_{13})$ , respectively. . . . .	59
3-4	Expected accuracy for $\sin^2\theta_{12}$ , $\Delta m_{21}^2$ and $\Delta m_{ee}^2$ after 6 years of running at JUNO (i.e., $\mathcal{O}(100\text{k})$ events). The solid curves are obtained with all other oscillation parameters fixed, while the parameters are set free for the dashed curves. . . . .	61
3-5	The precision of $\sin^2\theta_{12}$ with the rate plus shape information (solid curve) and rate-only information (dashed curve). . . . .	62
3-6	Dependence of the precision of $\sin^2\theta_{12}$ , $\Delta m_{21}^2$ and $\Delta m_{ee}^2$ with the neutrino energy resolution. . . . .	62
3-7	Different realizations of the unitarity violation test of the equation 3.1 in reactor antineutrino oscillations. See the text for details. . . . .	66

4-1	Three phases of neutrino emission from a core-collapse SN, from left to right: (1) In-fall, bounce and initial shock-wave propagation, including prompt $\nu_e$ burst. (2) Accretion phase with significant flavor differences of fluxes and spectra and time variations of the signal. (3) Cooling of the newly formed neutron star, only small flavor differences between fluxes and spectra. (Based on a spherically symmetric Garching model with explosion triggered by hand during 0.5–0.6 ms [168,169]. See text for details.) We show the flavor-dependent luminosities and average energies as well as the IBD rate in JUNO assuming either no flavor conversion (curves $\bar{\nu}_e$ ) or complete flavor swap (curves $\bar{\nu}_x$ ). The elastic proton (electron) scattering rate uses all six species and assumes a detection threshold of 0.2 MeV of visible proton (electron) recoil energy. For the electron scattering, two extreme cases of no flavor conversion (curves no osc.) and flavor conversion with a normal neutrino mass ordering (curves NH) are presented. . . . .	73
4-2	The neutrino event spectra with respect to the visible energy $E_d$ in the JUNO detector for a SN at 10 kpc, where no neutrino flavor conversions are assumed for illustration and the average neutrino energies are $\langle E_{\nu_e} \rangle = 12$ MeV, $\langle E_{\bar{\nu}_e} \rangle = 14$ MeV and $\langle E_{\nu_x} \rangle = 16$ MeV. The main reaction channels are shown together with the threshold of neutrino energies: (1) IBD (black and solid curve), $E_d = E_\nu - 0.8$ MeV; (2) Elastic $\nu$ - $p$ scattering (red and dashed curve), $E_d$ stands for the recoil energy of proton; (3) Elastic $\nu$ - $e$ scattering (blue and double-dotted-dashed curve), $E_d$ denotes the recoil energy of electron; (4) Neutral-current reaction $^{12}\text{C}(\nu, \nu')^{12}\text{C}^*$ (orange and dotted curve), $E_d \approx 15.1$ MeV; (5) Charged-current reaction $^{12}\text{C}(\nu_e, e^-)^{12}\text{N}$ (green and dotted-dashed curve), $E_d = E_\nu - 17.3$ MeV; (6) Charged-current reaction $^{12}\text{C}(\bar{\nu}_e, e^+)^{12}\text{B}$ (magenta and double-dotted curve), $E_d = E_\nu - 13.9$ MeV. . . . .	75
4-3	The light output of a recoiled proton in a LAB-based scintillator detector, where the Birk's constant is taken to be $k_B = 0.0098$ cm MeV $^{-1}$ according to the measurement in Ref. [187]. The energy deposition rates of protons in hydrogen and carbon targets are taken from the PSTAR database [188], and combined to give the deposition rate in a LAB-based scintillator according to the ratio of their weights in the detector. . . . .	77
4-4	Event spectrum of the elastic neutrino-proton scattering in JUNO. The average neutrino energies are $\langle E_{\nu_e} \rangle = 12$ MeV, $\langle E_{\bar{\nu}_e} \rangle = 14$ MeV and $\langle E_{\nu_x} \rangle = 16$ MeV. The total numbers of events have been calculated by imposing an energy threshold of 0.1 or 0.2 MeV. . . . .	77
4-5	Impact of energy threshold on the elastic $\nu$ - $p$ scattering events in JUNO, where the input parameters are the same as in Fig. 4-4. . . . .	78
4-6	Vertex distribution of the faked events created by coincidence of the PMT dark noise versus total photoelectrons. The data point and the error bar shows the mean value and $1 \sigma$ uncertainty for the Maxwell-Boltzmann distribution of the radius of the faked events. . . . .	80
4-7	Maximum IBD rate at JUNO as a function of the distance to a galactic SN. In the upper panel, the shaded range has been obtained by considering a class of SN models from the Basel [189], Garching [190,191] and Nakazato [192] groups. The insert refers to the SN candidate Betelgeuse with a distance of $0.197 \pm 0.045$ kpc [144]. In the lower panel, the SN probability in our galaxy has been given according to three different evaluations [141–143]. . . . .	81
4-8	The neutrino event rate in JUNO for a massive star of $20 M_\odot$ at the silicon-burning stage, where the distance is assumed to be 0.2 kpc, the same as that of the nearest possible SN progenitor Betelgeuse. . . . .	83

4-9	The upper bounds on the absolute scale of neutrino masses at the 95% CL for a SN at a distance of $D = 5$ kpc, 10 kpc, 20 kpc and 50 kpc in the parameterized model from Ref. [213], and a series of numerical models from Ref. [192], in which simulations have been performed for a progenitor-star mass $M = 13, 20, 30$ or 50 solar masses, a metallicity $Z = 0.02$ or 0.004, and a shock revival time $t_{\text{revive}} = 100$ ms or 300 ms. In our calculations, we have chosen fourteen numerical models, since a black hole is formed 842 ms after bounce in two models with $M = 30$ solar masses and $Z = 0.02$ . See Ref. [192] for more details about the numerical models, and the SN neutrino data are publicly available at the website <a href="http://asphwww.ph.noda.tus.ac.jp/snn/">http://asphwww.ph.noda.tus.ac.jp/snn/</a> . This figure is taken from Ref. [216] . . . . .	87
4-10	Numerical illustration for the splits in neutrino energy spectra after collective oscillations in the case of inverted mass hierarchy [218]. The initial spectra are indicated by dotted curves in the same color as the final ones, where one can observe a complete swap of the antineutrino spectra and a sharp split in the neutrino spectra. . . . .	88
5-1	Visible energy spectra of prompt DSNB events for $\langle E_{\bar{\nu}_e} \rangle = 12, 15, 18$ and 21 MeV for a fiducial volume of 17 kt (cf. section 5.3). Observation below 11 MeV is obstructed by the overwhelming background from reactor antineutrinos and cosmogenic background. . . . .	92
5-2	Prompt DSNB signal ( $\langle E_{\bar{\nu}_e} \rangle = 15$ MeV, $\Phi = \Phi_0$ ) and background spectra before ( <i>left</i> ) and after ( <i>right</i> ) the application of pulse-shape discrimination. The DSNB signal dominates all backgrounds for a large fraction of the observation window from 11 to 30 MeV. . . . .	95
5-3	JUNO’s discovery potential for the DSNB as a function of the mean energy of the SN spectrum $\langle E_{\bar{\nu}_e} \rangle$ and the DSNB flux normalization $\Phi$ (cf. section 5.2). We assume 10 yrs measuring time, 5% background uncertainty and a detected event spectrum corresponding to the sum of signal and background predictions. The significance is derived from a likelihood fit to the data. The star marks a theoretically well-motivated combination of DSNB parameters (cf. section 5.2). . . . .	98
5-4	Predicted exclusion contour (90% C.L.) if JUNO finds no signal of the DSNB above background. The upper limit is shown as a function of the mean energy of the SN spectrum $\langle E_{\bar{\nu}_e} \rangle$ and the DSNB flux normalization $\Phi$ (cf. section 5.2). It has been derived from a spectral likelihood fit assuming 5% background uncertainty, 10 yrs of measurement time and $N_{\text{det}} = \langle N_{\text{bg}} \rangle$ . The upper limit derived from the Super-Kamiokande results presented in [231] is shown for comparison. . . . .	98
6-1	Comparison between theoretical predictions and experimental results for the fluxes of ${}^8\text{B}$ ( $x$ -axis) and ${}^7\text{Be}$ ( $y$ -axis) solar neutrinos. The black, red, and blue ellipses represent the $1\sigma$ allowed regions, respectively in the high- $Z$ , low- $Z$ and low- $Z$ with increased opacity versions of the SSM. The $1\sigma$ experimental results for the two fluxes correspond to the horizontal and vertical black bars. Updated version of the figure from [289]. See also [290] and [291]. . . . .	103
6-2	Comparison between the theoretical predictions for the values of the ${}^8\text{B}$ ( $x$ -axis) and ${}^{13}\text{N} + {}^{15}\text{O}$ ( $y$ -axis) neutrino fluxes derived from different versions of the SSM (high- $Z$ in black, low- $Z$ in red, and low- $Z$ with increased opacity in blue). The shaded grey vertical region represents the $1\sigma$ region compatible with present data for ${}^8\text{B}$ neutrinos. The horizontal line indicates the Borexino measured CNO flux limit. Updated version of the figure from [289]. See also [290, 291]. . . . .	104
6-3	The expected singles spectra at JUNO with (a) the “baseline” and (b) the “ideal” radiopurity assumptions listed in Table 6-1. See text for details. . . . .	106

6-4	The simulated background spectra for the cosmogenics isotopes $^{11}\text{C}$ , $^{10}\text{C}$ , and $^{11}\text{Be}$ at JUNO. Furthermore, the expected $^8\text{B}$ ( $\nu - e$ ) spectrum is shown for comparison. A reduction of $^{10}\text{C}$ and $^{11}\text{C}$ should be possible by Three-Fold Coincidence but is not applied in the figure (see text for details). . . . .	109
7-1	The differential $(\nu_\mu + \bar{\nu}_\mu)$ flux density multiplied with $E^2$ versus energy and zenith angle (left) and flux ratios of different flavors versus energy averaged over all zenith angles (right). . . . .	112
7-2	Six relevant oscillograms of oscillation probabilities for atmospheric neutrinos and antineutrinos in the normal hierarchy hypothesis. . . . .	113
7-3	Maximum variations of oscillation probabilities in the energy and zenith angle plane for $P(\nu_e \rightarrow \nu_\mu)$ (left) and $P(\nu_\mu \rightarrow \nu_\mu)$ (right) cases where we scan the CP phase $\delta$ from 0 to $2\pi$ . . . . .	115
7-4	The initial neutrino energy $E_\nu$ versus the visible energy $E_{vis}$ (upper panels) and the initial neutrino direction $\theta_\nu$ versus the $\mu^\pm$ direction $\theta_\mu$ (lower panels) for all (left) and selected (right) $\nu_\mu/\bar{\nu}_\mu$ CC events . . . . .	117
7-5	Left panel: the neutrino and antineutrino per nucleon cross sections for the LS target [320]. Right panel: the expected spectra as a function of $E_{vis}$ for the 200 kton-years exposure. . . . .	118
7-6	The calculated spectra as a function of $E_{vis}/E_\nu$ (left) and $\theta_\mu - \theta_\nu$ (right) for the selected FC (green), PC (violet) and all (black) $\nu_\mu/\bar{\nu}_\mu$ CC events. The orange line describes the $E_\mu/E_\nu$ distribution for the FC events. . . . .	119
7-7	The expected FC (left) and PC (right) spectra as a function of the visible energy $E_{vis}$ for the $L_\mu \geq 5$ m $\nu_\mu/\bar{\nu}_\mu$ CC events. The blue and red lines denote $\nu_\mu$ and $\bar{\nu}_\mu$ , respectively. . . . .	120
7-8	The JUNO MH sensitivities from high energy muon neutrino events as a function of livetime for the true NH (left) and IH (right) hypotheses. . . . .	123
7-9	The future optimistic (blue) and pessimistic (red) MH sensitivities as a function of livetime for the true NH (left) and IH (right) hypotheses. . . . .	124
7-10	The JUNO sensitivities to the octant for high energy muon neutrino events as a function of true $\theta_{23}$ in the true NH (left) and IH (right) cases. . . . .	125
7-11	The JUNO's sensitivities to CP violation for high energy muon neutrino events as a function of true $\delta$ in the NH (left) and IH (right) cases. . . . .	126
7-12	The upper limit of the CP discovery sensitivity of JUNO in ten years. All statistics of $\nu_\mu$ , $\bar{\nu}_\mu$ , $\nu_e$ , and $\bar{\nu}_e$ in low energy are considered. . . . .	127
8-1	Geoneutrino signal contribution at JUNO. The cumulative geoneutrino signal and the percentage contributions of the Bulk Crust, Continental Lithospheric Mantle (CLM) and Mantle are represented as function of the distance from JUNO [332]. . .	129
8-2	(a) Sketch map showing major tectonic units around JUNO. NCC - North China Craton; SCB - South China Block. (b) Regional map showing the distribution of Mesozoic granites in the southeastern South China Block. Dashed purple lines show the provincial boundaries. (c) Geological map showing the age distribution of Mesozoic granites along the southern coastal region of the Guangdong Province, southeastern China). Stars highlight the plutons. New geochronological results are shown in bold. J-K-Jurassic and Cretaceous; P-T-Permian and Triassic [342]. . . .	132
8-3	Crustal thickness (exclusive water) in the surrounding area of JUNO from CRUST 1.0 model, $1^\circ$ degree [349]. Dashed thick blue line is plate boundary [350]. Thin blue lines denote the main tectonic units. . . . .	133

8-4	Result of a single toy Monte Carlo for 1-year measurement with fixed chondritic Th/U mass ratio; the bottom plot is in logarithmic scale to show background shapes. The data points show the energy spectrum of prompt candidates of events passing IBD selection cuts. The different spectral components are shown as they result from the fit; black line shows the total sum for the best fit. The geoneutrino signal with Th/U fixed to chondritic ratio is shown in red. The following colour code applies to the backgrounds: orange (reactor antineutrinos), green ( ${}^9\text{Li} - {}^8\text{He}$ ), blue (accidental), small magenta ( $\alpha, n$ ). The flat contribution visible in the lower plot is due to fast neutron background. . . . .	139
8-5	The three plots demonstrate the procedure of the sensitivity study to measure geoneutrinos in JUNO. In particular, the capability of the fit to reproduce the correct number of geoneutrino events (fixed ratio U/Th ratio) after 1 year live time after all cuts. Ten thousand simulations and fits have been performed: the upper left plot shows the distribution of the number of generated geoneutrino events, while the upper right plot the distribution of fit results. Finally, the lower plot gives the distribution of the ratio between reconstructed and generated number events. . . .	140
8-6	Distribution of the ratios of the reconstructed/generated number of events for geoneutrinos versus reactor antineutrinos. . . . .	142
8-7	Distributions of the ratios between reconstructed and generated number events for 1 year lifetime simulations, considering fixed Th/U ratio. Top left: reactor antineutrinos. Top right: ( $\alpha, n$ ) background. Bottom left: ${}^9\text{Li} - {}^8\text{He}$ events, Bottom right: accidental coincidences. . . . .	143
8-8	Result of a single toy Monte Carlo for 10-year measurement with Th and U components left free and independent. The data points show the energy spectrum of prompt candidates of events passing IBD selection cuts. The different spectral components are shown as they result from the fit; black line shows the total sum for the best fit. The U and Th signal are shown in red and black areas, respectively. The following colour code applies to the backgrounds: orange (reactor antineutrinos), green ( ${}^9\text{Li} - {}^8\text{He}$ ), blue (accidental), small magenta ( $\alpha, n$ ). . . . .	145
8-9	Correlations between the ratios of reconstructed-to-generated number of events in 5 years of lifetime (after cuts): Top left: U versus reactors antineutrinos. Top right: Th vs reactor antineutrinos. Bottom left: Th versus U. Bottom right: Th versus ( $\alpha, n$ ) background. . . . .	146
8-10	Distribution of the ratio reconstructed-to-generated U/Th ratio for 1 (blue line) and 10 (red line) years of lifetime after cuts. The simulations resulting in zero Th contribution are not plot here. . . . .	147
9-1	Four different scenarios of neutrino mass spectra in the (3+1) scheme, depending on the neutrino mass hierarchies of three active and one sterile neutrino mass eigenstates. The (2+2) scheme with two separate groups of mass eigenstates are already ruled out with the global analysis of solar and atmospheric neutrino data [367]. . . .	149
9-2	Energy and position dependence of the event numbers expected for a ${}^{144}\text{Ce}$ $\bar{\nu}_e$ source (50 kCi, 900 days) at the center of the detector. The top row of panels shows the signal of the antineutrino source without oscillations. The middle row illustrates the effect of $\bar{\nu}_e \rightarrow \bar{\nu}_s$ oscillations. The bottom row illustrates the event distribution expected for the reactor antineutrino background. In each row, the left panel shows the 2-dimension distribution of the event rates as a function of signal energy and the distance from the source. The middle panels are are one-dimensional projections of the energy spectrum, while right panels show the distance distributions. . . . .	155

9-3	Sensitivity of $\sin^2 2\theta_{14}$ at the 90% C.L. (for $\Delta m_{41}^2$ fixed at $1 \text{ eV}^2$ ): Default values are a running time of 450 days, an energy resolution of $3\%/\sqrt{E(\text{MeV})}$ , and a spatial resolution of 12 cm. While the other values are kept fixed, the left panel shows the dependence of the sensitivity on the running time, the middle on the energy resolution, and the right on the spatial resolution. . . . .	155
9-4	Sensitivity of a $\bar{\nu}_e$ disappearance search at JUNO to the oscillation parameters $\Delta m_{41}^2$ and $\sin^2 2\theta_{14}$ assuming a 50 kCi $^{144}\text{Ce}$ source at the detector center, with 450 days of data-taking. We show the 90, 95 and 99% confidence levels, with the reactor antineutrino background taken into account. . . . .	156
9-5	Sensitivity of a $\bar{\nu}_e$ disappearance search at JUNO to the oscillation parameters $\Delta m_{41}^2$ and $\sin^2 2\theta_{14}$ , placing a 100 kCi $^{144}\text{Ce}$ source outside the central detector. We assume a data taking time of 450 days and take the reactor antineutrino background into account. The exclusion limits shown represent 90, 95 and 99% confidence levels. The allowed regions are taken from the global analysis in Ref. [60]. . . . .	157
9-6	Oscillation signature in the $L/E$ space, with five years running, assuming (top) $\Delta m^2(\equiv \Delta m_{41}^2) = 1.0 \text{ eV}^2$ and $\sin^2 2\theta_{ee}(\equiv \sin^2 2\theta_{14}) = 0.1$ and (bottom) $\sin^2 2\theta_{ee} = 0.003$ . Black points corresponds to the simulation data, while the solid curve represents the oscillation probability without energy and position smearing. Plots from Ref. [382] . . . . .	158
9-7	The sensitivity of an oscillation search of JUNO@IsoDAR experiment in comparison to the parameter regions favored by the current anomalies. The blue curve indicates the $\Delta m^2(\equiv \Delta m_{41}^2)$ vs. $\sin^2 2\theta_{ee}(\equiv \sin^2 2\theta_{14})$ contours for which the null-oscillation hypothesis can be excluded at more than $5\sigma$ with IsoDAR@JUNO after five years of data-taking. The light (dark) gray area is the 99% allowed region for the Reactor Anomaly [58] (Global Oscillation Fit [60]) plotted as $\Delta m^2$ vs. $\sin^2 2\theta_{ee}$ . The purple area is the 99% CL for a combined fit to all $\bar{\nu}_e$ appearance data [374], plotted as $\Delta m^2$ vs. $\sin^2 2\theta_{e\mu}(\equiv 4\sin^2 \theta_{14}\sin^2 \theta_{24})$ . Plot is adapted from Ref. [382], . . . . .	159
9-8	Comparison of the 95% C.L. sensitivities for various combinations of neutrino mass hierarchies. . . . .	160
10-1	The 90% C.L. limits on the nucleon lifetimes in a variety of two-body decay modes of the nucleons [401]. Today's best limits are mostly from the Super-Kamiokande experiment using the water Cherenkov detector. . . . .	163
10-2	The simulated hit time distribution of photoelectrons (PEs) from a $K^+ \rightarrow \mu^+ \nu_\mu$ event at JUNO. . . . .	164
10-3	The 90% C.L. sensitivity to the proton lifetime in the decay mode $p \rightarrow K^+ + \bar{\nu}$ at JUNO as a function of time. In comparison, Super-Kamiokande's sensitivity is also projected to year 2030. . . . .	167
11-1	The energy-dependent efficiency $\epsilon(E_\nu)$ for selecting muon events with track length greater than 5 m in the detector. . . . .	171
11-2	The efficiency for collecting DM-induced neutrino events from the Sun with the cone half angle $\psi = 10^\circ, 20^\circ$ and $30^\circ$ . . . . .	172
11-3	The JUNO $2\sigma$ sensitivity in 5 years to the spin-dependent cross section $\sigma_{\chi p}^{\text{SD}}$ in 5 years. The constraints from the direct detection experiments are also shown for comparison. . . . .	173
11-4	The JUNO $2\sigma$ sensitivity in 5 years to the spin-independent cross section $\sigma_{\chi p}^{\text{SI}}$ . The recent constraints from the direct detection experiments are also shown for comparison. . . . .	174



12-1	The effects of NSIs in reactor $\bar{\nu}_e$ spectra at a baseline of 52.5 km [450]. For visualization, we set $\delta\varepsilon_1 - \delta\varepsilon_2 = 0, \pm 0.02$ in the upper panel and $\delta\varepsilon_1 - \delta\varepsilon_3 = 0, \pm 0.4$ in the lower panel. $\delta\varepsilon_1 - \delta\varepsilon_3$ is fixed at zero in the upper panel, and $\delta\varepsilon_1 - \delta\varepsilon_2$ is fixed at zero in the lower panel. The NH is assumed for illustration. . . . .	178
12-2	The shifts of mixing angles $\sin^2 \theta_{12}$ (left) and $\sin^2 \theta_{13}$ (right) induced by NSIs in fitting $(\theta_{12}, \Delta m_{21}^2)$ and $(\theta_{13}, \Delta m_{31}^2)$ to the simulated data [449]. The NSI effects are neglected in the fitting process. The black diamonds indicate the true values, whereas the crosses correspond to the extracted parameters. The dotted-dashed (green), dotted (yellow), and solid (red) curves stand for the $1\sigma$ , $2\sigma$ , and $3\sigma$ C.L., respectively. . . . .	179
12-3	The shifts of mass-squared differences induced by NSIs in fitting $(\Delta m_{21}^2, \Delta m_{31}^2)$ to the simulated data. The left and right panels are illustrated for $\delta\varepsilon_1 - \delta\varepsilon_2 = -0.54 \delta U$ , $\delta\varepsilon_1 - \delta\varepsilon_3 = -5.60 \delta U$ and $\delta\varepsilon_1 - \delta\varepsilon_2 = +3.00 \delta U$ , $\delta\varepsilon_1 - \delta\varepsilon_3 = +8.06 \delta U$ respectively, with $\delta U = 0.01$ [450]. The NSI effects are neglected in the fitting process.	179
12-4	The iso- $\Delta\chi^2$ contours for the MH sensitivity as a function of two effective NSI parameters $\delta\varepsilon_1 - \delta\varepsilon_2$ and $\delta\varepsilon_1 - \delta\varepsilon_3$ . [450] The NH is assumed for illustration. . . . .	180
12-5	The experimental constraints on the generic NSI parameters $\delta\varepsilon_1 - \delta\varepsilon_2$ and $\delta\varepsilon_1 - \delta\varepsilon_3$ , where the true values are fixed at $\delta\varepsilon_1 - \delta\varepsilon_2 = \delta\varepsilon_1 - \delta\varepsilon_3 = 0$ . [450] The NH is assumed for illustration. . . . .	180
12-6	The definition (left panel) of the sun-centered system [455,456], and definition (right panel) of $t = 0$ in the sun-centered system. . . . .	183
12-7	The definition of the earth-centered system (left panel) [455,456], and definition of the local coordinate system (right panel). . . . .	183
13-1	Neutrino yield per fission, the interaction cross section of the inverse beta decay, and the observable spectra of the listed isotopes. . . . .	188
13-2	Simulation of the fission fractions in the Daya Bay and Taishan cores with DRAGON packages for a normal burnup cycle. The simulation assumes a 18 months refueling cycle and average disassembly burnup at 45 MW · d/ton. Differences between the Daya Bay and Taishan cores are due to fuel enrichment. . . . .	190
13-3	Total p.e. for 1 MeV gamma uniformly generated in the central detector. . . . .	195
13-4	Vertex resolution as a function of energy (left) and PMT time resolution (right). . .	195
13-5	Mountain profile at the JUNO experimental site. . . . .	197

## List of Tables

1-1	The best-fit values, together with the $1\sigma$ , $2\sigma$ and $3\sigma$ intervals, for the six three-flavor neutrino oscillation parameters from a global analysis of current experimental data [27].	23
1-2	Summary of the thermal power and baseline to the JUNO detector for the Yangjiang (YJ) and Taishan (TS) reactor cores, as well as the remote reactors of Daya Bay (DYB) and Huizhou (HZ).	30
2-1	The efficiencies of antineutrino selection cuts, signal and backgrounds rates.	40
2-2	The MH sensitivity with the JUNO nominal setup of six year running.	47
2-3	Probability ratios with respect to several typical $\Delta\chi_{\text{MH}}^2$ values.	48
2-4	The background summary table for the analysis of reactor antineutrinos.	51
2-5	Different contributions for the MH determination. The first column is the statistical-only scenario with the equal baseline of 52.5 km, the second column considers the real distribution (dist.) of reactor cores, the third column defines the contribution of remote DYB and HZ NPPs, the fourth column stands for the reduction of the reactor shape uncertainty, the fifth and sixth columns are the contributions of the background statistical and shape uncertainties, the seventh column is the enhanced sensitivity from additional information of $ \Delta m_{\mu\mu}^2 $ .	53
3-1	Current precision for the five known oscillation parameters from the dominant experiments and the latest global analysis [29].	60
3-2	Precision of $\sin^2\theta_{12}$ , $\Delta m_{21}^2$ and $ \Delta m_{ee}^2 $ from the nominal setup to those including additional systematic uncertainties. The systematics are added one by one from left to right.	63
4-1	Numbers of neutrino events in JUNO for a SN at a typical distance of 10 kpc, where $\nu$ collectively stands for neutrinos and antineutrinos of all three flavors and their contributions are summed over. Three representative values of the average neutrino energy $\langle E_\nu \rangle = 12$ MeV, 14 MeV and 16 MeV are taken for illustration, where in each case the same average energy is assumed for all flavors and neutrino flavor conversions are not considered. For the elastic neutrino-proton scattering, a threshold of 0.2 MeV for the proton recoil energy is chosen.	75
4-2	Neutrino emission from a massive star of $20 M_\odot$ [197, 198].	82
5-1	Signal and background event rates before and after PSD in 10 years of JUNO data taking. An energy window $11 \text{ MeV} < E_\nu < 30 \text{ MeV}$ and a fiducial volume cut corresponding to 17 kt have been chosen for background suppression.	95
5-2	The expected detection significance after 10 years of data taking for different DSNB models with $\langle E_{\bar{\nu}_e} \rangle$ ranging from 12 MeV to 21 MeV ( $\Phi = \Phi_0$ ). Results are given based on either a rate-only or spectral fit analysis and assuming 5% or 20% for background uncertainty.	96
6-1	The requirements of singles background rates for doing low energy solar neutrino measurements and the estimated solar neutrino signal rates at JUNO.	105
6-2	Cosmogenic radioisotopes	108
7-1	The expected event numbers of four samples for 200 kton-years exposure.	121

8-1	Geoneutrino signals from U and Th expected in JUNO. The signals from different reservoirs (CLM = Continental Lithospheric Mantle, LS = Lithosphere, DM = Depleted Mantle, EM = Enriched Mantle) indicated in the first column are in TNU [332]. Total equals Total LS + DM + EM. The mantle signal can span between 1-19 TNU according to the composition of the Earth: here the geoneutrino signal produced by a primitive mantle having $m(\text{U})= 8.1 \cdot 10^{16}$ kg and $m(\text{Th})= 33 \cdot 10^{16}$ kg is reported. . . . .	130
8-2	Systematic uncertainties on the expected reactor antineutrino signal in the total energy window. See Eq. (8.3) and accompanying text for details. . . . .	136
8-3	Main non antineutrino background components assumed in the geoneutrino sensitivity study: the rates are intended as number of events per day after all cuts (refer to Section 2.2.2). The options of acrylic vessel and balloon have been compared in the $(\alpha, n)$ background evaluation. . . . .	137
8-4	Signal and backgrounds considered in the geoneutrino sensitivity study: the number of expected events for all components contributing to the IBD spectrum in the 0.7 - 12 MeV energy region of the prompt signal. We have assumed 80% antineutrino detection efficiency and 17.2 m radial cut (18.35 kton of liquid scintillator, $12.85 \times 10^{32}$ target protons). . . . .	141
8-5	Precision of the reconstruction of geoneutrino signal, as it can be obtained in 1, 3, 5, and 10 years of lifetime, after cuts. Different columns refer to the measurement of geoneutrino signal with fixed Th/U ratio, and U and Th signals fit as free and independent components. The given numbers are the position and RMS of the Gaussian fit to the distribution of the ratios between the number of reconstructed and generated events. It can be seen that while the RMS is decreasing with longer data acquisition time, there are some systematic effects which do not depend on the acquired statistics and are described in text. . . . .	144
8-6	Parametrization of asymmetric distributions of the reconstructed-to-generated U/Th ratio for 1, 3, 5, and 10 years of lifetime after cuts (see examples for 1 and 10 years on Fig. 8-10). Different columns give the position of the peak, RMS, and the fraction of fits in which Th component converges to zero. . . . .	144
12-1	The JUNO sensitivity at the 95% confidence level for the effective LIV coefficients $\mathcal{C}$ , and $\mathcal{A}/\mathcal{B}$ from the effects of spectral distortion and sidereal variation [454]. . . . .	186
13-1	Energy release per fission of the main fissile isotopes. . . . .	190
13-2	Correlation coefficients of isotope fission fraction uncertainties. . . . .	191
13-3	Baseline parameters in the JUNO MC simulation. . . . .	194
13-4	Factors that impact to the energy resolution. . . . .	196
13-5	IBD efficiency of different time cuts from MC simulation. . . . .	196
13-6	IBD efficiency of different distance cuts from MC simulation. . . . .	197
13-7	The simulated muon flux and mean energy at JUNO site. . . . .	197
13-8	The multiplicity of muons going through JUNO detector. . . . .	198
13-9	The estimated rates for cosmogenic isotopes in JUNO LS by FLUKA simulation, in which the oxygen isotopes are neglected. The decay modes and Q values are from TUNL Nuclear Data Group [479]. . . . .	199
13-10	The estimated radioactivity of JUNO detector construction materials. . . . .	200
13-11	The estimated radioactivity of JUNO LS. . . . .	201
13-12	The simulated singles rates from different detector components. . . . .	201
13-13	The summary of singles rates inside the Fiducial volume from the detector components, Radon in water and rock. . . . .	201

# 1 Introduction

## 1.1 Neutrino Oscillations in a Nutshell

The standard electroweak model is a successful theory which not only unifies the electromagnetic and weak interactions but also explains almost all the phenomena of this nature observed at or below the electroweak scale. When this theory was first formulated by Weinberg in 1967 [1], its particle content was so economical that the neutrinos were assumed to be massless and hence there was no lepton flavor mixing. But just one year later the solar neutrinos were observed by Davis *et al* [2], and a deficit of their flux as compared with the prediction from the standard solar model was also established by Bahcall *et al* [3, 4]. Such an anomaly turned out to be solid evidence for new physics beyond the standard model, because it was found to be attributed to the neutrino oscillation — a spontaneous and periodic change from one neutrino flavor to another, which does not take place unless neutrinos have finite masses and lepton flavors are mixed. Flavor oscillations can therefore serve as a powerful tool to study the intrinsic properties of massive neutrinos and probe other kinds of new physics.

### 1.1.1 Flavor mixing and neutrino oscillation probabilities

In the standard model the fact that the quark fields interact with both scalar and gauge fields leads to a nontrivial mismatch between their mass and flavor eigenstates, which is just the dynamical reason for quark flavor mixing and CP violation. Although a standard theory for the origin of tiny neutrino masses has not been established, one may expect a straightforward extension of the standard model in which the phenomena of lepton flavor mixing and CP violation emerge for a similar reason. In this case the weak charged-current interactions of leptons and quarks can be written as

$$- \mathcal{L}_{cc} = \frac{g}{\sqrt{2}} \left[ \overline{(e \ \mu \ \tau)_L} \gamma^\mu U \begin{pmatrix} \nu_1 \\ \nu_2 \\ \nu_3 \end{pmatrix}_L W_\mu^- + \overline{(u \ c \ t)_L} \gamma^\mu V \begin{pmatrix} d \\ s \\ b \end{pmatrix}_L W_\mu^+ \right] + \text{h.c.} , \quad (1.1)$$

where all the fermion fields are the mass eigenstates,  $U$  is the  $3 \times 3$  Maki-Nakagawa-Sakata-Pontecorvo (MNSP) matrix [5, 6], and  $V$  denotes the  $3 \times 3$  Cabibbo-Kobayashi-Maskawa (CKM) matrix [7, 8]. Note that unitarity is the only but powerful constraint, imposed by the standard model itself, on  $V$ . This property, together with the freedom of redefining the phases of six quark fields, allows one to parametrize  $V$  in terms of only four independent parameters, such as three mixing angles and one CP-violating phase. In contrast, whether the MNSP matrix  $U$  is unitary or not depends on the mechanism of neutrino mass generation [9]<sup>1</sup>. The bottom line is that any possible deviation of  $U$  from unitarity must be small, at most at the percent level, as constrained by the available experimental data [22, 23]. That is why  $U$  is simply assumed to be unitary in dealing with current neutrino oscillation data.

Given the basis in which the flavor eigenstates of three charged leptons are identified with their

---

Editors: Jun Cao (caoj@ihep.ac.cn) and Zhi-zhong Xing (xingzz@ihep.ac.cn)

<sup>1</sup>For example,  $U$  is exactly unitary in the type-II seesaw mechanism [10–14], but it is non-unitary in the type-I [15–20] and type-III [21] seesaw mechanisms due to the mixing of three light neutrinos with some heavy degrees of freedom.

mass eigenstates, the flavor eigenstates of three active neutrinos and  $n$  sterile neutrinos read as

$$\begin{pmatrix} \nu_e \\ \nu_\mu \\ \nu_\tau \\ \vdots \end{pmatrix} = \begin{pmatrix} U_{e1} & U_{e2} & U_{e3} & \cdots \\ U_{\mu 1} & U_{\mu 2} & U_{\mu 3} & \cdots \\ U_{\tau 1} & U_{\tau 2} & U_{\tau 3} & \cdots \\ \vdots & \vdots & \vdots & \ddots \end{pmatrix} \begin{pmatrix} \nu_1 \\ \nu_2 \\ \nu_3 \\ \vdots \end{pmatrix}. \quad (1.2)$$

where  $\nu_i$  is a neutrino mass eigenstate with the physical mass  $m_i$  (for  $i = 1, 2, \dots, 3 + n$ ). Eq. (1.1) tells us that a  $\nu_\alpha$  neutrino can be produced from the  $W^+ + \ell_\alpha^- \rightarrow \nu_\alpha$  interaction, and a  $\nu_\beta$  neutrino can be detected through the  $\nu_\beta \rightarrow W^+ + \ell_\beta^-$  interaction (for  $\alpha, \beta = e, \mu, \tau$ ). So the  $\nu_\alpha \rightarrow \nu_\beta$  oscillation may happen if the  $\nu_i$  beam with energy  $E \gg m_i$  travels a proper distance  $L$  in vacuum. The amplitude of the  $\nu_\alpha \rightarrow \nu_\beta$  oscillation turns out to be

$$\begin{aligned} A(\nu_\alpha \rightarrow \nu_\beta) &= \sum_i \left[ A(W^+ + \ell_\alpha^- \rightarrow \nu_i) \cdot \text{Prop}(\nu_i) \cdot A(\nu_i \rightarrow W^+ + \ell_\beta^-) \right] \\ &= \frac{1}{\sqrt{(UU^\dagger)_{\alpha\alpha}(UU^\dagger)_{\beta\beta}}} \sum_i \left[ U_{\alpha i}^* \exp\left(-i\frac{m_i^2 L}{2E}\right) U_{\beta i} \right] \end{aligned} \quad (1.3)$$

in the plane-wave expansion approximation [24, 25], where  $A(W^+ + \ell_\alpha^- \rightarrow \nu_i) = U_{\alpha i}^*/\sqrt{(UU^\dagger)_{\alpha\alpha}}$ ,  $\text{Prop}(\nu_i)$  and  $A(\nu_i \rightarrow W^+ + \ell_\beta^-) = U_{\beta i}/\sqrt{(UU^\dagger)_{\beta\beta}}$  describe the production of  $\nu_\alpha$  at the source, the propagation of free  $\nu_i$  over a distance  $L$  and the detection of  $\nu_\beta$  at the detector, respectively. It is then straightforward to obtain the probability of the  $\nu_\alpha \rightarrow \nu_\beta$  oscillation  $P(\nu_\alpha \rightarrow \nu_\beta) \equiv |A(\nu_\alpha \rightarrow \nu_\beta)|^2$ ; i.e.,

$$P(\nu_\alpha \rightarrow \nu_\beta) = \frac{\sum_i |U_{\alpha i}|^2 |U_{\beta i}|^2 + 2 \sum_{i < j} [\text{Re}(U_{\alpha i} U_{\beta j} U_{\alpha j}^* U_{\beta i}^*) \cos \Delta_{ij} - \text{Im}(U_{\alpha i} U_{\beta j} U_{\alpha j}^* U_{\beta i}^*) \sin \Delta_{ij}]}{(UU^\dagger)_{\alpha\alpha}(UU^\dagger)_{\beta\beta}} \quad (1.4)$$

where  $\Delta_{ij} \equiv \Delta m_{ij}^2 L / (2E)$  with  $\Delta m_{ij}^2 \equiv m_i^2 - m_j^2$ . The probability of the  $\bar{\nu}_\alpha \rightarrow \bar{\nu}_\beta$  oscillation can easily be read off from Eq. (1.4) by making the replacement  $U \rightarrow U^*$ .

As for the ‘‘disappearance’’ reactor antineutrino oscillations to be studied in this Yellow Book, we may simply take  $\alpha = \beta = e$  for Eq. (1.4) and then arrive at

$$P(\bar{\nu}_e \rightarrow \bar{\nu}_e) = 1 - \frac{4}{\left(\sum_i |U_{ei}|^2\right)^2} \sum_{i < j} \left( |U_{ei}|^2 |U_{ej}|^2 \sin^2 \frac{\Delta m_{ij}^2 L}{4E} \right). \quad (1.5)$$

Note that the denominator on the right-hand side of Eq. (1.5) is not equal to unity if there are heavy sterile antineutrinos which mix with the active antineutrinos but do not take part in the flavor oscillations (forbidden by kinematics). Note also that the terrestrial matter effects on  $P(\bar{\nu}_e \rightarrow \bar{\nu}_e)$  are negligibly small in most cases, because the typical value of  $E$  is only a few MeV and that of  $L$  is usually less than 100 km for a realistic reactor-based  $\bar{\nu}_e \rightarrow \bar{\nu}_e$  oscillation experiment.

If the  $3 \times 3$  MNSP matrix  $U$  is exactly unitary, it can be parametrized in terms of three flavor

mixing angles and three CP-violating phases in the following “standard” way:

$$\begin{aligned}
U &= \begin{pmatrix} 1 & 0 & 0 \\ 0 & c_{23} & s_{23} \\ 0 & -s_{23} & c_{23} \end{pmatrix} \begin{pmatrix} c_{13} & 0 & s_{13}e^{-i\delta} \\ 0 & 1 & 0 \\ -s_{13}e^{i\delta} & 0 & c_{13} \end{pmatrix} \begin{pmatrix} c_{12} & s_{12} & 0 \\ -s_{12} & c_{12} & 0 \\ 0 & 0 & 1 \end{pmatrix} P_\nu \\
&= \begin{pmatrix} c_{12}c_{13} & s_{12}c_{13} & s_{13}e^{-i\delta} \\ -s_{12}c_{23} - c_{12}s_{13}s_{23}e^{i\delta} & c_{12}c_{23} - s_{12}s_{13}s_{23}e^{i\delta} & c_{13}s_{23} \\ s_{12}s_{23} - c_{12}s_{13}c_{23}e^{i\delta} & -c_{12}s_{23} - s_{12}s_{13}c_{23}e^{i\delta} & c_{13}c_{23} \end{pmatrix} P_\nu, \quad (1.6)
\end{aligned}$$

where  $c_{ij} \equiv \cos\theta_{ij}$  and  $s_{ij} \equiv \sin\theta_{ij}$  (for  $ij = 12, 13, 23$ ) are defined, and  $P_\nu = \text{Diag}\{e^{i\rho}, e^{i\sigma}, 1\}$  denotes the diagonal Majorana phase matrix which has nothing to do with neutrino oscillations. In this case,

$$P(\bar{\nu}_e \rightarrow \bar{\nu}_e) = 1 - \sin^2 2\theta_{12}c_{13}^4 \sin^2 \frac{\Delta m_{21}^2 L}{4E} - \sin^2 2\theta_{13} \left[ c_{12}^2 \sin^2 \frac{\Delta m_{31}^2 L}{4E} + s_{12}^2 \sin^2 \frac{\Delta m_{32}^2 L}{4E} \right], \quad (1.7)$$

in which  $\Delta m_{32}^2 = \Delta m_{31}^2 - \Delta m_{21}^2$ . The oscillation terms driven by  $\Delta m_{21}^2$  and  $\Delta m_{31}^2 \simeq \Delta m_{32}^2$  can therefore be used to determine  $\theta_{12}$  and  $\theta_{13}$ , respectively. The JUNO experiment aims to measure the flux rate and energy spectrum of  $\bar{\nu}_e \rightarrow \bar{\nu}_e$  oscillations to an unprecedentedly good degree of accuracy, especially to pin down the sign of  $\Delta m_{31}^2$  or equivalently the neutrino mass ordering.

To test unitarity of the  $3 \times 3$  MNSP matrix  $U$  or to probe possible sterile neutrino effects in the foreseeable future, one should better make use of Eq. (1.5) instead of Eq. (1.7) to analyze the relevant experimental data. This point will be made much clearer later in the following sections.

### 1.1.2 Known and unknown neutrino oscillation parameters

In the standard three-flavor framework without any extra neutrino species, there are six independent parameters which govern the behaviors of neutrino oscillations: the neutrino mass-squared differences  $\Delta m_{21}^2$  and  $\Delta m_{31}^2$ , the flavor mixing angles  $\theta_{12}$ ,  $\theta_{13}$  and  $\theta_{23}$ , and the Dirac CP-violating phase  $\delta$ . Since 1998, a number of atmospheric, solar, accelerator and reactor experiments [26] have provided us with very compelling evidence for neutrino (or antineutrino) oscillations, from which  $\Delta m_{21}^2$ ,  $|\Delta m_{31}^2|$ ,  $\theta_{12}$ ,  $\theta_{13}$  and  $\theta_{23}$  have well been determined. The ongoing and future neutrino oscillation experiments are expected to fix the sign of  $\Delta m_{31}^2$  and probe the value of  $\delta$ .

A global three-flavor analysis of the currently available experimental data on solar (SNO, Super-Kamiokande, Borexino), atmospheric (Super-Kamiokande), accelerator (MINOS, T2K) and reactor (KamLAND, Daya Bay, RENO) neutrino (or antineutrino) oscillations has recently been done by several groups [27–29]. For simplicity, here we only quote the main results of Ref. [27] as summarized in Table 1.1<sup>2</sup>, in which the normal neutrino mass ordering ( $m_1 < m_2 < m_3$ ) and the inverted neutrino mass ordering ( $m_3 < m_1 < m_2$ ) are separately considered. Some comments are in order.

- The output values of  $\theta_{13}$ ,  $\theta_{23}$  and  $\delta$  in such a global fit are sensitive to the sign of  $\Delta m_{31}^2$ . That is why it is crucial to determine whether  $\Delta m_{31}^2 > 0$  or  $\Delta m_{31}^2 < 0$  (i.e., whether  $m_1$  or  $m_3$  is the smallest neutrino mass) in JUNO and a few other experiments.
- The hint  $\delta \neq 0^\circ$  (or  $180^\circ$ ) at the  $1\sigma$  level is preliminary but encouraging, because it implies a potential effect of leptonic CP violation which is likely to show up in some long-baseline neutrino oscillation experiments in the foreseeable future.

<sup>2</sup>Note that the notations  $\delta m^2 \equiv m_2^2 - m_1^2$  and  $\Delta m^2 \equiv m_3^2 - (m_1^2 + m_2^2)/2$  have been used in Ref. [27]. Their relations with  $\Delta m_{21}^2$  and  $\Delta m_{31}^2$  are rather simple:  $\Delta m_{21}^2 = \delta m^2$  and  $\Delta m_{31}^2 = \Delta m^2 + \delta m^2/2$ .

Table 1-1: The best-fit values, together with the  $1\sigma$ ,  $2\sigma$  and  $3\sigma$  intervals, for the six three-flavor neutrino oscillation parameters from a global analysis of current experimental data [27].

Parameter	Best fit	$1\sigma$ range	$2\sigma$ range	$3\sigma$ range
Normal neutrino mass ordering ( $m_1 < m_2 < m_3$ )				
$\Delta m_{21}^2/10^{-5} \text{ eV}^2$	7.54	7.32 — 7.80	7.15 — 8.00	6.99 — 8.18
$\Delta m_{31}^2/10^{-3} \text{ eV}^2$	2.47	2.41 — 2.53	2.34 — 2.59	2.26 — 2.65
$\sin^2 \theta_{12}/10^{-1}$	3.08	2.91 — 3.25	2.75 — 3.42	2.59 — 3.59
$\sin^2 \theta_{13}/10^{-2}$	2.34	2.15 — 2.54	1.95 — 2.74	1.76 — 2.95
$\sin^2 \theta_{23}/10^{-1}$	4.37	4.14 — 4.70	3.93 — 5.52	3.74 — 6.26
$\delta/180^\circ$	1.39	1.12 — 1.77	0.00 — 0.16 $\oplus$ 0.86 — 2.00	0.00 — 2.00
Inverted neutrino mass ordering ( $m_3 < m_1 < m_2$ )				
$\Delta m_{21}^2/10^{-5} \text{ eV}^2$	7.54	7.32 — 7.80	7.15 — 8.00	6.99 — 8.18
$\Delta m_{13}^2/10^{-3} \text{ eV}^2$	2.42	2.36 — 2.48	2.29 — 2.54	2.22 — 2.60
$\sin^2 \theta_{12}/10^{-1}$	3.08	2.91 — 3.25	2.75 — 3.42	2.59 — 3.59
$\sin^2 \theta_{13}/10^{-2}$	2.40	2.18 — 2.59	1.98 — 2.79	1.78 — 2.98
$\sin^2 \theta_{23}/10^{-1}$	4.55	4.24 — 5.94	4.00 — 6.20	3.80 — 6.41
$\delta/180^\circ$	1.31	0.98 — 1.60	0.00 — 0.02 $\oplus$ 0.70 — 2.00	0.00 — 2.00

- The possibility  $\theta_{23} = 45^\circ$  cannot be excluded at the  $2\sigma$  level, and thus a more precise determination of  $\theta_{23}$  is desirable in order to resolve its octant. The latter is important since it can help fix the geometrical structure of the MNSP matrix  $U$ .

Note also that  $|U_{\mu i}| = |U_{\tau i}|$  (for  $i = 1, 2, 3$ ), the so-called  $\mu$ - $\tau$  permutation symmetry of  $U$  itself, holds if either the conditions  $\theta_{13} = 0^\circ$  and  $\theta_{23} = 45^\circ$  or the conditions  $\delta = 90^\circ$  (or  $270^\circ$ ) and  $\theta_{23} = 45^\circ$  are satisfied. Now that  $\theta_{13} = 0^\circ$  has definitely been ruled out by the Daya Bay experiment [30–32], it is imperative to know the values of  $\theta_{23}$  and  $\delta$  as accurately as possible, so as to fix the strength of  $\mu$ - $\tau$  symmetry breaking associated with the structure of  $U$ .

## 1.2 Open Issues of Massive Neutrinos

There are certainly many open questions in neutrino physics, but here we concentrate on some intrinsic flavor issues of massive neutrinos which may more or less be addressed in the JUNO experiment.

### 1.2.1 The nature of neutrinos and their mass spectrum

*Question (1): Dirac or Majorana?* — If a massive neutrino is the Dirac particle, just like the electron, then it must be distinguishable from its antiparticle because they possess the opposite lepton numbers. By definition, a massive Majorana neutrino is its own antiparticle [33], leading to lepton number violation as a direct consequence. The tiny masses of three known neutrinos make it extremely difficult to identify their nature, i.e., whether they are the Dirac or Majorana particles. At present the only experimentally feasible way to probe the Majorana nature of massive neutrinos is to observe the neutrinoless double-beta ( $0\nu\beta\beta$ ) decays of some even-even nuclei,  $N(A, Z) \rightarrow N(A, Z + 2) + 2e^-$ , which occur via an exchange of the virtual Majorana neutrinos between two

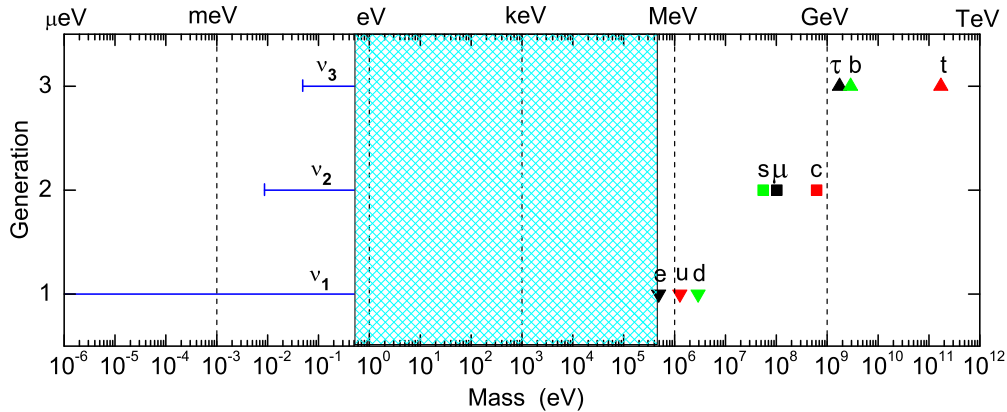


Figure 1-1: A schematic illustration of the “flavor hierarchy” and “flavor desert” in the fermion mass spectrum at the electroweak scale [38]. Here the neutrino masses are assumed to have a normal ordering.

associated beta decays [34]. The effective neutrino mass term in the  $0\nu\beta\beta$  decay is defined as

$$\langle m \rangle_{ee} \equiv \sum_i (m_i U_{ei}^2) , \quad (1.8)$$

which is in general sensitive to all the three neutrino masses (including the sign of  $\Delta m_{31}^2$ ), two of the three flavor mixing angles and two of the three CP-violating phases.

So far no convincing evidence for an occurrence of the  $0\nu\beta\beta$  decay has been established, although a lot of experimental efforts have been made in the past few decades. Within the standard three-flavor scheme, the inverted neutrino mass ordering (i.e.,  $\Delta m_{31}^2 < 0$ ) or a near neutrino mass degeneracy will allow  $|\langle m \rangle_{ee}| \geq 0.01$  eV [35–37], perhaps accessible in the next-generation  $0\nu\beta\beta$ -decay experiments.

*Question (2): Normal or inverted mass ordering?* — Now that  $\Delta m_{21}^2 > 0$  has been fixed but the sign of  $\Delta m_{31}^2$  remains unknown, we are left with two possibilities for the mass ordering of three active neutrinos whose family indices are specified by the weak charged-current interactions in Eq. (1.1): the normal case  $m_1 < m_2 < m_3$  and the inverted case  $m_3 < m_1 < m_2$ . The former is “normal” in the sense that it is parallel to the mass ordering of three charged leptons or three quarks of the same electric charge (i.e.,  $m_e \ll m_\mu \ll m_\tau$ ,  $m_u \ll m_c \ll m_t$  and  $m_d \ll m_s \ll m_b$ , as shown in Fig. 1.1). However, a good (model-independent) theoretical reason for either  $\Delta m_{31}^2 > 0$  or  $\Delta m_{31}^2 < 0$  has been lacking<sup>3</sup>.

The sign of  $\Delta m_{31}^2$  is of fundamental importance because it can impact on many important processes in particle physics, astrophysics and cosmology. The  $0\nu\beta\beta$  decay is just a typical example of this kind. In the atmospheric and long-baseline accelerator neutrino experiments, the behaviors of flavor oscillations are sensitive to a combination of  $\Delta m_{31}^2$  and the terrestrial matter term  $2\sqrt{2} G_F N_e E$ , where  $N_e$  denotes the number density of electrons in the matter background and  $E$  is the neutrino beam energy [39]. The supernova neutrino oscillations are also affected by the sign of  $\Delta m_{31}^2$  for a similar reason [40]. Meanwhile, the interference effects of two atmospheric mass-squared differences in reactor neutrino vacuum oscillations are sensitive to the sign of  $\Delta m_{31}^2$  [41]. It is therefore possible to probe the neutrino mass ordering via the atmospheric, long-baseline accelerator,

<sup>3</sup>If the neutrino mass ordering is finally found to be inverted, one may always “renormalize” it to  $m'_1 < m'_2 < m'_3$  by setting  $m'_1 = m_3$ ,  $m'_2 = m_1$  and  $m'_3 = m_2$ , equivalent to a transformation  $(\nu_1, \nu_2, \nu_3) \rightarrow (\nu'_2, \nu'_3, \nu'_1)$ . In this case the matrix elements of  $U$  must be reordered in a self-consistent way:  $U \rightarrow U'$ , in which  $U'_{\alpha 1} = U_{\alpha 3}$ ,  $U'_{\alpha 2} = U_{\alpha 1}$  and  $U'_{\alpha 3} = U_{\alpha 2}$  (for  $\alpha = e, \mu, \tau$ ). Therefore, such a treatment does not change any physical content of massive neutrinos.



reactor and supernova neutrino oscillations [42, 43]. On the other hand, the “right” sign of  $\Delta m_{31}^2$  may help the seesaw and leptogenesis mechanisms [44] work well to simultaneously interpret the origin of tiny neutrino masses and the observed baryon number asymmetry of the Universe [45, 46].

*Question (3): The absolute mass scale?* — Since the flavor oscillations of massive neutrinos are only sensitive to the neutrino mass-squared differences, a determination of the absolute neutrino mass scale has to rely on some non-oscillation experiments. Searching for the  $0\nu\beta\beta$  decay is one of the feasible ways for this purpose if massive neutrinos are the Majorana particles, because the magnitude of its effective mass  $\langle m \rangle_{ee}$  is governed by  $m_i$  as shown in Eq. (1.8). The upper bound of  $|\langle m \rangle_{ee}|$  has been set to be about 0.2 eV by the present  $0\nu\beta\beta$ -decay experiments [47], and the sensitivities of the future experiments are likely to reach the meV level [35–37]. Another way is to detect the effective neutrino mass

$$\langle m \rangle_e \equiv \sqrt{\sum_i (m_i^2 |U_{ei}|^2)} \quad (1.9)$$

in the beta decays, such as  ${}^3_1\text{H} \rightarrow {}^3_2\text{He} + e^- + \bar{\nu}_e$ . The most promising experiment of this kind is the KATRIN experiment, which may hopefully probe  $\langle m \rangle_e$  with a sensitivity of about 0.2 eV [48].

Furthermore, one may get useful information on the mass scale of light neutrinos from cosmology and astrophysics. A global analysis of current cosmological data (especially those on the cosmic microwave background and large-scale structures) has actually provided us with the most powerful sensitivity to the sum of light neutrino masses,

$$\Sigma_\nu \equiv \sum_i m_i. \quad (1.10)$$

For example,  $\Sigma_\nu < 0.23$  eV has recently been reported by the Planck Collaboration at the 95% confidence level [49]. Given the values of  $\Delta m_{21}^2$  and  $|\Delta m_{31}^2|$  extracted from current neutrino oscillation data, the results of  $|\langle m \rangle_{ee}|$ ,  $\langle m \rangle_e$  and  $\Sigma_\nu$  are all sensitive to the sign of  $\Delta m_{31}^2$ .

Let us restrict ourselves to the standard three-flavor case to illustrate the correlation among the above three effective mass terms in Fig. 1.2, where the  $3\sigma$  ranges of  $\Delta m_{21}^2$ ,  $|\Delta m_{31}^2|$ ,  $\theta_{12}$  and  $\theta_{13}$  as given in Table 1.1 are input, and the CP-violating phases of  $U$  are all allowed to vary in the  $[0^\circ, 360^\circ)$  interval.

### 1.2.2 Lepton flavor mixing pattern and CP violation

*Question (4): The octant of  $\theta_{23}$ ?* — Although the smallest neutrino mixing angle  $\theta_{13}$  has already been determined in the Daya Bay experiment [30–32], the geometric structure of the  $3 \times 3$  MNSP matrix  $U$  cannot be fully fixed until the octant of  $\theta_{23}$  and the value of  $\delta$  are both known. Current experimental data strongly support  $|U_{\mu i}| \simeq |U_{\tau i}|$  (for  $i = 1, 2, 3$ ), i.e., an approximate  $\mu$ - $\tau$  permutation symmetry of  $U$  itself [50]. In particular,  $\theta_{23} = 45^\circ$  is favored in many neutrino mass models as a consequence of the exact  $\mu$ - $\tau$  symmetry or some other kinds of flavor symmetries. In this sense the deviation of  $\theta_{23}$  from  $45^\circ$  serves for a useful model discriminator [51, 52] and deserves a precise measurement in the upcoming atmospheric and long-baseline neutrino oscillation experiments.

Taking account of  $\sin \theta_{12} < 1/\sqrt{2}$  and  $\sin \theta_{13} \ll 1$ , one may roughly expect  $|U_{e1}| > |U_{\mu 3}| \sim |U_{\tau 3}| \sim |U_{\mu 2}| \sim |U_{\tau 2}| \sim |U_{e2}| > |U_{\mu 1}| \sim |U_{\tau 1}| > |U_{e3}|$ , where “ $\sim$ ” means that the two MNSP matrix elements are comparable in magnitude. Hence the pattern of  $U$  seems to be partly anarchical and partly hierarchical. In comparison, the CKM quark flavor mixing matrix  $V$  is found to possess a clearly hierarchical structure:  $|V_{tb}| > |V_{ud}| > |V_{cs}| \gg |V_{us}| > |V_{cd}| \gg |V_{cb}| > |V_{ts}| \gg |V_{td}| > |V_{ub}|$  since its three mixing angles satisfy  $\vartheta_{12} \gg \vartheta_{23} \gg \vartheta_{13}$ , which should have something to do with the strong quark mass hierarchies.

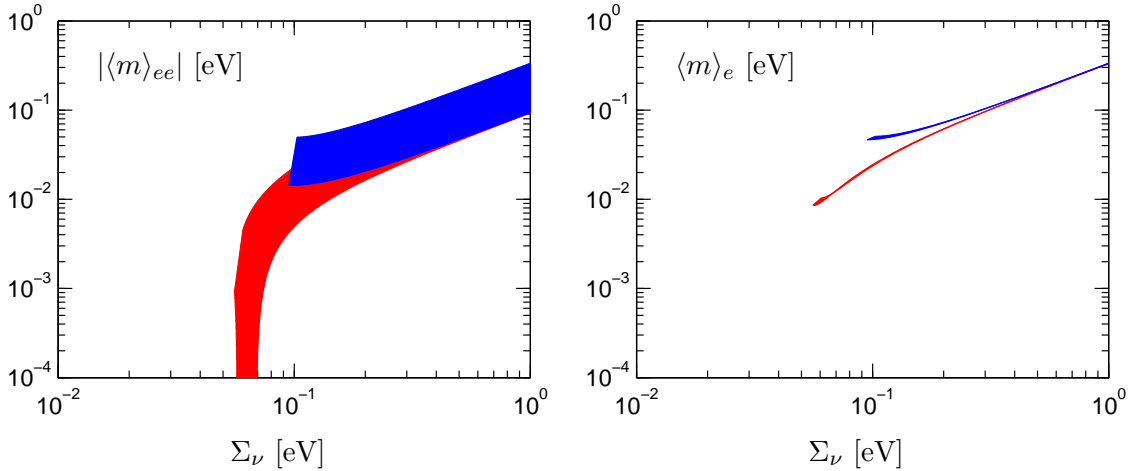


Figure 1-2: An illustration of the correlation between  $\Sigma_\nu$  and  $|\langle m \rangle_{ee}|$  (left panel) and that between  $\Sigma_\nu$  and  $\langle m \rangle_e$  (right panel) by using the  $3\sigma$  inputs as given in Table 1.1. Here the red (blue) region corresponds to the normal (inverted) neutrino mass ordering.

*Question (5): The Dirac CP-violating phase  $\delta$ ?* — In the standard three-flavor scheme the phase parameter  $\delta$  of  $U$  is fundamentally important because it uniquely controls the strength of leptonic CP and T violation in neutrino oscillations. Under CPT invariance, the CP- and T-violating asymmetries  $\mathcal{A}_{\alpha\beta} \equiv P(\nu_\alpha \rightarrow \nu_\beta) - P(\bar{\nu}_\alpha \rightarrow \bar{\nu}_\beta) = P(\nu_\alpha \rightarrow \nu_\beta) - P(\nu_\beta \rightarrow \nu_\alpha)$  in vacuum are explicitly given by

$$\mathcal{A}_{\alpha\beta} = 2 \sin 2\theta_{12} \cos \theta_{13} \sin 2\theta_{13} \sin 2\theta_{23} \sin \delta \sum_{\gamma} \epsilon_{\alpha\beta\gamma} \sin \frac{\Delta m_{21}^2 L}{4E} \sin \frac{\Delta m_{31}^2 L}{4E} \sin \frac{\Delta m_{32}^2 L}{4E}, \quad (1.11)$$

in which the Greek subscripts run over  $e$ ,  $\mu$  and  $\tau$ . It becomes obvious that CP or T violation is a three-flavor “appearance” effect, and a measurement of this effect will allow us to determine the value of  $\delta$ . Given the best-fit values  $\theta_{12} \simeq 33.7^\circ$ ,  $\theta_{13} \simeq 8.8^\circ$  and  $\theta_{23} \simeq 40.7^\circ$  in the normal neutrino mass ordering case, for example, the coefficient in front of the oscillating term of  $\mathcal{A}_{\alpha\beta}$  is about  $0.5 \times \sin \delta$ . Current neutrino oscillation data seem to hint at  $\delta \sim 270^\circ$  (see Table 1.1) — an encouraging implication of large CP violation in the lepton sector.

In a realistic medium- or long-baseline neutrino oscillation experiment, however, the terrestrial matter effects may modify the oscillation behaviors and thus affect the determination of  $\delta$ . This kind of contamination is negligible for a variety of experiments provided the neutrino beam energy  $E$  and the baseline length  $L$  satisfy the condition  $10^{-7} (L/\text{km})^2 (\text{GeV}/E) \ll 1$ . If the unitarity of the  $3 \times 3$  MNSP matrix  $U$  is slightly violated due to the existence of extra species of massive neutrinos, it is also possible for new CP-violating effects to show up in neutrino oscillations [9].

*Question (6): The Majorana CP-violating phases  $\rho$  and  $\sigma$ ?* — If the Majorana nature of massive neutrinos is finally established through a convincing measurement of the  $0\nu\beta\beta$  decay, one will be left with a question which is probably most challenging in neutrino physics — how to determine the CP-violating phases  $\rho$  and  $\sigma$  in the standard three-flavor scheme? Because the  $0\nu\beta\beta$  decay is a CP-conserving process, its effective mass term  $\langle m \rangle_{ee}$  can only provide some indirect information on the combinations of  $\delta$ ,  $\rho$  and  $\sigma$ . Hence a direct determination of  $\rho$  and  $\sigma$  depends on the observation of those processes which are both lepton-number-violating and CP-violating. Although the measurement of neutrino-antineutrino oscillations can in principle allow us to probe all the three CP-violating phases and even the absolute neutrino mass scale [53], it is in practice

impossible to do such an experiment since the corresponding oscillation probabilities are suppressed by the factors  $m_i^2/E^2 \lesssim 10^{-12}$ .

The  $3 \times 3$  Majorana neutrino mass matrix  $M_\nu$  can be reconstructed in terms of three neutrino masses, three flavor mixing angles and three CP-violating phases in the basis where the flavor eigenstates of three charged leptons are identified with their mass eigenstates, and its six independent elements are

$$\langle m \rangle_{\alpha\beta} \equiv \sum_i (m_i U_{\alpha i} U_{\beta i}) , \quad (1.12)$$

where  $\alpha$  and  $\beta$  run over  $e, \mu$  and  $\tau$ . Current experimental constraints on the magnitudes of  $\langle m \rangle_{\alpha\beta}$  can be found in Ref. [54]. While a theoretical model is always possible to predict the moduli and phases of  $\langle m \rangle_{\alpha\beta}$ , its correctness or wrongness will not be testable until sufficient information about the CP-violating phases of  $U$  is experimentally obtained.

### 1.2.3 Extra neutrino species and unitarity tests

*Question (7): Extra light or heavy sterile neutrinos?* — One of the fundamental questions in neutrino physics and cosmology is whether there exist extra species of neutrinos which do not directly participate in the standard weak interactions. Such *sterile* neutrinos are certainly hypothetical, but their possible existence is either theoretically motivated or experimentally implied [55]. For example, the canonical (type-I) seesaw mechanism [15–20] provides an elegant interpretation of the small masses of  $\nu_i$  (for  $i = 1, 2, 3$ ) with the help of two or three heavy sterile neutrinos, and the latter can even help account for the observed matter-antimatter asymmetry of the Universe via the leptogenesis mechanism [44]. On the experimental side, the LSND [56], MiniBooNE [57] and reactor antineutrino [58] anomalies can all be explained as the active-sterile antineutrino oscillations in the assumption of one or two species of sterile antineutrinos whose masses are below 1 eV [59,60]. Furthermore, a careful analysis of the existing data on the cosmic microwave background anisotropy, galaxy clustering and supernovae Ia seems to favor one species of sterile neutrinos at the sub-eV mass scale [61–63]. On the other hand, sufficiently long-lived sterile neutrinos in the keV mass range might serve as a good candidate for warm dark matter if they were present in the early Universe [64]. That is why a lot of attention has been paid to sterile neutrinos. No matter how small or how large the mass scale of sterile neutrinos is, they are undetectable unless they mix with three active neutrinos to some extent. The active-sterile neutrino mixing can slightly modify the behaviors of the standard three-flavor neutrino oscillations, as shown in Eqs. (1.2)–(1.4).

As for the  $\bar{\nu}_e \rightarrow \bar{\nu}_e$  oscillation in a reactor antineutrino experiment, its probability  $P(\bar{\nu}_e \rightarrow \bar{\nu}_e)$  is governed by Eq. (1.5). The heavy sterile antineutrinos do not participate in any flavor oscillations, but they may violate the unitarity of the  $3 \times 3$  MNSP matrix. In comparison, the light sterile antineutrinos can contribute extra oscillation terms to  $P(\bar{\nu}_e \rightarrow \bar{\nu}_e)$ . The JUNO experiment will therefore be a good playground to probe or constrain the effects of sterile antineutrinos.

*Question (8): Direct and indirect non-unitary effects?* — In the presence of small mixing between 3 active and  $n$  sterile neutrinos, the  $3 \times 3$  MNSP matrix becomes a submatrix of the  $(3+n) \times (3+n)$  unitary matrix which describes the overall flavor mixing effects, as shown in Eq. (1.2). Hence the  $3 \times 3$  MNSP matrix itself must be non-unitary. From the point of view of neutrino oscillations, one may classify its possible non-unitary effects into three categories [24,25]:

- the *indirect* non-unitary effect arising from the heavy sterile neutrinos which are kinematically forbidden to take part in neutrino oscillations;
- the *direct* non-unitary effect caused by the light sterile neutrinos which are able to participate in neutrino oscillations;

- the *interplay* of the direct and indirect non-unitary effects in a flavor mixing scenario including both light and heavy sterile neutrinos.

An experimental test of the unitarity of the  $3 \times 3$  MNSP matrix is therefore important to probe or constrain the flavor mixing parameters of possible new physics associated with sterile neutrinos, and it can theoretically shed light on the underlying dynamics responsible for neutrino mass generation and lepton flavor mixing (e.g., the  $3 \times 3$  MNSP matrix is exactly unitary in the type-II [10–14] seesaw mechanism but non-unitary in the type-I [15–20] and type-III [21] seesaw mechanisms).

In the quark sector, the unitarity of the CKM matrix  $V$  has been tested to an impressive degree of accuracy. For instance,  $|V_{ud}|^2 + |V_{us}|^2 + |V_{ub}|^2 = 0.9999 \pm 0.0006$  and  $|V_{ud}|^2 + |V_{cd}|^2 + |V_{td}|^2 = 1.000 \pm 0.004$  for the first row and column of  $V$ , respectively [26]. Hence the room for possible new physics which may violate the unitarity of  $V$  must be extremely small. In comparison, a preliminary constraint on the sum of  $|U_{e1}|^2$ ,  $|U_{e2}|^2$  and  $|U_{e3}|^2$  in the lepton sector is

$$|U_{e1}|^2 + |U_{e2}|^2 + |U_{e3}|^2 = 0.9979 \cdots 0.9998 \quad (1.13)$$

at the 90% confidence level [22, 23], implying that the  $3 \times 3$  MNSP matrix  $U$  is allowed to be non-unitary only at the  $\mathcal{O}(10^{-3})$  level. But it should be noted that such a stringent constraint is obtained in the assumption of *minimal unitarity violation*, and there might be the effects of unitarity violation at the percent level in the lepton sector. The JUNO experiment will allow us to determine  $|U_{e1}|$ ,  $|U_{e2}|$  and  $|U_{e3}|$  to a much better degree of accuracy via a precision measurement of the  $\bar{\nu}_e \rightarrow \bar{\nu}_e$  oscillation, and then examine whether the sum  $|U_{e1}|^2 + |U_{e2}|^2 + |U_{e3}|^2$  deviates from one or not.

Of course, there are many more open questions, which are more or less associated with massive neutrinos and their various consequences, in particle physics, astrophysics and cosmology. Typical examples of this kind include how to detect the cosmic neutrino (or antineutrino) background, how to detect the supernova neutrino burst and (or) the supernova relic neutrino background, how to detect the ultrahigh-energy cosmic neutrinos, etc. In any case the JUNO experiment is expected to clarify a part of the flavor issues in the lepton sector and help resolve some of the fundamental problems about the origin and evolution of the Universe.

### 1.3 JUNO Experiment

The Jiangmen Underground Neutrino Observatory (JUNO) is a multi-purpose neutrino experiment. It was proposed in 2008 to determine the neutrino mass hierarchy by detecting reactor antineutrinos from the Daya Bay nuclear power plant (NPP) [65–68], thus formerly known as “Daya Bay II experiment”. The mass hierarchy determination requires equal baselines from the detector to all reactor cores to avoid cancellation of the oscillation dephasing effect. Due to the complex and unclear layout of the future nuclear power plants in the neighborhood, the experiment was moved to Jiangmen city in Guangdong province in August 2012, and named as JUNO in 2013.

The site location is optimized to have the best sensitivity for the mass hierarchy determination, which is at 53 km from both the Yangjiang and Taishan NPPs [69]. The neutrino detector is a liquid scintillator (LS) detector with a 20 kton fiducial mass, deployed in a laboratory 700 meter underground. The experimental site and the detector will be described in this section.

The JUNO project was approved by Chinese Academy of Sciences in February 2013. Data taking is expected in 2020.

### 1.3.1 Experimental site

The JUNO experiment locates in Jinji town, Kaiping city, Jiangmen city, Guangdong province. The geographic location is east longitude  $112^{\circ}31'05''$  and north latitude  $22^{\circ}07'05''$ . The experimental site is 43 km to the southwest of the Kaiping city, a county-level city in the prefecture-level city Jiangmen in Guangdong province. There are five big cities, Guangzhou, Hong Kong, Macau, Shenzhen, and Zhuhai, all in  $\sim 200$  km drive distance, as shown in Fig. 1-3.



Figure 1-3: Location of the JUNO site. The distances to the nearby Yangjiang NPP and Taishan NPP are both 53 km. Daya Bay NPP is 215 km away. Huizhou and Lufeng NPPs have not been approved yet. Three metropolises, Hong Kong, Shenzhen, and Guangzhou, are also shown.

The experimental site is at  $\sim 53$  km from the Yangjiang NPP and Taishan NPP. Yangjiang NPP has six reactor cores of  $2.9 \text{ GW}_{\text{th}}$  each (thermal power). All cores are the 2nd generation pressurized water reactors CPR1000, which is a derivative of Framatome M310, with improvements on safety, refueling, and conventional island design. They are very similar in terms of nuclear core design. The distances between any two cores of Yangjiang NPP are between 88 m and 736 m. The first core started construction on Dec. 16, 2008 and began commercial operations on Mar. 26, 2014. The 6th core started construction on Dec. 23, 2013. All six cores will be running when JUNO starts data taking in 2020. Taishan NPP has planned four cores of  $4.59 \text{ GW}_{\text{th}}$  each. All cores are the 3rd generation pressurized water reactors EPR. The distances between any two cores are between 252 m and 1110 m. The first two cores started construction on Sep. 1, 2009 and Apr. 15, 2010, respectively. The first core is expected to begin commercial operation in 2015. The construction of the 3rd and 4th cores have not started yet. The total thermal power of the Yangjiang and Taishan NPPs would be  $35.73 \text{ GW}_{\text{th}}$ . It is possible that the last two cores in Taishan will not be available by 2020, in which case the total power will be  $26.55 \text{ GW}_{\text{th}}$  when JUNO will start data taking.

Daya Bay complex includes Daya Bay NPP, Ling Ao NPP, and Ling Ao-II NPP in a spread of 1.1 km, each with 2 cores of  $2.9 \text{ GW}_{\text{th}}$ . The Daya Bay and Ling Ao cores are Framatome M310 and the Ling Ao-II cores are CPR1000. The Daya Bay complex is 215 km away from the JUNO detector, and will contribute about 2.8% of the reactor antineutrino events. There are proposals for new NPPs in Huizhou and Lufeng, which is unclear now. The Huizhou site is 265 km from the JUNO detector and the Lufeng site is more than 300 km. There is no other NPP or planned NPP in 500 km around the JUNO experimental site. The thermal power of all cores and the baselines are listed in Table 1-2. The distances from the detector site to the Yangjiang and Taishan cores

are surveyed with a Global Positioning System (GPS) to a precision of 1 meter. All these NPPs are constructed and operated by the China General Nuclear Power Group (CGNPG).

Cores	YJ-C1	YJ-C2	YJ-C3	YJ-C4	YJ-C5	YJ-C6
Power (GW)	2.9	2.9	2.9	2.9	2.9	2.9
Baseline(km)	52.75	52.84	52.42	52.51	52.12	52.21
Cores	TS-C1	TS-C2	TS-C3	TS-C4	DYB	HZ
Power (GW)	4.6	4.6	4.6	4.6	17.4	17.4
Baseline(km)	52.76	52.63	52.32	52.20	215	265

Table 1-2: Summary of the thermal power and baseline to the JUNO detector for the Yangjiang (YJ) and Taishan (TS) reactor cores, as well as the remote reactors of Daya Bay (DYB) and Huizhou (HZ).

In absence of high mountains in the allowed area where the sensitivity to the mass hierarchy is optimized, the detector will be deployed in an underground laboratory under the Dashi hill. The elevation of the hill above the detector is 268 m, and that of the dome and the floor of the underground experimental hall is -433 m and -460 m, respectively. The detector is located in a cylindrical pit. The elevation of the detector center is -481.25 m. Therefore, the vertical overburden for the detector is more than 700 m. The experimental hall is designed to have two accesses. One is a 616 m-deep vertical shaft, and the other is a 1340 m long tunnel with a slope of 42.5%. The rock is granite. The average rock density along a 650 m borehole is measured to be  $2.61 \text{ g/cm}^3$ . The activities of the  $^{238}\text{U}$ ,  $^{232}\text{Th}$ , and  $^{40}\text{K}$  in the rock around the experimental hall are measured to be 130, 113, and 1062 Bq/kg, respectively. The muon rate and average energy in the JUNO detector are expected to be  $0.0030 \text{ Hz/m}^2$  and 215 GeV estimated by simulation with the surveyed mountain profile taken into account.

### 1.3.2 JUNO Detector

The JUNO detector consists of a central detector, a water Cherenkov detector and a muon tracker. The central detector is a liquid scintillator (LS) detector of 20 kton fiducial mass with an designed energy resolution of  $3\%/\sqrt{E(\text{MeV})}$ . The central detector is submerged in a water pool to be shielded from natural radioactivity from the surrounding rock and air. The water pool is equipped with Photomultiplier Tubes (PMTs) to detect the Cherenkov light from cosmic muons, acting as a veto detector. On top of the water pool, there is another muon detector to accurately measure the muon tracks. A schematic view of the JUNO detector is shown in Fig. 1-4. The detector design is still developing in the carrying on of R&D.

To achieve a  $3\%/\sqrt{E(\text{MeV})}$  energy resolution is very challenging. A Monte Carlo simulation has been developed based on the Monte Carlo of the Daya Bay experiment, as described in Sec. 13.2.1. The photoelectron yield has been tuned according to the Daya Bay data. To reach the required energy resolution, the following improvements from Daya Bay have to be accomplished.

- The PMT photocathode coverage  $\geq 75\%$ .
- The PMT photocathode quantum efficiency  $\geq 35\%$ .
- The attenuation length of the liquid scintillator  $\geq 20 \text{ m}$  at 430 nm, which corresponds to an absorption length of 60 m with a Rayleigh scattering length of  $30 \text{ m}^4$ .

<sup>4</sup>The Rayleigh scattering length of Linear alkybenzene was measured to be  $28.2 \pm 1.0 \text{ m}$  at 430 nm recently [70]

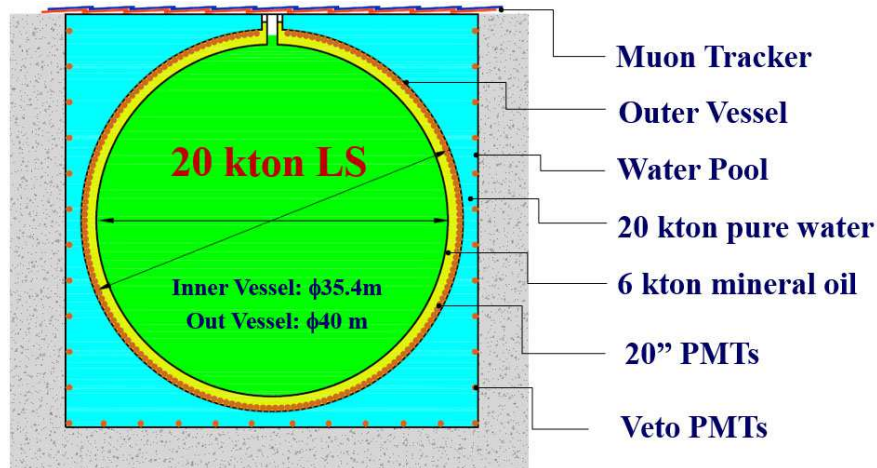


Figure 1-4: A schematic view of the JUNO detector.

The liquid scintillator has similar recipe as the Daya Bay LS without gadolinium loading. Linear alkylbenzene (LAB), a straight alkyl chain of 10-13 carbons attached to a benzene ring [10], is used as the detection medium due to its excellent transparency, high flash point, low chemical reactivity, and good light yield. The liquid scintillator also consists of 3 g/L 2,5-diphenyloxazole (PPO) as the fluor and 15 mg/L p-bis-(o-methylstyryl)-benzene (bis-MSB) as the wavelength shifter.

The density of the LS is 0.859 g/ml. Twenty thousand ton LS is contained in a spherical container of radius of 17.7 m. The light emitted by the LS is watched by about 17,000 20-inch PMTs. PMTs are installed on a spherical structure of a radius of 19.5 m, and submerged in a buffer liquid to protect the LS from the radioactivity of the PMT glass.

The mechanics of the central detector is also very challenging. Two options are under R&D. The “Acrylic Sphere” option uses an acrylic vessel to contain the LS. The buffer liquid is water, which is connected with the outer water Cherenkov detector but being optically separated. The PMTs are installed on the inner surface of the truss structure, which also supports the acrylic sphere. The “Balloon” option uses nylon bag instead of acrylic to contain the LS. The buffer liquid is non-scintillation LAB or mineral oil contained in a stainless steel sphere. The PMTs are installed on the inner surface of the stainless steel vessel. For both options, the PMTs have special protection in case of implosion. Taking into account the implosion container and mechanical clearance, the photocathode coverage can reach 75% to 78% for various options.

The central detector is submerged in a cylindrical water pool. At least 2 m water from any direction protects the central detector from the surrounding rock radioactivity. About 1600 20-inch PMTs are installed in the water pool. The muon detection efficiency is expected to be similar as that of the Daya Bay water Cherenkov detector, which is 99.8%.

The earth magnetic field intensity is about 0.5 gauss at the experimental site. It could have significant negative impact on the photoelectron collection efficiency of the large size PMTs. Both compensation coils surrounding the water pool and high- $\mu$  metal shielding for individual PMTs will be installed.

On the top of the water pool, muon tracker will be installed to accurately measure the muon direction. Plastic scintillator strips decommissioned from the target tracker of the OPERA experiment [71] will be reused as the JUNO top tracker. The OPERA target tracker is composed of 62 walls with a sensitive area of  $6.7 \times 6.7 \text{ m}^2$  each. Each wall consists of four vertical (x) and four horizontal (y) modules. A target tracker module is composed of 64 scintillating strips, 6.7 m long

and 26.4 mm wide. Each strip is read out on both sides by a Hamamatsu 64-channel multi-anode PMT. The total surface which could be covered by the 62 x-y walls is 2783 m<sup>2</sup>. Radioactivity from the surrounding rock of the experimental hall will induce extremely high noise rate in the plastic scintillator strips. Multi-layer design, at least 3 x-y layers, is needed to suppress the radioactivity background. Distance between two adjacent super-layers will be between 1 m and 1.5 m. The muon tracker will cover more than 25% of the area of the top surface of the water pool.

A chimney for calibration operation will connect the central detector to outside from the top. Special radioactivity shielding and muon detector will be designed for the chimney.



## 2 Identifying the Neutrino Mass Hierarchy

### 2.1 Introduction and motivation

After the discovery of non-zero  $\theta_{13}$  in recent reactor [30, 31, 72, 73] and accelerator [74, 75] neutrino experiments, the present status of the standard three-flavor neutrino oscillation [27–29, 76–78] can be summarized as follows:

- three non-zero mixing angles [26]  $\theta_{12}$ ,  $\theta_{23}$ , and  $\theta_{13}$  in the MNSP [5, 6] lepton mixing matrix have been measured with the precision from 4% to 10% <sup>1</sup>,
- two independent mass-squared differences  $|\Delta m_{31}^2| = |m_3^2 - m_1^2|$  (or  $|\Delta m_{32}^2| = |m_3^2 - m_2^2|$ ) and  $\Delta m_{21}^2 = m_2^2 - m_1^2$  have been measured with the precision better than 4% [26],
- the neutrino mass hierarchy (i.e., sign of the mass-squared difference  $\Delta m_{31}^2$ ) is unknown,
- the octant of the mixing angle  $\theta_{23}$  (i.e.,  $\theta_{23} < \pi/4$  or  $\theta_{23} > \pi/4$ ) is unknown,
- the leptonic CP-violating phase  $\delta$  in the MNSP matrix is unknown.

Therefore, the determination of the neutrino mass hierarchy and octant of the mixing angle  $\theta_{23}$ , as well as the measurement of the leptonic CP-violating phase constitutes the main focus of future neutrino oscillation experiments.

The neutrino mass hierarchy (MH) answers the question whether the third generation ( $\nu_3$  mass eigenstate) is heavier or lighter than the first two generations ( $\nu_1$  and  $\nu_2$ ). As shown in Fig. 2-1, the normal mass hierarchy (NH) refers to  $m_3 > m_1$  and the inverted mass hierarchy (IH) refers to  $m_3 < m_1$ .

The relatively large value of  $\theta_{13}$  has provided excellent opportunities to resolve the MH in different neutrino oscillation configurations, which include

- the medium baseline ( $\sim 50$  km) reactor antineutrino  $\bar{\nu}_e \rightarrow \bar{\nu}_e$  oscillation experiments (JUNO [65, 66, 69, 79, 80] and RENO-50 [81]),
- the long-baseline accelerator (anti-)neutrino  $\bar{\nu}_\mu \rightarrow \bar{\nu}_e$  oscillation experiments (NO $\nu$ A [82] and DUNE [83]),
- the atmospheric (anti-)neutrino  $\bar{\nu}_\mu \rightarrow \bar{\nu}_\mu$  oscillation experiments (INO [84], PINGU [85], ORCA [86], DUNE [83] and Hyper-K [87, 88]).

While the last two methods depend on the matter effect in neutrino oscillations (the charge-current interaction between (anti-) $\nu_e$  and electrons in the matter), the first method with reactor antineutrinos at a medium baseline only relies on the oscillation interference between  $\Delta m_{31}^2$  and  $\Delta m_{32}^2$  with  $\Delta m_{ij}^2 = m_i^2 - m_j^2$  [65, 66, 69, 79, 80].

Besides the neutrino oscillation experiments of determining the MH, the octant of  $\theta_{23}$  and the lepton CP-violating phase, the absolute neutrino mass scale and nature of the massive neutrinos (i.e., the Majorana or Dirac type) are questions of fundamental importance to be answered in future neutrino non-oscillation probes, including beta decays, neutrinoless double beta decays and cosmological observations.

The determination of the MH has profound impacts on our understanding of the neutrino physics, neutrino astronomy and neutrino cosmology.

---

Editors: Yufeng Li (liyufeng@ihep.ac.cn) and Liang Zhan (zhanl@ihep.ac.cn)

Major contributor: Xin Qian

<sup>1</sup>precision in terms of  $\sin^2 \theta_{12}$ ,  $\sin^2 \theta_{23}$ , and  $\sin^2 \theta_{13}$ .

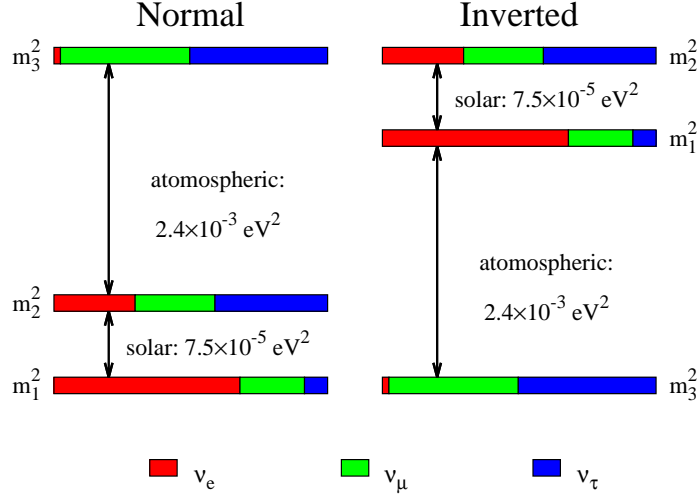


Figure 2-1: Illustration for the patterns of normal and inverted neutrino mass hierarchies.

- First, as illustrated in Fig. 2-2 [89], MH helps to define the goal of neutrinoless double beta decay ( $0\nu\beta\beta$ ) search experiments, which aim to reveal whether neutrinos are Dirac or Majorana particles. In particular, the chance to observe  $0\nu\beta\beta$  in the next-generation double beta decay experiments is greatly enhanced for an inverted MH and the Majorana nature of massive neutrinos. New techniques beyond the next generation are needed to explore the region covered by a normal MH.
- Second, MH is a crucial factor for measuring the lepton CP-violating phase. In the long-baseline accelerator (anti-)neutrino oscillation experiments, degenerate solutions for the MH and CP phase emerge, and the wrong MH would give a fake local minimum for the CP phase, thus reduce the significance of the CP measurement. This effect is even more important for accelerator neutrino experiments with a shorter baseline such as Hyper-K [87, 88] and MOMENT [90]. Therefore, a determination of the MH independent of the CP phase is important for the future prospect of neutrino physics.
- Third, MH is a key parameter of the neutrino astronomy and neutrino cosmology. On one hand, the spectral splits [91] in supernova neutrino fluxes would provide a smoking gun for collective neutrino oscillations induced by the neutrino self-interaction in the dense environment. The split patterns are significantly different for the normal and inverted MHs. MH is also important for the supernova nucleosynthesis, where the prediction of the  ${}^7\text{Li}/{}^{11}\text{B}$  ratio is also distinct for different MHs [92]. On the other hand, MH may have important implications on the cosmological probe of the neutrino mass scale (i.e.,  $\sum m_\nu$ ). As shown in Fig. 2-3, in the case of an inverted MH, future combined cosmological constraints would have a very high-precision detection, with  $1\sigma$  error shown as a blue band. In the case of a normal MH, future cosmology would detect the lowest  $\sum m_\nu$  at a level of  $\sim 4\sigma$ .
- Fourth, MH is one of the most important discriminators for model building of the neutrino masses and flavor mixing. To understand the origin of neutrino mass generation, the MH information is crucial. Due to the similar and complementary aspects of quarks and leptons, the normal MH could be related to the quark mass spectrum and attributed to the relations of Grand Unified Theories (GUTs). On the other hand, the inverted MH predicts a nearly-degenerate spectrum between the first and second mass eigenstates, which could be

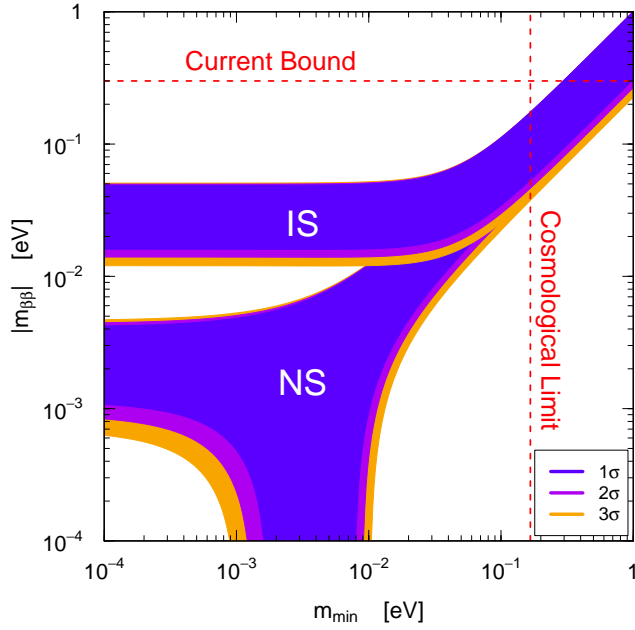


Figure 2-2: Values of the effective Majorana mass  $|m_{\beta\beta}|$  as a function of the lightest neutrino mass in the normal (NS, with  $m_{\min} = m_1$ ) and inverted (IS, with  $m_{\min} = m_3$ ) neutrino mass spectra after the measurement of non-zero  $\theta_{13}$ . The plot is taken from [89].

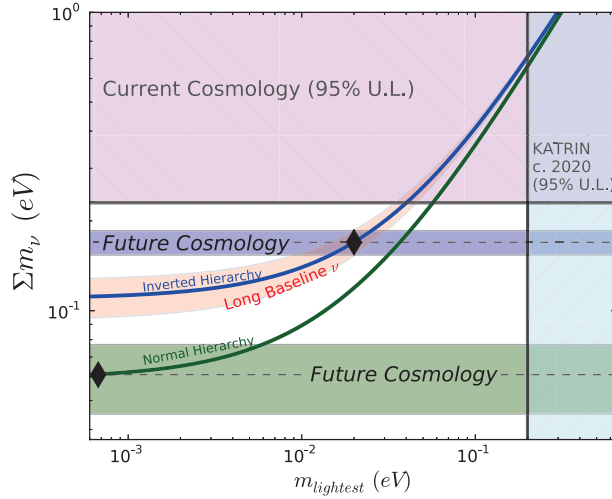


Figure 2-3: The current constraints and forecast sensitivity of cosmology to the neutrino mass in relation to MH [93]. In the case of an inverted MH in the upper curve, future combined cosmological constraints would have a very high-precision detection, with  $1\sigma$  error shown as the blue band. In the case of a normal MH in the lower curve, future cosmology would detect the lowest  $\sum m_{\nu}$  at a level of  $\sim 4\sigma$ .

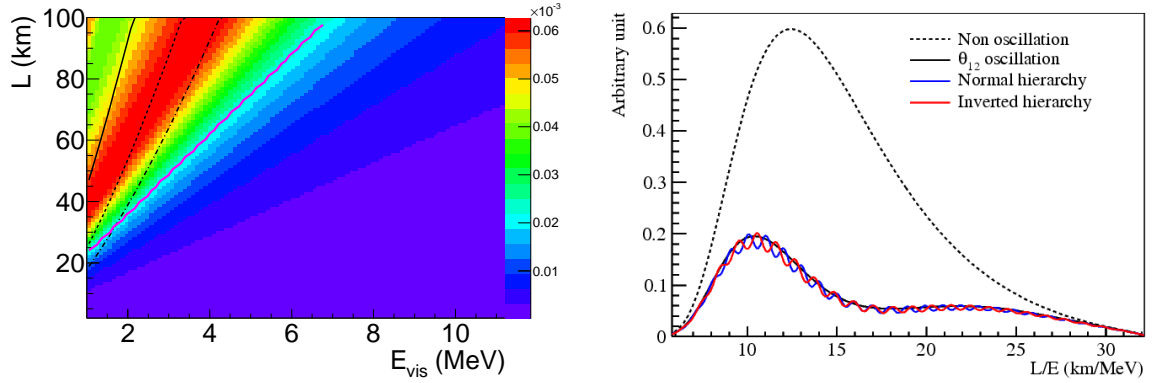


Figure 2-4: (left panel) The effective mass-squared difference shift  $\Delta m_\phi^2$  [79] as a function of baseline (y-axis) and visible prompt energy  $E_{\text{vis}} \simeq E_\nu - 0.8 \text{ MeV}$  (x-axis). The legend of color code is shown in the right bar, which represents the size of  $\Delta m_\phi^2$  in  $\text{eV}^2$ . The solid, dashed, and dotted lines represent three choices of detector energy resolution with 2.8%, 5.0%, and 7.0% at 1 MeV, respectively. The purple solid line represents the approximate boundary of degenerate mass-squared difference. (right panel) The relative shape difference [65, 66] of the reactor antineutrino flux for different neutrino MHs.

explained in the models with the discrete or  $U(1)$  flavor symmetries. Therefore, MH is a critical parameter to understand the origin of neutrino masses and mixing.

JUNO is designed to resolve the neutrino MH using precision spectral measurements of reactor antineutrino oscillations. Before giving the quantitative calculation of the MH sensitivity, we shall briefly review the principle of this method. The electron antineutrino survival probability in vacuum can be written as [69, 79, 94]:

$$\begin{aligned} P_{\bar{\nu}_e \rightarrow \bar{\nu}_e} &= 1 - \sin^2 2\theta_{13} (\cos^2 \theta_{12} \sin^2 \Delta_{31} + \sin^2 \theta_{12} \sin^2 \Delta_{32}) - \cos^4 \theta_{13} \sin^2 2\theta_{12} \sin^2 \Delta_{21} \\ &= 1 - \frac{1}{2} \sin^2 2\theta_{13} \left[ 1 - \sqrt{1 - \sin^2 2\theta_{12} \sin^2 \Delta_{21}} \cos(2|\Delta_{ee}| \pm \phi) \right] - \cos^4 \theta_{13} \sin^2 2\theta_{12} \sin^2 \Delta_{21}, \end{aligned} \quad (2.1)$$

where  $\Delta_{ij} \equiv \Delta m_{ij}^2 L / 4E$ , in which  $L$  is the baseline,  $E$  is the antineutrino energy,

$$\sin \phi = \frac{c_{12}^2 \sin(2s_{12}^2 \Delta_{21}) - s_{12}^2 \sin(2c_{12}^2 \Delta_{21})}{\sqrt{1 - \sin^2 2\theta_{12} \sin^2 \Delta_{21}}}, \quad \cos \phi = \frac{c_{12}^2 \cos(2s_{12}^2 \Delta_{21}) + s_{12}^2 \cos(2c_{12}^2 \Delta_{21})}{\sqrt{1 - \sin^2 2\theta_{12} \sin^2 \Delta_{21}}},$$

and [95, 96]

$$\Delta m_{ee}^2 = \cos^2 \theta_{12} \Delta m_{31}^2 + \sin^2 \theta_{12} \Delta m_{32}^2. \quad (2.2)$$

The  $\pm$  sign in the last term of Eq. (2.1) is decided by the MH with plus sign for the normal MH and minus sign for the inverted MH.

In a medium-baseline reactor antineutrino experiment (e.g., JUNO), oscillation of the atmospheric mass-squared difference manifests itself in the energy spectrum as the multiple cycles. The spectral distortion contains the MH information, and can be understood with the left panel of Fig. 2-4 which shows the energy and baseline dependence of the extra effective mass-squared difference,

$$\Delta m_\phi^2 = 4E\phi/L, \quad (2.3)$$

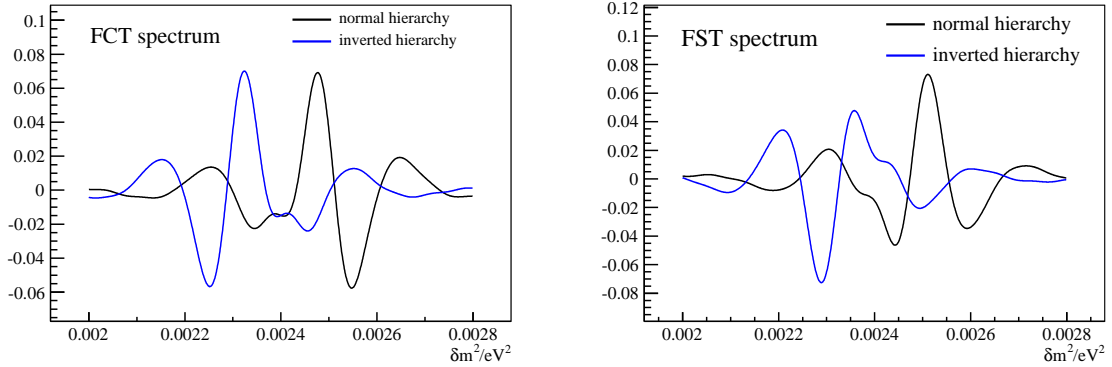


Figure 2-5: The Fourier cosine transform (FCT) (left panel) and Fourier sine transform (FST) (right panel) of the reactor antineutrino energy spectrum. The solid and dashed lines are for the normal MH and the inverted MH, respectively.

At baseline of  $\sim 50$  km,  $\Delta m_\phi^2$  at the low energy ( $\sim 3$  MeV) is larger than the  $\Delta m_\phi^2$  at the high energy ( $\sim 6$  MeV). For NH, the effective mass-squared difference  $2|\Delta m_{ee}^2| + \Delta m_\phi^2$  in Eq. (2.1) at low energies will be larger than that at high energies and vice versa for IH, in which the effective mass-squared difference is  $2|\Delta m_{ee}^2| - \Delta m_\phi^2$ . Therefore, the advancement or retardance of the oscillation phase illustrated in the right panel of Fig. 2-4 contains the useful MH information. However, in order to extract the MH information from the spectral distortion, an excellent energy resolution ( $3\%/\sqrt{E}$ ), a good understanding of the energy response (better than 1%), and a large statistics ( $\mathcal{O}(100k)$  inverse beta decay events) are required.

The oscillation interference effect is more evident in the frequency domain after a Fourier transform of the  $L/E$  spectrum of reactor antineutrinos [65, 66, 97]. In Fig 2-5 we illustrate the Fourier sine transform (FST) and Fourier cosine transform (FCT) of the reactor antineutrino energy spectrum, where the FST and FCT frequency spectra are defined as

$$\text{FST}(\omega) = \int_{t_{\min}}^{t_{\max}} F(t) \sin(\omega t) dt, \quad \text{FCT}(\omega) = \int_{t_{\min}}^{t_{\max}} F(t) \cos(\omega t) dt, \quad (2.4)$$

with  $\omega = 2.54 \times \Delta m_{ij}^2$  being the frequency, and  $t = L/E$  being the variable in the  $L/E$  space, varying from  $t_{\min} = L/E_{\max}$  to  $t_{\max} = L/E_{\min}$ .  $F(L/E)$  is written as

$$F(L/E) = \phi(E) \sigma(E) P_{\bar{\nu}_e \rightarrow \bar{\nu}_e}(L/E), \quad (2.5)$$

where  $\phi(E)$ ,  $\sigma(E)$  and  $P_{\bar{\nu}_e \rightarrow \bar{\nu}_e}(L/E)$  are the reactor antineutrino spectrum, the interaction cross section and the oscillation probability, respectively.  $\phi(E)$  and  $\sigma(E)$  will be discussed in the next section, and  $P_{\bar{\nu}_e \rightarrow \bar{\nu}_e}(L/E)$  is defined in Eq. (2.1). Distinctive features of the FST and FCT spectra for normal and inverted MHs can be observed in Fig 2-5. On the FCT spectrum (left panel), a valley appears at the left of the prominent peak for the IH, and a peak appears at the left of the valley for the NH. On the FST spectrum (right panel), there is a clear valley for the IH, and a clear peak for NH. Therefore, we can distinguish the MH from the Fourier transform spectra without any prior information on the neutrino mass-squared differences. More details on properties of the FCT and FST spectra in the MH determination can be found in Refs. [65, 66].

Beside the aforementioned interference between  $|\Delta m_{31}^2|$  and  $|\Delta m_{32}^2|$ , the precision measurement of  $|\Delta m_{ee}^2|$  in a medium-baseline reactor experiment can reveal additional information regarding the

MH, when combined with the precision  $|\Delta m_{\mu\mu}^2|$  measurements from the future muon (anti-)neutrino disappearance [95, 96]. Using the convention of Refs. [69, 95], we have

$$|\Delta m_{ee}^2| - |\Delta m_{\mu\mu}^2| = \pm \Delta m_{21}^2 (\cos 2\theta_{12} - \sin 2\theta_{12} \sin \theta_{13} \tan \theta_{23} \cos \delta), \quad (2.6)$$

where the positive and negative signs correspond to normal and inverted MHs, respectively. The precision measurements of both  $|\Delta m_{\mu\mu}^2|$  and  $|\Delta m_{ee}^2|$  would provide new information regarding the neutrino MH. Therefore, by combining these two types of information (interference and precision  $|\Delta m_{ee}^2|$  measurement), JUNO will have a robust path to resolve the neutrino MH [69].

## 2.2 Signal and Background

### 2.2.1 Reactor neutrino signal

Reactor neutrinos are electron antineutrinos emitted from subsequent  $\beta$ -decays of instable fission fragments. All reactors close to JUNO are pressurized water reactors (PWR), the same type as the Daya Bay reactors. In these reactors, fissions of four fuel isotopes,  $^{235}\text{U}$ ,  $^{238}\text{U}$ ,  $^{239}\text{Pu}$ , and  $^{241}\text{Pu}$ , generate more than 99.7% of the thermal power and reactor antineutrinos. Reactor neutrino fluxes per fission of each isotope are determined by inversion of the measured  $\beta$  spectra of fission products [98–102] or by calculation with the nuclear database [103, 104]. Their fission rates in a reactor can be estimated with the core simulation and thermal power measurements. The reactor neutrino flux can be predicted as

$$\Phi(E_\nu) = \frac{W_{\text{th}}}{\sum_i f_i e_i} \cdot \sum_i f_i \cdot S_i(E_\nu), \quad (2.7)$$

Where  $W_{\text{th}}$  is the thermal power of the reactor,  $f_i$ ,  $e_i$ , and  $S_i(E_\nu)$  are fission fraction, the thermal energy released in each fission, and the neutrino flux per fission for the  $i$ -th isotope, respectively. Such a prediction is expected to carry an uncertainty of 2-3% [30]. Recently, reactor neutrino experiments (Daya Bay [105], RENO [106] Double Chooz [107]) found a large discrepancy between the predicted and measured spectra in the 4-6 MeV region. Model independent prediction based on the new precision measurements could avoid this bias, and might be able to improve the precision to 1%. Detailed description on the reactor neutrino flux can be found in the Appendix of Sec. 13.

JUNO measures the reactor neutrino signal via the inverse beta decay (IBD) reaction

$$\bar{\nu}_e + p \rightarrow e^+ + n. \quad (2.8)$$

The reactor antineutrino  $\bar{\nu}_e$  interacts with a proton, creating a positron ( $e^+$ ) and a neutron. The positron quickly deposits its energy and annihilates into two 511-keV  $\gamma$ -rays, which gives a prompt signal. The neutron scatters in the detector until being thermalized. It is then captured by a proton  $\sim 200 \mu\text{s}$  later and releases a 2.2-MeV  $\gamma$ -ray. The coincidence of the prompt-delayed signal pair in such a short time significantly reduces backgrounds. Positron carries almost all energy of the neutrino in this reaction. Therefore, the observable neutrino spectrum shown in Fig. 2-6 can be obtained from the prompt signal with a  $\sim 0.8$  MeV shift. With reactors of 36 GW thermal power at 53 km, a 20-kton LS detector will have 83 IBD events per day.

The accidental background,  $^8\text{He}/^9\text{Li}$ , fast neutron and  $(\alpha, n)$  background are the major backgrounds for the reactor neutrino oscillation analysis. Fiducial volume cut can significantly reduce the accidental background and the  $(\alpha, n)$  background. Energy selection, time coincidence, and vertex correlation of the prompt and delayed signals are required for the reactor antineutrino selection to further suppress the accidental background. To reject the cosmogenic backgrounds such

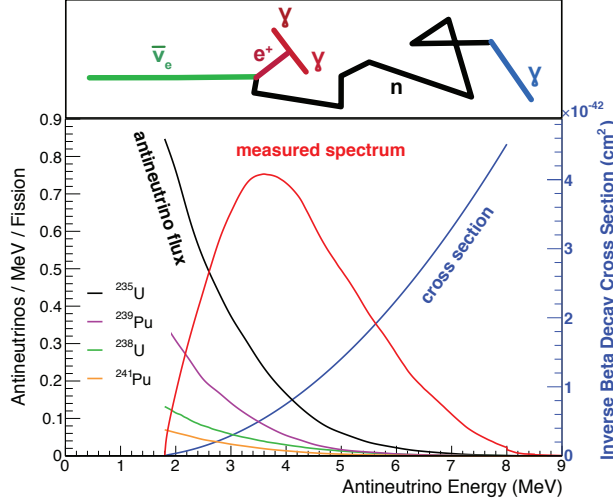


Figure 2-6: The observable  $\bar{\nu}_e$  spectrum (red line) is a product of the antineutrino flux from reactor and the cross section of inverse beta decay (blue line). The contributions of four fission isotopes to the antineutrino flux are shown for a typical pressurized water reactor. The steps involved in the detection are schematically drawn on the top of the figure [108].

as  ${}^9\text{Li}/{}^8\text{He}$  and fast neutron, muon veto cuts are necessary and need be optimized to reduce the loss of detector live time and dead volume. Detailed discussion on backgrounds will be presented later. A set of preliminary antineutrino selection criteria is listed below:

- fiducial volume cut  $r < 17$  m;
- the prompt energy cut  $0.7 \text{ MeV} < E_p < 12 \text{ MeV}$ ;
- the delayed energy cut  $1.9 \text{ MeV} < E_d < 2.5 \text{ MeV}$ ;
- time interval between the prompt and delayed signal  $\Delta T < 1.0$  ms;
- the prompt-delayed distance cut  $R_{p-d} < 1.5$  m;
- Muon veto criteria:
  - for muons tagged by Water Pool, veto the whole LS volume for 1.5 ms
  - for good tracked muons in central detector and water Cerenkov detector, veto the detector volume within  $R_{d2\mu} < 3$  m and  $T_{d2\mu} < 1.2$  s
  - for the tagged, non-trackable muons in central detector, veto the whole LS volume for 1.2 s

The antineutrino selection efficiency due to the fiducial volume is 91.8%. The energy cut, time cut, and vertex cut have efficiencies of 97.8%, 99.1%, and 98.7%, respectively, using Geant4-based Monte Carlo (MC) studies described in Sec. 13. Assuming 99% muons have good reconstructed track, the efficiency of above muon veto cut is estimated to be 83% by using the toy MC method. Tab. 2-1 summarizes the efficiencies of antineutrino selection cuts and the corresponding reduction to various backgrounds, which will be discussed in the next subsection. JUNO will observe 60 IBD events per day, with about 6% backgrounds.

Selection	IBD efficiency	IBD	Geo- $\nu$ s	Accidental	${}^9\text{Li}/{}^8\text{He}$	Fast $n$	$(\alpha, n)$
-	-	83	1.5	$\sim 5.7 \times 10^4$	84	-	-
Fiducial volume	91.8%	76	1.4	410	77	0.1	0.05
Energy cut	97.8%	73	1.3		71		
Time cut	99.1%						
Vertex cut	98.7%						
Muon veto	83%	60	1.1	0.9	1.6		
Combined	73%	60	3.8				

Table 2-1: The efficiencies of antineutrino selection cuts, signal and backgrounds rates.

### 2.2.2 Background estimation

**Accidental background** The rate of accidental backgrounds can be calculated as  $R_{\text{acc}} = R_p \cdot R_d \cdot \Delta T$ , where  $R_p$  and  $R_d$  are the rate of prompt and delayed signals, respectively, and  $\Delta T$  is the time coincidence window. A fiducial volume cut is essential to significantly suppress such background. The accidental background consists of mainly three types of random coincidence: (radioactivity, radioactivity), (radioactivity, cosmogenic isotope) and (radioactivity, spallation neutrons):

- (radioactivity, radioactivity): The singles rate obtained from MC simulation is about 7.6 Hz after fiducial volume cut (see Sec. 13.4.4), in which the fraction of neutron-like signals is  $\sim 8\%$ . Thus the rate of prompt-delayed coincidence within 1.0 ms is  $\sim 410/\text{day}$ . In addition, a toy MC study gives a factor of 380 suppression by requiring  $R_{p-d} < 1.5$  m, where  $R_{p-d}$  is the distance between the prompt-delayed pair, thus the accidental background rate is reduced to 1.1/day.
- (radioactivity, cosmogenic isotope): based on the rates of cosmogenic isotopes in Sec. 13.4.3, the neutron-like singles from cosmogenic isotopes is estimated to be  $\sim 340/\text{day}$ . The rate of accidental coincidence between radioactivity and those isotopes is  $< 0.01/\text{day}$  after  $\Delta T < 1.0$  ms and  $R_{p-d} < 1.5$  m cut.
- (radioactivity, spallation neutrons): Though the total rate of spallation neutrons is 1.8 Hz, after 1.5 ms muon veto the rate is reduced to  $\sim 45/\text{day}$ . The coincidence between radioactivity and the residual spallation neutrons is negligible after the time and spatial cut.

Thus the total rate of accidental backgrounds is estimated to be 0.9/day, after taking into account the efficiency of muon veto. During data taking, the rate of radioactivity can be precisely monitored, so can the neutron-like events from muon spallation. So the uncertainty of accidental background rate can be controlled within 1% and the uncertainty of spectrum shape is negligible due to the large statistics of prompt-like singles.

**${}^9\text{Li}/{}^8\text{He}$**  As noted in Sec. 13.4.3, the  $\beta$ -n decays from cosmogenic  ${}^8\text{He}$  and  ${}^9\text{Li}$  can mimic IBD interactions, thus are the most serious correlated background to reactor antineutrinos. The  ${}^9\text{Li}$  and  ${}^8\text{He}$  production cross section is often modelled empirically as being proportional to  $E_\mu^{0.74}$ , where  $E_\mu$  is the average energy of the muon at the detector. Considering the cross section measured in the KamLAND detector [109],  $2.2 \times 10^{-7} \mu^{-1} \text{g}^{-1} \text{cm}^2$  for  ${}^9\text{Li}$  and  $0.7 \times 10^{-7} \mu^{-1} \text{g}^{-1} \text{cm}^2$  for  ${}^8\text{He}$ , the predicted  ${}^9\text{Li}$  and  ${}^8\text{He}$  production rate at JUNO is 150 and 50 per day, respectively. The branching ratio of the  $\beta$ -n decay is 51% for  ${}^9\text{Li}$  and 16% for  ${}^8\text{He}$ , thus the total rate of  $\beta$ -n decays is 84/day. Taking into account the fiducial volume cut, the rate is reduced to 77/day. The delayed energy cut



and time cut efficiencies for  ${}^9\text{Li}$  are the same as those for IBDs, as shown in Tab. 2-1, while the prompt energy cut efficiency for  ${}^9\text{Li}$  is  $\sim 97\%$ . Thus the background rate is reduced to  $\sim 71/\text{day}$ . The FLUKA simulation results in Tab. 13-9 are smaller than this empirical extrapolation. It is pointed out that scaling with the muon average energy is not as accurate as the scaling with the energy loss of individual muons, which may explain the differences between the FLUKA-estimated yields and the empirical extrapolation [308].

In practice, the rate of  ${}^9\text{Li}/{}^8\text{He}$  can be measured from the distribution of the time since the last muon using the known decay times for these isotopes [110]. A toy MC based on the simulated muon data has been performed, and it's expected that  $<3\%$  rate uncertainty can be achieved with 6 years data.

The  ${}^9\text{Li}/{}^8\text{He}$  background is correlated with the parent muon in time and space. The lateral distance between the muon-induced isotopes and the parent muon trajectory is roughly exponential. The most effective approach to reject  ${}^9\text{Li}/{}^8\text{He}$  background is to veto a sufficient detector volume along the muon trajectory for a relative long time, e.g, a few times of the isotope's lifetime. Muons that are accompanied by electromagnetic or hadronic showers, usually named as showering muons, are the dominant producers ( $>85\%$ ) of the radioactive isotopes. With a muon simulation for JUNO, it is found that the showering muon rate is  $\sim 0.5$  Hz. The simulation also suggests that after producing a shower, the muon still survives and its direction changes negligibly. Thus the critical issue is how well the muon track reconstruction is, for both non-showering muons and showering muons.

For single non-showering muon, the track can be reconstructed using the first hit-time on PMTs. The methods to reconstruct the track of showering muons and the tracks in muon bundles (see Sec. 13.4.1) are under development. Initial track can be guessed by using the PMTs near the injecting point and outgoing point. The locations of spallation neutrons, if there is any, can be used to constrain their parent muon tracks. Particularly, the high multiplicity of spallation neutrons from the showering processes can give good estimation of where the showering happens, then it's possible to veto a spherical volume around the showering point to reject  ${}^9\text{Li}/{}^8\text{He}$ . If showering muons are poorly reconstructed, a whole volume cut is essential to reject the  ${}^9\text{Li}/{}^8\text{He}$  background.

To estimate the residual  ${}^9\text{Li}/{}^8\text{He}$  after the muon veto cuts listed in Sec. 2.2.1, we assume the efficiency of good track reconstruction for non-showering muon is more than 99%, based on the experience from KamLAND. For showering muons, we expect the track reconstruction can also reach 99% efficiency. Then the efficiency of the muon veto cuts is estimated to be 83% using toy MC, and 2.3% of  ${}^9\text{Li}/{}^8\text{He}$  will survive, thus the final residual  ${}^9\text{Li}$  and  ${}^8\text{He}$  background is 1.6/day.

The uncertainties on the residual  ${}^9\text{Li}/{}^8\text{He}$  background rate are mainly from the uncertainty from muon track reconstruction and the position reconstruction uncertainty of IBD candidates. We assume 20% relative uncertainty on the residual background rate. With the full statistics of  ${}^9\text{Li}/{}^8\text{He}$  events, the energy spectrum shape can be measured quite well. We can assign 10% bin-to-bin shape uncertainty.

**Fast neutron** The cosmic muons that only passing the surrounding rock of the water pool, as well as the corner clipping muons with very short track length in water, are not able to be tagged. The energetic neutrons produced by those muons can form a fast neutron background by scattering off a proton and then being captured in the LS detector. Based on a full simulation without optical processes, the rate of fast neutrons is estimated to be  $\sim 0.1/\text{day}$ . The signals produced by the energetic neutrons are found to be concentrated at the top of detector and near the equator where the water shielding is minimum. For the MH analysis, we assume the relative rate uncertainty is 100%. The prompt energy spectrum is consistent with a flat distribution. The tagged fast-neutrons

can actually provide good information about the energy spectrum. In this analysis, we assume the shape uncertainty is 20%.

**$^{13}\text{C}(\alpha, n)^{16}\text{O}$  background** The alpha particles from the U, Th radioactivities can react with the  $^{13}\text{C}$  in LS. The  $^{13}\text{C}(\alpha, n)^{16}\text{O}$  reaction could lead to a correlated background if the neutron is fast enough or there is a gamma from the de-excitation of the  $^{16}\text{O}$  excited states. Based on the estimated natural radioactivity concentrations, the  $(\alpha, n)$  background rate is estimated to be 0.05/day for the “Acrylic Sphere” option, and 0.01/day for the “Balloon” option due to the lower U/Th concentration. The highest energy of alpha’s from U/Th is about 9 MeV, and the cross section of  $^{13}\text{C}(\alpha, n)^{16}\text{O}$  reaction is known with a  $\sim 20\%$  uncertainty for an alpha with energy  $< 10$  MeV. Thus if the rate of alpha particles is well measured, the  $(\alpha, n)$  background can be predicted precisely. In this analysis, a 50% relative uncertainty for both the background rate and the energy spectrum shape is conservatively assumed.

**Geo-neutrino background** Antineutrinos produced from radioactive decays of Th and U inside the Earth constitute the geo-neutrino flux, which will also contribute to the background of reactor antineutrinos. The total event rate of geo-neutrinos at the JUNO site is 1.5/day, where contributions from Th and U are 23% and 77% respectively. After the IBD efficiency cut, the remaining geo-neutrino background is 1.1/day. The relative rate uncertainty of geo-neutrinos is estimated as 30%, where the crust uncertainty is 18% and the uncertainty of mantle prediction is assumed to be 100%. Experimentally the rate of geo-neutrinos can be measured with much better precision using the JUNO detector itself. Finally, we assume the relative shape uncertainty of geo-neutrinos to be 5%, because the  $\beta$ -decay spectra of Th and U are well known from the nuclear physics. More details on the geo-neutrino prediction and measurement are discussed in Sec. 8.

The background rates and the reduction with the antineutrino selection cuts are summarized in Tab. 2-1.

## 2.3 The MH Sensitivity

### 2.3.1 Basic Setup and Definition

In JUNO simulation, we assume a 20 kt LS detector, and the total thermal power of the two reactor complexes as  $36 \text{ GW}_{th}$ . We use the nominal running time of six years (i.e., 2000 effective days) and a detector energy resolution of  $3\%/\sqrt{E(\text{MeV})}$  as a benchmark. The IBD detection efficiency is estimated as 73% as show in Tab. 2-1. The energy  $E$  is referred as the visible energy of the IBD events [ $E(\text{MeV}) \simeq E_\nu(\text{MeV}) - 0.8$ ]. A normal MH is assumed to be the true one (unless mentioned explicitly) while the conclusion is the same for the other assumption. The relevant oscillation parameters are taken from the latest global analysis [27,76] as  $\Delta m_{21}^2 = 7.54 \times 10^{-5} \text{ eV}^{-2}$ ,  $(\Delta m_{31}^2 + \Delta m_{32}^2)/2 = 2.43 \times 10^{-3} \text{ eV}^{-2}$ ,  $\sin^2 \theta_{13} = 0.024$  and  $\sin^2 \theta_{12} = 0.307$ . The CP-violating phase will be specified when needed. Corrections to  $\Delta m_{21}^2$  and  $\sin^2 \theta_{12}$  from terrestrial matter effects are around 0.5%-1% (see Sec. 3) and the induced uncertainties are negligibly small ( $< 0.1\%$ ). Finally, the reactor antineutrino flux model from ILL and Vogel *et al.* [98–100,103] is adopted in our simulation<sup>2</sup>. Because only two of the three mass-squared differences ( $\Delta m_{21}^2$ ,  $\Delta m_{31}^2$  and  $\Delta m_{32}^2$ ) are independent, we choose  $\Delta m_{21}^2$  and  $\Delta m_{ee}^2$  [see Eq. (2.2)] as our working parameters.

<sup>2</sup>We have tried both the old [98–100,103] and new evaluations [101,102] of the reactor antineutrino fluxes. Both evaluations give consistent results on the MH determination.

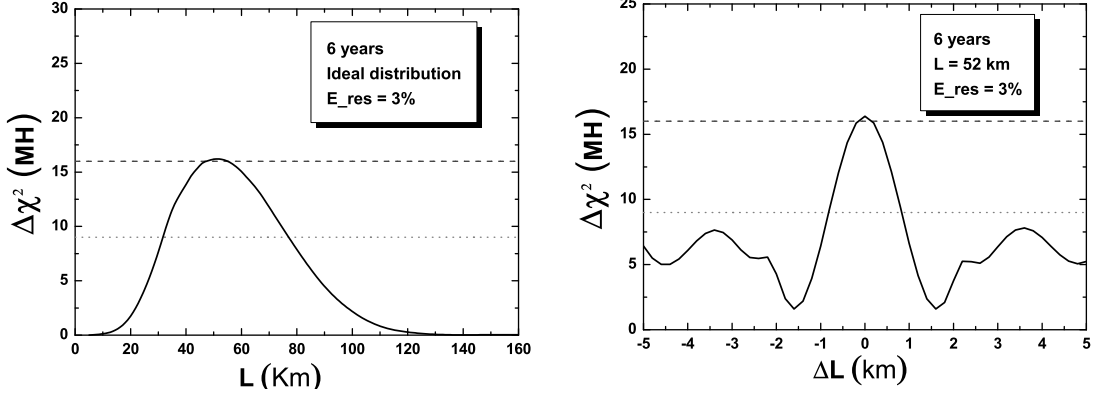


Figure 2-7: The MH discrimination ability as the function of the baseline (left panel) and function of the baseline difference of two reactors (right panel).

To obtain the MH sensitivity, we employ the least-squares method and construct a  $\chi^2$  function as <sup>3</sup>,

$$\chi_{\text{REA}}^2 = \sum_{i=1}^{N_{\text{bin}}} \frac{[M_i - T_i(1 + \sum_k \alpha_{ik}\epsilon_k)]^2}{M_i} + \sum_k \frac{\epsilon_k^2}{\sigma_k^2}, \quad (2.9)$$

where  $M_i$  is the measured neutrino events in the  $i$ -th energy bin,  $T_i$  is the predicted neutrino events with oscillations,  $\sigma_k$  is the systematic uncertainty,  $\epsilon_k$  is the corresponding pull parameter, and  $\alpha_{ik}$  is the fraction of neutrino event contribution of the  $k$ -th pull parameter to the  $i$ -th energy bin. The considered systematic uncertainties include the correlated (absolute) reactor uncertainty (2%), the uncorrelated (relative) reactor uncertainty (0.8%), the spectrum shape uncertainty (1%) and the detector-related uncertainty (1%). We use 200 equal-size bins for the incoming neutrino energy between 1.8 MeV and 8.0 MeV.

We fit the spectrum assuming the normal MH or inverted MH with the chisquare method and take the difference of the minima as a measure of the MH sensitivity. The discriminator of the MH can be defined as

$$\Delta\chi_{\text{MH}}^2 = |\chi_{\text{min}}^2(\text{N}) - \chi_{\text{min}}^2(\text{I})|, \quad (2.10)$$

where the minimization process is implemented for all the relevant oscillation parameters. Note that two local minima for each MH [ $\chi_{\text{min}}^2(\text{N})$  and  $\chi_{\text{min}}^2(\text{I})$ ] can be located at different positions of  $|\Delta m_{ee}^2|$ .

### 2.3.2 Baseline Optimization

The discriminator defined in Eq. (2.10) can be used to obtain the optimal baseline, which are shown in the left panel of Fig. 2-7. A sensitivity of  $\Delta\chi_{\text{MH}}^2 \simeq 16$  is obtained for the ideal case with identical baselines at around 50 km. The impact of the baseline difference due to multiple reactor cores is shown in the right panel of Fig. 2-7, by keeping the baseline of one reactor unchanged and varying that of another. A rapid oscillatory behavior is observed and demonstrates the importance of reducing the baseline differences of reactor cores. The worst case is at  $\Delta L \sim 1.7$  km, where the  $|\Delta m_{ee}^2|$  related oscillation is cancelled between two reactors.

<sup>3</sup>A different definition with the Poisson  $\chi^2$  function yields the consistent MH sensitivity [79, 80].

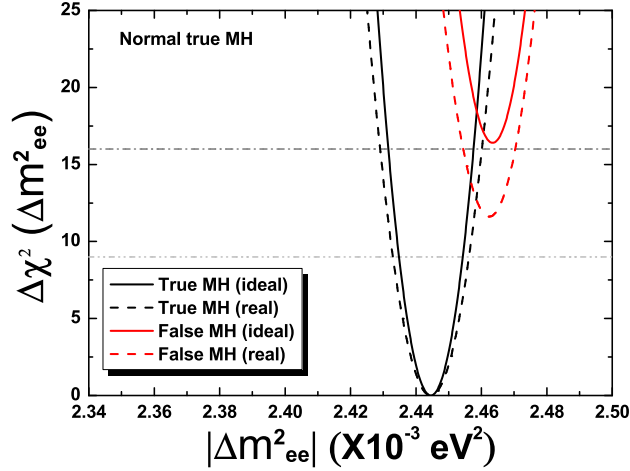


Figure 2-8: The comparison of the MH sensitivity for the ideal and actual distributions of the reactor cores. The real distribution gives a degradation of  $\Delta\chi_{\text{MH}}^2 \simeq 5$ .

Considering the baseline optimization and impact of the baseline difference, we select of the experimental site. A candidate site was identified by taking account of the physical performance and detailed geological survey. With the spatial coordinates of the experimental site and reactor cores, the actual power and baseline distributions for the reactor cores of Yangjiang (YJ) and Taishan (TS) NPPs are shown in Tab. 1-2. The remote reactors in the Daya Bay (DYB) and the possible Huizhou (HZ) NPP are also included. The reduction of sensitivity due to the actual distribution of reactor cores is shown in Fig. 2-8, which gives a degradation of  $\Delta\chi_{\text{MH}}^2 \simeq 5$ . The degradation includes  $\Delta\chi_{\text{MH}}^2 \simeq 3$  due to the baseline differences of Taishan and Yangjiang NPP, and  $\Delta\chi_{\text{MH}}^2 \simeq 1.7$  with the inclusion of Daya Bay and Huizhou NPPs. Other NPPs in operation and construction are much further away from the experimental site (larger than 400 km) and can be neglected in the MH studies (reduction of  $\Delta\chi_{\text{MH}}^2 < 0.2$ ). In all the following, the actual spacial distribution of reactor cores as shown in Tab. 1-2 is taken into account.

### 2.3.3 Requirement on the Energy Resolution

The energy resolution as or better than the size of  $\Delta m_{21}^2/|\Delta m_{31}^2|$  is required in order to precisely measure both the fast oscillations (driven by  $\Delta m_{31}^2$  and  $\Delta m_{32}^2$ ) and slow oscillation (driven by  $\Delta m_{21}^2$ ) at a medium baseline. In our nominal setup, the detector energy resolution  $3\%/\sqrt{E(\text{MeV})}$  is defined from the photon-electron statistics (1200 p.e./MeV), with the energy  $E$  defined as the visible energy of the positron. To show the effects of the energy resolution and event statistics, we illustrate the iso- $\Delta\chi_{\text{MH}}^2$  contour plot as a function of the two key factors in Fig. 2-9. The nominal luminosity is defined as the IBD event statistics in Sec. 2.3.1. From the figure, we can observe that the energy resolution of  $2.6\%/\sqrt{E(\text{MeV})}$  and  $2.3\%/\sqrt{E(\text{MeV})}$  is required to achieve the sensitivity of  $\Delta\chi_{\text{MH}}^2 \simeq 16$  or  $\Delta\chi_{\text{MH}}^2 \simeq 25$  with the nominal statistics, respectively. With an increase of the statistics by 50%, the energy resolution of  $2.9\%/\sqrt{E(\text{MeV})}$  and  $2.6\%/\sqrt{E(\text{MeV})}$  are required to achieve the same sensitivity of  $\Delta\chi_{\text{MH}}^2 \simeq 16$  or  $\Delta\chi_{\text{MH}}^2 \simeq 25$ .

For a real experimental environment, there are other important factors beyond the photon-electron statistics that affect the energy resolution, such as the dark noise from PMT and electronics, the detector non-uniformity and vertex resolution, as well as the PMT charge resolution. A generic

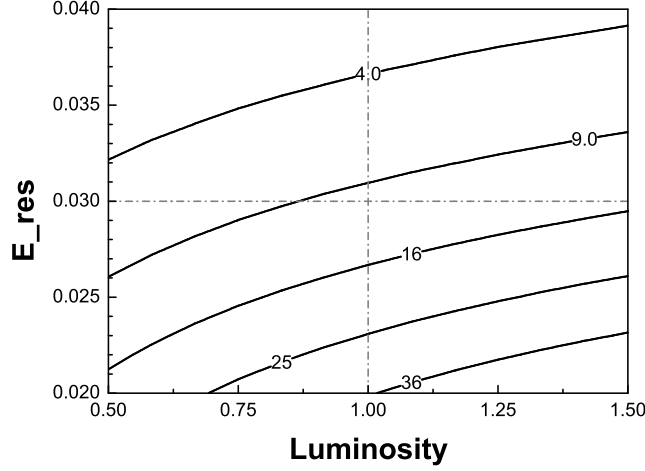


Figure 2-9: The iso- $\Delta\chi_{\text{MH}}^2$  contour plot as the function of the event statistics (luminosity) and the energy resolution, where the vertical dash-dotted line stands for the nominal running of six years with 80% signal efficiency.

parametrization for the detector energy resolution is defined as

$$\frac{\sigma_E}{E} = \sqrt{\left(\frac{a}{\sqrt{E}}\right)^2 + b^2 + \left(\frac{c}{E}\right)^2}, \quad (2.11)$$

where the visible energy  $E$  is in the unit of MeV.

Based on our numerical calculation of the MH sensitivity in terms of  $\Delta\chi_{\text{MH}}^2$ , we find an approximate relation for effects of non-stochastic terms (i.e.,  $b$ ,  $c$ ) using the equivalent  $a$  term,

$$\sqrt{\left(\frac{a}{\sqrt{E}}\right)^2 + b^2 + \left(\frac{c}{E}\right)^2} \simeq \sqrt{\left(\frac{a}{\sqrt{E}}\right)^2 + \left(\frac{1.6b}{\sqrt{E}}\right)^2 + \left(\frac{c}{1.6\sqrt{E}}\right)^2}, \quad (2.12)$$

which indicates that the influence of  $b$  is 1.6 times larger than the  $a$  term, and  $c$  is less significant than  $a$  by a factor of 1.6. Therefore, a requirement for the resolution of  $a/\sqrt{E}$  better than 3% is equivalent to the following requirement,

$$\sqrt{(a)^2 + (1.6 \times b)^2 + \left(\frac{c}{1.6}\right)^2} \leq 3\%. \quad (2.13)$$

Using Fig. 2-9 and the approximation in Eq. (2.12), we can study different effects of detector design parameters and optimize the corresponding requirements.

The energy resolution of the JUNO detector is projected in Appendix 13.2.2 with a full MC simulation. Toy MC is also used to study the degradation due to the PMT charge resolution, dark noise, quantum efficiency variation, and smearing from the vertex reconstruction, as shown in Tab. 13-4. Besides the detector response and reconstruction, the variation of the neutron recoil energy also degrades the resolution of the reconstructed neutrino energy, which introduces a degradation of  $\Delta\chi_{\text{MH}}^2 \simeq 0.1$  on the MH sensitivity.

### 2.3.4 Statistical Interpretation

In this section, we shall present a brief summary of the MH statistics and relation to the sensitivity. The following discussion is crucial to properly understand the sensitivity results shown in Fig. 2-8. The determination of MH is equivalent to resolving the sign of  $\Delta m_{31}^2$ . From the statistics point of view, the determination of MH is a test to distinguish two discrete hypotheses (NH vs. IH).

First let us employ the commonly used approach in the Frequentist statistics. Given a null hypothesis  $H_0$  and the alternative hypothesis  $H_1$ , we can choose a test statistic  $T$  in order to test whether data can reject the null hypothesis  $H_0$ . The confidence level (CL)  $(1 - \alpha)$  to reject  $H_0$  is related to the type-I error rate  $\alpha$ , where,

- *type-I error rate*  $\alpha$  is defined as the probability of rejecting the null hypothesis  $H_0$ , if  $H_0$  is true.

From the definition, one can define the relation between a critical value of the observation  $T_c^\alpha$  and the the type-I error rate  $\alpha$  as

$$\int_{T_c^\alpha}^{\infty} p(T|H_0)dT = \alpha, \quad (2.14)$$

with  $p(T|H_0)$  being the probability distribution function of  $T$  given that  $H_0$  is true. Moreover, we can further define the conversion between the double-sided Gaussian  $n\sigma$  and the value of  $\alpha$  as

$$\alpha(n) = \frac{2}{\sqrt{2\pi}} \int_n^{\infty} dx e^{-x^2/2} = \text{erfc} \left( \frac{n}{\sqrt{2}} \right), \quad (2.15)$$

where  $\text{erfc}(x)$  is the complementary error function. This definition implies that we identify standard deviations of  $1\sigma, 2\sigma, 3\sigma$  with a CL  $(1 - \alpha)$  of 68.27%, 95.45%, 99.73%, respectively.

On the other hand, the power of a given test  $T$  is related to the type-II error rate  $\beta$ , where

- *type-II error rate*  $\beta$  is defined as the probability of accepting the null hypothesis  $H_0$ , if  $H_1$  is true.

According to the definition,  $\beta$  is calculated as

$$\beta = P(T < T_c^\alpha | H_1) = \int_{-\infty}^{T_c^\alpha} p(T|H_1)dT, \quad (2.16)$$

where  $p(T|H_1)$  is the probability distribution function of  $T$  assuming the alternative hypothesis  $H_1$  is true.  $\beta$  depends on the CL  $(1 - \alpha)$  at which we want to reject  $H$ . A small value of  $\beta$  means that the type-II error rate is small, the power of the test (which is defined as  $1 - \beta$ ) is large.

Based on different choices of  $\beta$ , one can have different sensitivities, such as the median sensitivity [111, 112] ( $\beta = 50\%$ ) and the crossing sensitivity [112–115] ( $\beta = \alpha$ ). The former is defined for the expected sensitivity of an averaged experiment, and the latter corresponds to the CL at which exactly one of the two hypotheses can be rejected. By definition, the crossing sensitivity gives smaller confidence levels than the median sensitivity and is not necessarily connected to what would be expected from an designed experiment [112].

For the case of the MH determination at JUNO, we first define our working test statistics similar to the discriminator in Eq. (2.10),

$$T = \chi_{\min}^2(\text{I}) - \chi_{\min}^2(\text{N}). \quad (2.17)$$

According to the derivation in Refs. [112–115], the static  $T$  follows the Gaussian distribution with

$$T = \mathcal{N} \left( \pm \Delta \chi_{\text{MH}}^2, 2\sqrt{\Delta \chi_{\text{MH}}^2} \right), \quad (2.18)$$

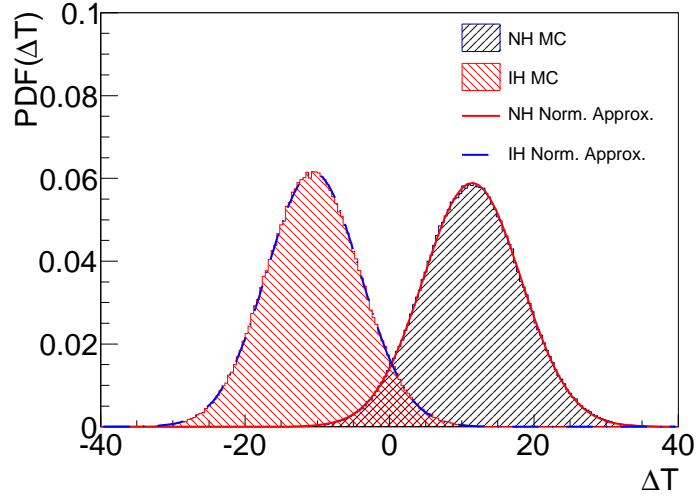


Figure 2-10: The  $T$  distribution function for the JUNO nominal setup of six year running.

	Median sens.	Standard sens.	Crossing sens.
Normal MH	$3.4 \sigma$	$3.3 \sigma$	$1.9 \sigma$
Inverted MH	$3.5 \sigma$	$3.4 \sigma$	$1.9 \sigma$

Table 2-2: The MH sensitivity with the JUNO nominal setup of six year running.

where the plus (minus) sign holds for the normal (inverted) MH. This distribution is validated with an explicit MC simulation in Fig. 2-10, showing the excellent agreement between the numerical and analytical calculations.

In Tab 2-2, we show the median sensitivity, standard sensitivity (defined as  $\sqrt{\Delta\chi_{\text{MH}}^2}\sigma$ ), and crossing sensitivity respectively for the JUNO nominal setup, where we can see that the commonly defined standard sensitivity is very close to the median sensitivity and can be regard as the expected sensitivity of a future experiment.

Before finishing the discussion on this approach, we want to stress that the Frequentist approach does not directly address the question how much one MH hypothesis is favored than the other MH hypothesis given the experimental data. In the MH determination one can choose the null hypothesis to be the NH, and the alternative hypothesis would be the IH. The result of this hypothesis testing will tell us whether the NH would be rejected or not, given the pre-defined rule. Similarly, one should also perform a second hypothesis testing by choosing null hypothesis to be the IH with the alternative hypothesis being the NH. The result of the second test will tell us whether the IH would be rejected or not.

On the other hand, the method of using the Bayesian statistics can tell us the comparison of two MH hypotheses. The Bayes' theorem gives the relationship of the posterior probability distribution function  $p(\text{MH}|\text{D}, \text{I})$ , the prior probability distribution function  $p(\text{MH}|\text{I})$  and the likelihood function  $L(\text{D}|\text{MH}, \text{I})$  as

$$p(\text{MH}|\text{D}, \text{I}) = \frac{L(\text{D}|\text{MH}, \text{I}) \cdot p(\text{MH}|\text{I})}{\int L(\text{D}|\text{MH}, \text{I}) \cdot p(\text{MH}|\text{I})}, \quad (2.19)$$

where D represents the data of a measurement, I is the prior information on the MH hypotheses and the integration are carried out for all the oscillation parameters. Given data from the measurement, one can calculate  $T_{\text{NH}} = -2\text{Log}[p(\text{NH}|\text{D},\text{I})]$  and  $T_{\text{IH}} = -2\text{Log}[p(\text{IH}|\text{D},\text{I})]$ .  $T_{\text{NH}}$  and  $T_{\text{IH}}$  are marginalized over all nuisance parameters including unknown parameters and systematic uncertainties of the experiment to obtain  $T_{\text{NH}}^{\text{mag}}$  and  $T_{\text{IH}}^{\text{mag}}$ , respectively <sup>4</sup>.

Assuming that the prior information of NH vs. IH is 50% vs. 50%, the probability ratio of the IH vs. NH, which is  $p(\text{IH}|\text{D},\text{I})$  vs.  $p(\text{NH}|\text{D},\text{I})$ , can be calculated as  $e^{-\Delta\tau/2}$  vs. 1, with  $\Delta\tau = T_{\text{IH}}^{\text{mag}} - T_{\text{NH}}^{\text{mag}}$ . As illustrated in Ref. [113], an approximation  $\Delta\tau \approx \Delta\chi_{\text{MH}}^2$  can be made in practice. More generally,  $\Delta\tau$  can be explicitly calculated through MC simulations or other advanced integration techniques. Tab. 2-3 lists a few values of  $\Delta\chi_{\text{MH}}^2$  and their corresponding probability ratios. The final results are then presented in terms of probability ratio which is a natural and simple way to present results for the MH determination.

$\Delta\tau \approx \Delta\chi_{\text{MH}}^2$	1	4	9	16	25
$p(\text{IH} \text{D},\text{I})$ vs. $p(\text{NH} \text{D},\text{I})$	38% vs. 62%	12% vs. 88%	1.1% vs. 98.9%	0.034% vs. 99.966%	$3.7 \times 10^{-6}$ vs. 100%
$p(\text{IH} \text{D},\text{I})/p(\text{NH} \text{D},\text{I})$	0.61	0.136	0.011	$3.4 \times 10^{-4}$	$3.7 \times 10^{-6}$

Table 2-3: Probability ratios with respect to several typical  $\Delta\chi_{\text{MH}}^2$  values.

## 2.4 Systematics

In this section, we shall discuss the effects of systematics in the MH measurement in reactor antineutrino oscillations, which includes the reactor related uncertainties, detector related uncertainties, background related uncertainties and the energy related uncertainties.

### 2.4.1 Reactor related uncertainties

As discussed before, the MH information is encoded in the spectral shape of reactor antineutrino oscillations. The absolute normalization uncertainty from the reactor flux at the current level has negligible impact on the MH determination. Therefore only the reactor-related shape uncertainty is considered in the following.

We incorporate the shape uncertainty to each bin by modifying the  $\chi^2$  definition in Eq. (2.9) as follows:

$$\chi_{\text{REA}}^2 = \sum_{i=1}^{N_{\text{bin}}} \frac{[M_i - T_i(1 + \sum_k \alpha_{ik}\epsilon_k)]^2}{M_i + (\sigma M_i)^2} + \sum_k \frac{\epsilon_k^2}{\sigma_k^2}, \quad (2.20)$$

where  $\sigma$  denotes the relative (uncorrelated) shape uncertainty. The  $\Delta\chi_{\text{REA}}^2$  degrades less than 1 when we set the 1% shape uncertainty ( $\sigma = 1\%$ ), while the degradation is about 2 in  $\Delta\chi_{\text{REA}}^2$  when we increase  $\sigma$  to 2%. Therefore, careful estimation and reduction of the energy uncorrelated shape uncertainties are mandatory to achieve the required sensitivity.

Because the model predictions for the reactor antineutrino spectrum are inconsistent with the measurement from ongoing reactor experiments (i.e., the bump between 4 ~ 6 MeV) [105–107]. Moreover, a recent theoretical calculation trying to understand the above inconsistency observes additional high-frequency fine structures [104] in the reactor antineutrino spectrum. Both of the

<sup>4</sup>In the marginalization process, one integrates the likelihood function over the entire phase space of nuisance parameters.



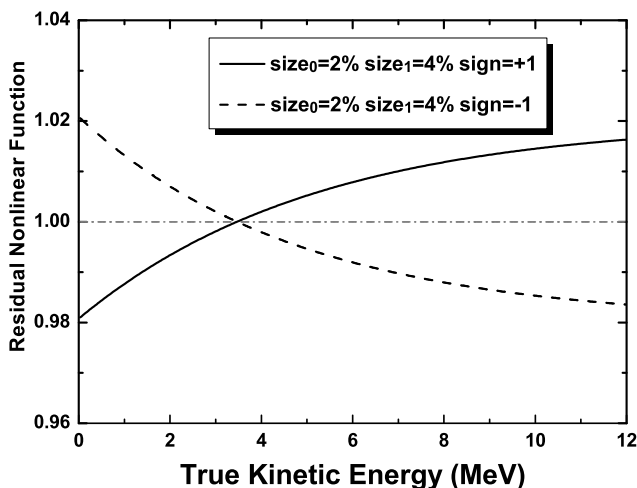


Figure 2-11: Two classes of typical examples for the residual non-linear functions in our simulation.

mentioned spectral structures may induce additional systematics of the shape uncertainty. MC studies of the MH sensitivity on the effects of these spectral structures are carried out, which show that the changes in  $\Delta\chi_{\text{REA}}^2$  can be controlled to be less than 1. In summary, it is crucial to control the effect of reactor spectral structures to reduce systematics of the shape uncertainty.

#### 2.4.2 Detector related uncertainties

Similar to the reactor normalization uncertainty, the uncertainty in the detection absolute efficiency also has negligible impact on the MH determination. Therefore it is desirable to study the energy related uncertainties.

A dedicated calibration of the detector energy non-linearity response is another critical factor to obtain reliable sensitivity of the MH determination. The uncertainty from the detector nonlinearity response can distort the antineutrino spectrum and is crucial for JUNO, since a precise energy spectrum of reactor antineutrinos is required to resolve the MH. Assuming the energy non-linearity correction is imperfect, we study the impact on the sensitivity by including in our simulation a residual non-linearity between the measured and expected neutrino spectra. By including the residual non-linearity with the assumed form shown in Fig 2-11, we obtain the  $\Delta\chi^2$  distribution as functions of the free parameter  $|\Delta m_{ee}^2|$  in Fig. 2-12, where the normal MH is assumed and the plus (left) and minus (right) signs of the non-linearity curves are implemented, respectively. The solid, dashed and dotted lines are for the cases with different sizes of the non-linearity.

From Fig. 2-12, we observe that non-linearity with the minus sign would significantly reduce the sensitivity of MH determination for the true normal MH. In principle, there is the worst case of non-linearity that the wrong MH may perfectly mimic the true one, which defines as

$$\frac{E_{\text{rec}}}{E_{\text{true}}} = \frac{2|\Delta' m_{ee}^2| + \Delta m_{\phi}^2}{2|\Delta m_{ee}^2| - \Delta m_{\phi}^2}, \quad (2.21)$$

where  $\Delta m_{ee}^2$  and  $\Delta' m_{ee}^2$  are the effective mass-squared differences in Eq. (2.2) for the true and false

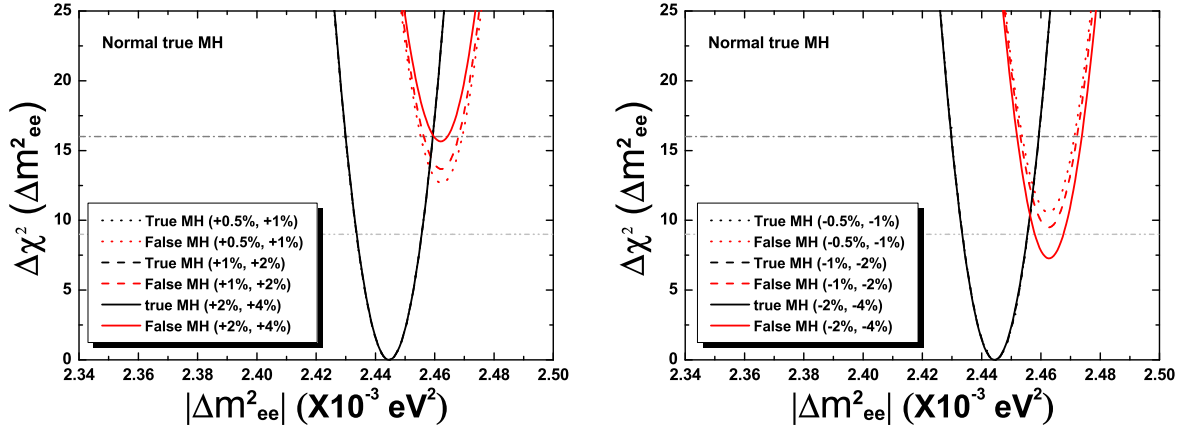


Figure 2-12:  $\Delta\chi^2$  distribution as functions of the free parameters  $|\Delta m_{ee}^2|$ , where the normal MH is assumed, and the plus (left) and minus (right) signs of the non-linearity curves in Fig 2-11 are implemented, respectively. The dashed and dotted lines are for the cases with reduced sizes of the non-linearity.

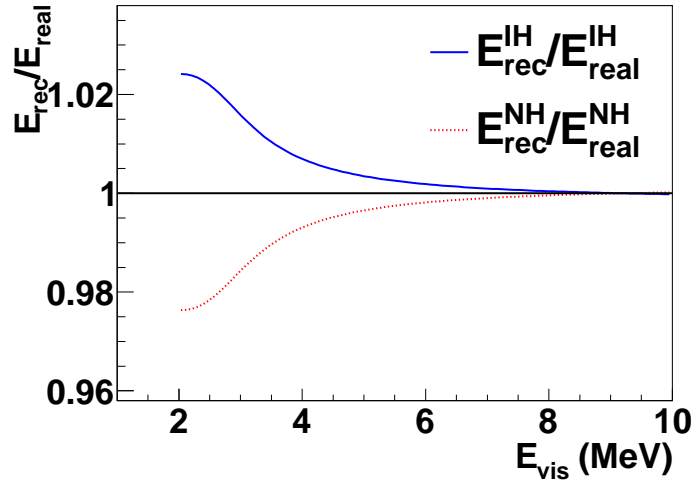


Figure 2-13: The non-linearity models with the largest effects of mimicking between the normal MH and inverted MH.

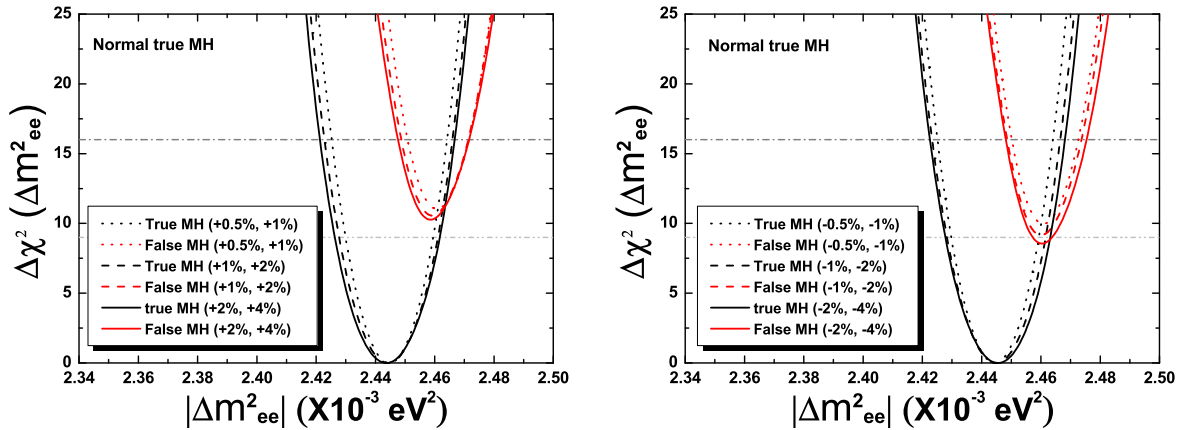


Figure 2-14: Effects of two classes of energy non-linearity models [with plus (left) and minus (right) signs] in determination of the MH with the self-calibration effect, where the normal MH is assumed.

Event type	Rate (per day)	Rate uncertainty (relative)	Shape uncertainty
IBD candidates	60	-	-
Geo- $\nu$ s	1.1	30%	5%
Accidental signals	0.9	1%	negligible
Fast- $n$	0.1	100%	20%
${}^9\text{Li}$ - ${}^8\text{He}$	1.6	20%	10%
${}^{13}\text{C}(\alpha, n){}^{16}\text{O}$	0.05	50%	50%

Table 2-4: The background summary table for the analysis of reactor antineutrinos.

MHs, respectively. Thanks to the current measurements of the neutrino oscillation parameters, we can illustrate the specific non-linearity curves for the normal MH and inverted MH in Fig. 2-13. With this residual non-linearity in the measurement of Eq. (2.9), we can obtain the degradation of  $\Delta\chi^2 \simeq 2.5$  in agreement with the effect in the right panel of Fig. 2-12.

For the reactor antineutrino experiment at a medium baseline, we can observe multiple peaks of the  $\Delta m_{ee}^2$  induced oscillation. Each of the peak position carries the information of  $\Delta m_{ee}^2$ . This redundancy can be used to evaluate the energy scale at different energies, providing a self-calibration way of measuring the energy non-linearity [69]. To illustrate, we consider a test quadratic non-linear function in the prediction of Eq. (2.9), where the coefficients of the function are arbitrary and will be determined in the fitting. Therefore, in the simplest way, we illustrate the self-calibration effect in Fig. 2-14, where the normal MH is assumed. We observe that the increase and reduction of the MH sensitivity due to unknown energy non-linearity can be resolved to some extent, and consistent sensitivity of the MH determination are obtained. Notice that the width of the  $\Delta\chi^2$  functions in Fig. 2-14 is broadened, because additional uncertainties from the parameters of test quadratic non-linearity are introduced.

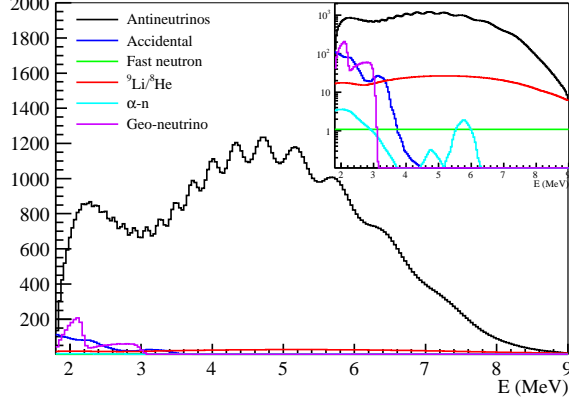


Figure 2-15: Spectra for the antineutrino signal and five kinds of main backgrounds, including the accidental,  ${}^8\text{He}/{}^9\text{Li}$ , fast neutron, and  ${}^{13}\text{C}(\alpha, n){}^{16}\text{O}$  and geo-neutrinos.

### 2.4.3 Background related uncertainties

We further study the effects of background related uncertainties. From Tab. 2-4, the total background to signal (B/S) ratio is 6.3%, which contributes to a reduction of  $\Delta\chi_{\text{MH}}^2 \simeq 0.6$ . Second, the rate uncertainties of backgrounds are negligible for the MH determination since they are nicely constrained in the precision spectral measurements. Finally, the expected energy spectra for five kinds of main backgrounds are shown in Fig. 2-15. The total background shape uncertainties contribute to a 0.4% bin-to-bin uncertainty, which can further reduce the MH sensitivity by  $\Delta\chi_{\text{MH}}^2 \simeq 0.1$ .

### 2.4.4 Systematics summary

To conclude, we summarize the decomposition of experimental systematics in the MH determination in Tab. 2-5.

- Ideal distribution of reactor cores with the equal baseline of 52.5 km gives the MH sensitivity of  $\Delta\chi_{\text{MH}}^2 \simeq 16$ .
- In reality, the real baseline distribution of reactor cores in Taishan and Yangjiang NPPs from Tab. 1-2 induces a degradation of  $\Delta\chi_{\text{MH}}^2 \simeq 3$ .
- An additional reduction of  $\Delta\chi_{\text{MH}}^2 \simeq 1.7$  is obtained due to inclusion of Daya Bay and Huizhou NPPs.
- The reactor shape uncertainty of 1% will further degrade the  $\Delta\chi_{\text{MH}}^2$  by 1.
- The statistical and shape uncertainties of backgrounds with the estimation of Tab. 2-4 contribute to  $\Delta\chi_{\text{MH}}^2 \simeq -0.6$  and  $\Delta\chi_{\text{MH}}^2 \simeq -0.1$ , respectively.
- As will be discussed in the next subsection, an increase of  $\Delta\chi_{\text{MH}}^2 \simeq +8$  can be obtained by including a measurement of  $|\Delta m_{\mu\mu}^2|$  at the 1% precision level.

	Stat.	Core dist.	DYB & HZ	Shape	B/S (stat.)	B/S (shape)	$ \Delta m_{\mu\mu}^2 $
Size	52.5 km	Tab. 1-2	Tab. 1-2	1%	6.3%	0.4%	1%
$\Delta\chi_{\text{MH}}^2$	+16	-3	-1.7	-1	-0.6	-0.1	+(4-12)

Table 2-5: Different contributions for the MH determination. The first column is the statistical-only scenario with the equal baseline of 52.5 km, the second column considers the real distribution (dist.) of reactor cores, the third column defines the contribution of remote DYB and HZ NPPs, the fourth column stands for the reduction of the reactor shape uncertainty, the fifth and sixth columns are the contributions of the background statistical and shape uncertainties, the seventh column is the enhanced sensitivity from additional information of  $|\Delta m_{\mu\mu}^2|$ .

## 2.5 MH Sensitivity with Precision $|\Delta m_{ee}^2|$ and $|\Delta m_{\mu\mu}^2|$ Measurements

Due to the intrinsic difference between  $|\Delta m_{ee}^2|$  and  $|\Delta m_{\mu\mu}^2|$ , precise measurements of these two mass-squared differences can provide additional sensitivity to MH, besides the sensitivity from the interference effects. To incorporate the contribution from the  $|\Delta m_{\mu\mu}^2|$  measurement in long-baseline muon-neutrino oscillation experiments, we define the following the extra pull function

$$\chi_{\text{pull}}^2(|\Delta m_{\mu\mu}^2|) = \frac{(|\Delta m_{\mu\mu}^2| - \overline{|\Delta m_{\mu\mu}^2|})^2}{\sigma^2(\Delta m_{\mu\mu}^2)}, \quad (2.22)$$

where  $\overline{|\Delta m_{\mu\mu}^2|}$  and  $\sigma(\Delta m_{\mu\mu}^2)$  are the central value and  $1\sigma$  uncertainty of the measurement. The combined  $\chi^2$  function is defined as

$$\chi_{\text{ALL}}^2 = \chi_{\text{REA}}^2 + \chi_{\text{pull}}^2(|\Delta m_{\mu\mu}^2|). \quad (2.23)$$

Because two of the three mass-squared differences ( $\Delta m_{21}^2$ ,  $\Delta m_{31}^2$  and  $\Delta m_{32}^2$ ) are independent, we choose  $\Delta m_{21}^2$  and  $\Delta m_{ee}^2$  defined in Eq. (2.2) as the free parameters. Proper values of  $\Delta m_{\mu\mu}^2$  can be calculated by the relations in Eq. (2.6).

To illustrate the effect of the external  $|\Delta m_{\mu\mu}^2|$  measurement, we calculate the separated and combined  $\chi^2$  functions in Eqs. (2.9) and (2.23) in Fig. 2-16, where a 1% (left panel) or 1.5% (right panel) relative error of  $\Delta m_{\mu\mu}^2$  is assumed. The black and red lines are for the true (normal) and false (inverted) MHs, respectively. The dashed and solid lines are for the reactor-only [in Eq. (2.9)] and combined distributions. Here a fixed CP-violating phase ( $\cos \delta = 0$ ) is assumed for illustration. We can get a value of  $\Delta\chi_{\text{MH}}^2 \simeq 10$  for the reactor-only analysis in the  $\chi^2$  method. As for the contribution from the external  $|\Delta m_{\mu\mu}^2|$  measurement, it is almost negligible if we choose the true (normal) MH in the fitting program. However, if the fitting MH is the false (inverted) one, the central value of  $\Delta m_{ee}^2$  in the  $\chi_{\text{pull}}^2$  function will change by two times the difference in Eq. (2.6), which accordingly results in a significant contribution to the combined  $\chi^2$  function. Finally we can achieve  $\Delta\chi_{\text{MH}}^2 \simeq 19$  and  $\Delta\chi_{\text{MH}}^2 \simeq 14$  for the 1% and 1.5% relative errors of the  $|\Delta m_{\mu\mu}^2|$  measurement, respectively. Considering the whole parameter space of  $\delta_{\text{MH}}^2$  from 0 to  $2\pi$ ,  $\Delta\chi^2$  can range from 14 to 22 for the 1% relative precision of  $|\Delta m_{\mu\mu}^2|$  [69].

## 2.6 Conclusions

The determination of the neutrino mass hierarchy is of great importance in neutrino physics, since the MH provides a crucial input for future searches of neutrinoless double beta decays, observation

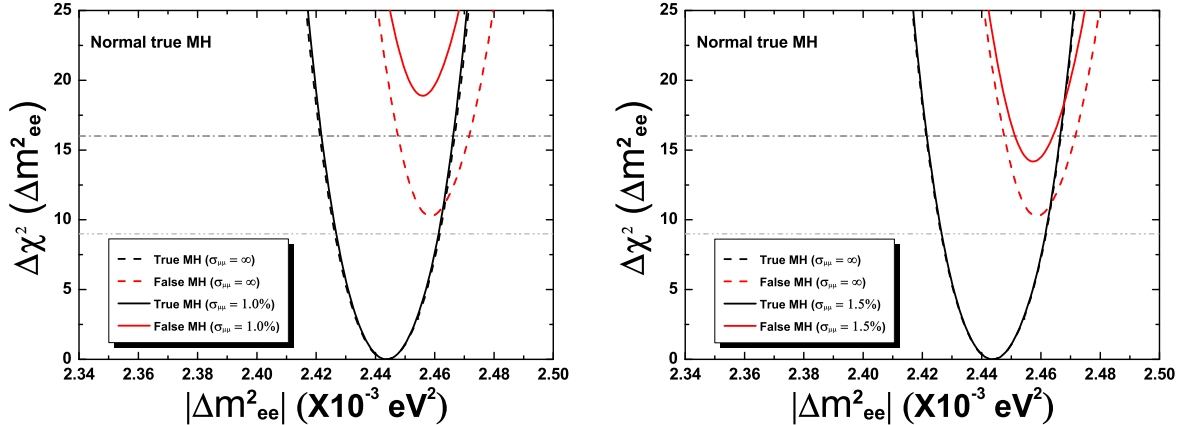


Figure 2-16: the reactor-only (dashed) and combined (solid) distributions of the  $\Delta\chi^2$  function in Eq. (2.9) and Eq. (2.23), where a 1% (left panel) or 1.5% (right panel) relative error of  $\Delta m_{\mu\mu}^2$  is assumed and the CP-violating phase ( $\delta$ ) is assigned to be  $90^\circ/270^\circ$  ( $\cos\delta = 0$ ) for illustration. The black and red lines are for the true (normal) and false (inverted) neutrino MH, respectively.

of supernova neutrino bursts, cosmological probe of neutrino properties, and model building of the neutrino masses and flavor mixing.

Thanks to the relatively large  $\theta_{13}$  discovered in recent reactor and accelerator neutrino experiments, precise measurements of the reactor antineutrino spectrum at a medium baseline of about 50 km can probe the interference effect of two fast oscillation modes (i.e., oscillations induced by  $\Delta m_{31}^2$  and  $\Delta m_{32}^2$ ) and sensitive to the neutrino MH. The corresponding sensitivity depends strongly on the energy resolution, the baseline differences and energy response functions. Moreover, the MH sensitivity can be improved by including a measurement of the effective mass-squared difference in the long-baseline muon-neutrino disappearance experiment due to flavor dependence of the effective mass-squared differences.

We have calculated the MH sensitivity at JUNO taking into account the real spatial distribution of reactor complexes, reactor related uncertainties, detector related uncertainties and background related uncertainties. We demonstrated that a median sensitivity of  $\sim 3\sigma$  can be achieved with the reasonable assumption of the systematics and six years of running. We emphasized that the reactor shape uncertainty and detector non-linearity response, are the important factors to be dealt with. In addition, we have studied the additional sensitivity by including precision measurements of  $|\Delta m_{\mu\mu}^2|$  from long baseline muon (anti)neutrino disappearance. A confidence level of  $\Delta\chi_{\text{MH}}^2 \sim 14$  ( $3.7\sigma$ ) or  $\Delta\chi_{\text{MH}}^2 \sim 19$  ( $4.4\sigma$ ) can be obtained, for the  $|\Delta m_{\mu\mu}^2|$  uncertainty of 1.5% or 1%.

Besides the spectral measurement of reactor antineutrino oscillations, there are other methods to resolve the MH using the matter-induced oscillation of accelerator or atmospheric neutrinos. Worldwide, there are many ongoing and planned experiments designed in this respect. These include the long baseline accelerator neutrino experiments (i.e. NO $\nu$ A and DUNE) and atmospheric neutrino experiments (i.e., INO, PINGU, Hyper-K). Using different oscillation patterns, different neutrino sources and different detector techniques, they are complementary in systematics and contain a great amount of synergies. Therefore, the mass hierarchy, being one of the most important undetermined fundamental parameters in neutrino physics, clearly deserves multiple experiments with preferably different experimental techniques. A consistent resolution of the MH from all these experiments will greatly increase our confidence in the MH determination.

## 3 Precision Measurements of Neutrinos

### 3.1 Introduction and motivation

JUNO is designed to collect a large number of reactor antineutrino events with excellent energy resolution [ $3\%/\sqrt{E}(\text{MeV})$ ] and accurate energy determination [better than 1%]. Therefore, besides the determination of the neutrino mass hierarchy (MH) [69, 79], in 6 years JUNO will also allow a detailed study of various aspects of neutrino oscillations, including the extractions of the mixing parameters  $\theta_{12}$ ,  $\Delta m_{21}^2$ , and  $|\Delta m_{ee}^2|$ , and probe the fundamental properties of neutrino oscillations. JUNO will be:

- the first experiment to simultaneously observe the neutrino oscillation driven by both atmospheric and solar neutrino mass-squared differences (Fig. 3-1). The pronounced dip around 3 MeV corresponds to the solar  $\Delta m^2$ , and the rapid oscillations correspond to the atmospheric  $\Delta m^2$ .
- the first experiment to observe multiple oscillation cycles of the atmospheric  $\Delta m^2$  (Fig. 3-1).
- the well place to have an unprecedented precision measurement of  $\sin^2 \theta_{12}$ ,  $\Delta m_{21}^2$  and  $|\Delta m_{ee}^2|$  to better than 1%.

Furthermore, together with long-baseline neutrino experiments (DUNE [83], Hyper-K [87, 88]), JUNO will usher in the new era of precision neutrino oscillation experiments.

It has to be stressed that on top of measuring the oscillation parameters precision tests of the oscillation pattern in a model-independent way is also very important to probe new physics beyond the Standard Model. The precision measurement of neutrino oscillation parameters is a very powerful tool to test the standard 3-flavor neutrino model ( $\nu\text{SM}$ ). In particular, precision measurement of the fundamental parameter  $\theta_{12}$  will:

- play a crucial role in the future unitarity test of the MNSP matrix  $U$ . The combination of short-baseline reactor antineutrino experiments (e.g., Daya Bay [30]), medium-baseline reactor antineutrino experiments as JUNO and solar neutrino experiments (e.g., SNO [116]) will enable the first direct unitarity test of the MNSP matrix [22–24, 117]:

$$|U_{e1}|^2 + |U_{e2}|^2 + |U_{e3}|^2 \stackrel{?}{=} 1. \quad (3.1)$$

With the combination of Daya Bay, JUNO and SNO, the above unitarity condition will be tested with the precision of 2.5% [117]. The precision is limited by the solar neutrino measurements and could be improved to better than 1% with future precision solar neutrino measurements.

- narrow down the parameter space of the effective mass (i.e.,  $|m_{ee}|$ ) of the neutrinoless double beta decay allowing a conclusive test for the scenario of inverted mass hierarchy (IH). In the case of  $m_3 \leq 0.05 \text{ eV}$ , the minimal value of the effective neutrino mass for IH can be written as [118]

$$|m_{ee}|_{\min}(\text{IH}) \simeq \cos^2 \theta_{13} \sqrt{|\Delta m_{31}^2|} \cos 2\theta_{12}. \quad (3.2)$$

---

Editors: Yufeng Li (liyufeng@ihep.ac.cn)  
Major contributor: Xin Qian

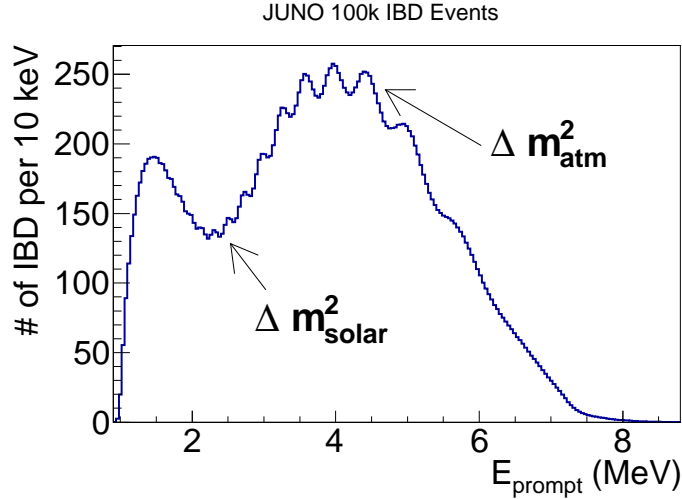


Figure 3-1: The expected prompt energy spectrum of JUNO with a nominal luminosity for six years of data taking with a 20 kt detector and 36  $\text{GW}_{th}$  reactor power (a total of 100k IBD events). A  $3\%/\sqrt{E}$  energy resolution is assumed.

As the uncertainty of  $\sin^2 \theta_{12}$  shrinks from the current level to better than 1%, the lower limit of the effective mass for IH can increase by a factor of two (see Fig. 3-2). In a background-dominated neutrinoless double beta decay experiment, a factor of two improvement in the effective mass sensitivity corresponds to a combined factor of 16 improvement for the experimental parameters of the running time, detector mass, background level and energy resolution [119, 120]. Therefore, the precision measurement of  $\sin^2 \theta_{12}$  is crucial for the next generation of the neutrinoless double beta decay experiments, which aim to cover the whole parameter space corresponding to IH.

- be a powerful discriminator for models of the neutrino masses and mixing. First,  $\theta_{12}$  is more sensitive than other mixing angles to the quantum corrections since  $\Delta m_{21}^2 \ll |\Delta m_{31}^2|$ . Therefore, neutrino-mixing models will be better constrained when the accuracy of  $\theta_{12}$  is improved. Second, taking the prediction of the tri-bimaximal mixing (TBM) [122–124] for  $\theta_{12}$  as an example:

$$\theta_{12}^{\text{TBM}} = \arcsin \frac{1}{\sqrt{3}} \simeq 35.3^\circ, \quad (3.3)$$

the value of non-zero  $\theta_{13}$  may induce further corrections for  $\theta_{12}$ . Depending on the sign of  $\theta_{12}$  corrections, two categories of mixing models, TM1 and TM2, are defined respectively [125]. TM1 and TM2 correspond to the mixing matrix keeping the first or second column of TBM unchanged. A measurement of  $\sin^2 \theta_{12}$  better than 1% is a powerful tool to discriminate between TM1 and TM2 and may shed light on the mechanism of the neutrino masses and mixing.

The muon (anti)neutrino and electron antineutrino disappearance effectively measure  $\Delta m_{\mu\mu}^2$  and  $\Delta m_{ee}^2$  [95, 96] (two different combinations of  $\Delta m_{31}^2$  and  $\Delta m_{32}^2$ ), respectively. When combined with the precision  $|\Delta m_{\mu\mu}^2|$  measurements from muon (anti)neutrino disappearance, the precision measurement of  $|\Delta m_{ee}^2|$  will:



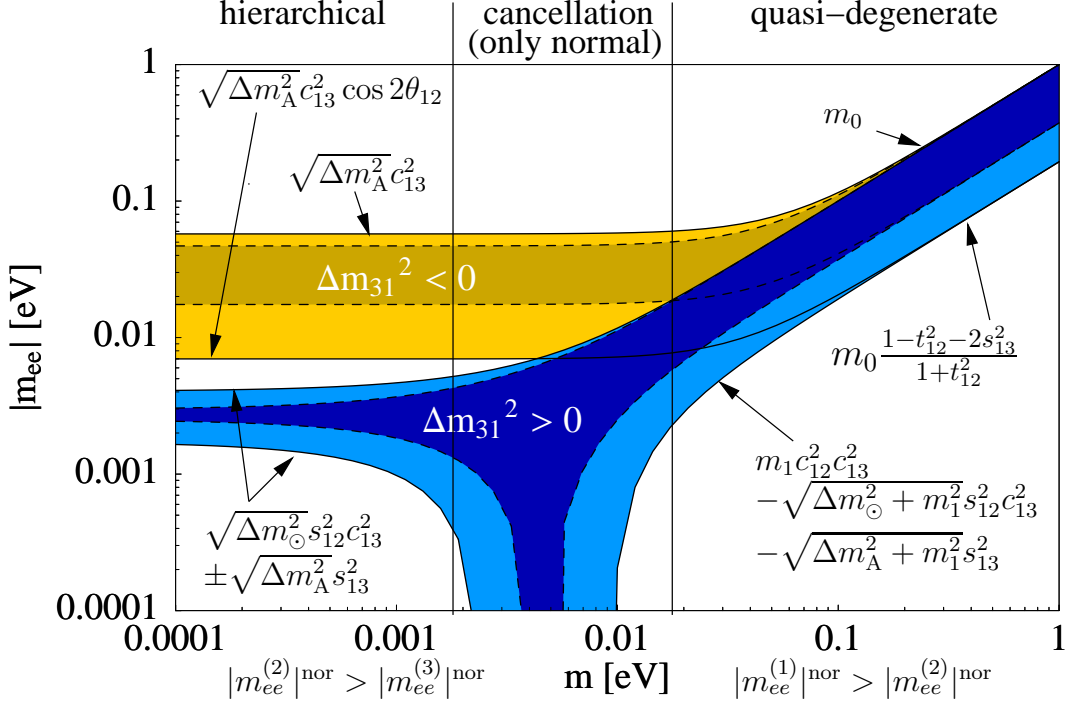


Figure 3-2: The main properties of the effective mass  $|m_{ee}|$  as a function of the smallest neutrino mass [121]. Here  $m$  denotes the common mass for the quasi-degenerate region and  $t_{ij} = \tan \theta_{ij}$ ,  $s_{ij} = \sin \theta_{ij}$ ,  $c_{ij} = \cos \theta_{ij}$ . Furthermore,  $\Delta m_A^2$  and  $\Delta m_\odot^2$  stands for the atmospheric mass-squared difference and the solar mass-squared difference, respectively.

- test the mass sum rule:

$$\Delta m_{13}^2 + \Delta m_{21}^2 + \Delta m_{32}^2 \stackrel{?}{=} 0, \quad (3.4)$$

which is an important prediction of the  $\nu$ SM. New physics like the light sterile neutrinos or non-standard interactions may induce non-trivial corrections to the effective oscillation frequencies  $\Delta m^2$ . Therefore, a precision test of the sum rule is an important probe of new physics beyond the Standard Model.

- reveal additional information regarding the neutrino mass hierarchy. As discussed in Refs. [69, 95], precision measurements of both  $|\Delta m_{ee}^2|$  and  $|\Delta m_{\mu\mu}^2|$  would provide new information for the neutrino mass hierarchy. A quantitative calculation is performed in Ref. [69], illustrating a significant improvement for the sensitivity of the neutrino mass hierarchy. The median sensitivity is increased from  $3 \div 3.5\sigma$  to  $4 \div 4.5\sigma$  [69] by considering a precision of 1% for  $|\Delta m_{\mu\mu}^2|$ . An individual 1.5% precision is estimated for both T2K [126] and NO $\nu$ A [82]. Therefore, a combined precision level [127] of 1% would be achievable by the moment when JUNO will start taking data.

In the following sections, the sensitivity of JUNO for precision measurements will be illustrated. Precision measurements of the oscillation parameters will be presented in Sec. 3.2. Moreover, the strategy for testing the unitarity of the lepton mixing matrix and the contribution of JUNO in this respect will be presented in Sec. 3.3. Finally, a summary will be given in Sec. 3.4.

### 3.2 Precision measurements of oscillation parameters

In the standard three-neutrino mixing framework, the relevant mass and mixing parameters for JUNO are  $\theta_{12}$ ,  $\theta_{13}$ ,  $\Delta m_{21}^2$  and  $\Delta m_{ee}^2$  (as the linear combination of  $\Delta m_{31}^2$  and  $\Delta m_{32}^2$ , see the definition in Eq. (2.2)). In the era of precision measurements, matter effects may not be negligible and deserve careful evaluations. In the presence of terrestrial matter effects, the survival probability of reactor antineutrinos is written as

$$P(\bar{\nu}_e \rightarrow \bar{\nu}_e) = 1 - \sin^2 2\theta_{13}^m [\cos^2 \theta_{12}^m \sin^2 \Delta_{31}^m + \sin^2 \theta_{12}^m \sin^2 \Delta_{32}^m] - \cos^4 \theta_{13}^m \sin^2 2\theta_{12}^m \sin^2 \Delta_{21}^m, \quad (3.5)$$

with  $\Delta_{ij}^m \equiv (\lambda_i^2 - \lambda_j^2)L/4E$ , and

$$\begin{aligned} \sin^2 2\theta_{12}^m &\simeq \sin^2 2\theta_{12} \left( 1 + 2 \frac{A_{CC}}{\Delta m_{21}^2} \cos 2\theta_{12} \right), \\ \lambda_2^2 - \lambda_1^2 &\simeq \Delta m_{21}^2 \left( 1 - \frac{A_{CC}}{\Delta m_{21}^2} \cos 2\theta_{12} \right), \end{aligned} \quad (3.6)$$

and

$$\begin{aligned} \sin^2 2\theta_{13}^m &\sim \sin^2 2\theta_{13} \left[ 1 + \mathcal{O}\left(\frac{A_{CC}}{\Delta m_{31}^2} \sin^2 \theta_{13}\right) \right], \\ \lambda_3^2 - \lambda_1^2 &\sim \Delta m_{31}^2 \left[ 1 + \mathcal{O}\left(\frac{A_{CC}}{\Delta m_{31}^2} \sin^2 \theta_{13}\right) \right]. \end{aligned} \quad (3.7)$$

Note that  $\lambda_i^2$  is the  $i$ th energy eigenvalue of the Hamiltonian in matter, and  $A_{CC} = 2\sqrt{2}EG_{\text{F}}N_e$  with  $N_e$  being the electron number density in matter and  $G_{\text{F}}$  the Fermi constant.. For the typical neutrino energy  $E$  and matter density  $\rho(x)$ , we obtain

$$\begin{aligned} \frac{A_{CC}}{\Delta m_{21}^2} \cos 2\theta_{12} &\simeq 0.5\% \times \frac{E}{4 \text{ MeV}} \times \frac{\rho(x)}{3 \text{ g/cm}}, \\ \frac{A_{CC}}{\Delta m_{31}^2} \sin^2 \theta_{13} &\simeq 1.5 \times 10^{-5} \times \frac{E}{4 \text{ MeV}} \times \frac{\rho(x)}{3 \text{ g/cm}}. \end{aligned} \quad (3.8)$$

For measurements with precision better than 1%, matter effects are negligible for the atmospheric neutrino oscillation parameters (i.e.,  $\theta_{13}$  and  $\Delta m_{31}^2$ ), but they are sizable (0.5%-0.1%) for the solar neutrino oscillation parameters (i.e.,  $\theta_{12}$  and  $\Delta m_{21}^2$ ). Therefore, it is important to consider matter effects when analyzing the real data. However, matter effects can be neglected for sensitivity studies as the corrections only affect the central values of oscillation parameters and not the sensitivity of MH and oscillation parameters.

In the history of neutrino oscillation observations, three different oscillation modes are observed in terms of effective two-flavor oscillations. The Super-Kamiokande Collaboration [128] observed the oscillation driven by  $(\Delta m_{32}^2, \sin^2 2\theta_{23})$  in the atmospheric muon neutrino disappearance channel (shown in the upper panel of Fig. 3-3). Later on, two reactor antineutrino experiments also presented the electron antineutrino survival probability as a function of  $L/E$ . The middle panel of Fig. 3-3 illustrates the oscillation determined by  $(\Delta m_{21}^2, \sin^2 2\theta_{12})$  at the KamLAND detector [129] with almost two complete cycles. The third case is shown in the lower panel of Fig. 3-3, which is characterized by  $(\Delta m_{31}^2, \sin^2 2\theta_{13})$  and observed in the Daya Bay spectral observation [130]. JUNO could be the first to observe an oscillation pattern containing two independent oscillation frequencies and multiple oscillation cycles. Because the reactor-detector distances are almost identical as

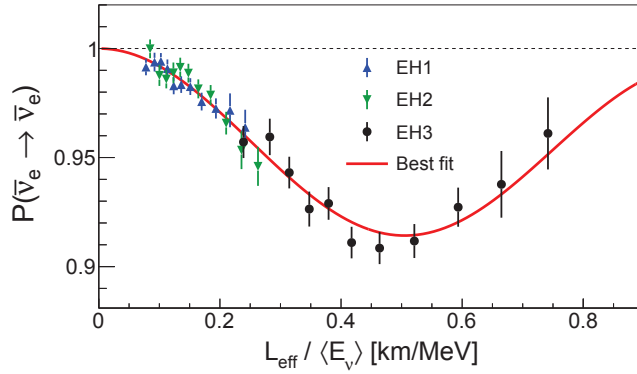
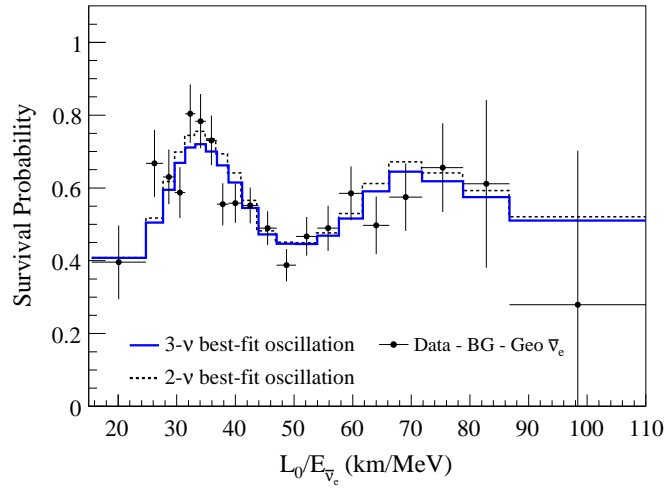
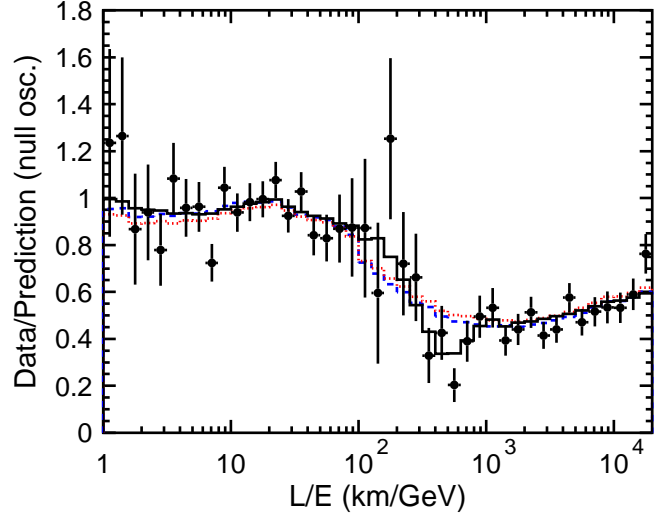


Figure 3-3: The observed neutrino events over the non-oscillation predictions as functions of  $L_{\text{eff}}$  (the effective baseline) over  $E$  (the neutrino energy) for Super-K [128] atmospheric neutrino oscillations (top), KamLAND [129] reactor antineutrino oscillations (middle) and Daya Bay [130] reactor antineutrino oscillations (bottom). They correspond to three different modes of effective two-flavor oscillations controlled by  $(\Delta m_{32}^2, \sin^2 2\theta_{23})$ ,  $(\Delta m_{21}^2, \sin^2 2\theta_{12})$  and  $(\Delta m_{31}^2, \sin^2 2\theta_{13})$ , respectively.

	$\Delta m_{21}^2$	$ \Delta m_{31}^2 $	$\sin^2 \theta_{12}$	$\sin^2 \theta_{13}$	$\sin^2 \theta_{23}$
Dominant Exps.	KamLAND	MINOS	SNO	Daya Bay	SK/T2K
Individual $1\sigma$	2.7% [129]	4.1% [131]	6.7% [116]	6% [130]	14% [132, 133]
Global $1\sigma$	2.6%	2.7%	4.1%	5.0%	11%

Table 3-1: Current precision for the five known oscillation parameters from the dominant experiments and the latest global analysis [29].

required by the MH measurement, antineutrinos from different reactors generate nearly identical energy spectra without smearing the oscillation patterns. This represents an important advantage for extracting the oscillation parameters with high precision. Fig. 3-1 shows the predicted prompt energy spectrum for the IBD events. Multiple oscillation patterns corresponding to the solar and atmospheric  $\Delta m^2$  scales are clearly visible.

Current precision for five known oscillation parameters are summarized in Table 3-1, where both the results from individual experiments and from the latest global analysis [29] are presented. Most of the oscillation parameters have been measured with an accuracy better than 10%. The least accurate case is for  $\theta_{23}$ , where the octant ambiguity hinders a precision determination. Among the four oscillation parameters accessible by JUNO,  $\theta_{13}$  can not be measured with a precision better than the Daya Bay one, which is expected to reach a 4% precision for this smallest mixing angle after 5 years of running. Therefore, we only discuss the prospect for precision measurements of  $\theta_{12}$ ,  $\Delta m_{21}^2$ , and  $|\Delta m_{ee}^2|$ <sup>1</sup>.

With the nominal setup [69] described in the MH measurement, the expected accuracy for the three relevant parameters is shown in Fig. 3-4, where the solid lines show the accuracy with all the other oscillation parameters fixed and the dashed lines show the accuracy with free oscillation parameters. The precision (dashed lines) of 0.54%, 0.24% and 0.27% can be obtained for  $\sin^2 \theta_{12}$ ,  $\Delta m_{21}^2$  and  $\Delta m_{ee}^2$ , respectively, after 6 years of running.

Several comments are listed as follows:

- Although only one single detector is considered, the precision on  $\theta_{12}$  at the sub-percent level is achievable because most of the sensitivity is from the spectral information. This property is illustrated in Fig. 3-5, showing the  $\theta_{12}$  accuracy with both the rate and shape information and with only the rate information.
- A precision of  $|\Delta m_{ee}^2|$  similar to  $\Delta m_{21}^2$  is obtained because each fast oscillation cycle gives a statistically independent measurement of  $|\Delta m_{ee}^2|$ . The combined result from the whole spectrum has a high statistical accuracy.
- The baseline differences may affect significantly the precision of  $\theta_{12}$  because different baselines can smear the oscillation pattern. For comparison, the precision of  $\theta_{12}$  could be improved from 0.54% to 0.35% if the baselines were identical for JUNO.
- The energy resolution impacts mainly  $|\Delta m_{ee}^2|$  because the relevant information is contained in the fine structure of fast oscillations. A quantitative dependence on the energy resolution for all the three oscillation parameters is shown in Fig. 3-6 with energy resolution ranging from 2% to 5%.

<sup>1</sup>There will be two degenerated solutions for  $|\Delta m_{ee}^2|$  in case of undetermined MH.

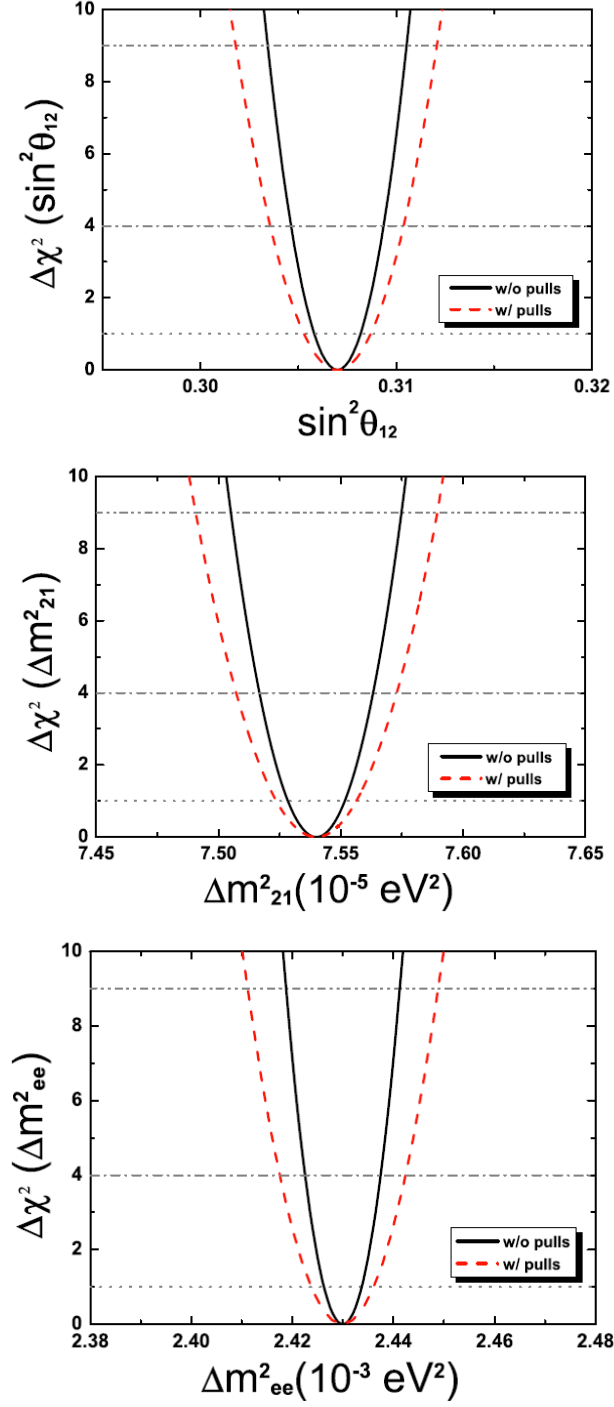


Figure 3-4: Expected accuracy for  $\sin^2\theta_{12}$ ,  $\Delta m^2_{21}$  and  $\Delta m^2_{ee}$  after 6 years of running at JUNO (i.e.,  $\mathcal{O}(100\text{k})$  events). The solid curves are obtained with all other oscillation parameters fixed, while the parameters are set free for the dashed curves.

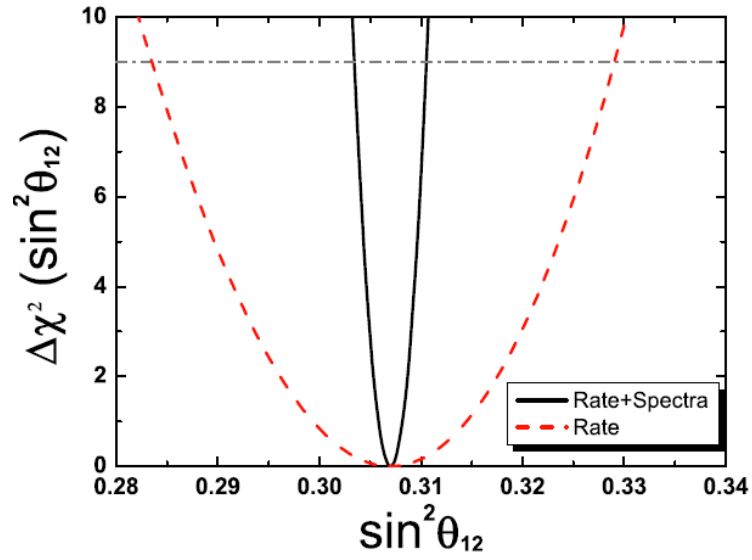


Figure 3-5: The precision of  $\sin^2 \theta_{12}$  with the rate plus shape information (solid curve) and rate-only information (dashed curve).

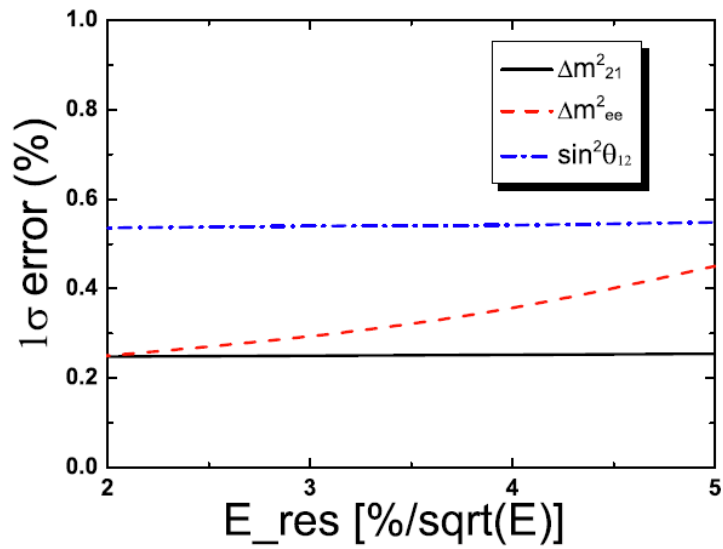


Figure 3-6: Dependence of the precision of  $\sin^2 \theta_{12}$ ,  $\Delta m_{21}^2$  and  $\Delta m_{ee}^2$  with the neutrino energy resolution.

	Nominal	+ B2B (1%)	+ BG	+ EL (1%)	+ NL (1%)
$\sin^2 \theta_{12}$	0.54%	0.60%	0.62%	0.64%	0.67%
$\Delta m_{21}^2$	0.24%	0.27%	0.29%	0.44%	0.59%
$ \Delta m_{ee}^2 $	0.27%	0.31%	0.31%	0.35%	0.44%

Table 3-2: Precision of  $\sin^2 \theta_{12}$ ,  $\Delta m_{21}^2$  and  $|\Delta m_{ee}^2|$  from the nominal setup to those including additional systematic uncertainties. The systematics are added one by one from left to right.

In the following a study of the effects of important systematic errors, including the bin-to-bin (B2B) energy uncorrelated uncertainty, the energy linear scale (EL) uncertainty and the energy non-linear (NL) uncertainty, will be discussed and the influence of background (BG) will be presented. As a benchmark, 1% precision for all the considered systematic errors is assumed. The background level and uncertainties are the same as in the previous chapter for the MH determination. In Table 3-2, we show the precision of  $\sin^2 \theta_{12}$ ,  $\Delta m_{21}^2$  and  $|\Delta m_{ee}^2|$  from the nominal setup to those including additional systematic uncertainties. The systematics are added one by one. Note the energy-related uncertainties are more important because the sensitivity is mostly from the spectrum distortion due to neutrino oscillations.

In summary, for the precision measurements of oscillation parameters, we can achieve the precision level of 0.5%–0.7% for the three oscillation parameters  $\sin^2 \theta_{12}$ ,  $\Delta m_{21}^2$  and  $|\Delta m_{ee}^2|$ . Therefore, precision tests of the unitarity of the lepton mixing matrix in Eq. (3.1), and the mass sum rule in Eq. (3.4) are feasible at unprecedented precision levels.

### 3.3 Tests of the standard three-neutrino paradigm

In this section, the strategy for testing the standard three-neutrino paradigm including the unitarity of the lepton mixing matrix and the sum rule of the mass-squared differences will be discussed. As only the lepton mixing elements of the electron flavor are accessible in reactor antineutrino oscillations, we here focus on testing the normalization condition in the first row of  $U$  as shown in Eq. (3.1). It should be noted that the  $\theta_{12}$  measurement in JUNO is mainly from the energy spectrum measurement, and  $\theta_{13}$  in Daya Bay is from the relative rate measurement. Therefore, an absolute rate measurement from either reactor antineutrino experiments or solar neutrino experiments is required to anchor the total normalization for the first row of  $U$ . For the test of the mass sum rule, an additional independent mass-squared difference is needed, where the most promising one is that from the long-baseline accelerator muon-neutrino disappearance channel, i.e.,  $\Delta m_{\mu\mu}^2$ .

To explain non-zero neutrino masses in new physics beyond the Standard Model (SM), a large class of models introduces additional fermion singlets to mix with the SM neutrinos. Thus the full neutrino mixing matrix will be enlarged, and an effective  $3 \times 3$  *non-unitary* mixing matrix emerges when one integrates out all those heavy fermion singlets (i.e., sterile neutrinos). The distinct effects within this class of SM extensions are well described by an effective field extension of the SM, called the Minimal Unitarity Violation (MUV) scheme. The MUV extension of the SM, characterized by two non-renormalizable effective operators, is defined as

$$\begin{aligned}
\mathcal{L}_{\text{MUV}} &= \mathcal{L}_{\text{SM}} + \delta\mathcal{L}^{d=5} + \delta\mathcal{L}^{d=6} \\
&= \mathcal{L}_{\text{SM}} + \frac{1}{2} c_{\alpha\beta}^{d=5} \left( \overline{L^c} \alpha \tilde{\phi}^* \right) \left( \tilde{\phi}^\dagger L_\beta \right) + c_{\alpha\beta}^{d=6} \left( \overline{L}_\alpha \tilde{\phi} \right) i \not{\partial} \left( \tilde{\phi}^\dagger L_\beta \right) + \text{H.c.}, \quad (3.9)
\end{aligned}$$

where  $\phi$  denotes the SM Higgs field, which breaks the electroweak (EW) symmetry spontaneously after acquiring the vacuum expectation value (vev)  $v_{\text{EW}} \simeq 246 \text{ GeV}$ , and  $L_\alpha$  represents the lepton

doublets. In addition, we use the notation  $\tilde{\phi} = i\tau_2\phi^*$ . The dimension-5 operator in Eq. (3.9) generates nonzero neutrino masses after EW symmetry breaking. On the other hand, the dimension-6 operator contributes to the kinetic terms of neutrinos, which leads to the *non-unitary* neutrino mixing matrix  $N$  after we canonically normalize the kinetic terms with a *non-unitary* transformation of the neutrino fields. Therefore, we can obtain the effective low-energy Lagrangian in the neutrino mass basis as

$$\begin{aligned} \mathcal{L}_{\text{MUV}} = & \frac{1}{2} (\bar{\nu}_i i \not{\partial} \nu_i - \bar{\nu}_i^c m_i \nu_i + \text{H.c.}) - \frac{g}{2\sqrt{2}} (W_\mu^+ \bar{l}_\alpha \gamma_\mu (1 - \gamma_5) N_{\alpha i} \nu_i + \text{H.c.}) \\ & - \frac{g}{2 \cos \theta_W} \left( Z_\mu \bar{\nu}_i \gamma^\mu (1 - \gamma_5) (N^\dagger N)_{ij} \nu_j + \text{H.c.} \right) + \dots \end{aligned} \quad (3.10)$$

where  $\nu_i$  denotes the four-component left-handed field for the  $i$ th neutrino mass eigenstate, and  $g$  is the coupling constant of the EW interactions. It should be noted that observable consequences of the *non-unitary* neutrino mixing matrix are encoded in the modifications of charged current (CC) and neutral current (NC) interactions of neutrinos in Eq. (3.10).

To test the unitarity violation, we first need a parametrization of the *non-unitary* neutrino mixing matrix  $N$ . Without loss of generality, one can write  $N$  as the product of a Hermitian matrix  $H$  and a unitary matrix  $U$ :

$$N = HU \equiv (1 + \eta)U, \quad (3.11)$$

where the elements of the  $\eta$  matrix are assumed to be  $\ll 1$  due to the smallness of the unitarity violation. Alternatively, one can use the parametrization for the Hermitian combination  $NN^\dagger$  as

$$(NN^\dagger)_{\alpha\beta} = (\mathbf{1}_{\alpha\beta} + \varepsilon_{\alpha\beta}), \quad (3.12)$$

where elements of the  $\varepsilon$  matrix are again assumed to be  $\ll 1$ , and can be related to the  $\eta$  matrix as

$$\varepsilon_{\alpha\beta} \simeq 2\eta_{\alpha\beta}, \quad (3.13)$$

up to higher orders of  $\eta_{\alpha\beta}$  and  $\varepsilon_{\alpha\beta}$ .

Unitarity violation can be tested in both the neutrino oscillation and EW interaction processes. There exist significant distinctions for the unitarity tests in the neutrino oscillation and EW interaction processes. For the neutrino oscillations, the neutrino flavors are tagged with the corresponding charged leptons in the production or detection processes, and the indices for neutrino mass eigenstates are distinguished using the interference effects. Thus we can determine the individual elements of the mixing matrix from neutrino oscillations [22, 24, 117]. On the other hand, in the EW interaction processes, neutrino mass eigenstates in the final states are not detected separately. The experiment rates correspond to sums over all possible mass eigenstates. Therefore, only the sums of products of the matrix elements (i.e.,  $NN^\dagger$ ) are measurable [22, 23].

In the following we shall briefly summarize the constraints of non-unitarity from the EW interaction processes [22, 23], which include both high and low energy observables:

- electroweak precision observables, including the weak mixing angle  $\sin^2 \theta_W$ ,  $Z$  decay parameters, the  $W$  boson mass and decay widths;
- leptonic universality tests;
- rare charged lepton decays (e.g.,  $\ell_\rho \rightarrow \ell_\sigma \gamma$ );
- CKM unitarity;



- NuTeV tests of weak interactions;
- low energy measurements of  $\sin^2 \theta_W$ , including parity non-conservation in Cesium, weak charge of the proton, and Möller scattering.

A global analysis of all above observables is performed to obtain the constraints on the elements of  $NN^\dagger$ . At 90% C.L., the constraints are [23]:

$$\left| NN^\dagger \right| = \begin{pmatrix} 0.9979 - 0.9998 & < 10^{-5} & < 0.0021 \\ < 10^{-5} & 0.9996 - 1.0 & < 0.0008 \\ < 0.0021 & < 0.0008 & 0.9947 - 1.0 \end{pmatrix}, \quad (3.14)$$

where the best-fit points for the off-diagonal  $\varepsilon_{\alpha\beta}$  and for  $\varepsilon_{\mu\mu}$  are at zero, and the preference of flavor-conserving non-unitarity is observed at 90% C.L. for  $\varepsilon_{ee}$  and below 90% CL for  $\varepsilon_{\tau\tau}$ . The off-diagonal non-unitarity parameters are mainly constrained from charged lepton flavor-changing decays. Particularly, the limit for  $\varepsilon_{e\mu}$  is dominated by the measurements of  $\mu \rightarrow e\gamma$ . The slight departure from zero for  $\varepsilon_{ee}$  is stemmed from the similar discrepancy in the invisible width of the  $Z$  boson, and that for  $\varepsilon_{\tau\tau}$  is from the internal correlation among  $\varepsilon_{\alpha\beta}$  in the MUV scheme. The EW interaction processes are only sensitive to the elements of  $NN^\dagger$ . The unitarity test in the form of  $N^\dagger N$  can only be inferred indirectly from Eq. (3.14) in the MUV scheme, where a precision level of around 3% can be obtained [22]. In this respect, the neutrino oscillations provide us an excellent opportunity to test the unitarity using the direct measurements of mixing matrix elements.

In the neutrino oscillation with a single transition channel, only one combination of the mixing matrix elements can be extracted from the oscillation amplitude. In addition, an absolute measurement of the zero-distance effect gives a direct test of unitarity conditions in  $NN^\dagger$  or  $N^\dagger N$ . For the former case, the global analysis of different oscillation channels is needed to test unitary conditions. As for the latter case, the level of unitarity tests from absolute rate measurements requires better understanding of the uncertainties in the neutrino flux normalization and detector efficiency. In the following part, we shall discuss the unique role of JUNO in the global picture of unitarity tests in neutrino oscillations.

For reactor antineutrino oscillations, only the  $\bar{\nu}_e$  survival probability is detectable, which can be expressed in the MUV scheme as

$$\begin{aligned} P_{\bar{\nu}_e \rightarrow \bar{\nu}_e} &= (|N_{e1}|^2 + |N_{e2}|^2 + |N_{e3}|^2)^2 \\ &- 4|N_{e1}|^2|N_{e2}|^2 \sin^2 \Delta_{21} - 4|N_{e3}|^2(|N_{e1}|^2 \sin^2 \Delta_{31} + |N_{e2}|^2 \sin^2 \Delta_{32}), \end{aligned} \quad (3.15)$$

where  $\Delta_{ij} = (m_i^2 - m_j^2)L/4E$ . It has to be noted that the mixing element  $N_{\alpha i}$  is only sensitive to the absolute measurements, which is directly compared to model predictions of the antineutrino production. To illustrate this effect, we define the effective mixing angles as

$$\sin^2 \tilde{\theta}_{13} \equiv \frac{|N_{e3}|^2}{|N_{e1}|^2 + |N_{e2}|^2 + |N_{e3}|^2}, \quad \tan^2 \tilde{\theta}_{12} \equiv \frac{|N_{e2}|^2}{|N_{e1}|^2}. \quad (3.16)$$

Therefore, we can rewrite Eq. (3.15) as

$$\begin{aligned} P_{\bar{\nu}_e \rightarrow \bar{\nu}_e} &= (|N_{e1}|^2 + |N_{e2}|^2 + |N_{e3}|^2) \times \left[ 1 - \cos^4 \tilde{\theta}_{13} \sin^2 2\tilde{\theta}_{12} \sin^2 \Delta_{21} \right. \\ &\left. - \sin^2 2\tilde{\theta}_{13} (\cos^2 \tilde{\theta}_{12} \sin^2 \Delta_{31} + \sin^2 \tilde{\theta}_{12} \sin^2 \Delta_{32}) \right]. \end{aligned} \quad (3.17)$$

Comparing to the probability in Eq. (2.1), it can be shown that only the rate normalization factor contributes to the unitarity test of Eq. (3.1), which mainly includes the uncertainties from the

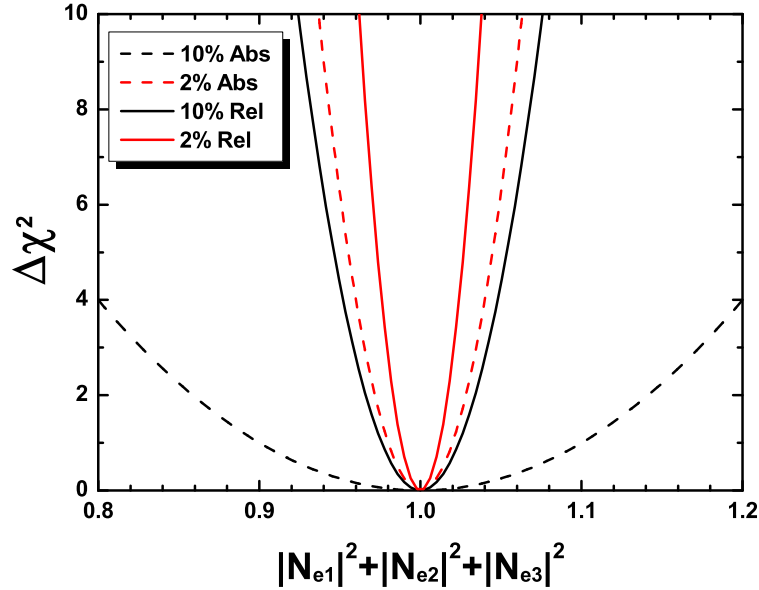


Figure 3-7: Different realizations of the unitarity violation test of the equation 3.1 in reactor antineutrino oscillations. See the text for details.

reactor flux normalization and detector efficiency. We refer this scenario as the absolute (Abs) measurement. On the other hand, we can define a relative (Rel) measurement, which combines the reactor spectral measurements of effective mixing parameters in Eq. (3.16) and the solar neutrino measurements to test the unitarity violation in an indirect way [117]. In Fig. 3-7, we present the two different scenarios of the unitarity test, which show obvious advantages for the combined analysis, for several considered uncertainties of reactor flux normalization. An additional 1% detector efficiency uncertainty is assumed. In the combined analysis, we assume a 4% final projected sensitivity for  $\sin^2 2\tilde{\theta}_{13}$  at Daya Bay, and a direct measurement of  $|N_{e2}|^2$  of the 4% level at a future SNO-like solar neutrino experiment. Finally, we may achieve the precision level of 1.2% for unitarity tests in the assumption of a 10% reactor normalization uncertainty, which could present a independent test of the reactor antineutrino anomaly.

Regarding the test of the mass sum rule in Eq. (3.4), JUNO is a powerful precision tool in measuring the two independent mass-squared differences  $\Delta m_{21}^2$  and  $|\Delta m_{ee}^2|$  as seen in Table 3-2, and can test the mass sum rule by inclusion of a third independent mass-squared difference in Eq. (2.6). Assuming a 1% precision level of  $|\Delta m_{\mu\mu}^2|$ , we can obtain the test of the mass sum rule in Eq. (3.4) at better than 1.8%, which represents an important test for the standard three-neutrino paradigm.

### 3.4 Conclusions

Precision measurement of the oscillation parameters and test of the standard three-neutrino framework constitute another important goal of the JUNO experiment. Among all the six oscillation parameters of neutrino oscillations, JUNO can measure  $\sin^2 \theta_{12}$ ,  $\Delta m_{21}^2$  and  $|\Delta m_{ee}^2|$  to the world-leading levels of 0.7%, 0.6%, and 0.5%, respectively. As a powerful detector with huge statistics, unprecedented energy resolution, the precision measurements of oscillation parameters are important for discrimination of the neutrino mixing patterns, the search of neutrinoless double beta decay, and test of the standard three-neutrino paradigm. Utilizing these above measurements, JUNO can

help in testing the unitarity relation of Eq. (3.1) and the mass sum rule of Eq. (3.4) to the levels of around 1.2% and 1.8%, respectively. Moreover, JUNO would be the first experiment to simultaneously observe neutrino oscillations from two different frequencies, and be the first experiment to observe more than two oscillation cycles.

## 4 Supernova Burst Neutrinos

Measuring the neutrino burst from the next nearby supernova (SN) is a premier target of low-energy neutrino physics and astrophysics. For a typical galactic distance of 10 kpc and typical SN parameters, JUNO will register about 5000 events from inverse beta decay (IBD),  $\bar{\nu}_e + p \rightarrow n + e^+$ , comparable to Super-Kamiokande, and many events from complementary channels, notably 2000 events from all-flavor elastic neutrino-proton scattering. With more than 300 events from neutrino-electron scattering, JUNO will also be the best detector for SN  $\nu_e$ . Such a high-statistics signal can determine a detailed neutrino “light curve” spectrum, and complete flavor information. In combination with other neutrino detectors, gravitational-wave detectors, and observations in various electromagnetic channels, a detailed astrophysical multi-messenger picture will emerge. In this way the standard paradigm of stellar core collapse will be confirmed, refuted or extended. The unique particle-physics lessons pioneered by the sparse SN 1987A data for the first time will be made precise and will extend to areas that depend on high statistics, good energy resolution, or flavor information, notably in the area of neutrino oscillations.

### 4.1 Core-collapse supernovae: What, where and when?

The baryonic matter in a spiral galaxy like our own Milky Way participates in an on-going cycle of star formation, nuclear processing, and ejection into interstellar space. Only low-mass stars with  $M \lesssim 0.85 M_\odot$ <sup>1</sup> live longer than the age of the universe of 14 billion years, whereas the progenitors of core-collapse SNe ( $M \gtrsim 6 \sim 8 M_\odot$ , depending on other parameters such as metallicity [134]) finish after less than a hundred million years. Intermediate-mass stars lose most of their mass during the red-giant phase in the form of a “stellar wind”, i.e., they mostly “evaporate”, leaving behind a white dwarf, a sub- $M_\odot$  compact star supported by electron degeneracy pressure. A more massive star, on the other hand, completes the nuclear reaction chains all the way to iron, forming a degenerate core. It ultimately collapses to nuclear density, ejects the remaining mass in a spectacular SN explosion, and emits 99% of the gravitational binding energy of the newly formed neutron star in the form of neutrinos and antineutrinos<sup>2</sup> of all flavors. The standard paradigm of how a core-collapse implosion reverses to a SN explosion is that a shock wave forms at core bounce, propagates outward, stalls at a radius of 100–200 km, and is finally revived by neutrino energy deposition [135, 136]. If this neutrino-driven explosion mechanism indeed captures the crucial physics remains open and could be tested with a high-statistics SN neutrino observation.

Core-collapse SNe encompass the spectral types Ib, Ic, and II, whereas SNe of Type Ia represent a different physical phenomenon [135, 137, 138]. The progenitor consists of a carbon-oxygen white dwarf, accreting matter from a binary companion until collapse (single degenerate scenario) or of two merging white dwarfs (double degenerate scenario), either way igniting explosive nuclear burning that disrupts the entire star—no stellar remnant survives. This thermonuclear explosion mechanism liberates a comparable amount of visible energy as a core-collapse SN which is driven by gravitational binding energy, liberates about 100 times more energy, but emits 99% of it in the form of neutrinos. The light curves of SNe Ia are very reproducible and they have been extensively used as cosmological standard candles, whereas core-collapse SNe are dimmer and show more diverse light curves. Core-collapse SNe occur in regions of active star formation, i.e., primarily the gaseous

---

Editors: Georg Raffelt (raffelt@mpp.mpg.de) and Shun Zhou (zhoush@ihep.ac.cn)

Major contributors: Gang Guo, Yufeng Li, Jiashu Lu, and Hao Wang

<sup>1</sup>In stellar astrophysics, masses are usually measured in units of the solar mass,  $1 M_\odot = 1.989 \times 10^{33}$  g, corresponding to  $1.20 \times 10^{57}$  nucleons.

<sup>2</sup>In the following we will generically use the term “neutrinos” to include both neutrinos and antineutrinos unless we explicitly distinguish between them.

and dust-filled disks of spiral galaxies, where around 2/3 of all SNe are of core-collapse type. Little star formation takes place in elliptical galaxies and they host only SNe Ia [137].

Core collapse may sometimes produce a black hole, but usually the compact remnant is a neutron star with a gravitational mass of up to  $2 M_{\odot}$ , often showing up as a pulsar. The collapse of this amount of matter to nuclear density, i.e., to a radius of 12–15 km, liberates 10–20% of its rest mass as gravitational binding energy, corresponding to some  $3 \times 10^{53}$  erg or  $2 \times 10^{59}$  MeV, exact numbers depending on the final neutron-star mass and the nuclear equation of state. Around 99% of this enormous amount of energy emerges as neutrinos, about 1% as kinetic energy of the explosion, and about 0.01% as light, still outshining the host galaxy. Star formation strongly favors low-mass stars, so core-collapse SNe are rare, yet the integrated cosmic energy density of SN neutrinos (the diffuse SN neutrino background or DSNB, see Sec. 5) is comparable to the integrated photon emission from all stars [139].

While every second a few core-collapse events happen in the visible universe, a JUNO-class detector covers only our own galaxy and its satellites, such as the Large Magellanic Cloud (LMC) at a distance of 50 kpc, the site of SN 1987A which provided the first and only observed SN neutrino signal [140]. A SN in Andromeda, at 750 kpc our nearest-neighbor big galaxy, would produce about one neutrino event in JUNO. Another SN in the LMC would produce around 200 events, a significant improvement on the SN 1987A statistics of a total of about two dozen events in three detectors. The most likely place of the next nearby SN, however, is the spiral disk of our own galaxy. The solar system is located close to the mid-plane of the disk at a distance of 8.7 kpc from the galactic center. The expected SN distance distribution has an average of around 10 kpc, usually taken as the fiducial distance, where JUNO would register around 5000 events.

However, the distance distribution is broad [141–143] and one cannot expect the next galactic SN to be “average” or “typical”. The distribution drops very quickly at or around 20 kpc, a distance that would still provide a whopping  $10^3$  events. On the other extreme, the distribution becomes very small at around 2 kpc, where the number of events would be around  $10^5$ . The nearest possible SN progenitor is the red supergiant Betelgeuse (Alpha Orionis) at a distance of around 0.2 kpc [144] producing around  $10^7$  events. Such a high event rate ( $\sim 20$  MHz at peak) is a big challenge for a huge liquid scintillator detector like JUNO. The data acquisition system of JUNO will be designed to accommodate as high event rates as possible to maintain the event by event detection.

Observing the next nearby SN in neutrinos is a once-in-a-lifetime opportunity that must not be missed. The galactic core-collapse SN rate is only one every few decades. It can be estimated from SN statistics in external galaxies [137, 145, 146], the galactic birth rate of massive stars [147], the pulsar birth rate [148, 149], the measured galactic abundance of the radioactive isotope  $^{26}\text{Al}$  which is produced in core-collapse SNe [150], and the historical SN rate over the past millennium [143, 151, 152]. A weak upper limit is obtained from the non-observation of a neutrino burst other than SN 1987A since 30 June 1980 when the Baksan Scintillator Telescope (BST) took up operation [153]. Together with subsequent neutrino detectors, no galactic SN neutrino burst would have been missed since that time. Assuming a galactic core-collapse rate of one every 30–40 years, the chances of observing a galactic SN burst over ten years of operation is around 30%, a great opportunity for a world-class fundamental observation. Coordination on detector maintenance with other big neutrino observatories, such as Super-Kamiokande and IceCube, will help to avoid missing a SN in all neutrino observatories simultaneously.

Our location in the mid-plane of the dust-filled galactic disk implies that visual SN observations are strongly impeded by obscuration. Therefore, only five historical SNe have been reported in the second millennium where the record may be reasonably complete [154]. Moreover, three out of these events were of the brighter type Ia (SNe 1006, 1572 and 1604). The two historical core-collapse SNe were the “Chinese SN” of 1054 that has produced the Crab Nebula and Crab Pulsar and

SN 1181. The Cas A remnant and non-pulsar hot neutron star may correspond to the uncertain SN observation of 1680 that would bring the historical second-millennium SNe up to six. These numbers are consistent with 2/3 or more of all galactic SNe being of core-collapse type and with a few galactic core-collapse events per century. Today, a galactic SN almost certainly would be observed in some electromagnetic band, notably in the near infra-red (IR) [143]. Actually, an IR record of the progenitor star almost certainly exists in the Two Micron All Sky Survey. The neutrino burst occurs several hours before the explosion and optical outburst, leaving time to issue a neutrino alert to the astronomical community. JUNO will join the Supernova Early Warning System (SNEWS) [155], a network of neutrino detectors, to participate in this important task.

## 4.2 Neutrino signature of core collapse

### 4.2.1 Neutrino-driven explosion

The neutrino signal from the next nearby, probably galactic, core-collapse SN will be picked up by many detectors that will measure tens to hundreds of events if the SN is at the fiducial distance of 10 kpc [156]. A completely different level of statistics will be provided by the large detectors Super-Kamiokande [157, 158] with around  $10^4$  reconstructed events and IceCube [159–161] with around  $10^6$  events of correlated noise increase. JUNO will play in this forefront league of large detectors that will provide detailed information about the neutrino signal and will have a number of unique capabilities, similar to the earlier LENA (Low-Energy Neutrino Astronomy) concept [162]. However, what is to be expected and what will it tell us?

The standard scenario of core-collapse SN explosion is the delayed, neutrino-driven explosion paradigm of Bethe and Wilson [163, 164]. The degenerate core of an evolved massive star becomes unstable by pressure loss due to electron absorption and photon dissociation on heavy nuclei. Usually this happens after completing all nuclear burning stages when the core consists of iron, the most tightly bound nucleus—the class of iron-core SNe. For the smallest progenitor masses of perhaps  $6\text{--}8 M_\odot$ , the dissociation begins before igniting the final burning stage when the oxygen-neon-magnesium core has become very degenerate—the class of electron-capture or O-Ne-Mg-core SNe. In both cases, the subsequent implosion on a near free-fall time is halted when nuclear density of around  $3 \times 10^{14} \text{ g cm}^{-3}$  is reached and the equation of state stiffens. This sudden “core bounce” forms a shock wave that propagates outward, ramming into the high- $Z$  material that keeps falling in at supersonic speed. Its dissociation absorbs energy and weakens the shock wave until it stagnates after reaching a radius of 100–200 km.

The absorption of electrons during infall produces a  $\nu_e$  flux until the core reaches densities of around  $10^{12} \text{ g cm}^{-3}$ . Afterwards neutrinos are trapped and the lepton number stored in the electron gas can no longer escape. This trapping at relatively low density is caused by the coherence of neutrino scattering on large nuclei. This effect means that the electron fraction per baryon,  $Y_e$ , after collapse is around 0.32, not much smaller than that of the pre-collapse core. Most of this trapped electron-lepton number will eventually escape by diffusion in the form of  $\nu_e$ . However, a “prompt  $\nu_e$  burst” or “deleptonization burst” lasting around 10 ms (Fig. 4-1), is released when the shock wave passes through the edge of the iron core, dissociates iron, and allows the outer layers to deleptonize by  $e^- + p \rightarrow n + \nu_e$ .

During the subsequent stalled-shock phase, or standing accretion shock phase, matter keeps falling in, heating the outer layers of the forming neutron star, and powering strong neutrino emission. Neutrinos and antineutrinos of all flavors are thermally produced and in addition a  $\nu_e$  excess flux emerges as a result of charged-current electron conversion fed by the electrons of the infalling material. The neutrino emission region with a thickness of a few tens of km above the

proto-neutron star preferentially emits  $\nu_e$  and  $\bar{\nu}_e$ . Heavy-flavor neutrino emission emerges from a somewhat deeper and hotter region. Typical neutrino energies of tens of MeV are too low to produce muon or tau leptons. Therefore,  $\nu_\mu$ ,  $\bar{\nu}_\mu$ ,  $\nu_\tau$  and  $\bar{\nu}_\tau$ , often collectively denoted as  $\nu_x$ , are not subject to charged-current reactions but rather are produced or absorbed in pairs. During the accretion phase  $L_{\nu_e}$  and  $L_{\bar{\nu}_e}$  are similar, but perhaps twice as large as each  $L_{\nu_x}$  (Fig. 4-1).

Neutrinos stream almost freely from the decoupling region or “neutrino sphere”, which however should be pictured as a broad region and depends on energy. Still,  $\nu_e$  and  $\bar{\nu}_e$  occasionally interact by charged-current reactions on nucleons on their way out, producing electrons and positrons. The balance of neutrino energy gain and loss is such that, midway between the neutrino sphere and the stalling shock wave, a “gain radius” develops such that there is a net gain of energy behind the shock wave. It is this effect that pumps energy back into this region, builds up pressure, and eventually revives the shock wave: The explosion takes off and the accretion flow is terminated. The proto-neutron star settles and the subsequent evolution is cooling and deleptonization, a detectable signal in JUNO lasting of order 10 s.

Numerical simulations, however, do not reliably produce explosions or sufficiently energetic explosions: neutrinos do not deposit quite enough energy. Spherically symmetric (one-dimensional, 1D) simulations produce explosions for the low-mass class of electron-capture SNe, but not for the higher-mass iron-core SNe. Early exploding models by the Livermore group had enhanced neutrino fluxes by the assumed effect of neutron-finger convection which today is no longer deemed realistic.

However, core-collapse SNe are generically 3D phenomena. The explosion of SN 1987A was strongly asymmetric, as seen in electromagnetic observations. Neutron stars often have large “kick velocities” of several hundreds to thousands of km/s, pointing to strong asymmetries in their birth process. 2D and 3D numerical simulations show the evolution of large-scale convective overturn between neutron star and standing shock wave after some 100 ms post bounce. Other dynamical instabilities have been discovered over the years, notably the standing accretion shock instability (SASI) [165], producing a large-scale sloshing or spiral motion and strong deformations of the shock front, and very recently the LESA phenomenon (lepton-emission self-sustained asymmetry) [166]. Multi-D effects may help with the explosion, for example by allowing the material to absorb more energy from the neutrino flux, yet explosions have not been systematically successful. A suite of axisymmetric (2D) models shows explosions, but in 3D the same models do not explode in current simulations [167].

Systematic 3D simulations with sophisticated multi-flavor Boltzmann neutrino transport are only beginning and still depend on significant approximations. Therefore, the question remains if numerical improvements, notably increased spatial resolution, will actually produce systematic explosions or if entirely new physical ingredients are required as some authors have argued. In principle, these could be of the astrophysical type (rotation, magnetic fields, new hydrodynamical effects) or of the particle physics type (e.g., energy transfer to the shock wave by new particles). It is also not known how strongly the explosion physics depends on details of the progenitor model and if some or many cases also fail in nature, leading to black-hole formation. These failed SNe would produce a strong neutrino signal because the black-hole collapse would occur only after a period of shock-wave stagnation. The non-observation of a galactic neutrino burst since 1980 provides only a weak upper limit on the galactic rate of failed SNe.

Core-collapse SNe probably create half of the chemical elements heavier than iron. The conditions depend on the proton-to-neutron ratio as well as the entropy in the hot SN outflows which are determined by neutrinos and particularly by the fluxes and spectra of  $\nu_e$  and  $\bar{\nu}_e$  through beta processes. Observations of nucleosynthesis yields in SNe provide some information about the conditions in this region, and conversely measuring the neutrino flavor-dependent neutrino fluxes provides crucial information on these conditions. Nucleosynthesis in the SN environment, like the explosion

mechanism itself, is a major subject of numerical study that would benefit from high-statistics neutrino data.

### 4.2.2 Three-phase neutrino signal

If the core-collapse scenario indeed roughly follows the stages described in the previous section, one expects a neutrino signal with three characteristic phases as shown in Fig. 4-1. In a high-statistics observation one should consider these essentially as three different experiments, each holding different and characteristic lessons for particle- and astrophysics. The shown example is a spherically symmetric model from the Garching group, based on a  $27 M_{\odot}$  model [168, 169]. The explosion is triggered “by hand” by quenching the accretion flow between 500–600 ms. The final neutron-star baryonic mass is  $1.762 M_{\odot}$  and it emits a total of  $3.24 \times 10^{53}$  erg of energy in neutrinos, corresponding to a mass equivalent of  $0.180 M_{\odot}$ . Its final gravitational mass is  $1.582 M_{\odot}$  and thus a typical neutron star. This model is comparable to the example from the Basel group shown in the LENA White Paper [162], except that the Garching models include nucleon recoils in the treatment of neutrino transport, leading to a much smaller flavor-dependent spread in average neutrino energies.

For each of the three phases ( $\nu_e$  Burst, Accretion, Cooling) we show the luminosities in  $\nu_e$ ,  $\bar{\nu}_e$ , and  $\nu_x$ , where the latter stands for any of  $\nu_{\mu}$ ,  $\bar{\nu}_{\mu}$ ,  $\nu_{\tau}$  and  $\bar{\nu}_{\tau}$ , and the average energies. We further show the IBD rate in JUNO for two cases: No flavor conversion at all (curves marked  $\bar{\nu}_e$ ) and assuming complete flavor conversion (curves marked  $\bar{\nu}_x$ ). The actual neutrino flavor conversions lead to an IBD rate lying between the curves of two extreme cases. Finally we show the rate of elastic proton scattering caused by all six species, assuming a detection threshold for proton recoils of 0.2 MeV visible energy. More discussions about the detection of SN neutrinos can be found in the following section. A few comments are in order on the three phases of neutrino signals:

**1. Infall, Bounce and Shock Propagation.**—During the core collapse, the electron capture on protons and heavy nuclei already starts to produce  $\nu_e$ . The first tens of ms after bounce show the characteristic prompt  $\nu_e$  burst, the emission of  $\bar{\nu}_e$  is at first suppressed, and emission of other flavors only begins. The flux and spectral characteristics are rather reproducible, independently of specific assumptions, e.g., concerning the progenitor mass and nuclear equation of state. The IBD rate shows a characteristic rise-time difference between  $\bar{\nu}_e$  and  $\bar{\nu}_x$  that can be used to diagnose neutrino flavor conversion.

**2. Accretion Phase (Shock Stagnation).**—Few tens to few hundreds of ms, depending on progenitor properties and other parameters. Neutrino emission is powered by accretion flow. Luminosities in  $\nu_e$  and  $\bar{\nu}_e$  perhaps as much as a factor of two larger than each of the  $\nu_x$  fluxes. Pronounced hierarchy of average energies  $\langle E_{\nu_e} \rangle < \langle E_{\bar{\nu}_e} \rangle < \langle E_{\nu_x} \rangle$ , energies increasing until explosion. Large-scale convection, SASI and LESA build up, implying fast time variations and directional dependence of the neutrino signal. The luminosity drop at around 200 ms represents the infall of the Si/O interface—the accretion rate and therefore luminosity clearly drops afterwards.

**3. Cooling.**—When the explosion has taken off (here triggered between 500–600 ms by numerically quenching the accretion flow) the luminosity drops and is subsequently powered by cooling of the proto-neutron star. Approximate luminosity equipartition between species and  $\langle E_{\nu_e} \rangle < \langle E_{\bar{\nu}_e} \rangle \sim \langle E_{\nu_x} \rangle$ . Number flux of  $\nu_e$  enhanced because of de-leptonization.

Finally, it is worth mentioning that there exist alternatives to the delayed, neutrino-driven explosion paradigm, such as the acoustic mechanism [170] and magnetohydrodynamically driven explosion [171]. A successful explosion could also be triggered by a QCD phase transition [172–174].



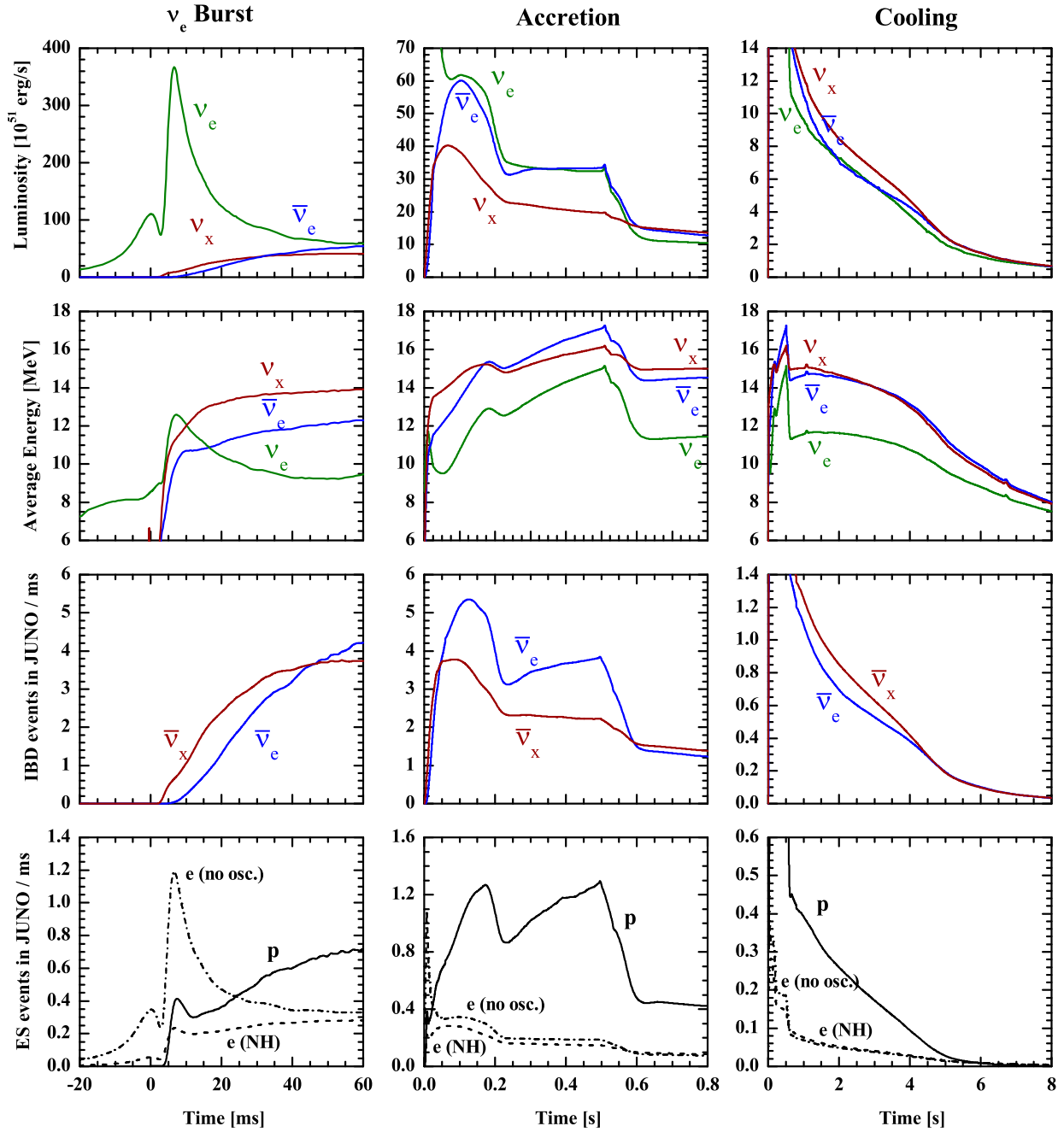


Figure 4-1: Three phases of neutrino emission from a core-collapse SN, from left to right: (1) Infall, bounce and initial shock-wave propagation, including prompt  $\nu_e$  burst. (2) Accretion phase with significant flavor differences of fluxes and spectra and time variations of the signal. (3) Cooling of the newly formed neutron star, only small flavor differences between fluxes and spectra. (Based on a spherically symmetric Garching model with explosion triggered by hand during 0.5–0.6 ms [168,169]. See text for details.) We show the flavor-dependent luminosities and average energies as well as the IBD rate in JUNO assuming either no flavor conversion (curves  $\bar{\nu}_e$ ) or complete flavor swap (curves  $\bar{\nu}_x$ ). The elastic proton (electron) scattering rate uses all six species and assumes a detection threshold of 0.2 MeV of visible proton (electron) recoil energy. For the electron scattering, two extreme cases of no flavor conversion (curves no osc.) and flavor conversion with a normal neutrino mass ordering (curves NH) are presented.

The neutrino signals in all these cases may be quite different from those shown in Fig. 4-1, and thus a high-statistics measurement of time and energy spectra of neutrino events can be used to distinguish one explosion mechanism from another.

### 4.3 Detection channels in JUNO

#### 4.3.1 Time-integrated event rates

In order to estimate the expected neutrino rates in JUNO, we assume a linear alkylbenzene (LAB) based liquid scintillator and a fiducial mass of 20 kiloton, implying about  $1.5 \times 10^{33}$  target protons. For a typical galactic SN at 10 kpc, there will be more than 5000 neutrino events solely from the IBD channel. Such a high-statistics observation definitely allows us to probe the time-dependent features of SN neutrinos. However, the time-integrated event rates will give a first impression on the capability of JUNO detector in SN neutrino detection. For simplicity, instead of taking the simulated results in Fig. 4-1 as input, we model the time-integrated neutrino spectra as  $f_\nu(E_\nu) \propto E_\nu^\alpha \exp[-(1 + \alpha)E_\nu/\langle E_\nu \rangle]$  with a nominal index  $\alpha = 3$  and  $\langle E_\nu \rangle$  being the average neutrino energy [175]. Furthermore, a total energy of  $3 \times 10^{53}$  erg is assumed to be equally distributed in neutrinos and antineutrinos of three flavors. As the average neutrino energies are both flavor- and time-dependent, we calculate the event rates for three representative values  $\langle E_\nu \rangle = 12$  MeV, 14 MeV and 16 MeV, and in each case the average energy is taken to be equal for all flavors so that one can easily observe the impact of average neutrino energies on the event rates. The total numbers of neutrino events for the main channels in JUNO are summarized in Table 4-1, where no neutrino flavor conversions are considered. For the numerical model introduced in the previous section, the time-dependent event rates for IBD are displayed in the third row of Fig. 4-1, while those for elastic proton and electron scattering are given in the fourth row. The neutrino event spectra with respect to the visible energy in six main reaction channels are shown in Fig. 4-2. Some comments on the different signal channels are in order.

(1) The IBD is the dominant channel for SN neutrino detection in both scintillator and water-Cherenkov detectors, in which a large number of free protons are available. In the IBD reaction

$$\bar{\nu}_e + p \rightarrow e^+ + n, \quad (4.1)$$

the neutrino energy threshold is  $E_\nu^{\text{th}} = \Delta + m_e \approx 1.806$  MeV, where  $\Delta \equiv m_n - m_p \approx 1.293$  MeV is the neutron-proton mass difference. The energy of the incident neutrino can be reconstructed from the positron energy via  $E_\nu \approx E_e + \Delta$ . The energy deposition and the annihilation of the positron with an ambient electron into 0.511-MeV  $\gamma$ 's give rise to a prompt signal. In addition, the neutron is captured on a free proton with an average lifetime of about 200  $\mu\text{s}$ , producing a 2.2-MeV  $\gamma$ . Hence the time coincidence of the prompt and delayed signals increases greatly the tagging power. A precise calculation of the IBD cross section has been performed in Ref. [176,177]. In general, the angular distribution of the positron is nearly isotropic, so it is difficult to extract the directional information of neutrinos. However, the forward shift of the neutron capture vertex may be used to further reduce backgrounds and locate the neutrino source [177,178].

(2) As an advantage of the scintillator detector, the charged-current (CC) interaction on  $^{12}\text{C}$  takes place for both  $\nu_e$  and  $\bar{\nu}_e$  via

$$\nu_e + {}^{12}\text{C} \rightarrow e^- + {}^{12}\text{N}, \quad (4.2)$$

$$\bar{\nu}_e + {}^{12}\text{C} \rightarrow e^+ + {}^{12}\text{B}. \quad (4.3)$$

The energy threshold for  $\nu_e$  is 17.34 MeV, while that for  $\bar{\nu}_e$  is 14.39 MeV. The subsequent beta decays of  $^{12}\text{B}$  and  $^{12}\text{N}$  with a 20.2 ms and 11 ms half-life, respectively, lead to a prompt-delayed

Channel	Type	Events for different $\langle E_\nu \rangle$ values		
		12 MeV	14 MeV	16 MeV
$\bar{\nu}_e + p \rightarrow e^+ + n$	CC	$4.3 \times 10^3$	$5.0 \times 10^3$	$5.7 \times 10^3$
$\nu + p \rightarrow \nu + p$	NC	$0.6 \times 10^3$	$1.2 \times 10^3$	$2.0 \times 10^3$
$\nu + e \rightarrow \nu + e$	ES	$3.6 \times 10^2$	$3.6 \times 10^2$	$3.6 \times 10^2$
$\nu + {}^{12}\text{C} \rightarrow \nu + {}^{12}\text{C}^*$	NC	$1.7 \times 10^2$	$3.2 \times 10^2$	$5.2 \times 10^2$
$\nu_e + {}^{12}\text{C} \rightarrow e^- + {}^{12}\text{N}$	CC	$0.5 \times 10^2$	$0.9 \times 10^2$	$1.6 \times 10^2$
$\bar{\nu}_e + {}^{12}\text{C} \rightarrow e^+ + {}^{12}\text{B}$	CC	$0.6 \times 10^2$	$1.1 \times 10^2$	$1.6 \times 10^2$

Table 4-1: Numbers of neutrino events in JUNO for a SN at a typical distance of 10 kpc, where  $\nu$  collectively stands for neutrinos and antineutrinos of all three flavors and their contributions are summed over. Three representative values of the average neutrino energy  $\langle E_\nu \rangle = 12$  MeV, 14 MeV and 16 MeV are taken for illustration, where in each case the same average energy is assumed for all flavors and neutrino flavor conversions are not considered. For the elastic neutrino-proton scattering, a threshold of 0.2 MeV for the proton recoil energy is chosen.

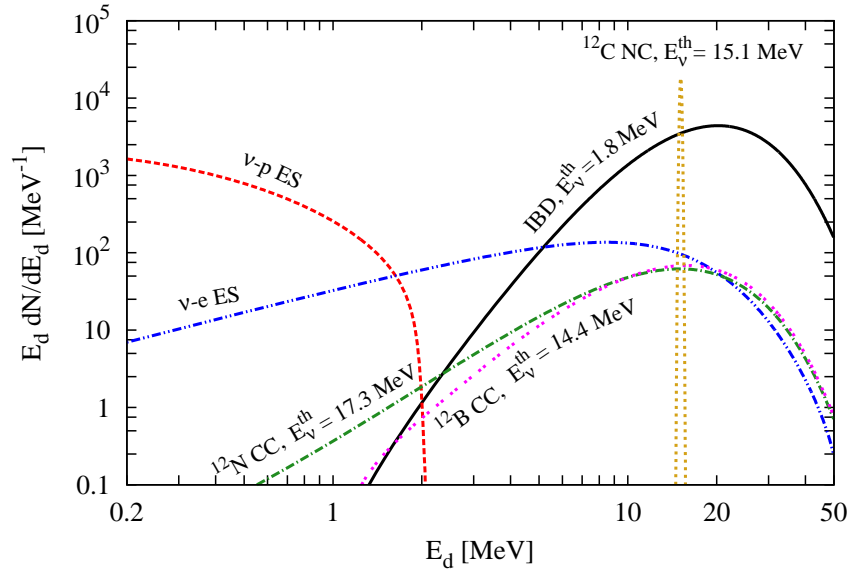


Figure 4-2: The neutrino event spectra with respect to the visible energy  $E_d$  in the JUNO detector for a SN at 10 kpc, where no neutrino flavor conversions are assumed for illustration and the average neutrino energies are  $\langle E_{\nu_e} \rangle = 12$  MeV,  $\langle E_{\bar{\nu}_e} \rangle = 14$  MeV and  $\langle E_{\nu_x} \rangle = 16$  MeV. The main reaction channels are shown together with the threshold of neutrino energies: (1) IBD (black and solid curve),  $E_d = E_\nu - 0.8$  MeV; (2) Elastic  $\nu$ - $p$  scattering (red and dashed curve),  $E_d$  stands for the recoil energy of proton; (3) Elastic  $\nu$ - $e$  scattering (blue and double-dotted-dashed curve),  $E_d$  denotes the recoil energy of electron; (4) Neutral-current reaction  ${}^{12}\text{C}(\nu, \nu'){}^{12}\text{C}^*$  (orange and dotted curve),  $E_d \approx 15.1$  MeV; (5) Charged-current reaction  ${}^{12}\text{C}(\nu_e, e^-){}^{12}\text{N}$  (green and dotted-dashed curve),  $E_d = E_\nu - 17.3$  MeV; (6) Charged-current reaction  ${}^{12}\text{C}(\bar{\nu}_e, e^+){}^{12}\text{B}$  (magenta and double-dotted curve),  $E_d = E_\nu - 13.9$  MeV.

coincident signal. Hence the charged-current reactions in Eqs. (4.2) and (4.3) provide a possibility to detect separately  $\nu_e$  and  $\bar{\nu}_e$  [179]. The cross section of neutrino interaction on  ${}^{12}\text{C}$  has been calculated in Ref. [180] by using a direct evaluation of nuclear matrix elements from experimental data at that time. Recent calculations based on the nuclear shell model and the random-phase

approximation can be found in Ref. [181]. The cross section has been measured in the LSND experiment, and the result is well compatible with theoretical calculations [182].

(3) The neutral-current (NC) interaction on  $^{12}\text{C}$  is of crucial importance to probe neutrinos of non-electron flavors, i.e.,

$$\nu + {}^{12}\text{C} \rightarrow \nu + {}^{12}\text{C}^*, \quad (4.4)$$

where  $\nu$  collectively denotes neutrinos and antineutrinos of all three flavors. A 15.11-MeV  $\gamma$  from the deexcitation of  $^{12}\text{C}^*$  to its ground state is a clear signal of SN neutrinos. The cross section can be found in Refs. [180, 181], and has also been measured in the LSND experiment [182]. Since the neutrinos of non-electron flavors  $\nu_x$  have higher average energies, the neutral-current interaction is most sensitive to  $\nu_x$ , offering a possibility to pin down the flavor content of SN neutrinos. However, the recoil energy of  $^{12}\text{C}$  is negligible and the final-state neutrino is invisible to current detectors, implying the impossibility to reconstruct neutrino energy event-by-event in this channel. Note that the neutral-current processes are not affected by the neutrino flavor oscillations.

(4) In the elastic scattering (ES) of neutrinos on electrons, the scattered electrons carry the directional information of incident neutrinos, and thus can be used to locate the SN. This is extremely important if a SN is hidden in the galactic gas and dust clouds and the optical signal is obscured. The elastic scattering

$$\nu + e^- \rightarrow \nu + e^- \quad (4.5)$$

is most sensitive to  $\nu_e$  because of its largest cross section, which is particularly useful in detecting the prompt  $\nu_e$  burst. The cross sections of neutrino- and antineutrino-electron elastic scattering have been computed and summarized in Ref. [183], where the electroweak radiative corrections are also included. Unlike water Cherenkov detectors such as Super-Kamiokande, it is challenging for a liquid scintillator detector to determine the SN direction by reconstructing the direction of the scattered electron, unless the PMT time response is quick enough and the detector is precisely understood. For high-energy electrons, it might be possible to make use of Cherenkov light to obtain some directional information.

(5) The elastic scattering of neutrinos on protons has been proposed as a promising channel to measure SN neutrinos of non-electron flavors [184, 185]:

$$\nu + p \rightarrow \nu + p. \quad (4.6)$$

Although the total cross section is about four times smaller than that of the IBD reaction, the contributions from all the neutrinos and antineutrinos of three flavors will compensate for the reduction of cross section, especially if the average energy of the SN neutrinos is large. In this channel, the proton recoil energy  $T_p \leq 2E_\nu^2/m_p$  is highly suppressed by the nucleon mass, so the precise determination of the proton quenching factor and a low energy threshold are required to reconstruct neutrino energy and accumulate sufficient statistics. The cross section of elastic neutrino-proton scattering was calculated a long time ago [186], and has been recently simplified for low-energy neutrinos [184]. However, the cross section receives a dominant contribution from the proton axial form factor, which at present is only known with a 30% uncertainty if the strange-quark contribution to the nucleon spin is taken into account.

### 4.3.2 Elastic neutrino-proton scattering

As shown in Refs. [184, 185], it is possible to reconstruct the energy spectrum of  $\nu_x$  at a large scintillator detector, which is very important to establish the flavor conversions and the total energy of SN neutrinos. Therefore, it is worthwhile to study in more detail the potential of JUNO to detect SN neutrinos in this channel.

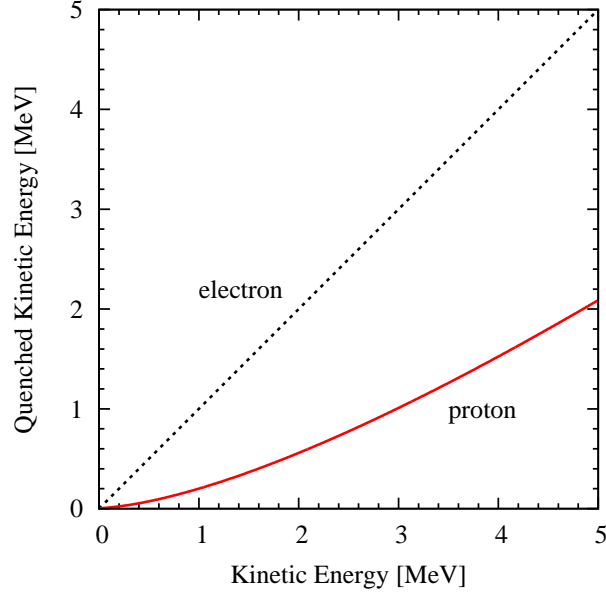


Figure 4-3: The light output of a recoiled proton in a LAB-based scintillator detector, where the Birk's constant is taken to be  $k_B = 0.0098 \text{ cm MeV}^{-1}$  according to the measurement in Ref. [187]. The energy deposition rates of protons in hydrogen and carbon targets are taken from the PSTAR database [188], and combined to give the deposition rate in a LAB-based scintillator according to the ratio of their weights in the detector.

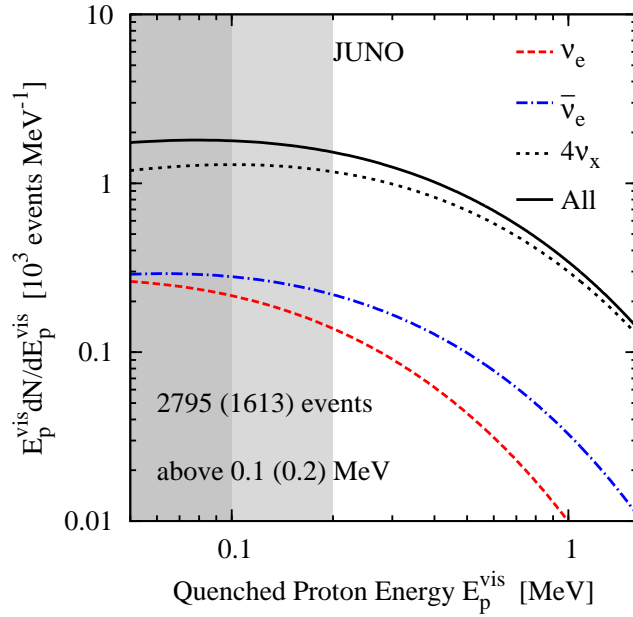


Figure 4-4: Event spectrum of the elastic neutrino-proton scattering in JUNO. The average neutrino energies are  $\langle E_{\nu_e} \rangle = 12 \text{ MeV}$ ,  $\langle E_{\bar{\nu}_e} \rangle = 14 \text{ MeV}$  and  $\langle E_{\nu_x} \rangle = 16 \text{ MeV}$ . The total numbers of events have been calculated by imposing an energy threshold of 0.1 or 0.2 MeV.

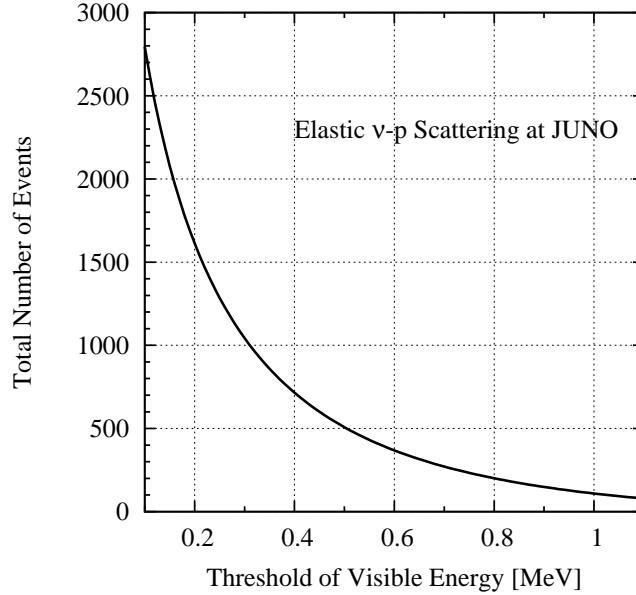


Figure 4-5: Impact of energy threshold on the elastic  $\nu$ - $p$  scattering events in JUNO, where the input parameters are the same as in Fig. 4-4.

For a realistic measurement of the neutrino energy spectrum, a low-energy threshold and a satisfactory reconstruction of proton recoil energy are required. The reason is simply that low-energy protons are highly ionizing particles, implying that their energy-loss rate is much higher compared to electrons of the same energy. From Fig. 4-3, one can observe that the light output of a low-energy proton is significantly quenched relative to an electron losing the same amount of energy. The measurement of the proton quenching factor for various liquid scintillators has been performed in Ref. [187], and further applied to the SN neutrino detection. For JUNO, the proton quenching factor will be measured for the ultimately implemented scintillator.

In Fig. 4-4, the event spectrum of elastic neutrino-proton scattering in JUNO has been given, where a hierarchical spectrum of average neutrino energies is assumed. It is evident that the events are dominated by the heavy-lepton flavors, for which the average energy is higher than that for the electron flavor. However, as indicated by the sophisticated numerical simulations, the average energies of  $\bar{\nu}_e$  and  $\nu_x$  are quite similar and larger than that of  $\nu_e$  in the late phases (see Fig. 4-1). Whereas the  $\bar{\nu}_e$  spectrum can be well measured in the IBD channel, the  $\nu_x$  spectrum can only be determined in the neutrino-proton channel. The reconstruction of neutrino energy spectrum allows us to figure out the total energy emitted in neutrinos and to extract the information of flavor conversions. Although the neutrino-proton scattering is most sensitive to the high-energy tail of the neutrino spectrum, one can fit the observed data by using a thermal spectrum with an unknown average energy [185]. In JUNO, the total number of events is about 1600 above a threshold of 0.2 MeV and 2800 above 0.1 MeV. Singles from radioactivity will be controlled to tens of Hz in the JUNO detector. The major impediment is the coincidence of PMT dark noise, limiting the energy threshold at  $\sim 0.3$  MeV. A sophisticated trigger approach that rejects low energy events with vertices at the detector center is under study, which could lower the energy threshold down to  $\sim 0.1$  MeV with negligible inefficiency. In Fig. 4-5, the dependence of total events on the energy threshold is illustrated, where one can see that the events decrease dramatically for a higher energy threshold. Even at the worst case, the threshold  $\sim 0.7$  MeV as required by reactor neutrino

physics, the neutrino-proton scattering is still the best channel to measure the SN neutrinos of heavy-lepton flavors. The time-dependent event rate for the Garching SN model has been shown in Fig. 4-1, where one can see that a few tens of proton scattering events can be observed for the prompt  $\nu_e$  burst, independently of the flavor oscillations. The reason is simply that the elastic proton scattering is governed by the NC interaction, which is flavor blind.

### 4.3.3 Backgrounds

There exist various backgrounds for SN neutrino detection, and the backgrounds may vary by the detector location and type, as well as the signal channel. In general, background is not a serious concern for a SN neutrino burst since it lasts only for about 10 seconds. Possible background sources for a given signal channel are natural radioactivities (less than 10 Hz at  $> 0.7$  MeV), cosmogenic backgrounds ( $\sim 3$  Hz muon rate in the JUNO liquid scintillator detector), the SN neutrinos themselves, and other neutrinos. Detailed background estimation can be found in the Appendix.

Inverse beta decay is the major signal channel of the SN burst detection in JUNO. Reactor neutrinos and geo-neutrinos contribute as backgrounds. In a 10-second interval, there will be 0.01 IBD from reactors and 0.0002 IBD from geo-neutrinos, which is totally negligible for any detectable SN. Other backgrounds, such as that from low-energy atmospheric antineutrinos, natural radioactivities, and cosmogenic isotopes are even smaller.

The other charged-current channels that produce  $^{12}\text{N}$  and  $^{12}\text{B}$  as delayed signals will not suffer from the reactor neutrinos and geo-neutrinos, either. Coincidence of IBD prompt signals from the SN burst is a major obstacle to identify these events, since the delayed signal from the decay of  $^{12}\text{N}$  or  $^{12}\text{B}$  has a long lifetime of tens of ms. Vertex correlation between the prompt  $e^-$  ( $e^+$ ) and the delayed  $^{12}\text{N}$  ( $^{12}\text{B}$ ) signals can reject the coincidence backgrounds to a negligible level, unless the SN neutrino rate is extremely high.

The neutral-current channel that produces a  $^{12}\text{C}^*$  can be identified with the 15.11 MeV  $\gamma$ , which is much higher than the natural radioactivities. There are 0.1  $^8\text{Li}$  and 0.1  $^{12}\text{B}/^{12}\text{N}$  in the cosmogenic isotopes in 10 seconds. With the energy selection around 15.11 MeV, they are negligible. The  $^{12}\text{C}^*$  signal locates in the energy region of the IBD prompt signal and the  $^{12}\text{N}$  and  $^{12}\text{B}$  decays of the SN neutrinos. Again, rejection can be done with vertex correlation and time correlation of the other two types of SN neutrinos.

Backgrounds should be estimated with more care for the elastic neutrino-proton scattering since they are singles of low visible energy. In the cosmogenic isotopes, there are 1.9  $^{11}\text{C}$ , 0.6  $^7\text{B}$ , and 0.6 other longlived isotopes in the 10 seconds interval. Radioactive decays of scintillator materials and surroundings lead to the dominant backgrounds. In the energy region from 0.2 to 1 MeV, it will arise from the  $\beta$ -decay of the noble gas  $^{85}\text{Kr}$  and the lead-daughter  $^{210}\text{Bi}$ , which is fed by the long-lived isotope  $^{210}\text{Pb}$  ( $\tau = 32$  yrs). The JUNO baseline design without distillation foresees an activity of  $50 \mu\text{Bq}/\text{m}^3$  for  $^{85}\text{Kr}$  and a concentration of  $1.4 \times 10^{-22}$  g/g for  $^{210}\text{Pb}$ . The corresponding background rates in the 10 second interval are 10 events of  $^{85}\text{Kr}$  and  $\sim 70$  events of  $^{210}\text{Bi}$ . Even assuming low spectral energies for the SN neutrinos, the proton recoil signal would be dominating by at least one order of magnitude.

The neutrino-electron scattering has similar backgrounds as the neutrino-proton scattering. It has higher visible energy since the quenching effect for the electron is small. If we select only high energy events, it has much less background than the neutrino-proton scattering.

Faked events created by random coincidences of the PMT dark noise can be rejected by vertex selection. Since the PMT hits are uniformly distributed, the vertex of the faked event is at the detector center. Fig. 4-6 shows the vertex distribution due to statistical fluctuation versus the

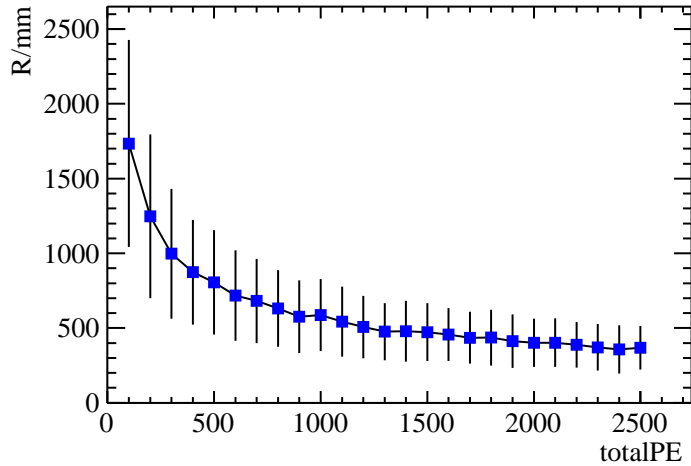


Figure 4-6: Vertex distribution of the faked events created by coincidence of the PMT dark noise versus total photoelectrons. The data point and the error bar shows the mean value and  $1\sigma$  uncertainty for the Maxwell-Boltzmann distribution of the radius of the faked events.

number of photoelectrons, while every 120 p.e. corresponds  $\sim 0.1$  MeV. Without online selection on vertex, the energy threshold will be limited at 0.3–0.4 MeV due to extremely high event rate. With an online trigger rejecting the events at the detector center and of an energy below 0.4 MeV, the threshold can be lowered to 0.1 MeV, with only a couple of percent inefficiency.

The rate of fake dark-noise triggers above a given energy threshold (defined by a coincident number of PMT hits, e.g. 240 hits for 0.2 MeV) depends on the dark rate of the individual PMTs,  $R_{\text{dn}}$ , and the length of the trigger gate  $t_{\text{gate}}$  for coincidences between hits and can be computed from Poisson statistics.

#### 4.3.4 Data acquisition

The large scintillator detector of JUNO has great potential of detecting galactic SN neutrinos, which however could have diverse energies and intensities. In the previous discussions, a typical distance of 10 kpc has been assumed for illustration. But it is important to notice that a galactic SN may occur at a much shorter distance. For instance, the red supergiant Betelgeuse is a very promising SN candidate, which is located just about 0.2 kpc away [144]. Hence, the electronic and data acquisition systems of JUNO should be designed to properly handle a huge number of neutrino events even in this extreme case.

To clarify the requirement for the detector not to be blinded by SN neutrinos, we calculate the maximum IBD rate in JUNO for a large number of SN models from the Basel [189], Garching [190, 191] and Nakazato [192] groups. The largest IBD rates for those models have been depicted as a function of the distance in Fig. 4-7, where the wide band can be viewed as the uncertainties of SN models. The insert in the upper panel refers to the case when Betelgeuse finally turns into a core-collapse SN. Taking account of the distance uncertainty, we can see that the maximal IBD rate reaches 100 MHz, and even the minimum exceeds 1 MHz, which is several orders of magnitude larger than the baseline value 1 kHz chosen for the determination of neutrino mass ordering. In the lower panel of Fig. 4-7, the SN probability in our galaxy has been shown for three different theoretical evaluations [141–143], where one can observe that the probability distribution is broad and the average distance is around 10 kpc.



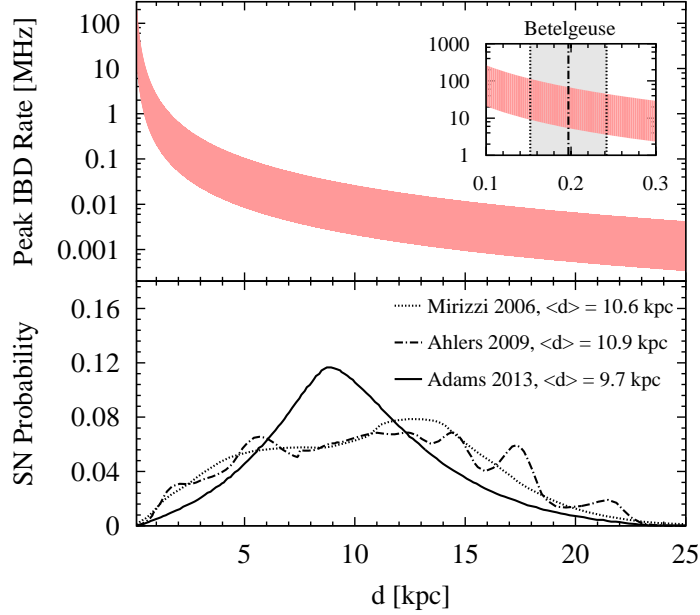


Figure 4-7: Maximum IBD rate at JUNO as a function of the distance to a galactic SN. In the upper panel, the shaded range has been obtained by considering a class of SN models from the Basel [189], Garching [190, 191] and Nakazato [192] groups. The insert refers to the SN candidate Betelgeuse with a distance of  $0.197 \pm 0.045$  kpc [144]. In the lower panel, the SN probability in our galaxy has been given according to three different evaluations [141–143].

In the best situation, the data acquisition system of JUNO should be able to work both for a “typical” SN at the most probable distance 10 kpc and the closest conceivable distance 0.2 kpc.

#### 4.4 Implications for astrophysics

A high-statistics observation of galactic SN neutrinos is of crucial importance for astrophysics, in particular for the evolution of massive stars, the core-collapse SN explosion and the production of heavy chemical elements [167, 193–195]. Moreover, the core-collapse SNe themselves are expected to be associated with the birth of neutron stars and black holes, and the emission of gravitational waves. Therefore, the neutrino signals at the JUNO detector could help us answer many fundamental questions in astrophysics:

- What are the conditions inside massive stars during their evolution, collapse, and explosion?
- How does the SN explosion take place? Is the delayed neutrino-driven mechanism of SN explosion correct?
- Is the compact remnant after the SN explosion a neutron star or a black hole?
- Do SNe provide adequate conditions for producing various elements, especially those heavier than iron?

In the following, we elaborate on the implications of SN neutrino detection for several important astrophysical issues that are related to the above important questions. Although many discussions in this subsection are based on the JUNO detector, it should be remembered that there will be

several SN neutrino detectors of scintillator, Cherenkov and liquid-argon [83] types in operation at the same time. Altogether, they will offer us valuable and complementary information.

#### 4.4.1 Pre-supernova neutrinos

Before a massive star collapses and forms a SN, it experiences various “stationary” burning phases. In the standard stellar evolution model, one can obtain the temperature and density for a given radius at any time. However, it is difficult to test the stellar models solely by using optical observations: photons come out of the core by diffusion, and any information about the core will be lost. During the advanced burning stages, the flux of neutrinos becomes much larger than that of photons. As neutrinos interact only weakly with stellar matter, they record faithfully the inner structure of the stars. Therefore, the detection of pre-SN neutrinos is vital for the verification of stellar models.

Inside a massive star neutrinos are produced via thermal processes, out of which the dominant one is  $e^+ + e^- \rightarrow \nu + \bar{\nu}$  [196]. At any given time, a massive star can be divided into many thin layers – each with approximately uniform temperature, density and chemical composition. One calculates neutrino production rate for each layer, and sum over all layers to derive the total neutrino flux and spectrum. In Table 4-2, neutrino fluxes and average energies at relevant burning stages are listed. The neutrino spectrum at the silicon-burning stage, in contrast with the solar neutrinos (e.g.,  $pp$  and  ${}^8\text{B}$  neutrinos), can be found in Ref. [197, 198]. Generally speaking, the neutrino production rate increases significantly with temperature, and so do the average energies of neutrinos and antineutrinos. Therefore, the detection of pre-SN neutrinos becomes relatively easier for the nuclear burning at later stages.

Burning phase	Average energy [MeV]	Total energy [erg]	Duration [days]
C	0.71	$7.0 \times 10^{49}$	$10^5$
Ne	0.99	$1.4 \times 10^{50}$	140
O	1.13	$1.2 \times 10^{51}$	180
Si	1.85	$5.4 \times 10^{50}$	2

Table 4-2: Neutrino emission from a massive star of  $20 M_{\odot}$  [197, 198].

The IBD reaction is the dominant channel to probe pre-SN neutrinos from massive stars. Fig. 4-8 shows the expected event rates in JUNO for the nearest possible SN progenitor, i.e., the red supergiant Betelgeuse, whose mass is taken to be  $20 M_{\odot}$  and distance is 0.2 kpc. The salient feature in the neutrino “light curve” – a quick rise starting at a few hours prior to core collapse – makes the JUNO detector an ultimate pre-warning system of SN explosion. As shown in Fig. 4-8, the rate drops rapidly down to 60 events per day around 0.6 day before SN explosion. The reason is that the silicon has been burnt out in the center and the core temperature decreases, leading to a reduced neutrino production. This dip in the neutrino “light curve” could serve as a discriminator for different progenitor star masses. The signal rate is time dependent, and there are about 400 events in the whole detector in the last day before core collapse.

Within the same energy window as for reactor neutrinos, any backgrounds of reactor neutrino experiments also act as backgrounds for detecting thermal neutrinos from massive stars. Those standard backgrounds include  ${}^9\text{Li}$ - ${}^8\text{He}$  events, fast- $n$  events, accidental coincidences,  $(\alpha, n)$  events, geo-neutrinos, and so on. Among all possible  $\bar{\nu}_e$  sources, the reactor neutrino itself could be the main background for pre-SN neutrino detection. The event rates from reactor neutrinos and geoneutrinos are 0.25 and 0.05 per kiloton per day, respectively. Here the expected event rate is estimated in the energy region  $1.8 \text{ MeV} < E < 3.3 \text{ MeV}$  and a 100% detection efficiency is assumed.

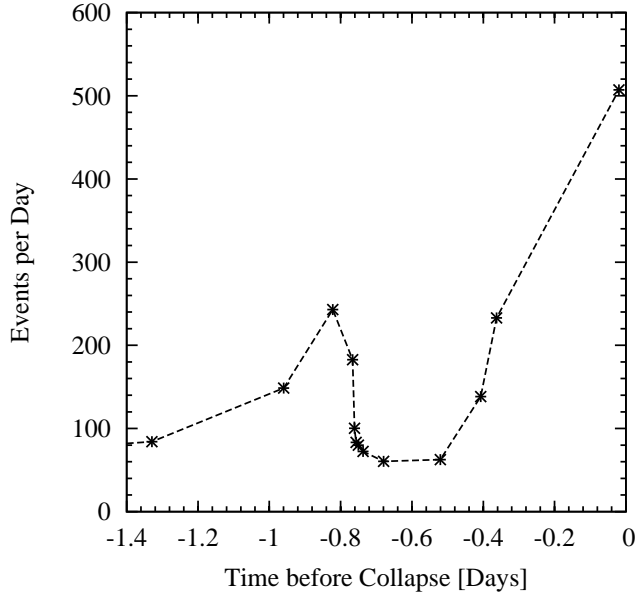


Figure 4-8: The neutrino event rate in JUNO for a massive star of  $20 M_{\odot}$  at the silicon-burning stage, where the distance is assumed to be 0.2 kpc, the same as that of the nearest possible SN progenitor Betelgeuse.

However, it is worthwhile to point out that the detection of pre-SN neutrinos is only possible for a very close progenitor star. For a SN at 10 kpc, the event rate will be reduced by about four orders of magnitude, rendering the detection of pre-SN neutrinos in JUNO or the detector of similar size extremely difficult.

#### 4.4.2 Locating the supernova

As mentioned before, the SN neutrinos arrive at the Earth several hours earlier than the optical signals, providing an early-time alert to the astronomical community. Moreover, if the optical display is hidden behind the dense gas and dust clouds of a star-forming region, the neutrino burst will be a unique tool to locate the SN [199, 200].

In general, there are two distinct methods to determine the location. First, the angular correlation between the final-state particle and the incident neutrino can be directly fixed in large Cherenkov detectors, such as Super-Kamiokande and its possible upgrade Hyper-Kamiokande. Second, two detectors separated at a long distance can locate the SN by neutrino triangulation.

According to the kinematics, the outgoing neutrons in the IBD reaction have a forward angular distribution. For a JUNO-like scintillator detector, it is possible to separately reconstruct the positions of positron and neutron. Therefore, the direction along the line connecting these two points is, at least statistically, related to the neutrino direction [177]. This method has been used by the CHOOZ experiment to determine the incoming direction of reactor antineutrinos in Ref. [178]. It has been found that the direction of the neutrino source can be fixed within a cone of half-aperture angle  $18^{\circ}$  at the 68% confidence level, based on 2700 collected  $\bar{\nu}_e$  events. For a galactic SN, if the total number of IBD events is about 5000, it is possible to measure the sky coordinates of the SN with an uncertainty of about  $9^{\circ}$ . It is expected that the JUNO detector will do better in this aspect. In the scintillator detector, it is also possible to observe the Cherenkov light from electrons, which are boosted to a high velocity in the elastic neutrino-electron scattering,

so the direction of recoiled electron can help locate the SN.

On the other hand, in neutrino triangulation, the key point is to estimate the neutrino arrival time and figure out the time delay  $\Delta t$  between two detectors at the distance  $d$ . In this case, the angle  $\theta$  between the SN direction and the line connecting these two detectors is given by  $\cos\theta = \Delta t/d$ , and the uncertainty is dominated by the error in the measurement of  $\Delta t$ . Taking a detector similar to JUNO with 5000 events and a distance of 30 ms, we obtain an uncertainty of about  $\delta(\cos\theta) \sim 0.21$ , following the strategy in Ref. [199]. Evidently, the precision for neutrino triangulation is not comparable to the statistical method.

#### 4.4.3 Coincidence with gravitational waves

Besides neutrinos, the gravitational waves are good messengers to probe the interior of a SN. A gravitational-wave signal provides useful information on non-radial deformation and non-spherical hydrodynamic motions, whereas a high-statistics neutrino signal allows us to follow directly the different stages of core collapse without additional assumptions. As predicted by all theoretical SN models, the prompt  $\nu_e$  burst is a robust and uniform landmark structure. Since the energy threshold of JUNO can be as low as 0.2 MeV, it offers a unique possibility of identifying this feature via elastic electron and proton scattering. One could use the prompt  $\nu_e$  burst in JUNO for coincidence measurements with the gravitational wave burst that may arise at core bounce. Using the prompt  $\nu_e$  burst could provide an even sharper coincidence than can be achieved with the onset of the  $\bar{\nu}_e$  signal in Super-Kamiokande and IceCube.

After core collapse, the luminosities of  $\nu_e$  and  $\bar{\nu}_e$  in the accretion phase depends on the mass infall rate and thus on the progenitor-dependent structure of the stellar core, with more massive cores producing higher luminosities. During this phase, the luminosity variations are accompanied by sizable gravitational-wave emission at several hundred Hz, the observation of neutrino and gravitational-wave signals would confirm the presence of violent hydrodynamic instabilities stirring the accretion flow around the assembling neutron star [201]. Such activity and a several hundred millisecond delay of the onset of the explosion are expected within the framework of the delayed neutrino-driven mechanism. A pronounced drop of the  $\nu_e$  and  $\bar{\nu}_e$  luminosities, followed by a close similarity to those of heavy-lepton neutrinos, would finally signal the end of the accretion phase and the launch of the outgoing SN blast wave. The cooling signature of a nascent neutron star is characterized by a monotonic and gradual decline of the neutrino emission. It would be prolonged if additional energy was released by phase transitions in the nuclear matter. Exotic scenarios might predict a secondary  $\nu_e$  burst, such as a QCD phase transition, or an abrupt end of neutrino emission if the collapse to a black hole occurred.

#### 4.4.4 SN nucleosynthesis

Another advantage of the JUNO detector is its superior energy resolution, which could help to disentangle source-imposed spectral features from those caused by neutrino-flavor conversions. Moreover, detecting significant numbers not only of  $\bar{\nu}_e$  but also of  $\nu_e$  and heavy-lepton neutrinos would yield at least time-averaged spectral information for different emission channels. Conceivably one could extract information on the neutron-to-proton ratio in the neutrino-processed SN outflows, presently also a sensitive result of numerical modeling of a multitude of complex processes. The relative abundance of neutrons and protons determines the conditions for nucleosynthesis and are set by competing  $\nu_e$  and  $\bar{\nu}_e$  captures, which in turn depend delicately on the relative fluxes and spectral distributions of these neutrinos [195]. A JUNO measurement of a SN burst may offer the only direct empirical test of the possibility for  $r$ -processing in the SN core, except for an extremely

challenging in-situ measurement of  $r$ -process nuclei in fresh SN ejecta [202].

In addition to the  $r$ -process for the production of heavy chemical elements, the neutrinos emitted from the core collapse and the subsequent cooling of the proto-neutron star will interact with outer layers of the SN, producing some rare nuclei such as  $^{11}\text{B}$  and  $^7\text{Li}$ . This neutrino process is crucially important for the  $^{11}\text{B}$  and  $^7\text{Li}$  production [203–205]. In particular, the SN neutrinos of heavy-lepton flavors, which may have higher average energies, will dominate the generation of galactic light chemical elements. Therefore, the measurement of  $\nu_x$  energy spectra at JUNO is necessary to directly pin down whether the neutrino process is really the true mechanism for producing the present galactic inventory of light nuclei.

One should notice that the flavor oscillations of SN neutrinos, which could lead to modification of neutrino energy spectra and fluxes, will affect both  $r$ - and neutrino processes [206].

## 4.5 Implications for particle physics

Neutrino signals of a core-collapse SN have also profound implications for elementary particle physics. If the standard scenario of delayed neutrino-driven explosion is confirmed by future observations of SN neutrinos and the cooling phase of neutrino emission is firmly established, the energy-loss argument will result in robust and restrictive constraints on a large number of particle physics models where new weakly-interacting particles are introduced, such as axions, majorons, and sterile neutrinos [207]. Numerous results derived from the sparse SN 1987A data can be refined.

If neutrinos are Majorana particles, spin-flavor conversions caused by the combined action of magnetic fields and matter effects can transform some of the prompt  $\nu_e$  burst to  $\bar{\nu}_e$ , leading to a huge inverse-beta signal. Such an observation would provide smoking-gun evidence for neutrino transition magnetic moments. Non-radiative decays would also produce a  $\nu_e \rightarrow \bar{\nu}_e$  conversion during the prompt burst. On the other hand, null results of observing those conversions will set restrictive bounds on the neutrino transition magnetic moments [208]. In addition, the existence of eV-mass sterile neutrinos may have great impact on the supernova explosion and nucleosynthesis [209, 210]

The core-collapse SNe serve as laboratories to probe intrinsic properties of neutrinos themselves. The SN neutrino observations will shed light on important fundamental problems in particle physics:

- What is the absolute scale of neutrino masses?
- What is the neutrino mass ordering?
- Are there collective neutrino oscillations?
- Are there exotic neutrino interactions?

In the following, we elaborate on a few important topics that are associated with these fundamental questions, and study the role that JUNO will play in this connection.

### 4.5.1 Bound on neutrino masses

Since neutrinos are massive, their flight time from a SN core to the detector at the Earth will be delayed, compared to massless particles [211]. For SN neutrinos, the time delay can be written as

$$\Delta t(m_\nu, E_\nu) = 5.14 \text{ ms} \left( \frac{m_\nu}{\text{eV}} \right)^2 \left( \frac{10 \text{ MeV}}{E_\nu} \right)^2 \frac{D}{10 \text{ kpc}}, \quad (4.7)$$

where  $E_\nu$  is the neutrino energy, and  $D$  is the distance between SN and detector. Thus a time-delay at the millisecond level is expected for neutrinos from a typical galactic SN. However, the average

energy and luminosity of neutrinos evolve in time, which complicates the extraction of neutrino mass information. In order to derive a mass bound, one has to know the time evolution of neutrino energies and fluxes, and take into account neutrino flavor conversions.

The sharply rising and falling luminosity of prompt  $\nu_e$  burst can be implemented to probe the time-delay effects of massive neutrinos, since the time structure is very unique and the characteristic timescale is around tens of milliseconds. However, the total number of neutrino-electron scattering events in JUNO is limited and it is impossible to reconstruct neutrino energy, which may reduce the sensitivity to neutrino masses. An abrupt termination of neutrino signals after the black-hole formation should be a perfect scenario to probe absolute neutrino masses [212].

As the IBD is the dominant channel for SN neutrino detection, we concentrate on the  $\bar{\nu}_e$  flux  $\Phi_{\bar{\nu}_e}^0$  in the accretion and cooling phases. In Ref. [213], a simple parametrization of  $\Phi_{\bar{\nu}_e}^0$  has been proposed to capture essential physics of neutrino production and the main features of numerical simulations. In the cooling phase, the  $\bar{\nu}_e$  flux  $\Phi_c^0$  is parametrized by three model parameters: the initial temperature  $T_c$ , the radius of neutrino sphere  $R_c$ , and the cooling time scale  $\tau_c$ . More explicitly, we have

$$\Phi_c^0(t, E_\nu) = \frac{1}{4\pi D^2} \frac{1}{8\pi^2} \left\{ 4\pi R_c^2 \frac{E_\nu^2}{1 + \exp[E_\nu/T_c(t)]} \right\}, \quad (4.8)$$

where the temperature evolves as  $T_c(t) = T_c \exp[-t/(4\tau_c)]$ . In the accretion phase, one has to model the time evolution of neutron number and positron temperature in order to figure out the  $\bar{\nu}_e$  flux  $\Phi_a^0$ . This can be done by introducing the accretion time scale  $\tau_a$ , and requiring the resultant neutrino energy and luminosity to follow numerical simulations. In addition, the initial number of neutrons depends on an initial accreting mass  $M_a$ , and a thermal energy spectrum of positrons with an initial temperature  $T_a$  is reasonable. The flux of  $\bar{\nu}_e$  is determined by the interaction between neutrons and positrons, so it can be written as

$$\Phi_a^0(t, E_\nu) = \frac{1}{4\pi D^2} \frac{1}{\pi^2} \left\{ N_n(t) \sigma_{ne^+}(E_\nu) \frac{\bar{E}_{e^+}^2}{1 + \exp[\bar{E}_{e^+}/T_a(t)]} \right\}, \quad (4.9)$$

where the average positron energy is evaluated as  $\bar{E}_{e^+} = (E_\nu - 1.293 \text{ MeV})/(1 - E_\nu/m_n)$ . For the neutrino energies of our interest (i.e., from 5 to 40 MeV), the cross section is approximately given by  $\sigma_{ne^+}(E_\nu) \approx 4.8 \times 10^{-44} \text{ cm}^2/[1 + E_\nu/(260 \text{ MeV})]$ . The time evolution of neutron number  $N_n(t) = 0.6M_a j_k(t) T_a^6 / \{ [1 + t/(0.5 \text{ s})] T_a^6(t) \}$  and the temperature function  $T_a(t) = T_a + (0.6 T_c - T_a)(t/\tau_a)^2$  are properly chosen to ensure a continuous neutrino average energy and to capture the numerical features [213]. Putting all together, the total flux is [213, 214]

$$\Phi_{\bar{\nu}_e}^0(t, E_\nu) = f_r(t) \Phi_a^0(t, E_\nu) + [1 - j_k(t)] \Phi_c^0(t, E_\nu), \quad (4.10)$$

where  $f_r(t) = 1 - \exp(-t/\tau_r)$  with the rising time scale  $\tau_r$  further introduces fine early time structure, and  $j_k(t) = \exp[-(t/\tau_a)^k]$  with a default value of  $k = 2$  is the time function interpolating the accretion and cooling phases of neutrino emission.

However, neutrino flavor conversions take place when they propagate from the SN core to the detector. In particular, the Mikheyev-Smirnov-Wolfenstein (MSW) matter effects in the SN mantle will significantly change neutrino flavor content. Given a relatively large  $\theta_{13}$ , the electron antineutrino flux at the detector is  $\Phi_{\bar{\nu}_e} = \cos^2 \theta_{12} \Phi_{\bar{\nu}_e}^0 + \sin^2 \theta_{12} \Phi_{\bar{\nu}_x}^0$  for normal neutrino mass ordering, while  $\Phi_{\bar{\nu}_e} = \Phi_{\bar{\nu}_x}^0$  for inverted neutrino mass ordering.

It is now straightforward to figure out the neutrino event rate  $R(t, E)$  as a function of emission time and neutrino energy, which are related to the detection time and positron energy, given a

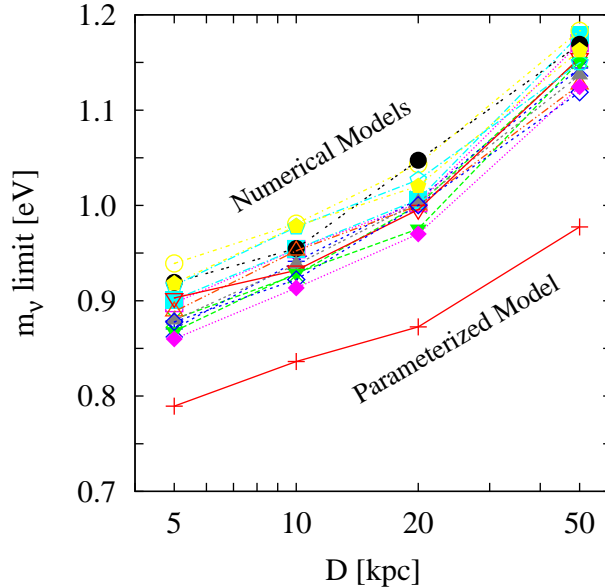


Figure 4-9: The upper bounds on the absolute scale of neutrino masses at the 95% CL for a SN at a distance of  $D = 5$  kpc, 10 kpc, 20 kpc and 50 kpc in the parameterized model from Ref. [213], and a series of numerical models from Ref. [192], in which simulations have been performed for a progenitor-star mass  $M = 13, 20, 30$  or 50 solar masses, a metallicity  $Z = 0.02$  or 0.004, and a shock revival time  $t_{\text{revive}} = 100$  ms or 300 ms. In our calculations, we have chosen fourteen numerical models, since a black hole is formed 842 ms after bounce in two models with  $M = 30$  solar masses and  $Z = 0.02$ . See Ref. [192] for more details about the numerical models, and the SN neutrino data are publicly available at the website <http://asphwww.ph.noda.tus.ac.jp/snn/>. This figure is taken from Ref. [216]

definite neutrino mass. The strategy is to generate neutrino events, denoted by a detection time  $t_i$  and a positron energy  $E_i$ , according to the event rate  $R(t, E)$ . The simulated data are fitted by the event rate with neutrino mass scale  $m_\nu$  as an additional parameter. The maximum likelihood approach is implemented, and the likelihood function has been constructed by taking account of every single event [215]. Assuming a nearly-degenerate neutrino mass spectrum and the normal mass ordering, we obtain a neutrino mass upper bound  $m_\nu < (0.83 \pm 0.24)$  eV at 95% confidence level, where  $1\sigma$  Gaussian error has been attached to the best-fit value [216]. In order to illustrate the impact of the SN distance on the mass limit, we have calculated the mass bound for different distances  $D = 5$  kpc, 10 kpc, 20 kpc and 50 kpc, where the last one corresponds to the case of SN 1987A. It is generally expected that a closer SN offers a larger number of neutrino events, implying a better upper limit on neutrino masses. Furthermore, to take account of SN model uncertainties, we show in Fig. 4-9 the results for the previous parametrized model of SN neutrino fluxes and a dozen of numerical SN models. In the latter case, the upper bound could be worsened by 0.15 eV or so, which should be regarded as a kind of systematic uncertainty.

#### 4.5.2 Impact of mass ordering

Flavor conversions of SN neutrinos are very interesting. Neutrinos propagating through the SN mantle and envelope encounter a large range of matter densities, allowing for MSW conversions driven first by the neutrino mass-squared difference  $\Delta m_{31}^2$  and the mixing angle  $\theta_{13}$ , and then by

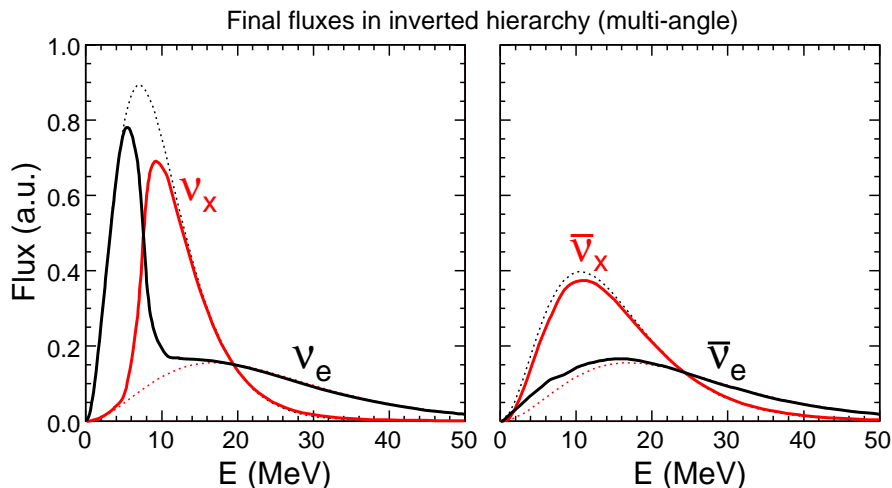


Figure 4-10: Numerical illustration for the splits in neutrino energy spectra after collective oscillations in the case of inverted mass hierarchy [218]. The initial spectra are indicated by dotted curves in the same color as the final ones, where one can observe a complete swap of the antineutrino spectra and a sharp split in the neutrino spectra.

$\Delta m_{21}^2$  and  $\theta_{12}$ . A SN neutrino signal is sensitive to the unknown neutrino mixing parameter: the ordering of neutrino masses that could be in the normal (NH) or inverted hierarchy (IH). In the former case, the  $\bar{\nu}_e$  flux outside the SN envelope will be a superposition of both initial  $\bar{\nu}_e$  and  $\nu_x$  fluxes, and the ratio between these two components is determined by the mixing angle  $\theta_{12}$ . In the latter case, the final  $\bar{\nu}_e$  flux at the Earth will be entirely the initial  $\nu_x$  flux. Note in both cases, the final fluxes needed to be scaled by the square of SN distance.

Although the difference caused by flavor conversions can be seen from the third row of Fig. 4-1, where the IBD event rate is calculated and the complete flavor conversion has been assumed, it remains to find a model-independent way to extract the information of mass ordering directly from the experimental observations. As another example, in the fourth row of Fig. 4-1, we can observe that the neutrino mass ordering significantly affects the event rate of neutrino-electron scattering. One possible way to determine the neutrino mass ordering may be to compare the event rates in the IBD channel with that of elastic neutrino-proton scattering, since the latter is not changed by flavor conversions.

### 4.5.3 Collective neutrino oscillations

The picture of SN neutrino oscillations has recently been changed drastically by the insight that the neutrino-neutrino refractive effect is crucial. These self-induced collective flavor conversions occur within a few hundred km above the neutrino sphere; see Ref. [217] for a review of the recent torrent of literature on this topic. The most important observational consequence is a swap of the  $\nu_e$  and  $\bar{\nu}_e$  spectrum with that of  $\nu_x$  and  $\bar{\nu}_x$  in certain energy intervals. The sharp spectral features at the edges of these swap intervals are known as “spectral splits”. Their development depends on the neutrino mass hierarchy as well as on the ordering of the flavor fluxes at the source. Therefore, the split features can depend on time in interesting ways. For instance, in Ref. [218], it has been shown in the case of inverted neutrino mass hierarchy that SN neutrinos in the accretion phase will undergo collective oscillations, leading to a complete swap between  $\bar{\nu}_e$  and  $\bar{\nu}_x$  spectra and a



sharp split around 7 MeV in the neutrino spectra, as in Fig. 4-10. The average neutrino energies  $\langle E_{\nu_e} \rangle = 10$  MeV,  $\langle E_{\bar{\nu}_e} \rangle = 15$  MeV and  $\langle E_{\nu_x} \rangle = 24$  MeV, together with a total neutrino energy of  $3 \times 10^{53}$  erg equally distributed in six neutrino species, are assumed. In the case of normal hierarchy, no significant flavor conversions are observed [217,218].

The main problem to detect oscillation features is that one can not rely on detailed theoretical predictions of the flavor-dependent fluxes and spectra. Therefore, model-independent signatures are crucial. One case in point is the energy-dependent modulation of the neutrino survival probability caused by Earth matter effects that occur if SN neutrinos arrive at the detector “from below”. The appearance of Earth effects depends on the flux and mixing scenario. Therefore, its detection could give hints about the primary SN neutrino fluxes, as well as on the neutrino mass hierarchy [219,220].

The excellent energy resolution of JUNO leads to a particular advantage for discovering small energy-dependent flux modulations caused by Earth effects, but of course depends on seeing the SN shadowed by the Earth. Additional signatures of flavor conversions can be imprinted by matter effects of the shock fronts in the SN envelope. The number of events, average energy, or the width of the spectrum may display dips or peaks for short time intervals. Such signatures yield valuable information about shock-wave propagation and the neutrino mass hierarchy [221]. However, realistic chances to detect shock features remain unclear. The flavor-dependent spectral differences in the antineutrino channel are probably small during the cooling phase. Moreover, strong turbulence in the post-shock regions could affect these signatures [222].

#### 4.5.4 Constraining new physics

It is well known that the stars can be ideal places to constrain new physics scenarios beyond the standard model of elementary particles [207]. If the standard picture of SN explosion is verified by a high-statistics observation, the duration of neutrino signal in the long cooling phase will be precisely measured. According to the standard energy-loss argument, any weakly-interacting exotic particles that can be copiously produced in the SN core will carry away a large amount of energies, significantly reducing the neutrino signal. To avoid excessive energy loss, the new particles should be interacting with matter and neutrinos so strongly that they are captured in the SN core, or so weakly that the production of new particles is inefficient. Therefore, by requiring the agreement between observations and theoretical prediction, we can draw restrictive constraints on the interaction strengths of new elementary particles. This approach has been applied to numerous new physics scenarios, such as axions, sterile neutrinos, majorons, and hidden photons.

As the neutrino energy spectra and flavors can be determined in future observations of SN neutrinos, new possibilities other than the energy-loss argument will be opened to set bounds on new physics.

## 4.6 Summary

A high-statistics detection of neutrinos from a galactic SN will provide us with precious information about the explosion mechanism and intrinsic properties of neutrinos themselves. For a galactic SN at a distance of 10 kpc, there are around 5000 events in the IBD channel, 2000 events for elastic neutrino-proton scattering, and 300 events for elastic neutrino-electron scattering in the JUNO detector. The time evolution, energy spectra and flavor contents of SN neutrinos can in principle be established and used to verify or disprove the neutrino-driven explosion mechanism. With experimental observations, many interesting questions in astronomy, astrophysics and particle physics, such as the early warning of SNe, the SN location, SN nucleosynthesis, absolute neutrino masses and neutrino mass ordering, can hopefully be revised or addressed.

## 5 Diffuse Supernova Neutrino Background (DSNB)

The integrated neutrino flux from all past core-collapse events in the visible universe forms the diffuse supernova neutrino background (DSNB), holding information on the cosmic star-formation rate, the average core-collapse neutrino spectrum, and the rate of failed SNe. The Super-Kamiokande water Cherenkov detector has provided first limits and eventually may achieve a measurement at the rate of a few events per year, depending on the implementation of its gadolinium upgrade. A JUNO-class detector has the potential to achieve a comparable measurement, benefitting from the excellent intrinsic capabilities of liquid scintillator detectors for antineutrino tagging and background rejection. The most critical background is created by neutral-current interactions of atmospheric neutrinos. Depending on the performance of pulse-shape discrimination techniques, this background may prove too high for a clear detection. However, a positive signal at the  $3\sigma$  level is conceivable for a 10-year measurement and typical DSNB parameters. A non-detection would strongly improve current limits and exclude a significant range of DSNB parameter space.

### 5.1 Motivation and Opportunities

While core-collapse SNe are rare, and in a galaxy like our own Milky Way occur only once every few decades, the energy release is so large that the integrated neutrino flux from all past SNe, the diffuse SN neutrino background (DSNB), adds up to a large cosmic radiation density [139,223–228]. It is comparable to the extra-galactic background light, the photons emitted from all stars, and corresponds to around 10% of the energy density of the cosmic microwave background. Note that the big-bang relic neutrinos are today non-relativistic, contributing a small hot dark matter component, so the DSNB is actually the largest cosmic neutrino *radiation* background, unless the lightest mass eigenstate of the big-bang neutrinos remains relativistic after all. It has been recognized for a long time that for  $E_\nu \gtrsim 10$  MeV, above reactor neutrino energies, the DSNB is the dominant local anti-neutrino flux. The primary detection channel is inverse-beta decay (IBD),  $\bar{\nu}_e + p \rightarrow n + e^+$ , where the solar  $\nu_e$  flux does not contribute even though it reaches up to about 15 MeV and dominates in this low-energy range.<sup>1</sup> The DSNB flux component in  $\bar{\nu}_e$  is around  $20 \text{ cm}^{-2} \text{ s}^{-1}$ , details depending on the cosmic SN rate as a function of redshift and the average core-collapse  $\bar{\nu}_e$  flux spectrum, including the effect of flavor conversion.

The DSNB can be detected if backgrounds, notably caused by atmospheric neutrinos, can be controlled. In this regard, a scintillator detector has an inherent advantage over the water-Cherenkov technique because neutron tagging of IBD events is a generic feature. The most restrictive current limits on the DSNB derive from Super-Kamiokande I–III without neutron tagging [230,231], already excluding the most extreme models for the DSNB flux spectrum. With a completely revised data-acquisition system, Super-Kamiokande IV now has limited sensitivity to the 2.2 MeV  $\gamma$ -ray caused by neutron capture on protons. A new DSNB limit based on this technique has recently become available [232], but is not yet competitive with the earlier Super-Kamiokande I–III results. Limits by the much smaller SNO [233] and KamLAND [234] detectors are also not competitive. In future, gadolinium as an efficient neutron absorber may be dissolved in Super-Kamiokande [235], a technique currently studied at the EGADS facility [236,237], probably allowing them to detect the DSNB at a rate of perhaps a few events per year [238]. Super-Kamiokande has around  $1.5 \times 10^{33}$  protons in its 22.5 kt of fiducial volume for DSNB detection, whereas JUNO has

---

Editors: Georg Raffelt (raffelt@mpp.mpg.de) and Michael Wurm (michael.wurm@uni-mainz.de)

Major contributor: Randolph Möllenberg, Zhimin Wang

<sup>1</sup>In principle,  $\nu_e \rightarrow \bar{\nu}_e$  transitions in the Sun caused by spin-flavor transitions of Majorana neutrinos could produce a solar background signal in this low-energy range [229].

around  $1.2 \times 10^{33}$  protons in the fiducial volume of 17kt to be used for the DSNB analysis (see below). Therefore, JUNO will be comparable and complementary to the Super-Kamiokande effort, and it will be unique if the gadolinium upgrade would not be implemented after all.

Following Ref. [139], the expected DSNB flux depends on two main ingredients, the core-collapse rate as a function of cosmic redshift and the number and spectrum of neutrinos and anti-neutrinos per flavor emitted by an average core-collapse event, including flavor conversion effects. These quantities bear significant uncertainties. The core-collapse SN rate rises from its local value by about an order of magnitude up to redshift  $z \sim 1$ , then levels off and eventually decreases [226, 227, 239–242]. If the  $\bar{\nu}_e$  detection threshold is above some 10 MeV, the overall detection rate is dominated by SNe with  $z \lesssim 1$ . However, the SN rate predicted from the observed star-formation rate appears to be systematically a factor of 2 smaller than the directly observed SN rate [242]. Additional contributions likely arise from sub-luminous SNe and from failed SNe, i.e. those core-collapse events leading to a black hole rather than an actual explosion [243–251]. Both outcomes lead to a neutrino flux comparable to that of a standard SN.

The total liberated energy in a core collapse depends on the final neutron-star mass and the nuclear equation of state, introducing a significant uncertainty even if we ignore the unknown contribution by failed SNe. The predicted flux spectra of the different flavors depend on details of the neutrino interaction rates and the numerical implementation of neutrino transport. Flavor conversion during neutrino propagation in the SN environment partly swaps the spectra so that the detectable  $\bar{\nu}_e$  flux is some combination of the original  $\bar{\nu}_e$ ,  $\bar{\nu}_\mu$  and  $\bar{\nu}_\tau$  fluxes emitted by the SN core. One expects large variability for most of these effects between different core-collapse events because of the large range of progenitor masses and other properties.

In principle, the DSNB is a treasure trove of valuable information on the astrophysics of core collapse, failed SNe and black-hole formation, and flavor-dependent neutrino propagation and flavor conversion. However, a detailed spectral DSNB measurement is clearly out of reach with near-term detectors of the JUNO and Super-Kamiokande class. Neutrino astronomy is a field in its infancy where only solar neutrinos have been observed with robust statistical detail. At this stage, the very detection of the DSNB is the first milestone and will be a fundamental discovery in its own right.

## 5.2 Parametric DSNB flux spectrum

In this situation, a detailed parameter study of the various DSNB ingredients is not warranted for a JUNO sensitivity forecast. Rather, we follow the practice adopted in the LENA physics study [162] and adopt a simple parametric representation of the DSNB. Its isotropic flux spectrum is given by the line-of-sight integral over cosmic redshift  $z$

$$\frac{dF_{\bar{\nu}_e}}{dE_{\bar{\nu}_e}} = \frac{c}{H_0} \int_0^{z_{\max}} dz \frac{R_{\text{SN}}(z)}{\sqrt{\Omega_{\text{m}}(1+z)^3 + \Omega_{\Lambda}}} \frac{dN_{\bar{\nu}_e}(E'_{\bar{\nu}_e})}{dE'_{\bar{\nu}_e}}. \quad (5.1)$$

The maximum redshift of star-formation  $z_{\max}$  is taken to be 5, but the exact value is irrelevant because  $z \lesssim 1$  dominates for the detectable part of the spectrum.  $H_0 = 70 \text{ km s}^{-1} \text{ Mpc}^{-1}$  is the present-day Hubble parameter and  $c$  the speed of light.  $R_{\text{SN}}(z)$  is the redshift-dependent co-moving SN rate, i.e., the number of SNe per year and per cubic-Mpc. The cosmological model is taken to be flat with a matter-density parameter  $\Omega_{\text{m}} = 0.30$  and cosmological-constant density parameter  $\Omega_{\Lambda} = 0.70$ . The cosmological parameters are rather well established, but our results do not directly depend upon them because they also enter the determination of  $R_{\text{SN}}(z)$ . Finally,  $dN_{\bar{\nu}_e}(E'_{\bar{\nu}_e})/dE'_{\bar{\nu}_e}$  is the total number spectrum of  $\bar{\nu}_e$  from an average core collapse, with flavor-conversion effects already included. Note that  $E'_{\bar{\nu}_e} = (1+z)E_{\bar{\nu}_e}$  is the neutrino energy in the rest frame of a SN at redshift  $z$ .

For the cosmic SN rate as a function of redshift we specifically adopt the functional form proposed by Porciani and Madau [239] in the form of equations (4) and (5) of reference [226] with the choice  $f^* = 1.5$ . The SN rate in the local universe is thus taken to be  $R_{\text{SN}}(0) = 1.25 \times 10^{-4} \text{ yr}^{-1} \text{ Mpc}^{-3}$  in agreement with reference [238]. A different parametrization provided in reference [241] leads to similar DSNB results because the main contribution arises from  $z \lesssim 1$  so that differences of  $R_{\text{SN}}(z)$  at larger redshifts have little impact on the overall result. For each individual core collapse we assume that, after flavor conversion effects have been included, a total energy  $E_{\text{tot}} = 0.5 \times 10^{53} \text{ erg}$  is emitted in  $\bar{\nu}_e$  with average energy  $\langle E_{\bar{\nu}_e} \rangle$ . While the instantaneous emission spectra tend to be “pinched”, i.e., less broad than a thermal distribution, the time-averaged spectra may be close to thermal. So we assume a Maxwell-Boltzmann distribution, normalized to  $tE_{\text{tot}}$ , of the form [175, 252]

$$\frac{dN_{\bar{\nu}_e}}{dE_{\bar{\nu}_e}} = \frac{0.5 \times 10^{53} \text{ erg}}{\langle E_{\bar{\nu}_e} \rangle} \frac{27}{2} \frac{E_{\bar{\nu}_e}^2}{\langle E_{\bar{\nu}_e} \rangle^3} e^{-3E_{\bar{\nu}_e}/\langle E_{\bar{\nu}_e} \rangle}. \quad (5.2)$$

Overall, this corresponds effectively to a two-parameter representation of the DSNB flux spectrum: one parameter is  $\langle E_{\bar{\nu}_e} \rangle$ , the other a global flux normalization  $\Phi$  which depends on the product of the SN rate at  $z = 0$  and the average energy per SN emerging in the form of  $\bar{\nu}_e$ . As a reference for the flux normalization, we define a default value  $\Phi_0 = E_{\text{tot}} \cdot R_{\text{SN}}(0)$  that corresponds to the most likely SN rate and total energy as described above.

In the following, we will explicitly consider  $\langle E_{\bar{\nu}_e} \rangle = 12, 15, 18$  and  $21 \text{ MeV}$ , where the upper end is certainly beyond what is nowadays expected for core-collapse SNe, but is meant to represent an extreme case. Figure 5-1 displays the corresponding DSNB antineutrino energy spectra for JUNO. Depending on  $\langle E_{\bar{\nu}_e} \rangle$ , the position of the spectral peak varies around  $10 \text{ MeV}$ . The corresponding event rate is  $0.2\text{--}0.5$  per (kt·yr) .

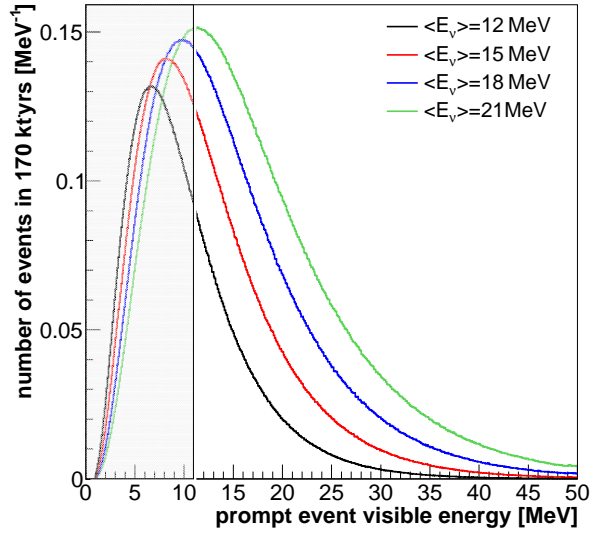


Figure 5-1: Visible energy spectra of prompt DSNB events for  $\langle E_{\bar{\nu}_e} \rangle = 12, 15, 18$  and  $21 \text{ MeV}$  for a fiducial volume of  $17 \text{ kt}$  (cf. section 5.3). Observation below  $11 \text{ MeV}$  is obstructed by the overwhelming background from reactor antineutrinos and cosmogenic background.

### 5.3 Signal and background sources in JUNO

The following section lines out the expected signal and background sources for the DSNB search in JUNO and proposes a viable analysis strategy based on event selection cuts and event identification to enable a positive detection of the DSNB in spite of the significant backgrounds. The projected sensitivity is laid out in section 5.4.

**DSNB antineutrino signal.** While the DSNB consists of approximately equal fluxes of neutrinos and antineutrinos of all flavors, the primary signal in liquid-scintillator detectors is the IBD reaction  $\bar{\nu}_e + p \rightarrow e^+ + n$ . The energy of the interacting antineutrino can be inferred by the signal of prompt positron that is shifted by  $\sim 0.8$  MeV to lower energies. The expected event rates and prompt event spectra have been derived by the convolution of the DSNB spectrum described in section 5.2 and the parametrized cross-section proposed in [176]. From this, the expected signal can be derived as a function of the mean energy of the SN spectrum  $\langle E_{\bar{\nu}_e} \rangle$ , the flux normalization  $\Phi$ , the number of protons contained in the fiducial mass  $m_{\text{fid}}$  and the detection efficiency  $\varepsilon_\nu$ . For  $m_{\text{fid}} = 17$  kt,  $\Phi = \Phi_0$  and  $\langle E_{\bar{\nu}_e} \rangle \in [12; 21]$  MeV, we expect an event rate of 1.5 to 2.9 events per year. The DSNB signal spectra of figure 5-1 have been obtained by a toy MC assuming a 3% energy resolution at 1 MeV.

The DSNB provides a clear coincidence signature of prompt positron and delayed neutron capture on hydrogen ( $E_\gamma = 2.2$  MeV,  $\tau_{np} \sim 220$   $\mu$ s) which allows for an efficient suppression of single-event background. However, there are several sources of correlated background events that must be taken into account when defining the energy window, fiducial volume and pulse shape selection criteria for DSNB detection (see below). The corresponding visible energy spectra are mostly derived from a modified version of the LENA detector simulation [253] but provide a good approximation of the expected signal in JUNO. On the other hand, the background created by fast neutrons is much more dependent on the detector geometry and has therefore been taken from a dedicated simulation of the JUNO setup [254].

**Reactor antineutrino background.**  $\bar{\nu}_e$ 's from neutron-rich fission products provide a large IBD signal in the energy region below 10 MeV that effectively impedes a detection of the DSNB in this energy range. Due to the relative proximity to the nuclear power stations at Taishan and Yanjiang, the  $\bar{\nu}_e$  background flux will be large compared to other proposed sites [255]. The expected rate is  $\sim 800$  events per (kt·yr). In particular, this will lead to a substantial number of events in the high-energy tail of the reactor  $\bar{\nu}_e$  spectrum that potentially extends to energies as high as 13 MeV [255]. To avoid this irreducible background, the energy threshold for DSNB detection has been set to a visible energy of 11 MeV, indicated by the shaded region in figure 5-1.

**Cosmogenic isotopes.** The decay events of the  $\beta n$ -emitters  ${}^9\text{Li}$  and  ${}^8\text{He}$  that are induced by cosmic muons pose with  $\sim 70$   $\text{d}^{-1}$  a large background for low-energy  $\bar{\nu}_e$  detection. However, the spectral endpoints of both radioisotopes effectively lie below the lower analysis of 11 MeV defined due to the reactor antineutrino signal. Therefore, this background can be safely neglected in the further discussion.

**Atmospheric neutrino CC interactions.** The events created by the IBDs of atmospheric  $\bar{\nu}_e$ 's on the target protons constitute a further source of indiscriminable background and start to dominate the DSNB signal for energies of 30 MeV and higher. Compared to other sites, Jiangmen is at a low geographical latitude (22.6°N), which leads to a relatively low atmospheric  $\nu$  flux. The corresponding background spectrum of IBD events (scaled from reference [255]) is shown in figure 5-1.

Unlike in water Cherenkov detectors, the background rate originating from the CC interactions of the large flux of atmospheric  $\nu_\mu$ 's and  $\bar{\nu}_\mu$ 's is far less problematic in liquid scintillator. In this events, the presence of final state muons can be very efficiently tagged based on both the coincidence tag provided by the Michel electrons and the characteristic pulse shape of muon events. This background is therefore considered to be negligible in this analysis. However, a determination of a potential residual rate will be addressed in future, more elaborate studies.

**Atmospheric neutrino NC interactions.** The search for antineutrinos at energies above 8 MeV that has been performed by KamLAND has demonstrated that neutral current reactions of high-energy atmospheric neutrinos in liquid scintillator can result in an IBD-like signature, either by neutron knock-out or by more complicated processes [234]. The corresponding event rate is more than an order of magnitude above the DSNB signal in the region of interest. In many cases, a  $^{11}\text{C}$ -nucleus will remain in the end state of such reactions. Its delayed decay has the potential to reject about 50% of this background. Moreover, a significant reduction can be achieved if pulse-shape discrimination (PSD) techniques are applied to the prompt signal [253]. In the following, we assume that the PSD efficiencies derived for the LENA setup in reference [253] can be transferred without loss to JUNO. This approach is supported by the use of identical scintillators and neglects the positive impact of the considerably higher light yield in JUNO. In this way, the residual background rate within the observational window can be reduced to  $0.6\text{ yr}^{-1}$  in the fiducial volume, corresponding to  $\varepsilon_{\text{NC}} = 1.1\%$  of the original rate. In spite of this rather stringent cut, the signal efficiency is still at  $\varepsilon_\nu = 50\%$  [253].

**Fast neutron (FN) background.** Due to the relatively low depth of the JUNO detector cavern ( $\sim 700\text{ m}$  of rock shielding), neutrons created by cosmic muons passing through the rock close-by the detector are relatively frequent and constitute a relevant source of background. While spallation neutrons can be easily discarded if the parent muon crosses the outer veto or the water pool, neutrons from further-out muons have a non-zero probability to pass undetected through the Cherenkov veto region and to mimic the IBD signature by a prompt proton recoil and a delayed capture of the thermalized neutron. Based on a muon flux of  $\sim 20\text{ m}^{-2}\text{ h}^{-1}$  and a mean muon energy of  $\langle E_\mu \rangle = 215\text{ GeV}$ , the expected FN background rate inside the JUNO target volume is of the order of 20 events per year.

Two factors allow a considerable reduction of this background: Because of the finite mean free path of the neutrons most of the events are concentrated towards the verge of the scintillator volume, clustering at the equator and the north pole of the spherical vessel. A soft fiducial volume cut rejecting all events at radii greater than 16.8 m reduces the residual background rate to  $\sim 1\text{ yr}^{-1}$  in the remaining target mass of 17 kt. Moreover, the PSD analysis (see above) is sensitive to the prompt proton recoils, decreasing the residual rate to  $\varepsilon_{\text{FN}} = 1.3\%$  of the initial value, corresponding to a negligible FN rate of  $\sim 0.01\text{ yr}^{-1}$ .

Reactor and atmospheric neutrino IBD signals define an observational window reaching from 11 to  $\sim 30\text{ MeV}$ . Corresponding numbers for signal and background events with and without PSD have been compiled in table 5-1 for a 10-year measuring period. The beneficial impact of PSD is illustrated in figure 5-2: In the left panel before PSD, atmospheric NC and fast neutron backgrounds dominate the DSNB signal, while they are greatly reduced in the right panel that reflects the situation after application of the PSD. The signal-to-background ratio is expected to exceed 1:1, creating very favorable conditions for a positive detection of the DSNB.

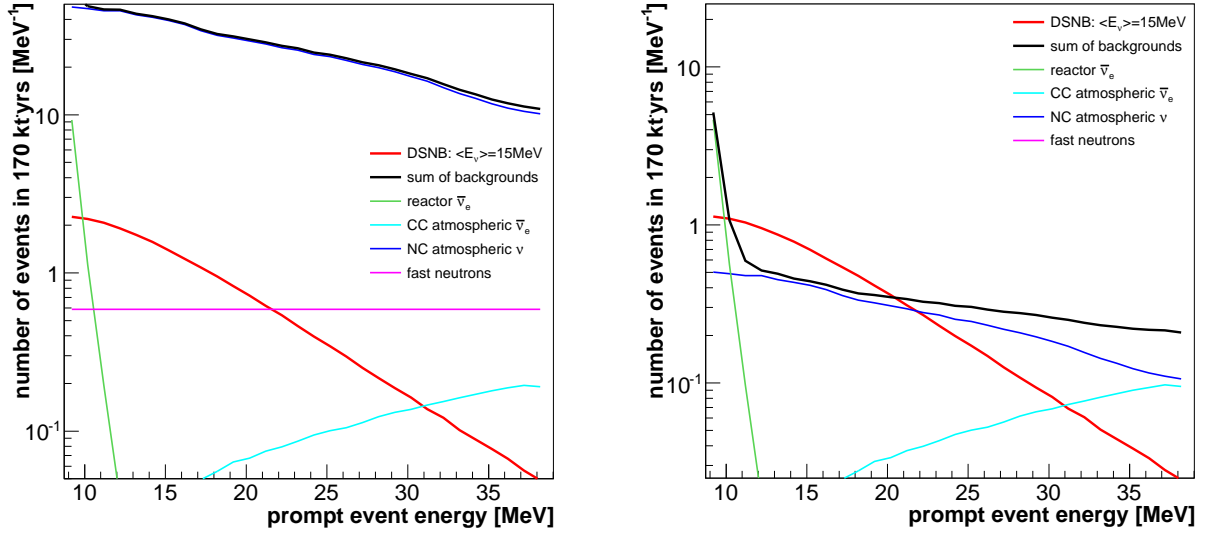


Figure 5-2: Prompt DSNB signal ( $\langle E_{\bar{\nu}_e} \rangle = 15 \text{ MeV}$ ,  $\Phi = \Phi_0$ ) and background spectra before (*left*) and after (*right*) the application of pulse-shape discrimination. The DSNB signal dominates all backgrounds for a large fraction of the observation window from 11 to 30 MeV.

Item		Rate (no PSD)	PSD efficiency	Rate (PSD)
Signal	$\langle E_{\bar{\nu}_e} \rangle = 12 \text{ MeV}$	13	$\varepsilon_{\nu} = 50 \%$	7
	$\langle E_{\bar{\nu}_e} \rangle = 15 \text{ MeV}$	23		12
	$\langle E_{\bar{\nu}_e} \rangle = 18 \text{ MeV}$	33		16
	$\langle E_{\bar{\nu}_e} \rangle = 21 \text{ MeV}$	39		19
Background	reactor $\bar{\nu}_e$	0.3	$\varepsilon_{\nu} = 50 \%$	0.13
	atm. CC	1.3	$\varepsilon_{\nu} = 50 \%$	0.7
	atm. NC	$6 \cdot 10^2$	$\varepsilon_{\text{NC}} = 1.1 \%$	6.2
	fast neutrons	11	$\varepsilon_{\text{FN}} = 1.3 \%$	0.14
	$\Sigma$			7.1

Table 5-1: Signal and background event rates before and after PSD in 10 years of JUNO data taking. An energy window  $11 \text{ MeV} < E_{\nu} < 30 \text{ MeV}$  and a fiducial volume cut corresponding to 17 kt have been chosen for background suppression.

## 5.4 Expected sensitivity

We have investigated two possible approaches for determining the potential of a positive DSNB detection by JUNO: Optimal sensitivity can be achieved in case the spectral shapes and rates of all backgrounds are well known, allowing for an energy-dependent fit of signal and background spectra to the data. Alternatively, we investigate a more conservative ansatz where detection significance is evaluated based on a rate-only analysis inside the observation window. Finally, the dependence of the sensitivity on the systematic uncertainty associated with the background normalizations is studied.

**Spectral fit.** The sensitivity of the DSNB search will depend on the knowledge on spectral

shape and normalization of the various background sources. Reactor and atmospheric antineutrino IBD spectra and fluxes can be extrapolated from the regions outside the observation window and will play only a minor role for most of the region of interest. For the more important FN and atmospheric NC backgrounds, rates and spectra can probably be determined with good accuracy if the energy-dependent PSD efficiencies are well understood.

Figure 5-3 depicts the significance of a positive DSNB measurement as a function of DSNB parametrization. Both the flux normalization  $\Phi$  and the mean spectral energy have been varied around the most probable values  $\Phi_0$  and  $\langle E_{\bar{\nu}_e} \rangle = 15$  MeV (cf. section 5.2). Assuming 170 kt-yr of exposure, event spectra based on the predictions for signal and all background sources have been generated for the energy range of 10-40 MeV. Based on these data samples, likelihood fits have been performed to the spectra above a prompt-event visible energy of 11 MeV, with and without including a contribution from the DSNB<sup>2</sup>. The likelihood function employed is

$$\mathcal{L}(\langle E_{\bar{\nu}_e} \rangle, \Phi, f_j) = \sum_i -2 \log \left[ P\left(n_i, \Phi s_i + \sum_j f_j b_{j,i}\right) \right] + \sum_j \frac{(f_j - 1)^2}{\sigma_j^2}, \quad (5.3)$$

where  $P$  is the Poissonian probability to obtain  $n_i$  events in the  $i^{\text{th}}$  bin based on the prediction for signal  $s_i$  and backgrounds  $b_{j,i}$ ,  $\Phi$  and  $f_j$  are the spectral normalizations of signal and backgrounds, respectively. The  $\sigma_j$  are the systematic uncertainties on the background normalization. The profile of figure 5-3 assumes  $\sigma_j = 5\%$ , while table 5-2 also lists the expected sensitivities for  $\sigma_j = 20\%$ . For the favored DSNB parameters, a  $3\sigma$  evidence for the DSNB signal seems well within reach (cf. table 5-2).

**Rate-only analysis.** Assuming no accurate knowledge on spectral shapes of signal and background, the detection potential can be calculated based merely on the detected event rate (table 5-1). This more conservative analysis is based on the integrated event rates within the nominal observational window of 11–30 MeV. The detection significance is evaluated according to the same likelihood function (5.3), but assuming only a single energy bin  $i$ . Resulting sensitivities are listed in table 5-2. Again, 5% and 20% are considered as systematic uncertainties for the individual background contributions. While the sensitivity is in all cases somewhat reduced, a  $3\sigma$  evidence for  $\langle E_{\bar{\nu}_e} \rangle = 15$  MeV can be still expected. Compared to the rate-only result, the inclusion of spectral information provides only a mild benefit due to the overall low statistics and the similarity in the spectral shapes of the DSNB and the background dominated by the atmospheric  $\nu$  NC interactions.

Syst. uncertainty BG	5%		20%	
	rate only	spectral fit	rate only	spectral fit
$\langle E_{\bar{\nu}_e} \rangle$				
12 MeV	2.3 $\sigma$	2.5 $\sigma$	2.0 $\sigma$	2.3 $\sigma$
15 MeV	3.5 $\sigma$	3.7 $\sigma$	3.2 $\sigma$	3.3 $\sigma$
18 MeV	4.6 $\sigma$	4.8 $\sigma$	4.1 $\sigma$	4.3 $\sigma$
21 MeV	5.5 $\sigma$	5.8 $\sigma$	4.9 $\sigma$	5.1 $\sigma$

Table 5-2: The expected detection significance after 10 years of data taking for different DSNB models with  $\langle E_{\bar{\nu}_e} \rangle$  ranging from 12 MeV to 21 MeV ( $\Phi = \Phi_0$ ). Results are given based on either a rate-only or spectral fit analysis and assuming 5% or 20% for background uncertainty.

<sup>2</sup>In particular, the median sensitivities have been obtained by using the Asimov sample (without statistical fluctuations).



**Upper limit on DSNB flux.** If there is no positive detection of the DSNB, the current limit can be significantly improved. Assuming that the detected event spectrum equals the background expectation in overall normalization and shape, the upper limit on the DSNB flux above 17.3 MeV would be  $\sim 0.2 \text{ cm}^{-2} \text{ s}^{-1}$  (90% C.L.) after 10 years for  $\langle E_{\bar{\nu}_e} \rangle = 18 \text{ MeV}$ . This limit is almost an order of magnitude better than the current value from Super-Kamiokande [231]. In figure 5-4 we show the corresponding exclusion contour as function of  $\langle E_{\bar{\nu}_e} \rangle$  (90% C.L.).

## 5.5 Outlook on further studies

A precise estimate of the DSNB detection potential in JUNO requires further studies. Most important is the determination of the PSD efficiency. The current estimates for the detection potential (section 5.4) are based on the assumption that the pulse-shape cut has the same efficiency as in the LENA study. But due to the higher light yield in JUNO, the pulse shape cut should actually be more efficient. If the signal efficiency can be increased, the information extracted on the DSNB will be more detailed and might allow us to obtain some information on the spectral mean energy  $\langle E_{\bar{\nu}_e} \rangle$ . On the other hand, PSD efficiency will also greatly depend on the time resolution of the light sensors, for which we here assumed a rather optimistic value of 1 ns ( $1\sigma$ ). While first studies indicate that a moderate reduction in time resolution will have only a small impact on PSD efficiencies, more detailed investigations are mandatory.

Another important issue that needs to be studied is how precise the expected value for the number of background events can be determined. While it is relatively easy to estimate the amount of radioactive, fast-neutron and CC atmospheric background events, the critical task will be to determine the expected value of the atmospheric NC events after the pulse-shape cut [253].

Finally, it should be investigated whether shape and rate uncertainties of the fast neutron background might be constrained by a dedicated muon sampler above the detector. Such a device will allow us to track a sample of rock muons and to study the induced signals of particle showers and especially neutrons in the water and scintillator volumes.

## 5.6 Conclusions

Large liquid-scintillator detectors are probably the most powerful approach to measure the long-sought DSNB. Despite its shallow depth, the relatively small size and the large atmospheric NC background, the superior detector properties of JUNO may be able to provide a DSNB detection at the  $3\sigma$  level. If no signal is detected, significant limits in the plausible parameter space can be achieved, improving on the existing limits from Super-Kamiokande which has approximately a 50% larger fiducial mass for DSNB detection. In case the gadolinium upgrade of Super-Kamiokande is implemented, it will have a realistic chance of measuring the DSNB. Adding the measurements of the two detectors will roughly double the overall statistics while reducing systematic uncertainties due to the differences in background and detection uncertainties. A combined analysis will either provide a more significant detection or more restrictive limits for the DSNB.

A detailed spectral study of the DSNB will not be possible with detectors of the JUNO or Super-Kamiokande size. In the more distant future, larger detectors such as the original LENA concept may be realized. For example, if the megaton Hyper-Kamiokande water Cherenkov detector is built, Super-Kamiokande might be converted to a 50 kt scintillator observatory.

The neutrino observation of a galactic SN is quite conceivable over the time span until the JUNO measurements have been completed. Such an observation would go a long way to give us confidence in theoretical expectations of SN neutrino emission parameters, strongly improving on the sparse SN 1987A data. However, the large variability of core-collapse events, the signal even

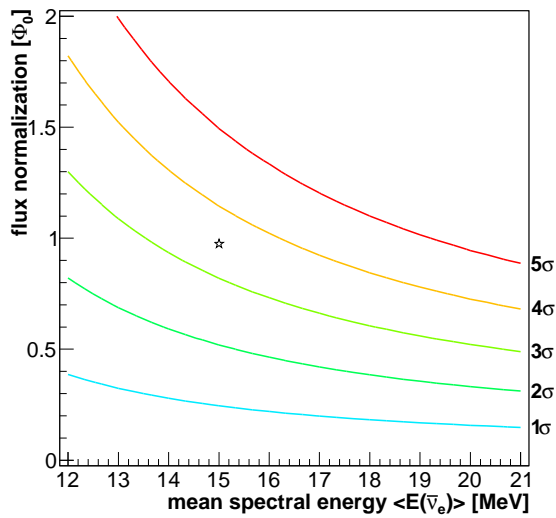


Figure 5-3: JUNO’s discovery potential for the DSNB as a function of the mean energy of the SN spectrum  $\langle E_{\bar{\nu}_e} \rangle$  and the DSNB flux normalization  $\Phi$  (cf. section 5.2). We assume 10 yrs measuring time, 5% background uncertainty and a detected event spectrum corresponding to the sum of signal and background predictions. The significance is derived from a likelihood fit to the data. The star marks a theoretically well-motivated combination of DSNB parameters (cf. section 5.2).

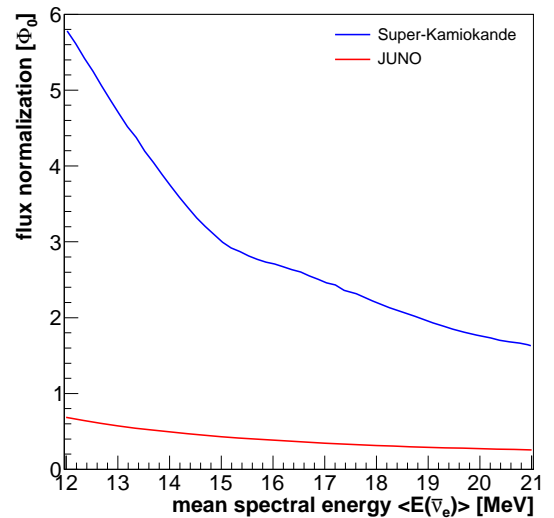


Figure 5-4: Predicted exclusion contour (90% C.L.) if JUNO finds no signal of the DSNB above background. The upper limit is shown as a function of the mean energy of the SN spectrum  $\langle E_{\bar{\nu}_e} \rangle$  and the DSNB flux normalization  $\Phi$  (cf. section 5.2). It has been derived from a spectral likelihood fit assuming 5% background uncertainty, 10 yrs of measurement time and  $N_{\text{det}} = \langle N_{\text{bg}} \rangle$ . The upper limit derived from the Super-Kamiokande results presented in [231] is shown for comparison.

depending on observer direction [166,256], will prevent one from an unambiguous prediction of the average core-collapse neutrino emission properties.

In the more distant future, one may therefore construct a multi-megaton detector that can measure SN neutrinos out to distances of several Mpc, although only a few events per SN [257]. Yet by stacking such measurements, over time one can build up an average  $\bar{\nu}_e$  flux spectrum that could be used to interpret DSNB measurements in terms of SN rates, notably failed SNe and black-hole formation. One possible implementation of such a program could be a dense infill of the IceCube detector. At present, the PINGU infill is being considered for studying atmospheric neutrino oscillations, and a further step could bring the energy threshold down to the level required for low-energy neutrino astronomy, the MICA concept [258].

Neutrino astronomy is a field in its infancy and high-statistics observations exist only for solar neutrinos. JUNO will play a leading role in pushing the low-energy frontier of this exciting field and may be the first instrument ever to measure low-energy neutrinos from the edge of the visible universe.

## 6 Solar Neutrinos

The Sun is a powerful source of electron neutrinos with the energy of  $\mathcal{O}(1)$  MeV, produced in the thermonuclear fusion reactions in the solar core. The two fusion reactions involved in combining four protons into a  ${}^4\text{He}$  nucleus,  $4p \rightarrow {}^4_2\text{He} + 2e^+ + 2\nu_e$ , are known as the  $pp$  chain and the CNO cycle. Because the total mass of the four protons is larger than the total mass of the final state particles, extra energy is released in the form of photons or of neutrino kinetic energy. The  $pp$  chain constitutes around 99% of the neutrino flux out of the Sun, which includes the  $pp$  neutrinos,  $pep$  neutrinos,  $hep$  neutrinos,  ${}^7\text{Be}$  neutrinos, and  ${}^8\text{B}$  neutrinos. The names of these neutrinos are defined according to their respective fusion reactions. On the other hand, neutrinos from nuclei decays (i.e.,  ${}^{13}\text{N}$ ,  ${}^{15}\text{O}$  and  ${}^{17}\text{F}$ ) of the CNO cycle are often referred to as the CNO neutrinos.

The study of solar neutrinos has already contributed significantly to the development of elementary particle physics and of astrophysics, reinforcing the synergy between these two disciplines. Over the last decades, together with the atmospheric [259], accelerator [260] and reactor [261] neutrino experiments, the experimental studies using solar neutrinos [262, 263] have obtained compelling evidence of neutrino oscillations. Nowadays, the issue is not any more to prove that neutrinos are massive and oscillating particles. However, important questions are still open for relevant solutions. Besides testing of the Mikheyev-Smirnov-Wolfenstein (MSW) [264, 265] matter effect in particle physics, we can also improve significantly our knowledge of fundamental solar physics, such as the mechanism ruling the dynamics of the Sun, the solar metallicity problem, and the agreement between solar models and the data from helioseismology.

Using a liquid scintillator detector as KamLAND [261] and Borexino [266] but with a much larger mass comparable to the Super-Kamiokande water Cherenkov detector [267], and with a very good energy resolution and hopefully an high radiopurity level, the JUNO experiment can have the potentiality to contribute significantly to the solar neutrino measurements, both from the astrophysical side and the elementary particle side. In this section we discuss the possibilities of doing solar neutrino physics at JUNO, with particular attention to the  ${}^7\text{Be}$  and  ${}^8\text{B}$  neutrino measurements.

### 6.1 History of solar neutrino experiments

The long-standing solar neutrino problem (SNP) was caused by the observed flux deficit in Homestake [2, 268], KamiokaNDE [269], Super-Kamiokande [267], and Gallium experiments (Gallex [270], GNO [271], and SAGE [272]) and it was solved finally by the SNO experiment [273] in 2002. The SNO results confirmed the validity of the Standard Solar Models (SSM) [274] using the neutral current signal that measured all active neutrino flavors. By comparing these results with the  $\nu_e$  flux recovered by the charged current signal, they offered a clear proof of the electron neutrino conversion into other active flavors [275]. The combination of the SNO result with the previous solar neutrino experiments defined a complete oscillation solution to the SNP, and together with the data from the reactor experiment KamLAND [261], the so-called large mixing angle (LMA) solution was found as the correct neutrino mixing parameter set. These results had great impact both on nuclear astrophysics and on elementary particle physics. In combination with atmospheric neutrino [259] and long baseline accelerator experiments [260], they proved in an undeniable way that neutrinos oscillate and have non-zero masses. Therefore, they gave the first clear hint of the need to go beyond the Standard Model of elementary particle physics.

---

Editors: Emanuela Meroni (emanuela.meroni@mi.infn.it), Lothar Oberauer (lothar.oberauer@tum.de), and Chao Zhang (chao@bnl.gov)

Major contributors: Vito Antonelli, Marco Grassi, Yufeng Li and Lino Miramonti

In the last years, the liquid scintillator experiments Borexino and KamLAND reached a low energy threshold in the sub-MeV region. The solar  ${}^7\text{Be}$ -neutrinos have been measured with high precision [276,277], and for the first time solar  $pep$  and  $pp$  neutrinos have been observed [278,279]. These measurements allow the new insight into the mechanism of thermal nuclear fusion processes in the center of the Sun. In addition, the predicted MSW matter effect on neutrino oscillations was found to be in general agreement with the experimental observations.

Moreover, a global three neutrino analysis [280], including all the solar neutrino experiments (assuming the fluxes predicted by the high- $Z$  version of SSM) and KamLAND data (assuming the  $CPT$  invariance), gave the following values for the mixing angles and the mass-squared difference:  $\tan^2 \theta_{12} = 0.457_{-0.025}^{+0.038}$ ;  $\sin^2 \theta_{13} = 0.023_{-0.018}^{+0.014}$ ;  $\Delta m_{21}^2 = 7.50_{-0.21}^{+0.18} \times 10^{-5} \text{ eV}^2$ , which are very similar to other global analyses of all neutrino data performed in the three neutrino framework [27–29] and other similar works published in 2012 [76–78].

## 6.2 Relevant open questions in solar neutrino physics

Despite the great achievements of the last decades, there are still important aspects of solar neutrino physics to clarify and some questions of great relevance for astrophysics and elementary particle physics are waiting for definite solutions. The issues can be summarized as the need for a better determination of the oscillation parameters, the solution of the solar metallicity problem, and the detailed analysis of the energy dependence for the oscillation probability in the region corresponding to the low-energy solar  ${}^8\text{B}$  neutrinos.

For the measurements of oscillation parameters, there could be a significant improvement with respect to the present situation, thanks to the precision measurements of reactor antineutrino oscillations at JUNO. As shown in the previous chapters, three of the oscillation parameters, including the solar oscillation parameters  $\sin^2 \theta_{12}$ ,  $\Delta m_{21}^2$  and the larger mass-squared difference  $\Delta m_{ee}^2$  (i.e., a linear combination of  $\Delta m_{31}^2$  and  $\Delta m_{32}^2$ ), can be measured with the precision level of 0.5%–0.7%. In this respect, one could enter the precision oscillation era in combination with other future long baseline experiments [83,87,88]. Moreover, solar neutrino oscillations itself can make the independent measurements of oscillation parameters without the assumption of  $CPT$  invariance, which is very important to test the consistency of the standard three neutrino framework and probe new physics beyond the Standard Model [281]. As also discussed previously, the combination of the data from medium baseline reactor antineutrino experiments (like JUNO) and from short baseline reactor (like Daya Bay) and solar experiments can offer a direct unitarity test of the MNSP mixing matrix, i.e.,  $|U_{e1}|^2 + |U_{e2}|^2 + |U_{e3}|^2 \stackrel{?}{=} 1$ . On the other hand, further improvement in the oscillation parameters from the solar experiment side is difficult in the post-SNO era.

Regarding the solar metallicity problem [282,283], so far we have observed neutrinos from the  $pp$  chain and still missing is a measurement of the sub-dominant solar CNO cycle. The best limits for its contribution to the solar energy generation are coming so far from the Borexino data, however a CNO neutrino measurement with the accuracy of about 10% would be necessary to shed light on the solar metallicity problem, which became apparent within the last years. The former excellent agreement between the SSM and the solar data has been compromised by the revision of the solar surface heavy-element content from  $(Z/X) = 0.0229$  [284] to  $(Z/X) = 0.0165$  [285], leading to a discrepancy between the SSM and helioseismology results<sup>1</sup>. Solution to this puzzle would imply either to revise the physical inputs of the SSM or to modify the core abundances, in particular those of C, N, O, Ne, and Ar. In 2009, a complete revision of the solar photospheric abundances for nearly all elements has been done [286], including a new three dimensional hydrodynamical

---

<sup>1</sup> $X$  and  $Z$  are the mass fractions of hydrogen and metals respectively

solar atmosphere model with the improved radiative transfer and opacity. The obtained results give a solar abundance  $(Z/X) = 0.0178$ . The three different sets of solar abundances, GS98 [284], AGS05 [285], and AGSS09 [286], have been used to construct different versions of the SSM [287]. The predictions of these SSM versions differ also for the  $^8\text{B}$  and  $^7\text{Be}$  neutrino fluxes. Therefore, a possible improvement at JUNO of the accuracy in the determination of these fluxes, together with data (coming from other future experiments) about the CNO fluxes could help solving this central problem of nuclear astrophysics, which will be explained further in the next subsection.

Coming, finally, to the study of energy dependence of the electron neutrino survival probability, the vacuum-oscillation and matter-oscillation dominated regions are separated at around 1–3 MeV. The continuous solar  $^8\text{B}$  neutrino spectrum is in principle a perfect tool to study the MSW-modulated energy dependence. According to the standard LMA-MSW solution one would expect a continuous transition between the vacuum and matter related  $\nu_e$ -survival probabilities. However, the data of existing detectors did not observe a clear evidence of this up-turn going towards the low energy part of the solar  $^8\text{B}$  spectrum, which gave rise to a series of theoretical discussions of sub-leading non-standard effects of the neutrino survival probability. The Super-Kamiokande data published in 2014 [288], including a combined analysis of all the four phases of this experiment, slightly indicated the presence of the up-turn. However, an independent and high-significance test of the up-turn effect would be extremely important to confirm the consistency of the standard LMA-MSW solution, or to indicate any possible deviations from this standard paradigm.

### 6.3 Motivation of solar neutrino measurements at JUNO

Solar neutrino measurement at JUNO is performed via the elastic neutrino electron scattering. A low energy threshold and a very good energy resolution should be accomplished at JUNO. Due to its much larger volume, significantly larger statistics can be reached as compared with Borexino. The larger detector size will also help suppress external gamma background by defining a fiducial volume and the self-shielding of the detector can be very good, provided that the intrinsic radiopurity of the scintillator is comparable to that reached in Borexino. However, the overburden is significantly lower with respect to the Gran Sasso underground laboratory of Borexino and therefore one has to see how cosmogenic background events can be rejected at JUNO. In the following, we discuss motivations and prospects of the low (i.e.,  $E \sim 1$  MeV) and high energy solar neutrinos measurements.

A new, accurate and independent measurement of the  $^7\text{Be}$  flux, that presently is essentially determined by the Borexino data within 5% of accuracy, would be interesting for a precise study of the vacuum dominated MSW-region. It could also shed some light on the solar metallicity problem, which is one of the present central astrophysical puzzles [282, 283]. In addition to the already cited high- $Z$  [284] and low- $Z$  [285, 286] versions of the SSM, in literature one can find also models in which the effect of reduced metallicity is partially compensated by an increase in the radiative opacity. In this way it is possible to reproduce the opacity profile and restore a good agreement with helioseismology, but this increased opacity can be only partially justified by theoretical arguments.

The values of the different solar neutrino fluxes can be used as observables to solve the present ambiguity between the different versions of the SSM (high- $Z$ , low- $Z$  and low- $Z$  with increased opacity), as shown in Fig. 6-1. The relatively large uncertainty of theoretical models and the fact that present experimental results fall in the middle between different SSM predictions make it impossible to draw any final conclusion at present. It is also clear that, due to the ambiguity between the high- $Z$  SSM and a low- $Z$  solution with increased opacity, there is the need for complementary information, like the values of CNO neutrino fluxes, that would represent the real breakthrough

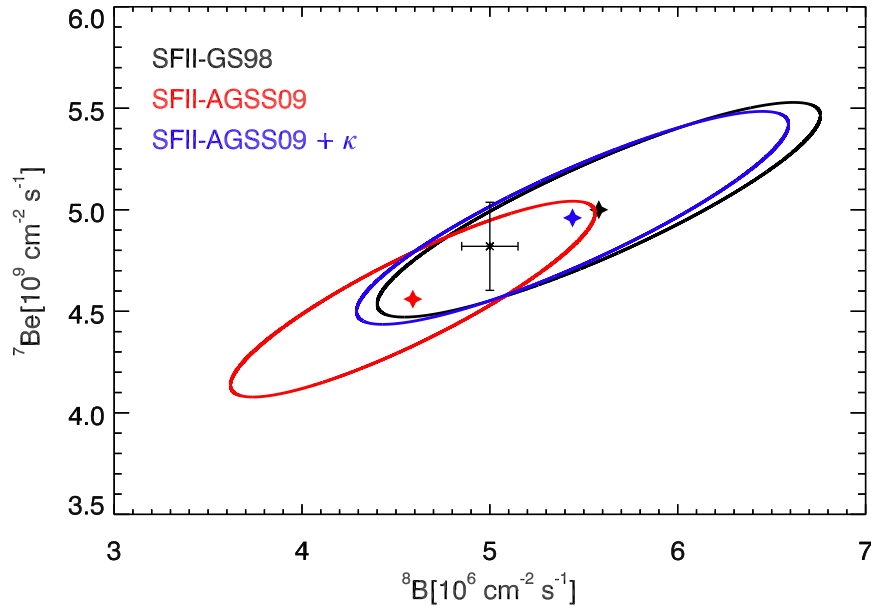


Figure 6-1: Comparison between theoretical predictions and experimental results for the fluxes of  ${}^8\text{B}$  ( $x$ -axis) and  ${}^7\text{Be}$  ( $y$ -axis) solar neutrinos. The black, red, and blue ellipses represent the  $1\sigma$  allowed regions, respectively in the high- $Z$ , low- $Z$  and low- $Z$  with increased opacity versions of the SSM. The  $1\sigma$  experimental results for the two fluxes correspond to the horizontal and vertical black bars. Updated version of the figure from [289]. See also [290] and [291].

in this field. Nevertheless, a  ${}^7\text{Be}$  flux measurement with the reduced uncertainty, possibly complemented by a parallel reduction of the theoretical model uncertainties, could give an important contribution to the solution of this puzzle, especially in the case of central value moving towards one of the two solutions (high or low- $Z$ ).

A further improved measurement of  ${}^7\text{Be}$  solar neutrinos could be also relevant to the search for the anomalous magnetic moment of neutrinos. In the Standard Model of electroweak interactions the magnetic moments of neutrinos are predicted to be very small,  $\mu_\nu \leq 10^{-20} \mu_B$  (where  $\mu_B = e/2m_e$  is the Bohr-magneton), therefore, any significantly larger value of the neutrino magnetic moment would be a clear signal of new physics [292–294]. The current experimental upper limit from particle physics experiments on the neutrino anomalous magnetic moment has been obtained by experiments studying reactor antineutrinos [295–297] and it is of the order of  $\sim 3 \times 10^{-11} \mu_B$ . Even more stringent (of almost one order of magnitude lower) indirect limits can be derived from astrophysical experiments and studies [208, 298]. The Borexino experiment also studied the anomalous neutrino magnetic moment, using the data of the elastic scattering of  ${}^7\text{Be}$  neutrinos on electrons. Due to the oscillations, the incident neutrinos are a mixture of three flavors, and this means that what is measured is an effective magnetic moment [299]. A further improvement of the neutrino effective magnetic moment at JUNO could offer important information [300] complementary to the reactor antineutrino studies and to the astrophysical studies.

A precise measurement of  ${}^8\text{B}$  solar neutrino flux from JUNO will also shed light on the metallicity problem with similar consideration as for the  ${}^7\text{Be}$  neutrinos. It is worthwhile to notice that, as shown in Fig. 6-2, even in the case of CNO neutrino fluxes being accurately extracted by the future measurements, e.g. in Borexino or SNO+ [301, 302], there could still be (in case of low values

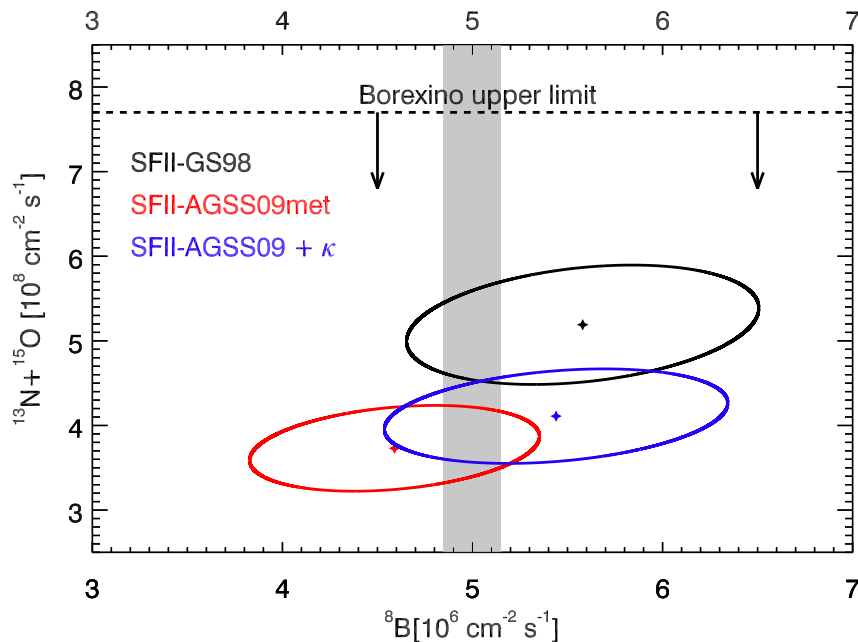


Figure 6-2: Comparison between the theoretical predictions for the values of the  ${}^8\text{B}$  ( $x$ -axis) and  ${}^{13}\text{N} + {}^{15}\text{O}$  ( $y$ -axis) neutrino fluxes derived from different versions of the SSM (high- $Z$  in black, low- $Z$  in red, and low- $Z$  with increased opacity in blue). The shaded grey vertical region represents the  $1\sigma$  region compatible with present data for  ${}^8\text{B}$  neutrinos. The horizontal line indicates the Borexino measured CNO flux limit. Updated version of the figure from [289]. See also [290, 291].

for these fluxes) an ambiguity in the solution between the low- $Z$  version of the SSM and the low- $Z$  with increased opacity. Therefore, an additional measurement with the increased accuracy of at least one of the two fluxes of  ${}^8\text{B}$  and  ${}^7\text{Be}$  solar neutrinos would be useful to break the degeneracy between the metallicity and opacity.

The measurement of the  ${}^8\text{B}$  solar neutrinos would be relevant also to test the consistency of the standard LMA-MSW paradigm. A first example is given by the study of the day-night asymmetry (i.e., defined as  $A_{\text{DN}}$ ). The outcome of the recent Super-Kamiokande analysis [303] found a value of  $A_{\text{DN}}$  different from zero at  $2.7\sigma$  and an even more robust hint when combining with the SNO data. However, it still needs a confirmation with higher statistical significance. Even more compelling information comes from the detailed analysis of the lower energy part of the  ${}^8\text{B}$  neutrino spectrum (around 3 MeV), which corresponds to the transition part between the matter enhanced and vacuum dominated regions. Considering the current ambiguity [288] in the up-turn behavior of the solar neutrino survival probability, an improved accuracy of this measurement in the region around 3 MeV would be essential to test the consistency of the LMA-MSW solution and definitely exclude (or confirm) more exotic sub-leading effects. Using the liquid scintillator and taking advantage of the low energy threshold, good energy resolution, low radioactive background, and large statistics, JUNO could be promising to arrive at a definite solution to this problem.

#### 6.4 Measurement of low energy solar neutrinos at JUNO

In this section, we describe in details the requirements for low energy solar neutrino measurement at JUNO, in particular for  ${}^7\text{Be}$  neutrinos. The measurement of the higher energy  ${}^8\text{B}$  solar neutrinos will be discussed in the next section. In a liquid scintillator detector such as JUNO, the solar



neutrinos of all flavors (via neutrino oscillations) are detected by means of their elastic scattering off electrons:

$$\nu_{e,\mu,\tau} + e^- \rightarrow \nu_{e,\mu,\tau} + e^- . \quad (6.1)$$

In contrast to the reactor  $\bar{\nu}_e$  IBD reaction where a coincidence signature exists to largely suppress background, the detection of solar neutrinos appears as a single flash of light. Only a fraction of the neutrino energy is transferred to the electron, therefore the electron recoil spectrum is continuous even in the case of mono-energetic neutrinos. The expected solar neutrino rates at JUNO are summarized in Tab. 6-1. The rates are calculated using the BP05(OP) [304] flux model, convolved with the neutrino-electron elastic scattering cross sections for all flavors. The standard three neutrino oscillation is applied with the solar LMA-MSW effect included. All the rates are estimated without any energy threshold cuts.

The emission of scintillation light is isotropic and any information about the initial direction of solar neutrinos is lost. Neutrino elastic scattering events in a liquid scintillator are thus intrinsically indistinguishable on an event-by-event basis from the background due to  $\beta$  or  $\gamma$  decays. Therefore, high radiopurity is required in order for JUNO to have the capability of measuring low energy solar neutrinos. Two internal purity levels are considered in Table 6-1 to calculate the intrinsic radioactive background. The “baseline” column is the minimum requirement of the purity level. The signal-to-background ratio at this level is approximately 1 : 3. The “ideal” column is the purity level at which the signal-to-background ratio is approximately 2 : 1. As a comparison, the “baseline” requirement is at approximately the KamLAND solar phase purity level (in the cleanest region) [277], and the “ideal” requirement is at about the Borexino phase-I (before 2010) purity level [280]. The exceptions are  $^{238}\text{U}$  and  $^{232}\text{Th}$ , for which both KamLAND and Borexino have reached better than “ideal” requirement since the beginning.

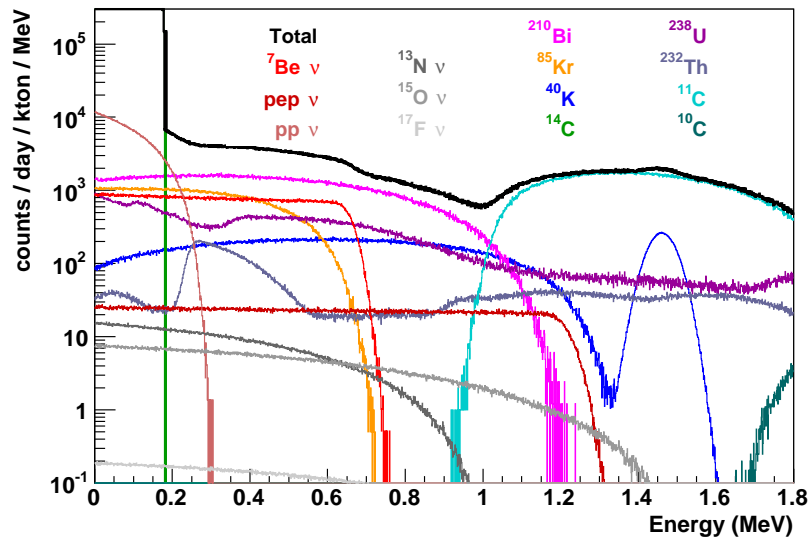
Table 6-1: The requirements of singles background rates for doing low energy solar neutrino measurements and the estimated solar neutrino signal rates at JUNO.

Internal radiopurity requirements		
	baseline	ideal
$^{210}\text{Pb}$	$5 \times 10^{-24}$ [g/g]	$1 \times 10^{-24}$ [g/g]
$^{85}\text{Kr}$	500 [counts/day/kton]	100 [counts/day/kton]
$^{238}\text{U}$	$1 \times 10^{-16}$ [g/g]	$1 \times 10^{-17}$ [g/g]
$^{232}\text{Th}$	$1 \times 10^{-16}$ [g/g]	$1 \times 10^{-17}$ [g/g]
$^{40}\text{K}$	$1 \times 10^{-17}$ [g/g]	$1 \times 10^{-18}$ [g/g]
$^{14}\text{C}$	$1 \times 10^{-17}$ [g/g]	$1 \times 10^{-18}$ [g/g]
Cosmogenic background rates [counts/day/kton]		
$^{11}\text{C}$	1860	
$^{10}\text{C}$	35	
Solar neutrino signal rates [counts/day/kton]		
pp $\nu$	1378	
$^7\text{Be}$ $\nu$	517	
pep $\nu$	28	
$^8\text{B}$ $\nu$	4.5	
$^{13}\text{N}/^{15}\text{O}/^{17}\text{F}$ $\nu$	7.5/5.4/0.1	

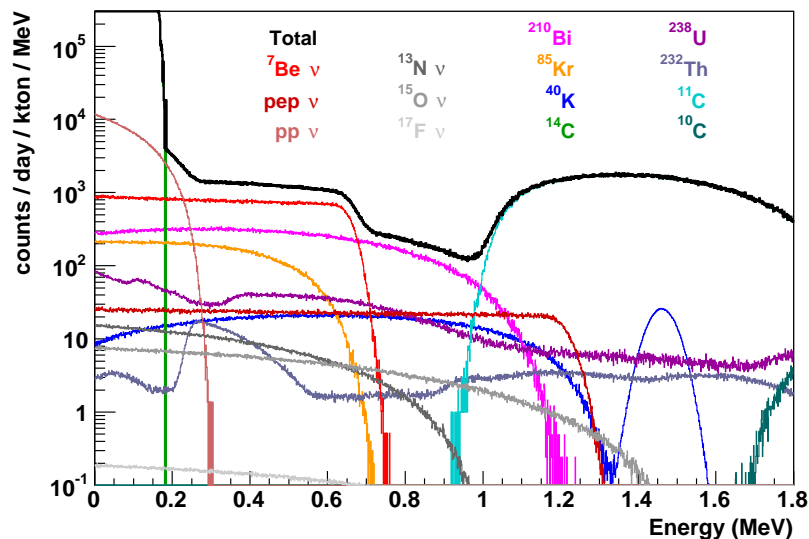
The expected cosmogenic  $^{11}\text{C}$  and  $^{10}\text{C}$  rates given in Table 6-1 are scaled from KamLAND spallation measurements (Table IV of Ref. [109].) As an example, for  $^{11}\text{C}$ , the KamLAND measurement is  $866 \times 10^{-7} \mu^{-1} \text{g}^{-1} \text{cm}^2$ . At the JUNO site, the mean muon energy is smaller than

KamLAND and the spallation production rate is about 0.9 times lower. The muon rate in the whole detector (20 kton) is about 3 Hz. The mean muon track length is about 23 m. The density is about 0.8 g/cc. Therefore, the scaled  $^{11}\text{C}$  rate at JUNO is  $\sim 1000$  counts per day per kton. All other cosmogenic backgrounds are assumed to be minor at the low energy [109,305] and are ignored in the calculation.

Fig. 6-3 shows the expected singles spectra at JUNO with the “baseline” and the “ideal” radiopurity assumptions listed in Table 6-1. The energy resolution is assumed to be  $\sigma(E) = 3\% \times \sqrt{E(\text{MeV})}$ . For simplicity, no energy non-linearity is applied to the spectrum.



(a)



(b)

Figure 6-3: The expected singles spectra at JUNO with (a) the “baseline” and (b) the “ideal” radiopurity assumptions listed in Table 6-1. See text for details.

In calculating  $^{238}\text{U}$  and  $^{232}\text{Th}$  decay spectra, secular equilibrium is assumed along the decay chains. The only non-equilibrium isotope considered is  $^{210}\text{Pb}$  (and the subsequent  $^{210}\text{Bi}$  decay) which has a 22-year half life and could break out of secular equilibrium by Rn contamination. When calculating all beta decay spectra, the Fermi correction, screening correction, finite size correction, and weak magnetism correction are applied to the shape of allowed decay spectrum. A shape correction to forbidden decays is also applied based on the spin and parity difference between the initial and final states.

A few backgrounds are neglected when calculating the rate and spectrum for Table 6-1 and Fig. 6-3:  $^{39}\text{Ar}$  rate is assumed to be two orders of magnitude lower than  $^{85}\text{Kr}$  (as it is in the air), thus is neglected in the calculation. We assume that the external gamma background can be removed with fiducial volume cuts. Since the signal rate is high, we assume we can always afford to cut deep into the cleanest region of the detector, therefore only internal radioactivity from the liquid scintillator itself is considered. We assume that with FADC waveform analysis, pile-up events can be largely removed and thus are neglected in the calculation. We further assume that the alpha-decay events (e.g.  $^{210}\text{Po}$  and alpha-decays in the  $^{238}\text{U}$  and  $^{232}\text{Th}$  decay chains) can be statistically subtracted from the singles spectrum with high precision, using the pulse-shape discrimination as demonstrated by Borexino [280]. Therefore, only beta and gamma decays are considered when calculating the singles spectra. The reactor  $\bar{\nu}_e$  elastic scattering rate is estimated to be only about 0.5 per day per kton and is neglected in the calculation.

As shown in Fig. 6-3 (a), the only solar neutrino branch that can be observed at the “baseline” purity level is the  $^7\text{Be}$  solar neutrino, which manifests itself as an edge around  $T_{\text{max}} = 665$  keV above the background. The extraction of this signal, however, requires a precise determination of the  $^{210}\text{Bi}$  background from the spectrum fit. On the other hand, the cosmogenic  $^{11}\text{C}$  doesn’t cause background to the solar  $^7\text{Be}$  neutrinos, because it undergoes  $\beta+$  decay, thus has a minimum energy of 1.022 MeV. JUNO’s high energy resolution (3%) makes sure that there is no leakage into the  $^7\text{Be}$  spectrum. At the “baseline” purity level, besides the dominating  $^{210}\text{Bi}$  background coming from the decay of  $^{210}\text{Pb}$ ,  $^{85}\text{Kr}$ ,  $^{238}\text{U}$ , and  $^{40}\text{K}$  all contribute non-negligibly in the  $^7\text{Be}$  signal range, thus need to be determined by other means (e.g., spectrum fitting, independent sample measurement, coincidence tagging, etc.) Detection of other low energy solar neutrino branches is difficult. The solar *pep* (and CNO) neutrino signal is overwhelmed by  $^{210}\text{Bi}$  at the low energy and by  $^{11}\text{C}$  at the high energy. The *pp* solar neutrino signal is overwhelmed by  $^{14}\text{C}$  at the low energy and by  $^{210}\text{Bi}$  at the high energy.

Assuming that the “ideal” purity level in Table 6-1 can be achieved (via online distillation and other means), the signal-to-background ratio will be largely improved, as shown in Fig. 6-3 (b). The  $^7\text{Be}$  solar neutrino signal rate will be about three times higher than the total of all other backgrounds. The ES scattering edge is clearly visible in Fig. 6-3 (b).

JUNO’s high energy resolution even makes it possible to observe the solar *pp* neutrinos. This is because the intrinsic  $^{14}\text{C}$  background ends at 156 keV, therefore there exists a window from approximately 160 keV to 230 keV where the *pp* neutrino flux is the dominating component of the singles spectrum. It manifests itself as a rising edge above the  $^7\text{Be}$  solar neutrino spectrum, as shown in Fig. 6-3 (b). The observation of *pp* solar neutrinos, however, requires a good pulse-shape discrimination to remove the low energy quenched alpha events, a clean removal of pile-up events with waveform analysis, as well as good understanding of low energy noise events.

## 6.5 Measurement of $^8\text{B}$ solar neutrinos at JUNO

The measurement of  $^8\text{B}$  solar neutrinos with a low energy threshold is possible at JUNO. Due to the much larger target mass, the counting statistics will be enlarged significantly with respect to the

Isotope	Decay Type	Q-Value [MeV]	Life time	Yield [109,305] $10^{-7} (\mu\text{g}/\text{cm}^2)^{-1}$	Rate [cpd/kton]
$^{11}\text{C}$	$\beta^+$	2.0	29.4 min	866	1860
$^{10}\text{C}$	$\beta^+$	3.7	27.8 s	16.5	35
$^{11}\text{Be}$	$\beta^-$	11.5	19.9 s	1.1	2

Table 6-2: List of the cosmogenic radioisotopes whose lifetimes are above 2s, which are the main backgrounds for  $^8\text{B}$  solar neutrino detection. Shorter-lifetime spallation products can be efficiently suppressed with proper muon veto cuts (see text for details).

previous liquid scintillator experiments such as Borexino and KamLAND. The higher photoelectron yield makes it possible for JUNO to lower the energy threshold further. Similar to other solar neutrino components, the detection of  $^8\text{B}$  solar neutrinos is through the neutrino-electron elastic scattering (ES) channel. The signal is a single event in contrast to the prompt-delayed signal pair in the case of reactor antineutrino IBD reaction. Therefore, background need to be controlled to a low level. The intrinsic background, external background, reactor background, and cosmogenic background that are relevant for solar  $^8\text{B}$  neutrino detection will be discussed in the following.

The intrinsic background at high energy is dominated by the decay of  $^{208}\text{Tl}$  ( $Q = 5.0\text{ MeV}$ ,  $\tau_{1/2} = 3\text{ min}$ ), which comes from the contamination of  $^{232}\text{Th}$  in the liquid scintillator. As an internal radioactive impurity, the total energy from the cascading  $\beta^-$  and  $\gamma$ -decays adds up to the Q-value of 5 MeV. This background cannot be removed by the fiducial volume cut. Assuming that secular equilibrium is reached, the  $^{208}\text{Tl}$  internal background can be measured via the  $\beta$ - $\alpha$  delayed coincidence from the  $^{212}\text{Bi}$ - $^{212}\text{Po}$  decay chain and then statistically subtracted. Nonetheless, the internal  $^{232}\text{Th}$  contamination need to be controlled to  $10^{-17}\text{ g/g}$  level in order to lower the analysis threshold to much below 5 MeV.

The external background, at the low energy end, is dominated by the 2.6 MeV  $\gamma$ -rays from  $^{208}\text{Tl}$  from the PMTs. Higher energy external gamma rays mainly come from the  $(n, \gamma)$  reaction in the surrounding materials. For example, neutron captures on stainless steel yield 6-MeV and 8.5-MeV gamma rays that can penetrate into the central detector. Energetic neutrons can also excite heavy nuclei in the surrounding material and produce high energy gamma rays. The external background can be efficiently reduced by applying a fiducial volume cut. A preliminary Monte Carlo study indicates that at least 5 m shielding is necessary [306], which will significantly reduce the fiducial mass by more than 50%.

The reactor background arises via elastic scattering (ES) of reactor antineutrinos off electrons in the liquid scintillator. The reactor ES event rate is estimated to be about 0.5 per day per kton, spanning over an energy range from 1 to 8 MeV. In total, the reactor ES background contribution is at about 5% level of the  $^8\text{B}$  solar neutrino signal. Furthermore, its contribution can be measured accurately from the IBD reaction and statistically subtracted with high precision.

Above 5 MeV, the dominant background is caused by the cosmogenic isotopes, which are produced in-situ by spallation reactions of cosmic muons on the carbon nuclei in the liquid scintillator. The muon rate in the 20-kton JUNO central detector is 3 Hz. The spallation products are typically unstable and undergo  $\beta^-/\beta^+$  decays. From the Monte Carlo study, the short-lived spallation isotopes ( $\tau \lesssim 1\text{ s}$ ) can be efficiently suppressed by vetoing a cylindrical volume with 1 m radius around each traversing muon track for 6.5 seconds. Since some of the muon events are muon bundles (multiple muons in one event), and some of the muons produce electromagnetic and hadronic showers (showering muons), good track reconstructions for muon bundles and showering muons are necessary (see the reactor neutrino chapter for details of muon reconstructions) for an efficient

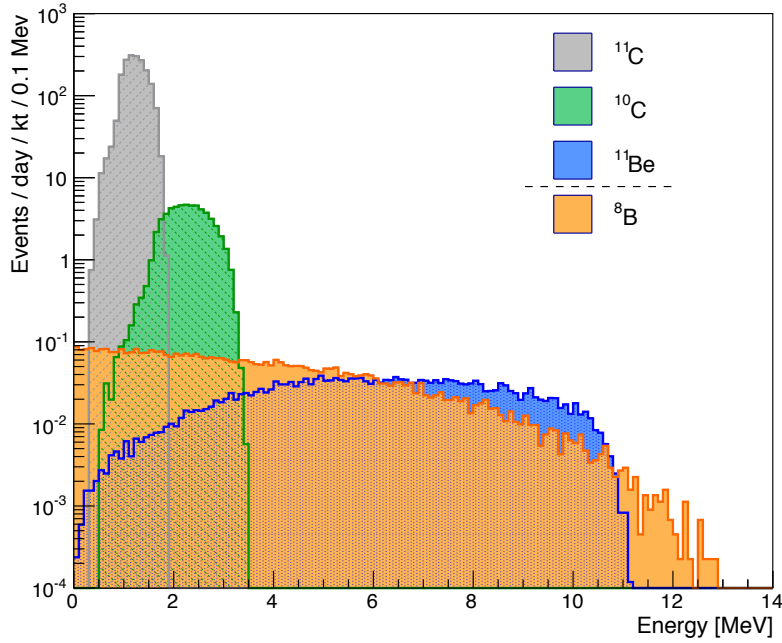


Figure 6-4: The simulated background spectra for the cosmogenics isotopes  $^{11}\text{C}$ ,  $^{10}\text{C}$ , and  $^{11}\text{Be}$  at JUNO. Furthermore, the expected  $^8\text{B}$  ( $\nu - e$ ) spectrum is shown for comparison. A reduction of  $^{10}\text{C}$  and  $^{11}\text{C}$  should be possible by Three-Fold Coincidence but is not applied in the figure (see text for details).

rejection of short-lived spallation backgrounds.

The remaining long-lived spallation radioisotopes are  $^{11}\text{C}$  ( $\beta^+$ ,  $\tau = 29.4$  min),  $^{10}\text{C}$  ( $\beta^+$ ,  $\tau = 27.8$  s), and  $^{11}\text{Be}$  ( $\beta^-$ ,  $\tau = 19.9$  s). Due to the long lifetime, they are difficult to remove without losing a large fraction of detector livetime. Therefore, their rates and spectra need to be measured accurately and subtracted. Their decay information, spallation yields, and estimated rates at JUNO are summarized in Table 6-2. The expected rates are scaled from the KamLAND and Borexino spallation measurements [109, 305] similarly as described in the previous low energy solar neutrino section. Their expected energy spectra at JUNO are shown in Fig. 6-4, together with the expected  $^8\text{B}$  solar neutrino signal spectrum. The energy resolution is assumed to be  $\sigma(E) = 3\% \times \sqrt{E(\text{MeV})}$ . For simplicity, no energy non-linearity is applied to the spectrum. One can see that due to the relatively shallow depth of JUNO, the long-lived spallation radioisotopes are the major background sources for  $^8\text{B}$  solar neutrino detection.

Typically, neutrons are produced along with the spallation products. For example, the primary processes to produce the  $^{11}\text{C}$  and  $^{10}\text{C}$  isotopes are  $(\gamma, n)$  and  $(\pi^+, np)$ , respectively. Therefore, a Three-Fold Coincidence (cosmic muon, neutron capture, and isotope decay) can be used to further suppress the  $^{11}\text{C}$  and  $^{10}\text{C}$  backgrounds. Since neutrons are captured with a lifetime of about  $200 \mu\text{s}$ , the electronics needs to recover within a few microseconds after high-multiplicity events in order to minimize the dead time and to have a high neutron tagging efficiency. The effect of neutrons leaking out of the scintillation region can be mitigated by a fiducial volume cut. Further rejection is possible by studying the underlining mechanism of spallation production and possible signatures

from them [307,308]. We note that the rates and the spectra of the spallation products can also be measured in-situ with enhanced samples by selecting the candidates inside the veto volume close to the muon tracks.

## 6.6 Conclusions

The JUNO detector has many advantages in performing solar neutrinos measurements compared with previous detectors. Being a liquid scintillator detector similar to Borexino and KamLAND, it has the benefit of high light yield and, therefore, very high energy resolution and low energy threshold. Being a massive 20 kton detector it will have large statistics comparable to the Super-Kamiokande water Cherenkov detector. This makes JUNO an attractive detector to further improve the measurement precision of various components of the solar neutrino flux, shed light on the solar metallicity problem, and probe the transition region between the vacuum-dominated and MSW-dominated neutrino oscillations. The solar neutrino measurements, however, demand challengingly low levels of radio-impurities and accurate determination of cosmogenic backgrounds. Since JUNO is optimized for reactor antineutrino measurements with relatively lenient background requirement, dedicated efforts to realize the low background phase for solar neutrino measurements are necessary.

# 7 Atmospheric Neutrinos

## 7.1 Introduction

A compelling three-flavor neutrino oscillation framework has been established by various atmospheric, solar, reactor, and accelerator neutrino experiments so far. Reviews of the progress can be found in many articles, for example, in Ref. [27]. Precision of the oscillation parameters has been improved significantly with recent experiments. However, there are still several major unknowns in neutrino oscillation physics. Many new experiments with various neutrino sources and detector technologies are designed to address these questions [309]. Here, we explore the capabilities of JUNO to determine the neutrino mass hierarchy (MH), the octant of atmospheric mixing angle  $\theta_{23}$  and the Dirac CP violation phase  $\delta$  using atmospheric neutrinos.

Atmospheric neutrinos are a very important neutrino source to study the neutrino oscillation physics. In 1998, the Super-Kamiokande experiment reported the first evidence of neutrino oscillations based on a zenith angle dependent deficit of atmospheric muon neutrinos [259]. Atmospheric neutrinos have a broad range in baseline (15 km  $\sim$  13000 km) and energy (0.1 GeV  $\sim$  10 TeV), and contain neutrinos and antineutrinos of all flavors. When they pass through the Earth, the Mikheyev-Smirnov-Wolfenstein (MSW) matter effect [264,265] will play a key role in answering the above three open questions. Super-Kamiokande has reported the preliminary results on these issues based on 4538 days of data [132]. Future atmospheric neutrino experiments, such as PINGU [85], ORCA [310] Hyper-Kamiokande [87,88] and INO [84], anticipate improved sensitivities.

The JUNO central detector as a liquid scintillator (LS) calorimeter has a very low energy threshold and can measure atmospheric neutrinos with excellent energy resolution. Characteristic signals from Michel electrons, neutron captures and unstable daughter nuclei are helpful for the particle recognition. Note that the JUNO LS detector also has some capabilities to reconstruct the directions of charged leptons in terms of the timing pattern of the first-hit on the PMTs (See appendix and Refs. [162,311]). Based on the above capabilities, JUNO is a promising detector for atmospheric neutrino oscillation measurements.

## 7.2 Atmospheric Neutrino Oscillations

Atmospheric neutrinos are produced in the Earth's atmosphere as a result of cosmic ray interactions and the weak decays of secondary mesons, in particular pions and kaons. The competition between the particle's decay and re-interaction probabilities leads to characteristic shapes for neutrino's energy spectrum and angular distributions. At energies relevant for JUNO the production of  $\nu_\mu$  and  $\bar{\nu}_\mu$  is dominated by the decay chains

$$\pi^+ \rightarrow \mu^+ + \nu_\mu, \quad \mu^+ \rightarrow e^+ + \bar{\nu}_\mu + \nu_e; \quad (7.1)$$

$$\pi^- \rightarrow \mu^- + \bar{\nu}_\mu, \quad \mu^- \rightarrow e^- + \nu_\mu + \bar{\nu}_e. \quad (7.2)$$

At low energies below typically one GeV, all parent particles in the decay chain decay at equal probability and the expected flux ratios reflect the production ratios of parent mesons  $\frac{\phi_{\nu_\mu}}{\phi_{\bar{\nu}_\mu}} \simeq 1$ ,  $\frac{\phi_{\nu_e}}{\phi_{\bar{\nu}_e}} \simeq 1$  and  $\frac{\phi_{\nu_\mu} + \phi_{\bar{\nu}_\mu}}{\phi_{\nu_e} + \phi_{\bar{\nu}_e}} \geq 2$ . These ratios increase at higher energies as muons are less likely to decay before hitting ground. The neutrino energy spectrum initially follows the primary cosmic ray spectrum  $\propto E^{-2.7}$  and becomes steeper at higher energy reflecting the decreasing decay probability of parent particles. The angular distribution exhibits a characteristic shape with an increased flux

---

Editors: Wanlei Guo (guowl@ihep.ac.cn) and Christopher Wiebusch (wiebusch@physik.rwth-aachen.de)

Major contributors: Michael Soiron and Zhe Wang

towards the horizon due to the effects of the longer path length together with lower interaction probability at the high altitude. At even higher energies of the order of  $\sim 100$  GeV the decay of kaons becomes more important, because of their shorter lifetime with respect to pions. The flux of atmospheric neutrinos has been simulated with increasing precision over the last decades. The flux of atmospheric muon neutrinos ( $\nu_\mu + \bar{\nu}_\mu$ ) resulting from the recent calculation [312] is shown in Fig. 7-1. An up-down asymmetry appears at sub-GeV energies due to the Earth magnetic field and depends on the geographical location of the experiment. The suppression of the electron neutrino flux becomes apparent above about 1 GeV. Note that the above calculations show the fluxes at production level and do not include flavor oscillations during propagation through the Earth which are discussed below.

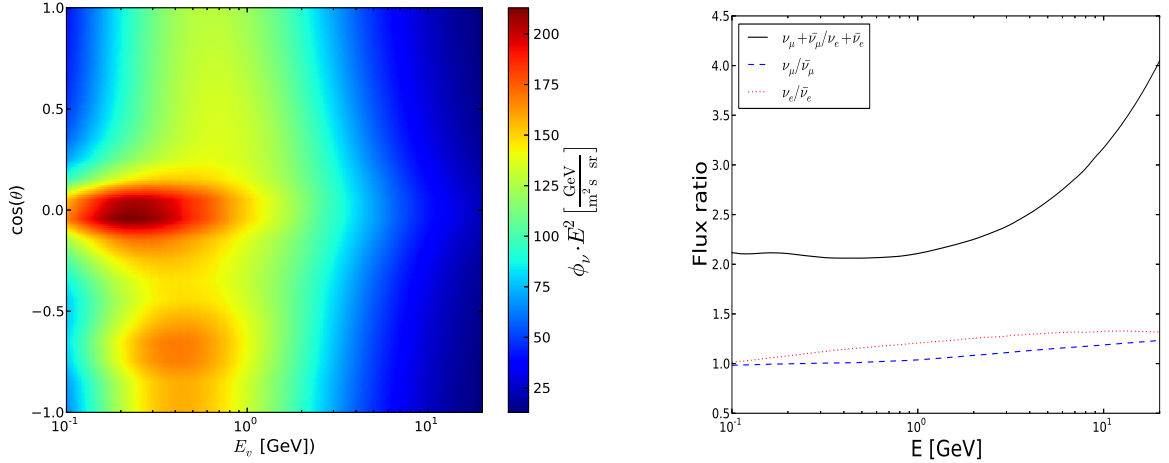


Figure 7-1: The differential ( $\nu_\mu + \bar{\nu}_\mu$ ) flux density multiplied with  $E^2$  versus energy and zenith angle (left) and flux ratios of different flavors versus energy averaged over all zenith angles (right).

When atmospheric neutrinos propagate in the Earth, the evolution of the flavor eigenstates is given by

$$i \frac{d\nu_f}{dt} = \left( U \frac{M^2}{2E\nu_f} U^\dagger + V \right) \nu_f, \quad (7.3)$$

with  $M^2 = \text{diag}(m_1^2, m_2^2, m_3^2)$  and  $V = \text{diag}(\sqrt{2}G_F N_e, 0, 0)$ . For the antineutrinos, Eq. (7.3) is still valid when replacing the leptonic mixing matrix  $U \rightarrow U^*$  and the effective potential  $V \rightarrow -V$ .  $G_F$  is the Fermi coupling constant and  $N_e = Y_e \rho$  is the electron number density with  $Y_e = 0.466$  for the core and  $Y_e = 0.494$  for the mantle [313]. In terms of the PREM Earth density profile [314], we numerically solve Eq. (7.3) and calculate six typical oscillation probabilities by use of nuCraft [315] for the normal hierarchy (NH) hypothesis as shown in Fig. 7-2. Here we take the Dirac CP phase  $\delta = 0$  and use the current best known values of the following oscillation parameters [27]:

$$\begin{aligned} \sin^2 \theta_{12} &= 0.308_{-0.049}^{+0.051}, \\ \sin^2 \theta_{13} &= 0.0234_{-0.0058}^{+0.0061}, \\ \sin^2 \theta_{23} &= 0.437_{-0.063}^{+0.187}, \\ \Delta m_{21}^2 &= 7.54_{-0.55}^{+0.64} \times 10^{-5} \text{eV}^2, \\ \Delta m_{atm}^2 &= 2.43_{-0.20}^{+0.18} \times 10^{-3} \text{eV}^2, \end{aligned} \quad (7.4)$$



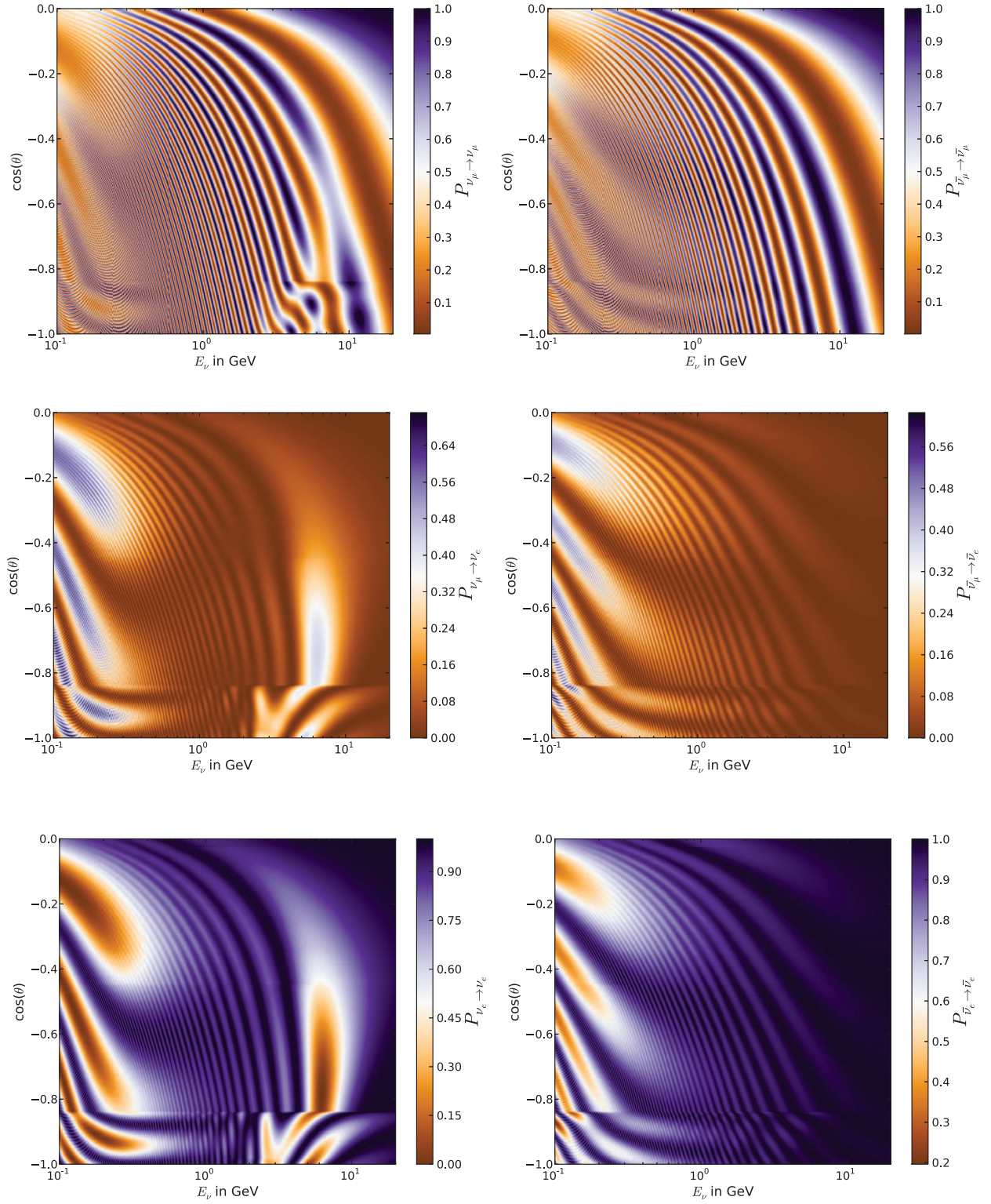


Figure 7-2: Six relevant oscillograms of oscillation probabilities for atmospheric neutrinos and antineutrinos in the normal hierarchy hypothesis.

where  $\Delta m_{atm}^2 = m_3^2 - (m_1^2 + m_2^2)/2$ . The matter effects for neutrinos traveling through the dense Earth core ( $\cos(\theta) \leq -0.82$ ) is obvious. In particular, in the GeV region the structures strongly differ for neutrinos and antineutrinos, and these structures swap between neutrinos and antineutrinos for the inverted hierarchy (IH) hypothesis.

A set of analytical expressions of the oscillation probabilities in Fig. 7-2 are very convenient for us to understand the oscillation features. For illustrative purposes we adopt the ‘‘one dominant mass scale’’ approximation ( $\Delta m_{21}^2 \ll |\Delta m_{31}^2|$ ) and have the following formulas [316–319]:

$$P(\nu_e \rightarrow \nu_e) \approx 1 - \sin^2 2\theta_{13}^m \sin^2 \left[ 1.27(\Delta m_{31}^2)^m \frac{L}{E_\nu} \right]; \quad (7.5)$$

$$P(\nu_e \rightarrow \nu_\mu) \approx P(\nu_\mu \rightarrow \nu_e) \approx \sin^2 \theta_{23} \sin^2 2\theta_{13}^m \sin^2 \left[ 1.27(\Delta m_{31}^2)^m \frac{L}{E_\nu} \right]; \quad (7.6)$$

$$\begin{aligned} P(\nu_\mu \rightarrow \nu_\mu) \approx & 1 - \cos^2 \theta_{13}^m \sin^2 2\theta_{23} \sin^2 \left[ 1.27 \frac{\Delta m_{31}^2 + A + (\Delta m_{31}^2)^m}{2} \frac{L}{E_\nu} \right] \\ & - \sin^2 \theta_{13}^m \sin^2 2\theta_{23} \sin^2 \left[ 1.27 \frac{\Delta m_{31}^2 + A - (\Delta m_{31}^2)^m}{2} \frac{L}{E_\nu} \right] \\ & - \sin^4 \theta_{23} \sin^2 2\theta_{13}^m \sin^2 \left[ 1.27(\Delta m_{31}^2)^m \frac{L}{E_\nu} \right], \end{aligned} \quad (7.7)$$

where  $A = 2\sqrt{2}G_F N_e E_\nu$  and the superscript  $m$  denotes the effective quantities in matter. The units of  $L$ ,  $E_\nu$  and  $\Delta m_{31}^2$  are in units of km, GeV and  $\text{eV}^2$ , respectively. The effective mass squared difference  $(\Delta m_{31}^2)^m$  and mixing angle  $\sin^2 2\theta_{13}^m$  are given by

$$(\Delta m_{31}^2)^m = \Delta m_{31}^2 \sqrt{(\cos 2\theta_{13} - A/\Delta m_{31}^2)^2 + \sin^2 2\theta_{13}}, \quad (7.8)$$

$$\sin^2 2\theta_{13}^m = \frac{\sin^2 2\theta_{13}}{(\cos 2\theta_{13} - A/\Delta m_{31}^2)^2 + \sin^2 2\theta_{13}}. \quad (7.9)$$

It should be worthwhile to stress that Eqs. (7.5-7.7) are valid when  $\Delta m_{21}^2 L/E_\nu \ll 1$ , namely  $L/E_\nu \ll 13263 \text{ km/GeV}$ . The expansion in the small parameters ( $\sin \theta_{13}$  and  $\Delta m_{21}^2$ ) can be found in Ref. [318]. For antineutrinos, the corresponding oscillation probabilities  $P(\bar{\nu}_e \rightarrow \bar{\nu}_e)$ ,  $P(\bar{\nu}_e \rightarrow \bar{\nu}_\mu)$  and  $P(\bar{\nu}_\mu \rightarrow \bar{\nu}_\mu)$  can be derived from Eqs. (7.5-7.9) with  $A \rightarrow -A$ . It is clear that neutrinos and antineutrinos have the same oscillation probabilities for the opposite mass hierarchies:

$$P_{\text{NH}}(\nu_\alpha \rightarrow \nu_\beta) = P_{\text{IH}}(\bar{\nu}_\alpha \rightarrow \bar{\nu}_\beta), P_{\text{IH}}(\nu_\alpha \rightarrow \nu_\beta) = P_{\text{NH}}(\bar{\nu}_\alpha \rightarrow \bar{\nu}_\beta). \quad (7.10)$$

Therefore, one can image the oscillation probabilities in the IH case from Fig. 7-2 if the condition  $\Delta m_{21}^2 L/E_\nu \ll 1$  is satisfied.

When the matter potential term  $A \ll |\Delta m_{31}^2| \cos 2\theta_{13}$  for the downward atmospheric neutrinos ( $\cos(\theta) > 0$ ), we may neglect  $A$  and obtain the vacuum oscillation probabilities from the above equations. Then, these vacuum oscillation probabilities are the same for the NH and IH cases. If  $A = \Delta m_{31}^2 \cos 2\theta_{13}$ , the MSW resonance will significantly enhance the effective mixing angle  $\sin^2 2\theta_{13}^m \rightarrow 1$ . Note that the MSW resonance enhancement occurs for neutrinos in the normal mass hierarchy and for antineutrinos in the inverted mass hierarchy. The resonance energy can be written as

$$E_\nu = \frac{\Delta m_{31}^2 \cos 2\theta_{13}}{2\sqrt{2}G_F N_e} = 32.1 \text{ GeV} \frac{g/\text{cm}^3}{\rho} \frac{0.5}{Y_e} \frac{\Delta m_{31}^2}{2.43 \times 10^{-3} \text{ eV}^2} \cos 2\theta_{13}. \quad (7.11)$$

Considering the Earth density profile, we can obtain the resonance energy range  $E_\nu \approx 3 - 10$  GeV for the atmospheric neutrinos passing through the Earth. In the resonance case, the oscillation probabilities in Eqs. (7.5-7.7) have significant differences for the NH and IH hypotheses. With the help of Eq. (7.10), we can easily find these differences from Fig.7-2. Therefore the upward atmospheric neutrinos can be used to probe the neutrino mass hierarchy.

The oscillation probabilities in Eqs. (7.5-7.7) do not include the CP phase  $\delta$  because we have ignored the subleading terms. Note that these approximated expressions are only valid in the case of  $\Delta m_{21}^2 L/E_\nu \ll 1$ . In order to estimate the impact of the CP phase  $\delta$ , we numerically calculate the oscillation probabilities in the neutrino energy and zenith angle plane while scanning  $\delta$  from 0 to  $2\pi$ . In Fig. 7-3, we plot the maximum variations due to  $\delta$  for  $P(\nu_e \rightarrow \nu_\mu)$  and  $P(\nu_\mu \rightarrow \nu_\mu)$ . Note that  $P(\nu_\mu \rightarrow \nu_e)$  and  $P(\nu_e \rightarrow \nu_e)$  have the same results since

$$P(\nu_\alpha \rightarrow \nu_\beta) = P(\nu_\beta \rightarrow \nu_\alpha)(\delta \rightarrow -\delta) \quad (7.12)$$

for constant or symmetric matter density profiles [318]. In addition, the  $P(\nu_e \rightarrow \nu_e)$  case is not sensitive to  $\delta$ . Since only upward going neutrinos are influenced by matter effects we only see differences for these directions as shown in Fig. 7-3. Because the expected rates are higher towards lower energies, we find that the best region to search for the CP phase is the sub-GeV region.

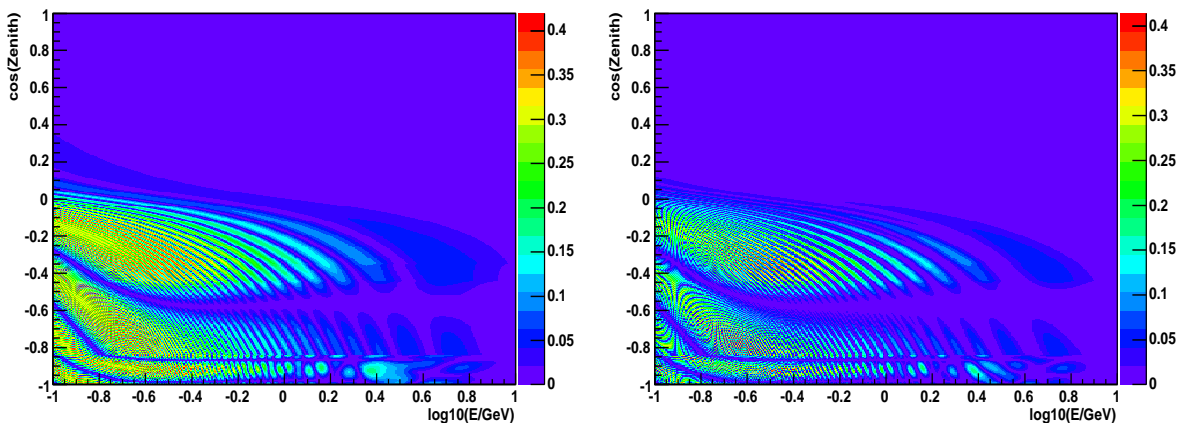


Figure 7-3: Maximum variations of oscillation probabilities in the energy and zenith angle plane for  $P(\nu_e \rightarrow \nu_\mu)$  ( left) and  $P(\nu_\mu \rightarrow \nu_\mu)$  (right) cases where we scan the CP phase  $\delta$  from 0 to  $2\pi$ .

## 7.3 Detector Performance

### 7.3.1 Monte Carlo Simulation

According to the detector properties described in appendix, we simulate atmospheric neutrino events using GENIE as generator (Version 2.8.0) [320] and Geant4 for detector simulation. We use the atmospheric neutrino event generation application in GENIE to generate 5 million events in JUNO detector including oscillation effects and additionally 25 million neutrino events which are later reweighted using the oscillation probability with nuCraft [315]. Unless otherwise specified, we take the best fit values in Eq. (7.4),  $\delta = 0$  and the normal hierarchy to calculate the neutrino oscillation probabilities in this subsection. For the first 5 million simulated events we have performed

a full detector simulation where the resulting particles are propagated using the Geant4 simulation [321]. Geant4 then provide various quantities for each neutrino event, such as the event vertex radius  $R_\nu$ , visible energy  $E_{vis}$ , charged lepton's zenith angles  $\theta_e$  and  $\theta_\mu$ , muon track length in the LS  $L_\mu$ , captured neutron numbers  $N_n$  and the Michel electron numbers  $N_e$ , etc. The JUNO central detector can measure the neutrino energy very well. For illustration, we plot the energy  $E_\nu$  versus the visible energy in the target region  $E_{vis}$  for the  $\nu_\mu/\bar{\nu}_\mu$  CC interactions in the upper-left panel of Fig. 7-4. Since some particles can escape the LS region with partially deposited energy, one finds  $E_{vis} \ll E_\nu$  for many events. If the event vertex  $R_\nu < 16.7$  m and  $\mu^\pm$  stops in the LS, the  $E_{vis}$  smearing is small as shown in the upper-right panel of Fig. 7-4. In the lower panels of Fig. 7-4, we plot  $\theta_\nu$  versus  $\theta_\mu$  for all (left) and  $L_\mu \geq 5$  m (right)  $\nu_\mu/\bar{\nu}_\mu$  CC events. It is found that  $\theta_\mu$  has smaller smearing for  $L_\mu \geq 5$  m case.

The expected number of the atmospheric neutrino CC events in every bin of the neutrino energy and zenith angle can be expressed as:

$$T_{ij,\nu_\alpha} = 2\pi MT \int_{\cos \theta_z^{i,min}}^{\cos \theta_z^{i,max}} d \cos \theta_z \int_{E_\nu^{j,min}}^{E_\nu^{j,max}} dE_\nu F_\alpha(\cos \theta_z, E_\nu) \sigma_{\nu_\alpha}, \quad (7.13)$$

with

$$F_\alpha(\cos \theta_z, E_\nu) = \sum_{l=(e,\mu,\tau)} c_{\nu_l} \phi_{\nu_l} \cdot P(\nu_l \rightarrow \nu_\alpha), \quad (7.14)$$

where  $\nu_\alpha = (\nu_e, \nu_\mu, \nu_\tau)$ ,  $M = 20$  kton is the LS target mass,  $T$  is the exposure time,  $\cos \theta_z^{i,min/max}$  and  $E_\nu^{j,min/max}$  are the borders of the bin  $i, j$  in zenith angle and energy. Unless otherwise specified, the 200 kton-years exposure will be used in this section.  $\phi_{\nu_l}$  are the initial atmospheric neutrino fluxes from Ref. [312]. For the flux normalization terms  $c_{\nu_l}$ , we set  $c_{\nu_e} = c_{\nu_\mu} = 1$  and  $c_{\nu_\tau} = 0$ .  $\sigma_{\nu_\alpha}$  is the  $\nu_\alpha$  per nucleon CC cross section [320] as shown in left panel of Fig. 7-5. Here we have considered that the LS target includes 12%  $^1\text{H}$  and 88%  $^{12}\text{C}$ . Considering the different cross sections, fluxes and oscillation probabilities the above expression applies also to antineutrinos. Applying it to JUNO we find that 8662  $\nu_\mu$  CC events, 3136  $\bar{\nu}_\mu$  CC events, 6637  $\nu_e$  CC events, 2221  $\bar{\nu}_e$  CC events, 90  $\nu_\tau$  CC events, 44  $\bar{\nu}_\tau$  CC events and a total of 12255 NC events. Comparing the event numbers per bin of the MC simulation and theoretical prediction, we determine the weight value for every MC event. Then the expected event sample can be obtained for the given neutrino interaction and oscillation parameters. In the right panel of Fig. 7-5, we plot the expected spectra as a function of the visible energy  $E_{vis}$ . Note that 88.5% of the NC events have visible energies smaller than 1.0 GeV since the final state neutrino does not deposit energy and the final state hadrons have large quenching effect.

### 7.3.2 Reconstruction Potential

The JUNO central detector can measure the visible energy  $E_{vis}$  of atmospheric neutrinos very well. In the Geant4 detector simulation, we have considered the quenching effect for different final state particles. The visible energy resolution depends on the statistical fluctuation in the scintillation photon emission and the quenching fluctuation. Here we assume  $\sigma_{E_{vis}} = 0.01\sqrt{E_{vis}/\text{GeV}}$  for the following analysis. The JUNO central detector can also reconstruct the track direction of the energetic charged particle by use of the time profile per PMT. The scintillation lights are emitted isotropically for every energy deposition point of the track. However, the first photon arriving at

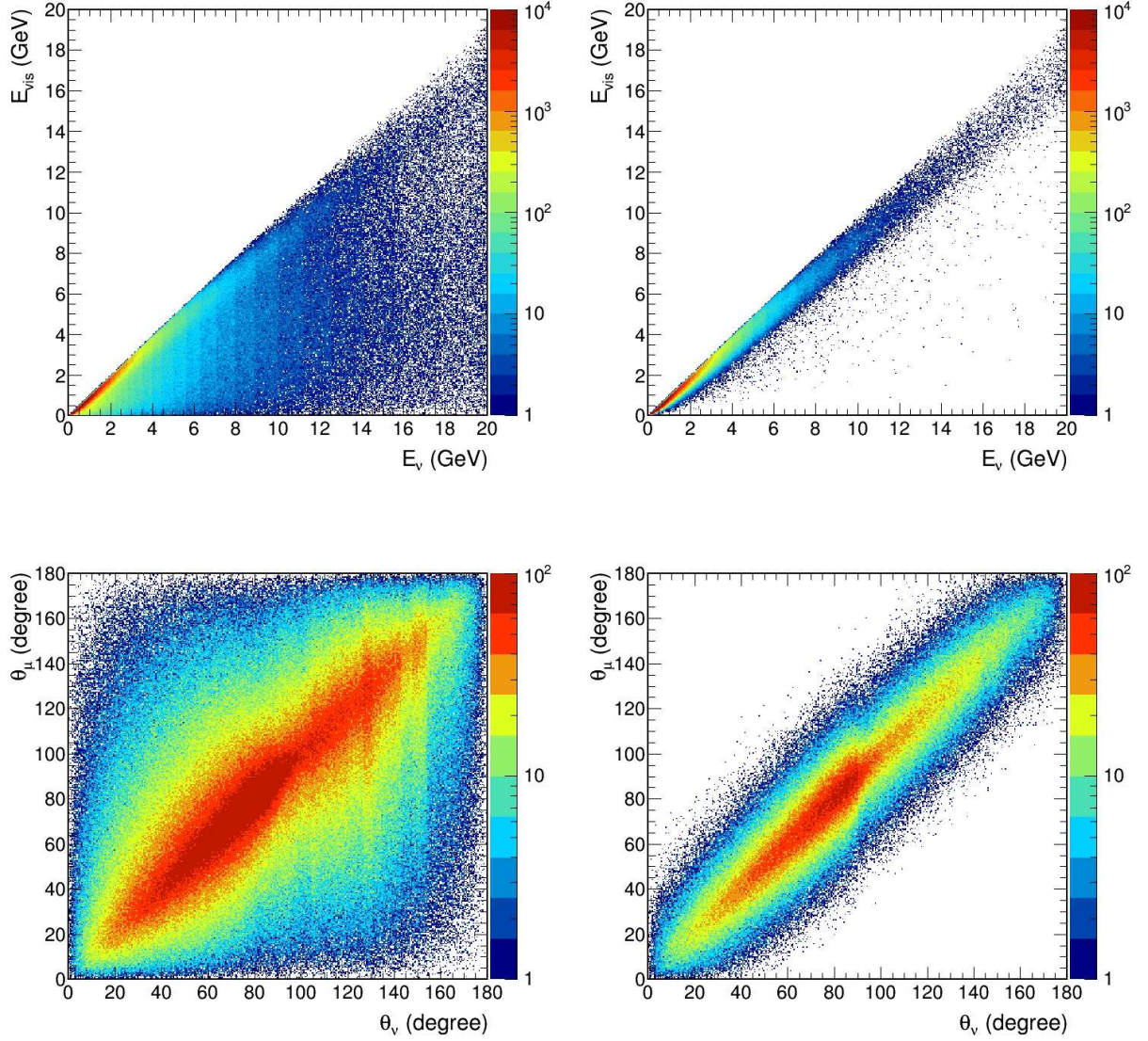


Figure 7-4: The initial neutrino energy  $E_\nu$  versus the visible energy  $E_{vis}$  (upper panels) and the initial neutrino direction  $\theta_\nu$  versus the  $\mu^\pm$  direction  $\theta_\mu$  (lower panels) for all (left) and selected (right)  $\nu_\mu/\bar{\nu}_\mu$  CC events

any PMT from this track are not isotropic when the energetic particle travels faster than light in the LS [311]. This first photon surface coinciding with the Cherenkov surface is directly correlated with the particle position and its time evolution hence includes all information about the track. With the help of the above principle, one may reconstruct the cosmic muon direction and suppress the corresponding backgrounds. More importantly, we can measure the charged lepton direction for the atmospheric neutrino CC events.

We have made a toy MC simulation for single muon tracks in the JUNO's central detector. For the track reconstruction, algorithms using the first photons registered in each PMT show promising

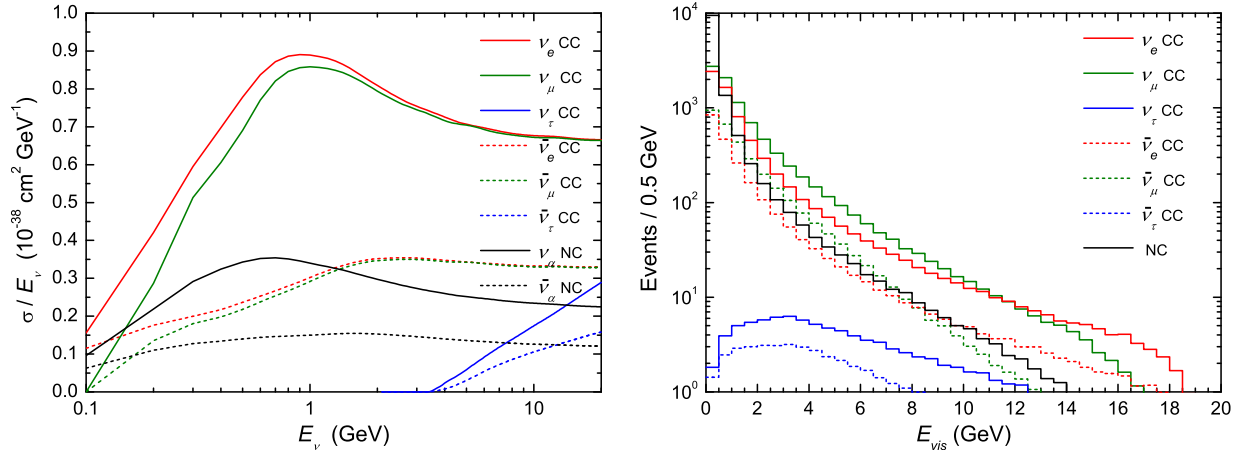


Figure 7-5: Left panel: the neutrino and antineutrino per nucleon cross sections for the LS target [320]. Right panel: the expected spectra as a function of  $E_{vis}$  for the 200 kton-years exposure.

results for JUNO (See the appendix for details). It is found that the direction and track length  $L_\mu$  resolutions mainly depend on the intrinsic PMT timing resolution. If it is better than 4 ns, the muon track length resolution is better than 0.5% and the angular resolution is better than  $1^\circ$  when  $L_\mu \geq 5$  m. For  $1 \text{ m} < L_\mu < 5$  m,  $L_\mu$  and angular resolution are better than 1% and  $10^\circ$ , respectively.

In the atmospheric neutrino CC interactions, the final states consist of a charged lepton and several hadrons. The charged lepton takes on average about 60% of the initial neutrino energy and several hadronic particles will share the residual energy. The existence of hadronic final state particles will have a negative effect on the expected resolutions for the charged lepton direction. On the other hand, these hadronic particles can also affect the charged lepton flavor recognition even if the signals from the single  $\mu^\pm$  track and  $e^\pm$  shower have clear differences. In addition, a substantial fraction of  $\pi^\pm$  ( $\gamma$  from  $\pi^0 \rightarrow \gamma\gamma$ ) from the NC interactions will be misidentified as  $\mu^\pm$  ( $e^\pm$ ) [162]. In this case, the  $\pi^\pm$  or  $\gamma$  direction will be reconstructed as the charged lepton direction and the atmospheric neutrino NC events become the main backgrounds. Note that the direction reconstruction, lepton flavor recognition and misidentification efficiencies have not been fully explored so far [162, 322, 323]. The related studies are under way.

To significantly increase the muon recognition capability and suppress the misidentification efficiencies, we select tracks with a length of at least a few meters. The final state hadrons ( $p, n$  and  $\pi^\pm$ ) usually have the shorter track length than  $\mu^\pm$  since they would undergo hadronic interactions. For the JUNO LS, the nuclear and pion interaction lengths are about 0.9m and 1.3m, respectively. The electromagnetic shower from  $e^\pm$  and  $\pi^0$  will not give a very long track because of the 0.5m radiation length. It is clear that muons with longer track lengths are easier to identify and reconstruct.

### 7.3.3 Event Selection and Classification

To identify charged leptons, we conservatively require a track length of  $\geq 5$  m and only consider the  $\nu_\mu/\bar{\nu}_\mu$  CC events. The selection efficiency of  $L_\mu \geq 5$  m is 29.2% for a MC sample of 11798  $\nu_\mu/\bar{\nu}_\mu$  CC events. For these selected events, we assume that the final state  $\mu^\pm$  can be fully reconstructed and identified. The corresponding  $\mu^\pm$  angular resolution is assumed to be  $1^\circ$ . Note that the Michel

electron from  $\mu^\pm$  decay can also help us to optimize the algorithm for distinguishing muon track from electron shower. For the selected CC events, the NC backgrounds are negligible based on the following three reasons. Firstly, event rates for the NC interaction is far lower than those from the  $\nu_\mu/\bar{\nu}_\mu$  CC interactions for  $E_{vis} > 1$  GeV as shown in the right panel of Fig. 7-5. This is because that the NC events are suppressed due to the  $E_\nu^{-2.7}$  energy dependence of the neutrino flux and hadron quenching effect for a given visible energy. Secondly, the energetic  $\pi^\pm$  production rates are largely suppressed since several hadrons share this visible energy. Finally, it is very rare for these  $\pi^\pm$  to produce a long straight track for the 1.3m pion interaction length. As shown in right panel of Fig. 7-5, the  $\nu_\tau/\bar{\nu}_\tau$  CC backgrounds can also be ignored when we consider the 17.36% branching ratio of  $\tau^- \rightarrow \mu^- \bar{\nu}_\mu \nu_\tau$ .

According to the characteristics of the reconstructed muon track, the selected  $\nu_\mu$  and  $\bar{\nu}_\mu$  CC events will be classified as fully contained (FC) or partially contained (PC) events, where FC and PC refers to muon track being fully or partially contained in the LS region. Note that the Michel electron can also help us to distinguish the FC from PC events. For the specified sample we find 1932 FC and 1510 PC events with  $L_\mu \geq 5$  m. The FC sample (green line) has a better correlation between  $E_{vis}$  and  $E_\nu$  than those from the PC (violet line) sample and all 11798 events (black line) as shown in left panel of Fig. 7-6. Here we have also plotted the spectrum (orange line) of the FC sample as a function of the  $\mu^\pm$  visible energy  $E_\mu$  over  $E_\nu$ . It is found that the PC events in the JUNO LS detector and the FC events in the Cherenkov detector have the similar energy smearing. As shown in the right panel of Fig. 7-6, the PC sample has the smaller angle smearing  $\theta_\mu - \theta_\nu$  than the FC sample and all  $\nu_\mu/\bar{\nu}_\mu$  CC events. We will focus on the 1932 FC and 1510 PC events with  $L_\mu \geq 5$  m and plot their expected spectra as a function of  $E_{vis}$  in Fig. 7-7. The FC and PC samples include 67.7% and 63.6%  $\nu_\mu$ , respectively.

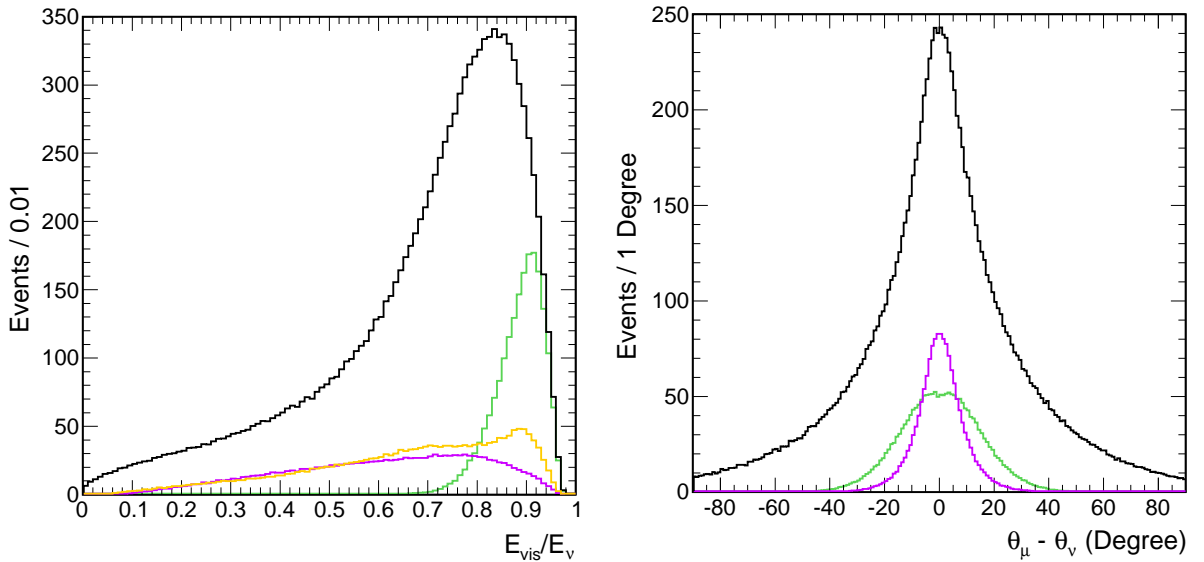


Figure 7-6: The calculated spectra as a function of  $E_{vis}/E_\nu$  (left) and  $\theta_\mu - \theta_\nu$  (right) for the selected FC (green), PC (violet) and all (black)  $\nu_\mu/\bar{\nu}_\mu$  CC events. The orange line describes the  $E_\mu/E_\nu$  distribution for the FC events.

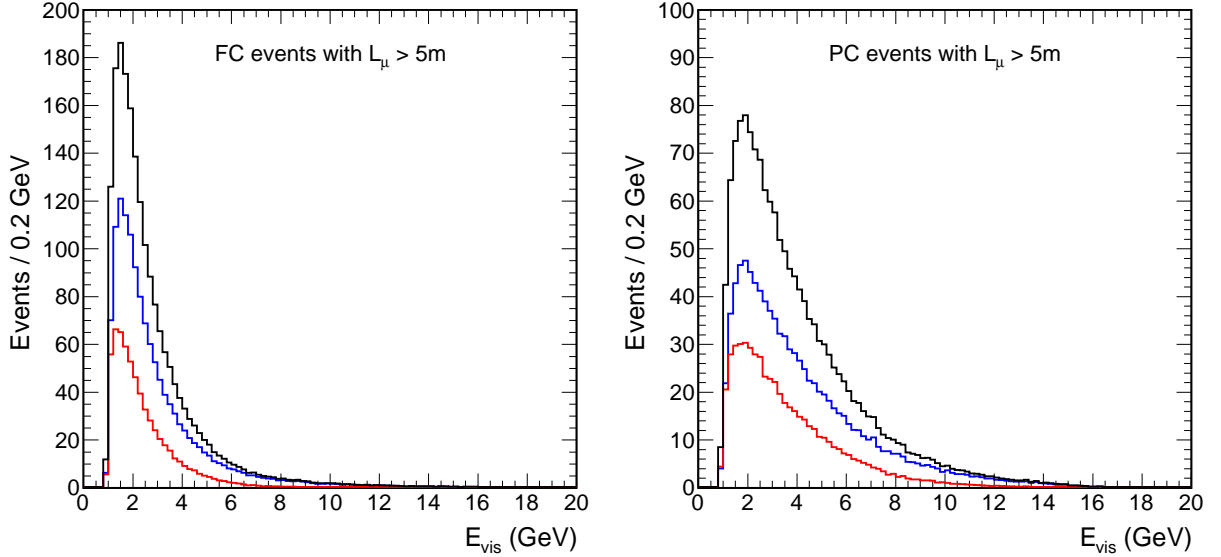


Figure 7-7: The expected FC (left) and PC (right) spectra as a function of the visible energy  $E_{vis}$  for the  $L_\mu \geq 5$  m  $\nu_\mu/\bar{\nu}_\mu$  CC events. The blue and red lines denote  $\nu_\mu$  and  $\bar{\nu}_\mu$ , respectively.

Because of the oscillation effects of different neutrino flavors, a neutrino and antineutrino mixed sample would have a smaller sensitivity than each of its constituents. As a non-magnetic detector, JUNO can not directly measure the charge of the muon tracks to distinguish neutrino from antineutrino events. However, we can choose other methods to statistically distinguish neutrinos from antineutrinos [324] which can improve the JUNO sensitivities to the neutrino mass hierarchy, the octant of  $\theta_{23}$  and the CP phase  $\delta$ . In JUNO we could use the following effects to discriminate between neutrinos and antineutrinos. Firstly, the primary  $\mu^-$  can be captured by a nucleus to form a muonic atom after the  $\mu^-$  loses its kinematic energy. In this case,  $\mu^-$  has a 8% capture probability on the nucleus of  $^{12}\text{C}$  and no Michel electron is produced. This feature allows a clear identification of  $\nu_\mu$  if the primary  $\mu^-$  does not escape the LS region. Secondly, the neutrino statistically shall transfer, on average, more momentum to the hadronic final states than the antineutrino in CC interactions. These primary hadrons may produce secondary particles through the final state interaction (FSI) in the nuclear environment and the inelastic scattering process in the LS. Therefore, the neutrino events on average have more Michel electrons (from  $\pi^\pm$  and  $\mu^\pm$  decay) than the antineutrino events [325]. Finally, we can deduce the visible energy of the hadron showers  $E_h$  from  $E_{vis}$  and the muon track length since the muons can be assumed to be minimum ionizing which leads to a constant energy deposition. Then the measured relative energy transfer  $Y_{vis} = E_h/E_{vis}$  may be used to statistically distinguish  $\nu_\mu$  from  $\bar{\nu}_\mu$  based on the same principle as in the second method.

We now group the selected FC and PC events into  $\nu_\mu$ -like and  $\bar{\nu}_\mu$ -like samples based on the  $\mu^-$  capture of nucleus, Michel electron numbers  $N_e$  and the relative energy transfer  $Y_{vis}$ . Firstly the FC events with  $N_e \geq 2$  or the  $\mu^-$  capture on nucleus of  $^{12}\text{C}$  will be classified into the FC  $\nu_\mu$ -like sample. Then, the other FC events with  $Y_{vis} \geq 0.5$  also get classified as FC  $\nu_\mu$ -like events. Finally, we classify the residual FC events into the FC  $\bar{\nu}_\mu$ -like sample. For the PC events, the PC  $\nu_\mu$ -like and PC  $\bar{\nu}_\mu$ -like samples can be obtained when we only replace  $N_e \geq 2$  with  $N_e \geq 1$ . In Table 7-1, we list the expected  $\nu_\mu$ ,  $\bar{\nu}_\mu$  and total event numbers of four samples for 200 kton-years exposure. It is worthwhile to stress that the Michel electron numbers  $N_e$  plays a key role in the



above classification. For example, the selection  $N_e \geq 2$  will result in 524  $\nu_\mu$  and 62  $\bar{\nu}_\mu$  events in the FC  $\nu_\mu$ -like sample. In addition to the above event classification, we have also performed a simplified classification in track-like and point-like events. Track-like events are all CC  $\nu_\mu$  events with an inelasticity  $E_h/E_\nu < 0.65$ . All other interactions are called point-like, because the cascade at the interaction vertex dominates the visible energy. This classification based on 25 million simulation events will be used for the pessimistic analysis of the MH sensitivity.

	$\nu_\mu$ events	$\bar{\nu}_\mu$ events	Total events	$\nu_\mu$ purity
FC $\nu_\mu$ -like	656	83	739	88.8%
FC $\bar{\nu}_\mu$ -like	652	541	1193	54.6%
PC $\nu_\mu$ -like	577	166	743	77.7%
PC $\bar{\nu}_\mu$ -like	383	384	767	50.0%

Table 7-1: The expected event numbers of four samples for 200 kton-years exposure.

### 7.3.4 Identification of $\nu_\mu$ , $\bar{\nu}_\mu$ , $\nu_e$ , and $\bar{\nu}_e$ for the CP-Violation analysis

As shown in Fig. 7-3, the sub-GeV region is most sensitive to the CP phase  $\delta$ . Below 100 MeV, the current atmospheric neutrino flux prediction has a large uncertainty, and the discrepancy between models can be as large as 50%. Therefore, it is a difficult region to study. Above 100 MeV, the CC quasi elastic processes are open for  $\nu_\mu$  and  $\nu_e$ . Around 300 MeV, the CC resonance production process is open. In this case, the final states include the charged lepton, pions and the daughter nuclei. For a liquid scintillator detector, which is weak in detecting multiple tracks for the sub-GeV neutrino events, it is also difficult to distinguish  $\mu^\pm$  ( $e^\pm$ ) from  $\pi^\pm$  ( $\pi^0$ ).

For the identification of the sub-GeV  $\nu_\mu$ ,  $\bar{\nu}_\mu$ ,  $\nu_e$ , and  $\bar{\nu}_e$ , the [100, 300] MeV region is very interesting since it may be a region with relatively low background. For example, the final state  $\mu^-$  will on average take 74% of the initial 200 MeV energy in the  $\nu_\mu$  CC interaction. It is possible for us to reconstruct the track length and direction of the charged lepton as discussed in appendix. Besides the quenching effect, the energy of  $\mu^\pm$  and  $e^\pm$  can be measured. Another advantage of the [100, 300] MeV region is that we may distinguish neutrinos from antineutrinos by use of the different daughter nuclei. In the [100, 300] MeV region, the  $\bar{\nu}_e$  and  $\nu_e$  CC processes can be written as

$${}^{12}\text{C}(\bar{\nu}_e, e^+){}^{12}\text{B}^*, \quad {}^{12}\text{C}(\bar{\nu}_e, e^+){}^{12}\text{B}(\text{g.s.}), \quad (7.15)$$

$${}^{12}\text{C}(\nu_e, e^-){}^{12}\text{N}^*, \quad {}^{12}\text{C}(\nu_e, e^-){}^{12}\text{N}(\text{g.s.}), \quad (7.16)$$

where the ground states  ${}^{12}\text{N}(\text{g.s.})$  and  ${}^{12}\text{B}(\text{g.s.})$  can be identified by the JUNO detector since they have different lifetimes and Q-values. The excited states  ${}^{12}\text{B}^*$  and  ${}^{12}\text{N}^*$  have characteristic decay modes. For example,  ${}^{12}\text{N}^*$  may decay into a proton and a  ${}^{11}\text{C}$ . The  $\beta^+$  decay of  ${}^{11}\text{C}$  can be identified since JUNO has a very low energy threshold. JUNO can also detect  $\bar{\nu}_e$  through IBD process  $p(\bar{\nu}_e, e^+)n$ . The same principle can be applied to  $\bar{\nu}_\mu$  and  $\nu_\mu$ . The final state muon with a 2.2  $\mu\text{s}$  lifetime can decay into a Michel electron plus neutrinos. This delayed coincidence feature can be used to distinguish muon neutrinos. In this case, a triple coincidence from prompt muon production, the Michel electron from muon decay, and the decay of the daughter nuclei are required.

It is promising to use double (triple) coincidence detection for  $\bar{\nu}_e$  and  $\nu_e$  ( $\bar{\nu}_\mu$  and  $\nu_\mu$ ), and to rely on different daughter nuclei to distinguish neutrinos from antineutrinos. However it is very hard to precisely predict the cross sections for different daughter nuclei in present nuclear structure models. Some experiments only measure the ground state cross section. Studies on the particle

identification and reconstruction are in progress for the [100, 300] MeV atmospheric neutrinos. Therefore the NC and CC backgrounds are not yet certain. In the [100, 300] MeV region, we shall take the idealized assumptions and only present a very optimistic upper limit of the JUNO detector for the CP research.

## 7.4 Atmospheric Neutrino Analysis

### 7.4.1 The $\chi^2$ Function

In the following we will investigate different data samples using the visible neutrino energy  $E_{vis}$  and the  $\mu^\pm$  zenith angle  $\theta_\mu$ . For most of the analysis we will use a  $\chi^2$  function, where we adopt the Poisson form:

$$\chi^2 = 2 \sum_{ij} \left[ \tilde{T}_{ij} - N_{ij} + N_{ij} \ln \frac{N_{ij}}{\tilde{T}_{ij}} \right] + \sum_{k=1}^4 \xi_k^2, \quad (7.17)$$

with

$$\tilde{T}_{ij} = T_{ij} \left( 1 + \sum_{k=1}^4 \pi_{ij}^k \xi_k \right), \quad (7.18)$$

where the subscripts  $i$  and  $j$  run over the energy and angle bins, respectively. For the range  $-1 \leq \cos \theta_\mu \leq 1$ , the number of bins is chosen to be 10, namely a bin width of 0.2. Then we divide the visible energy into several bins and require the experimental event numbers  $N_{ij} \geq 5$  for every bin. Adopting a set of oscillation parameters as the true values, we can calculate  $N_{ij}$  based on the MC efficiency per bin. The expected event numbers  $T_{ij}$  can be obtained from Eq. (7.13) with any input values of oscillation parameters. Using the method of pulls, we take into account the neutrino flux and cross section systematic uncertainties [326]. The pull variable  $\xi_1$  describes the 10% normalization error of neutrino cross section.  $\xi_2$  is the pull for the overall 20% neutrino flux error.  $\xi_3$  and  $\xi_4$  parameterize the 5% uncertainties on the energy and zenith angle dependence of atmospheric neutrino fluxes, respectively. The ‘‘coupling’’  $\pi_{ij}^k$  describes the fractional change of  $T_{ij}$  when the corresponding uncertainty has  $1\sigma$  deviation. Finally, we minimize  $\chi^2$  over the above four pull variables for a set of input oscillation parameters and derive the best-fit minimal  $\chi^2(\text{test})$ . For the test NH and IH hypotheses, the difference  $\Delta\chi^2 = |\chi^2(\text{IH}) - \chi^2(\text{NH})|$  will be used to calculate the JUNO MH sensitivity with  $N\sigma = \sqrt{\Delta\chi^2}$ .

### 7.4.2 Neutrino Mass Hierarchy

As discussed in Sec. 7.2,  $\nu_\mu$  and  $\bar{\nu}_\mu$  have opposite contributions to the MH sensitivity in the absence of the charge identification. That is because  $P(\nu_\mu \rightarrow \nu_\mu)$  and  $P(\nu_e \rightarrow \nu_\mu)$  in the NH case is approximately equal to the corresponding antineutrino oscillation probabilities in the IH case. Due to different fluxes and cross sections one expects a higher neutrino rate compared to antineutrinos which allows a measurement of the MH without distinguishing between the two. The statistical separation of  $\nu_\mu$  and  $\bar{\nu}_\mu$  events in Sec. 7.3.3 will obviously improve the sensitivity further.

For the upward atmospheric neutrinos, the oscillation probabilities  $P(\nu_\mu \rightarrow \nu_\mu)$  and  $P(\nu_e \rightarrow \nu_\mu)$  in the NH and IH cases have obvious differences due to the MSW resonance effect. These differences can be easily found from Eqs. (7.6-7.7) and Fig. 7-2 with the help of Eq. (7.10). It is clear that the approximated oscillation probabilities  $P(\nu_\mu \rightarrow \nu_\mu)$  and  $P(\nu_e \rightarrow \nu_\mu)$  in Eqs. (7.6-7.7) do not depend on  $\theta_{12}, \delta$  and  $\Delta m_{21}^2$ . In addition, the MH sensitivity is also insensitive to  $\theta_{13}$  since the

effective mixing angle  $\sin^2 2\theta_{13}^m$  will approach 1 in the MSW resonance case. Unless otherwise specified, we shall take  $\theta_{12}, \theta_{13}$  and  $\Delta m_{21}^2$  at their best values of Eq. (7.4), and the CP violation phase  $\delta = 0^\circ$  for the following analysis. Here we will analyze the dependence on  $\theta_{23}$  and  $\Delta m_{atm}^2$ . For three typical  $\sin^2 \theta_{23} = 0.4, 0.5, 0.6$ , we have calculated the theoretical and experimental event numbers per bin through varying  $\Delta m_{atm}^2$ . Then the JUNO MH sensitivity can be determined from Eqs. (7.17) and (7.18). The minimal  $\Delta\chi^2$  has been found at  $\Delta m_{atm}^2 = -2.40 \times 10^{-3} \text{eV}^2$  and  $\Delta m_{atm}^2 = 2.47 \times 10^{-3} \text{eV}^2$  for the true  $\Delta m_{atm}^2 = 2.43 \times 10^{-3} \text{eV}^2$  and  $\Delta m_{atm}^2 = -2.43 \times 10^{-3} \text{eV}^2$ , respectively. Using the two values as the test  $\Delta m_{atm}^2$ , we calculate the MH sensitivity as a function of livetime as shown in Fig. 7-8. It is found that JUNO has a  $0.9\sigma$  MH sensitivity with 10 year data and  $\sin^2 \theta_{23} = 0.5$ . The larger  $\sin^2 \theta_{23}$  gives better MH sensitivity. In the absence of the statistical separation of neutrinos and antineutrinos, about 20% reduction of the JUNO MH sensitivity is expected.

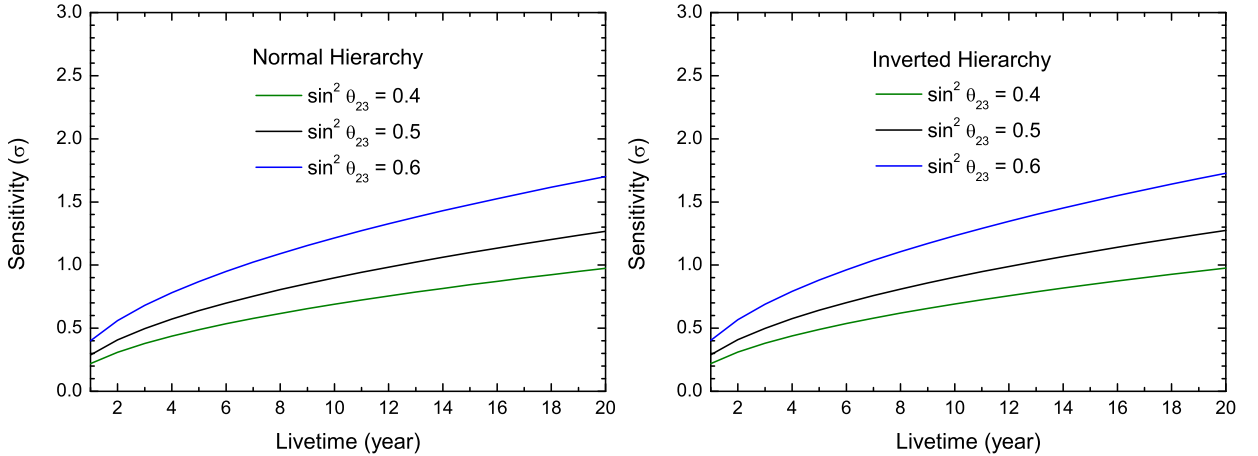


Figure 7-8: The JUNO MH sensitivities from high energy muon neutrino events as a function of livetime for the true NH (left) and IH (right) hypotheses.

In the following, we will discuss an optimistic estimation for the neutrino mass hierarchy based on few reasonable assumptions. Firstly, the  $\nu_e/\bar{\nu}_e$  CC events can be identified and reconstructed very well in the  $e^\pm$  visible energy  $E_{vis}^e > 1 \text{ GeV}$  and  $Y_{vis} < 0.5$  case. Secondly, we extend the selection condition  $L_\mu > 5\text{m}$  to  $L_\mu > 3\text{m}$  for the  $\nu_\mu/\bar{\nu}_\mu$  CC events. Finally, we replace the charged lepton direction with the neutrino direction for this physical analysis and assume  $10^\circ$  angular resolution. As shown in Fig. 7-9, we numerically calculate the optimistic MH sensitivities from  $\nu_\mu/\bar{\nu}_\mu$  (dashed lines) and  $\nu_e/\bar{\nu}_e$  (dotted lines) with a fixed  $\sin^2 \theta_{23} = 0.5$ . It is found that the  $\nu_\mu/\bar{\nu}_\mu$  contributions have a small enhancement with respect to the results in Fig. 7-8. The  $\nu_e/\bar{\nu}_e$  events have the larger sensitivities than  $\nu_\mu/\bar{\nu}_\mu$  events since most of  $\nu_e/\bar{\nu}_e$  events can deposit their energies in the LS region. The selected  $\nu_e/\bar{\nu}_e$  events only are divided into two samples in terms of the Michel electron number  $N_e = 0$  and  $N_e \geq 1$ . The combined sensitivities can reach  $1.8\sigma$  and  $2.6\sigma$  for 10 and 20 year data, respectively. Note that the predicted MH sensitivity will have a 13% reduction when we take  $20^\circ$  angular resolution.

Before the JUNO particle reconstruction and identification capabilities are fully understood, we should consider a more pessimistic case. For this analysis we adopt a different analytical method and assume that it will be only possible to distinguish muon tracks from other cascading events. We therefore divide the data into the point-like and track-like samples. The track-like sample contains only  $\nu_\mu/\bar{\nu}_\mu$  CC events with a  $E_h/E_\nu < 0.65$  inelasticity and the point-like sample all other CC

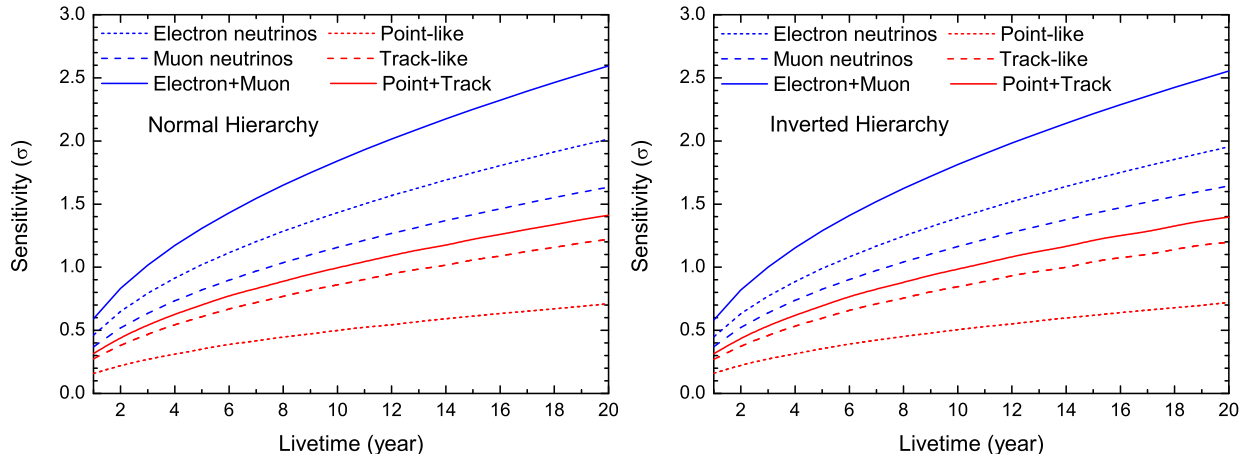


Figure 7-9: The future optimistic (blue) and pessimistic (red) MH sensitivities as a function of livetime for the true NH (left) and IH (right) hypotheses.

and NC events. Here we do not consider the statistical separation of neutrinos and antineutrinos, and do not discriminate the FC and PC events. In contrast to the optimistic case, we take the  $5\%\sqrt{E_{vis}}$  and  $37.2^\circ/\sqrt{E_\nu}$  for the visible energy and the neutrino direction resolutions, respectively.  $37.2^\circ/\sqrt{E_\nu}$  corresponds to the mean angle between the lepton and neutrino directions. In order to calculate the MH sensitivity we weight a simulated dataset of 25 million events according to the best fit parameters [27] of both NH and IH hierarchies. For the experimental event numbers  $N_{ij}$  in Eq. (7.17), we dice pseudo experiments for each hierarchy using a poisson distribution. This yields the Gaussian distributed  $\chi^2$  values. The MH sensitivity under the assumption that one hierarchy is true is the distance between the expectation values  $\mu_{\text{true}}$  and  $\mu_{\text{false}}$  expressed in units of the false hierarchy standard deviation  $\sigma_{\text{false}}$ . The estimated sensitivity  $N\sigma = |\mu_{\text{true}} - \mu_{\text{false}}|/\sigma_{\text{false}}$  can be seen in Fig. 7-9. After a 10 year measurement one would expect a  $1.0\sigma$  combined sensitivity from the point and track-like samples. The results are pessimistic compared to the optimistic case which is mostly due to the assumed angular uncertainties. Additionally, the sensitivity of the point-like sample is decreased by a high contamination of NC events and deep inelastic muon neutrino interactions while the track-like sample has a higher uncertainty on energy resolution due to a high number of PC events.

### 7.4.3 Atmospheric Mixing Angle $\theta_{23}$

For the atmospheric mixing angle  $\theta_{23}$ , the MINOS disappearance data indicates a non-maximal  $\theta_{23}$  [131]. However, the T2K disappearance data prefer a nearly maximal mixing  $\theta_{23} = 45^\circ$  [133]. It is an open question whether or not  $\theta_{23}$  is maximal. If  $\theta_{23}$  deviates from  $45^\circ$ , one can get both the lower octant (LO)  $\theta_{23} < 45^\circ$  and higher octant (HO)  $\theta_{23} > 45^\circ$  solutions, because the  $\nu_\mu/\bar{\nu}_\mu$  survival probability is mainly sensitive to the  $\sin^2 2\theta_{23}$  terms of Eq. (7.7) for the MINOS and T2K experiments. When the MSW resonance happens, the  $\sin^4 \theta_{23}$  term in Eq. (7.7) will be enlarged due to  $\sin^2 2\theta_{13}^m \rightarrow 1$ . Then the  $\sin^4 \theta_{23}$  term can help us to distinguish the  $\theta_{23}$  octant since  $\sin^4 \theta_{23}$  is different for the  $\theta_{23}$  and  $\pi/2 - \theta_{23}$  solutions. In addition, we should consider the oscillation probability  $P(\nu_e \rightarrow \nu_\mu)$  which is proportional to  $\sin^2 \theta_{23}$  as shown in Eq. (7.6). It is worthwhile to stress that the octant sensitivity from antineutrinos (neutrinos) is largely suppressed by  $\sin^2 2\theta_{13}^m \rightarrow \sin^2 2\theta_{13}$  when we take the NH (IH) hypothesis as the true mass hierarchy. Therefore

the statistical separation of neutrinos and antineutrinos can suppress the statistical errors and improve the octant sensitivity.

For the octant analysis, we assume a prior knowledge of mass hierarchy and hence consider the normal (inverted) hierarchy as the true hierarchy. For a given true  $\theta_{23}$ , we take the correct octant solution  $\theta_{23}$  and the wrong octant solution  $\pi/2 - \theta_{23}$  as the test values to calculate the best fit minimal difference  $\Delta\chi^2 = \chi^2(\pi/2 - \theta_{23}) - \chi^2(\theta_{23})$ . Then we can derive the JUNO octant sensitivity  $\sqrt{\Delta\chi^2}$ . In Fig. 7-10, we have plotted the JUNO sensitivities to the octant for the true NH and IH cases. The wrong  $\theta_{23}$  octant could be ruled out at  $1.8\sigma$  (NH) and  $0.9\sigma$  (IH) for the true  $\theta_{23} = 35^\circ$ . Note that the inverted hierarchy has the smaller octant sensitivity than the normal hierarchy, because neutrinos have more events than antineutrinos as shown in Fig. 7-7 and the MSW resonance occurs in the NH (IH) case for neutrinos (antineutrinos). We have also considered the  $\Delta m_{atm}^2$  impact on the octant sensitivity. As shown in Fig. 7-10, the JUNO octant sensitivity has a weak dependence on  $\Delta m_{atm}^2$ .

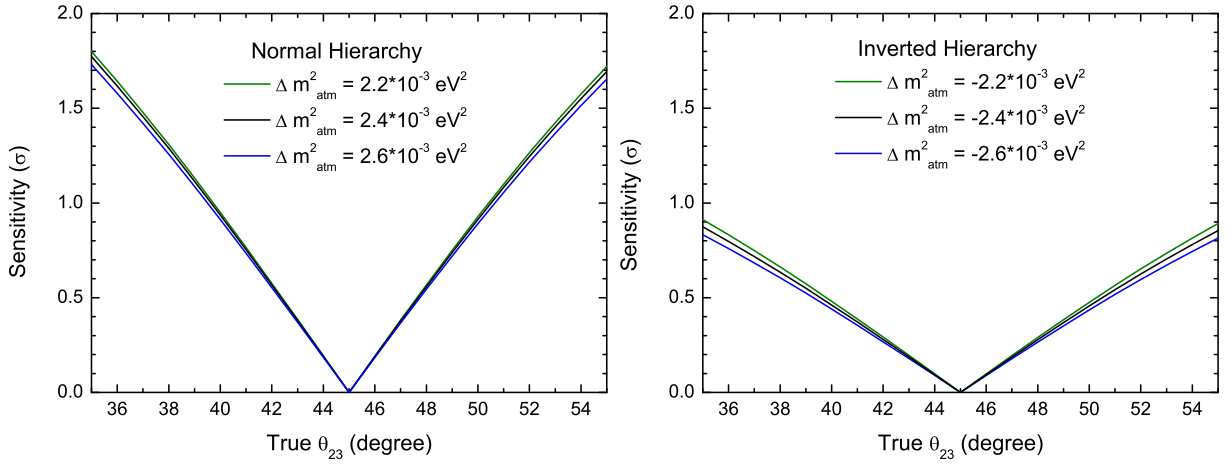


Figure 7-10: The JUNO sensitivities to the octant for high energy muon neutrino events as a function of true  $\theta_{23}$  in the true NH (left) and IH (right) cases.

#### 7.4.4 CP Phase $\delta$

As shown in Fig. 7-3, both  $P(\nu_e \rightarrow \nu_\mu)$  and  $P(\nu_\mu \rightarrow \nu_e)$  can be used to measure the CP phase  $\delta$ . However only the appearance oscillation probabilities are possible for us to discover the CP violation phenomenon, because  $P(\nu_\alpha \rightarrow \nu_\alpha) = P(\bar{\nu}_\alpha \rightarrow \bar{\nu}_\alpha)$  from the CPT invariance. The disappearance  $P(\nu_\mu \rightarrow \nu_\mu)$  only contain the  $\cos\delta$  terms which are invariant in the CP transformation ( $\delta \rightarrow -\delta$ ). The appearance  $P(\nu_e \rightarrow \nu_\mu)$  includes both  $\sin\delta$  and  $\cos\delta$  terms as shown in the approximated expressions of Ref. [318]. The  $\sin\delta$  terms can help us to discover the CP violation phenomenon, namely  $P(\nu_\alpha \rightarrow \nu_\beta) \neq P(\bar{\nu}_\alpha \rightarrow \bar{\nu}_\beta)$ . Note that  $\delta = 0$  and  $\delta = \pi$  correspond to the CP conservation. For a given true  $\delta$ , the CP violation sensitivity comes from whether or not it can be distinguished from the CP conservation. We take  $\delta = 0$  and  $\delta = \pi$  as the test values to calculate the best fit minimal differences  $\Delta\chi_0^2 = \chi^2(0) - \chi^2(\delta)$  and  $\Delta\chi_\pi^2 = \chi^2(\pi) - \chi^2(\delta)$ . Then we define the minimal value of  $\sqrt{\Delta\chi_0^2}$  and  $\sqrt{\Delta\chi_\pi^2}$  as the JUNO CP violation sensitivity. Since the  $\sin\delta$  terms have the opposite signs for neutrinos and antineutrinos, the statistical separation of  $\nu_\mu$  and  $\bar{\nu}_\mu$  signals will improve the sensitivity.

In Sec. 7.3.3, we have required  $L_\mu \geq 5$  m which means the  $\nu_\mu$  and  $\bar{\nu}_\mu$  energy is larger than 0.9

GeV. For these high energy  $\nu_\mu$  and  $\bar{\nu}_\mu$ , the oscillation probabilities  $P(\nu_\mu \rightarrow \nu_\mu)$  and  $P(\nu_e \rightarrow \nu_\mu)$  are sensitive to the CP phase  $\delta$  as shown in Fig. 7-3. However the kinematical smearing will obviously suppress the CP violation sensitivity. As shown in Fig. 7-11, the JUNO sensitivity to CP violation is very small for these high energy  $\nu_\mu$  and  $\bar{\nu}_\mu$  events where we have taken the best fit values of  $\Delta m_{atm}^2$ . It is found that different  $\sin^2 \theta_{23}$  can change the predicted sensitivity.

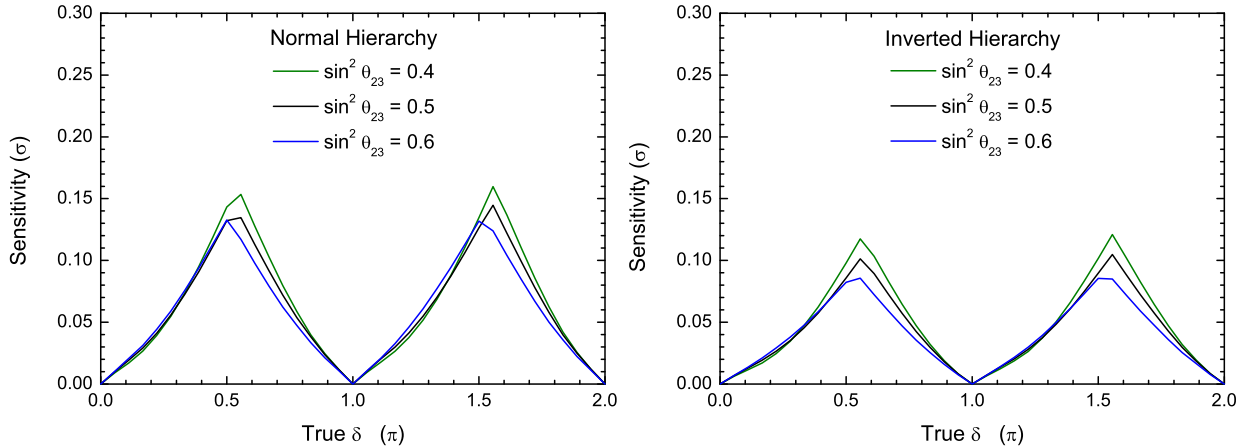


Figure 7-11: The JUNO's sensitivities to CP violation for high energy muon neutrino events as a function of true  $\delta$  in the NH (left) and IH (right) cases.

The lower energy [100, 300] MeV neutrinos have more sensitivity to measure CP phase  $\delta$  as shown in Fig. 7-3. With the techniques discussed in Sec. 7.3.4, it is possible to pursue such a measurement. The major uncertainty comes from the lack of knowledge of the daughter nuclei, which might spoil the idea. There might be also some backgrounds from the NC and CC processes of high energy neutrinos. An estimate of the maximal JUNO sensitivity is made by ignoring the above unknowns. The pure statistical sensitivity of JUNO detector in ten years is shown in Fig. 7-12 where all  $\nu_\mu$ ,  $\bar{\nu}_\mu$ ,  $\nu_e$ , and  $\bar{\nu}_e$  are considered. Direction reconstruction of electron and muon is not crucial, because it is only weakly correlated to the initial neutrino direction at these low energies.

#### 7.4.5 Summary

We have investigated atmospheric neutrinos in JUNO and discussed their contributions to the MH, octant and CP violation. In terms of the reconstruction potential of the JUNO detector, we conservatively use the atmospheric  $\nu_\mu$  and  $\bar{\nu}_\mu$  with the track length larger than 5 m for our physical analysis. These events have been classified into the FC  $\nu_\mu$ -like, FC  $\bar{\nu}_\mu$ -like, PC  $\nu_\mu$ -like and PC  $\bar{\nu}_\mu$ -like samples based on the  $\mu^\pm$  track and the statistical charge separation. Our numerical results have shown that the JUNO's MH sensitivity can reach  $0.9\sigma$  for a 200 kton-years exposure and  $\sin^2 \theta_{23} = 0.5$ , which is complementary to the JUNO reactor neutrino results. The wrong  $\theta_{23}$  octant could be ruled out at  $1.8\sigma$  ( $0.9\sigma$ ) for the true normal (inverted) hierarchy and  $\theta_{23} = 35^\circ$ . It is found that the JUNO sensitivity to CP violation is very small when we only consider the high energy  $\nu_\mu$  and  $\bar{\nu}_\mu$ . In contrast to the high energy neutrinos, the low energy neutrinos may give the dominant contributions to the CP violation sensitivity even if we do not use the direction information. In our analysis of the high-energy neutrino events, all  $\nu_e/\bar{\nu}_e$  and the sub-GeV  $\nu_\mu/\bar{\nu}_\mu$  data have been discarded from the conservative point of view. According to the optimistic and

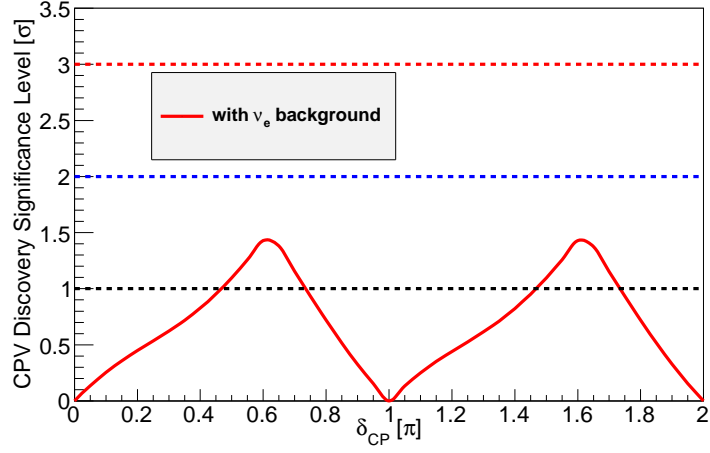


Figure 7-12: The upper limit of the CP discovery sensitivity of JUNO in ten years. All statistics of  $\nu_\mu$ ,  $\bar{\nu}_\mu$ ,  $\nu_e$ , and  $\bar{\nu}_e$  in low energy are considered.

pessimistic estimations, atmospheric neutrinos in JUNO may give a better sensitivity to the mass hierarchy. In the future, we shall investigate the particle reconstruction and identification of the JUNO detector in detail. In addition, we shall analyze the upward through-going and stopping muon events those are produced by atmospheric neutrinos in the rock and water pool. The future atmospheric neutrino exploration in JUNO can also help us to probe new physics beyond the standard model, such as the non-standard neutrino interactions, sterile neutrinos and new long range forces, etc.

## 8 Geoneutrinos

### 8.1 Introduction

For half a century we have established with considerable precision the Earth's surface heat flow as  $46 \pm 3$  TW [327, 328]. However we are vigorously debating what fraction of this power comes from primordial versus radioactive sources. This debate touches on the composition of the Earth, the question of chemical layering in the mantle, the nature of mantle convection, the energy needed to drive plate tectonics, and the power source of the geodynamo, which powers the magnetosphere that shields the Earth from the harmful cosmic ray flux.

Over the last decade particle physicists have detected the Earth's geoneutrino flux [329, 330], electron antineutrinos that are derived from naturally occurring, radioactive beta-decay events inside the Earth [223, 331]. Matter, including the Earth, is mostly transparent to these elusive messengers that reveal the sources of heat inside the Earth as they virtually escape detection, being that the Earth's geoneutrino flux is some  $10^6 \text{ cm}^{-2} \text{ s}^{-1}$ . However, by detecting a few particles per years we are now measuring the geoneutrino flux from thorium and uranium inside the planet, which in turn allows us to estimate the amount of radiogenic power driving the Earth's engine.

Today we are experiencing a renaissance in neutrino studies, in part driven by the fact that 15 years ago physicists revealed the phenomenon of neutrino oscillations and thus the fact that neutrinos have non-zero mass. Neutrino science is now bringing us fundamental insights into the nature of nuclear reactions, revealing for us the nuclear fusion in the core of the sun, nuclear fission in man-made nuclear reactors, and identifying our planet's nuclear fuel cycle, as reflected in the heat produced during radioactive decay. Geology is the fortunate recipient of the particle physicists' efforts to detect the Earth's emission of geoneutrinos.

How does geoneutrino detection serve the geological community and what transformational insights will it bring? It directly estimates the radiogenic heating in the Earth from thorium and uranium. These elements, along with potassium, account for more than 99% of the radiogenic heat production in the Earth. This component, along with the primordial energy of accretion and core segregation, define the total planetary power budget of the planet. By defining the absolute abundance of Th and U in the Earth, with accuracy and precision, we can:

1. define the building blocks, the chondritic meteorites, that formed the Earth,
2. resolve ever vexing paradoxes (e.g.  $^4\text{He}$ -heat flow, Ar budget and degassing) that fuel the debates of compositionally layered mantle structures or not,
3. discriminate models of parameterized mantle convection that define the thermal evolution ( $dT/dt$ ) of the Earth,
4. potentially identify and characterize deep, hidden reservoirs (or not) in the mantle, and
5. fix the radiogenic contribution to the terrestrial heat flow.

Moreover, such studies can place stringent limits on the power of any natural nuclear reactor in or near the Earth's core.

---

Editors: Ran Han (hanran@ncepu.edu.cn), Livia Ludhova (ludhova@gmail.com), and Bill McDonough (mcdonoug@umd.edu)

Major contributors: Fabio Mantovani, Barbara Ricci, Liangjian Wen, Oleg Smirnov, Yufei Xi, and Sandra Zavatarelli



## 8.2 Expected geoneutrino signal

The amount of U and Th and their distribution in a reservoir (e.g. crust and mantle) affects the integrated geoneutrino flux at a location on the Earth's surface. The unoscillated geoneutrino flux produced by a source volume  $\Delta V$  at the detector position<sup>1</sup> can be calculated with:

$$\Phi(\Delta V) = \frac{1}{4\pi} \int_{\Delta V} d^3r \frac{A(\vec{r})}{|\vec{R} - \vec{r}|^2}, \quad (8.1)$$

where  $A$  is the rate of geoneutrinos produced in the volume  $\Delta V$ , which depends on density, antineutrino production rates per unit mass and U and Th abundances. The intensity of the flux depends on the inverse-square of the distance to the sources, and thus the crust surrounding the detector, which contains a relative small amount of the Earth's U and Th budget, gives a large contribution to the signal. It is predicted that the first  $\sim 500$  km from the KamLAND detector contributes about 50% of the measured geoneutrino signal, with this volume containing  $\sim 0.1\%$  of the total crustal U and Th mass [332]. For the JUNO site it is predicted that the first 550 km from the detector contribute some 50% of the measured geoneutrino signal (Fig. 8-1).

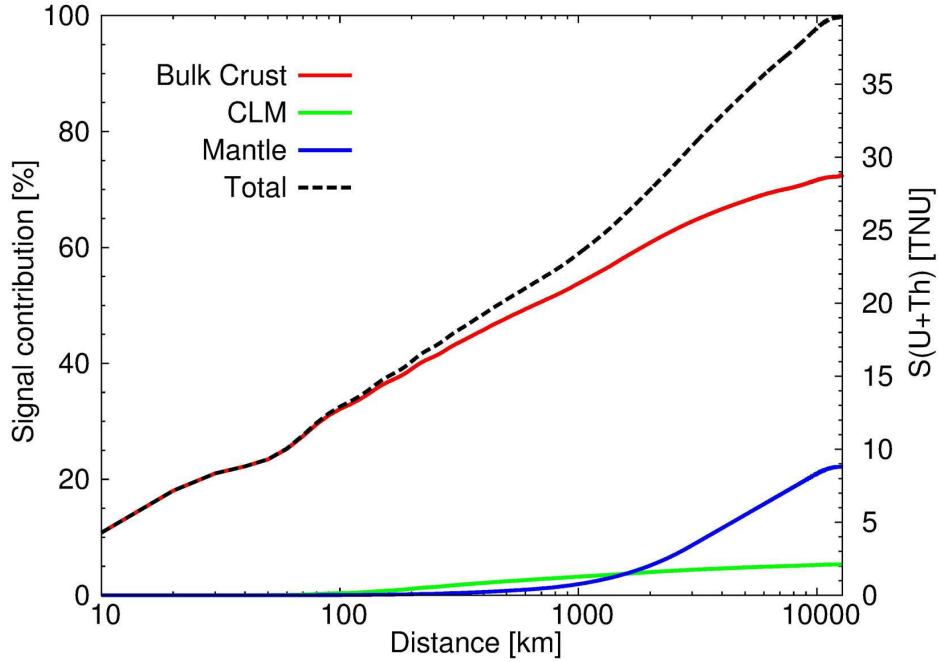


Figure 8-1: Geoneutrino signal contribution at JUNO. The cumulative geoneutrino signal and the percentage contributions of the Bulk Crust, Continental Lithospheric Mantle (CLM) and Mantle are represented as function of the distance from JUNO [332].

The geophysical structure of the global crustal model described in [333] takes into account data from different studies: body wave studies using reflection and refraction methods, surface wave dispersion studies and gravity surveys. On the basis of this model, the expected geoneutrino signal at JUNO, which originates from the U and Th in the global Bulk Crust (BC) and in the

<sup>1</sup>In the case of detector near the Earth surface  $|\vec{R}|$  is the radius of the Earth.

Continental Lithospheric Mantle (CLM), are  $S_{BC} = 28.2^{+5.2}_{-4.5}$  TNU<sup>2</sup> and  $S_{CLM} = 2.1^{+2.9}_{-1.3}$  TNU respectively (Tab. 8-1) [332]. The  $1\sigma$  asymmetric uncertainties reflect the propagation of non-Gaussian distributions of U and Th abundances in the deep BC and CLM, together with the Gaussian distributions of the errors associated with the geophysical inputs.

Table 8-1: Geoneutrino signals from U and Th expected in JUNO. The signals from different reservoirs (CLM = Continental Lithospheric Mantle, LS = Lithosphere, DM = Depleted Mantle, EM = Enriched Mantle) indicated in the first column are in TNU [332]. Total equals Total LS + DM + EM. The mantle signal can span between 1-19 TNU according to the composition of the Earth: here the geoneutrino signal produced by a primitive mantle having  $m(\text{U}) = 8.1 \cdot 10^{16}$  kg and  $m(\text{Th}) = 33 \cdot 10^{16}$  kg is reported.

	S(U)	S(Th)	S(U+Th)
Bulk crust	$21.3^{+4.8}_{-4.2}$	$6.6^{+1.9}_{-1.2}$	$28.2^{+5.2}_{-4.5}$
CLM	$1.3^{+2.4}_{-0.9}$	$0.4^{+1.0}_{-0.3}$	$2.1^{+2.9}_{-1.3}$
Total LS	$23.2^{+5.9}_{-4.8}$	$7.3^{+2.4}_{-1.5}$	$30.9^{+6.5}_{-5.2}$
DM	4.1	0.8	4.9
EM	2.9	0.9	3.8
Total	$30.3^{+5.9}_{-4.8}$	$9.0^{+2.4}_{-1.5}$	$39.7^{+6.5}_{-5.2}$

The Total predicted geoneutrino signal at JUNO  $S_{TOT} = 39.7^{+6.5}_{-5.2}$  TNU [332], which is obtained assuming a predicted Mantle contribution of  $S_M \sim 9$  TNU according to a mass balance argument. The adopted mantle model, divided into two spherically symmetric domains (Depleted Mantle and Enriched Mantle), refers to a Bulk Silicate Earth based on a primitive mantle having U and Th mass of  $m(\text{U}) = 8.1 \cdot 10^{16}$  kg and  $m(\text{Th}) = 33 \cdot 10^{16}$  kg, respectively [331]. Alternatively, another class of Earth models [334], with a global composition similar to that observed in enstatite chondrites, is characterized by smaller amounts of U and Th (i.e.  $m(\text{U}) = 4.9 \cdot 10^{16}$  kg and  $m(\text{Th}) = 20 \cdot 10^{16}$  kg). Consequently, assuming the same lithospheric contribution and mass balance arguments, this model has a minimum signal from the mantle of  $S_M \sim 1$  TNU [335]. On the other hand, models based on the energetics of mantle convection and on the observed surface heat loss [336] require a high concentration of U and Th in the primitive mantle (e.g.  $m(\text{U}) = 12.5 \cdot 10^{16}$  kg and  $m(\text{Th}) = 52 \cdot 10^{16}$  kg). In this scenario the present mantle signal could reach  $S_M \sim 19$  TNU. Ranges of geoneutrino signals produced by symmetric and asymmetric distributions of U and Th in the mantle are extensively discussed in [337]. The present crustal models are affected by uncertainties that are comparable to the mantle's contribution: this comes mainly from understanding the abundance and distribution of Th and U in the regional crystalline rocks. Upper crustal estimates for Th and U abundances vary by 10% and 22%, respectively, whereas larger uncertainties exist for their

<sup>2</sup>TNU: Terrestrial Neutrino Units. 1 TNU = 1 event/yr/ $10^{32}$  target protons, which is approximately the number of free protons in 1 kiloton liquid scintillation.

estimates in middle and lower crustal lithologies [333].

Thus, to understand the relative contributions from the crust and mantle to the total geoneutrino signal at JUNO an accurate estimation of the geoneutrino flux from the crustal region surrounding JUNO is a priority. Detailed geological, geochemical, and geophysical studies were performed in the areas surrounding the KamLAND detector at Kamioka, Japan [338,339], the Borexino detector at Gran Sasso, Italy [340], and the SNO+ detector at Sudbury, Canada [341]. The present geoneutrino flux prediction for JUNO [332] is recognized as being a first step and is not based on data specifically from the local region. This estimate was generated from a set of global databases, including a compositional estimate of the average upper crust, physical structure of crustal rocks, and models of the seismic and gravity properties of the crust (see [333]). To improve upon the accuracy and precision of this estimate, future studies of JUNO will necessarily require input from geological, geochemical and geophysical studies of the area surrounding JUNO, up to some 550 km away from the detector. The survey distance from the JUNO detector can be fixed by resolution studies, with trade offs between distance, limits on uncertainty, and costs of survey.

Thus, a refined model for predicting the geoneutrino flux at JUNO is needed. To meet this need, an integrated effort is required and will involve an exciting and collaborative research effort between particle physicists and Earth scientists.

### 8.3 The local geology study around JUNO

The JUNO detector is to be built near the southern continental margin of China close to the South China Sea (Fig. 8-2). This passive margin area has an extensive continental shelf and represents the transition between continental and oceanic plates.

The JUNO detector will accumulate a signal from the regional distribution of Th and U, as well as from the rest of the planet. The local contribution (the immediate several hundred km of crust surrounding the detector) typically contributes about half of the signal at the detector. So it will be important for the geological community to map out carefully and identify the abundance and distribution of Th and U in this region. Models for calculating the total geoneutrino signal from an area surrounding a detector and the rest of the planet requires extensive integration of spatially resolved local geological, geochemical, and geophysical data that is then integrated into a global model for the distribution of geoneutrino sources. Detailed characterization of the local region also brings additional fundamental benefits to the geoscience community.

Eastern China is documented, relative to a global perspective, as being a region of elevated heat flow and the Guangdong province specifically, has hot springs and anomalously high heat flow zones associated with deep crustal fractures and fluid flow. Regionally, southern and southeastern China have large surface areas covered with Mesozoic (circa 250 to 70 million years ago) granites containing high concentrations of K, Th and U (the heat producing elements) (Fig. 8-2b).

The Jurassic ( $\sim 160$  million years old) high-K granites are ubiquitous, extending from the continental interior to the coastal area [343] and possess the highest amount of heat producing elements. The petrogenesis of granitic rocks and the tectonic evolution in the southeastern China continue to attract attention (e.g., [343–348]) as they are a relevant source of economic minerals and geothermal energy. Lithologically the granites are heterogeneous, rich in heat producing elements, and important source rocks producing geoneutrinos [332].

The thickness of the continental crust immediately surrounding JUNO has been modeled using CRUST 2.0 and 1.0 [332, 333, 349]; it varies between 26 and 32 km (Fig. 8-3). At some 350 km distance to the south of JUNO, the oceanic crust outcrops (approximately 8 km thick and containing  $\sim 1/10$  of the concentration of Th and U as compared to the continental crust) and will contribute approximately to 0.2% of the total expected geoneutrino signal. On the basis of

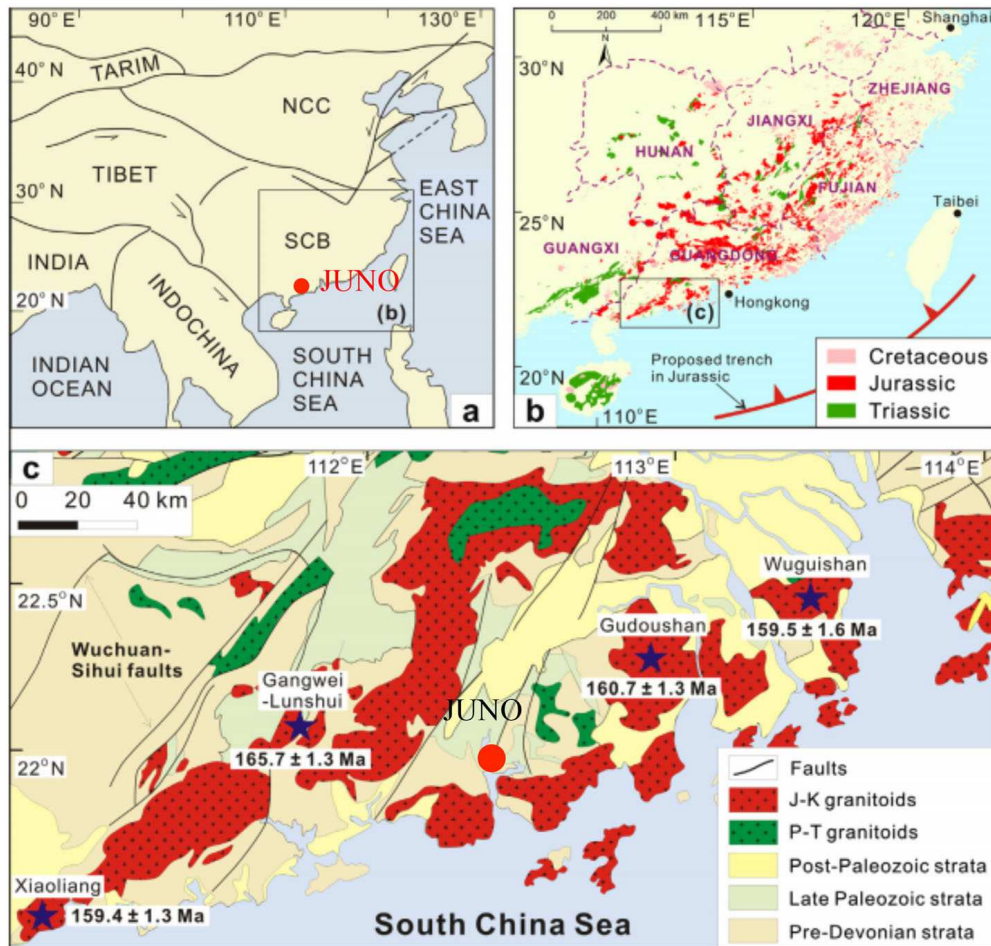


Figure 8-2: (a) Sketch map showing major tectonic units around JUNO. NCC - North China Craton; SCB - South China Block. (b) Regional map showing the distribution of Mesozoic granites in the southeastern South China Block. Dashed purple lines show the provincial boundaries. (c) Geological map showing the age distribution of Mesozoic granites along the southern coastal region of the Guangdong Province, southeastern China). Stars highlight the plutons. New geochronological results are shown in bold. J-K-Jurassic and Cretaceous; P-T-Permian and Triassic [342].

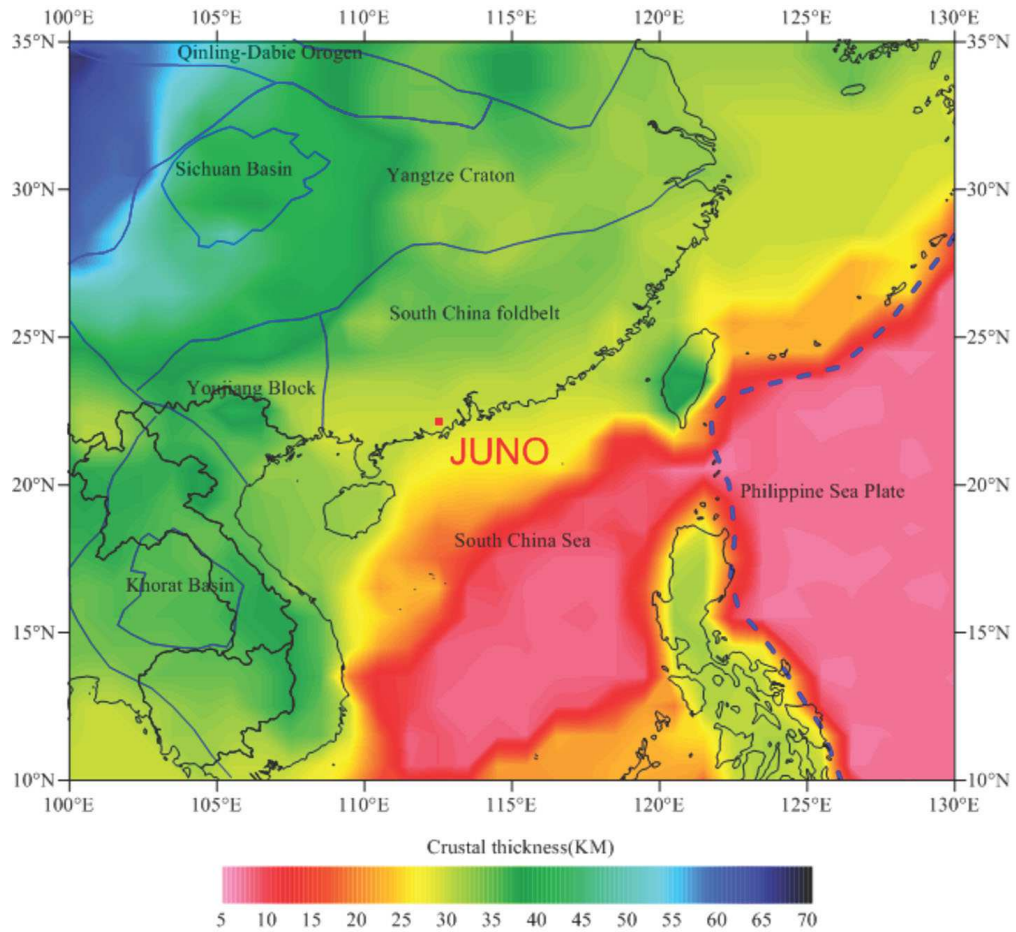


Figure 8-3: Crustal thickness (exclusive water) in the surrounding area of JUNO from CRUST 1.0 model, 1° degree [349]. Dashed thick blue line is plate boundary [350]. Thin blue lines denote the main tectonic units.

an existing global reference model for the Earth [333], an initial estimate of the local geoneutrino signal expected at JUNO is  $S_{\text{LOC}} = 17.4_{-2.8}^{+3.3}$  TNU [332]. This flux contribution corresponds to  $\sim 44\%$  of the expected geoneutrino signal at JUNO and exceeds the signal from the whole mantle. The  $2^\circ \times 2^\circ$  region including and to the north of JUNO is the area with the greatest thickness of sediments and crystalline crust and it alone has been identified as contributing  $\sim 27\%$  of the geoneutrino signal [332]. Thus, these early studies have identified significant regional targets that will require further intensive research to predict better the JUNO geoneutrino signal.

The main tasks for predicting the JUNO geoneutrino signal include surveys and descriptions of the geology, seismology, heat flow, and geochemistry of the regional lithosphere (the Earth's outer conductive layer that includes the crust and the mechanically coupled layer of mantle beneath it). Geological surveys define the surface lithologies, major structures, and geological provenances. Seismological surveys include refraction and reflection mapping, receiver function and ambient noise tomography of the crust and lithospheric mantle; these studies provide a 3-dimensional image of the structures of the deep crust and lithospheric mantle, specifically in terms of major boundaries and the vertical and horizontal variations in density, acoustic velocity and Poisson's ratio. Heat flow surveys will map out the surface variation in heat flow, as well as the heat production and thermal conductivity of the immediate lithologies, and from this develop models of near surface productivity versus reduced heat flow. Gravity surveys record the variations in density structure of the lithosphere and mantle; these surveys can be coupled with heat flow and seismic surveys to cross check and refine models of the lithosphere. Finally a wide range of geochemical studies, including mapping the spatial variations in the abundance of K, Th and U, local helium gas flux measurements, and gamma ray spectroscopy, will define the nature and composition of the near surface and set up the potential for projecting the 3-dimensional variation in the abundances of these elements at depth.

In addition to these survey studies it is vitally important to involve computational geological studies, where all of the geological, geophysical and geochemical data are geo-located into an integrated, 3-dimensional model that is the essential physical and chemical database of the Earth system. The global and regional contributions of the geoneutrino flux need to be predicted for the area surrounding the JUNO detector, as have been previously done at the existing detectors KamLAND (Japan) [338,339], Borexino (Italy) [340] and SNO+ (Canada) [341].

The area of Kaiping, China, the site of the JUNO experiment, is close to the continental margin of south China. Beyond the shores of this area is a significant region of continental shelf. This regional study therefore represents a golden opportunity to investigate in detail a passive continental margin, a tectonic boundary that we know little of its nature. These broad continental margins typically host considerable petroleum reserves and thus understanding their nature and structure might provide critical insights into identifying further energy resources. Moreover, integration of the matrix of geophysical, geochemical and geological data into a single, self-consistent solution is required in order to calculate the geoneutrino flux at JUNO.

## 8.4 Detecting geoneutrino signal

The full strength of geoneutrino studies comes from the synergistic activities of geology and physics, neither acting independently of the other and both accepting the challenge of knowing better the Earth and its secrets. These studies represent the ultimate opportunity for geologists and particle physicists to independently measure and test our predictions of the structure and composition of the planet's interior [329]. Thus, by 2020, when the JUNO detector will be built and begin data taking, we will have our best prediction of the expected signal. At that time we will wait and see what the measurement reveals. It is a rare moment in geology where we predict and then receive

independent assessment of the strength of our prediction.

Detectors like JUNO are sited deep underground and are enormous (20 kiloton) structures; their size enhances their potential for detection and their overburden shields them from cosmic ray fluxes. These factors, combined with their ultra-clean construction, will allow these detectors to extract the geoneutrino signal.

Geoneutrinos from  $^{238}\text{U}$  and  $^{232}\text{Th}$  (not those from  $^{235}\text{U}$  and  $^{40}\text{K}$ ) are above threshold for the classical antineutrino ( $\bar{\nu}_e$ ) detection reaction, the inverse beta decay (IBD) on free protons ( $p$ ):

$$\bar{\nu}_e + p \rightarrow e^+ + n - 1.806 \text{ MeV}. \quad (8.2)$$

The characteristic temporal and spatial coincidence of prompt positron ( $e^+$ ) and delayed neutron ( $n$ ) flash events offers a clean signature that resolves them from background signals.

The first geoneutrino measurements were reported in 2005 by the KamLAND team [351], where they recorded 25 events over two years of exposure. The KamLAND detector is sited deep in the Japanese Alps, opposite Tokyo, on the island of Honshu and is 1 kiloton in scale. Another active detector is the Borexino experiment, located beneath the Apennine Mountains near the town of L'Aquila in Italy. This detector, which is smaller (300 tons), reported in 2010 its measurement of the Earth's geoneutrino flux at the 99.997% C.L ( $5\sigma$ ) [352]. Both experiments provided new updated measurements [329, 330], on the occasion of the inter-disciplinary Neutrino Geoscience conference series, in 2013 held in Takayama, Japan.

A third, new detector, SNO+ is a re-deployed Sudbury Neutrino Observatory. It is a second kiloton detector and it is situated in Sudbury, Ontario, Canada, on the ancient stable Superior Craton [353]. JUNO will then join these detectors in 2020, being 20 times larger than all the existing devices. In its first year of operation, JUNO will record more geoneutrino events than all other detectors combined will have accumulated to that time. Before discussing the detection of geoneutrino events we will discuss the various experimental backgrounds coming from nuclear reactors and other sources.

## 8.5 Reactor antineutrino background

Determination of the expected signal from reactor  $\bar{\nu}_e$ 's requires a wide set of information, spanning from characteristics of nuclear cores placed around the world to neutrino properties. In this section, the number of expected reactor events and the corresponding spectral shape have been calculated as follows:

$$N_{ev} = \epsilon N_p \tau \sum_{r=1}^{N_{react}} \frac{P_r}{4\pi L_r^2} \langle LF_r \rangle \times \int dE_{\bar{\nu}_e} \sum_{i=1}^4 \frac{p_i}{Q_i} \phi_i(E_{\bar{\nu}_e}) \sigma(E_{\bar{\nu}_e}) P_{ee}(E_{\bar{\nu}_e}, \hat{\theta}, L_r), \quad (8.3)$$

where  $\epsilon$  is the detection efficiency,  $N_p$  is the number of target protons, and  $\tau$  is the data-taking time. The index  $r$  cycles over the number of reactors considered:  $P_r$  is the nominal thermal power,  $L_r$  is the reactor-detector distance,  $\langle LF_r \rangle$  indicates the average Load Factor (LF)<sup>3</sup> in the period  $\tau$ ,  $E_{\bar{\nu}_e}$  is the antineutrino energy. The index  $i$  stands for the different nuclear-fuel components ( $^{235}\text{U}$ ,  $^{238}\text{U}$ ,  $^{239}\text{Pu}$ ,  $^{241}\text{Pu}$ ),  $p_i$  is the power fraction,  $Q_i$  is the energy released per fission of the component  $i$ , and  $\phi_i(E_{\bar{\nu}_e})$  is the antineutrino energy spectrum originated by the fission of component  $i$ .  $\sigma(E_{\bar{\nu}_e})$  is the inverse-beta-decay cross section.  $P_{ee}$  is the energy-dependent survival probability of electron antineutrinos traveling the baseline  $L_r$ , for mixing parameters  $\hat{\theta} = (\delta m^2, \Delta m^2, \sin^2 \theta_{12}, \sin^2 \theta_{13})$ .

---

<sup>3</sup>Load Factor reflects the ratio between the delivered and the nominal reactor power. The shut-down periods are taken into account.

We express the expected reactor antineutrino signal in unit of TNU, same as the geoneutrinos. This means that in Eq. (8.3) we assume a 100% detection efficiency for a detector containing  $N_p = 10^{32}$  target protons and operating continuously for  $\tau = 1$  year. We consider all the nuclear cores in the world operating in the year 2013, plus all the cores of the Taishan and Yangjiang nuclear power plants that will enter operation in 2020. Information on the nominal thermal power and Load Factor for each existing nuclear core comes from the International Agency of Atomic Energy (IAEA) [354]. For each core the distance  $L_r$  has been calculated taking into account the position of the JUNO detector (22.12 N, 112.52 E) [69] and the positions of all the cores in the world according to the database adopted in [355]. For the future Taishan and Yangjiang nuclear plants, we considered the thermal power of 18.4 GW and 17.4 GW, the distance of 52.7 and 53.0 km, respectively, and we assumed 80% Load Factor. Typical power fractions for the PWR and BWR type reactors are adopted to be equal to the averaged value of the Daya Bay nuclear cores:  $^{235}\text{U} : ^{238}\text{U} : ^{239}\text{Pu} : ^{241}\text{Pu} = 0.577 : 0.076 : 0.295 : 0.052$ . As in [329], we have considered for the European reactors using Mixed OXide technology that 30% of their thermal power originates from the fuel with power fractions  $0.000 : 0.080 : 0.708 : 0.212$ , respectively and for the cores in the world using heavy-water moderator  $p_i = 0.543 : 0.024 : 0.411 : 0.022$ , respectively.

The  $\phi_i(E_{\bar{\nu}_e})$  energy spectra are taken from [102], the  $Q_i$  energy released per fission of component  $i$  are from [356], and the interaction cross section  $\sigma(E_{\bar{\nu}_e})$  for inverse beta decay reaction is from [176]. For the vacuum survival probability  $P_{ee}$  and the corresponding mixing parameters we adopt the most recent determinations by Capozzi et al. [27] for the Normal Hierarchy.

Tab 8-2 gives an overview of different contributions to the total error on the expected reactor antineutrino signal in the total energy window ( $1.8 \text{ MeV} < E_{\bar{\nu}_e} < 10 \text{ MeV}$ ).

Table 8-2: Systematic uncertainties on the expected reactor antineutrino signal in the total energy window. See Eq. (8.3) and accompanying text for details.

Source	Error [%]	Source	Error [%]
Fuel composition	1.0	$\sin^2 \theta_{12}$	3.6
$\phi_i(E_{\bar{\nu}_e})$	3.4	$\sin^2 \theta_{13}$	0.21
$P_r$	2.0	$\Delta m^2$	$< 10^{-2}$
$\sigma(E_{\bar{\nu}_e})$	0.4	$\delta m^2$	1.2
$Q_i$	0.09		
Total			5.6

The error due to the fuel composition reflects the possible differences among different cores and the unknown stage of burn-up in each of them. This error is determined as the variance of a uniform distribution, assumed for different signals calculated with the sets of power fractions available in the literature (see Tab. 1 of [355]).

The uncertainty due to  $\phi_i(E_{\bar{\nu}_e})$  energy spectra is very conservatively quoted as 3.4%, which is determined as the difference in the expected signal computed with the reference spectra of [102] and with the spectra published by [357].

The uncertainty due to the thermal power  $P_r$  is conservatively assumed to be 2%. Although thermal powers can be measured at sub-percent level, the adopted uncertainty reflects the regulatory specifications for Japan and United States (see e.g., Refs. [358] and [359]), furthermore allowing to account for the fact that the Load Factors reported in the IAEA database refer to the electrical power and not to the thermal one.



Table 8-3: Main non antineutrino background components assumed in the geoneutrino sensitivity study: the rates are intended as number of events per day after all cuts (refer to Section 2.2.2). The options of acrylic vessel and balloon have been compared in the  $(\alpha, n)$  background evaluation.

Background type	Rate after IBD+ muon cuts [events/day]	Uncertainty in Rate [%]	Uncertainty in Shape [%]
$^9\text{Li} - ^8\text{He}$	1.6	20	10
Fast neutrons	0.1	100	20
Accidental events	0.9	1	negl.
$^{13}\text{C}(\alpha, n)^{16}\text{O}$ (acrylic vessel)	0.05	50	50
$^{13}\text{C}(\alpha, n)^{16}\text{O}$ (balloon)	0.01	50	50

The effect of the uncertainties of oscillation parameters is calculated by varying each parameter one at the time in the  $1\sigma$  range and assuming a uniform distribution of the obtained signals; note that the dominant contribution arises from the  $\theta_{12}$  mixing angle. A more extensive treatment of the uncertainties can be found in [355], where a Monte Carlo based approach has been adopted in the determination of the uncertainty budget as well as of the signal central values.

In conclusion, the expected reactor antineutrino signal in the total energy window is  $(1569 \pm 88)$  TNU<sup>4</sup>. The signal in the geoneutrino energy window ( $1.8 \text{ MeV} < E_{\bar{\nu}_e} < 3.27 \text{ MeV}$ ) is  $(351 \pm 27)$  TNU, where the Taishan and Yangjiang nuclear power stations contribute more than 90% of the total.

We want to stress that JUNO will measure neutrino oscillations parameters with unprecedented precision. Thus, as a consequence, the total error on the expected antineutrino flux will be strongly reduced. In the geoneutrino sensitivity studies presented here, we have adopted the 5.6% uncertainty, since it reflects the current knowledge of the estimation of the reactor antineutrino background for JUNO geoneutrino measurement. As we will discuss below, the reactor antineutrino background is not constrained and is kept as a free fit parameter in our simulations of possible JUNO geoneutrino measurements. Thus, the error on the predicted reactor-antineutrino rate enters the simulations only as a parameter defining the signal-to-background ratio. We have checked, that considering an error of 2.4% (instead of 5.6%) does not significantly change our results on geoneutrino sensitivity.

## 8.6 Non antineutrino background

The coincidence tag used in the  $\bar{\nu}_e$ -detection is a very powerful tool in background suppression. Nevertheless, the event rate expected from geoneutrino interactions is quite small (few hundreds of events/year) and a number of non antineutrino background events faking geoneutrino interactions has to be properly accounted for in the sensitivity study.

A detailed description of expected background in JUNO is given elsewhere. Here we briefly summarise the most relevant backgrounds for the geoneutrino analysis. They can be divided into three main categories:

- Cosmic-muons spallation products, namely:

<sup>4</sup>The signal value does not include the matter effect in the neutrino-oscillation mechanism, which represents an additional increase of +1.1% with respect to the vacuum oscillation. Furthermore, the contribution of antineutrinos emitted from spent nuclear fuel (SNF) can be considered as +1.9% signal increase [360]

- ${}^9\text{Li}$  and  ${}^8\text{He}$  isotopes decaying in ( $\beta + \text{neutron}$ ) branches perfectly mimicking antineutrino interactions;
- fast neutrons able to penetrate through construction materials and giving a delayed coincidence if scattered off by one or many protons before being captured;
- Accidental coincidences of non-correlated events.
- Backgrounds induced by radioactive contaminants of scintillator and detector materials. In particular, alpha particles emitted in the  ${}^{238}\text{U}$  and  ${}^{232}\text{Th}$  decay chains or by off-equilibrium  ${}^{210}\text{Po}$  can induce  ${}^{13}\text{C}(\alpha, n){}^{16}\text{O}$  reactions on the scintillator  ${}^{13}\text{C}$  nuclides. In these interactions, the prompt signal can be induced by three different processes: *i*) de-excitation of  ${}^{16}\text{O}$  nuclides, if produced in an excited state; *ii*) 4 MeV  $\gamma$  ray from the de-excitation of  ${}^{12}\text{C}$  excited by neutron, and *iii*) protons scattered off by the thermalizing neutron before its capture.

In the second column of Tab. 8-3 the rates of events surviving the IBD selection cuts and muon cuts are reported. The muon cut properly vetoes in time and space the detector after each muon crossing the water pool or the central detector and it is effective in reducing the  ${}^9\text{Li}$  and  ${}^8\text{He}$  backgrounds by a factor 44 (refer to Tab. 2-1).

A fiducial volume of 18.35 ktons corresponding to a radial cut of  $R = 17.2$  m was chosen since it is particularly effective in reducing the accidental background mostly arising from  ${}^{238}\text{U}/{}^{232}\text{Th}/{}^{40}\text{K}$  contamination of the acrylic vessel, PMT's glass, steel supports, and copper fasteners.

In the ( $\alpha, n$ ) background evaluation, the options of acrylic vessel ( ${}^{238}\text{U}$ : 10 ppt,  ${}^{232}\text{Th}$ : 10 ppt) and ballon ( ${}^{238}\text{U}$ : 2 ppt,  ${}^{232}\text{Th}$ : 4 ppt) have been compared: after the fiducial volume cut, the corresponding ( $\alpha, n$ ) event rates of 0.05 counts/day and negligible were found, respectively. A  $10^{-15}$  g/g  ${}^{238}\text{U}/{}^{232}\text{Th}$  contamination of the liquid scintillator would be responsible for less than 0.01 ( $\alpha, n$ ) events/day. Considering the  ${}^{210}\text{Pb}$  contamination of the scintillator of the order of  $1.4 \cdot 10^{-22}$  g/g, the  $\alpha$ -decay rate of  ${}^{210}\text{Po}$  in equilibrium with  ${}^{210}\text{Pb}$  would give a negligible contribution to ( $\alpha, n$ ) background.

## 8.7 JUNO potential in measuring geoneutrinos

JUNO will be able to detect geoneutrinos in spite of the noticeable background coming from various sources - and mainly from nearby nuclear power plants. In order to assess the detectability and the measurement accuracy, the predicted total antineutrino spectrum (signal and backgrounds) has been studied under different possible conditions. The expected geoneutrino signal, as well as reactor antineutrino and non-antineutrino backgrounds have been described above in this section. For convenience, Tab. 8-4 summarizes the number of expected events for all components contributing to the IBD spectrum in the 0.7 - 12 MeV energy region of the prompt signal. We have assumed 80% antineutrino detection efficiency and 17.2 m radial cut (18.35 kton of liquid scintillator). In the simulations described below, we have considered Gaussian distributions for all spectral components according to this table. For simplicity, this is valid also for the geoneutrino signal, taking the mean of the left and right variances described above as the variance of symmetric Gaussian.

The main assumptions concerning the signal searched for (U and Th chains in the Earth, assumed to be in secular equilibrium) are the ones about their relative value (the Th/U ratio). One possibility, described in Sec. 8.7.1, is to consider in the analysis the fixed chondritic mass Th/U ratio of 3.9. Because the cross-section of the IBD detection interaction increases with energy, the ratio of the signals expected in the detector is  $\text{Th}/\text{U} = 0.27$ . The other obvious choice in the analysis, described in Sec. 8.7.2, is to leave both Th and U contributions free and independent (keeping both

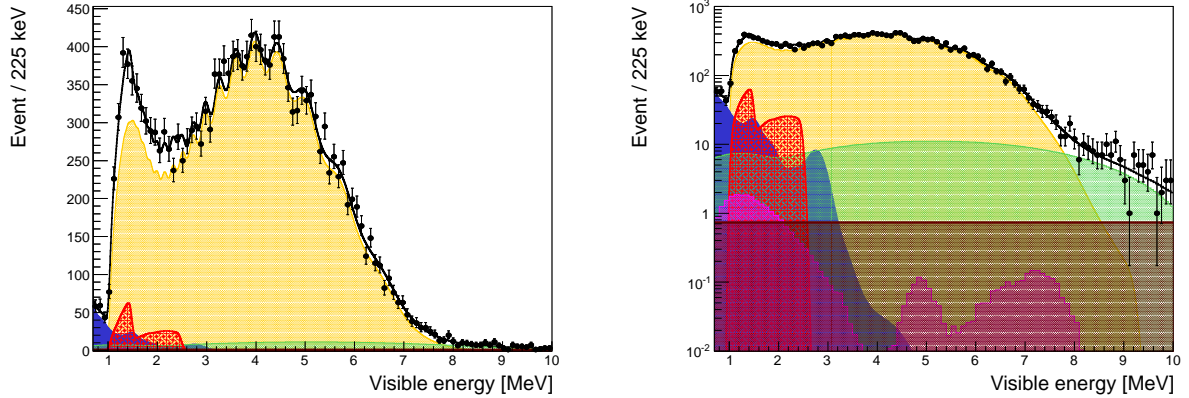


Figure 8-4: Result of a single toy Monte Carlo for 1-year measurement with fixed chondritic Th/U mass ratio; the bottom plot is in logarithmic scale to show background shapes. The data points show the energy spectrum of prompt candidates of events passing IBD selection cuts. The different spectral components are shown as they result from the fit; black line shows the total sum for the best fit. The geoneutrino signal with Th/U fixed to chondritic ratio is shown in red. The following colour code applies to the backgrounds: orange (reactor antineutrinos), green ( ${}^9\text{Li} - {}^8\text{He}$ ), blue (accidental), small magenta ( $\alpha, n$ ). The flat contribution visible in the lower plot is due to fast neutron background.

chains in secular equilibrium) and to study if the relative Th/U signal ratio is compatible with the expected chondritic mass ratio.

### 8.7.1 Geoneutrino signal assuming chondritic mass Th/U ratio

We have simulated several thousand possible JUNO geoneutrino measurements using a toy Monte Carlo. In each simulation, we have attributed to each spectral component a rate randomly extracted from the Gaussian distributions according to Tab. 8-4. We have used theoretical spectral shapes for geoneutrinos; Th and U components were summed in a proportion according to chondritic mass Th/U ratio of 3.9. The method of calculation of reactor antineutrino spectrum was described in Sec. 8.5. For non-antineutrino backgrounds (accidental coincidences,  $(\alpha, n)$ ,  ${}^9\text{Li} - {}^8\text{He}$ ) we have used spectral shapes as they have been measured in Daya Bay. For fast neutrons, we have used a simple flat spectral shape.

In the simulations we have not included the shape uncertainties of the reactor neutrino spectrum. The shape uncertainty for the Huber-Muller model is about 2% in average. Recently the reactor neutrino experiments, Daya Bay, Double Chooz, and RENO, have found discrepancies between the observed shape and the models, especially in the 4-6 MeV region. With these high precision measurements, it is possible to constrain the shape of the reactor neutrino spectrum to 1%. Comparing to the statistic uncertainty of the reactor spectrum (several percent for each bin), the shape uncertainty is not critical for this sensitivity study.

The possible precision of geoneutrino measurement under these conditions was evaluated for 1, 3, 5, and 10 years of full live time after cuts, including muon-veto cuts that require 17% loss of real DAQ time.

Figure 8-4 shows one of the possible total spectra (geoneutrinos and backgrounds) as simulated assuming a data taking period of one year (full livetime after cuts), with Th/U fixed at the

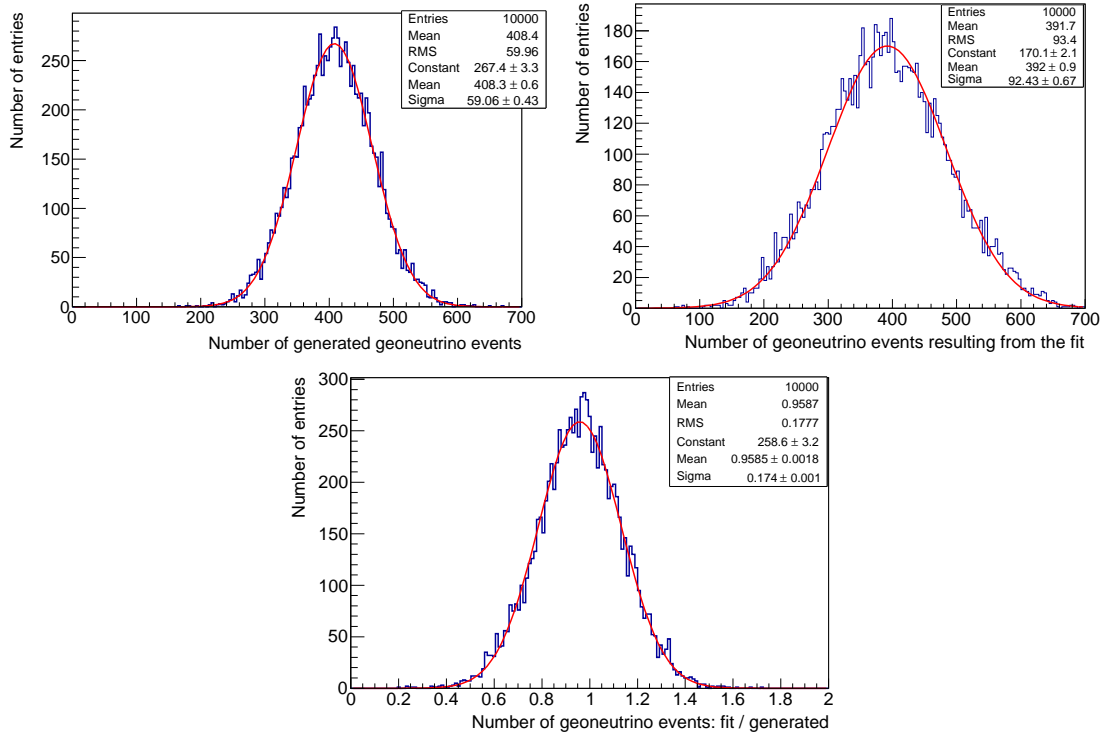


Figure 8-5: The three plots demonstrate the procedure of the sensitivity study to measure geoneutrinos in JUNO. In particular, the capability of the fit to reproduce the correct number of geoneutrino events (fixed ratio U/Th ratio) after 1 year live time after all cuts. Ten thousand simulations and fits have been performed: the upper left plot shows the distribution of the number of generated geoneutrino events, while the upper right plot the distribution of fit results. Finally, the lower plot gives the distribution of the ratio between reconstructed and generated number events.

Table 8-4: Signal and backgrounds considered in the geoneutrino sensitivity study: the number of expected events for all components contributing to the IBD spectrum in the 0.7 - 12 MeV energy region of the prompt signal. We have assumed 80% antineutrino detection efficiency and 17.2 m radial cut (18.35 kton of liquid scintillator,  $12.85 \times 10^{32}$  target protons).

Source	Events/year
Geoneutrinos	$408 \pm 60$
U chain	$311 \pm 55$
Th chain	$92 \pm 37$
Reactors	$16100 \pm 900$
Fast neutrons	$36.5 \pm 36.5$
${}^9\text{Li} - {}^8\text{He}$	$657 \pm 130$
${}^{13}\text{C}(\alpha, n){}^{16}\text{O}$	$18.2 \pm 9.1$
Accidental coincidences	$401 \pm 4$

chondritic value. After the simulation, the data are fit with the same spectral components used in the data generation. The amplitudes of geoneutrino and reactor antineutrino components are left as free fit parameters, while the non-antineutrino background components are constrained to their expectation value within  $\pm 1\sigma$  range.

This procedure was then repeated 10,000 times for 1, 3, 5, and 10 years of lifetime after cuts, as it is demonstrated in Fig. 8-5 for a specific case of 1 year. The upper left plot shows the number of geoneutrino events randomly generated in each simulation; the Gaussian fit is compatible with the values from the first input of Tab. 8-4. The upper right plot is the distribution of the absolute number of reconstructed geoneutrino events as resulting from the fit. The goodness of the procedure can be appreciated by the third plot, showing the distribution of ratios, calculated for each simulation, between the number of geoneutrinos reconstructed by the fit and the true number of generated events. This distribution is centered at about 0.96, thus systematically shifted to lower values by about 4% with respect to an ideal case centered at 1. Considering the width of this distribution, an error of about 17% is expected for the JUNO geoneutrino measurement, assuming a fixed U/Th ratio and one year statistics (after cuts). The correlation between geoneutrinos and reactor antineutrinos is demonstrated in Fig. 8-6 showing the distribution of the ratios of the reconstructed/generated number of events for geoneutrinos versus reactor antineutrinos for 1 year lifetime after cuts.

The distributions of ratios between reconstructed and generated number events for reactor antineutrinos and for  $(\alpha, n)$ ,  ${}^9\text{Li} - {}^8\text{He}$ , and accidental backgrounds are shown in Fig. 8-7. The -4% systematic shift in the reconstruction of geoneutrino signal (see lower part of Fig. 8-5) is mostly due to the correlation with reactor antineutrino background: 0.1% overestimate of the reactor background corresponds to 4% decrease in the reconstructed geoneutrino signal. The  $(\alpha, n)$  background tends to be overestimated and is correlated with the  ${}^9\text{Li} - {}^8\text{He}$  background. Background due to the accidental coincidences is well reconstructed.

This analysis has been repeated also for 3, 5, and 10 years of lifetime (after cuts). The precision of the geoneutrino measurement with fixed Th/U ratio is summarised in the 2<sup>nd</sup> column of Tab 8-5. As it can be seen, the -4% systematic shift in the reconstruction of the geoneutrino signal remains also for long data taking periods. The width of the distributions of the reconstructed/generated number of geoneutrino events decreases, and thus the statistical error on the measurement decreases

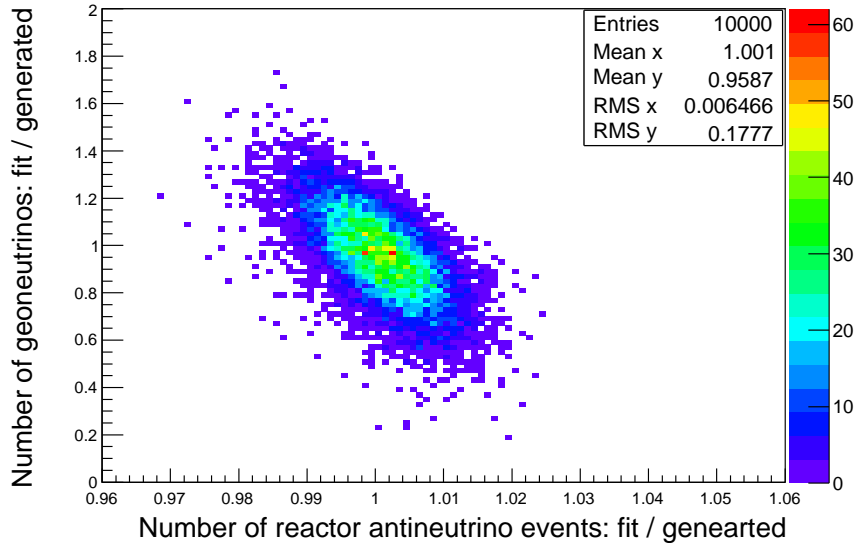


Figure 8-6: Distribution of the ratios of the reconstructed/ generated number of events for geoneutrinos versus reactor antineutrinos.

with higher statistics, as expected. With 1, 3, 5, and 10 years of data, this error amounts to 17, 10, 8, and 6%, respectively.

### 8.7.2 Potential to measure Th/U ratio

The large size of the JUNO detector and the significant number of geoneutrino events recorded each year offers the potential to measure individually the U and Th contributions. The same study as described in Sec. 8.7.1 has been repeated, but this time the constraint on the Th/U chondritic ratio has been removed and we allowed independent contributions from the two main natural radioactive chains. The Th and U signal has been generated from Gaussian distributions according to Tab. 8-4. As an example, Fig. 8-8 shows the spectrum that could be obtained in 10 years of the JUNO data (after cuts).

The precision of the free U and Th signal measurements for 1, 3, 5, and 10 years of lifetime are summarised in the 3<sup>rd</sup> and 4<sup>th</sup> columns of Tab 8-5, respectively. One year of data collection would result in a significant statistical error on the estimates of both U and Th, while the situation improves greatly with time. On the other hand, a systematic bias, at the level of 3% overestimate of the U signal and 20% underestimate of the Th signal is not eliminated with increased statistics. This is due to the correlations among different spectral components, as it is demonstrated on Fig. 8-9 for 5 years of lifetime after cuts. The correlation between U and reactor antineutrinos is stronger than between Th and reactor antineutrinos (top plots). The correlation between U and Th is quite strong (bottom left). The ( $\alpha$ , n) background gets overestimated but is not strongly correlated with Th (and neither U), as it is shown on the bottom right plot, but it is correlated with  ${}^9\text{Li} - {}^8\text{He}$  background.

Accordingly, we have studied how well we can reconstruct the U/Th ratio. Figure 8-10 shows the asymmetric distribution of the ratio reconstructed-to-generated U/Th ratio for 1 and 10 years of lifetime after cuts, excluding simulations in which the Th contribution converges to 0. Tab. 8-6

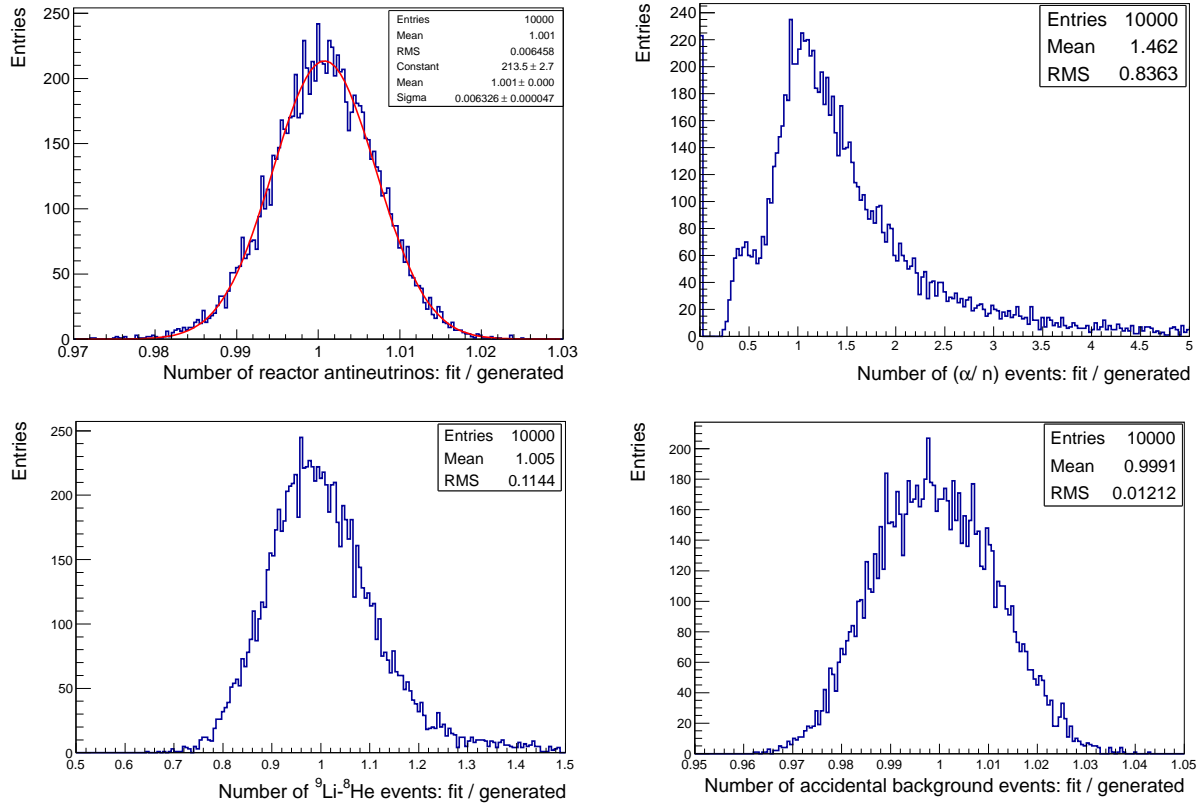


Figure 8-7: Distributions of the ratios between reconstructed and generated number events for 1 year lifetime simulations, considering fixed Th/U ratio. Top left: reactor antineutrinos. Top right: ( $\alpha$ , n) background. Bottom left:  ${}^9\text{Li}$  -  ${}^8\text{He}$  events, Bottom right: accidental coincidences.

Table 8-5: Precision of the reconstruction of geoneutrino signal, as it can be obtained in 1, 3, 5, and 10 years of lifetime, after cuts. Different columns refer to the measurement of geoneutrino signal with fixed Th/U ratio, and U and Th signals fit as free and independent components. The given numbers are the position and RMS of the Gaussian fit to the distribution of the ratios between the number of reconstructed and generated events. It can be seen that while the RMS is decreasing with longer data acquisition time, there are some systematic effects which do not depend on the acquired statistics and are described in text.

Number of years	U + Th (fixed chondritic Th/U ratio)	U (free)	Th (free)
1	$0.96 \pm 0.17$	$1.02 \pm 0.32$	$0.83 \pm 0.60$
3	$0.96 \pm 0.10$	$1.03 \pm 0.20$	$0.80 \pm 0.38$
5	$0.96 \pm 0.08$	$1.03 \pm 0.16$	$0.80 \pm 0.28$
10	$0.96 \pm 0.06$	$1.03 \pm 0.11$	$0.80 \pm 0.19$

Table 8-6: Parametrization of asymmetric distributions of the reconstructed-to-generated U/Th ratio for 1, 3, 5, and 10 years of lifetime after cuts (see examples for 1 and 10 years on Fig. 8-10). Different columns give the position of the peak, RMS, and the fraction of fits in which Th component converges to zero.

Number of years	Peak position	RMS	Fits with Th(fit) = 0 [%]
1	0.7	2.43	8.2
3	0.9	2.23	3.6
5	1.0	2.22	2.7
10	1.1	1.84	1.8

parametrizes such distributions for 1, 3, 5, and 10 years of lifetime after cuts and gives position of the peak, left and right RMS. The last column shows the fraction of fits in which the Th component converges to zero. We can see, that at least few years of lifetime are required in order to measure the Th/U ratio.

## 8.8 Directionality measurement

The average forward shift of neutrons in the direction of incoming antineutrinos have been observed by reactor experiments (i.e. by CHOOZ collaboration [178]). More recent theoretical considerations with respect to the geoneutrino detection can be found in [361]. The basic idea is to search for the statistical displacement of the capture vertex of the neutron with respect to the vertex of the prompt positron event ( $\Delta \vec{R} = \vec{R}_{prompt} - \vec{R}_{delayed}$ ).

The neutron from the inverse beta decay of geoneutrino carries energy up to tens of keV and is emitted in a relatively narrow range (below  $\sim 55$  degrees [361]) of angles around the incoming antineutrino. Emitted neutron is thermalized and then captured on hydrogen in liquid scintillator. The average forward displacement of the neutron capture vertex is about 1.7 cm, as observed by CHOOZ for reactor neutrinos, while the spread due to neutron drifting is about 10 cm. The gravity of energy deposit in liquid scintillator of the gamma released by the neutron capture will further



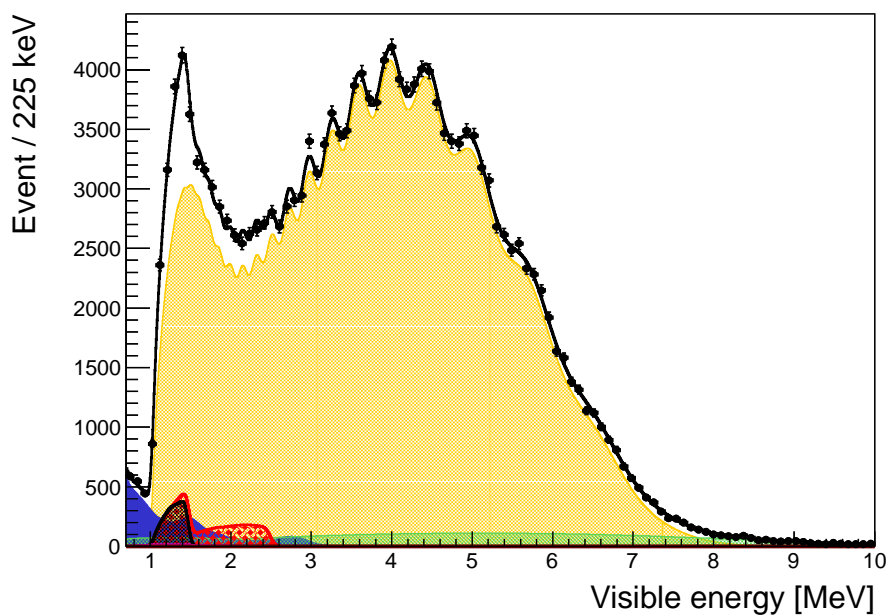


Figure 8-8: Result of a single toy Monte Carlo for 10-year measurement with Th and U components left free and independent. The data points show the energy spectrum of prompt candidates of events passing IBD selection cuts. The different spectral components are shown as they result from the fit; black line shows the total sum for the best fit. The U and Th signal are shown in red and black areas, respectively. The following colour code applies to the backgrounds: orange (reactor antineutrinos), green ( ${}^9\text{Li} - {}^8\text{He}$ ), blue (accidental), small magenta ( $\alpha, n$ ).

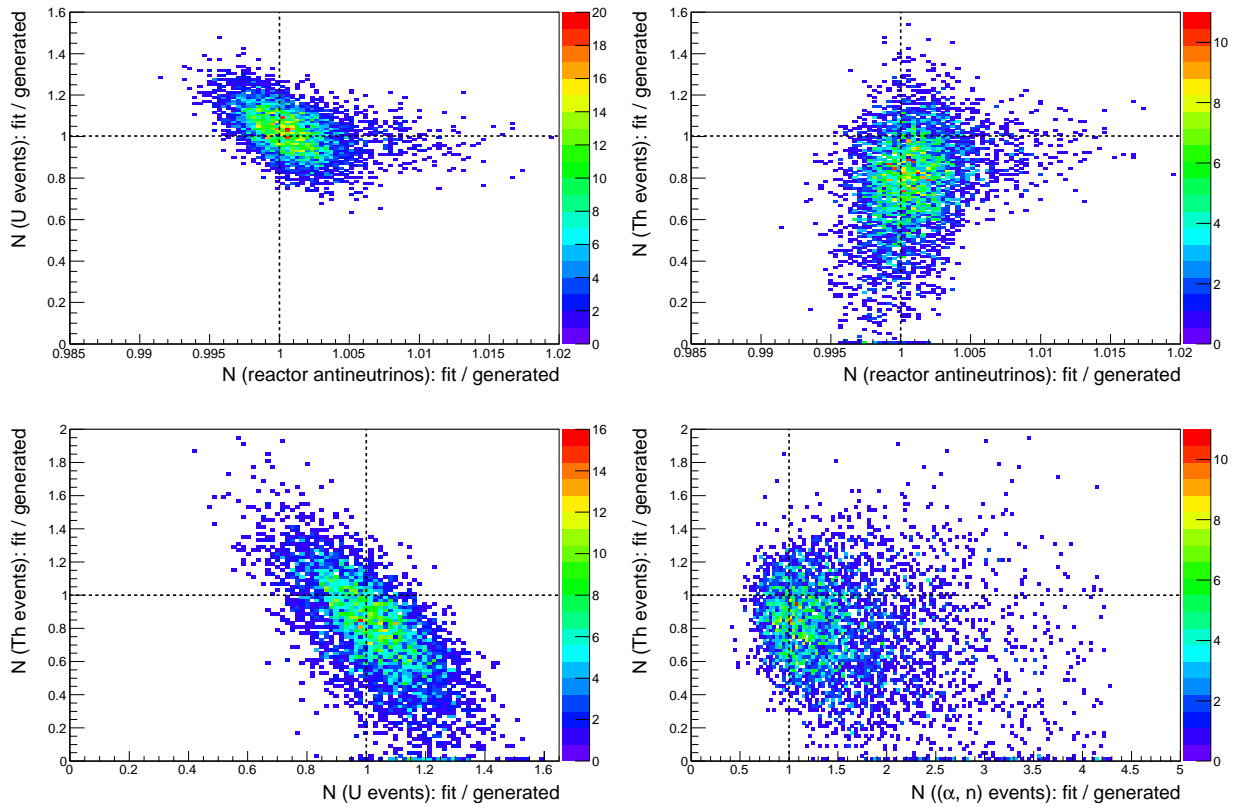


Figure 8-9: Correlations between the ratios of reconstructed-to-generated number of events in 5 years of lifetime (after cuts): Top left: U versus reactors antineutrinos. Top right: Th vs reactor antineutrinos. Bottom left: Th versus U. Bottom right: Th versus  $(\alpha, n)$  background.

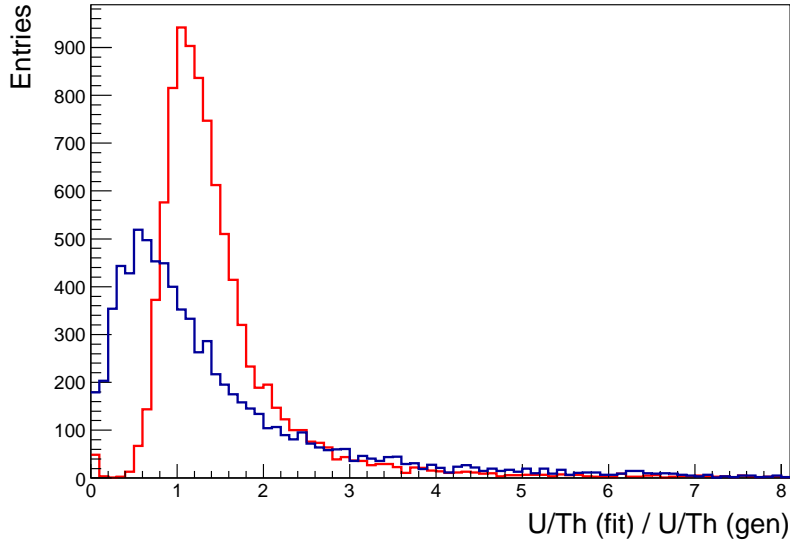


Figure 8-10: Distribution of the ratio reconstructed-to-generated U/Th ratio for 1 (blue line) and 10 (red line) years of lifetime after cuts. The simulations resulting in zero Th contribution are not plot here.

smear the vertex by about 20 cm, together with the vertex reconstruction resolution, a few to 10 cm for JUNO. The prompt event has relatively smaller vertex smearing, a few cm due to the energy deposit and a few to 10 cm due to vertex reconstruction. Given the small displacement ( $\sim 1.7$  cm) and the large intrinsic smearing ( $\sim 25$  cm), the direction of the reconstructed antineutrino is only meaningful statistically and needs large statistics.

The positron is almost isotropic in direction with respect to the incoming antineutrino. It can not provide directional information of the antineutrino directly. Optimistically, if the PMT time response is good enough, JUNO could reconstruct the direction of the positron, which could constrain the reconstruction of the neutron displacement since kinematically they are in the same plane. A simulation shows that the reconstructed direction of a supernova could be improved from  $11.2^\circ$  to  $8.6^\circ$  with 5000 events.

Because the direction to the reactors in JUNO is known, it looks promising exploiting the fit of displacement ( $\overrightarrow{\Delta R}$ ) distribution with predicted separate distributions from geo and reactor neutrinos in conjunction with the spectral fit. An attempt to separate the crust and mantle geoneutrino components could be made. Both tasks need extensive MC studies.

## 8.9 Conclusions

JUNO represents a fantastic opportunity to measure geoneutrinos. Its unprecedented size and sensitivity allows for the recording of 300 to 500 geoneutrino interactions per year. In approximately six months JUNO would match the present world sample of recorded geoneutrino interactions, which is less than 150 events.

This contribution investigates the prospects for extracting the geoneutrino signal at JUNO from the considerable background of reactor antineutrinos and non-antineutrino sources. Using a well constrained estimate of the reactor signal and reasonable estimates of the non-antineutrino sources,

the conclusion of the presented analysis is that geoneutrinos are indeed observable at JUNO. This encouraging result motivates continued studies of the potential to perform neutrino geoscience with JUNO.

With this illumination of the potential importance of JUNO to geological sciences it becomes important to explore fully the sensitivity of JUNO to geoneutrino observations. For example, radiogenic heating in the mantle, which is closely related to the mantle geoneutrino signal, is of critical geological significance. Maximizing the precision of the mantle geoneutrino measurement at JUNO requires detailed knowledge of the uranium and thorium content in the crust within several hundreds of kilometers of JUNO. Moreover, the statistical power of the geoneutrino signal at JUNO enables a measurement of the thorium to uranium ratio, which provides valuable insight to the Earth's origin and evolution.

Fully realizing JUNO's potential contributions to neutrino geosciences recommends the following studies: detailed investigations of the sensitivity of JUNO to geoneutrinos, including refining details of the geoneutrino signal and background Monte Carlo; and a geological examination of the local crust.

In summary, this contribution reveals the unprecedented opportunity to explore the origin and thermal evolution of the Earth by recording geoneutrino interactions with JUNO. It motivates continued studies to fully realize the indicated potential. There is an experienced and dedicated community of neutrino geoscientists that is eager to take advantage of this unique opportunity.

## 9 Sterile Neutrinos

### 9.1 Introduction

Sterile neutrinos are hypothesized gauge singlets of the Standard Model. They do not participate in standard weak interactions but couple to the active neutrinos through non-zero mixing between active and sterile flavors. Heavy sterile neutrinos featuring masses near the Grand Unified Theory (GUT) scale can explain the smallness of the three active neutrino masses via the traditional type-I seesaw mechanism [15–20], and play a pivotal role in the leptogenesis explanation of the cosmological matter-antimatter asymmetry [44,46]. On the other hand, light sterile neutrinos are also a hot topic in particle physics and cosmology. A sterile neutrino at the keV mass scale is a promising candidate for Warm Dark Matter [362]. Moreover, sterile neutrinos at the eV or sub-eV scale [93,363] are well-motivated by the short-baseline neutrino oscillation anomalies, which include the LSND [56] and MiniBooNE [57]  $\bar{\nu}_\mu \rightarrow \bar{\nu}_e$  event excess, the Reactor Antineutrino Anomaly [58,101] and the Gallium anomaly [364]. Finally, the standard LMA-MSW solution [264,265] of solar neutrino oscillations predicts an energy-dependent variation (upturn) in the mid-energy regime of the solar neutrino spectrum that is not observed in current solar neutrino data [116,288]. A hypothetical super-light sterile neutrino at the  $\Delta m^2$  scale of  $\mathcal{O}(10^{-5})$  eV<sup>2</sup> has been proposed to explain the suppression of the upturn in the 5-MeV region [365,366].

In the following, we investigate JUNO’s potential to search for sterile neutrino oscillation with  $\Delta m^2$  values on the scale of eV<sup>2</sup> and  $\mathcal{O}(10^{-5})$  eV<sup>2</sup>. For the former case, we consider both a radioactive (anti-)neutrino source inside or near the JUNO detector and a cyclotron-produced neutrino beam to directly test the short baseline anomalies. For the latter one, an additional  $\Delta m^2$  near the solar mass-squared difference could be discovered in JUNO by studying reactor antineutrino oscillations as the experiment is very sensitive to both the solar and atmospheric mass-squared differences. We will restrict ourselves to the simplest (3 + 1) scheme, which includes three active and one sterile neutrino mass eigenstate. Depending on the neutrino mass hierarchy, there are four different scenarios of neutrino mass spectra, which are shown in Fig. 9-1.

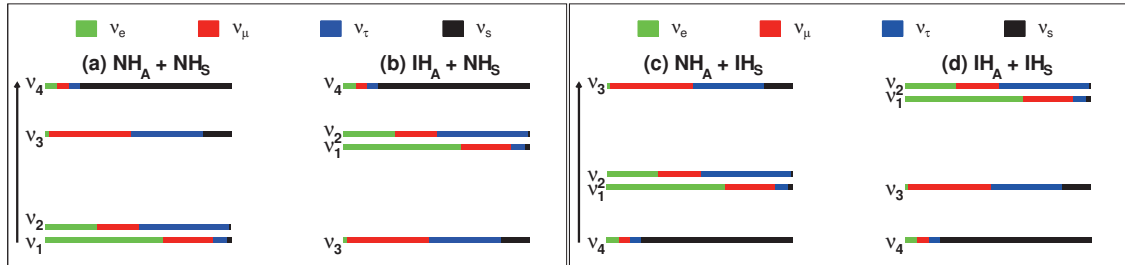


Figure 9-1: Four different scenarios of neutrino mass spectra in the (3+1) scheme, depending on the neutrino mass hierarchies of three active and one sterile neutrino mass eigenstates. The (2+2) scheme with two separate groups of mass eigenstates are already ruled out with the global analysis of solar and atmospheric neutrino data [367].

According to the general expression in Eq. 1.5, the electron (anti)neutrino survival probability

---

Editors: Yufeng Li (liyufeng@ihep.ac.cn), Weili Zhong (zhongwl@ihep.ac.cn)

Major contributors: Janet Conrad, Chao Li, Jiajie Ling, Gioacchino Ranucci, and Mike Shaevitz

in the (3+1) scheme is given by

$$P(\bar{\nu}_e^{(-)} \rightarrow \bar{\nu}_e^{(-)}) = 1 - 4 \sum_{i=1}^3 \sum_{j>i}^4 |U_{ei}|^2 |U_{ej}|^2 \sin^2 \frac{\Delta m_{ji}^2 L}{4E}, \quad (9.1)$$

where  $U$  is the neutrino mixing matrix defined in Eq. 1.2, and  $\Delta m_{ji}^2 \equiv m_j^2 - m_i^2$  for  $(1 \leq i < j \leq 4)$ . For the elements of  $U$ , we define  $U_{e1} \equiv \cos \theta_{14} \cos \theta_{13} \cos \theta_{12}$ ,  $U_{e2} \equiv \cos \theta_{14} \cos \theta_{13} \sin \theta_{12}$ ,  $U_{e3} \equiv \cos \theta_{14} \sin \theta_{13}$ , and  $U_{e4} \equiv \sin \theta_{14}$ . Using the mixing angles defined above, the survival probability in Eq. 9.1 can be written as

$$\begin{aligned} P(\bar{\nu}_e^{(-)} \rightarrow \bar{\nu}_e^{(-)}) = 1 & - \cos^4 \theta_{14} \cos^4 \theta_{13} \sin^2 2\theta_{12} \sin^2 \Delta_{21} \\ & - \cos^4 \theta_{14} \sin^2 2\theta_{13} (\cos^2 \theta_{12} \sin^2 \Delta_{31} + \sin^2 \theta_{12} \sin^2 \Delta_{32}) \\ & - \cos^4 \theta_{13} \sin^2 2\theta_{14} (\cos^2 \theta_{12} \sin^2 \Delta_{41} + \sin^2 \theta_{12} \sin^2 \Delta_{42}) \\ & - \sin^2 \theta_{13} \sin^2 2\theta_{14} \sin^2 \Delta_{43}, \end{aligned} \quad (9.2)$$

with  $\Delta_{ij} \equiv \Delta m_{ij}^2 L / 4E$ . The oscillation parameters from the three neutrino framework [26] are assumed to remain unchanged by the inclusion of the light sterile neutrino.

In the case of an eV-scale sterile neutrino, we can simplify Eq. 9.1 to an effective two-neutrino survival probability,

$$P(\bar{\nu}_e^{(-)} \rightarrow \bar{\nu}_e^{(-)}) = 1 - \sin^2 2\theta_{14} \sin^2 \frac{\Delta m_{41}^2 L}{4E}, \quad (9.3)$$

and the neutrino transition probability to

$$P(\bar{\nu}_\mu^{(-)} \rightarrow \bar{\nu}_e^{(-)}) = 4 \sin^2 \theta_{14} \sin^2 \theta_{24} \sin^2 \frac{\Delta m_{41}^2 L}{4E}, \quad (9.4)$$

with  $\theta_{24}$  being a further active-sterile mixing angle defined by  $|U_{\mu 4}|^2 \equiv \sin^2 \theta_{24}$ . Comparing the above oscillation probabilities, the amplitudes of the  $\bar{\nu}_e^{(-)} \rightarrow \bar{\nu}_e^{(-)}$  and  $\bar{\nu}_\mu^{(-)} \rightarrow \bar{\nu}_e^{(-)}$  channels are related with each other. A test of one of these channels can be used to restrict the other and vice versa.

## 9.2 Indications of eV-scale sterile neutrinos

In the past decades, there has been a number of experimental results that appear as anomalies in the context of the standard three-neutrino framework. This includes,

- the event excess of electron antineutrinos in a muon antineutrino beam [56] in the LSND experiment;
- the event excess of electron antineutrinos in a muon antineutrino beam [57] in the MiniBooNE experiment;
- the antineutrino rate deficit in reactor short-baseline experiments based on a recent evaluation of the reactor antineutrino flux model [58, 101];
- the neutrino rate deficit in the calibration runs performed with radioactive sources in the Gallium solar neutrino experiments [364].

It is quite interesting that all the above anomalies can be consistently described by short-baseline oscillations via a  $\Delta m^2$  of around 1 eV<sup>2</sup>. Given that solar neutrino oscillations indicate a value of  $\Delta m_{21}^2 \simeq 7.5 \times 10^{-5}$  eV<sup>2</sup> and atmospheric neutrino oscillations correspond to  $|\Delta m_{31}^2| \simeq 2.4 \times 10^{-3}$

$eV^2$ , the new mass-squared difference requires a fourth neutrino mass and thus also flavor eigenstate. However, results from the Large Electron-Positron collider (LEP) at CERN on the invisible decay width of  $Z$  bosons show that there are only three species of light neutrinos coupling to the  $Z$  featuring masses lower than half of the  $Z$  mass [368]. Therefore, the fourth neutrino flavor, if it exists, must be a sterile neutrino without direct coupling to standard model gauge bosons.

The LSND experiment used a pion decay-at-rest beam in the 20-60 MeV energy range to study neutrino oscillations at a baseline of 30 meters. Within the muon antineutrino beam, LSND observed an excess of electron-antineutrino events. The statistical significance of the observed excess is about  $3.8 \sigma$  [56]. In the follow-up, the MiniBooNE experiment was designed to test the LSND signal at a similar  $L/E$  ratio but both baseline and energy larger by about one order of magnitude. The result observed by MiniBooNE was inconclusive with regards to the LSND signal as there was no  $\bar{\nu}_e$  excess observed in the same  $L/E$  region. However, an anomalous excess was identified in the low-energy bins [57].

In the electron (anti-)neutrino disappearance channel, the recent re-evaluations of the reactor antineutrino spectrum resulted in a 3% increase in the interaction rates expected for neutrino detectors with respect to earlier calculations. Meanwhile, the experimental value for neutron lifetime decreased, which in turn implied a larger inverse  $\beta$ -decay cross section. Including previously-neglected effects on the rate expectation caused by long-lived isotopes not reaching equilibrium in a nuclear reactor core during the detector running time, the overall expectation value for the antineutrino rate from nuclear reactors increased by about 6%. As a result, more than 30 years of data from short-baseline reactor antineutrino experiments, which formerly agreed well with the flux prediction, featured now an apparent 6% deficit in their electron antineutrino event rates.

Another hint consistent with short-baseline oscillations arose from the source calibrations performed for the radio-chemical Gallium experiments for solar neutrino detection. High-intensity sources based on the radioisotopes  $^{51}\text{Cr}$  and  $^{37}\text{Ar}$ , which both decay via electron capture and emit mono-energetic electron neutrinos, were placed in close proximity to the detector and the resulting event rates were measured. Compared to the rates predicted based on the source strengths and reaction cross-sections, a 5-20% deficit of the measured count rate was observed.

At the same time, a number of measurements disfavor the interpretation of a sterile neutrino state with a mass of around 1 eV. Neither muon neutrino disappearance in MINOS [369], nor electron neutrino appearance was observed in KARMEN [370], NOMAD [371], ICARUS [372] and OPERA [373]. Several global analyses [59, 60, 374] that include all the available short-baseline data show strong tension between the appearance and disappearance data. A careful analysis of the existing data on the cosmic microwave background (CMB) anisotropies, galaxy clustering and supernovae Ia seems to favor one additional sterile neutrino species at the sub-eV mass scale [61–63]. However, the full thermalization of the additional degree of freedom before the CMB decoupling is disfavored.

In summary, a number of short baseline neutrino experiments support the sterile neutrino hypothesis, but some others do not. Considering the ambiguity of the available data, an unambiguous confirmation or refusal of the existence of light sterile neutrinos by a dedicated short-baseline oscillation experiments is a pressing requirement.

### 9.3 Requirements for future measurements

The neutrino community is engaging itself in an experimental effort to confirm or defy the existence of light sterile neutrinos (or an equivalent mechanism which would be consistent with the observed phenomena). In this context, the question arises how to define satisfactory criteria for a positive measurement. The current situation seems to suggest that a mere rate excess or deficit, although

statistically significant, may not be sufficient. Therefore, future experiments are required to test the anomalies with as little model-dependence as possible and by complementary methods to obtain as complete a picture as possible.

Future short-baseline accelerator neutrino experiments, such as the three detector short-baseline neutrino oscillation program laid out for the Fermilab Booster neutrino beam [375], will use charged-current reactions to observe both appearance and disappearance signals. Meanwhile, reactor antineutrino experiments may provide a charged-current measurement of the baseline-dependence of  $\bar{\nu}_e$  disappearance oscillations, as has been recently demonstrated by the Daya Bay experiment [376]. Currently, a new strategy emerges based on experiments with high-intensity radioactive neutrino sources at large liquid-scintillator detectors. The intense sources currently proposed are either based on electron-capture nuclei emitting mono-energetic electron neutrinos detected via elastic scattering of electrons or on high-endpoint  $\beta^-$ -emitters providing a sizable flux of electron antineutrinos above the detection threshold of the inverse beta decay. Corresponding experiments like SOX [377] or CeLAND [378] provide a test of both the distance and energy dependence expected for short-baseline oscillations. If very low energy thresholds were reached, a detection of all active neutrino flavors via neutral-current coherent scattering might become available, providing the most direct test of active-neutrino disappearance. Only multiple experiments using different channels will allow for a robust interpretation of the data as sterile neutrino oscillations. In addition, cosmological constraints [93] as well as a direct neutrino mass measurement at KATRIN [379] may provide the final orthogonal check for the existence of light sterile neutrinos.

Under the assumption of  $CPT$  invariance, the  $\bar{\nu}_e$  disappearance parameter space must contain the  $\bar{\nu}_\mu \rightarrow \bar{\nu}_e$  appearance parameter space. This is because  $CPT$  invariance requires that  $P(\bar{\nu}_\mu \rightarrow \bar{\nu}_e) = P(\nu_e \rightarrow \nu_\mu)$  and  $P(\nu_e \rightarrow \nu_e) = P(\bar{\nu}_e \rightarrow \bar{\nu}_e)$ . However, it must also hold  $P(\nu_e \rightarrow \nu_e) > P(\nu_e \rightarrow \nu_\mu)$ , since the latter is only a single appearance channel. Thus, if a  $\bar{\nu}_e$  disappearance experiment such as IsoDAR@JUNO will provide sufficient sensitivity to cover the entire parameter space for the observation of  $\bar{\nu}_\mu \rightarrow \bar{\nu}_e$  appearance, this experiment offers a decisive test.

#### 9.4 JUNO potential for light sterile neutrino searches

The JUNO experiment is designed to deploy a single (far) detector at baselines of about 53 km from both the Yangjiang and Taishan NPPs. Without an additional near detector, reactor antineutrino oscillations cannot be used to search for eV-scale sterile neutrinos. However, the diameter of the JUNO central detector will be around 35 meters, which is perfectly suitable for a short-baseline oscillation experiment with a radioactive neutrino source sensitive to eV-scale sterile neutrinos.

Source-based initiatives add a complementary approach to the reactor and accelerator short baseline programs because of both the purity of their source and the possibility to probe the baseline-dependence of the oscillation signal. In addition, source-based experiments are less susceptible to uncertainties arising from the normalization of both flux and cross-section. The possibility to perform orthogonal measurements by using multiple detection channels (i.e. elastic, neutral current, and charged current scattering) may provide the necessary orthogonal measurement to positively claim the existence of sterile neutrinos.

However, the production of MCi neutrino sources (e.g.,  $^{51}\text{Cr}$ ,  $^{37}\text{Ar}$ ) depends on reactor facilities for irradiation, while kCi antineutrino sources (e.g.,  $^{144}\text{Ce}$ - $^{144}\text{Pr}$ ) are based on fission isotopes won from spent nuclear fuel. Therefore, they can only be produced in countries that feature the corresponding facilities for the reprocessing of nuclear fuel. Further, short half-lives and regulatory issues complicate the transport of such sources, especially across international borders.

There are two basic options for the radioactive sources that can be deployed in a liquid scintillator detector like JUNO: A monochromatic  $\nu_e$  emitter, such as  $^{51}\text{Cr}$  or  $^{37}\text{Ar}$ , or a  $\bar{\nu}_e$  emitter



with a continuous  $\beta$ -spectrum. Regarding the former case, the signature is provided by  $\nu_e$  elastic scattering off electrons in the LS target. This signature can be mimicked by beta-decays or the Compton scattering of gamma-rays induced by radioactive and cosmogenic background sources and as well the elastic scattering of solar neutrinos. Especially if deployed outside of the detector target, an oscillation experiment with a  $\nu_e$  source requires a very high source activity of 5 – 10 MCi to overcome these backgrounds. In the second approach,  $\bar{\nu}_e$  are detected via the inverse beta decay, in which the delayed coincidence signature of positron and neutron provides efficient rejection power for the above-mentioned backgrounds. Therefore, we focus our studies on this second option.

A suitable  $\bar{\nu}_e$  source must feature a  $Q_\beta$  value larger than 1.8 MeV (i.e., threshold of the inverse beta decay) and a sufficiently long lifetime  $\tau_{1/2}$  ( $\geq 1$  month) to allow for the production and transportation to the detector. All candidate sources that have been proposed feature a long-lived low- $Q$  nucleus that decays to a short-lived high- $Q$  nucleus (e.g. [380]). Several suitable pairs have been identified:

- $^{144}\text{Ce}$ - $^{144}\text{Pr}$ , with  $Q_\beta(\text{Pr})=2.996$  MeV and  $\tau_{1/2}(\text{Ce})=285$  d,
- $^{106}\text{Ru}$ - $^{106}\text{Rh}$ , with  $Q_\beta(\text{Rh})=3.54$  MeV and  $\tau_{1/2}(\text{Ru})=372$  d,
- $^{90}\text{Sr}$ - $^{90}\text{Y}$ , with  $Q_\beta(\text{Y})=2.28$  MeV and  $\tau_{1/2}(\text{Sr})=28.9$  y,
- $^{42}\text{Ar}$ - $^{42}\text{K}$ , with  $Q_\beta(\text{K})=3.52$  MeV and  $\tau_{1/2}(\text{Ar})=32.9$  y,

The first three candidates are common fission products from nuclear reactors, which can be extracted from spent fuel rods. Since the  $Q_\beta$  of  $^{144}\text{Ce}$  is larger than that of  $^{90}\text{Sr}$ , and the chemical production of  $^{144}\text{Ce}$  is easier than for  $^{106}\text{Ru}$ , we will focus in the following on a  $^{144}\text{Ce}$ - $^{144}\text{Pr}$   $\bar{\nu}_e$  source to study the sensitivity of a sterile neutrino search in JUNO. This source can be either positioned at the center of the detector or outside the central detector, right next to the wall of the detector vessel.

#### 9.4.1 Sensitivity using an antineutrino source at the detector center

In this section, we study the deployment of a  $^{144}\text{Ce}$ - $^{144}\text{Pr}$   $\bar{\nu}_e$  antineutrino source featuring an energy spectrum  $S(E_\nu)$ , a mean lifetime  $\tau$ , and an initial activity  $A_0 = 50$  kCi. The source is encapsulated by a tungsten and copper shielding sphere and positioned at the detector center. We consider a running time  $t_e$  and a detection efficiency of 76%. The expected number of inverse beta decay interactions at radius  $R$  from the source and energy  $E_\nu$  can be written as

$$\frac{d^2 N(R, E_\nu)}{dR dE_\nu} = A_0 \cdot n \cdot \sigma(E_\nu) \cdot S(E_\nu) \cdot P(R, E_\nu) \int_0^{t_e} e^{-t/\tau} dt; \quad (9.5)$$

where  $n$  is the number density of free protons in the detector target,  $6.4 \times 10^{28}$  protons/m<sup>3</sup> for JUNO,  $\sigma(E_\nu)$  is the IBD cross-section, and  $P(R, E_\nu)$  is the oscillation probability given in Eq. 9.1.

The radius range considered for the oscillation search ranges from 1 m to 16 m with respect to the source. The total event number from inverse beta decays will reach  $2 \times 10^5$  for 900 days of data taking. The main background will be caused by coincidences among the 2.185 MeV gamma rays emitted in the decay of  $^{144}\text{Pr}$  with a branching ratio of 0.7% branch. This background will be reduced by a factor of  $5 \times 10^9$  when shielded by 33 cm of tungsten and 2 cm of copper. The remaining background is mainly given by the reactor antineutrinos emitted from the Taishan and Yangjiang reactor cores. Corresponding event numbers can be derived based on the respective thermal powers (total power of 35.8 GW) and baselines given in Tab. 1-2.

The expected sensitivity has been calculated based on a standard least-squares function,

$$\chi^2 = \sum_i \sum_j \frac{(N_{i,j}^{\text{obs}} - N_{i,j}^{\text{exp}})^2}{N_{i,j}^{\text{exp}} (1 + \sigma_b^2 N_{i,j}^{\text{exp}})} + \left(\frac{\alpha_s}{\sigma_s}\right)^2 + \left(\frac{\alpha_r}{\sigma_r}\right)^2 + \left(\frac{\alpha_d}{\sigma_d}\right)^2, \quad (9.6)$$

where the indices  $i$  and  $j$  refer to bins in the detected energy and position respectively.  $N_{i,j}^{\text{obs}}$  is the antineutrino events detected in each bin, including the possible sterile neutrino oscillation effect. The expected number of events assuming no sterile neutrino oscillation  $N_{i,j}^{\text{exp}}$  is the sum of events from the source  $S_{i,j}^{\text{exp}}$  and the background from reactor antineutrinos  $R_{i,j}^{\text{exp}}$ :

$$N_{i,j}^{\text{exp}} = (1 + \alpha_d)[(1 + \alpha_s)S_{i,j}^{\text{exp}} + (1 + \alpha_r)R_{i,j}^{\text{exp}}]. \quad (9.7)$$

For the observed and expected number of events, the survival probabilities for reactor and source antineutrinos are both calculated with the full 3+1 scheme oscillation probability assuming normal hierarchies for three active and one sterile mass eigenstates (as shown in panel (a) of Fig. 9-1). The expected number of events is allowed to vary within the systematic uncertainties via nuisance parameters.  $\alpha_d$  accounts for detector efficiency variations ( $\sigma_d$ , 2%), while  $\alpha_s$  and  $\alpha_r$  account for the source ( $\sigma_s$ , 2%) and reactor ( $\sigma_r$ , 3%) normalization uncertainties. In addition,  $\sigma_b$  is the bin-to-bin uncertainty of 0.3%.

Fig. 9-2 shows the distance and energy distributions expected for the antineutrino source signal (first row) as well as the reactor antineutrino background (third row). The second row illustrates the spectral features introduced by the presence of short-baseline disappearance oscillations, assuming a mass-squared difference of  $\Delta m_{41}^2 = 1 \text{ eV}^2$ , and an active-sterile mixing amplitude of  $\sin^2 2\theta_{14} = 0.1$ . Based on the above  $\chi^2$  function, we have performed a scan of the sensitivity to  $\sin^2 2\theta_{14}$  as a function of running time, energy resolution and spatial resolution, assuming a fixed mass-squared difference  $\Delta m_{41}^2$  is  $1 \text{ eV}^2$ . The results are shown in Fig. 9-3. As the default value for the calculation of the final sensitivity, we choose 450 days as a practical data-taking time, a spatial resolution of 12 cm according to the current detector design, and an energy resolution of  $3\%/\sqrt{E(\text{MeV})}$ . When varying these parameters, the resulting sensitivity shows only weak dependence on the spatial resolution, while the dependence on the energy resolution is significant.

Assuming these default values, the final sensitivity as a function of both  $\sin^2 2\theta_{14}$  and  $\Delta m_{41}^2$  is shown in Fig. 9-4. Despite the lower activity of the source and a shorter running time, JUNO will surpass the sensitivity of CeLAND [378] in the  $\Delta m_{41}^2$  region from 0.1 to  $10 \text{ eV}^2$ .

#### 9.4.2 Sensitivity with the antineutrino sources outside the detector

In case the kCi  $^{144}\text{Ce}$  source is deployed outside the central detector, we determine the sensitivity of a sterile neutrino search following the approach described in [381]. Specifically, the sensitivity is quantified using a  $\chi^2$  analysis along the lines of Eq. 9.6. The corresponding exclusion contours have been derived using the null-oscillation hypothesis, in which the observed event number  $N_{i,j}^{\text{obs}}$  is calculated assuming the absence of oscillations. On the other hand, the predicted  $N_{i,j}^{\text{exp}}$  profile includes the possibility of short-baseline oscillations with the oscillation parameters  $\Delta m_{41}^2$  and  $\sin^2 2\theta_{14}$ . The background from reactor antineutrinos is included in the analysis. The uncorrelated systematic bin-to-bin error is assumed to be 2%, and an additional pull term has been included to quantify the uncertainty in the knowledge of the source intensity, which has been set to 1.5%. Other inputs used in the calculations are the distance from the center of the detector, 20 m, the strength of the source, 100 kCi, the overall data taking period, 1.5 years, and the spatial resolution, 12 cm. For illustration, the energy resolution is set to be  $5\%/\sqrt{E(\text{MeV})}$  here as that of the Borexino

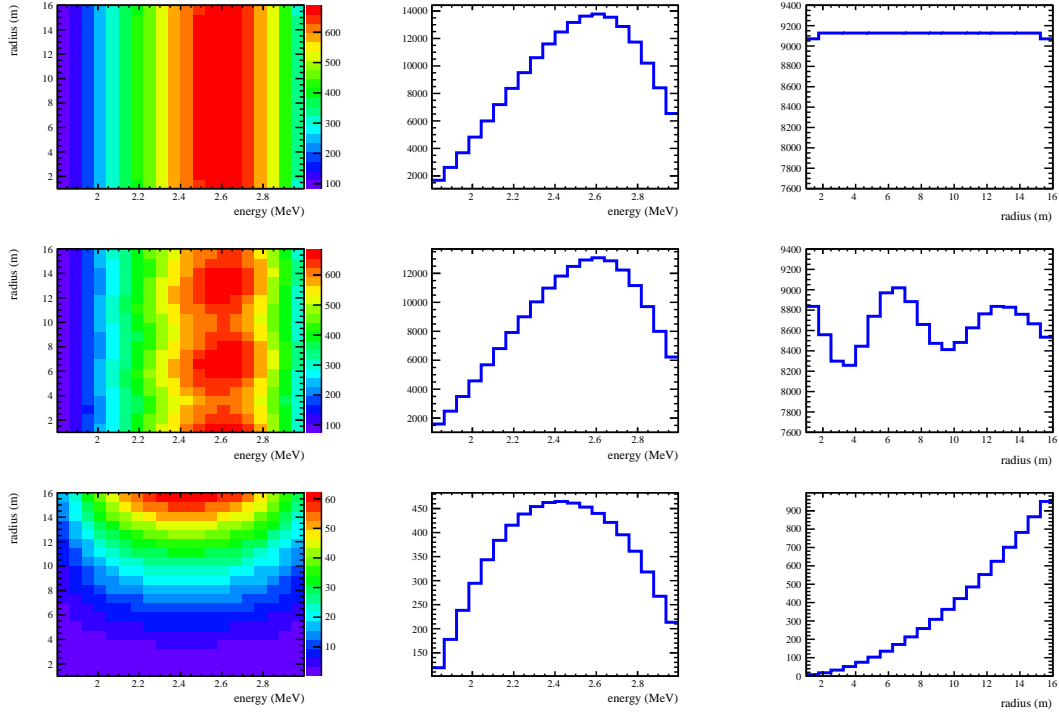


Figure 9-2: Energy and position dependence of the event numbers expected for a  $^{144}\text{Ce}$   $\bar{\nu}_e$  source (50 kCi, 900 days) at the center of the detector. The top row of panels shows the signal of the antineutrino source without oscillations. The middle row illustrates the effect of  $\bar{\nu}_e \rightarrow \bar{\nu}_s$  oscillations. The bottom row illustrates the event distribution expected for the reactor antineutrino background. In each row, the left panel shows the 2-dimension distribution of the event rates as a function of signal energy and the distance from the source. The middle panels are one-dimensional projections of the energy spectrum, while right panels show the distance distributions.

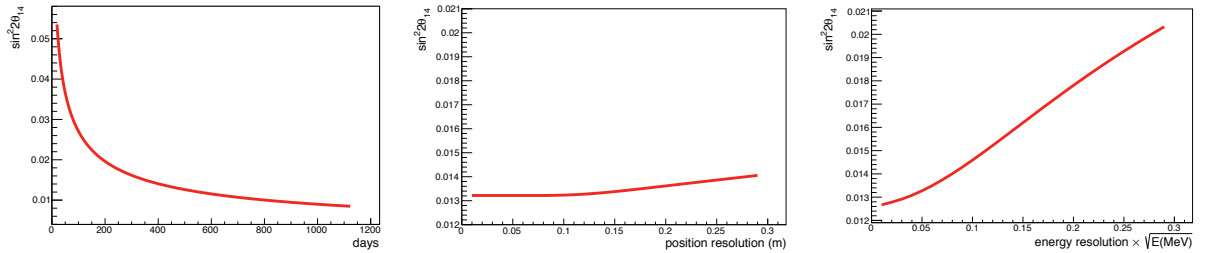


Figure 9-3: Sensitivity of  $\sin^2 2\theta_{14}$  at the 90% C.L. (for  $\Delta m_{41}^2$  fixed at  $1 \text{ eV}^2$ ): Default values are a running time of 450 days, an energy resolution of  $3\%/\sqrt{E(\text{MeV})}$ , and a spatial resolution of 12 cm. While the other values are kept fixed, the left panel shows the dependence of the sensitivity on the running time, the middle on the energy resolution, and the right on the spatial resolution.

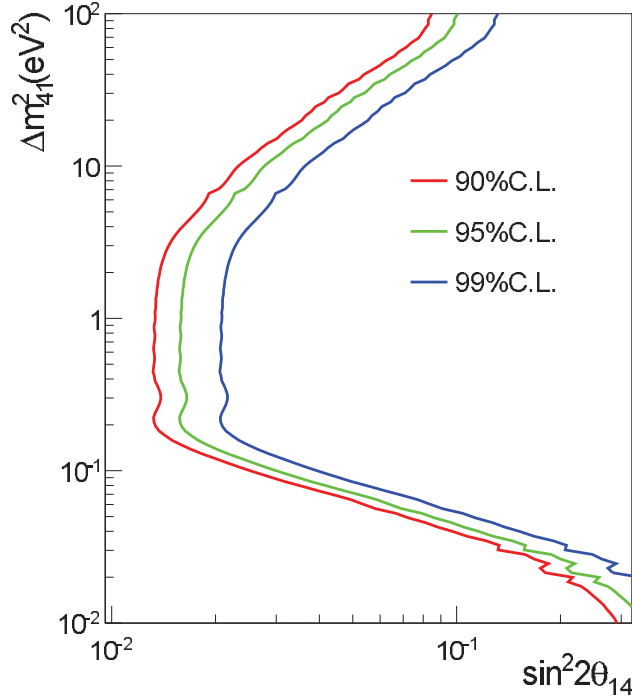


Figure 9-4: Sensitivity of a  $\bar{\nu}_e$  disappearance search at JUNO to the oscillation parameters  $\Delta m_{41}^2$  and  $\sin^2 2\theta_{14}$  assuming a 50 kCi  $^{144}\text{Ce}$  source at the detector center, with 450 days of data-taking. We show the 90, 95 and 99% confidence levels, with the reactor antineutrino background taken into account.

detector. The exclusion contours, stemming from Eq. 9.6 and reported in Fig. 9-5, are obtained with the 90, 95 and 99% C.L. of the  $\chi^2$  distribution for two degrees of freedom.

Comparing to the experiment placing the antineutrino source at the detector center as described before, the sensitivity in  $\sin^2 2\theta_{14}$  seems comparable. Note, however, that the experiment with the external source assumes a twice higher source activity as well as slightly different systematic uncertainties.

### 9.5 Sensitivity of a cyclotron-driven $^8\text{Li}$ source (IsoDAR)

IsoDAR@JUNO uses the decay of cyclotron-produced  $^8\text{Li}$  as a pure  $\bar{\nu}_e$  source located at short distance from the JUNO detector. The combination of high antineutrino flux and the large target volume of the JUNO detector allows the experiment to make an extremely sensitive search for antineutrino disappearance in the parameter region favored by the sterile-neutrino anomalies. Based on the small spatial diameter of the  $^8\text{Li}$  production region and the excellent position resolution of JUNO, such an experiment will be able to detect oscillations by observing the rate deficit that is induced by the oscillation wave as a function of the ratio of distance over energy ( $L/E$ ). An analysis of survival probabilities in  $L/E$  is well suited to detect oscillations but also highly effective in reducing the systematic uncertainties introduced by background and flux normalizations. In the following, we investigate the sensitivity of IsoDAR@JUNO for the oscillation parameter range indicated by the current experimental anomalies.

**Neutrino source.** A 60 MeV/amu cyclotron accelerator produces deuterons that impinge on a beryllium target, such producing copious amounts of neutrons. The target is surrounded on all

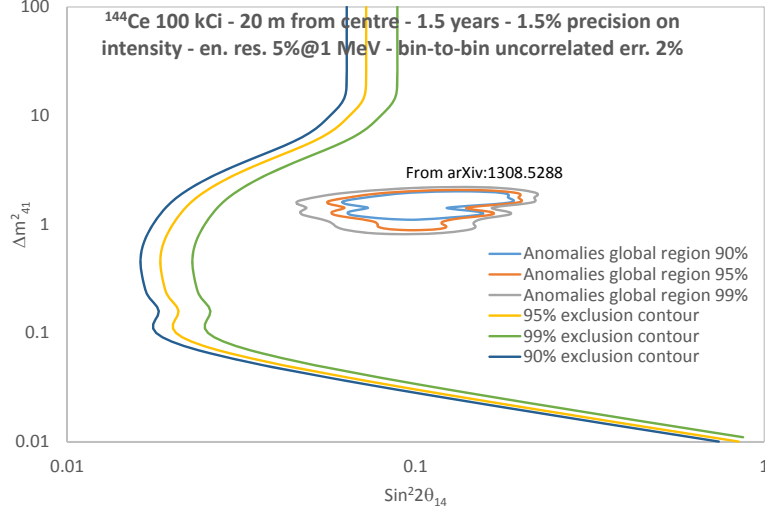


Figure 9-5: Sensitivity of a  $\bar{\nu}_e$  disappearance search at JUNO to the oscillation parameters  $\Delta m_{41}^2$  and  $\sin^2 2\theta_{14}$ , placing a 100 kCi  $^{144}\text{Ce}$  source outside the central detector. We assume a data taking time of 450 days and take the reactor antineutrino background into account. The exclusion limits shown represent 90, 95 and 99% confidence levels. The allowed regions are taken from the global analysis in Ref. [60].

sides by a high-purity (99.99%)  $^7\text{Li}$  sleeve, where neutron capture results in  $^8\text{Li}$  production. The subsequent  $\beta^-$ -decay of the  $^8\text{Li}$  nuclei created produces an isotropic  $\bar{\nu}_e$  flux with an average energy of  $\sim 6.5$  MeV and an endpoint of  $\sim 13$  MeV. The spatial extension of the source leads to an uncertainty of 40 cm ( $1\sigma$ ) regarding the origin of the antineutrinos emitted. The source requires substantial iron and concrete shielding to contain the neutrons that escape the  $^7\text{Li}$  sleeve. For this analysis, we assume that the center of the source is located 5.0 m from the edge of the active region of JUNO. Electron antineutrinos are observed via the inverse beta decay (IBD),  $\bar{\nu}_e + p \rightarrow e^+ + n$ . The neutrino energy is reconstructed from the visible energy of the positron:  $E_\nu = E_{e^+} + 0.8$  MeV. The vertex position is reconstructed using the arrival time of the scintillation light. For the preliminary analysis published in Ref. [382], the following parameters have been used for JUNO:

- an active target of 34.5 m in diameter, with a fiducial volume of 20 ktons.
- PMTs are located at a diameter of 37.5 m.
- Veto region extends 1.5 m beyond the PMTs
- rock overburden corresponding to  $\sim 2000$  m.w.e.
- an energy resolution of  $3\%/\sqrt{E(\text{MeV})}$ .
- a vertex resolution of  $12 \text{ cm}/\sqrt{E(\text{MeV})}$ .

The analysis for the sterile-neutrino sensitivity follows the method presented in Ref. [383], that assumes anormalization uncertainty of 5% and a detection efficiency of 90%. Since  $L$  and  $E$  can be measured rather precisely, this analysis exploits the  $L/E$  dependence of the possible oscillation probability to estimate the  $\Delta m_{41}^2$ - $\sin^2 2\theta_{14}$  regions where the null-oscillation hypothesis can be excluded at the  $5\sigma$  confidence level.

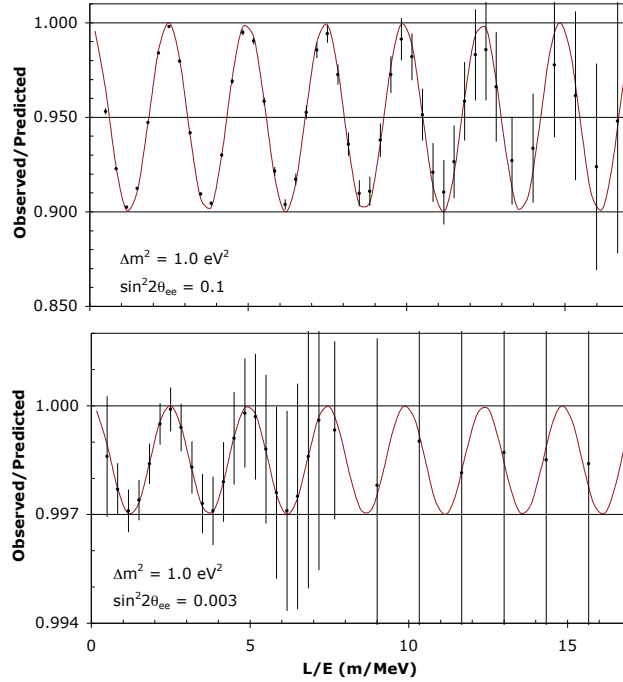


Figure 9-6: Oscillation signature in the  $L/E$  space, with five years running, assuming (top)  $\Delta m^2 (\equiv \Delta m_{41}^2) = 1.0 \text{ eV}^2$  and  $\sin^2 2\theta_{ee} (\equiv \sin^2 2\theta_{14}) = 0.1$  and (bottom)  $\sin^2 2\theta_{ee} = 0.003$ . Black points corresponds to the simulation data, while the solid curve represents the oscillation probability without energy and position smearing. Plots from Ref. [382]

We assume 5 years of running time. Fig. 9-6 shows example oscillation waves for parameter combinations motivated by the global oscillation analyses for sterile neutrinos. The parameters for the top example are  $\Delta m_{41}^2 = 1.0 \text{ eV}^2$  and  $\sin^2 2\theta_{14} = 0.1$ , which corresponds to the allowed parameter region for  $\bar{\nu}_e$  disappearance derived in Ref. [60]. The bottom example assumes parameter values of  $\Delta m_{41}^2 = 1.0 \text{ eV}^2$  and  $\sin^2 2\theta_{14} = 0.003$ , which is a solution in agreement with the allowed region for the  $\bar{\nu}_\mu \rightarrow \bar{\nu}_e$  appearance signal [374]. The bottom plot illustrates that even for the lowest values  $\sin^2 2\theta_{e\mu} (\equiv 4 \sin^2 \theta_{14} \sin^2 \theta_{24})$  allowed by the LSND anomaly, IsoDAR@JUNO will be able to definitively map out the oscillation wave.

Fig. 9-7 shows the sensitivity curve for IsoDAR@JUNO (blue line). Such an experiment could not only perform a decisive test of the parameter regions favored by the reactor anomaly (light gray) and the corresponding global analysis region for electron-flavor disappearance in a (3+1) model (dark gray). It also covers completely the “global  $\bar{\nu}_e$  appearance” region (purple) at a significance level greater than  $5\sigma$ . If no oscillation signal was observed, sterile neutrinos mixing could be excluded at  $5\sigma$  level as the cause of all of the present anomalies, including LSND and MiniBooNE. In case of a positive detection of short-baseline oscillations, the precise measurement of the  $L/E$  dependence will allow to quantify the emerging oscillation pattern in order to trace the complicated wave behavior and assess the consistency with oscillation models featuring one (3+1) or two (3+2) sterile in addition to the three active neutrino flavors. Currently, there are no other experiments proposed that would match the sensitivity of IsoDAR@JUNO.

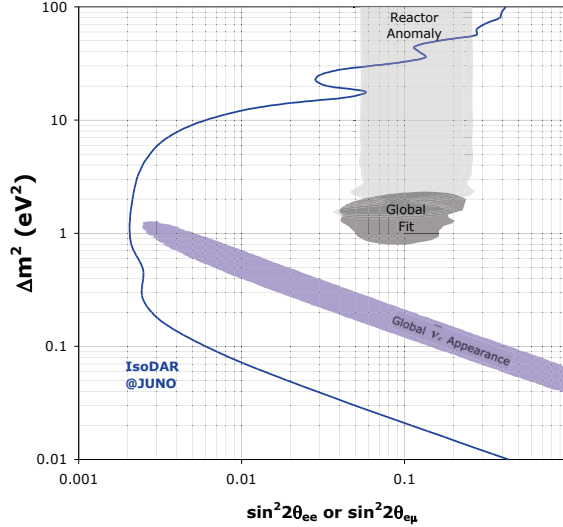


Figure 9-7: The sensitivity of an oscillation search of JUNO@IsoDAR experiment in comparison to the parameter regions favored by the current anomalies. The blue curve indicates the  $\Delta m^2 (\equiv \Delta m_{41}^2)$  vs.  $\sin^2 2\theta_{ee} (\equiv \sin^2 2\theta_{14})$  contours for which the null-oscillation hypothesis can be excluded at more than  $5\sigma$  with IsoDAR@JUNO after five years of data-taking. The light (dark) gray area is the 99% allowed region for the Reactor Anomaly [58] (Global Oscillation Fit [60]) plotted as  $\Delta m^2$  vs.  $\sin^2 2\theta_{ee}$ . The purple area is the 99% CL for a combined fit to all  $\bar{\nu}_e$  appearance data [374], plotted as  $\Delta m^2$  vs.  $\sin^2 2\theta_{e\mu} (\equiv 4\sin^2 \theta_{14} \sin^2 \theta_{24})$ . Plot is adapted from Ref. [382],

## 9.6 Sensitivity with reactor antineutrino oscillations

Super-light sterile neutrinos on a  $\Delta m^2$  scale of  $\mathcal{O}(10^{-5})$  eV<sup>2</sup> [387, 388] could be discovered not only by a precision measurement of the solar MSW-LMA oscillation transition region but also by a medium-baseline reactor neutrino experiment such as JUNO. In the following, we will study the sensitivity of a corresponding search in JUNO.

The JUNO detector, a 20 kton liquid scintillator detector, is located at a baseline of 53 km from two reactor complexes, with a total thermal power of 36 GW. The targeted energy resolution is  $3\%/\sqrt{E(\text{MeV})}$ . We assume the uncertainty of the absolute energy scale for positron signals is similar to the Daya Bay experiment [32], which corresponds to about 1% between 1 and 10 MeV. With 6 years of running at full reactor power, a total of  $\sim 100,000$  IBD events will be collected. The reactor neutrino data will be used to determine the mass hierarchy as well as precision measurement of three oscillation parameters. However, if super-light sterile neutrinos exist, additional distortion could be observed in the reactor neutrino spectrum.

For the three active neutrinos, two neutrino mass hierarchies are still allowed by experiment. They are usually referred to as the normal mass hierarchy if  $m_3 > m_1$ , and inverted mass hierarchy if  $m_3 < m_1$ . Similarly, there are also two possible mass orderings for the new sterile neutrino mass eigenstate,  $m_4$ , with respect to  $m_1$ . Following the convention, we define  $m_4 > m_1$  as the sterile neutrino normal mass hierarchy, and  $m_4 < m_1$  as the inverted mass hierarchy. In order to distinguish those two arrangements, we denote the conventional active neutrino normal and inverted mass hierarchies as NH<sub>A</sub> and IH<sub>A</sub>, and NH<sub>S</sub> and IH<sub>S</sub> for the sterile neutrino cases. As illustrated in Fig. 9-1, there are in the extended case four possible combinations for the neutrino mass hierarchy. Note that since the JUNO experiment has a 3-4 $\sigma$  medium sensitivity to determine the mass hierarchy of the active neutrinos we may end up with only two scenarios.

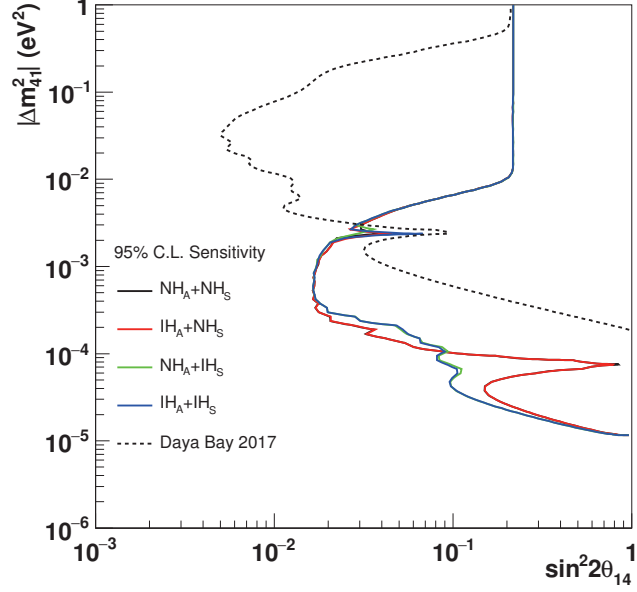


Figure 9-8: Comparison of the 95% C.L. sensitivities for various combinations of neutrino mass hierarchies.

In order to calculate the sensitivity for oscillations into super-light sterile neutrinos, we follow the method used in the Daya Bay reactor sterile neutrino search [390]. A binned log-likelihood method is adopted with nuisance parameters reflecting the uncertainty on the detector response and a covariance matrix encapsulating the reactor flux uncertainties as given in the Huber [101] and Mueller [102] flux models. Since there is no near detector to constrain the flux [391], the rate uncertainty of the reactor neutrino flux was enlarged to 6%. The fit uses  $|\Delta m_{32}^2| = (2.41 \pm 0.10) \times 10^{-3} \text{eV}^2$  [131]. The values of  $\sin^2 2\theta_{14}$ ,  $\sin^2 2\theta_{13}$ ,  $\sin^2 2\theta_{12}$ ,  $\Delta m_{41}^2$  and  $\Delta m_{32}^2$  are unconstrained. Fig. 9-8 shows the 95% C.L. sensitivity contours in the oscillation parameters  $\sin^2 2\theta_{14}$  and  $|\Delta m_{41}^2|$  for different combinations of the neutrino mass hierarchy. The search is most sensitive in the region  $10^{-5} < |\Delta m_{41}^2| < 10^{-2} \text{eV}^2$ . For the region of  $|\Delta m_{41}^2| > 10^{-2} \text{eV}^2$ , the fast oscillation pattern is smeared out in energy as the detector resolution is no longer sufficient. Therefore, the sensitivity in this region depends only on the uncertainty of the flux normalization, and no further information on  $|\Delta m_{41}^2|$  can be obtained.

For different mass hierarchies, there are some clearly distinctive features. For the sterile neutrino normal hierarchy  $\text{NH}_S$ , there appears a large dip in sensitivity at  $|\Delta m_{41}^2| = 7 \times 10^{-5} \text{eV}^2$ . This is caused by  $|\Delta m_{41}^2| \approx \Delta m_{21}^2$  as the masses of  $m_4$  and  $m_2$  become degenerate. However, this degeneracy is broken for other mass configurations that result in a different value of  $|\Delta m_{42}^2|$ . As shown in Fig. 9-1, for the  $\text{NH}_S$  case,  $|\Delta m_{42}^2| = |\Delta m_{41}^2| - \Delta m_{21}^2$ ; and for the  $\text{IH}_S$  case,  $|\Delta m_{42}^2| = |\Delta m_{41}^2| + \Delta m_{21}^2$ . According to the oscillation probability in Eq. 9.1, the  $|U_{e2}|^2 |U_{e4}|^2 \sin^2(\Delta m_{42}^2 L/4E)$  term becomes quite different for those two cases. Interestingly, there is a smaller dip structure at  $|\Delta m_{41}^2| = 2.4 \times 10^{-3} \text{eV}^2$  for all neutrino mass hierarchies. Similarly when masses  $m_4$  and  $m_3$  become degenerate at  $|\Delta m_{41}^2| \approx |\Delta m_{31}^2|$ ,  $|\Delta m_{43}^2|$  itself is different for the four cases. However, the oscillation term associated with  $|\Delta m_{43}^2|$ ,  $|U_{e3}|^2 |U_{e4}|^2 \sin^2(\Delta m_{43}^2 L/4E)$ , is suppressed by the smallness of  $|U_{e3}|^2 \approx 0.02$ , compared with  $|U_{e2}|^2 \approx 0.3$  for the case of degeneracy of  $m_2$  and  $m_4$ . Since JUNO has sensitivity to the active neutrino mass hierarchy determination, the dip structure shows up at slightly different locations for the  $\text{NH}_A$  and  $\text{IH}_A$  cases.

In summary, the precision measurement of reactor antineutrino oscillations in JUNO provides



sensitivity to search for super-light sterile neutrinos at a  $\Delta m^2$  scale of  $\mathcal{O}(10^{-5})$  eV<sup>2</sup>. The most sensitive region is located at  $10^{-5} < |\Delta m_{41}^2| < 10^{-2}$  eV<sup>2</sup>. If it is combined with the results of the sterile neutrino search conducted by the Daya Bay experiment [390], which is sensitive to  $10^{-3} < |\Delta m_{41}^2| < 0.3$  eV<sup>2</sup>, the sensitive region will cover about four orders of magnitude in  $|\Delta m_{41}^2|$ , from  $10^{-5}$  eV<sup>2</sup> to 0.3 eV<sup>2</sup>. Combined with one of the experiment approaches searching for eV-scale sterile neutrinos that have been described above, the whole region of interest for light sterile neutrinos can be covered.

## 9.7 Conclusion

The JUNO detector has multiple advantages in searching for light sterile neutrinos, including its large dimensions, unprecedented energy resolution and excellent position accuracy. Placing a 50 to 100 kCi source of antineutrinos extracted from spent reactor fuel, inside or outside the detector for a 1.5 year run, JUNO is sensitive to the entire global analysis region for electron-flavor disappearance in the (3+1) scheme, at a more than  $3\sigma$  confidence level. It has the greatest sensitivity for 0.1 - 10 eV<sup>2</sup>-scale sterile neutrinos among all current and planned experiments with various proposed sources. Using a <sup>8</sup>Li antineutrino source produced from a 60 MeV/amu cyclotron accelerator (IsoDAR@JUNO) located 5 m away from the detector would provide sensitivity to 1 eV<sup>2</sup>-scale sterile neutrinos. Assuming 5 years of data-taking, the sensitivity curve of IsoDAR@JUNO covers the allowed reactor anomaly region, the 3+1 scheme global analysis region for electron-flavor disappearance, and the global  $\bar{\nu}_e$  appearance region (i.e., all present anomaly regions) at a greater than  $5\sigma$  confidence level. In addition to the excellent sensitivity to 1 eV<sup>2</sup>-scale light sterile neutrinos, the JUNO experiment can search for super-light sterile neutrinos at the  $\Delta m^2$  scale of  $\mathcal{O}(10^{-5})$  eV<sup>2</sup> using reactor antineutrinos. With a total of 100,000 IBD events from reactor antineutrinos collected over 6 years of full-power running, the most sensitive region is  $10^{-5} < |\Delta m_{41}^2| < 10^{-2}$  eV<sup>2</sup>. Combined with the sterile neutrino exclusion region of the Daya Bay experiment, i.e.,  $10^{-3} < |\Delta m_{41}^2| < 0.3$  eV<sup>2</sup>, the JUNO experiment will have good sensitivity across the entire range of light sterile neutrino searches, about seven orders of magnitude in  $|\Delta m_{41}^2|$ , when using antineutrinos both from sources and reactors.

## 10 Nucleon Decays

Being a large liquid scintillator detector deep underground, JUNO is in an excellent position to search for nucleon decays. In particular, in the SUSY-favored decay channel  $p \rightarrow K^+ + \bar{\nu}$ , JUNO will be competitive with or complementary to those experiments using either water Cherenkov or liquid argon detectors.

### 10.1 A brief overview of nucleon decays

To explain the observed matter-antimatter asymmetry of the universe, baryon number violation is one of the prerequisites [392]. However, there has been no experimental evidence for baryon number violation. Unlike the electric charge, the baryon number is only a global symmetry in the Standard Model (SM) and its natural extensions. In many Grand Unified Theories (GUTs) that unify strong and weak interactions, baryon number conservation is only an approximate symmetry (i.e., it is slightly broken). A recent review of the GUT models can be found in Ref. [393]. The gauge coupling unification scale of such GUT models is typically of the order of  $10^{16}$  GeV, which can never be touched by any man-made particle accelerators in the foreseeable future. Fortunately, an indirect experimental test of the GUTs is possible through an observation of the proton decays — one of the unique predictions of the GUTs.

The first experiment in search of the proton decay dates back to 1954, when Reines *et al* [394] set a lower limit on the lifetime of protons with the help of a 300-liter liquid scintillator detector:  $\tau > 10^{22}$  yrs. Since then many larger-scale experiments, such as Kolar Gold Field [395], NUSEX [396], FREJUS [397], SOUDAN [398], IMB [399] and Kamiokande [400], have been done for this purpose. Today the largest running experiment of this kind is the Super-Kamiokande, a 50 kton (22.5 kton fiducial mass) water Cherenkov detector located in Kamioka in Japan. Thanks to these experiments, the lower bound on the lifetime of the proton has been improved by many orders of magnitude in the past 60 years.

The two decay modes which have often been searched for are  $p \rightarrow \pi^0 e^+$  and  $p \rightarrow K^+ \bar{\nu}$ . The first one is expected to be the leading mode in many GUTs, in particular in those non-SUSY GUTs which typically predict the lifetime of the proton to be about  $10^{35}$  yrs. This decay mode has also been constrained to the best degree of accuracy because of the high efficiency and background rejection of the water Cherenkov detectors. The current limit is  $\tau(p \rightarrow \pi^0 e^+) > 1.4 \times 10^{34}$  yrs at 90% C.L. from the Super-Kamiokande experiment [401].

In comparison, the decay mode  $p \rightarrow K^+ \bar{\nu}$  is favored by a number of SUSY GUTs which typically predict the lifetime of the proton to be less than a few  $\times 10^{34}$  yrs. The search for this mode in a large water Cherenkov detector is hindered by the decay kinematics. The momentum of the  $K^+$  in this two-body decay is 339 MeV/c (kinetic energy of 105 MeV), which is below the Cherenkov threshold in water. Therefore, both of the final-state particles are invisible. Nonetheless, the daughter particles originating from the two main decay channels of  $K^+$  (i.e.,  $K^+ \rightarrow \mu^+ \nu_\mu$  and  $K^+ \rightarrow \pi^+ \pi^0$ ) can be reconstructed in a water Cherenkov detector. A photon-tagging technique from the de-excitation of  $^{15}\text{N}$ , which is emitted from the decay of a proton bound in  $^{16}\text{O}$ , can be further used to increase the detection efficiency. But the overall efficiency remains rather low in a water Cherenkov detector. Today's best limit is  $\tau(p \rightarrow K^+ \bar{\nu}) > 5.9 \times 10^{33}$  yrs at 90% C.L. reported by the Super-Kamiokande collaboration [401].

There are some other decay modes of the proton, which are also interesting from a theoretical point of view. In some GUTs, for example, the branching ratios of  $p \rightarrow \mu^+ \pi^0$  and  $p \rightarrow e^+ \eta$  are of the order of 10–20%. Note that the lifetime of bound neutrons is expected to be comparable with

---

Editor: Chao Zhang (chao@bnl.gov)

that of protons. The 90% C.L. limits on the nucleon lifetimes in various two-body decay modes of the nucleons are graphically presented in Fig. 10-1. Most of the most stringent limits are achieved from the Super-Kamiokande experiment [402–404].

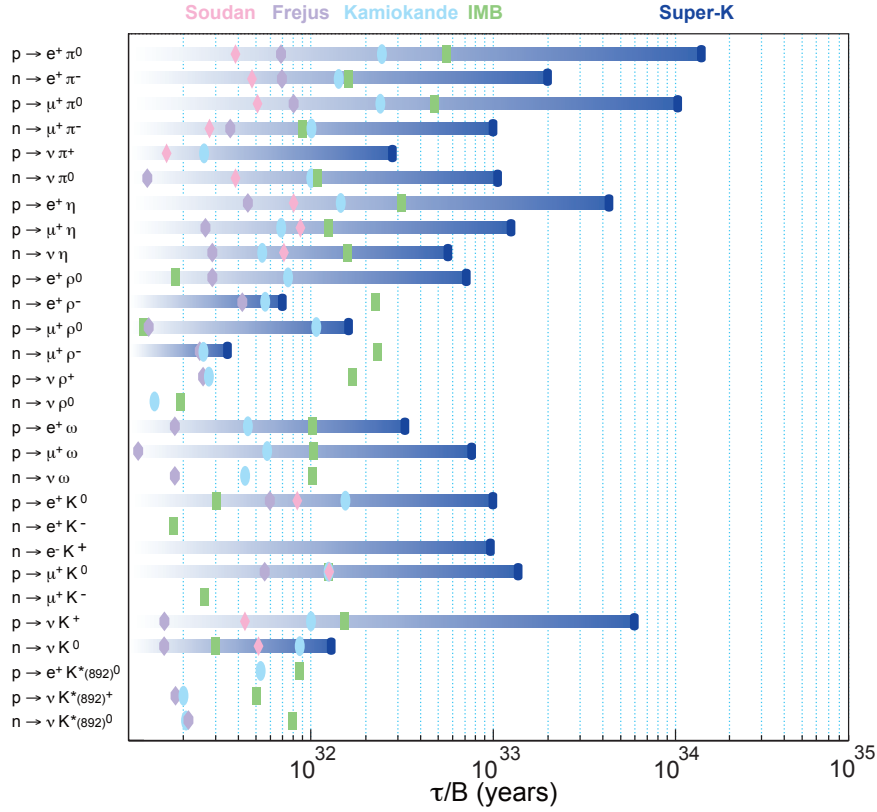


Figure 10-1: The 90% C.L. limits on the nucleon lifetimes in a variety of two-body decay modes of the nucleons [401]. Today’s best limits are mostly from the Super-Kamiokande experiment using the water Cherenkov detector.

The Super-Kamiokande detector (22.5 kt) and the future Hyper-Kamiokande detector (560 kt) are certainly larger than the JUNO detector (20 kt) in mass. Compared with the water Cherenkov detectors, however, the liquid scintillator detectors have the unique advantages in detecting some proton decay modes, in particular  $p \rightarrow K^+ \bar{\nu}$  [405]. The tagging efficiency for the proton decay can be largely improved due to the large scintillation signal created by the  $K^+$  itself, which is invisible in a water Cherenkov detector. For most other decay modes, the liquid scintillator does not provide any immediate advantages over water in the aspects of the signal efficiency and background. Thus we shall mainly focus on the  $p \rightarrow K^+ \bar{\nu}$  channel in the following.

## 10.2 Detection principle in liquid scintillator

Let us focus on the  $p \rightarrow K^+ \bar{\nu}$  channel. The protons in the JUNO detector are from both hydrogen and carbon nuclei. Using the Daya Bay liquid scintillator as a reference, the H-to-C molar ratio is 1.639. For a 20 kt fiducial volume detector, the number of protons from hydrogen (free protons) is  $1.45 \times 10^{33}$ , and that from carbon (bound protons) is  $5.30 \times 10^{33}$ .

$p \rightarrow K^+ \bar{\nu}$  is a two-body decay. If the decaying proton is from hydrogen, then it decays at rest. In this case the kinetic energy of  $K^+$  is fixed to be 105 MeV, which yields a prompt signal in the

liquid scintillator. The  $K^+$  meson has a lifetime of 12.4 nanoseconds and can quickly decay via the following major channels:

- $K^+ \rightarrow \mu^+ \nu_\mu$  (63.43%),
- $K^+ \rightarrow \pi^+ \pi^0$  (21.13%),
- $K^+ \rightarrow \pi^+ \pi^+ \pi^-$  (5.58%),
- $K^+ \rightarrow \pi^0 e^+ \nu_e$  (4.87%),
- $K^+ \rightarrow \pi^+ \pi^0 \pi^0$  (1.73%).

We mainly consider the two most important decay modes:  $K^+ \rightarrow \mu^+ \nu_\mu$  and  $K^+ \rightarrow \pi^+ \pi^0$ . In either case there is a shortly delayed ( $\sim 12$  ns) signal from the daughter particle(s). If the  $K^+$  meson decays into  $\mu^+ \nu_\mu$ , the delayed signal comes from  $\mu^+$ , which has a fixed kinetic energy of 152 MeV as required by kinematics. Then the decay  $\mu^+ \rightarrow e^+ \nu_e \bar{\nu}_\mu$  happens about  $2.2 \mu s$  later, leading to the third long-delayed signal with a well-known (Michel electron) energy spectrum. If the  $K^+$  meson decays into  $\pi^+ \pi^0$ , the  $\pi^+$  deposits its kinetic energy (108 MeV) and the  $\pi^0$  instantaneously decays into two gamma rays with the sum of the energies equal to the total energy of  $\pi^0$  (246 MeV). The delayed signal includes all of the aforementioned deposited energies. Then the  $\pi^+$  meson decays primarily into  $\mu^+ \nu_\mu$ . The  $\mu^+$  itself has very low kinetic energy (4.1 MeV), but it decays into  $e^+ \nu_e \bar{\nu}_\mu$  about  $2.2 \mu s$  later, yielding the third long-delayed decay positron signal. The simulated hit time distribution of a  $K^+ \rightarrow \mu^+ \nu_\mu$  event is shown in Figure. 10-2, which displays a clear three-fold coincidence.

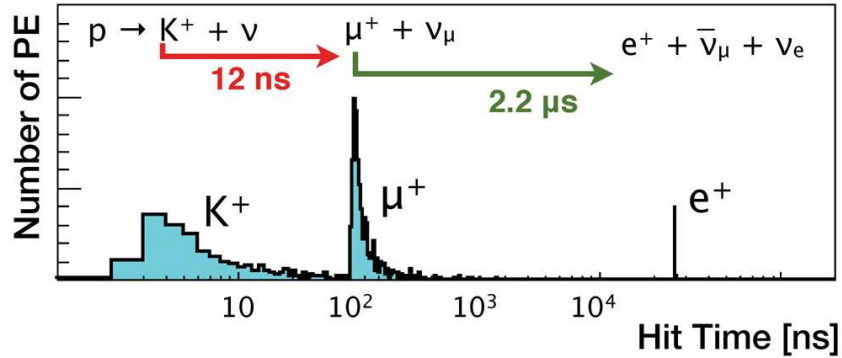


Figure 10-2: The simulated hit time distribution of photoelectrons (PEs) from a  $K^+ \rightarrow \mu^+ \nu_\mu$  event at JUNO.

If a proton decays in a carbon nucleus, the nuclear effects have to be taken into account. In particular, the binding energy and Fermi motion modify the decaying proton's effective mass and momentum, leading to a change of the kinematics of the decay process. In Ref. [405], the limiting values for the ranges of the kinetic energy of  $K^+$  are calculated to be 25.1—198.8 MeV for protons in the s-state and 30.0—207.2 MeV for protons in the p-state. The  $K^+$  meson may also rescatter inside the nucleus, producing the intranuclear cascades. This possibility has been discussed in Ref. [406].

In summary, the signatures of  $p \rightarrow K^+ \bar{\nu}$  in the JUNO experiment are:

- A prompt signal from  $K^+$  and a delayed signal from its decay daughters with a time coincidence of 12 ns.

- Both the prompt and delayed signals have well-defined energies.
- There is one and only one decay positron with a time coincidence of  $2.2 \mu\text{s}$  from the prompt signals.

The time coincidence and well-defined energies provide a powerful tool to reject the background, which is crucial in the search for proton decays.

### 10.3 Signal selection and efficiency

Because the decay time of  $K^+$  is very short (i.e., about 12 ns), the signal pulses from  $K^+$  and from its daughter particles (e.g.  $\mu^+$ ) will typically be in fast sequence or even partially overlapped. A fast response and high resolution waveform digitizer (e.g. a Giga-Hz flash ADC) is required to separate the prompt and delayed signals. Even so, if the  $K^+$  decays early, the prompt and delayed pulses may mix together and will resemble a single muon event from the quasi-elastic interactions of atmospheric muon neutrinos.

The combined photon hit time distribution recorded by all the PMTs can be used to distinguish a two-pulse event (the signal of proton decays) from a one-pulse event (the atmospheric muon neutrino background). The hit time distribution depends on the scintillation light time profile, light yield, light attenuation, PMT time jitter and electronic signal response. Here we use Ref. [405] as a baseline for the efficiency estimation. In Ref. [405] a pulse shape discrimination criterion ( $\Delta T_{15\%-85\%}$ ) is constructed using the time difference between the moments for which the pulse reaches 15% and 85% of the maximum pulse height.  $\Delta T_{15\%-85\%}$  is typically longer for a two-pulse signal-like event than a one-pulse background-like event. A cut at  $\Delta T_{15\%-85\%} > 7$  ns retains 65% of the signals while rejecting 99.995% of the muon background induced by the quasi-elastic interactions of atmospheric neutrinos.

Scaled from the Super-Kamiokande detector [407], the upper limit on the charged-current interaction rate of atmospheric muon neutrinos in the related energy range is estimated to be  $4.8 \times 10^{-2} \text{ MeV}^{-1}\text{kt}^{-1}\text{y}^{-1}$ . Further background rejection can be achieved by an energy cut on the two shortly correlated events, i.e. the sum of the deposited energies ( $E_{\text{sum}}$ ) from  $K^+$  and the daughter particles of its decay. For  $K^+ \rightarrow \mu^+\nu_\mu$ ,  $E_{\text{sum}}$  includes  $E_{K^+}$  (105 MeV) and  $E_{\mu^+}$  (152 MeV), a total of 257 MeV. For  $K^+ \rightarrow \pi^+\pi^0$ ,  $E_{\text{sum}}$  includes  $E_{K^+}$  (105 MeV),  $E_{\pi^+}$  (108 MeV) and  $E_{\pi^0 \rightarrow \gamma\gamma}$  (246 MeV), a total of 459 MeV. When defining the visible energy window, one has to take into account that the light output is quenched, especially for heavy ionizing particles. The quenching mechanism can be reasonably well described by the Birk's formula:

$$\left. \frac{dE}{dx} \right|_{\text{dep}} = \frac{dE}{dx} \left( 1 + k_B \cdot \frac{dE}{dx} \right)^{-1}, \quad (10.1)$$

where  $k_B$  is around 0.01 cm/MeV for typical liquid scintillators. A cut of  $150 \text{ MeV} < E_{\text{sum}} < 650 \text{ MeV}$  retains 99% of the signals [405]. In a more realistic simulation, the hadronic interactions will reduce the energy resolution and slightly decrease the energy cut efficiency. The background rate from the quasi-elastic interactions of atmospheric muon neutrinos in this 500 MeV energy window is estimated to be at most  $0.024 \text{ yr}^{-1}$  by taking into account the previously described pulse shape discrimination.

In the proton decay  $p \rightarrow K^+\bar{\nu}$ , there will be only a single decay positron from the decay of  $\mu^+$  — the descendant of  $K^+$ . This is in contrast with most of the hadronic processes from atmospheric neutrinos that produce kaons, which are the potential backgrounds of the proton decay. Apart from kaons, there are some other hadrons produced from these processes, such as  $\Lambda^0$ . By requiring

precisely one single decay positron, we can efficiently reject the backgrounds producing more than one decay positron. We require  $\mu^+$  to decay later than 100 ns to prevent its light leaking into  $E_{\text{sum}}$ , also to separate it from the daughter positron. We further require the energy of the decay positron to be larger than 1 MeV to reduce the contribution from random coincidences with the radioactive background events. The efficiency of the decay positron cut is estimated to be 99%. The total signal efficiency by combining the pulse shape cut, energy cut and decay positron cut, is estimated to be 64%.

## 10.4 Background estimation

In the search of a rare event, such as the proton decay, the understanding of the background is crucial. JUNO is located deep underground with an overburden of  $\sim 1900$  m.w.e, thus the cosmic-muon-related background is largely suppressed. The muon rate in the detector is about 3 Hz with the average muon energy of about 215 GeV. The outer muon system can efficiently veto muons which are in the energy range that can mimic the events of  $p \rightarrow K^+\bar{\nu}$ , as well as any short-lived particles and isotopes produced by the muon spallation. For the long-lived isotopes, their beta decays are in the low energy region ( $< 20$  MeV) and do not cause any background to the proton decay. On the other hand, neutral particles (e.g., neutrons, neutral kaons and  $\Lambda^0$  particles produced by muons outside the veto system) can penetrate the scintillator before being tagged. These neutral particles have energy spectra extending from a few MeV to a few GeV [408]. Fast neutrons will be thermalized inside the detector and captured on hydrogen within 200  $\mu\text{s}$ . The capture process emits a 2.2 MeV gamma ray and can be used to veto fast neutrons. The lack of the decay  $e^+$  signal further reduces the fast neutron background to a negligible level. The production of  $\Lambda^0$  is about  $10^{-4}$  relative to the production of neutrons [408] therefore is negligible. Finally,  $K_L^0$  could mimic a signal event either through the charge exchange and converting to a  $K^+$  in the detector, or via its decay (e.g.,  $K_L^0 \rightarrow \pi^+e^-\bar{\nu}_e$  and  $K_L^0 \rightarrow \pi^-e^+\nu_e$ ) with the right amount of deposited energy. The production rate of  $K_L^0$  is estimated to be about 1:500 relative to that of the neutron in Ref. [408]. However, due to the passive shielding from the water pool, we expect a stronger suppression of the  $K_L^0$  (and  $\Lambda^0$ ) background as compared with the estimate given in Ref. [408].

This leaves atmospheric neutrinos as the main background for the proton decay search. The background from  $\nu_\mu n \rightarrow \mu^- p$  and  $\bar{\nu}_\mu p \rightarrow \mu^+ n$  has been discussed in the previous subsection. Such a background can be largely rejected by combining the prompt energy cut and the pulse shape cut. The background rate from the quasi-elastic interactions of atmospheric muon neutrinos is estimated to be  $0.024 \text{ yr}^{-1}$ . The charged-current single pion production has smaller cross sections and can be further suppressed by the decay positron cut, and hence it is negligible.

Now let us consider the neutrino-triggered production of strange particles, in particular with the  $K^+$  mesons in the final state. The first category is relevant for the processes in which the strangeness is conserved (i.e.,  $\Delta S = 0$ ). The typical process of this kind is  $\nu_\mu n \rightarrow \mu^- K^+ \Lambda^0$ . In such processes a  $\Lambda^0$  particle is usually produced. The  $\Lambda^0$  decays shortly ( $\tau_{\Lambda^0} = 0.26$  ns) primarily via  $\Lambda^0 \rightarrow p\pi^-$  and  $\Lambda^0 \rightarrow n\pi^0$ . The decay daughters of  $\Lambda^0$  combined with  $\mu^-, K^+$  result in a larger prompt signal than that expected from a true proton decay. These events can be further rejected because there are three or more decay electrons or positrons from the decay chains. The second category is associated with the processes in which the strangeness is not conserved. The representative process of this kind is  $\nu_\mu p \rightarrow \mu^- K^+ p$ . Although the cross sections of such processes are Cabbibo-suppressed as compared with those  $\Delta S = 0$  reactions, they are the potential background events in case the prompt energy is similar to the expectation from the proton decay and one of the decay electrons is missed due to the low pulse height or the overlap with the prompt signal. Such a background can be largely removed if sophisticated particle ID algorithms can be developed to distinguish a muon-like event

from a kaon-like event in the scintillator (e.g., using the Cherenkov and range information). Here we simply scale the result obtained in Ref. [405]. The estimated background in this channel that produces strange particles in the final state is  $0.026 \text{ yr}^{-1}$ . The total background, combining the quasi-elastic channel, is estimated to be  $0.05 \text{ yr}^{-1}$ .

## 10.5 Sensitivity

The sensitivity to the proton lifetime can be expressed as

$$\tau(p \rightarrow K^+ + \bar{\nu}) = N_p T R \frac{\epsilon}{S}, \quad (10.2)$$

where  $N_p = 6.75 \times 10^{33}$  is the total number of protons,  $T$  is the measurement time which is assumed to be 10 years,  $R = 84.5\%$  is the branching ratio of the  $K^+$  decays being included in the analysis,  $\epsilon = 65\%$  is the total signal efficiency, and  $S$  is the upper limit on the number of signal events at a certain confidence interval which depends on the number of observed events and the expected number of background events. We follow the Feldman-Cousins approach [409] in our analysis. The expected background is 0.5 events in 10 years. If no event is observed, the 90% C.L. upper limit is  $S = 1.94$ . The corresponding sensitivity to the proton lifetime is  $\tau > 1.9 \times 10^{34}$  yrs. This represents “a factor of three” improvement over today’s best limit from the Super-Kamiokande experiment [401], and starts to approach the region of interest predicted by some GUT models [393].

In a realistic experiment, the sensitivity may decrease if there is an upward fluctuation of the background. In the case that one event is observed (30% probability), the 90% C.L. upper limit is  $S = 3.86$ . The corresponding sensitivity to the proton lifetime is  $\tau > 9.6 \times 10^{33}$  yrs. If two events are observed (7.6% probability), the sensitivity is further reduced to  $\tau > 6.8 \times 10^{33}$  yrs.

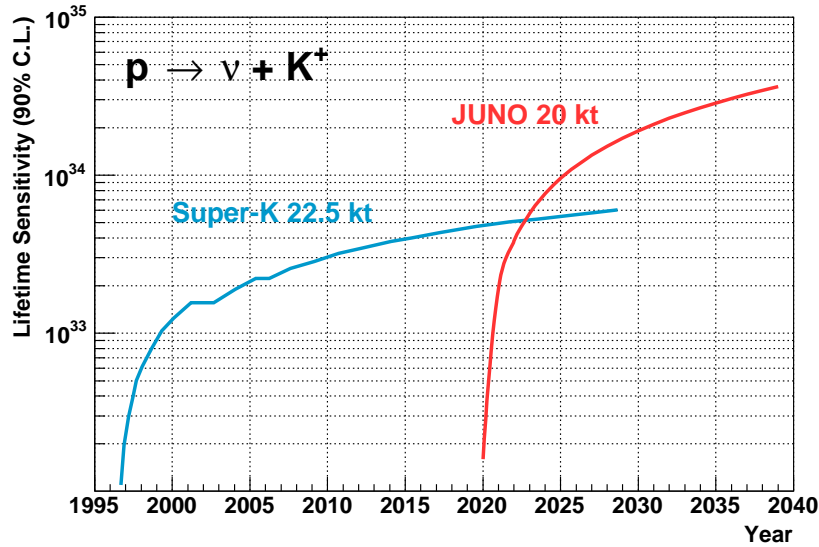


Figure 10-3: The 90% C.L. sensitivity to the proton lifetime in the decay mode  $p \rightarrow K^+ + \bar{\nu}$  at JUNO as a function of time. In comparison, Super-Kamiokande’s sensitivity is also projected to year 2030.

In Figure. 10-3 we plot the 90% C.L. sensitivity to the proton lifetime in the decay mode  $p \rightarrow K^+ + \bar{\nu}$  at JUNO as a function of time. Due to the high efficiency in measuring this mode, JUNO’s sensitivity will surpass Super-Kamiokande’s in only 3 years since its data taking.

# 11 Neutrinos from Dark Matter

## 11.1 Introduction

The existence of non-baryonic dark matter (DM) in the Universe has been well established by astronomical observations. For most spiral galaxies, the rotation curve of stars or gas far from the galactic center does not decline with increasing distance but rather stays as a constant. This strongly indicates the existence of a massive dark halo which envelops the galactic disk and extends well beyond the size of the visible part of the galaxy [410]. At cluster scales, the mass of a cluster determined by the radial velocity distribution [411, 412], or the gravitational lensing of background galaxies in the cluster [413], or the measurements of the X-ray temperature of hot gas in the cluster, is typically an order of magnitude larger than that inferred from the visible part of the cluster. The observation of the bullet cluster (1E0657-558) [414] and the large-scale structure filament in superclusters (Abell 222/223) [415] also strongly support the existence of DM.

The most accurate determination of the DM energy density comes from the measurement of the anisotropy of the cosmic microwave background. The recent measurement gives [49]

$$\Omega_{\text{DM}}h^2 = 0.1198 \pm 0.0026, \quad (11.1)$$

where  $h = 0.673 \pm 0.012$  is the Hubble constant. The contribution from baryonic matter is  $\Omega_{\text{b}}h^2 = 0.02207 \pm 0.00027$  [49]. Thus DM contributes to nearly 85% of the total mass in the Universe.

The DM candidate must be stable on the cosmological time scale, and must only have very weak interactions with ordinary matter and electromagnetic radiation. The N-body simulations suggest that DM particles should be cold (or non-relativistic) at the time of galaxy formation. The Standard Model (SM) of particle physics, although extremely successful in explaining the data, can not provide a viable cold DM candidate. In the particle content of the SM, only the neutrinos are electromagnetically neutral and interact with matter very weakly. However, the relic density of the neutrinos is too low today:  $\Omega_{\nu}h^2 \leq 0.0062$  at 95% CL [49], and they could only serve as hot (or relativistic) DM particles in the early Universe. Therefore, the existence of cold DM is also a striking indication of new physics beyond the SM.

A widely studied class of DM candidates are the Weakly Interacting Massive Particles (WIMPs). The masses of WIMPs are in the range of  $\mathcal{O}(1)$  GeV to  $\mathcal{O}(1)$  TeV, and their interaction strengths with the SM particles are around the weak interaction scale. Such WIMPs can naturally fit the observed DM density through decoupling from the thermal equilibrium with electromagnetic radiation fields, which is due to the expansion and cooling of the early Universe. Well-motivated WIMP candidates exist in the supersymmetric (SUSY) extensions of the SM. If the  $R$ -parity is conserved, the lightest neutral supersymmetric particle (LSP) is stable and can be a cold DM candidate. The LSP can be the lightest neutralino or sneutrino, and the latter is stringently constrained by the direct detection experiments. In models with universal extra dimensions, the Kaluza-Klein (KK) excitations of the SM particles have odd KK-parity while the SM particles are all KK-even. Thus the lightest neutral KK excitation particle (LKP) is stable and can be a WIMP. A possible DM candidate of this kind is the first KK excitation of the hypercharge field  $B^{(1)}$ . In a variety of the little Higgs models, a new discrete symmetry  $T$  is introduced to avoid the constraints from the electroweak precision measurements. The lightest  $T$ -odd particle is also a viable WIMP candidate. Besides the well-motivated WIMP candidates, one can construct “minimal” DM models, such as the SM singlet scalar models, singlet fermion models, etc. The motivation of such DM models does not seem to be compelling, but they can have rich phenomenology. Non-WIMP candidates,

---

Editor: Guey-Lin Lin (glin@mail.nctu.edu.tw)

Major contributors: Wanlei Guo, Yen-Hsun Lin, and Yufeng Zhou



such as the primordial black holes, axions and keV sterile neutrinos, also exist and attract some attentions [416]. Gravitinos and axionos, the respective supersymmetric partners of gravitons and axions, can be the cold DM candidates with the relic density obtained through the nonthermal processes.

DM can be detected either directly or indirectly. The former is to observe the nucleus recoil as DM interacts with the target nuclei in the detector, and the latter is to detect the final-state particles resulting from DM annihilation or decays. A direct detection of DM is possible because the DM particles constantly bombard the Earth as the Earth sweeps through the local halos. Some of the direct detection experiments have observed the preliminary excesses of candidate events over known backgrounds, such as DAMA [417], CoGeNT [418–420], CRESS-II [421], and CDMS-Si [422]. In contrast, other experiments have only obtained stringent upper limits on DM, such as those from XENON100 [423, 424], LUX [425], superCDMS [426], SIMPLE [427], and CDEX [428].

DM can be indirectly detected by measuring the cosmic-ray particle fluxes which may receive extra contributions from DM annihilation or decays in the galactic halo. The recent measurements by PAMELA [429], ATIC-2 [430], Fermi-LAT [431], and AMS-02 [432] have indicated an excess in the fraction of cosmic-ray positrons, but whether it points to DM or not remains an open question.

DM can also be detected indirectly by looking for the neutrino signature from DM annihilation or decays in the galactic halo, the Sun or the Earth. In particular, the search for the DM-induced neutrino signature from the Sun has given quite tight constraints on the spin-dependent (SD) DM-proton scattering cross section  $\sigma_{\chi p}^{\text{SD}}$  [433]. In the following we shall study the sensitivities of the JUNO detector to  $\sigma_{\chi p}^{\text{SD}}$  and spin-independent (SI) DM-proton scattering cross section  $\sigma_{\chi p}^{\text{SI}}$  by focusing on the neutrino signature from the Sun as well.

## 11.2 The neutrino flux from DM annihilation in the Sun

To facilitate our discussions, let us define  $dN_{\nu_\alpha}^f/dE_\nu$  as the energy spectrum of  $\nu_\alpha$  (for  $\alpha = e, \mu, \tau$ ) produced per DM annihilation  $\chi\chi \rightarrow f\bar{f}$  in the Sun. The differential neutrino flux of flavor  $\beta$  (for  $\beta = e, \mu, \tau$ ) arriving at the terrestrial neutrino detector is

$$\frac{d\Phi_{\nu_\beta}^{\text{DM}}}{dE_\nu} = P_{\nu_\alpha \rightarrow \nu_\beta}(E_\nu, D) \frac{\Gamma_A}{4\pi D^2} \sum_f B_\chi^f \frac{dN_{\nu_\alpha}^f}{dE_\nu}, \quad (11.2)$$

where  $\Gamma_A$  is the DM annihilation rate,  $B_\chi^f$  is the branching ratio for the DM annihilation channel  $\chi\chi \rightarrow f\bar{f}$ ,  $D$  is the distance between the source and detector, and  $P_{\nu_\alpha \rightarrow \nu_\beta}(E_\nu, D)$  is the neutrino oscillation probability from the source to the detector.  $P_{\nu_\alpha \rightarrow \nu_\beta}(E_\nu, D)$  can be calculated with the best fit neutrino oscillation parameters given by Ref. [27]. The DM annihilation rate  $\Gamma_A$  can be determined by the following argument. When the Sun sweeps through the DM halo, a WIMP could collide with matter inside the Sun and lose its speed. If the WIMP speed becomes less than its escape velocity, the WIMP can be captured by the Sun's gravitational force and then sinks into the core of the Sun. After a long period of accumulation, WIMPs inside the Sun can begin to annihilate into the SM particles at an appreciable rate. Among the final states of DM annihilation, neutrinos can be detected by a neutrino telescope, such as the JUNO detector. Defining  $N(t)$  as the number of WIMPs in the Sun at time  $t$ , we have

$$\frac{dN}{dt} = C_c - C_a N^2 - C_e N, \quad (11.3)$$

where  $C_c$  is the capture rate,  $C_a N^2$  is the annihilation rate, and  $C_e N$  is the evaporation rate. It has been shown that WIMPs with masses below 3 to 4 GeV may evaporate from the Sun [434–437].

The critical mass scale for WIMP evaporation may be raised by about 1 GeV if the WIMP self-interaction is taken into account [438]. In this case Eq. (11.3) should be modified by including the self-interaction effect. Here we shall not address the issue of DM self-interaction.

Taking the nominal values of  $C_c$ ,  $C_a$  and  $C_e$ , one can show that the total DM number in the Sun has already reached to the equilibrium, i.e., the right hand side of Eq. (11.3) vanishes.. For the mass range in which DM evaporation is negligible (i.e.,  $C_e \rightarrow 0$ ), it is easy to see that  $\Gamma_A(t) = C_c/2$ , i.e., the DM annihilation rate in this case only depends on the capture rate  $C_c$ . Since  $C_c$  depends on the DM-nucleon scattering cross section and the chemical composition of the Sun, the constraint on the SD cross section  $\sigma_{\chi p}^{\text{SD}}$  and that on the SI cross section  $\sigma_{\chi p}^{\text{SI}}$  can be extracted by searching for the DM-induced neutrinos from the Sun.

For spin-dependent (SD) interactions, the capture rate is given by [439, 440]

$$C_c^{\text{SD}} \simeq 3.35 \times 10^{24} \text{ s}^{-1} \left( \frac{\rho_0}{0.3 \text{ GeV/cm}^3} \right) \left( \frac{270 \text{ km/s}}{\bar{v}} \right)^3 \left( \frac{\text{GeV}}{m_\chi} \right)^2 \times \left( \frac{\sigma_{\text{H}}^{\text{SD}}}{10^{-6} \text{ pb}} \right), \quad (11.4)$$

where  $\rho_0$  is the local DM density,  $\bar{v}$  is the velocity dispersion,  $\sigma_{\text{H}}^{\text{SD}} \equiv \sigma_{\chi p}^{\text{SD}}$  is the SD DM-hydrogen scattering cross section, and  $m_\chi$  is the DM mass. The capture rate for spin-independent (SI) scattering behaves like [439, 440]

$$C_c \propto \frac{\rho_0}{\text{GeV cm}^{-3}} \times \frac{\text{km s}^{-1}}{\bar{v}} \times \frac{\text{GeV}}{m_\chi} \times \frac{\sigma_{\chi p}^{\text{SI}}}{\text{pb}} \times \sum_{A_i} F_{A_i}^*(m_\chi), \quad (11.5)$$

with  $A_i$  the atomic number of chemical element  $i$  in the Sun,  $F_{A_i}^*(m_\chi)$  is the product of various factors including the mass fraction of element  $i$ , the gravitational potential for element  $i$ , kinematic suppression factor, form factor, and a factor of reduced mass.

The DM evaporation rate in the Sun,  $C_e$ , has been well investigated in Refs. [435, 437]. Here we do not discuss it further since we shall focus on the DM mass range in which the neutrino flux from the Sun is not suppressed.

### 11.3 The sensitivities of the JUNO detector

In general, DM inside the Sun can annihilate into leptons, quarks and gauge bosons. The neutrino flux results from the decays of such final-state particles. Here we consider two annihilation channels  $\chi\chi \rightarrow \tau^+\tau^-$  and  $\chi\chi \rightarrow \nu\bar{\nu}$  as a benchmark. We shall focus on the detection of muon-neutrino flux from the above two annihilation channels. Hence we consider track events induced by charged current interactions of  $\nu_\mu$  and  $\bar{\nu}_\mu$ . The differential muon-neutrino flux arriving at the terrestrial neutrino detector can be calculated with the help of Eq. (11.2). For simplicity, we set the branching fraction  $B_\chi^{\tau,\nu} = 1$ . We employ `WimpSim` [441] with a total of 50,000 Monte Carlo generated events. The muon-neutrino event rate in the detector reads

$$N_{\text{DM}} = \int_{E_{\text{th}}}^{m_\chi} \frac{d\Phi_\nu^{\text{DM}}}{dE_\nu} A_\nu(E_\nu) dE_\nu d\Omega, \quad (11.6)$$

where  $E_{\text{th}}$  is the detector's threshold energy,  $d\Phi_\nu^{\text{DM}}/dE_\nu$  is the muon-neutrino flux from DM annihilation,  $A_\nu$  is the detector's effective area, and  $\Omega$  is the solid angle. The angular resolution of muon-neutrino track event has been presented in Chapter 7. It is shown there that, to reconstruct the muon direction in a good precision, one requires the muon track length to be greater than 5 m

within the JUNO detector. In such a condition, the angular resolution of the muon track is better than  $1^\circ$ . This sets the lower limit of  $\nu_\mu$  ( $\bar{\nu}_\mu$ ) energy to be about 1 GeV. Hence we set  $E_{\text{th}} = 1$  GeV. The effective area of the JUNO detector is expressed as

$$A_\nu(E_\nu) = M_{\text{LS}} \left( \frac{N_A}{m} \right) [n_p \sigma_{\nu p}(E_\nu) + n_n \sigma_{\nu n}(E_\nu)] \epsilon(E_\nu), \quad (11.7)$$

where  $M_{\text{LS}}$  is the target mass of the JUNO detector,  $N_A$  is the Avogadro constant,  $m$  is the mass of liquid scintillator per mole,  $n_p$  and  $n_n$  are the number of protons and neutrons, respectively, in a liquid scintillator molecule,  $\sigma_{\nu p}$  and  $\sigma_{\nu n}$  are the neutrino-proton and neutrino-neutron scattering cross sections, respectively, and  $\epsilon(E_\nu)$  is the energy-dependent efficiency for selecting muon events with track length greater than 5 m in the detector. This efficiency has been studied in Chap. 7 where  $\epsilon$  is found to be less than 1% for  $E_\nu = 1$  GeV and it is greater than 70% for  $E_\nu > 5$  GeV. We plot the efficiency  $\epsilon(E_\nu)$  in Fig. 11-1. The selected track events are classified as fully contained (FC) and partially contained (PC) events. PC events begin to dominate FC events for  $E_\nu > 5$  GeV. At  $E_\nu = 20$  GeV,  $N_{\text{PC}}/N_{\text{FC}} > 10$ .

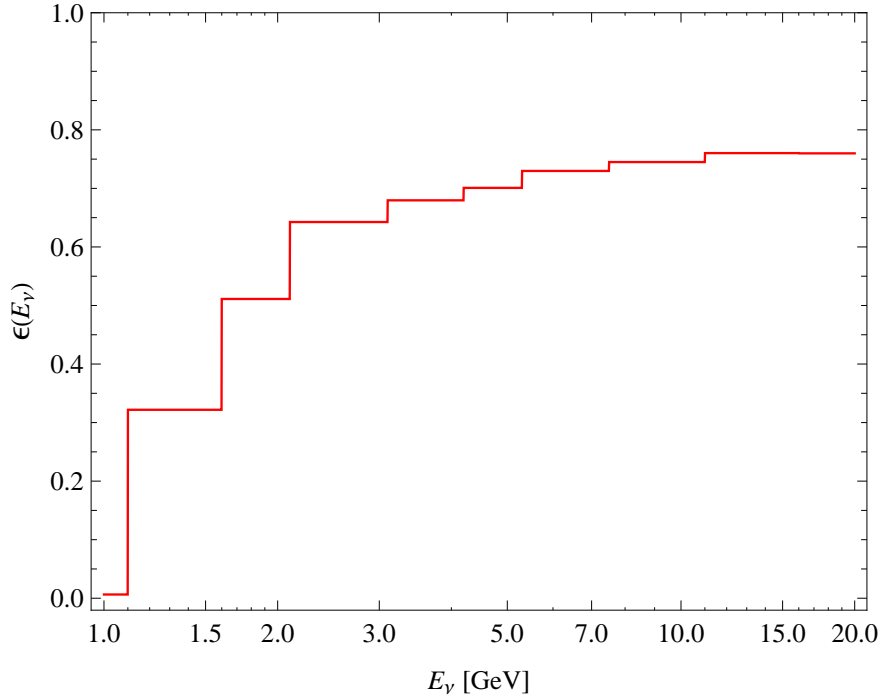


Figure 11-1: The energy-dependent efficiency  $\epsilon(E_\nu)$  for selecting muon events with track length greater than 5 m in the detector.

The effective area for anti-neutrino interactions can be calculated by the same equation with the replacements  $\sigma_{\nu p} \rightarrow \sigma_{\bar{\nu} p}$  and  $\sigma_{\nu n} \rightarrow \sigma_{\bar{\nu} n}$ . We use the results in [320] for the above cross sections in our interested energy range  $1 \text{ GeV} \leq E_\nu \leq 20 \text{ GeV}$ . Here we take  $\rho = 0.86 \text{ g/cm}^3$  for the density of liquid scintillator which has been used in the Daya Bay experiment. The mass fractions of carbon and hydrogen in the liquid scintillator are taken to be 88% and 12%, respectively. These fractions are also quoted from those used in the Daya Bay experiment. As the neutrinos propagate from the source to the detector, they encounter the high-density medium in the Sun, the vacuum

in space, and the Earth medium. The matter effects on neutrino oscillations have been considered in  $P_{\nu_\alpha \rightarrow \nu_\beta}$  in Eq. (11.2).

The atmospheric background event rate can also be calculated by using Eq. (11.6) with  $d\Phi_\nu^{\text{DM}}/dE_\nu$  replaced by the atmospheric neutrino flux. Hence

$$N_{\text{atm}} = \int_{E_{\text{th}}}^{E_{\text{max}}} \frac{d\Phi_\nu^{\text{atm}}}{dE_\nu} A_\nu(E_\nu) dE_\nu d\Omega. \quad (11.8)$$

In our calculations the atmospheric neutrino flux  $d\Phi_\nu^{\text{atm}}/dE_\nu$  is quoted from Refs. [442, 443]. We set  $E_{\text{max}} = m_\chi$  so as to compare with the DM signal. The threshold energy  $E_{\text{th}}$  is taken to be 1 GeV.

To estimate the JUNO sensitivity to the DM-induced neutrino flux from the Sun, we focus on events coming from a chosen solid angle range surrounding the direction of the Sun. The solid angle range  $\Delta\Omega$  is related to the half angle of the observation cone by  $\Delta\Omega = 2\pi(1 - \cos\psi)$ . Due to the spreading of muon direction relative to the direction of original  $\nu_\mu$ , which has been extensively studied in Chap.7, there is an efficiency factor corresponding to each choice of  $\psi$  for collecting the neutrino events from the Sun. This collection efficiency is plotted in Fig. 11-2. We choose

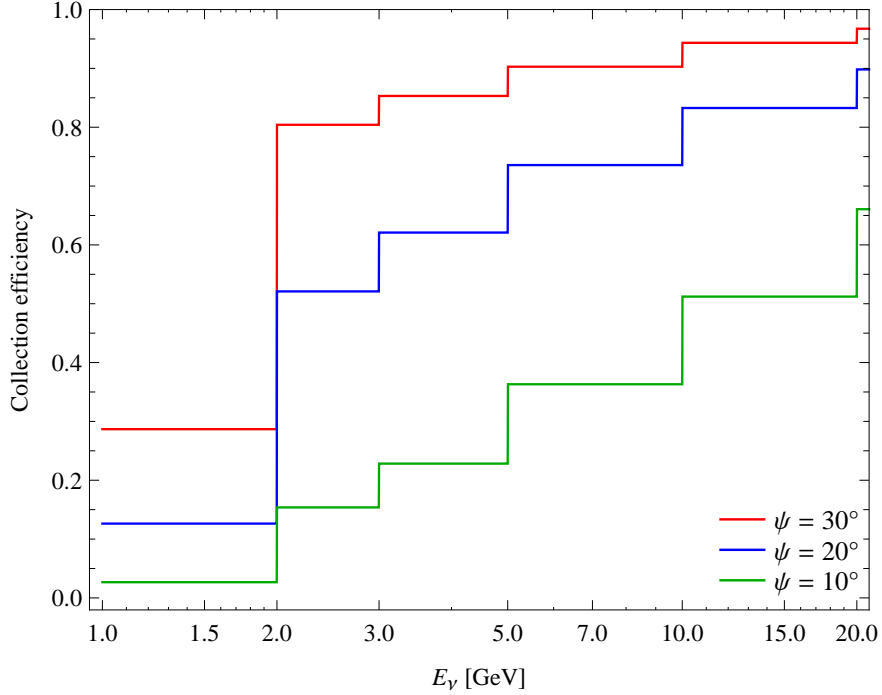


Figure 11-2: The efficiency for collecting DM-induced neutrino events from the Sun with the cone half angle  $\psi = 10^\circ$ ,  $20^\circ$  and  $30^\circ$ .

$\psi = 30^\circ$  for our sensitivity calculation since the collection efficiency is greater than 80% for the relevant DM mass range,  $m_\chi > 3$  GeV. The DM-induced neutrino event rate given by Eq. (11.6) is then corrected by the collection efficiency. The sensitivities to  $\sigma_{\chi p}^{\text{SD}}$  and  $\sigma_{\chi p}^{\text{SI}}$  are taken to be the  $2\sigma$  significance for 5 years of data taking. We extract the sensitivities using

$$\frac{s}{\sqrt{s+b}} = 2.0, \quad (11.9)$$

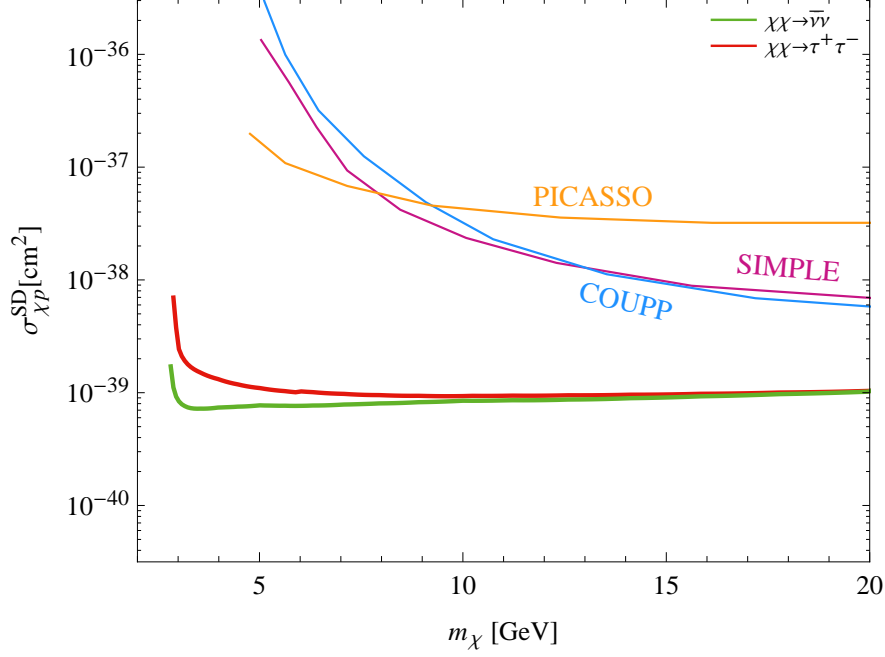


Figure 11-3: The JUNO  $2\sigma$  sensitivity in 5 years to the spin-dependent cross section  $\sigma_{\chi p}^{\text{SD}}$  in 5 years. The constraints from the direct detection experiments are also shown for comparison.

where  $s$  is the DM signal,  $b$  is the atmospheric background, and 2.0 refers to the  $2\sigma$  detection significance. The results of our sensitivity calculations are given in Fig. 11-3 and Fig. 11-4. It is clearly seen that the JUNO sensitivities to  $\sigma_{\chi p}^{\text{SD,SI}}$  through  $\chi\chi \rightarrow \nu\bar{\nu}$  channel are essentially identical to those through  $\chi\chi \rightarrow \tau^+\tau^-$  channel. This follows from our definition of sensitivity as the excess of total neutrino event rate integrated from  $E_{\text{th}}$  to  $m_\chi$ . If we consider the spectral feature of  $\chi\chi \rightarrow \nu\bar{\nu}$  annihilation channel, the JUNO sensitivities to  $\sigma_{\chi p}^{\text{SD,SI}}$  can be significantly improved. In Fig. 11-3 one can see that the JUNO sensitivity to  $\sigma_{\chi p}^{\text{SD}}$  is much better than the current direct detection constraints set by COUPP [444], SIMPLE [427] and PICASSO [445] experiments. For  $m_\chi < 3$  GeV, the sensitivity becomes poor due to the DM evaporation from the Sun. Fig. 11-4 shows that the direct detection experiments, such as XENON100 [423], LUX [425] and CDMSlite [446], can set very stringent constraints on  $\sigma_{\chi p}^{\text{SI}}$  for  $m_\chi > 7$  GeV. On the other hand, JUNO is more sensitive than the direct detection experiments for  $m_\chi < 7$  GeV. This advantage continues until the evaporation mass scale.

## 11.4 Summary

In this chapter we first reviewed the developments of dark matter physics and the status of dark matter detection search. We then discussed the sensitivities of the JUNO detector to spin-dependent DM-nucleon scattering cross section  $\sigma_{\chi p}^{\text{SD}}$  and the spin-independent one  $\sigma_{\chi p}^{\text{SI}}$  by searching for DM-induced neutrino events from the core of the Sun. The sensitivities are calculated based upon the excess of neutrino events beyond the atmospheric background. We focus on muon neutrino events resulting from DM annihilation channels  $\chi\chi \rightarrow \tau^+\tau^-$  and  $\chi\chi \rightarrow \nu\bar{\nu}$ . We select those events with the muon track length greater than 5 m within the detector. In such a case, the direction of the muon track can be reconstructed with an accuracy better than  $1^\circ$ . To search for DM-induced neutrino events from the Sun, we choose an observation cone with a cone half angle  $\psi = 30^\circ$ . We have found

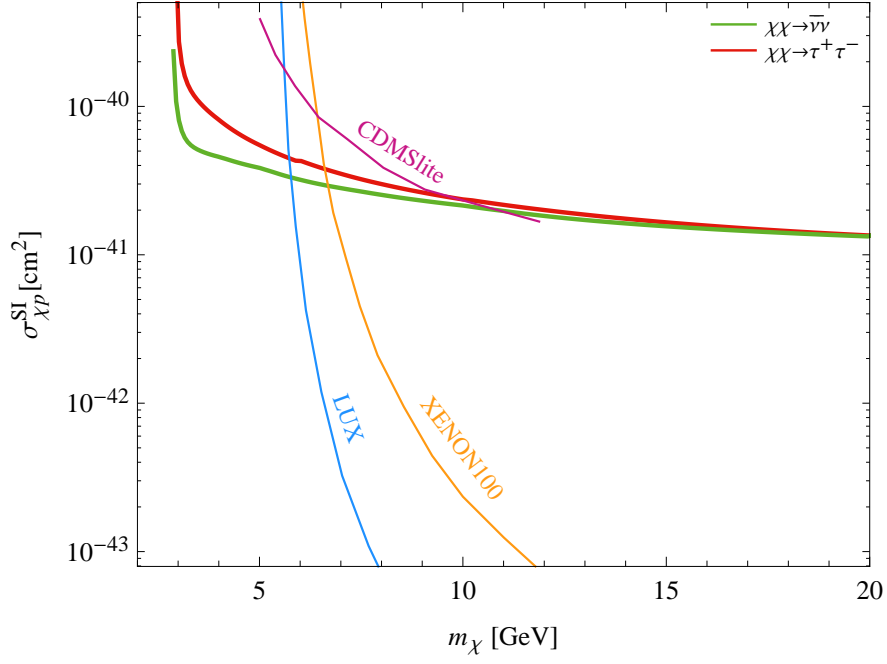


Figure 11-4: The JUNO  $2\sigma$  sensitivity in 5 years to the spin-independent cross section  $\sigma_{\chi p}^{\text{SI}}$ . The recent constraints from the direct detection experiments are also shown for comparison.

that JUNO sensitivity to  $\sigma_{\chi p}^{\text{SD}}$  is much better than the current direct detection constraints. In the case of  $\sigma_{\chi p}^{\text{SI}}$ , JUNO is competitive with direct detection experiments for  $m_\chi < 7$  GeV.

## 12 Exotic Searches with Neutrinos

The standard three-neutrino mixing paradigm, characterized by two mass-squared differences ( $\Delta m_{21}^2$  and  $\Delta m_{31}^2$ ), three mixing angles ( $\theta_{12}$ ,  $\theta_{13}$  and  $\theta_{23}$ ) and one Dirac CP-violating phase  $\delta$ , can describe most of the phenomena of solar, atmospheric, reactor, and accelerator neutrino oscillations [26]. However, other new physics mechanisms can operate at a sub-leading level, and may appear at the stage of precision measurements of neutrino oscillations.

Among different possibilities, the hypotheses of light sterile neutrinos, unitarity violation, non-standard interactions (NSIs), and Lorentz invariance violation (LIV), are of particular importance at JUNO.

- The light sterile neutrinos in light of short baseline oscillation anomalies have attracted active research attention in both the experimental searches and phenomenological implications. At JUNO, the hypothesis of light sterile neutrinos could be tested either using radioactive sources or with reactor antineutrinos. This part is thoroughly explored in Sec. 9.
- Unitarity violation in the lepton mixing matrix is the generic consequence of a large class of seesaw models, where the light active neutrinos are mixed with heavy fermion degrees of freedom. Tests of unitarity violation have been discussed in Sec. 3.3 in the MUV framework.
- High-dimensional operators from the new physics contributions can affect the neutrino oscillation in the form of NSIs [281, 447–450], which emerge as effective four fermion interactions after integrating out the heavy particles beyond the SM. NSIs can modify both the neutrino production and detection processes, and induce shifts for both the mixing angles and mass-squared differences at reactor antineutrino oscillations.
- LIV is one of the most important evidence for Quantum Gravity [451]. The low energy phenomena of LIV can be systematically studied in the framework of the Standard Model Extension (SME) [452, 453]. In reactor antineutrino experiments, LIV can be tested in terms of both the spectral distortion and sidereal variation effects [454].

In this section, we shall concentrate on the tests of NSIs and LIV at JUNO with reactor antineutrino oscillations. We shall also give brief discussions on other aspects of exotic searches beyond the SM.

### 12.1 Non-standard Interactions

NSIs can occur in the neutrino production, propagation and detection processes in the experiments of neutrino oscillations. The NSI effects in the propagation process are negligible because of the suppression of the neutrino energy and terrestrial matter density. The neutrino and antineutrino states produced in the source and observed in the detector are superpositions of neutrino and antineutrino flavor states [449, 450]

$$\begin{aligned} |\nu_\alpha^s\rangle &= \frac{1}{N_\alpha^s} \left( |\nu_\alpha\rangle + \sum_\beta \epsilon_{\alpha\beta}^s |\nu_\beta\rangle \right), & |\bar{\nu}_\alpha^s\rangle &= \frac{1}{N_\alpha^s} \left( |\bar{\nu}_\alpha\rangle + \sum_\beta \epsilon_{\alpha\beta}^{s*} |\bar{\nu}_\beta\rangle \right), \\ \langle \nu_\beta^d| &= \frac{1}{N_\beta^d} \left( \langle \nu_\beta| + \sum_\alpha \epsilon_{\alpha\beta}^d \langle \nu_\alpha| \right), & \langle \bar{\nu}_\beta^d| &= \frac{1}{N_\beta^d} \left( \langle \bar{\nu}_\beta| + \sum_\alpha \epsilon_{\alpha\beta}^{d*} \langle \bar{\nu}_\alpha| \right), \end{aligned} \quad (12.1)$$

where  $\epsilon_{\alpha\beta}^s$  and  $\epsilon_{\alpha\beta}^d$  denote the NSI parameters at the source and detector, respectively, and

$$N_\alpha^s = \sqrt{\sum_\beta |\delta_{\alpha\beta} + \epsilon_{\alpha\beta}^s|^2}, \quad N_\beta^d = \sqrt{\sum_\alpha |\delta_{\alpha\beta} + \epsilon_{\alpha\beta}^d|^2} \quad (12.2)$$

---

Editor: Yufeng Li (liyufeng@ihep.ac.cn)

are normalization factors. In order to measure the average and difference between neutrino production and detection processes, we introduce two sets of new NSI parameters as

$$\tilde{\epsilon}_{\alpha\beta} = (\epsilon_{\alpha\beta}^s + \epsilon_{\beta\alpha}^{d*})/2, \quad \delta\epsilon_{\alpha\beta} = (\epsilon_{\alpha\beta}^s - \epsilon_{\beta\alpha}^{d*})/2, \quad (12.3)$$

to rewrite the NSI effects.

Including the NSI effects at the source and detector, the amplitude of the  $\bar{\nu}_\alpha \rightarrow \bar{\nu}_\alpha$  transition can be written as

$$\tilde{\mathcal{A}}_{\alpha\alpha} = \langle \bar{\nu}_\alpha^d | e^{-iHL} | \bar{\nu}_\alpha^s \rangle = \sum_{\beta\gamma} \langle \bar{\nu}_\alpha^d | \bar{\nu}_\gamma \rangle \langle \bar{\nu}_\gamma | e^{-iHL} | \bar{\nu}_\beta \rangle \langle \bar{\nu}_\beta | \bar{\nu}_\alpha^s \rangle = (\delta_{\gamma\alpha} + \epsilon_{\gamma\alpha}^{d*}) \mathcal{A}_{\beta\gamma} (\delta_{\alpha\beta} + \epsilon_{\alpha\beta}^{s*}), \quad (12.4)$$

where  $L$  is the baseline, and

$$\mathcal{A}_{\beta\gamma} = \langle \bar{\nu}_\gamma | e^{-iHL} | \bar{\nu}_\beta \rangle = \sum_i U_{\gamma i}^* U_{\beta i} \exp\left(-i \frac{m_i^2 L}{2E}\right) \quad (12.5)$$

is the amplitude of  $\bar{\nu}_\beta \rightarrow \bar{\nu}_\gamma$  without NSIs. It is useful to define

$$\tilde{U}_{\alpha i} = \frac{1}{\tilde{N}_\alpha} \sum_\beta (\delta_{\alpha\beta} + \tilde{\epsilon}_{\alpha\beta}^*) U_{\beta i}, \quad \delta U_{\alpha i} = \frac{1}{\tilde{N}_\alpha} \sum_\beta \delta\epsilon_{\alpha\beta}^* U_{\beta i}, \quad (12.6)$$

where

$$\tilde{N}_\alpha = \sqrt{\sum_\beta |\delta_{\alpha\beta} + \tilde{\epsilon}_{\alpha\beta}|^2} = \sqrt{N_\alpha^s N_\alpha^d} + \mathcal{O}(\delta\epsilon^2), \quad (12.7)$$

and  $\sum_i |\tilde{U}_{\alpha i}|^2 = 1$  is required. Thus we can obtain  $\tilde{\mathcal{A}}_{\alpha\alpha}$  as

$$\tilde{\mathcal{A}}_{\alpha\alpha} = \sum_i (\tilde{U} - \delta U)_{\alpha i}^* (\tilde{U} + \delta U)_{\alpha i} \exp\left(-i \frac{m_i^2 L}{2E}\right) + \mathcal{O}(\delta\epsilon^2), \quad (12.8)$$

and the survival probability for  $\bar{\nu}_\alpha \rightarrow \bar{\nu}_\alpha$  is expressed as

$$\tilde{P}_{\alpha\alpha} = |\tilde{\mathcal{A}}_{\alpha\alpha}|^2 = 1 - 4 \sum_{i<j} |\tilde{U}_{\alpha i}|^2 |\tilde{U}_{\alpha j}|^2 \left[ \sin^2 \Delta_{ji} + \text{Im} \left( \frac{\delta U_{\alpha i}}{\tilde{U}_{\alpha i}} - \frac{\delta U_{\alpha j}}{\tilde{U}_{\alpha j}} \right) \sin 2\Delta_{ji} \right] + \mathcal{O}(\delta\epsilon^2) \quad (12.9)$$

Due to the smallness of  $\delta U_{\alpha i}/\tilde{U}_{\alpha i}$ , we can rewrite the above equation as

$$\tilde{P}_{\alpha\alpha} = 1 - 4 \sum_{i<j} |\tilde{U}_{\alpha i}|^2 |\tilde{U}_{\alpha j}|^2 \sin^2 \tilde{\Delta}_{ji}^\alpha + \mathcal{O}(\delta\epsilon^2) \quad (12.10)$$

with

$$\tilde{\Delta}_{ji}^\alpha = \Delta_{ji} + \text{Im} \left( \frac{\delta U_{\alpha i}}{\tilde{U}_{\alpha i}} - \frac{\delta U_{\alpha j}}{\tilde{U}_{\alpha j}} \right). \quad (12.11)$$

For the effective mass-squared differences we have

$$\Delta \tilde{m}_{ji}^{2\alpha}(E/L) = \Delta m_{ji}^2 + \text{Im} \left( \frac{\delta U_{\alpha i}}{\tilde{U}_{\alpha i}} - \frac{\delta U_{\alpha j}}{\tilde{U}_{\alpha j}} \right) \frac{4E}{L}, \quad (12.12)$$



which is an energy/baseline- and flavor-dependent effective quantity.

With Eq. (12.10) we have obtained a standard-like expression for the antineutrino survival probability in vacuum in the presence of NSIs. The corresponding NSI effects are encoded in the effective mass and mixing parameters. The average parts induce constant shifts for the neutrino mixing elements, and the difference parts generate energy and baseline dependent corrections to the mass-squared differences.

In reactor antineutrino oscillations, only the electron antineutrino survival probability is relevant because of the high threshold of the  $\mu/\tau$  production. We can rewrite  $\tilde{P}_{\bar{e}\bar{e}}$  with these effective mixing parameters as

$$\begin{aligned}\tilde{P}_{\bar{e}\bar{e}} &= 1 - \tilde{c}_{13}^4 \sin^2 2\tilde{\theta}_{12} [\sin^2 \tilde{\Delta}_{21} + (\delta\varepsilon_1 - \delta\varepsilon_2) \sin 2\tilde{\Delta}_{21}] \\ &\quad - \tilde{c}_{12}^2 \sin^2 2\tilde{\theta}_{13} [\sin^2 \tilde{\Delta}_{31} + (\delta\varepsilon_1 - \delta\varepsilon_3) \sin 2\tilde{\Delta}_{31}] \\ &\quad - \tilde{s}_{12}^2 \sin^2 2\tilde{\theta}_{13} [\sin^2 \tilde{\Delta}_{32} + (\delta\varepsilon_2 - \delta\varepsilon_3) \sin 2\tilde{\Delta}_{32}] + \mathcal{O}(\delta\varepsilon^2) \\ &= 1 - \tilde{c}_{13}^4 \sin^2 2\tilde{\theta}_{12} \sin^2 \tilde{\Delta}_{21} - \tilde{c}_{12}^2 \sin^2 2\tilde{\theta}_{13} \sin^2 \tilde{\Delta}_{31} \\ &\quad - \tilde{s}_{12}^2 \sin^2 2\tilde{\theta}_{13} \sin^2 \tilde{\Delta}_{32} + \mathcal{O}(\delta\varepsilon^2),\end{aligned}\tag{12.13}$$

with

$$\begin{aligned}\tilde{\Delta}_{ji} &= \Delta_{ji} + \delta\varepsilon_i - \delta\varepsilon_j, \\ \delta\varepsilon_1 &= \frac{\text{Im}(\delta U_{e1})}{\tilde{c}_{12}\tilde{c}_{13}}, \quad \delta\varepsilon_2 = \frac{\text{Im}(\delta U_{e2})}{\tilde{s}_{12}\tilde{c}_{13}}, \quad \delta\varepsilon_3 = \frac{\text{Im}(\delta U_{e3})}{\tilde{s}_{13}},\end{aligned}\tag{12.14}$$

where the superscript  $\alpha = e$  in  $\tilde{\Delta}_{ji}^e$  has been ignored, and the effective mixing angles  $\tilde{\theta}_{13}$  and  $\tilde{\theta}_{12}$  are defined through  $\tilde{s}_{13} = |\tilde{U}_{e3}|$  and  $\tilde{s}_{12} = |\tilde{U}_{e2}|/\tilde{c}_{13}$ . Correspondingly we have  $|\tilde{U}_{e1}| = \tilde{c}_{12}\tilde{c}_{13}$  by using the normalization relation  $|\tilde{U}_{e1}|^2 + |\tilde{U}_{e2}|^2 + |\tilde{U}_{e3}|^2 = 1$ .

The average part  $\tilde{\varepsilon}$  can be treated as constant shifts to mixing angles  $\theta_{12}$  and  $\theta_{13}$ , and the difference part  $\delta\varepsilon$  leads to energy- and baseline-dependent shifts to the mass-squared differences  $\Delta m_{ji}^2$  as

$$\Delta \tilde{m}_{ji}^2(E/L) = \Delta m_{ji}^2 + (\delta\varepsilon_i - \delta\varepsilon_j)4E/L.\tag{12.15}$$

However, only two combinations of the three parameters  $\delta\varepsilon_i$  contribute to the oscillation probability thanks to the relation  $(\delta\varepsilon_2 - \delta\varepsilon_3) = (\delta\varepsilon_1 - \delta\varepsilon_3) - (\delta\varepsilon_1 - \delta\varepsilon_2)$ . It is notable that one cannot distinguish the effects of mixing angle shifts from the scenario of three neutrino mixing using reactor antineutrino oscillation experiments. On the other hand, the shifts of mass-squared differences are clearly observable due to the baseline- and energy-dependent corrections in the reactor antineutrino spectrum.

Following the nominal setup defined in the MH sensitivity study, we numerically show the NSI effects at JUNO. We illustrate how the NSI effects shift the mixing angles and mass-squared differences, how it influences the mass ordering measurement and to what extent we can constrain the NSI parameters. The relevant oscillation parameters are  $\tilde{\theta}_{12}$ ,  $\tilde{\theta}_{13}$ ,  $\Delta m_{21}^2$  and  $\Delta m_{ee}^2$  and the NSI parameters are  $\delta\varepsilon_1 - \delta\varepsilon_2$ ,  $\delta\varepsilon_1 - \delta\varepsilon_3$ . We directly employ the mixing angles measured in recent reactor antineutrino experiments as our effective mixing angles, which can be shown as

$$\sin^2 2\tilde{\theta}_{13} = \sin^2 2\theta_{13}^D = 0.084, \quad \tan^2 \tilde{\theta}_{12} = \tan^2 \theta_{12}^K = 0.481,\tag{12.16}$$

where the measured mixing angles  $\theta_{13}^D$  and  $\theta_{12}^K$  are from Daya Bay [130] and KamLAND [330], respectively. On the other hand, because the current uncertainties of mass-squared differences

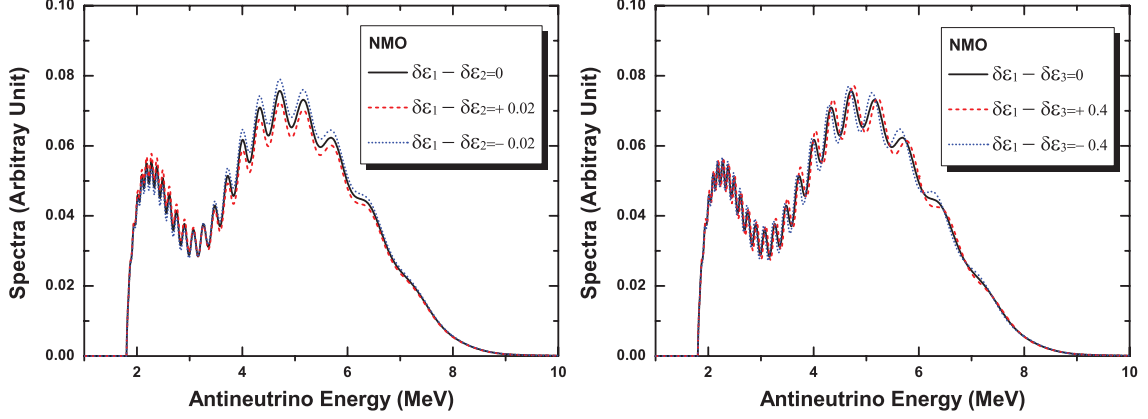


Figure 12-1: The effects of NSIs in reactor  $\bar{\nu}_e$  spectra at a baseline of 52.5 km [450]. For visualization, we set  $\delta\varepsilon_1 - \delta\varepsilon_2 = 0, \pm 0.02$  in the upper panel and  $\delta\varepsilon_1 - \delta\varepsilon_3 = 0, \pm 0.4$  in the lower panel.  $\delta\varepsilon_1 - \delta\varepsilon_3$  is fixed at zero in the upper panel, and  $\delta\varepsilon_1 - \delta\varepsilon_2$  is fixed at zero in the lower panel. The NH is assumed for illustration.

from Daya Bay and KamLAND are much larger than the NSI corrections, we simply take the measured mass-squared differences as the true parameters,

$$\Delta m_{ee}^2 = \Delta m_{ee}^{2D} = 2.44 \times 10^{-3} \text{ eV}^2, \quad (12.17)$$

$$\Delta m_{21}^2 = \Delta m_{21}^{2K} = 7.54 \times 10^{-5} \text{ eV}^2. \quad (12.18)$$

We show the effects of NSIs in the reactor  $\bar{\nu}_e$  spectra at a baseline of 52.5 km in Fig. 12-1, where the influences of  $\delta\varepsilon_1 - \delta\varepsilon_2$  and  $\delta\varepsilon_1 - \delta\varepsilon_3$  are presented in the upper panel and lower panel, respectively. In the upper panel, we fix  $\delta\varepsilon_1 - \delta\varepsilon_3 = 0$  and find that non-zero  $\delta\varepsilon_1 - \delta\varepsilon_2$  introduces the spectral distortion to the slow oscillation term  $\Delta_{21}$ . For  $\delta\varepsilon_1 - \delta\varepsilon_2 = 0.02$ , the spectrum is suppressed in the high energy region with  $E > 3$  MeV and enhanced for the low energy range  $2 \text{ MeV} < E < 3$  MeV. In comparison, negative  $\delta\varepsilon_1 - \delta\varepsilon_2$  gives the opposite effect on the spectrum distortion. In the lower panel, we set  $\delta\varepsilon_1 - \delta\varepsilon_2 = 0$  and observe that  $\delta\varepsilon_1 - \delta\varepsilon_3$  can affect the spectral distribution for the fast oscillation term  $\Delta_{31}$ . The non-trivial NSI effects will contribute a small phase advancement or retardance to the fast oscillation depending on the sign of  $\delta\varepsilon_1 - \delta\varepsilon_3$ .

The NSI-induced shifts of mixing angles and mass squared differences are presented in Figs. 12-2 and 12-3 respectively, where the true scenario is the generic scenario with the NSI effects, and the best-fit values of  $\theta_{12}$ ,  $\theta_{13}$ ,  $\Delta m_{21}^2$  and  $\Delta m_{31}^2$  are obtained from the minimization process without the NSI effects. One can observe from Fig. 12-2 that the average part (i.e.,  $\varepsilon_{e\mu} = 0.02$ ) of NSIs introduces constant shifts of  $\theta_{12}$  and  $\theta_{13}$  [449]. On the other hand, from Fig. 12-3, the difference part of NSIs induce the shifts to  $\Delta m_{21}^2$  and  $\Delta m_{31}^2$ , where the left and right panels are illustrated for  $\delta\varepsilon_1 - \delta\varepsilon_2 = -0.54 \delta U$ ,  $\delta\varepsilon_1 - \delta\varepsilon_3 = -5.60 \delta U$  and  $\delta\varepsilon_1 - \delta\varepsilon_2 = +3.00 \delta U$ ,  $\delta\varepsilon_1 - \delta\varepsilon_3 = +8.06 \delta U$  respectively, with  $\delta U = 0.01$  [450].

Next we shall discuss the NSI effects on the MH measurement. The iso- $\Delta\chi^2$  contours are illustrated in Fig. 12-4 for the MH sensitivity as a function of two effective NSI parameters  $\delta\varepsilon_1 - \delta\varepsilon_2$  and  $\delta\varepsilon_1 - \delta\varepsilon_3$ . The NH is assumed for illustration. We can learn from the figure that the smaller  $\delta\varepsilon_1 - \delta\varepsilon_2$  and larger  $\delta\varepsilon_1 - \delta\varepsilon_3$  will reduce the possibility of the MH measurement. If  $\delta\varepsilon_1 - \delta\varepsilon_2$  decreases by 0.03 or  $\delta\varepsilon_1 - \delta\varepsilon_3$  increases by 0.05,  $\Delta\chi^2$  will be suppressed by 2 units.

Finally we want to present the constraints on NSI parameters with JUNO. In our calculation,

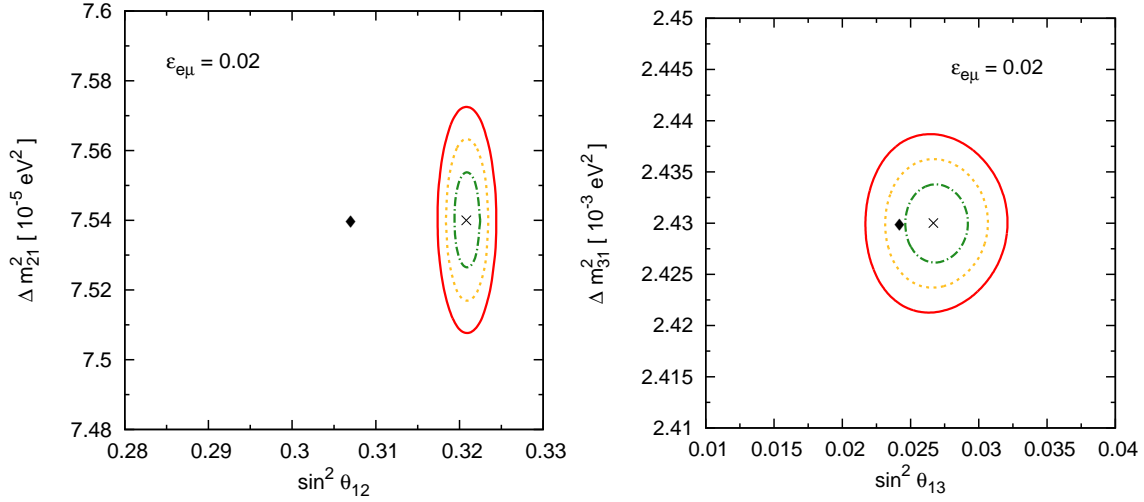


Figure 12-2: The shifts of mixing angles  $\sin^2 \theta_{12}$  (left) and  $\sin^2 \theta_{13}$  (right) induced by NSIs in fitting  $(\theta_{12}, \Delta m_{21}^2)$  and  $(\theta_{13}, \Delta m_{31}^2)$  to the simulated data [449]. The NSI effects are neglected in the fitting process. The black diamonds indicate the true values, whereas the crosses correspond to the extracted parameters. The dotted-dashed (green), dotted (yellow), and solid (red) curves stand for the  $1\sigma$ ,  $2\sigma$ , and  $3\sigma$  C.L., respectively.

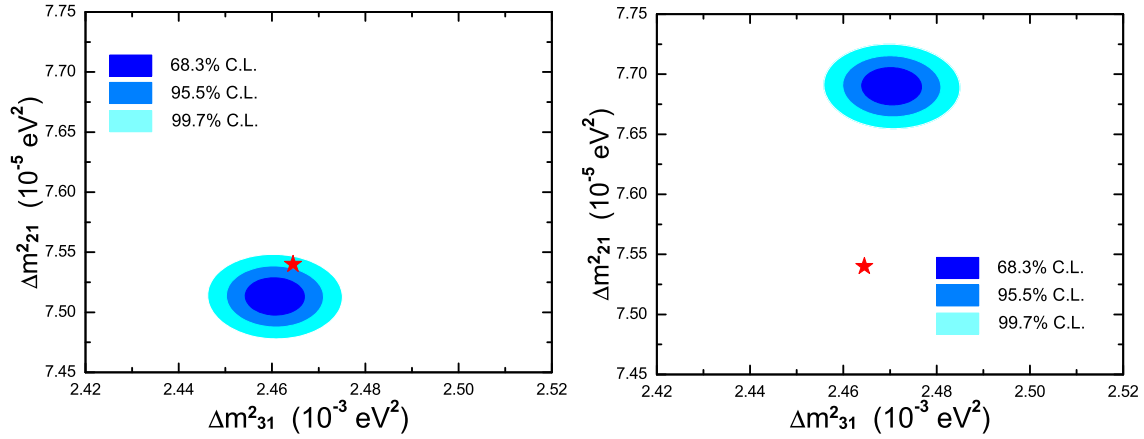


Figure 12-3: The shifts of mass-squared differences induced by NSIs in fitting  $(\Delta m_{21}^2, \Delta m_{31}^2)$  to the simulated data. The left and right panels are illustrated for  $\delta\varepsilon_1 - \delta\varepsilon_2 = -0.54\delta U$ ,  $\delta\varepsilon_1 - \delta\varepsilon_3 = -5.60\delta U$  and  $\delta\varepsilon_1 - \delta\varepsilon_2 = +3.00\delta U$ ,  $\delta\varepsilon_1 - \delta\varepsilon_3 = +8.06\delta U$  respectively, with  $\delta U = 0.01$  [450]. The NSI effects are neglected in the fitting process.

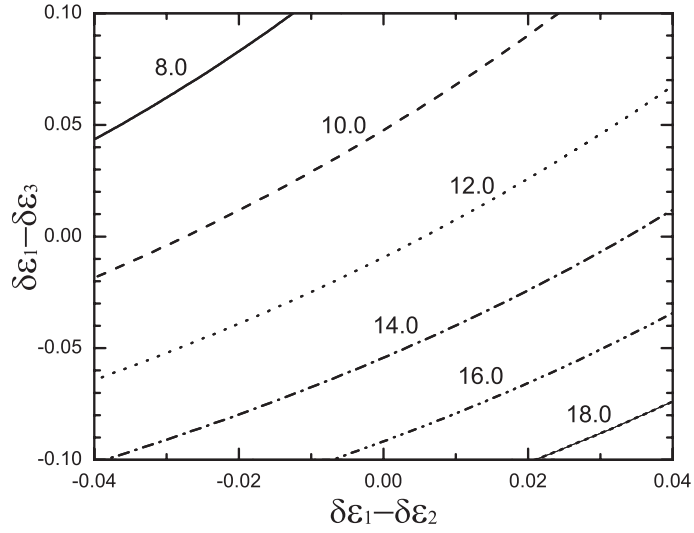


Figure 12-4: The iso- $\Delta\chi^2$  contours for the MH sensitivity as a function of two effective NSI parameters  $\delta\varepsilon_1 - \delta\varepsilon_2$  and  $\delta\varepsilon_1 - \delta\varepsilon_3$ . [450] The NH is assumed for illustration.

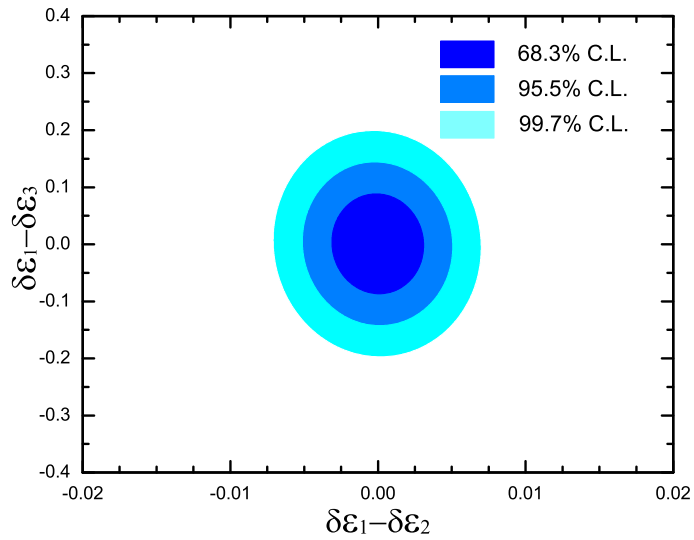


Figure 12-5: The experimental constraints on the generic NSI parameters  $\delta\varepsilon_1 - \delta\varepsilon_2$  and  $\delta\varepsilon_1 - \delta\varepsilon_3$ , where the true values are fixed at  $\delta\varepsilon_1 - \delta\varepsilon_2 = \delta\varepsilon_1 - \delta\varepsilon_3 = 0$ . [450] The NH is assumed for illustration.

the true NSI parameters are taken as  $\delta\varepsilon_1 - \delta\varepsilon_2 = \delta\varepsilon_1 - \delta\varepsilon_3 = 0$ , but the corresponding fitted ones are free. The constraints on the NSI parameters are shown in Fig. 12-5, where the limits on these two parameters are at the  $1\sigma$ ,  $2\sigma$ ,  $3\sigma$  confidence levels respectively. For  $\delta\varepsilon_1 - \delta\varepsilon_2$ , the precision is much better than 1%. However, the precision for  $\delta\varepsilon_1 - \delta\varepsilon_3$  is around the 10% level. JUNO is designed for a precision spectral measurement at the oscillation maximum of  $\Delta m_{21}^2$ . From Eq. (12.13), the precision for  $\delta\varepsilon_1 - \delta\varepsilon_2$  can be compatible with that of  $\sin^2 2\theta_{12}$ , where a sub-percent level can be achieved. On the other hand, the precision for  $\sin^2 2\theta_{13}$  is also at the 10% level, also consistent with that of  $\delta\varepsilon_1 - \delta\varepsilon_3$  in our numerical simulation. Because  $\delta\varepsilon_1 - \delta\varepsilon_3$  is suppressed by  $\sin \theta_{13}$ , the above two constraints are actually compatible if we consider the physical NSI parameters  $\delta\epsilon_{\alpha\beta}$  defined in Eq. (12.3).

## 12.2 Lorentz Invariance Violation

Special Relativity is a fundamental theory describing the Lorentz space-time symmetry, which is a consequence of the homogeneous and isotropic space-time and the relativity principle among different inertial frames. Although Lorentz invariance has been widely accepted, well-motivated models with LIV are anticipated from the principle of Quantum Gravity [451]. As one of the most important low energy phenomena, neutrino oscillations provide an opportunity to test the Lorentz invariance violation.

The low energy phenomena of LIV can be systematically studied in the framework of the Standard Model Extension (SME) [452, 453], which includes all possible LIV terms formed by the SM fields in the Lagrangian,

$$\mathcal{L}_{LV} \simeq -(a_L)_\mu \bar{\psi}_L \gamma^\mu \psi_L - (c_L)_{\mu\nu} \bar{\psi}_L i \gamma^\mu \partial^\nu \psi_L. \quad (12.19)$$

Notice that  $a_L$  violates both the Lorentz and CPT symmetries, but  $c_L$  is CPT-even and only violates the Lorentz invariance. Although the LIV coefficients are very small due to the suppression factor of the order of the electro-weak scale divided by the Planck scale (i.e.,  $10^{-17}$ ), they provide an accessible test to the Planck scale physics.

The SME framework predicts distinct behaviors of neutrino flavor conversions, which are different from the standard picture of three neutrino oscillations. The transition probability depends on the ratio of neutrino propagation baseline  $L$  to energy  $E$  (i.e.,  $L/E$ ) in the standard oscillation framework, but in the SME it depends on either  $L$  or  $L \times E$  for the contribution induced by  $a_L$  or  $c_L$ . On the other hand, LIV also predicts the breakdown of space-time's isotropy, which manifests as a sidereal modulation of the neutrino events for experiments with both the neutrino source and detector fixed on the earth. The sidereal time is defined on the basis of the orientation of the earth with respect to the sun-centered reference inertial frame. At JUNO both the sidereal variation and spectral distortion effects will be employed to test the LV. We shall analyze the LIV effects in the reference frame of the sun [455, 456] and present the sensitivity of JUNO to LIV coefficients.

According to the SME, the effective Hamiltonian for Lorentz violating neutrino oscillations is written as [457]

$$H_{\alpha\beta} = \frac{1}{E} \left[ \frac{m^2}{2} + (a_L)_\mu p^\mu + (c_L)_{\mu\nu} p^\mu p^\nu \right]_{\alpha\beta}, \quad (12.20)$$

where  $E$  and  $p^\mu$  are the neutrino energy and 4-momentum,  $\alpha$  and  $\beta$  are flavor indices, and  $(m^2)_{\alpha\beta} = U \text{diag}(m_1^2, m_2^2, m_3^2) U^\dagger$  is the mass-squared matrix in the flavor basis. To derive the oscillation probabilities from the Hamiltonian, we employ the perturbation treatment [458] to factorize the LIV part from the conventional neutrino oscillation part.

By defining  $\delta H = [(a_L)_\mu p^\mu + (c_L)_{\mu\nu} p^\mu p^\nu]/E$  and taking the perturbative expansion, we derive the time evolution operator as

$$S = e^{-iHt} = \left( e^{-iH_0 t - i\delta H t} e^{iH_0 t} \right) e^{-iH_0 t} = \left( 1 - i \int_0^t dt_1 e^{-iH_0 t_1} \delta H e^{iH_0 t_1} + \dots \right) S^{(0)}. \quad (12.21)$$

Therefore, the oscillation probability is expanded as

$$P_{\alpha \rightarrow \beta} = |S_{\alpha\beta}|^2 = \left| S_{\alpha\beta}^{(0)} \right|^2 + 2 \operatorname{Re} \left[ (S_{\alpha\beta}^{(0)})^* S_{\alpha\beta}^{(1)} \right] = P_{\alpha \rightarrow \beta}^{(0)} + P_{\alpha \rightarrow \beta}^{(1)}. \quad (12.22)$$

In particular, the expression of  $P_{\alpha \rightarrow \beta}^{(1)}$  can be written as [458]

$$P_{\alpha \rightarrow \beta}^{(1)} = \sum_{i,j} \sum_{\rho,\sigma} 2L \operatorname{Im} \left[ (S_{\alpha\beta}^{(0)})^* U_{\alpha i} U_{\rho i}^* \tau_{ij} \delta H_{\rho\sigma} U_{\sigma j} U_{\beta j}^* \right], \quad (12.23)$$

with

$$\tau_{ij} = \begin{cases} \exp\{-iE_i L\} & \text{when } i = j \\ \frac{\exp\{-iE_i L\} - \exp\{-iE_j L\}}{-i(E_i - E_j)L} & \text{when } i \neq j \end{cases}. \quad (12.24)$$

$\delta H_{\rho\sigma}$  is required to be real when  $\rho = \sigma$  and  $\delta H_{\rho\sigma} = \delta H_{\sigma\rho}^*$  when  $\rho \neq \sigma$ . For the former case the LIV terms can be extracted directly as

$$P_{\alpha \rightarrow \beta}^{(1)} = \sum_{i,j} \sum_{\rho=\sigma} 2L \operatorname{Im} \left[ (S_{\alpha\beta}^{(0)})^* U_{\alpha i} U_{\rho i}^* \tau_{ij} U_{\sigma j} U_{\beta j}^* \right] \delta H_{\rho\sigma}. \quad (12.25)$$

On the other hand, the LIV terms with  $\rho \neq \sigma$  can be expressed as

$$\begin{aligned} P_{\alpha \rightarrow \beta}^{(1)} &= \sum_{i,j} \sum_{\rho \neq \sigma} L \operatorname{Im} \left[ (S_{\alpha\beta}^{(0)})^* U_{\alpha i} U_{\rho i} \tau_{ij} U_{\sigma j} U_{\beta j} (\delta H_{\rho\sigma} + \delta H_{\sigma\rho}) \right] \\ &= \sum_{i,j} \sum_{\rho \neq \sigma} 2L \operatorname{Im} \left[ (S_{\alpha\beta}^{(0)})^* U_{\alpha i} U_{\rho i} \tau_{ij} U_{\sigma j} U_{\beta j} \right] \operatorname{Re} \delta H_{\rho\sigma}, \end{aligned} \quad (12.26)$$

where the CP-violating phase in the MNSP matrix has been neglected for simplicity. We notice from Eqs. (12.25) and (12.26) that contributions from the mass term and LIV terms can be factorized. Therefore, we define the quantity  $I_{\alpha\beta}^{\rho\sigma}$  as an indicator of the sensitivity to  $\delta H_{\rho\sigma}$  in a certain oscillation channel  $P_{\alpha \rightarrow \beta}$ ,

$$I_{\alpha\beta}^{\rho\sigma} = \sum_{i,j} 2L \operatorname{Im} \left[ (S_{\alpha\beta}^{(0)})^* U_{\alpha i} U_{\rho i} \tau_{ij} U_{\sigma j} U_{\beta j} \right]. \quad (12.27)$$

This indicator can be used to understand the distinct properties of different LIV components  $\delta H_{\rho\sigma}$  in the following numerical analysis.

Since the LIV coefficients  $(a_L)_\mu$  and  $(c_L)_{\mu\nu}$  are direction-dependent, a reference frame should be specified when an experiment is going to report the LIV results. The sun-centered system [455,456] can take on this responsibility, which is depicted in the left panel of Fig. 12-6 and defined in the following way:

- Point  $S$  is the center of the sun;
- The  $Z$  axis has the same direction as the earth's rotational axis, so the  $X$ - $Y$  plane is parallel to the earth's equator;

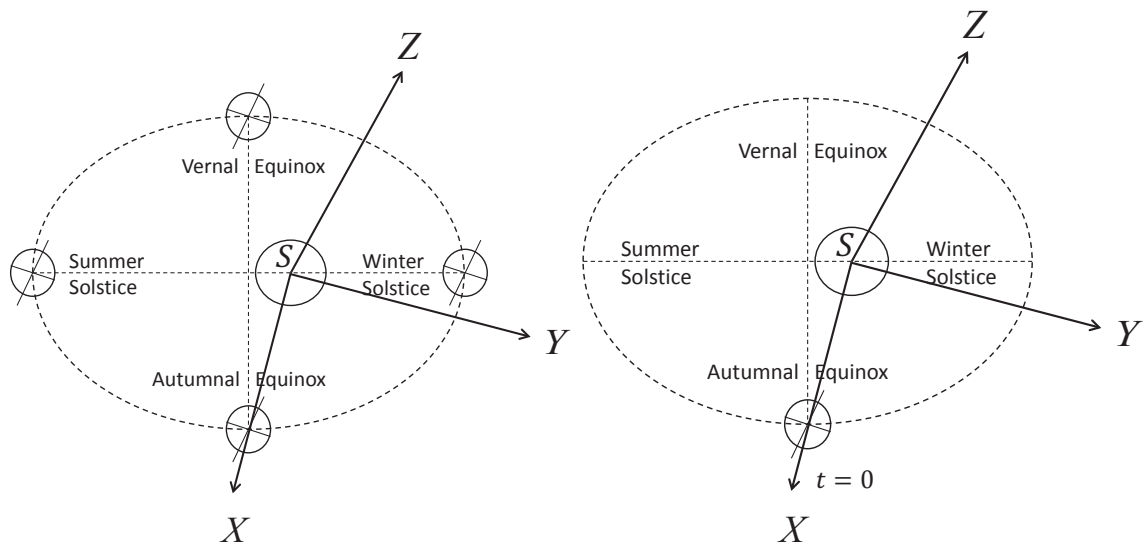


Figure 12-6: The definition (left panel) of the sun-centered system [455, 456], and definition (right panel) of  $t = 0$  in the sun-centered system.

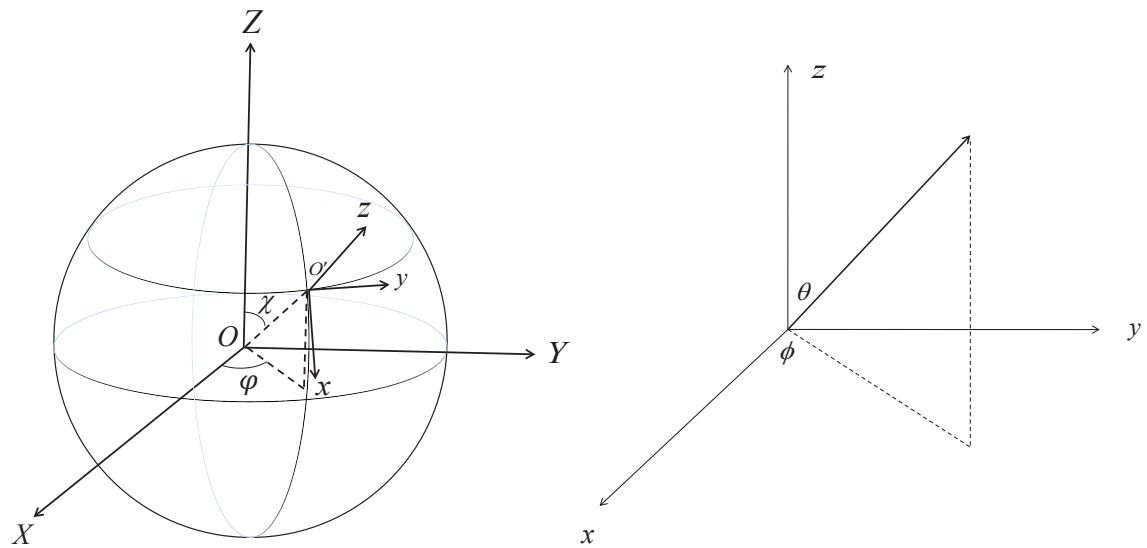


Figure 12-7: The definition of the earth-centered system (left panel) [455, 456], and definition of the local coordinate system (right panel).

- The  $X$  axis is parallel to the vector pointed from the sun to the autumnal equinox, while the  $Y$  axis completes the right-handed system.

In a terrestrial experiment, the direction of neutrino propagation is described by its components along the  $X, Y, Z$  axes (i.e.,  $\hat{N}^X, \hat{N}^Y$  and  $\hat{N}^Z$ ). For convenience, the origin of the sun-centered system can be defined to sit in the center of the earth  $O$  due to the invariance of spatial translation, as shown in the left panel of Fig. 12-7. In order to express  $\hat{N}^X, \hat{N}^Y$  and  $\hat{N}^Z$  in terms of local geographical information, a local coordinate system  $(x, y, z)$  is also introduced:

- point  $O'$  is the site of the neutrino source, and  $\chi$  (i.e., the angle between  $OO'$  and  $Z$  axis) denotes its colatitude;
- the  $z$  axis is defined to be upward;
- the  $x$  and  $y$  axes point to the south and east, respectively.

In the local coordinate system depicted in the right panel of Fig. 12-7, the direction of neutrino propagation is parameterized by two angles, of which  $\theta$  is the angle between the beam direction and  $z$  axis and  $\phi$  is the angle between the beam direction and  $x$  axis.

Because the neutrino source and detector are fixed on the earth, the rotation of the earth will induce a periodic change of the neutrino propagation directions relative to the standard reference frame, with an angular frequency  $\omega = 2\pi/T_s$ . Here  $T_s \simeq 23$  h 56 min is the period of a sidereal day. For this reason, a reference time origin should be specified. Without loss of generality, we can set the local midnight when the earth arrives at the autumnal equinox to be  $t = 0$  (see the right panel of Fig. 12-6). At this moment, the  $x$ - $z$  plane coincides with the  $X$ - $Z$  plane, resulting in the coordinate transformation between the coordinate in the sun-centered system and that in the local system as

$$\begin{aligned}\hat{N}^X &= \cos \chi \sin \theta \cos \phi + \sin \chi \cos \theta, \\ \hat{N}^Y &= \sin \theta \sin \phi, \\ \hat{N}^Z &= -\sin \chi \sin \theta \cos \phi + \cos \chi \cos \theta.\end{aligned}\tag{12.28}$$

Therefore, the direction of neutrino propagation  $\widehat{p}^\mu = (1, \widehat{p}^X, \widehat{p}^Y, \widehat{p}^Z)$  is a periodic function of the time  $t$

$$\begin{aligned}\widehat{p}^X &= \hat{N}^X \cos \omega t - \hat{N}^Y \sin \omega t, \\ \widehat{p}^Y &= \hat{N}^X \sin \omega t + \hat{N}^Y \cos \omega t, \\ \widehat{p}^Z &= \hat{N}^Z.\end{aligned}\tag{12.29}$$

Accordingly,  $\delta H_{\rho\sigma}$  can be decomposed as

$$\begin{aligned}\delta H_{\rho\sigma} &= \mathcal{C}_{\rho\sigma} + (\mathcal{A}_s)_{\rho\sigma} \sin \omega t + (\mathcal{A}_c)_{\rho\sigma} \cos \omega t \\ &\quad + (\mathcal{B}_s)_{\rho\sigma} \sin 2\omega t + (\mathcal{B}_c)_{\rho\sigma} \cos 2\omega t.\end{aligned}\tag{12.30}$$

Note that the above coefficients (i.e.,  $\mathcal{C}$ ,  $\mathcal{A}_s$ ,  $\mathcal{A}_c$ ,  $\mathcal{B}_s$  and  $\mathcal{B}_c$ ) are linear combinations of the LIV coefficients  $(a_L)_\mu$  and  $(c_L)_{\mu\nu}$ .  $\mathcal{A}_s$ ,  $\mathcal{A}_c$ ,  $\mathcal{B}_s$  and  $\mathcal{B}_c$  (written as  $\mathcal{A}/\mathcal{B}$  for short) associated terms are time-dependent and can induce periodic variations for the oscillation probability. On the other hand, the  $\mathcal{C}$  term can modify the absolute value of the oscillation probability with unconventional energy and baseline dependence, while the contributions of  $\mathcal{A}/\mathcal{B}$  cancel out in a full sidereal period.

In our numerical calculation of the JUNO sensitivity to LIV coefficients, we take the same setup as that in the MH studies when using the spectral information. However, we simplify the reactor complexes in Yangjiang and Taishan NPPs as two virtual reactors with equal baselines (i.e.,



52.5 km). When we discuss the sidereal variation of IBD event rates, a sidereal day is divided into 24 bins. Notice that a normalization factor has a negligible effect in the sidereal variation analysis. Thus we only consider the statistical uncertainty and the time-dependent uncorrelated uncertainty of the 1% level for this study.

The upper limits at the 95% confidence level for those LIV coefficients responsible for the spectral distortion (i.e.,  $\mathcal{C}_{\rho\sigma}^{\text{eff}}$ ) are listed in the first row of Tab. 12-1. The relative differences in the power of constraining these six coefficients can be understood by the quantity defined in Eq. (12.27), which indicates that the flavor components with larger  $I_{\alpha\beta}$  will get more severe constraints. The 95% upper limits for those LIV coefficients from the sidereal variation (i.e.,  $\mathcal{A}/\mathcal{B}_{\rho\sigma}^{\text{eff}}$ ) are listed in the second row of Tab. 12-1, where the  $\tau\tau$  component gets the worst sensitivity, but the  $e\tau$  coefficient turns out to be the most severely constrained parameter. The order of magnitude for  $\mathcal{A}/\mathcal{B}_{\rho\sigma}^{\text{eff}}$  is  $10^{-24}$  GeV, which is much smaller than that for  $\mathcal{C}_{\rho\sigma}^{\text{eff}}$  (i.e.,  $10^{-22}$  GeV). This is because the uncertainties of the spectrum and oscillation parameters do not enter the sidereal variation of IBD events.

It is straightforward to transfer the limits for  $\mathcal{C}_{\rho\sigma}^{\text{eff}}$  and  $\mathcal{A}/\mathcal{B}_{\rho\sigma}^{\text{eff}}$  to that for each space component of the physical parameters  $a_L^\mu$  and  $c_L^{\mu\nu}$ . Using the real positions of the reactor cores and experiment site, we can present explicit relations between the effective parameters and the physical parameters [454]. The expansion coefficients for antineutrinos coming from Yangjiang are given as follows:

$$\begin{aligned}
(\mathcal{C}_{\rho\sigma}^*)_1 &= -a_{\rho\sigma}^T + 0.81 a_{\rho\sigma}^Z + [0.42 c_{\rho\sigma}^{TT} - 0.48 c_{\rho\sigma}^{ZZ}] E, \\
((\mathcal{A}_s)_{\rho\sigma}^*)_1 &= -0.49 a_{\rho\sigma}^X - 0.33 a_{\rho\sigma}^Y - [0.98 c_{\rho\sigma}^{TX} + 0.65 c_{\rho\sigma}^{TY} - 0.79 c_{\rho\sigma}^{XZ} - 0.52 c_{\rho\sigma}^{YZ}] E, \\
((\mathcal{A}_c)_{\rho\sigma}^*)_1 &= -0.33 a_{\rho\sigma}^X + 0.49 a_{\rho\sigma}^Y - [0.65 c_{\rho\sigma}^{TX} - 0.98 c_{\rho\sigma}^{TY} - 0.52 c_{\rho\sigma}^{XZ} + 0.79 c_{\rho\sigma}^{YZ}] E, \\
((\mathcal{B}_s)_{\rho\sigma}^*)_1 &= -0.16 c_{\rho\sigma}^{XX} + 0.16 c_{\rho\sigma}^{YY} + 0.13 c_{\rho\sigma}^{XY}, \\
((\mathcal{B}_c)_{\rho\sigma}^*)_1 &= -0.067 c_{\rho\sigma}^{XX} + 0.067 c_{\rho\sigma}^{YY} + 0.32 c_{\rho\sigma}^{XY}.
\end{aligned} \tag{12.31}$$

Meanwhile, expansion coefficients for antineutrinos coming from Taishan are given as

$$\begin{aligned}
(\mathcal{C}_{\rho\sigma}^*)_2 &= -a_{\rho\sigma}^T + 0.41 a_{\rho\sigma}^Z - [0.59 c_{\rho\sigma}^{TT} - 0.25 c_{\rho\sigma}^{ZZ}] E, \\
((\mathcal{A}_s)_{\rho\sigma}^*)_2 &= 0.90 a_{\rho\sigma}^X - 0.17 a_{\rho\sigma}^Y + [1.8 c_{\rho\sigma}^{TX} - 0.34 c_{\rho\sigma}^{TY} - 0.73 c_{\rho\sigma}^{XZ} + 0.14 c_{\rho\sigma}^{YZ}] E, \\
((\mathcal{A}_c)_{\rho\sigma}^*)_2 &= -0.17 a_{\rho\sigma}^X - 0.90 a_{\rho\sigma}^Y - [0.34 c_{\rho\sigma}^{TX} + 1.8 c_{\rho\sigma}^{TY} - 0.14 c_{\rho\sigma}^{XZ} - 0.73 c_{\rho\sigma}^{YZ}] E, \\
((\mathcal{B}_s)_{\rho\sigma}^*)_2 &= 0.15 c_{\rho\sigma}^{XX} - 0.15 c_{\rho\sigma}^{YY} + 0.77 c_{\rho\sigma}^{XY}, \\
((\mathcal{B}_c)_{\rho\sigma}^*)_2 &= -0.39 c_{\rho\sigma}^{XX} + 0.39 c_{\rho\sigma}^{YY} - 0.30 c_{\rho\sigma}^{XY}.
\end{aligned} \tag{12.32}$$

Here the subscript “ $L$ ” for  $a_L$  and  $c_L$  is omitted for simplicity.

One should keep in mind that the degrees of freedom in  $a_L^\mu$  and  $c_L^{\mu\nu}$  are much larger than those in the effective LIV coefficients. In order to obtain independent constraints, it is thus more reasonable to use the effective coefficients. On the other hand, it is better to derive the limits of  $a_L^\mu$  and  $c_L^{\mu\nu}$  when we compare and combine the limits from different oscillation experiments.

### 12.3 Discussions

Besides the exotic search with the reactor neutrino oscillation, there are many other possibilities in the aspect of new physics studies.

Rare decays and similar processes related to the baryon number and lepton number violation, constitute a large group of fundamental issues in the new physics searches beyond the SM. Future

	$\mathcal{C}_{ee}^{\text{eff}}$	$\mathcal{C}_{e\mu}^{\text{eff}}$	$\mathcal{C}_{e\tau}^{\text{eff}}$	$\mathcal{C}_{\mu\mu}^{\text{eff}}$	$\mathcal{C}_{\mu\tau}^{\text{eff}}$	$\mathcal{C}_{\tau\tau}^{\text{eff}}$
$10^{-22}$ GeV	1.5	0.5	0.4	4.4	3.4	1.1
	$\mathcal{A}/\mathcal{B}_{ee}^{\text{eff}}$	$\mathcal{A}/\mathcal{B}_{e\mu}^{\text{eff}}$	$\mathcal{A}/\mathcal{B}_{e\tau}^{\text{eff}}$	$\mathcal{A}/\mathcal{B}_{\mu\mu}^{\text{eff}}$	$\mathcal{A}/\mathcal{B}_{\mu\tau}^{\text{eff}}$	$\mathcal{A}/\mathcal{B}_{\tau\tau}^{\text{eff}}$
$10^{-24}$ GeV	3.7	3.7	2.7	5.4	6.6	11.6

Table 12-1: The JUNO sensitivity at the 95% confidence level for the effective LIV coefficients  $\mathcal{C}$ , and  $\mathcal{A}/\mathcal{B}$  from the effects of spectral distortion and sidereal variation [454].

prospects of nucleon decays at JUNO are discussed in Sec. 10, with the special attention to the  $p \rightarrow K^+ + \bar{\nu}$  channel of proton decays. Solar and supernova neutrino studies at JUNO also provide us useful astrophysical probes for testing new physics scenarios, among which tests of neutrino electromagnetic properties are of fundamental importance [300]. In solar neutrinos, effects of neutrino magnetic dipole moments could appear in the  $\nu_e$ - $e$  scattering cross section and spin-flavor precession mechanism. Through the solar  ${}^7\text{Be}$  and  ${}^8\text{B}$  neutrino observations at JUNO, the neutrino magnetic moment can be tested at a level comparable to that using reactor antineutrinos. On the other hand, with the high-precision supernova neutrino detection at JUNO, it might be possible to reveal the collective spin-flavor oscillation effects with the Majorana transition magnetic moments as small as  $10^{-22} \mu_B$  [459, 460].

In summary, as a multi-purpose underground neutrino observatory, JUNO will provide us the unique opportunity to study new physics beyond the SM.

## 13 Appendix

### 13.1 Reactor Neutrinos

#### 13.1.1 Introduction

Reactor neutrinos are electron antineutrinos that emitted from subsequent  $\beta$ -decays of instable fission fragments. All reactors close to JUNO are pressurized water reactors (PWR). In these reactors, fission of four fuel isotopes,  $^{235}\text{U}$ ,  $^{238}\text{U}$ ,  $^{239}\text{Pu}$ , and  $^{241}\text{Pu}$ , makes up more than 99.7% of the thermal power and reactor antineutrinos. Reactor neutrino fluxes per fission of each isotope are determined by inversion of the measured  $\beta$  spectra of fissioning [98–102] or by calculation with nuclear database [103, 104]. Their fission rates in a reactor can be estimated with the core simulation and the thermal power measurements. Therefore, the reactor neutrino flux can be predicted as  $\Phi(E_\nu) = \sum_i F_i S_i(E_\nu)$ , where  $F_i$  is the fission rate of isotope  $i$  and  $S_i(E_\nu)$  is the neutrino flux per fission, summing over the four isotopes [358]. Such a prediction is expected to carry an uncertainty of 2-3% [30–32]. Recently, reactor neutrino experiments (i.e., Daya Bay [105], RENO [106] Double Chooz [107]) found a large discrepancy between the predicted and measured spectra in 4-6 MeV. Model independent prediction based on the new precision measurements could avoid this bias, and might be able to improve the precision to 1%.

#### 13.1.2 Neutrino flux per fission

Neutrino flux per fission for each isotope could be calculated by superposing thousands of beta decays of the fission fragments. However, such a first-principle calculation is challenging due to missing or inaccurate data even with modern nuclear databases. In general the uncertainty is  $\sim 10\%$  [103].

Several direct measurements were done at ILL in 1980s to determine the neutrino fluxes and energy spectra of the thermal fissile isotopes  $^{235}\text{U}$ ,  $^{239}\text{Pu}$  and  $^{241}\text{Pu}$ . In these measurements, sample foils were placed into a reactor and exposed to neutrons for one or two days. A high precision electron spectrometer recorded the emitted  $\beta$  spectra, which were then inverted to the antineutrino spectra by fitting the observed  $\beta$  spectra to a set of 30 virtual  $\beta$ -branches. With the Q-value and the branching ratios of the virtual  $\beta$ -branches, the corresponding neutrino spectra could be computed out [98–100].

These measurements didn't include  $^{238}\text{U}$  which fissions only with fast neutrons. A theoretical calculation of the  $^{238}\text{U}$  neutrino spectrum has been computed by Vogel *et al.* [103]. Since  $^{238}\text{U}$  contributes only  $\sim 10\%$  antineutrinos in a typical PWR, the error by using this calculated  $^{238}\text{U}$  neutrino spectrum should be less than 1%. The neutrino fluxes per fission of the four isotopes determined in above literature, which is called ILL+Vogel model, are shown in Fig. 13-1. The inverted neutrino spectrum were compared with the Bugey-3 data [461] and showed reasonable agreement in both the total rate and energy spectrum.

The neutrino flux per fission was recently improved by Huber [101], in which the ILL  $\beta$  spectra were re-analyzed with higher order corrections in the  $\beta$  decay spectrum taken into account. The spectrum of  $^{238}\text{U}$  was also updated with an *ab initio* calculation by Mueller *et al.* [102]. Comparing to the ILL+Vogel model, the Huber+Mueller model shows a 3.5% increase in total flux and a small excess in the high energy part of the spectra. The flux uncertainty is reduced to 2% from 2.7% of

---

Editors: Jun Cao (caoj@ihep.ac.cn), Miao He (hem@ihep.ac.cn), Liangjian Wen (wenlj@ihep.ac.cn), and Weili Zhong (zhongwl@ihep.ac.cn)

Major Contributors: Ziyang Deng and Xinying Li

the ILL+Vogel model. The upward shift in the total flux introduces tension with short baseline reactor neutrino experiments, which is called Reactor Neutrino Anomaly [58].

The reactor antineutrinos are generally detected via the inverse beta decay (IBD) reaction  $\bar{\nu}_e + p \rightarrow n + e^+$ . The reaction cross section  $\sigma(E_\nu)$  is calculated to the order of  $1/M$  in Ref. [177]. The observable reactor neutrino spectrum is the multiplication of the neutrino flux per fission and the cross section, which is shown in Fig. 13-1 for the four isotopes.

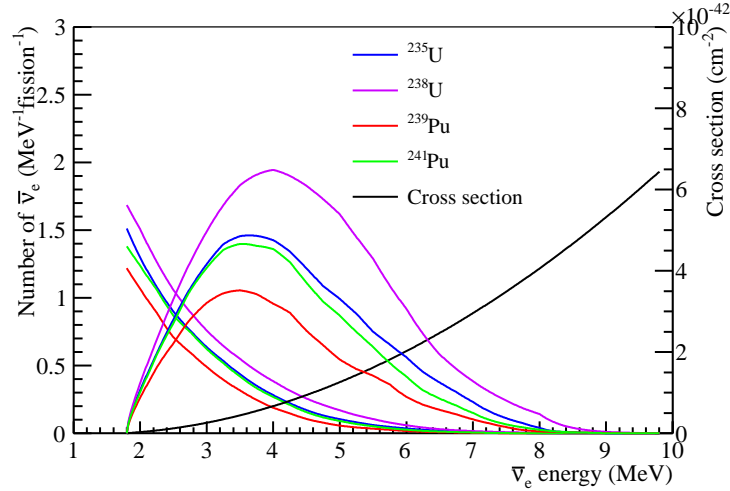


Figure 13-1: Neutrino yield per fission, the interaction cross section of the inverse beta decay, and the observable spectra of the listed isotopes.

### 13.1.3 Reactor Power and Fuel Evolution

Fission rates of isotopes (at nominal power) as a function of time, as well as the fuel composition, can be obtained via core simulation. Since the fission rates are correlated with the reactor power, normally we use fission fraction in the core simulation, which is the ratio of the fission rate of an isotope over the total fission rate. Fresh fuel contains only uranium. The plutonium isotopes are gradually generated via the neutron capture of  $^{238}\text{U}$  and the subsequent evolution. Generally a PWR core refuels every 12-18 months, and replaces 1/4 to 1/3 fuel assemblies each time. To describe the fuel evolution as a function of time, burnup of the fuel is defined as

$$B(t) = \frac{W \cdot D}{M_{init-U}}, \quad (13.1)$$

where  $W$  is the fission power of the fuel,  $D$  is the fissioning days, and  $M_{init-U}$  is the initial mass of the uranium. The unit of the burnup is  $\text{MW} \cdot \text{d}/\text{ton}$ . Since a fuel assembly will stay in the core for 3-4 refueling cycles, and fuel assemblies have different burnup, a more convenient variable “cycle burnup” is defined to describe the aging of a reactor core within a refueling cycle. The cycle burnup has the same expression as Eq. (13.1), but with  $W$  being the total nuclear power of the reactor core,  $D$  being the fissioning days since the beginning of the refueling cycle, and  $M_{init-U}$  being the total initial uranium mass in the reactor core. Cycle burnup can be calculated by using the daily thermal power which are obtained by the power monitoring system.

The most accurate thermal power measurement is the Secondary Heat Balance method. Detailed description of this measurement can be found, for example, in Ref. [462]. It is an offline

measurement, normally done weekly or monthly. Primary Heat Balance test are online thermal power measurement. Normally it is calibrated to the Secondary Heat Balance measurement weekly. Daya Bay power plants control the difference between these two measurements to less than 0.1% of the full power. This data is good for neutrino flux analysis. To 0.1% level, it can be taken as the Secondary Heat Balance measurement. The power plants also monitor the ex-core neutron flux, which gives the nuclear power. This monitoring is online, for safety and reactor operation control. It is normally calibrated to the Primary Heat Balance measurement daily. The ex-core neutron measurement is less accurate, controlled to be less than 1.5% of the full power by the Daya Bay power plant. Using the Primary Heat Balance measurement, the thermal power uncertainty is estimated to be 0.5% per core for the Daya Bay experiment [30–32]. The Yangjiang and Taishan NPPs use similar reactors as the Daya Bay NPP. The power uncertainty is also taken as 0.5% for JUNO in the analyses.

The reactor power plants simulate the fuel evolution in every refueling cycle to reconfigure the location of the fuel assemblies of different burnup in the core. Simulations are done for possible configurations before the refueling to optimize the safety factor and operation efficiency, and are redone with actual power history and in-core neutron flux measurements to better estimate the burnup of the fuel assemblies when the cycle completes. Fission fraction and fuel composition can be extracted from these simulations. The simulation is performed by Daya Bay power plants with a validated and licensed commercial software SCIENCE developed by CEA, France. Its core component is APOLLO2 [463]. Uncertainties of the simulation were estimated by comparing the simulated fuel composition at different burnup with isotopic analyses of spent fuel samples taking from the reactors. The uncertainties of the fission fractions reported by SCIENCE are estimated to be  $\sim 5\%$ . Another simulation package based on DRAGON [464], a public available software, was developed by the Daya Bay experiment to cross check the simulation done by the power plant and to evaluate the correlation of uncertainties.

The Yangjiang reactors are CPR1000+. The nuclear cores are almost identical to the Daya Bay cores (Framatone M310) and Ling Ao cores (CP1000, a derivative of M310). The fresh fuel enrichment is  $\sim 4.5\%$ . A refueling cycle lasts for 12-18 months. The Taishan reactors use the EPR technology of the French AREVA company. The fresh fuel enrichment is about 7.44%. A refueling cycle could be 18-22 months. When refueling for a new cycle, the fuel elements are configured in the reactor core around the center as symmetrical as possible, which makes the center of gravity being stable at the core center. The fission fractions versus burnup for the Tainshan core are simulated with DRAGON packages, and compared to the Daya Bay core, as shown in Fig. 13-2. Due to the different enrichment, there are slight differences between the Daya Bay (Yangjiang) core and the Taishan core. The uncertainty of the fission fraction will be taken as 5% for both core types, while further investigation will be done in the future.

### 13.1.4 Antineutrino Spectrum and Uncertainties

With the thermal power  $W_{th}$  and fission fractions of four main isotopes  $f_i$ , the expected neutrino flux emitted from a reactor is predicted as:

$$\Phi(E_\nu) = \frac{W_{th}}{\sum_i f_i e_i} \cdot \sum_i f_i \cdot S_i(E_\nu), \quad (13.2)$$

Where  $e_i$  and  $S_i(E_\nu)$  are the thermal energy released in each fission and the neutrino flux per fission for the  $i$ -th isotope, respectively. Eq. (13.2) is equivalent to the expression  $\sum_i F_i S_i(E_\nu)$  in the introduction since  $W_{th}/\sum_i f_i e_i$  is the total fission rate, and the fission rate of the  $i$ -th isotope is  $F_i = W_{th}/\sum_i f_i e_i \cdot f_i$ .

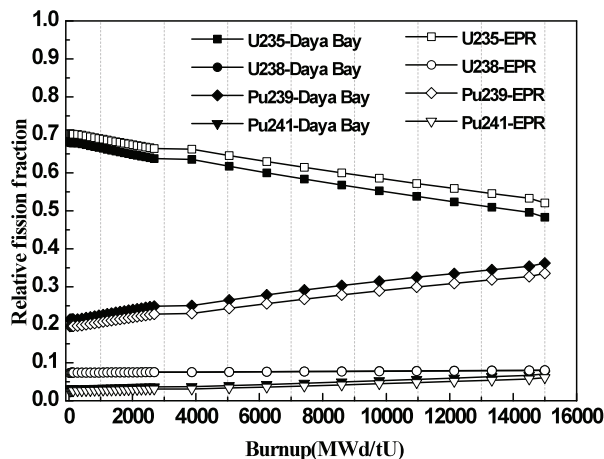


Figure 13-2: Simulation of the fission fractions in the Daya Bay and Taishan cores with DRAGON packages for a normal burnup cycle. The simulation assumes a 18 months refueling cycle and average disassembly burnup at 45 MW · d/ton. Differences between the Daya Bay and Taishan cores are due to fuel enrichment.

Fission energies of the four isotopes could be obtained by reactor core simulation or analytical calculation. The typical values and their uncertainties are listed in Tab. 13-1 which were calculated by Kopeikin *et al.* [465] and updated by Ma *et al.* [356] recently.

isotope	$^{235}\text{U}$	$^{238}\text{U}$	$^{239}\text{Pu}$	$^{241}\text{Pu}$
Kopeikin (MeV)	$201.92 \pm 0.46$	$205.52 \pm 0.96$	$209.99 \pm 0.60$	$213.60 \pm 0.65$
Ma (MeV)	$202.36 \pm 0.26$	$205.99 \pm 0.52$	$211.12 \pm 0.34$	$214.26 \pm 0.33$

Table 13-1: Energy release per fission of the main fissile isotopes.

The fission fractions predicted by the core simulation carry relatively large uncertainty. But they are not independent. On one hand, they are strongly constrained by the more accurate total thermal power. As a consequence, the uncertainty is greatly reduced. On the other hand, they are correlated in the fuel evolution. For example, if  $^{239}\text{Pu}$  is over-estimated,  $^{241}\text{Pu}$  will also be over-estimated since they come from the same neutron capture process on  $^{238}\text{U}$ . The correlations were studied with the DRAGON simulation by systematically varying the intermediate fuel composition. Tab. 13-2 shows the correlation of the fission fractions that were simulated at several burnup stages for Daya Bay cores [466]. Similar simulations will be done for JUNO.

The expected neutrino spectrum in the detector without oscillation effect is

$$S(E_\nu) = \frac{1}{4\pi L^2} \cdot \Phi(E_\nu) \cdot \epsilon \cdot N_p \cdot \sigma(E_\nu), \quad (13.3)$$

where  $L$  is the distance from the reactor to the detector,  $\epsilon$  is the detection efficiency,  $N_p$  is the target proton number, and  $\sigma(E_\nu)$  is the inverse  $\beta$  decay cross section. The calculated cross section relates to the neutron lifetime, whose uncertainty is 0.2%. The multiplication of cross section and total isotope antineutrino spectrum is defined as 'reaction cross section'.

	$^{235}\text{U}$	$^{238}\text{U}$	$^{239}\text{Pu}$	$^{241}\text{Pu}$
$^{235}\text{U}$	1.0	-0.22	-0.53	-0.18
$^{238}\text{U}$	-0.22	1.0	0.18	0.26
$^{239}\text{Pu}$	-0.53	0.18	1.0	0.49
$^{241}\text{Pu}$	-0.18	0.26	0.49	1.0

Table 13-2: Correlation coefficients of isotope fission fraction uncertainties.

In ILL measurements, fissile samples were exposed in neutrons for one to two days. Therefore, the beta decays from some of the long-lived fission fragments not reaching equilibrium were missed in the ILL measurements. The long lived fission fragments accumulate in core during operation and contribute an extra antineutrino flux at low energy. This effect can be evaluated with nuclear database by using the cumulative yields of the known long-lived ( e.g. lifetime longer than 10 hours) fission fragments which has Q-values above the inverse  $\beta$  decay threshold (1.8 MeV ) [102]. On the other hand, after refueling the reactor cores, the spent fuel taken out from the previous cycle are moved to a cooling pool adjacent to the core. The long-lived isotopes will continue decay and generate antineutrinos. This contributions to the total antineutrinos can also be evaluated by using the cumulative yields [360, 467–470]. The contribution to IBD events from off-equilibrium of long-lived isotopes in reactor cores and from spent fuel pools in the Daya Bay experiment were evaluated to be both less than 0.3%. The uncertainties of them were taken as 100%, or 0.3% in terms of the total IBD events. For JUNO experiment, the similar calculation could be done with the reactor core and spent fuel pool information. The total neutrino spectrum should then be modified by including the contributions from the off-equilibrium long-lived isotopes in reactor cores and from the spent fuel pools,

$$S_\nu(E_\nu) = S(E_\nu) + S_{\text{offEq}} + S_{\text{SNF}}. \quad (13.4)$$

The event rate of the IBD reactions in the  $k$ -th energy bin  $[E_k^{\min}, E_k^{\max}]$  of a detector from several reactor cores is given by

$$R_k(E_\nu) = \sum_r \frac{1}{4\pi L_r^2} \cdot \frac{W_{th}^r}{\sum_i f_i^r e_i^r} \cdot \sum_i f_i^r \int_{E_k^{\min}}^{E_k^{\max}} S_i(E_\nu) \cdot \sigma(E_\nu) dE_\nu \cdot \epsilon \cdot N_p, \quad (13.5)$$

where  $k$  is the bin index and  $r$  is the index of the reactor cores.

The flux uncertainties can be propagated using Eq. (13.5). The reaction cross section uncertainties are considered to be correlated between isotopes. The reactor-related uncertainties are categorized into the reactor-correlated ones and reactor-uncorrelated ones, respectively. The correlated uncertainties includes those from energy per fission (0.2%) and reaction cross section (2.7%). The uncorrelated uncertainties are the combination of the thermal power (0.5%), fission fraction (0.6% with the thermal power constraint and correlation among isotopes), off-Equilibrium (0.3%) and spent fuel (0.3%).

The shape uncertainties can also be propagated using Eq. (13.5). There are two categories basically, energy dependent and energy independent uncertainties. The energy independent uncertainties are same as flux uncertainties, such as power and fission energies. The energy dependent uncertainties includes the uncertainties of antineutrino flux per fission of each fuel isotope, the uncertainties of off-equilibrium and SNF corrections, and the uncertainties introduced by fission

fraction uncertainty. These energy dependent uncertainties are categorized as bin-to-bin correlated and uncorrelated uncertainties. The  $^{235}\text{U}$ ,  $^{239}\text{Pu}$  and  $^{241}\text{Pu}$  spectra have both bin-to-bin uncorrelated uncertainties (statistical uncertainties) and bin-to-bin correlated uncertainties (systematic uncertainties from ILL measurements, and beta-antineutrino conversion), while the  $^{238}\text{U}$  spectrum only has bin-to-bin correlated uncertainties since it is from theoretical calculation. The off-equilibrium uncertainties, spent fuel uncertainties and fission fraction uncertainties are treated as energy correlated, but reactor uncorrelated.

### 13.1.5 Model Independent Prediction of the Antineutrino Spectrum

Recently, Daya Bay [105], RENO [106] Double Chooz [107] have found significant local inconsistency (at  $4 \sim 6$  MeV) between the measured reactor neutrino spectrum and the predicted spectrum, no matter using the ILL+Vogel or the Huber+Mueller flux model. The largest deviation reaches  $\sim 10\%$ , significantly larger than the expected uncertainty 2-3%. In 2014, there were new evaluations of the shape uncertainties of the antineutrino flux per fission from ILL measurement, which claimed that the uncertainties of the inversion from the  $\beta$  spectra to the antineutrino spectrum is underestimated. The energy dependent uncertainty should be no less than 4% [391]. Further more, the latest calculation of the antineutrino flux per fission with the  $\beta$  branch information in database of the fission fragments indicates similar local structure of isotope antineutrino spectrum as the measurements in the reactor antineutrino experiments [104].

One possible way to do more precise prediction of the expected antineutrino spectrum for JUNO is to use the measured positron spectrum of the Daya Bay experiment directly. The principle is to treat Daya Bay as a virtual near detector of the JUNO experiment. The reactor cores of Yangjiang and Taishan will be constructed and operated by the same company as Daya Bay. Similar core technology and simulation enable a virtual near/far relative measurement, where the reactor related uncertainties are almost cancelled, and the relative detector uncertainties between near and far site is the main contribution of final uncertainty. Detector simulation would help to determine the relative uncertainty of energy scale between the antineutrino detectors of JUNO and Daya Bay. The current absolute energy scale uncertainty of Daya Bay is within 1% and the energy non-linearity has been determined to  $\sim 1\%$ .

We expect that the shape uncertainties of the measured positron spectrum for JUNO could be determined to 1% with further studies. As an alternative method, the antineutrino spectrum from unfolding of the direct measurement of Daya Bay could be also used for spectrum prediction. The unfolded spectrum is independent of the Daya Bay detector effect, could be used more generally, such as comparing with different reactor models of antineutrino spectrum, and predicting the measured positron spectrum by applying their own detector effects of the experiments [105].

## 13.2 Monte Carlo Simulation and Reconstruction

### 13.2.1 Monte Carlo Simulation

A Geant4 [321, 472] based computer simulation (Monte Carlo, MC) of the detectors and readout electronics is used to study the detector response and optimize the detector design. It consists of five components: kinematic generator, detector simulation, electronics simulation, trigger simulation and readout simulation. The JUNO MC is developed based on the Daya Bay MC simulation, which has been carefully tuned to match observed detector distributions, such as the liquid scintillator light yield, charge response, and energy non-linearity.

The antineutrino generator reads from a database that stored the reactor antineutrino spectra.



The cosmic muons in the underground laboratory are simulated using a digitized topographic map of the site and Muon Simulation Code [473] (MUSIC), which calculates the energy loss and multiple scattering due to the rock overburden. The muon generator for Geant4 reads randomly from a library of muon events generated with MUSIC. The software generators for the calibration sources and the simulation of the decay sequences for natural radionuclides found in our detectors are customized based on data from the ENDF database [474].

All physical processes in Geant4 relevant to the reactor neutrino experiment have been validated. The gamma spectra of neutron capture and muon capture on many nuclei are incorrectly modeled in Geant4. Since a systematic correction is complex, we implement corrections on a case by case basis. Furthermore, the simulation of thermal neutron scattering is improved by considering the molecular binding energy of the scattering nuclei.

The details of the electronics simulation can be found in Ref. [475, 476]. Using the timing and number of photoelectron (p.e.) generated in PMTs, an analog signal pulse for each PMT is generated and tracked through the digitization process, taking into account the non-linearity, dark rate, pre-pulsing, after-pulsing and ringing of the waveform. The simulated analog pulse is then used as input to a trigger system simulation.

Most of the properties of the detector materials are borrowed from the Daya Bay experiment. The elemental concentrations of the liquid scintillator were measured and incorporated into the MC. All relevant optical properties of the detector components are derived from measurements, including refractive indices of the liquids as well as the acrylic or nylon components, time constants and photon emission spectra of the liquid scintillator, and the reflectivity of the detector materials. Photon absorption and re-emission processes in liquid scintillator are modeled based on measurements in order to properly simulate the propagation of scintillation photons and contributions from Cherenkov process.

The major differences from the Daya Bay MC include the detector geometry, the attenuation length and the rayleigh scattering length of the liquid scintillator, and the PMT geometry and quantum efficiency. The detector is spherical, of a diameter of 35.4 m for the liquid scintillator container. Currently there are two options for the central detector to be determined with R&D. One use an acrylic ball as the LS container. PMTs are installed on a truss and look inward in the water buffer. The water cherenkov detector for muon veto is optically separated from the water buffer for the center detector. Another option is a nylon balloon as the LS container. PMTs are installed on the inner wall of a stainless steel sphere and shielded with non-scintillation liquid. Both options are implemented in the MC and simulated to compare the detector performance. To achieve an energy resolution of  $3\%/\sqrt{E}$ , 17746 20-inch PMTs corresponding to 77% photocathode coverage are used. The quantum efficiency is set to be 35%. The attenuation length of the LS is set to be 20 m, larger than 15 m for the Daya Bay. Recently we have measured the rayleigh scattering length of the liquid scintillator to be  $\sim 30$  m. The light yield of the liquid scintillator is tuned to the data of the Daya Bay detector. We find that the  $3\%/\sqrt{E}$  energy resolution is achieved with the above settings. Therefore, they served as the requirements for the JUNO detector design. The baseline parameters of the JUNO MC are shown in Tab. 13-3, as well as in the following.

**Detector dimensions.** The scintillator volume is 35.4 m in diameter, surrounded by a buffer medium with a thickness of 1.5 m, either water in the acrylic ball option or non-scintillation oil in the balloon option. PMTs are assumed to be 20-inch PMTs, with their bulk center located at 19.5 m in radius. The number of PMTs is 17746. The water pool, as the cherenkov detector for muons, is a cylinder of 42.5 m in diameter and 42.5 m in height.

**Light emission.** The light yield of the liquid scintillator is about 10000 photons per MeV. The exact value may vary by the order of 10% depending on the scintillator solvent and fluor concentrations. For different settings in the simulation, we normalize the light yield to the response

target mass	20 kt
target radius	17.7 m
target density	0.856 g/cm <sup>3</sup>
mass fraction of C	0.8792
mass fraction of H	0.1201
light yield	10400 /MeV
birks1	$6.5 \times 10^{-3}$ g/cm <sup>2</sup> /MeV
birks2	$1.5 \times 10^{-6}$ (g/cm <sup>2</sup> /MeV) <sup>2</sup>
emission time $\tau_1$	4.93 ns
emission time $\tau_2$	20.6 ns
emission time $\tau_3$	190 ns
$\tau_1$ weight	0.799
$\tau_2$ weight	0.171
$\tau_3$ weight	0.03
attenuation length	20 m
absorption length	60 m
rayleigh scat. length	30 m
optical coverage	75%
quantum efficiency	35%

Table 13-3: Baseline parameters in the JUNO MC simulation.

of the Daya Bay detector. The light output also depends on the energy loss rate  $dE/dx$  of the ionizing particle, resulting in a quenched visible energy. This effect is taken into account by the Birks' law,

$$\text{Quenched Energy} = \frac{\text{Energy Deposit}}{1 + C_1 \frac{dE}{dx} + C_2 \left(\frac{dE}{dx}\right)^2}. \quad (13.6)$$

The light is emitted following a time profile described by a superposition of exponential decays. The simulation uses a description of three components with time constants  $\tau_1$ ,  $\tau_2$ , and  $\tau_3$ , respectively.

**Light propagation.** The scintillation light is produced in a relatively broad span of wavelengths. The emission spectrum of liquid scintillator is from the Daya Bay measurements. The photon absorption, re-emission, and Rayleigh scattering are simulated.

**Light detection.** The baseline design for JUNO assumes an photocathode coverage of 77% and 35% peak quantum efficiency of the PMTs. The quantum efficiency spectrum is scaled from the Daya Bay PMTs.

Based on these configurations, the p.e. yield per deposited energy can be obtained as a function of the vertex position inside the target volume. The p.e. yield significantly depends on vertex position, the transparency of liquid scintillator container, and the refractive indices of liquid materials, as shown in Figure 13-3.

### 13.2.2 Reconstruction and performance

Since the energy of the reactor antineutrino is mainly below 10 MeV, it can be approximated as a point-like source in the JUNO detector. The vertex can be determined by the measurement of

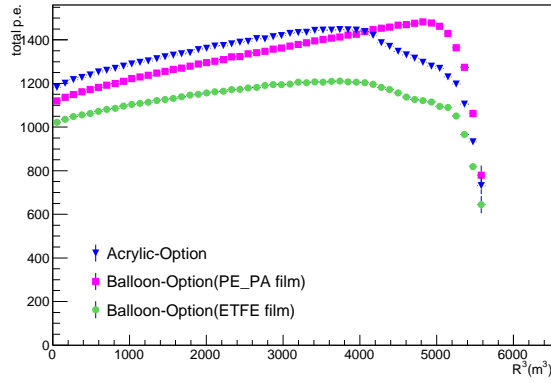


Figure 13-3: Total p.e. for 1 MeV gamma uniformly generated in the central detector.

the time of flight to each PMT. In case of multiple photoelectrons that hit on the same PMT, only the first hit time is used in the reconstruction because the latter ones may be distorted due to the response of electronics. The vertex resolution depends on the PMT time resolution as well as the time spread of the light emission of the liquid scintillator.

The performance of the vertex reconstruction is studied using single  $\gamma$  or positron uniformly distributed in the detector. Fig. 13-4 (left) shows the vertex resolution as a function of visible energy, assuming a PMT time resolution of 1 ns. Fig. 13-4 (right) shows the impact of the PMT time resolution. It dominates the vertex performance when larger than 4 ns, while the decay time of the scintillation light becomes significant when it is better than 2 ns.

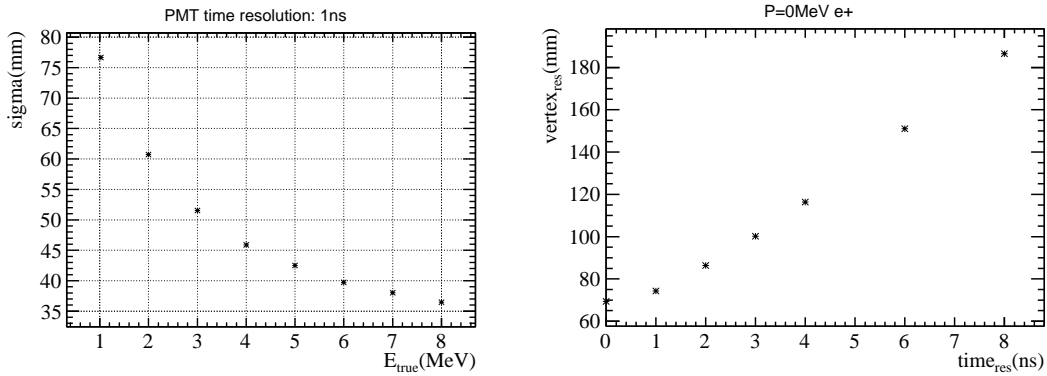


Figure 13-4: Vertex resolution as a function of energy (left) and PMT time resolution (right).

The visible energy in the detector is reconstructed by comparing the measured charge of each PMT with the expectation, which relies on the event vertex, the light emission and propagation, and the photon detection with PMTs. The energy solution as a function of the visible energy can be described with a 3-parameter function

$$\frac{\sigma}{E} = \sqrt{\left(\frac{p_0}{\sqrt{E}}\right)^2 + p_1^2 + \left(\frac{p_2}{E}\right)^2}, \quad (13.7)$$

where  $E$  refers to the visible energy in MeV,  $p_0$  is the leading term dominated by the photon statistics,  $p_1$  and  $p_2$  come from detector effects such as PMT dark noise, variation of the PMT QE,

and the reconstructed vertex smearing. Toy MC samples are generated to study each term, which is shown in Tab. 13-4.

effects	p0	p1	p2
statistical fluctuation	2.68	0	0
PMT charge resolution(30%)	2.8	0	0
PMT dark noise(50kHz per PMT)	2.68	0	0.9
PMT QE difference(20%)	2.68	0.26	0
vertex smearing(11cm @1MeV)	2.68	0.17	0

Table 13-4: Factors that impact to the energy resolution.

Muon tracking is important for the cosmogenic background rejection and the atmospheric neutrino study. Similar to the vertex reconstruction, a track is determined by the the first hit time of each PMT. For the muons that go through the detector, the PMTs around the injection point and the outgoing point see more lights and form two clusters, which can be used to estimate the initial tracking parameters. Toy MC samples are used to estimate the tracking performance. Assuming the intrinsic PMT time resolution is better than 4 ns, for a muon track longer than 5 m (i.e.  $> 1$  GeV), the track length resolution is better than 0.5% and the angular resolution is better than 1 degree. For a muon track between 1 m and 5 m (i.e.  $0.2 \text{ GeV} < E < 1 \text{ GeV}$ ), the track length resolution is better than 1% and the angular resolution is better than 10 degree. Tracking of electrons and identification of muon/electron are still under development.

### 13.3 Antineutrino Detection in JUNO

Antineutrinos from reactors are detected by LS via the inverse beta decay reaction (shorten as IBD in the following contents):

$$\bar{\nu}_e + p \rightarrow e^+ + n$$

The prompt positron signal and delayed neutron capture signal constitute an anti-neutrino event. In LS, neutron are captured by free protons or Carbon with a capture time of  $\sim 216\mu\text{s}$  obtained by MC simulation. The delayed signal, 2.2 MeV  $\gamma$ -ray emitted after neutron captured on proton, can be contaminated by the natural radioactivity. Thus, a triple-coincidence criteria of energy, time and space is necessary to suppress the accidental background.

Full MC simulation and reconstruction is performed to obtain the antineutrino detection efficiency. The efficiency of (0.7 MeV, 12 MeV) energy cut on prompt signal is 100%. The efficiency of (1.9 MeV, 2.5 MeV) cut on the delayed signal is 97.8%, and the in-efficiency is mainly due to neutron-capture on Carbon. The efficiency for different time-, and space- correlation cuts are listed in Tab. 13-5 and Tab. 13-6.

Time Cut ( $\mu\text{s}$ )	300	500	1000	1500	2000
Efficiency (%)	74.55	89.57	98.68	99.49	99.60

Table 13-5: IBD efficiency of different time cuts from MC simulation.

Distance Cut (m)	0.5	1	1.5	2.0	2.5
Efficiency (%)	76.66	95.90	99.08	99.74	99.89

Table 13-6: IBD efficiency of different distance cuts from MC simulation.

## 13.4 Backgrounds in JUNO

### 13.4.1 Cosmic Muons at JUNO experimental site

For underground neutrino observatories, sufficient amount of overburden above the detector is the most effective approach to suppress the cosmogenic backgrounds. The JUNO experimental site is chosen to be under a 286-m high mountain, and the detector will be at -480 m depth. The mountain profile is shown in Figure. 13-5, converted from a high precision, digitized topographic map. The JUNO experimental site is at the coordinate of (0, 0, -480 m) in the map. The shortest distance from the mountain surface is 664 m. A modified Gaisser formula [477] is used to describe the muon flux at sea level. With the mountain profile data, the cosmic muons are transported from the sea level to the underground JUNO detector site using the MUSIC [473] package. A uniform rock density of  $2.60\text{g/cm}^3$  is assumed. The simulated muon rate and flux is shown in Tab. 13-7.

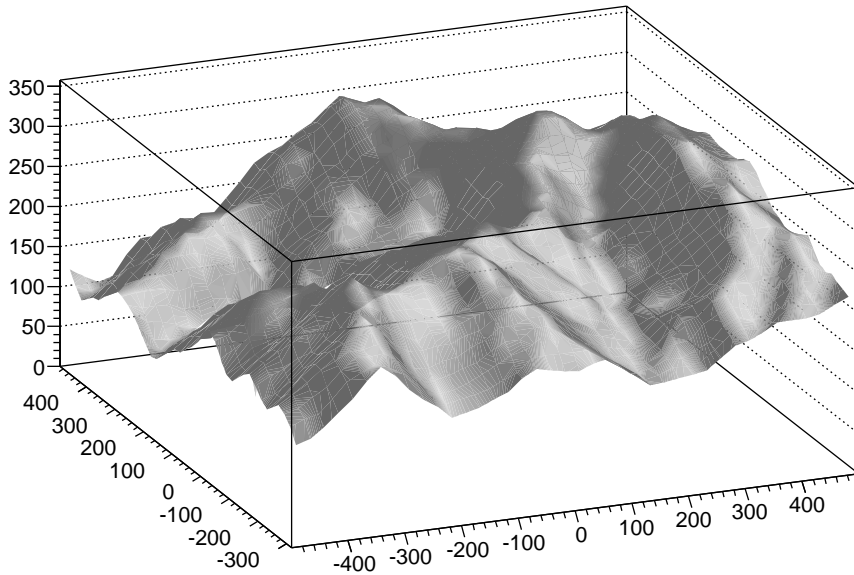


Figure 13-5: Mountain profile at the JUNO experimental site.

Overburden	Muon flux	$\langle E_\mu \rangle$	$R_\mu$ in CD	$R_\mu$ in WP
748 m	$0.003 \text{ Hz/m}^2$	215 GeV	3.0 Hz	1.0 Hz

Table 13-7: The simulated muon flux and mean energy at JUNO site.

A parametrization method [478] is used to investigate the muon bundles, and it gives 20% probability of muon bundle at the depth of JUNO detector. The probability of multiple muon

bundle reduces to 10% after taking into account the JUNO detector geometry. MC simulation indicates the muons in the bundle are almost in parallel within  $0.2^\circ$ . The multiplicity of muons going through JUNO detector is shown in Table. 13-8.

Multiplicity	1	2	3	4	5	6
Fraction	89.6%	7.7%	1.8%	0.6%	0.3%	0.07%

Table 13-8: The multiplicity of muons going through JUNO detector.

### 13.4.2 Neutrons

The neutron production depends on the muon flux and the average energy at the JUNO detector. Full muon simulation using Geant4 gives  $\sim 1.8$  Hz spallation neutrons in JUNO LS.

Neutron produced by muons passing through the JUNO LS will be tagged with almost 100% efficiency. Neutron produced in water buffer can be tagged with an efficiency of 99.8%, since their parent muons pass through the muon systems. The 0.2% inefficiency is mainly from the corner clipping muons. The tagged neutrons can be rejected by sufficient time veto after the tagged muons to suppress the possible correlated background.

Neutrons produced by the un-tagged corner clipping muons and in the surrounding rocks arise from the muons missing muon systems, have to traverse at least 3.2 m for the “Sphere Acrylic” option (or 2.5 m for “Balloon” option) to reach JUNO LS. The “un-tagged” neutrons can enter LS and produce prompt proton-recoil signal then captured by H or C in LS. These events, namely the fast neutron events, can mimic the anti-neutrino signal as correlated backgrounds. A full MC simulation is performed to propagate the neutrons produced by cosmic muons in water pool and surrounding rocks, and the fast neutrons mimicking the anti-neutrino events are estimated to be  $\sim 0.1/\text{day}$ .

### 13.4.3 Cosmogenic Isotopes

In the liquid scintillator, the energetic cosmic muons and subsequent showers can interact with  $^{12}\text{C}$  and produce radioactive isotopes with  $Z \leq 6$  by electromagnetic or hadronic processes. Among them,  $^9\text{Li}$  and  $^8\text{He}$  with half-lives of 0.178 s and 0.119 s, respectively, are the most serious correlated background source to reactor anti-neutrinos, because they can decay by emitting both a beta and a neutron which mimics as an anti-neutrino signal. The estimation of  $^9\text{Li}$  and  $^8\text{He}$  is discussed in detail in Section 2.2.2. Other isotopes, such as  $^{11}\text{Li}$ ,  $^{12}\text{Be}$ ,  $^{14}\text{B}$ ,  $^{16}\text{C}$ ,  $^{17}\text{N}$  and  $^{18}\text{N}$ , are also beta-neutron emitters but have much less contribution to the background.

The other long-lived cosmogenic isotopes have beta decay without an accompanying neutron. They can not form correlated backgrounds by themselves but can contribute the neutron-like signal if they have beta decay energy in the 1.9-2.5 MeV range. Measuring the isotopes production yield in JUNO detector is useful for understanding the muon shower spallation processes. The rates of those cosmogenic radioactive isotopes from FLUKA MC simulation are listed in Table. 13-9. Recently there are measurements from KamLAND [109] and Borexino [305]. Physics-driven model is built to analyze the cosmogenic backgrounds in Super-K [307, 308], which could significantly reduce the backgrounds, and also increase the live time by well defining the shower position. Cosmogenic backgrounds in JUNO detector will be elaborated with these studies.

Isotopes	Q (MeV)	$T_{1/2}$	Rate (per day)
$^3\text{H}$	0.0186 ( $\beta^-$ )	12.31 year	$1.14 \times 10^4$
$^6\text{He}$	3.508 ( $\beta^-$ )	0.807 s	544
$^7\text{Be}$	$Q_{EC}=0.862$ (10.4% $\gamma$ , $E_\gamma = 0.478$ )	53.22 day	5438
$^8\text{He}$	10.66 ( $\beta^- \gamma$ : 84%), 8.63 ( $\beta^- n$ : 16%)	0.119 s	11
$^8\text{Li}$	16.0 ( $\beta^-$ )	0.839 s	938
$^8\text{B}$	16.6 ( $\beta^+$ )	0.770 s	225
$^9\text{Li}$	13.6 ( $\beta^-$ : 49%), 11.94 ( $\beta^- n$ : 51%)	0.178 s	94
$^9\text{C}$	15.47 ( $\beta^+ p$ : 61.6%, $\beta^+ \alpha$ : 38.4%)	0.126 s	31
$^{10}\text{Be}$	0.556 ( $\beta^-$ )	1.51e6 year	1419
$^{10}\text{C}$	2.626 ( $\beta^+ \gamma$ )	19.29 s	482
$^{11}\text{Li}$	20.55 ( $\beta^- n$ : 83%, $\beta^- 2n$ : 4.1%)	0.00875 s	0.06
$^{11}\text{Be}$	11.51 ( $\beta^- \gamma$ : 96.9%), 2.85 ( $\beta^- \alpha$ : 3.1%)	13.76 s	24
$^{11}\text{C}$	0.960 ( $\beta^+$ )	20.36 min	$1.62 \times 10^4$
$^{12}\text{Be}$	11.708 ( $\beta^- \gamma$ , $\beta^- n$ : 0.5%)	0.0215 s	0.45
$^{12}\text{B}$	13.37 ( $\beta^- \gamma$ )	0.0202 s	966
$^{12}\text{N}$	16.316 ( $\beta^+ \gamma$ )	0.0110 s	17
$^{13}\text{B}$	13.437 ( $\beta^- \gamma$ )	0.0174 s	12
$^{13}\text{N}$	1.198 ( $\beta^+$ )	9.965 min	19
$^{14}\text{B}$	20.644 ( $\beta^- \gamma$ , $\beta^- n$ : 6.1%)	0.0126 s	0.021
$^{14}\text{C}$	0.156 ( $\beta^-$ )	5730 year	132
$^{15}\text{C}$	9.772 ( $\beta^-$ )	2.449 s	0.6
$^{16}\text{C}$	8.010 ( $\beta^- n$ : 99%)	0.747 s	0.012
$^{16}\text{N}$	10.42 ( $\beta^- \gamma$ )	7.130 s	13
$^{17}\text{N}$	8.680 ( $\beta^- \gamma$ : 5%), 4.536 ( $\beta^- n$ : 95%)	4.173 s	0.42
$^{18}\text{N}$	13.896 ( $\beta^- \gamma$ : 93%), 5.851 ( $\beta^- n$ : 7%)	0.620 s	0.009
neutron			155 000

Table 13-9: The estimated rates for cosmogenic isotopes in JUNO LS by FLUKA simulation, in which the oxygen isotopes are neglected. The decay modes and Q values are from TUNL Nuclear Data Group [479].

#### 13.4.4 Natural Radioactivity

Natural radioactivity exists in the material of JUNO detector components and its surroundings. Particular care need be taken to select low radioactivity materials and design the passive shielding to control the radioactivity background. For JUNO experiment, the radioactivity comes from various sources. For simplicity, the radioactive isotopes  $^{238}\text{U}$ ,  $^{232}\text{Th}$ ,  $^{222}\text{Rn}$ ,  $^{85}\text{Kr}$ ,  $^{60}\text{Co}$ ,  $^{40}\text{K}$  are shorten as U, Th, Rn, Kr, Co, K in the following text. The radioactive sources include:

- U/Th/K in the rocks around the detector hall
- U/Th/K and Rn dissolved in the water buffer
- U/Th/K/Co in the stainless steel (vessel or strut)

- Rn and Kr in air
- U/Th/K in the PMT glass
- U/Th/K in the liquid scintillator container (acrylic or polymer film)
- U/Th/K/Kr/Ar in the liquid scintillator
- Dust and other impurities

In the following, the rate of singles means signals from radioactivity depositing  $>0.7$  MeV of visible energy in LS.

Assuming the radioactivity of the rock at JUNO experimental site is similar as that measured at Daya Bay site:  $\sim 10$  ppm for U,  $\sim 30$  ppm for Th and  $\sim 5$  ppm for K. Since a full MC simulation would be extremely time consuming, thus a numerical calculation is performed to estimate the effect of the rock radioactivity: 1) divide the 50 cm-thick rock around the water pool into small voxels; 2) the activities of  $\gamma$  rays with different energies are calculated for each voxel by using the radioactivity generator; 3) then for each gamma energy, the effective solid angle of each voxel to the LS detector is calculated by taking into account the attenuation of different water thickness; 4) in the end the singles rate is obtained by summing the contributions from all voxels. With the shielding of 3.2 meter buffer, there are  $\sim 0.61$  Hz,  $\sim 6.74$  Hz and  $\sim 0.07$  Hz singles rates in all LS volume for U/Th/K, respectively. After fiducial volume cut ( $R < 17.2$  m), the total singles rate reduces to 0.98 Hz.

The water buffer of JUNO will be circulated and purified to achieve a long absorption length for Cherenkov photons as well as low radioactivity. In addition, there will be nitrogen flow on the top of water pool and anti-Rn liner (e.g, 2 mm HDPE film) on the water pool walls to control Radon permeation into water buffer. In the ‘‘Acrylic Sphere’’ option of central detector, water acts as the buffer liquid and is just outside LS, thus the Radon dissolved in water will contribute more singles than the ‘‘Balloon’’ option. A MC simulation gives 16 Hz singles rate in all LS volume if the Radon concentration in water is  $0.2$  Bq/m<sup>3</sup>, and the rate will reduce to 1.3 Hz inside the  $R < 17.2$ m volume.

Based on the experience from the existing neutrino experiments, the projected radioactivity of detector materials such as PMT glass, acrylic, polymer film, steel and copper is listed in Table. 13-10.

Detector material	<sup>238</sup> U	<sup>238</sup> Th	<sup>40</sup> K	<sup>60</sup> Co
PMT glass	22 ppb	20 ppb	3.54 ppb	-
Acrylic	10 ppt	10 ppt	10 ppt	-
Polymer film	2 ppt	4 ppt	1 ppt	-
Steel	0.096 ppb	1.975 ppb	0.049 ppb	0.002 Bq/kg
Copper	1.23 mBq/kg	0.405 mBq/kg	0.0377 mBq/kg	-

Table 13-10: The estimated radioactivity of JUNO detector construction materials.

Above external radioactivity can be rejected by proper fiducial volume cut since their energy deposits are mainly at the LS edge. Thus, the internal LS radio-purity is very important to the JUNO experiment and should be well controlled. The fractional distillation process at the last step of raw LAB production and water extraction of the fluors are necessary to improve the radio-purity of raw LS materials. There will be nitrogen protection during LS production and handling to



suppress Radon contamination. In addition, the residual Radon contamination will lead to non-equilibrium isotope  $^{210}\text{Pb}$  (and the subsequent  $^{210}\text{Bi}$  decay) which has 22-year half life. The  $^{210}\text{Pb}$  isotope is the dominant background in searching solar neutrinos, as discussed in Section.6. On-line purification, such as distillation, is required to remove  $^{210}\text{Pb}$  from LS to open the opportunity to observe  $^7\text{Be}$  solar neutrino. In the JUNO experiment, an initial purity level of  $10^{-15}$  g/g U/Th,  $10^{-16}$  g/g K and  $1.4 \cdot 10^{-22}$  g/g  $^{210}\text{Pb}$  can be achieved without distillation. After setting up the on-line distillation, we believe two orders of magnitude better purity level can be achieved:  $10^{-17}$  g/g U/Th,  $10^{-18}$  g/g K and  $10^{-24}$  g/g  $^{210}\text{Pb}$ . The purity level of other isotope such as  $^{85}\text{Kr}$  and  $^{39}\text{Ar}$  is also listed.

LS	$^{238}\text{U}$	$^{238}\text{Th}$	$^{40}\text{K}$	$^{210}\text{Pb}$	$^{85}\text{Kr}$	$^{39}\text{Ar}$
No distillation	$10^{-15}$ g/g	$10^{-15}$ g/g	$10^{-16}$ g/g	$1.4 \cdot 10^{-22}$ g/g	$50 \mu\text{Bq}/\text{m}^3$	$50 \mu\text{Bq}/\text{m}^3$
After distillation	$10^{-17}$ g/g	$10^{-17}$ g/g	$10^{-18}$ g/g	$10^{-24}$ g/g	$1 \mu\text{Bq}/\text{m}^3$	-

Table 13-11: The estimated radioactivity of JUNO LS.

Full MC simulation is performed to obtain the singles rates from LS and other detector construction materials. Taking the ‘‘Acrylic Sphere’’ option of central detector, the singles rates in different volumes are listed in Table. 13-12.

Fiducial Cut	LS (Hz)	PMT (Hz)	Acrylic (Hz)	Strut (Hz)	Fastener (Hz)	Sum (Hz)
R<17.7 m	2.39	2.43	69.23	0.89	0.82	75.75
R<17.6 m	2.35	1.91	41.27	0.66	0.55	46.74
R<17.5 m	2.31	1.03	21.82	0.28	0.32	25.75
R<17.4 m	2.27	0.75	12.23	0.22	0.19	15.66
R<17.3 m	2.24	0.39	6.47	0.13	0.12	9.33
R<17.2 m	2.20	0.33	3.61	0.083	0.087	6.31
R<17.1 m	2.16	0.23	1.96	0.060	0.060	4.47
R<17.0 m	2.12	0.15	0.97	0.009	0.031	3.28

Table 13-12: The simulated singles rates from different detector components.

A fiducial volume cut is necessary to reject the external radioactivity thus reduce the accidental background and  $(\alpha, n)$  background, as discussed in Section.2. The total singles rate will reduce to  $\sim 7.6$  Hz if applying an R< 17.2 m fiducial volume cut, as shown in Table. 13-13.

Fiducial Cut	Detector Components	Radon in water	Rock	Total
R<17.2 m	6.3 Hz	1.3 Hz	0.98 Hz	7.63 Hz

Table 13-13: The summary of singles rates inside the Fiducial volume from the detector components, Radon in water and rock.

## Acknowledgement

The JUNO Experiment is supported by the Chinese Academy of Sciences, the Ministry of Science and Technology of China, the National Natural Science Foundation of China, Shanghai Jiao Tong University, and Tsinghua University in China, the Belgian Fonds de la Recherche Scientifique, FNRS in Belgium, the Charles University in Prague, Czech Republic, the CNRS National Institute of Nuclear and Particle Physics (IN2P3) in France, the Deutsche Forschungsgemeinschaft (DFG), Helmholtz Alliance for Astroparticle Physics (HAP), and Helmholtz Gemeinschaft (HGF) in Germany, the Istituto Nazionale di Fisica Nucleare (INFN) in Italy, the Joint Institute for Nuclear Research (JINR) in Russia, and the NSFC-RFBR joint research program. We acknowledge the generous support of the Guangdong provincial government and the Jiangmen and Kaiping Municipal Government. We are grateful for the ongoing cooperation from the China General Nuclear Power Group (CGNPC).

## References

- [1] S. Weinberg, Phys. Rev. Lett. **19**, 1264 (1967).
- [2] R. Davis, Jr., D. S. Harmer and K. C. Hoffman, Phys. Rev. Lett. **20**, 1205 (1968).
- [3] J. N. Bahcall, N. A. Bahcall and G. Shaviv, Phys. Rev. Lett. **20**, 1209 (1968).
- [4] J. N. Bahcall, W. F. Huebner, S. H. Lubow, P. D. Parker and R. K. Ulrich, Rev. Mod. Phys. **54**, 767 (1982).
- [5] Z. Maki, M. Nakagawa and S. Sakata, Prog. Theor. Phys. **28**, 870 (1962).
- [6] B. Pontecorvo, Sov. Phys. JETP **26**, 984 (1968) [Zh. Eksp. Teor. Fiz. **53**, 1717 (1967)].
- [7] N. Cabibbo, Phys. Rev. Lett. **10**, 531 (1963).
- [8] M. Kobayashi and T. Maskawa, Prog. Theor. Phys. **49**, 652 (1973).
- [9] Z. z. Xing and S. Zhou, “Neutrinos in particle physics, astronomy and cosmology,” Springer-Verlag, Berlin Heidelberg (2011).
- [10] W. Konetschny and W. Kummer, Phys. Lett. B **70**, 433 (1977).
- [11] M. Magg and C. Wetterich, Phys. Lett. B **94**, 61 (1980).
- [12] T. P. Cheng and L. F. Li, Phys. Rev. D **22**, 2860 (1980).
- [13] G. Lazarides, Q. Shafi and C. Wetterich, Nucl. Phys. B **181**, 287 (1981).
- [14] R. N. Mohapatra and G. Senjanovic, Phys. Rev. D **23**, 165 (1981).
- [15] P. Minkowski, Phys. Lett. B **67**, 421 (1977).
- [16] T. Yanagida, in *Proceedings of the Workshop on Unified Theory and the Baryon Number of the Universe*, edited by O. Sawada and A. Sugamoto (KEK, Tsukuba, 1979), p. 95.
- [17] M. Gell-Mann, P. Ramond, and R. Slansky, in *Supergravity*, edited by P. van Nieuwenhuizen and D. Freedman (North Holland, Amsterdam, 1979), p. 315.
- [18] S. L. Glashow, in *Quarks and Leptons*, edited by M. Lévy *et al.* (Plenum, New York, 1980), p. 707.
- [19] R. N. Mohapatra and G. Senjanovic, Phys. Rev. Lett. **44**, 912 (1980).
- [20] J. Schechter and J. W. F. Valle, Phys. Rev. D **22**, 2227 (1980).
- [21] R. Foot, H. Lew, X. G. He and G. C. Joshi, Z. Phys. C **44**, 441 (1989).
- [22] S. Antusch, C. Biggio, E. Fernandez-Martinez, M. B. Gavela and J. Lopez-Pavon, JHEP **0610**, 084 (2006) [hep-ph/0607020].
- [23] S. Antusch and O. Fischer, JHEP **1410**, 94 (2014) [arXiv:1407.6607 [hep-ph]].
- [24] Z. z. Xing, Phys. Lett. B **718**, 1447 (2013) [arXiv:1210.1523 [hep-ph]].

- [25] Y. F. Li and S. Luo, arXiv:1508.00052 [hep-ph].
- [26] K. A. Olive *et al.* [Particle Data Group Collaboration], Chin. Phys. C **38**, 090001 (2014).
- [27] F. Capozzi, G. L. Fogli, E. Lisi, A. Marrone, D. Montanino and A. Palazzo, Phys. Rev. D **89**, 093018 (2014) [arXiv:1312.2878 [hep-ph]].
- [28] D. V. Forero, M. Tortola and J. W. F. Valle, Phys. Rev. D **90**, no. 9, 093006 (2014) [arXiv:1405.7540 [hep-ph]].
- [29] M. C. Gonzalez-Garcia, M. Maltoni and T. Schwetz, JHEP **1411**, 052 (2014) [arXiv:1409.5439 [hep-ph]].
- [30] F. P. An *et al.* [Daya Bay Collaboration], Phys. Rev. Lett. **108**, 171803 (2012) [arXiv:1203.1669 [hep-ex]].
- [31] F. P. An *et al.* [Daya Bay Collaboration], Chin. Phys. C **37**, 011001 (2013) [arXiv:1210.6327 [hep-ex]].
- [32] F. P. An *et al.* [Daya Bay Collaboration], Phys. Rev. Lett. **112**, 061801 (2014) [arXiv:1310.6732 [hep-ex]].
- [33] E. Majorana, Nuovo Cim. **14**, 171 (1937).
- [34] W. H. Furry, Phys. Rev. **56**, 1184 (1939).
- [35] W. Rodejohann, Int. J. Mod. Phys. E **20**, 1833 (2011) [arXiv:1106.1334 [hep-ph]].
- [36] S. Dell’Oro, S. Marcocci and F. Vissani, Phys. Rev. D **90**, no. 3, 033005 (2014) [arXiv:1404.2616 [hep-ph]].
- [37] S. M. Bilenky and C. Giunti, Int. J. Mod. Phys. A **30**, no. 04n05, 1530001 (2015) [arXiv:1411.4791 [hep-ph]].
- [38] Y. F. Li and Z. z. Xing, Phys. Lett. B **695**, 205 (2011) [arXiv:1009.5870 [hep-ph]].
- [39] J. Bernabeu, S. Palomares Ruiz and S. T. Petcov, Nucl. Phys. B **669**, 255 (2003) [hep-ph/0305152].
- [40] A. S. Dighe and A. Y. Smirnov, Phys. Rev. D **62**, 033007 (2000) [hep-ph/9907423].
- [41] S. T. Petcov and M. Piai, Phys. Lett. B **533**, 94 (2002) [hep-ph/0112074].
- [42] X. Qian and P. Vogel, Prog. Part. Nucl. Phys. **83**, 1 (2015) [arXiv:1505.01891 [hep-ex]].
- [43] R. B. Patterson, arXiv:1506.07917 [hep-ex].
- [44] M. Fukugita and T. Yanagida, Phys. Lett. B **174**, 45 (1986).
- [45] W. Buchmuller, P. Di Bari and M. Plumacher, Annals Phys. **315**, 305 (2005) [hep-ph/0401240].
- [46] S. Davidson, E. Nardi and Y. Nir, Phys. Rept. **466**, 105 (2008) [arXiv:0802.2962 [hep-ph]].
- [47] M. Agostini *et al.* [GERDA Collaboration], Phys. Rev. Lett. **111**, no. 12, 122503 (2013) [arXiv:1307.4720 [nucl-ex]].

- [48] L. Bornschein [KATRIN Collaboration], eConf C **030626**, FRAP14 (2003) [hep-ex/0309007].
- [49] P. A. R. Ade *et al.* [Planck Collaboration], *Astron. Astrophys.* **571**, A16 (2014) [arXiv:1303.5076 [astro-ph.CO]].
- [50] Z. z. Xing and S. Zhou, *Phys. Lett. B* **737**, 196 (2014) [arXiv:1404.7021 [hep-ph]].
- [51] S. Luo and Z. z. Xing, *Phys. Rev. D* **90**, no. 7, 073005 (2014) [arXiv:1408.5005 [hep-ph]].
- [52] Y. L. Zhou, arXiv:1409.8600 [hep-ph].
- [53] Z. z. Xing and Y. L. Zhou, *Phys. Rev. D* **88**, 033002 (2013) [arXiv:1305.5718 [hep-ph]].
- [54] Z. z. Xing, Z. h. Zhao and Y. L. Zhou, arXiv:1504.05820 [hep-ph].
- [55] K. N. Abazajian, M. A. Acero, S. K. Agarwalla, A. A. Aguilar-Arevalo, C. H. Albright, S. Antusch, C. A. Argüelles and A. B. Balantekin *et al.*, arXiv:1204.5379 [hep-ph].
- [56] A. Aguilar-Arevalo *et al.* [LSND Collaboration], *Phys. Rev. D* **64**, 112007 (2001) [hep-ex/0104049].
- [57] A. A. Aguilar-Arevalo *et al.* [MiniBooNE Collaboration], *Phys. Rev. Lett.* **105**, 181801 (2010) [arXiv:1007.1150 [hep-ex]].
- [58] G. Mention, M. Fechner, T. Lasserre, T. A. Mueller, D. Lhuillier, M. Cribier and A. Letourneau, *Phys. Rev. D* **83**, 073006 (2011) [arXiv:1101.2755 [hep-ex]].
- [59] J. Kopp, P. A. N. Machado, M. Maltoni and T. Schwetz, *JHEP* **1305**, 050 (2013) [arXiv:1303.3011 [hep-ph]].
- [60] C. Giunti, M. Laveder, Y. F. Li and H. W. Long, *Phys. Rev. D* **88**, 073008 (2013) [arXiv:1308.5288 [hep-ph]].
- [61] J. Hamann, S. Hannestad, G. G. Raffelt, I. Tamborra and Y. Y. Y. Wong, *Phys. Rev. Lett.* **105**, 181301 (2010) [arXiv:1006.5276 [hep-ph]].
- [62] J. Hamann, S. Hannestad, G. G. Raffelt and Y. Y. Y. Wong, *JCAP* **1109**, 034 (2011) [arXiv:1108.4136 [astro-ph.CO]].
- [63] E. Giusarma, M. Corsi, M. Archidiacono, R. de Putter, A. Melchiorri, O. Mena and S. Pandolfi, *Phys. Rev. D* **83**, 115023 (2011) [arXiv:1102.4774 [astro-ph.CO]].
- [64] P. Bode, J. P. Ostriker and N. Turok, *Astrophys. J.* **556**, 93 (2001) [astro-ph/0010389].
- [65] L. Zhan, Y. Wang, J. Cao and L. Wen, *Phys. Rev. D* **78**, 111103 (2008) [arXiv:0807.3203 [hep-ex]].
- [66] L. Zhan, Y. Wang, J. Cao and L. Wen, *Phys. Rev. D* **79**, 073007 (2009) [arXiv:0901.2976 [hep-ex]].
- [67] Yifang Wang, talk at ICFA seminar, (2008). [http://www-conf.slac.stanford.edu/icfa2008/Yifang\\_Wang\\_102808.pdf](http://www-conf.slac.stanford.edu/icfa2008/Yifang_Wang_102808.pdf)
- [68] Jun Cao, talk at Neutrino Telescope, (2009). <http://neutrino.pd.infn.it/NEUTEL09/Talks/Cao.pdf>

- [69] Y. F. Li, J. Cao, Y. Wang and L. Zhan, Phys. Rev. D **88**, 013008 (2013) [arXiv:1303.6733 [hep-ex]].
- [70] Q. Liu, X. Zhou, W. Huang, Y. Zhang, W. Wu, W. Luo, M. Yu and Y. Zheng *et al.*, Nucl. Instrum. Meth. A **795**, 284 (2015) [arXiv:1504.01001 [physics.ins-det]].
- [71] T. Adam, E. Baussan, K. Borer, J. E. Campagne, N. Con-Sen, C. de La Taille, N. Dick and M. Dracos *et al.*, Nucl. Instrum. Meth. A **577**, 523 (2007) [physics/0701153].
- [72] Y. Abe *et al.* [Double Chooz Collaboration], Phys. Rev. Lett. **108**, 131801 (2012) [arXiv:1112.6353 [hep-ex]].
- [73] J. K. Ahn *et al.* [RENO Collaboration], Phys. Rev. Lett. **108**, 191802 (2012) [arXiv:1204.0626 [hep-ex]].
- [74] K. Abe *et al.* [T2K Collaboration], Phys. Rev. Lett. **107**, 041801 (2011) [arXiv:1106.2822 [hep-ex]].
- [75] P. Adamson *et al.* [MINOS Collaboration], Phys. Rev. Lett. **107**, 181802 (2011) [arXiv:1108.0015 [hep-ex]].
- [76] G. L. Fogli, E. Lisi, A. Marrone, D. Montanino, A. Palazzo and A. M. Rotunno, Phys. Rev. D **86**, 013012 (2012) [arXiv:1205.5254 [hep-ph]].
- [77] D. V. Forero, M. Tortola and J. W. F. Valle, Phys. Rev. D **86**, 073012 (2012) [arXiv:1205.4018 [hep-ph]].
- [78] M. C. Gonzalez-Garcia, M. Maltoni, J. Salvado and T. Schwetz, JHEP **1212**, 123 (2012) [arXiv:1209.3023 [hep-ph]].
- [79] X. Qian, D. A. Dwyer, R. D. McKeown, P. Vogel, W. Wang and C. Zhang, Phys. Rev. D **87**, 033005 (2013) [arXiv:1208.1551 [physics.ins-det]].
- [80] A. B. Balantekin, H. Band, R. Betts, J. J. Cherwinka, J. A. Detwiler, S. Dye, K. M. Heeger and R. Johnson *et al.*, arXiv:1307.7419 [hep-ex].
- [81] S. B. Kim, arXiv:1412.2199 [hep-ex].
- [82] D. S. Ayres *et al.* [NO $\nu$ A Collaboration], hep-ex/0503053.
- [83] C. Adams *et al.* [LBNE Collaboration], arXiv:1307.7335 [hep-ex].
- [84] S. Ahmed *et al.* [ICAL Collaboration], arXiv:1505.07380 [physics.ins-det].
- [85] M. G. Aartsen *et al.* [IceCube PINGU Collaboration], arXiv:1401.2046 [physics.ins-det].
- [86] V. Van Elewyck [KM3NeT Collaboration], J. Phys. Conf. Ser. **598**, 012033 (2015).
- [87] K. Abe, T. Abe, H. Aihara, Y. Fukuda, Y. Hayato, K. Huang, A. K. Ichikawa and M. Ikeda *et al.*, arXiv:1109.3262 [hep-ex].
- [88] K. Abe *et al.* [Hyper-Kamiokande Proto- Collaboration], PTEP **2015**, no. 5, 053C02 (2015) [arXiv:1502.05199 [hep-ex]].

- [89] S. M. Bilenky and C. Giunti, *Mod. Phys. Lett. A* **27**, 1230015 (2012) [arXiv:1203.5250 [hep-ph]].
- [90] J. Cao, M. He, Z. L. Hou, H. T. Jing, Y. F. Li, Z. H. Li, Y. P. Song and J. Y. Tang *et al.*, *Phys. Rev. ST Accel. Beams* **17**, 090101 (2014) [arXiv:1401.8125 [physics.acc-ph]].
- [91] G. G. Raffelt and A. Y. Smirnov, *Phys. Rev. D* **76**, 081301 (2007) [*Phys. Rev. D* **77**, 029903 (2008)] [arXiv:0705.1830 [hep-ph]].
- [92] T. Kajino, G. J. Mathews and T. Hayakawa, *J. Phys. G* **41**, 044007 (2014).
- [93] K. N. Abazajian *et al.* *Astropart. Phys.* **63**, 66 (2015) [arXiv:1309.5383 [astro-ph.CO]].
- [94] H. Minakata, H. Nunokawa, S. J. Parke and R. Zukanovich Funchal, *Phys. Rev. D* **76**, 053004 (2007) [*Phys. Rev. D* **76**, 079901 (2007)] [hep-ph/0701151].
- [95] H. Nunokawa, S. J. Parke and R. Zukanovich Funchal, *Phys. Rev. D* **72**, 013009 (2005) [hep-ph/0503283].
- [96] A. de Gouvea, J. Jenkins and B. Kayser, *Phys. Rev. D* **71**, 113009 (2005) [hep-ph/0503079].
- [97] J. Learned, S. T. Dye, S. Pakvasa and R. C. Svoboda, *Phys. Rev. D* **78**, 071302 (2008) [hep-ex/0612022].
- [98] F. Von Feilitzsch, A. A. Hahn and K. Schreckenbach, *Phys. Lett. B* **118**, 162 (1982).
- [99] K. Schreckenbach, G. Colvin, W. Gelletly and F. Von Feilitzsch, *Phys. Lett. B* **160**, 325 (1985).
- [100] A. A. Hahn, K. Schreckenbach, G. Colvin, B. Krusche, W. Gelletly and F. Von Feilitzsch, *Phys. Lett. B* **218**, 365 (1989).
- [101] P. Huber, *Phys. Rev. C* **84**, 024617 (2011) [*Phys. Rev. C* **85**, 029901 (2012)] [arXiv:1106.0687 [hep-ph]].
- [102] T. A. Mueller, D. Lhuillier, M. Fallot, A. Letourneau, S. Cormon, M. Fechner, L. Giot and T. Lasserre *et al.*, *Phys. Rev. C* **83**, 054615 (2011) [arXiv:1101.2663 [hep-ex]].
- [103] P. Vogel, G. K. Schenter, F. M. Mann and R. E. Schenter, *Phys. Rev. C* **24**, 1543 (1981).
- [104] D. A. Dwyer and T. J. Langford, *Phys. Rev. Lett.* **114**, 012502 (2015) [arXiv:1407.1281 [nucl-ex]].
- [105] W. L. Zhong, for Daya Bay collaboration, talk at ICHEP 2014; F. P. An, for Daya Bay collaboration, talk at NuFact 2014; See also L. Zhan [Daya Bay Collaboration], arXiv:1506.01149 [hep-ex].
- [106] S. H. Seo [RENO Collaboration], arXiv:1410.7987 [hep-ex].
- [107] Y. Abe *et al.* [Double Chooz Collaboration], *JHEP* **1410**, 086 (2014) [*JHEP* **1502**, 074 (2015)] [arXiv:1406.7763 [hep-ex]].
- [108] P. Vogel, L. Wen and C. Zhang, *Nature Communications* **6**, 6935 (2015) [arXiv:1503.01059 [hep-ex]].

- [109] S. Abe *et al.* [KamLAND Collaboration], Phys. Rev. C **81**, 025807 (2010) [arXiv:0907.0066 [hep-ex]].
- [110] L. Wen, J. Cao, K. Luk, Y. Ma, Y. Wang and C. Yang, Nucl. Instrum. Meth. A **564**, 471 (2006) [hep-ex/0604034].
- [111] T. Schwetz, Phys. Lett. B **648**, 54 (2007) [hep-ph/0612223].
- [112] M. Blennow, P. Coloma, P. Huber and T. Schwetz, JHEP **1403**, 028 (2014) [arXiv:1311.1822 [hep-ph]].
- [113] X. Qian, A. Tan, W. Wang, J. J. Ling, R. D. McKeown and C. Zhang, Phys. Rev. D **86**, 113011 (2012) [arXiv:1210.3651 [hep-ph]].
- [114] S. F. Ge, K. Hagiwara, N. Okamura and Y. Takaesu, JHEP **1305**, 131 (2013) [arXiv:1210.8141 [hep-ph]].
- [115] E. Ciuffoli, J. Evslin and X. Zhang, JHEP **1401**, 095 (2014) [arXiv:1305.5150 [hep-ph]].
- [116] B. Aharmim *et al.* [SNO Collaboration], Phys. Rev. C **88**, 025501 (2013) [arXiv:1109.0763 [nucl-ex]].
- [117] X. Qian, C. Zhang, M. Diwan and P. Vogel, arXiv:1308.5700 [hep-ex].
- [118] M. Lindner, A. Merle and W. Rodejohann, Phys. Rev. D **73**, 053005 (2006) [hep-ph/0512143].
- [119] A. Dueck, W. Rodejohann and K. Zuber, Phys. Rev. D **83**, 113010 (2011) [arXiv:1103.4152 [hep-ph]].
- [120] S. F. Ge and W. Rodejohann, arXiv:1507.05514 [hep-ph].
- [121] W. Rodejohann, J. Phys. G **39**, 124008 (2012) [arXiv:1206.2560 [hep-ph]].
- [122] P. F. Harrison, D. H. Perkins and W. G. Scott, Phys. Lett. B **530**, 167 (2002) [hep-ph/0202074].
- [123] Z. z. Xing, Phys. Lett. B **533**, 85 (2002) [hep-ph/0204049].
- [124] X. G. He and A. Zee, Phys. Lett. B **560**, 87 (2003) [hep-ph/0301092].
- [125] C. H. Albright and W. Rodejohann, Eur. Phys. J. C **62**, 599 (2009) [arXiv:0812.0436 [hep-ph]].
- [126] Y. Itow *et al.* [T2K Collaboration], hep-ex/0106019.
- [127] S. K. Agarwalla, S. Prakash and W. Wang, arXiv:1312.1477 [hep-ph].
- [128] Y. Ashie *et al.* [Super-Kamiokande Collaboration], Phys. Rev. Lett. **93**, 101801 (2004) [hep-ex/0404034].
- [129] A. Gando *et al.* [KamLAND Collaboration], Phys. Rev. D **83**, 052002 (2011) [arXiv:1009.4771 [hep-ex]].
- [130] F. P. An *et al.* [Daya Bay Collaboration], arXiv:1505.03456 [hep-ex].
- [131] P. Adamson *et al.* [MINOS Collaboration], Phys. Rev. Lett. **110**, 251801 (2013) [arXiv:1304.6335 [hep-ex]].



- [132] R. Wendell [Super-Kamiokande Collaboration], arXiv:1412.5234 [hep-ex].
- [133] K. Abe *et al.* [T2K Collaboration], Phys. Rev. Lett. **112**, 181801 (2014) [arXiv:1403.1532 [hep-ex]].
- [134] N. Langer, Ann. Rev. Astron. Astrophys. **50**, 107 (2012) [arXiv:1206.5443].
- [135] A. Burrows, Nature **403**, 727 (2000).
- [136] H.-Th. Janka, Ann. Rev. Nucl. Part. Sci. **62**, 407 (2012) [arXiv:1206.2503].
- [137] E. Cappellaro and M. Turatto, Astrophys. Space Sci. Libr. **264**, 199 (2001) [astro-ph/0012455].
- [138] P. A. Mazzali, F. K. Röpke, S. Benetti and W. Hillebrandt, Science **315**, 825 (2007) [astro-ph/0702351].
- [139] J. F. Beacom, Ann. Rev. Nucl. Part. Sci. **60**, 439 (2010) [arXiv:1004.3311].
- [140] M. Koshiya, Phys. Rept. **220**, 229 (1992).
- [141] A. Mirizzi, G. G. Raffelt and P. D. Serpico, JCAP **0605**, 012 (2006) [astro-ph/0604300].
- [142] M. Ahlers, P. Mertsch and S. Sarkar, Phys. Rev. D **80**, 123017 (2009) [arXiv:0909.4060].
- [143] S. M. Adams, C. S. Kochanek, J. F. Beacom, M. R. Vagins and K. Z. Stanek, Astrophys. J. **778**, 164 (2013) [arXiv:1306.0559].
- [144] G. M. Harper, A. Brown and E. F. Guinan, Astron. J. **135**, 1430 (2008).
- [145] S. van den Bergh and R. D. McClure, Astrophys. J. **425**, 205 (1994).
- [146] W. Li, R. Chornock, J. Leaman, A. V. Filippenko, D. Poznanski, X. Wang, M. Ganeshalingam and F. Mannucci, Mon. Not. R. Astron. Soc. **412**, 1473 (2011) [arXiv:1006.4613].
- [147] B. C. Reed, Astron. J. **130**, 1652 (2005) [astro-ph/0506708].
- [148] C.-A. Faucher-Giguère and V. M. Kaspi, Astrophys. J. **643**, 332 (2006) [astro-ph/0512585].
- [149] E. F. Keane and M. Kramer, Mon. Not. R. Astron. Soc. **391**, 2009 (2008) [arXiv:0810.1512].
- [150] R. Diehl *et al.*, Nature **439**, 45 (2006).
- [151] R. G. Strom, Astron. Astrophys. **288**, L1 (1994).
- [152] G. A. Tammann, W. Löffler and A. Schröder, Astrophys. J. Suppl. **92**, 487 (1994).
- [153] E. N. Alekseev *et al.*, Zh. Eksp. Teor. Fiz. **104**, 2897 (1993) [J. Exp. Theor. Phys. **77**, 339 (1993)].
- [154] D. A. Green and F. R. Stephenson, Lect. Notes Phys. **598**, 7 (2003) [astro-ph/0301603].
- [155] P. Antonioli *et al.*, New J. Phys. **6**, 114 (2004) [astro-ph/0406214]. For the SNEWS project homepage see <http://snews.bnl.gov/>
- [156] K. Scholberg, Ann. Rev. Nucl. Part. Sci. **62**, 81 (2012).

- [157] K. Abe *et al.* (Super-Kamiokande Collaboration), Nucl. Instrum. Meth. A **737**, 253 (2014).
- [158] T. Mori (for Super-Kamiokande Collaboration), Nucl. Instrum. Meth. A **732**, 316 (2013).
- [159] R. Abbasi *et al.* (IceCube Collaboration), Astron. Astrophys. **535**, A109 (2011).
- [160] M. Salathe, M. Ribordy and L. Demirors, Astropart. Phys. **35**, 485 (2012).
- [161] M. G. Aartsen *et al.* (IceCube Collaboration), arXiv: 1309.7008.
- [162] M. Wurm *et al.* (LENA Collaboration), Astropart. Phys. **35**, 685 (2012) [arXiv:1104.5620].
- [163] H. A. Bethe and J. Wilson, R., Astrophys. J. **295**, 14 (1985).
- [164] H. A. Bethe, Rev. Mod. Phys. **62**, 801 (1990).
- [165] J. M. Blondin, A. Mezzacappa and C. DeMarino, Astrophys. J. **584**, 971 (2003) [astro-ph/0210634].
- [166] I. Tamborra, F. Hanke, H. T. Janka, B. Mller, G. G. Raffelt and A. Marek, Astrophys. J. **792**, no. 2, 96 (2014) [arXiv:1402.5418].
- [167] H.-Th. Janka, F. Hanke, L. Hüdepohl, A. Marek, B. Müller and M. Obergaulinger, PTEP **2012**, 01A309 (2012) [arXiv:1211.1378].
- [168] L. Hüdepohl, PhD Thesis, Technische Universität München (2013). Neutrino model data can be made available upon request at <http://www.mpa-garching.mpg.de/ccsnarchive/>
- [169] A. Mirizzi, I. Tamborra, H. T. Janka, N. Saviano, K. Scholberg, R. Bollig, L. Hudepohl and S. Chakraborty, arXiv:1508.00785 [astro-ph.HE].
- [170] A. Burrows, E. Livne, L. Dessart, C. Ott and J. Murphy, Astrophys. J. **640**, 878 (2006) [astro-ph/0510687].
- [171] S. Akiyama, J. C. Wheeler, D. L. Meier and I. Lichtenstadt, Astrophys. J. **584**, 954 (2003) [astro-ph/0208128].
- [172] N. A. Gentile, M. B. Aufderheide, G. J. Mathews, F. D. Swesty and G. M. Fuller, Astrophys. J. **414**, 701 (1993).
- [173] Z. G. Dai, Q. H. Peng and T. Lu, Astrophys. J. **440**, 815 (1995).
- [174] I. Sagert, T. Fischer, M. Hempel, G. Pagliara, J. Schaffner-Bielich, A. Mezzacappa, F.-K. Thielemann and M. Liebendorfer, Phys. Rev. Lett. **102**, 081101 (2009) [arXiv:0809.4225].
- [175] M. Th. Keil, G. G. Raffelt and H.-Th. Janka, Astrophys. J. **590**, 971 (2003) [astro-ph/0208035].
- [176] A. Strumia and F. Vissani, Phys. Lett. B **564**, 42 (2003) [astro-ph/0302055].
- [177] P. Vogel and J. F. Beacom, Phys. Rev. D **60**, 053003 (1999) [hep-ph/9903554].
- [178] M. Apollonio *et al.* [CHOOZ Collaboration], Phys. Rev. D **61**, 012001 (2000) [hep-ex/9906011].
- [179] R. Laha, J. F. Beacom and S. K. Agarwalla, arXiv:1412.8425.

- [180] M. Fukugita, Y. Kohyama and K. Kubodera, Phys. Lett. B **212**, 139 (1988).
- [181] C. Volpe, N. Auerbach, G. Colo, T. Suzuki and N. Van Giai, Phys. Rev. C **62**, 015501 (2000) [nucl-th/0001050].
- [182] L. B. Auerbach *et al.* [LSND Collaboration], Phys. Rev. C **64**, 065501 (2001) [hep-ex/0105068].
- [183] W. J. Marciano and Z. Parsa, J. Phys. G **29**, 2629 (2003) [hep-ph/0403168].
- [184] J. F. Beacom, W. M. Farr and P. Vogel, Phys. Rev. D **66**, 033001 (2002) [hep-ph/0205220].
- [185] B. Dasgupta and J. F. Beacom, Phys. Rev. D **83**, 113006 (2011) [arXiv:1103.2768].
- [186] S. Weinberg, Phys. Rev. D **5**, 1412 (1972).
- [187] B. von Krosigk, L. Neumann, R. Nolte, S. Rottger and K. Zuber, Eur. Phys. J. C **73**, 2390 (2013) [arXiv:1301.6403].
- [188] PSTAR Database: <http://physics.nist.gov/PhysRefData/Star/Text/PSTAR.html>
- [189] T. Fischer, S. C. Whitehouse, A. Mezzacappa, F.-K. Thielemann and M. Liebendorfer, Astron. Astrophys. **517**, A80 (2010) [arXiv:0908.1871].
- [190] R. Buras, H. T. Janka, M. Rampp and K. Kifonidis, Astron. Astrophys. **457**, 281 (2006) [astro-ph/0512189].
- [191] P. D. Serpico, S. Chakraborty, T. Fischer, L. Hudepohl, H. T. Janka and A. Mirizzi, Phys. Rev. D **85**, 085031 (2012) [arXiv:1111.4483 [astro-ph.SR]].
- [192] K. Nakazato, K. Sumiyoshi, H. Suzuki, T. Totani, H. Umeda and S. Yamada, Astrophys. J. Suppl. **205**, 2 (2013) [arXiv:1210.6841].
- [193] A. Burrows, Rev. Mod. Phys. **85**, 245 (2013) [arXiv:1210.4921 [astro-ph.SR]].
- [194] G. M. Fuller, R. Mayle, B. S. Meyer, and J. R. Wilson, Astrophys. J. **389**, 517 (1992).
- [195] Y. Z. Qian, G. M. Fuller, G. J. Mathews, R. Mayle, J. R. Wilson and S. E. Woosley, Phys. Rev. Lett. **71**, 1965 (1993).
- [196] N. Itoh, H. Hayashi, A. Nishikawa and Y. Kohyama, Astrophys. J. Suppl. **102**, 411 (1996).
- [197] A. Odrzywolek, M. Misiaszek and M. Kutschera, Astropart. Phys. **21**, 303 (2004) [astro-ph/0311012].
- [198] A. Odrzywolek and A. Heger, Acta Phys. Polon. B **41**, 1611 (2010).
- [199] J. F. Beacom and P. Vogel, Phys. Rev. D **60**, 033007 (1999) [astro-ph/9811350].
- [200] R. Tomàs, D. Semikoz, G. G. Raffelt, M. Kachelrieß and A. S. Dighe, Phys. Rev. D **68**, 093013 (2003) [hep-ph/0307050].
- [201] E. Müller, M. Rampp, R. Buras, H.-Th. Janka and D. H. Shoemaker, Astrophys. J. **603**, 221 (2004) [astro-ph/0309833].
- [202] Y. Z. Qian, Prog. Part. Nucl. Phys. **50**, 153 (2003) [astro-ph/0301422].

- [203] S. E. Woosley, D. H. Hartmann, R. D. Hoffman and W. C. Haxton, *Astrophys. J.* **356**, 272 (1990).
- [204] A. Heger, E. Kolbe, W. C. Haxton, K. Langanke, G. Martínez-Pinedo and S. E. Woosley, *Phys. Lett. B* **606**, 258 (2005) [astro-ph/0307546].
- [205] T. Yoshida, T. Kajino and D. H. Hartmann, *Phys. Rev. Lett.* **94**, 231101 (2005) [astro-ph/0505043].
- [206] M. R. Wu, Y. Z. Qian, G. Martínez-Pinedo, T. Fischer and L. Huther, *Phys. Rev. D* **91**, no. 6, 065016 (2015) [arXiv:1412.8587].
- [207] G. G. Raffelt, *Stars as Laboratories for Fundamental Physics* (Chicago University Press, Chicago, 1996).
- [208] G. G. Raffelt, *Phys. Rept.* **320**, 319 (1999).
- [209] I. Tamborra, G. G. Raffelt, L. Hüdepohl and H.-Th. Janka, *JCAP* **1201**, 013 (2012) [arXiv:1110.2104].
- [210] M. R. Wu, T. Fischer, L. Huther, G. Martínez-Pinedo and Y. Z. Qian, *Phys. Rev. D* **89**, 061303 (2014) [arXiv:1305.2382].
- [211] G. T. Zatsepin, *Pisma Zh. Eksp. Teor. Fiz.* **8**, 333 (1968).
- [212] J. F. Beacom, R. N. Boyd and A. Mezzacappa, *Phys. Rev. Lett.* **85**, 3568 (2000) [hep-ph/0006015].
- [213] G. Pagliaroli, F. Vissani, M. L. Costantini and A. Ianni, *Astropart. Phys.* **31**, 163 (2009) [arXiv:0810.0466].
- [214] G. Pagliaroli, F. Vissani, E. Coccia and W. Fulgione, *Phys. Rev. Lett.* **103**, 031102 (2009) [arXiv:0903.1191].
- [215] G. Pagliaroli, F. Rossi-Torres and F. Vissani, *Astropart. Phys.* **33**, 287 (2010) [arXiv:1002.3349].
- [216] J. S. Lu, J. Cao, Y. F. Li and S. Zhou, *JCAP* **1505**, 044 (2015) [arXiv:1412.7418].
- [217] H. Duan, G. M. Fuller and Y. Z. Qian, *Ann. Rev. Nucl. Part. Sci.* **60**, 569 (2010) [arXiv:1001.2799].
- [218] G. L. Fogli, E. Lisi, A. Marrone and A. Mirizzi, *JCAP* **0712**, 010 (2007) [arXiv:0707.1998].
- [219] A. S. Dighe, M. T. Keil and G. G. Raffelt, *JCAP* **0306**, 005 (2003) [hep-ph/0303210].
- [220] A. S. Dighe, M. T. Keil and G. G. Raffelt, *JCAP* **0306**, 006 (2003) [hep-ph/0304150].
- [221] R. Tomas, M. Kachelriess, G. Raffelt, A. Dighe, H.-T. Janka and L. Scheck, *JCAP* **0409**, 015 (2004) [astro-ph/0407132].
- [222] E. Borriello, S. Chakraborty, H. T. Janka, E. Lisi and A. Mirizzi, *JCAP* **1411**, no. 11, 030 (2014) [arXiv:1310.7488].
- [223] L. M. Krauss, S. L. Glashow and D. N. Schramm, *Nature* **310**, 191 (1984).

- [224] G. S. Bisnovatyi-Kogan and S. F. Seidov, *Annals N. Y. Acad. Sci.* **422**, 319 (1984).
- [225] S. E. Woosley, J. R. Wilson and R. Mayle, *Astrophys. J.* **302**, 19 (1986).
- [226] S. Ando and K. Sato, *New J. Phys.* **6**, 170 (2004) [astro-ph/0410061].
- [227] C. Lunardini, *Astropart. Phys.* **26**, 190 (2006) [astro-ph/0509233].
- [228] C. Lunardini and I. Tamborra, *JCAP* **1207**, 012 (2012) [arXiv:1205.6292].
- [229] G. Raffelt and T. Rashba, *Phys. Atom. Nucl.* **73**, 609 (2010) [arXiv:0902.4832].
- [230] M. Malek *et al.* (Super-Kamiokande Collaboration), *Phys. Rev. Lett.* **90**, 061101 (2003) [hep-ex/0209028].
- [231] K. Bays *et al.* (Super-Kamiokande Collaboration), *Phys. Rev. D* **85**, 052007 (2012) [arXiv:1111.5031].
- [232] H. Zhang *et al.* (Super-Kamiokande Collaboration), *Astropart. Phys.* **60**, 41 (2014) [arXiv:1311.3738].
- [233] B. Aharmim *et al.* (SNO Collaboration), *Astrophys. J.* **653**, 1545 (2006) [hep-ex/0607010].
- [234] A. Gando *et al.* (KamLAND Collaboration), *Astrophys. J.* **745**, 193 (2012) [arXiv:1105.3516].
- [235] J. F. Beacom and M. R. Vagins, *Phys. Rev. Lett.* **93**, 171101 (2004) [hep-ph/0309300].
- [236] H. Watanabe *et al.* (Super-Kamiokande Collaboration), *Astropart. Phys.* **31**, 320 (2009) [arXiv:0811.0735].
- [237] M. R. Vagins, *Nucl. Phys. Proc. Suppl.* **229–232**, 325 (2012).
- [238] S. Horiuchi, J. F. Beacom and E. Dwek, *Phys. Rev. D* **79**, 083013 (2009) [arXiv:0812.3157].
- [239] C. Porciani and P. Madau, *Astrophys. J.* **548**, 522 (2001) [astro-ph/0008294].
- [240] A. M. Hopkins and J. F. Beacom, *Astrophys. J.* **651**, 142 (2006) [astro-ph/0601463].
- [241] H. Yüksel, M. D. Kistler, J. F. Beacom and A. M. Hopkins, *Astrophys. J.* **683**, L5 (2008) [arXiv:0804.4008].
- [242] S. Horiuchi, J. F. Beacom, C. S. Kochanek, J. L. Prieto, K. Z. Stanek and T. A. Thompson, *Astrophys. J.* **738**, 154 (2011) [arXiv:1102.1977].
- [243] A. Heger, C. L. Fryer, S. E. Woosley, N. Langer and D. H. Hartmann, *Astrophys. J.* **591**, 288 (2003) [astro-ph/0212469].
- [244] T. Fischer, S. C. Whitehouse, A. Mezzacappa, F.-K. Thielemann and M. Liebendörfer, *Astron. Astrophys.* **499**, 1 (2009) [arXiv:0809.5129].
- [245] K. Nakazato, K. Sumiyoshi, H. Suzuki and S. Yamada, *Phys. Rev. D* **78**, 083014 (2008); Erratum *ibid.* **79**, 069901 (2009) [arXiv:0810.3734].
- [246] C. S. Kochanek, J. F. Beacom, M. D. Kistler, J. L. Prieto, K. Z. Stanek, T. A. Thompson and H. Yüksel, *Astrophys. J.* **684**, 1336 (2008) [arXiv:0802.0456].

- [247] C. Lunardini, Phys. Rev. Lett. **102**, 231101 (2009) [arXiv:0901.0568].
- [248] E. O’Connor and C. D. Ott, Astrophys. J. **730**, 70 (2011) [arXiv:1010.5550].
- [249] M. Ugliano, H.-T. Janka, A. Marek and A. Arcones, Astrophys. J. **757**, 69 (2012) [arXiv:1205.3657].
- [250] J. G. Keehn and C. Lunardini, Phys. Rev. D **85**, 043011 (2012) [arXiv:1012.1274].
- [251] C. S. Kochanek, Astrophys. J. **785**, 28 (2014) [arXiv:1308.0013].
- [252] I. Tamborra, B. Müller, L. Hüpdepohl, H.-T. Janka and G. Raffelt, Phys. Rev. D **86**, 125031 (2012) [arXiv:1211.3920].
- [253] R. M?llenberg, F. von Feilitzsch, D. Hellgartner, L. Oberauer, M. Tippmann, V. Zimmer, J. Winter and M. Wurm, Phys. Rev. D **91**, no. 3, 032005 (2015) [arXiv:1409.2240 [astro-ph.IM]].
- [254] Jilei Xu, “Rock Neutron Background Simulation”, JUNO General Meeting, Guangzhou (2015)
- [255] M. Wurm, F. von Feilitzsch, M. Göger-Neff, K. A. Hochmuth, T. Marrodán Undagoitia, L. Oberauer and W. Potzel, Phys. Rev. D **75**, 023007 (2007) [astro-ph/0701305].
- [256] I. Tamborra, G. Raffelt, F. Hanke, H.-T. Janka and B. Müller, Phys. Rev. D **90**, 045032 (2014) [arXiv:1406.0006].
- [257] M. D. Kistler, H. Yüksel, S. Ando, J. F. Beacom and Y. Suzuki, Phys. Rev. D **83**, 123008 (2011) [arXiv:0810.1959].
- [258] A. Gross (for the IceCube/PINGU Collaboration), Talk at the NNN 2013 Conference, Kashiwa, Japan, (2013).
- [259] Y. Fukuda *et al.* [Super-Kamiokande Collaboration], Phys. Rev. Lett. **81** (1998) 1562.
- [260] M. H. Ahn *et al.* [K2K Collaboration], Phys. Rev. Lett. **90** (2003) 041801.
- [261] K. Eguchi *et al.* [KamLAND Collaboration], Phys. Rev. Lett. **90**, 021802 (2003) [hep-ex/0212021].
- [262] W. C. Haxton, R. G. Hamish Robertson and A. M. Serenelli, Ann. Rev. Astron. Astrophys. **51**, 21 (2013) [arXiv:1208.5723 [astro-ph.SR]].
- [263] V. Antonelli, L. Miramonti, C. Pena Garay and A. Serenelli, Adv. High Energy Phys. **2013**, 351926 (2013) [arXiv:1208.1356 [hep-ex]].
- [264] L. Wolfenstein, Phys. Rev. D **17**, 2369 (1978).
- [265] S. P. Mikheev and A. Y. Smirnov, Sov. J. Nucl. Phys. **42**, 913 (1985) [Yad. Fiz. **42**, 1441 (1985)].
- [266] G. Alimonti *et al.* [Borexino Collaboration], Nucl. Instrum. Meth. A **600**, 568 (2009) [arXiv:0806.2400 [physics.ins-det]].

- [267] Y. Fukuda *et al.* [Super-Kamiokande Collaboration], Phys. Rev. Lett. **81**, 1158 (1998) [Phys. Rev. Lett. **81**, 4279 (1998)] [hep-ex/9805021].
- [268] B. T. Cleveland, T. Daily, R. Davis, Jr., J. R. Distel, K. Lande, C. K. Lee, P. S. Wildenhain and J. Ullman, Astrophys. J. **496**, 505 (1998).
- [269] K. S. Hirata *et al.* [Kamiokande-II Collaboration], Phys. Rev. Lett. **63**, 16 (1989).
- [270] W. Hampel *et al.* [GALLEX Collaboration], Phys. Lett. B **447**, 127 (1999).
- [271] M. Altmann *et al.* [GNO Collaboration], Phys. Lett. B **616**, 174 (2005) [hep-ex/0504037].
- [272] J. N. Abdurashitov *et al.* [SAGE Collaboration], Phys. Rev. Lett. **83**, 4686 (1999) [astro-ph/9907131].
- [273] N. Jelley, A. B. McDonald and R. G. H. Robertson, Ann. Rev. Nucl. Part. Sci. **59**, 431 (2009).
- [274] J. N. Bahcall and M. H. Pinsonneault, Phys. Rev. Lett. **92**, 121301 (2004) [astro-ph/0402114].
- [275] Q. R. Ahmad *et al.* [SNO Collaboration], Phys. Rev. Lett. **87**, 071301 (2001) [nucl-ex/0106015].
- [276] C. Arpesella *et al.* [Borexino Collaboration], Phys. Rev. Lett. **101**, 091302 (2008) [arXiv:0805.3843 [astro-ph]].
- [277] A. Gando *et al.* [KamLAND Collaboration], arXiv:1405.6190 [hep-ex].
- [278] G. Bellini *et al.* [Borexino Collaboration], Phys. Rev. Lett. **108**, 051302 (2012) [arXiv:1110.3230 [hep-ex]].
- [279] G. Bellini *et al.* [BOREXINO Collaboration], Nature **512**, 383 (2014).
- [280] G. Bellini *et al.* [Borexino Collaboration], Phys. Rev. D **89**, 112007 (2014) [arXiv:1308.0443 [hep-ex]].
- [281] T. Ohlsson, Rept. Prog. Phys. **76**, 044201 (2013) [arXiv:1209.2710 [hep-ph]].
- [282] F. L. Villante, A. M. Serenelli, F. Delahaye and M. H. Pinsonneault, Astrophys. J. **787**, 13 (2014) [arXiv:1312.3885 [astro-ph.SR]].
- [283] M. Bergemann and A. Serenelli, arXiv:1403.3097 [astro-ph.SR].
- [284] N. Grevesse and A. J. Sauval, Space Sci. Rev. **85**, 161 (1998).
- [285] M. Asplund, N. Grevesse and J. Sauval, Nucl. Phys. A **777**, 1 (2006) [ASP Conf. Ser. **336**, 25 (2005)] [astro-ph/0410214].
- [286] M. Asplund, N. Grevesse, A. J. Sauval and P. Scott, Ann. Rev. Astron. Astrophys. **47**, 481 (2009) [arXiv:0909.0948 [astro-ph.SR]].
- [287] A. Serenelli, S. Basu, J. W. Ferguson and M. Asplund, Astrophys. J. **705**, L123 (2009) [arXiv:0909.2668 [astro-ph.SR]].
- [288] A. Renshaw [Super-Kamiokande Collaboration], Phys. Procedia **61**, 345 (2015) [arXiv:1403.4575 [hep-ex]].

- [289] A. M. Serenelli, talk given at “A special Borexino event - Borexino Mini-Workshop”, Gran Sasso, (2014).
- [290] K. Zuber, PoS NICXII , 012 (2012).
- [291] A. M. Serenelli, *Astrophys. Space Sci.* **328**, 13 (2010) [arXiv:0910.3690 [astro-ph.SR]].
- [292] M. B. Voloshin, *Phys. Rev. Lett.* **105**, 201801 (2010) [*Phys. Rev. Lett.* **106**, 059901 (2011)] [arXiv:1008.2171 [hep-ph]].
- [293] C. Giunti and A. Studenikin, arXiv:1403.6344 [hep-ph].
- [294] C. Brogгинi, C. Giunti and A. Studenikin, *Adv. High Energy Phys.* **2012**, 459526 (2012) [arXiv:1207.3980 [hep-ph]].
- [295] A. G. Beda, V. B. Brudanin, V. G. Egorov, D. V. Medvedev, V. S. Pogosov, E. A. Shevchik, M. V. Shirchenko and A. S. Starostin *et al.*, *Phys. Part. Nucl. Lett.* **10**, 139 (2013).
- [296] H. T. Wong *et al.* [TEXONO Collaboration], *Phys. Rev. D* **75**, 012001 (2007) [hep-ex/0605006].
- [297] Z. Daraktchieva *et al.* [MUNU Collaboration], *Phys. Lett. B* **615**, 153 (2005) [hep-ex/0502037].
- [298] N. Viaux, M. Catelan, P. B. Stetson, G. Raffelt, J. Redondo, A. A. R. Valcarce and A. Weiss, *Phys. Rev. Lett.* **111**, 231301 (2013) [arXiv:1311.1669 [astro-ph.SR]].
- [299] J. F. Beacom and P. Vogel, *Phys. Rev. Lett.* **83**, 5222 (1999) [hep-ph/9907383].
- [300] C. Giunti, K. A. Kouzakov, Y. F. Li, A. V. Lokhov, A. I. Studenikin and S. Zhou, arXiv:1506.05387 [hep-ph].
- [301] C. Kraus *et al.* [SNO+ Collaboration], *Prog. Part. Nucl. Phys.* **64**, 273 (2010).
- [302] M. Mottram [SNO+ Collaboration], PoS EPS **-HEP2013**, 524 (2013).
- [303] A. Renshaw *et al.* [Super-Kamiokande Collaboration], *Phys. Rev. Lett.* **112**, 091805 (2014) [arXiv:1312.5176 [hep-ex]].
- [304] J. N. Bahcall, A. M. Serenelli and S. Basu, *Astrophys. J.* **621**, L85 (2005) [astro-ph/0412440].
- [305] G. Bellini *et al.* [Borexino Collaboration], *JCAP* **1308**, 049 (2013) [arXiv:1304.7381 [physics.ins-det]].
- [306] R. Mollenberg, “Monte Carlo Study of Solar  $^8\text{B}$  Neutrinos and the Diffuse Supernova Neutrino Background in LENA,” PhD thesis, TU München (2013). see <http://mediatum.ub.tum.de/node?id=1175550>
- [307] S. W. Li and J. F. Beacom, *Phys. Rev. C* **89**, 045801 (2014) [arXiv:1402.4687 [hep-ph]].
- [308] S. W. Li and J. F. Beacom, *Phys. Rev. D* **91**, 105005 (2015) [arXiv:1503.04823 [hep-ph]].
- [309] A. de Gouvea *et al.* [Intensity Frontier Neutrino Working Group Collaboration], arXiv:1310.4340 [hep-ex].



- [310] U. F. Katz [KM3NeT Collaboration], [arXiv:1402.1022 [astro-ph.IM]].
- [311] J. G. Learned, arXiv:0902.4009 [hep-ex].
- [312] M. Honda, T. Kajita, K. Kasahara and S. Midorikawa, Phys. Rev. D **83**, 123001 (2011) [arXiv:1102.2688 [astro-ph.HE]].
- [313] E. Lisi and D. Montanino, Phys. Rev. D **56**, 1792 (1997) [hep-ph/9702343].
- [314] A. M. Dziewonski and D. L. Anderson, Phys. Earth Planet. Interiors **25**, 297 (1981).
- [315] M. Wallraff and C. Wiebusch, arXiv:1409.1387 [astro-ph.IM].
- [316] A. Cervera, A. Donini, M. B. Gavela, J. J. Gomez Cadenas, P. Hernandez, O. Mena and S. Rigolin, Nucl. Phys. B **579**, 17 (2000) [Nucl. Phys. B **593**, 731 (2001)] [hep-ph/0002108].
- [317] M. Freund, Phys. Rev. D **64**, 053003 (2001) [hep-ph/0103300].
- [318] E. K. Akhmedov, R. Johansson, M. Lindner, T. Ohlsson and T. Schwetz, JHEP **0404**, 078 (2004) [hep-ph/0402175].
- [319] S. Choubey and P. Roy, Phys. Rev. D **73**, 013006 (2006) [hep-ph/0509197].
- [320] C. Andreopoulos, A. Bell, D. Bhattacharya, F. Cavanna, J. Dobson, S. Dytman, H. Gallagher and P. Guzowski *et al.*, Nucl. Instrum. Meth. A **614**, 87 (2010) [arXiv:0905.2517 [hep-ph]].
- [321] S. Agostinelli *et al.* [GEANT4 Collaboration], Nucl. Instrum. Meth. A **506**, 250 (2003).
- [322] J. Peltoniemi, arXiv:0909.4974 [physics.ins-det].
- [323] J. Peltoniemi, arXiv:0911.4876 [hep-ex].
- [324] P. Huber and T. Schwetz, Phys. Lett. B **669**, 294 (2008) [arXiv:0805.2019 [hep-ph]].
- [325] K. Abe *et al.* [Super-Kamiokande Collaboration], Phys. Rev. Lett. **107**, 241801 (2011) [arXiv:1109.1621 [hep-ex]].
- [326] M. C. Gonzalez-Garcia and M. Maltoni, Phys. Rev. D **70**, 033010 (2004) [hep-ph/0404085].
- [327] C. Jaupart, S. Labrosse, and J. C. Mareschal, “Temperatures, Heat and Energy in the Mantle of the Earth”, In: Bercovici, Schubert, eds. Treatise on Geophysics, vol. 7: Mantle dynamics. Elsevier B-V, 253-303 (2007).
- [328] J. H. Davies and D. R. Davies, Solid Earth **1**, 5 (2010).
- [329] G. Bellini *et al.* [Borexino Collaboration], Phys. Lett. B **722**, 295 (2013) [arXiv:1303.2571 [hep-ex]].
- [330] A. Gando *et al.* [KamLAND Collaboration], Phys. Rev. D **88**, 033001 (2013) [arXiv:1303.4667 [hep-ex]].
- [331] W. F. McDonough, J. G. Learned and S. T. Dye, Phys. Today **65N3**, 46 (2012).
- [332] V. Strati, M. Baldoocini, I. Callegari, F. Mantovani, W. F. McDonough, B. Ricci and G. Xhixha, Progress in Earth and Planetary Science **2**, 1 (2015).

- [333] Y. Huang *et al.*, *Geochemistry Geophysics Geosystems* **14**, 2003 (2013).
- [334] M. Javoy *et al.*, *Earth Planet. Sci. Lett.* **293**, 259 (2010).
- [335] G. Fiorentini, G. L. Fogli, E. Lisi, F. Mantovani and A. M. Rotunno, *Phys. Rev. D* **86**, 033004 (2012) [arXiv:1204.1923 [hep-ph]].
- [336] D.L. Turcotte and G. Schubert, “Geodynamics, Applications of Continuum Physics to Geological Problems”, second ed., Cambridge University Press (2002).
- [337] O. Sramek, W. F. McDonough, E. S. Kite, V. Lekic, S. Dye and S. Zhong, *Earth Planet. Sci. Lett.* **361**, 356 (2013) [arXiv:1207.0853 [physics.geo-ph]].
- [338] S. Enomoto *et al.*, *Earth Planet. Sci. Lett.* **258**, 147 (2007).
- [339] G. Fiorentini, M. Lissia, F. Mantovani and R. Vannucci, *Phys. Rev. D* **72**, 033017 (2005) [hep-ph/0501111].
- [340] M. Coltorti, R. Boraso, F. Mantovani, M. Morsilli, G. Fiorentini, A. Riva, G. Rusciadelli and R. Tassinari *et al.*, *Geochim. Cosmochim. Acta* **75**, 2271 (2011) [arXiv:1102.1335 [astro-ph.EP]].
- [341] Y. Huang, V. Strati, F. Mantovani, S. B. Shirey, R. L. Rudnick and W. F. McDonough, *Geochem. Geophys. Geosyst.* **15**, 3925 (2014) [arXiv:1404.6692 [physics.geo-ph]].
- [342] H-Q. Huang, *et al.*, *J. Asian Earth Sci.* **74**, 280 (2013).
- [343] X. M. Zhou, W. X. Li., *Tectonophysics* **326**, 269 (2000).
- [344] S. A. Gilder *et al.*, *J. Geophysical Research* **101**, B7, 16137 (1996).
- [345] Y. L. Niu, *Geological J. China Universities*, **11**, 9 (2005).
- [346] X. Zhou *et al.*, *Episodes*, **29**, 26 (2006).
- [347] Z-X. Li, X-H. Li, *Geology*, **35**, 179 (2007).
- [348] Y-T. Yang, *Earth Sci. Reviews*, **126**, 96 (2013).
- [349] G. Laske, G. Masters, Z. Ma, and M. Pasyanos, *Geophys. Research Abstracts*, **15**, 2658 (2013).
- [350] C. DeMets *et al.*, *Geophys. J. International*, **101**, 425 (1990).
- [351] T. Araki, S. Enomoto, K. Furuno, Y. Gando, K. Ichimura, H. Ikeda, K. Inoue and Y. Kishimoto *et al.*, *Nature* **436**, 499 (2005).
- [352] G. Bellini *et al.* [Borexino Collaboration], *Phys. Lett. B* **687**, 299 (2010) [arXiv:1003.0284 [hep-ex]].
- [353] M. C. Chen, *Earth Moon Planets* **99**, 221 (2006).
- [354] J. Mandula, Nuclear Power Engineering Section, IAEA-PRIS database 2013.
- [355] M. Baldoncini, I. Callegari, G. Fiorentini, F. Mantovani, B. Ricci, V. Strati and G. Xhixha, *Phys. Rev. D* **91**, 065002 (2015) [arXiv:1411.6475 [physics.ins-det]].

- [356] X. B. Ma, W. L. Zhong, L. Z. Wang, Y. X. Chen and J. Cao, Phys. Rev. C **88**, no. 1, 014605 (2013) [arXiv:1212.6625 [nucl-ex]].
- [357] P. Huber and T. Schwetz, Phys. Rev. D **70**, 053011 (2004) [hep-ph/0407026].
- [358] J. Cao, Nucl. Phys. Proc. Suppl. **229-232**, 205 (2012) [arXiv:1101.2266 [hep-ex]].
- [359] Z. Djurcic, J. A. Detwiler, A. Piepke, V. R. Foster, Jr., L. Miller and G. Gratta, J. Phys. G **36**, 045002 (2009) [arXiv:0808.0747 [hep-ex]].
- [360] B. Zhou, X. C. Ruan, Y. B. Nie, Z. Y. Zhou, F. P. An and J. Cao, Chin. Phys. C **36**, 1 (2012).
- [361] M. Batygov, Earth, Moon, and Planets **183**, 192 (2006).
- [362] A. Kusenko, Phys. Rept. **481**, 1 (2009) [arXiv:0906.2968 [hep-ph]].
- [363] S. Gariazzo, C. Giunti, M. Laveder, Y. F. Li and E. M. Zavanin, arXiv:1507.08204 [hep-ph].
- [364] C. Giunti and M. Laveder, Phys. Rev. C **83**, 065504 (2011) [arXiv:1006.3244 [hep-ph]].
- [365] P. C. de Holanda and A. Y. Smirnov, Phys. Rev. D **69**, 113002 (2004) [hep-ph/0307266].
- [366] P. C. de Holanda and A. Y. Smirnov, Phys. Rev. D **83**, 113011 (2011) [arXiv:1012.5627 [hep-ph]].
- [367] M. Maltoni, T. Schwetz, M. A. Tortola and J. W. F. Valle, Nucl. Phys. B **643**, 321 (2002) [hep-ph/0207157].
- [368] S. Schael *et al.* [ALEPH and DELPHI and L3 and OPAL and SLD and LEP Electroweak Working Group and SLD Electroweak Group and SLD Heavy Flavour Group Collaborations], Phys. Rept. **427**, 257 (2006) [hep-ex/0509008].
- [369] A. Sousa [MINOS and MINOS+ Collaborations], arXiv:1502.07715 [hep-ex].
- [370] B. Armbruster *et al.* [KARMEN Collaboration], Phys. Rev. D **65**, 112001 (2002) [hep-ex/0203021].
- [371] P. Astier *et al.* [NOMAD Collaboration], Phys. Lett. B **570**, 19 (2003) [hep-ex/0306037].
- [372] M. Antonello *et al.* [ICARUS Collaboration], Eur. Phys. J. C **73**, 2599 (2013) [arXiv:1307.4699 [hep-ex]].
- [373] N. Agafonova *et al.* [OPERA Collaboration], JHEP **1307**, 004 (2013) [JHEP **1307**, 085 (2013)] [arXiv:1303.3953 [hep-ex]].
- [374] J. M. Conrad, C. M. Ignarra, G. Karagiorgi, M. H. Shaevitz and J. Spitz, Adv. High Energy Phys. **2013**, 163897 (2013) [arXiv:1207.4765 [hep-ex]].
- [375] M. Antonello *et al.* [MicroBooNE and LAr1-ND and ICARUS-WA104 Collaborations], arXiv:1503.01520 [physics.ins-det].
- [376] D. A. Dwyer, K. M. Heeger, B. R. Littlejohn and P. Vogel, Phys. Rev. D **87**, no. 9, 093002 (2013) [arXiv:1109.6036 [hep-ex]].

- [377] G. Bellini *et al.* [Borexino Collaboration], JHEP **1308**, 038 (2013) [arXiv:1304.7721 [physics.ins-det]].
- [378] A. Gando, Y. Gando, S. Hayashida, H. Ikeda, K. Inoue, K. Ishidoshiro, H. Ishikawa and M. Koga *et al.*, arXiv:1312.0896 [physics.ins-det].
- [379] A. S. Riis and S. Hannestad, JCAP **1102**, 011 (2011) [arXiv:1008.1495 [astro-ph.CO]].
- [380] V. N. Kornoukhov, ITEP-90-94.
- [381] M. Cribier, M. Fechner, T. Lasserre, A. Letourneau, D. Lhuillier, G. Mention, D. Franco and V. Kornoukhov *et al.*, Phys. Rev. Lett. **107**, 201801 (2011) [arXiv:1107.2335 [hep-ex]].
- [382] J. M. Conrad and M. H. Shaevitz, Phys. Rev. D **89**, 057301 (2014) [arXiv:1310.3857 [hep-ex]].
- [383] S. K. Agarwalla, J. M. Conrad and M. H. Shaevitz, JHEP **1112**, 085 (2011) [arXiv:1105.4984 [hep-ph]].
- [384] B. Aharmim *et al.* [SNO Collaboration], Phys. Rev. Lett. **101**, 111301 (2008) [arXiv:0806.0989 [nucl-ex]].
- [385] J. Hosaka *et al.* [Super-Kamiokande Collaboration], Phys. Rev. D **73**, 112001 (2006) [hep-ex/0508053].
- [386] S. Abe *et al.* [KamLAND Collaboration], Phys. Rev. Lett. **100**, 221803 (2008) [arXiv:0801.4589 [hep-ex]].
- [387] P. Bakhti and Y. Farzan, JHEP **1310**, 200 (2013) [arXiv:1308.2823 [hep-ph]].
- [388] I. Girardi, D. Meloni, T. Ohlsson, H. Zhang and S. Zhou, JHEP **1408**, 057 (2014) [arXiv:1405.6540 [hep-ph]].
- [389] A. Palazzo, JHEP **1310**, 172 (2013) [arXiv:1308.5880 [hep-ph]].
- [390] F. P. An *et al.* [Daya Bay Collaboration], Phys. Rev. Lett. **113**, 141802 (2014) [arXiv:1407.7259 [hep-ex]].
- [391] A. C. Hayes, J. L. Friar, G. T. Garvey, G. Jungman and G. Jonkmans, Phys. Rev. Lett. **112**, 202501 (2014) [arXiv:1309.4146 [nucl-th]].
- [392] A. D. Sakharov, JETP Lett. **5**, 27 (1967) [Pisma Zh. Eksp. Teor. Fiz. **5**, 36 (1967)].
- [393] P. Nath and P. Fileviez Perez, Phys. Rept. **441**, 191 (2007) [hep-ph/0601023].
- [394] F. Reines, C. L. Cowan and M. Goldhaber, Phys. Rev. **96**, 1157 (1954).
- [395] M. R. Krishnaswamy, M. G. K. Menon, N. K. Mondal, V. S. Narasimham, B. V. Sreekantan, N. Ito, S. Kawakami and Y. Hayashi *et al.*, Phys. Lett. B **106**, 339 (1981).
- [396] G. Battistoni, E. Bellotti, C. Bloise, G. Bologna, P. Campana, C. Castagnoli, V. Chiarella and O. Cremonesi *et al.*, Nucl. Instrum. Meth. A **245**, 277 (1986).
- [397] C. Berger *et al.* [FREJUS Collaboration], Nucl. Instrum. Meth. A **262**, 463 (1987).
- [398] J. L. Thron, Nucl. Instrum. Meth. A **283**, 642 (1989).

- [399] R. Becker-Szendy, C. B. Bratton, D. R. Cady, D. Casper, R. Claus, S. T. Dye, W. Gajewski and M. Goldhaber *et al.*, Nucl. Instrum. Meth. A **324**, 363 (1993).
- [400] K. S. Hirata *et al.* [Kamiokande-II Collaboration], Phys. Lett. B **220**, 308 (1989).
- [401] E. Kearns, talk presented at the ISOUP Symposium (2013).
- [402] H. Nishino *et al.* [Super-Kamiokande Collaboration], Phys. Rev. D **85**, 112001 (2012) [arXiv:1203.4030 [hep-ex]].
- [403] C. Regis *et al.* [Super-Kamiokande Collaboration], Phys. Rev. D **86**, 012006 (2012) [arXiv:1205.6538 [hep-ex]].
- [404] K. Abe *et al.* [Super-Kamiokande Collaboration], Phys. Rev. Lett. **113**, no. 12, 121802 (2014) [arXiv:1305.4391 [hep-ex]].
- [405] T. M. Undagoitia, F. von Feilitzsch, M. Goger-Neff, C. Grieb, K. A. Hochmuth, L. Oberauer, W. Potzel and M. Wurm, Phys. Rev. D **72**, 075014 (2005) [hep-ph/0511230].
- [406] D. Stefan and A. M. Ankowski, Acta Phys. Polon. B **40**, 671 (2009) [arXiv:0811.1892 [nucl-th]].
- [407] Y. Hayato *et al.* [Super-Kamiokande Collaboration], Phys. Rev. Lett. **83**, 1529 (1999) [hep-ex/9904020].
- [408] A. Bueno, Z. Dai, Y. Ge, M. Laffranchi, A. J. Melgarejo, A. Mereaglia, S. Navas and A. Rubbia, JHEP **0704**, 041 (2007) [hep-ph/0701101].
- [409] G. J. Feldman and R. D. Cousins, Phys. Rev. D **57**, 3873 (1998) [physics/9711021 [physics.data-an]].
- [410] V. C. Rubin and W. K. Ford, Jr., Astrophys. J. **159**, 379 (1970).
- [411] F. Zwicky, Helv. Phys. Acta **6**, 110 (1933).
- [412] F. Zwicky, Astrophys. J. **86**, 217 (1937).
- [413] H. Hoekstra, H. Yee and M. Gladders, New Astron. Rev. **46**, 767 (2002) [astro-ph/0205205].
- [414] D. Clowe, M. Bradac, A. H. Gonzalez, M. Markevitch, S. W. Randall, C. Jones and D. Zaritsky, Astrophys. J. **648**, L109 (2006) [astro-ph/0608407].
- [415] J. P. Dietrich, N. Werner, D. Clowe, A. Finoguenov, T. Kitching, L. Miller and A. Simionescu, Nature **487**, 202 (2012) [arXiv:1207.0809 [astro-ph.CO]].
- [416] J. L. Feng, Ann. Rev. Astron. Astrophys. **48**, 495 (2010) [arXiv:1003.0904 [astro-ph.CO]].
- [417] R. Bernabei *et al.* [DAMA and LIBRA Collaborations], Eur. Phys. J. C **67**, 39 (2010) [arXiv:1002.1028 [astro-ph.GA]].
- [418] C. E. Aalseth *et al.* [CoGeNT Collaboration], Phys. Rev. Lett. **106**, 131301 (2011) [arXiv:1002.4703 [astro-ph.CO]].
- [419] C. E. Aalseth *et al.* [CoGeNT Collaboration], Phys. Rev. Lett. **107**, 141301 (2011) [arXiv:1106.0650 [astro-ph.CO]].

- [420] C. E. Aalseth *et al.* [CoGeNT Collaboration], arXiv:1401.3295 [astro-ph.CO].
- [421] G. Angloher *et al.*, Eur. Phys. J. C **72**, 1971 (2012) [arXiv:1109.0702 [astro-ph.CO]].
- [422] R. Agnese *et al.* [CDMS Collaboration], Phys. Rev. Lett. **111**, 251301 (2013) [arXiv:1304.4279 [hep-ex]].
- [423] E. Aprile *et al.* [XENON100 Collaboration], Phys. Rev. Lett. **109**, 181301 (2012) [arXiv:1207.5988 [astro-ph.CO]].
- [424] E. Aprile *et al.* [XENON100 Collaboration], Phys. Rev. Lett. **111**, 021301 (2013) [arXiv:1301.6620 [astro-ph.CO]].
- [425] D. S. Akerib *et al.* [LUX Collaboration], Phys. Rev. Lett. **112**, 091303 (2014) [arXiv:1310.8214 [astro-ph.CO]].
- [426] R. Agnese *et al.* [SuperCDMS Collaboration], Phys. Rev. Lett. **112**, 241302 (2014) [arXiv:1402.7137 [hep-ex]].
- [427] M. Felizardo *et al.* (SIMPLE Collaboration), Phys. Rev. Lett. **108**, 201302 (2012) [arXiv:1106.3014 [astro-ph.CO]].
- [428] Q. Yue *et al.* [CDEX Collaboration], Phys. Rev. D **90**, 091701 (2014) [arXiv:1404.4946 [hep-ex]].
- [429] O. Adriani *et al.* [PAMELA Collaboration], Nature **458**, 607 (2009) [arXiv:0810.4995 [astro-ph]].
- [430] J. Chang *et al.*, Nature **456**, 362 (2008).
- [431] A. A. Abdo *et al.* [Fermi LAT Collaboration], Phys. Rev. Lett. **102**, 181101 (2009) [arXiv:0905.0025 [astro-ph.HE]].
- [432] M. Aguilar *et al.* [AMS Collaboration], Phys. Rev. Lett. **110**, 141102 (2013).
- [433] M. G. Aartsen *et al.* [IceCube Collaboration], Phys. Rev. Lett. **110**, 131302 (2013).
- [434] L. M. Krauss, M. Srednicki and F. Wilczek, Phys. Rev. D **33**, 2079 (1986).
- [435] K. Griest and D. Seckel, Nucl. Phys. B **283**, 681 (1987) [Erratum-ibid. B **296**, 1034 (1988)].
- [436] M. Nauenberg, Phys. Rev. D **36**, 1080 (1987).
- [437] A. Gould, Astrophys. J. **321**, 560 (1987).
- [438] C. S. Chen, F. F. Lee, G. L. Lin and Y. H. Lin, JCAP **1410**, 049 (2014) [arXiv:1408.5471 [hep-ph]].
- [439] G. Jungman, M. Kamionkowski and K. Griest, Phys. Rept. **267**, 195 (1996) [hep-ph/9506380].
- [440] G. Bertone, D. Hooper and J. Silk, Phys. Rept. **405**, 279 (2005) [hep-ph/0404175].
- [441] M. Blennow, J. Edsjo and T. Ohlsson, JCAP **0801**, 021 (2008).
- [442] M. G. Aartsen *et al.* [IceCube Collaboration], Phys. Rev. Lett. **110**, 151105 (2013).

- [443] M. Honda, M. S. Athar, T. Kajita, K. Kasahara and S. Midorikawa, arXiv:1502.03916 [astro-ph.HE].
- [444] E. Behnke *et al.* [COUPP Collaboration], Phys. Rev. D **86**, 052001 (2012) [arXiv:1204.3094 [astro-ph.CO]].
- [445] S. Archambault *et al.* [PICASSO Collaboration], Phys. Lett. B **711**, 153 (2012) [arXiv:1202.1240 [hep-ex]].
- [446] R. Agnese *et al.* [SuperCDMS Collaboration], Phys. Rev. Lett. **112**, 041302 (2014) [arXiv:1309.3259 [physics.ins-det]].
- [447] S. Antusch, J. P. Baumann and E. Fernandez-Martinez, Nucl. Phys. B **810**, 369 (2009) [arXiv:0807.1003 [hep-ph]].
- [448] N. Severijns, M. Beck and O. Naviliat-Cuncic, Rev. Mod. Phys. **78**, 991 (2006) [nucl-ex/0605029].
- [449] T. Ohlsson, H. Zhang and S. Zhou, Phys. Lett. B **728**, 148 (2014) [arXiv:1310.5917 [hep-ph]].
- [450] Y. F. Li and Y. L. Zhou, Nucl. Phys. B **888**, 137 (2014) [arXiv:1408.6301 [hep-ph]].
- [451] V. A. Kostelecky and S. Samuel, Phys. Rev. D **39**, 683 (1989).
- [452] D. Colladay and V. A. Kostelecky, Phys. Rev. D **55**, 6760 (1997) [hep-ph/9703464].
- [453] D. Colladay and V. A. Kostelecky, Phys. Rev. D **58**, 116002 (1998) [hep-ph/9809521].
- [454] Y. F. Li and Z. h. Zhao, Phys. Rev. D **90**, no. 11, 113014 (2014) [arXiv:1409.6970 [hep-ph]].
- [455] V. A. Kostelecky and M. Mewes, Phys. Rev. Lett. **87**, 251304 (2001) [hep-ph/0111026].
- [456] V. A. Kostelecky and M. Mewes, Phys. Rev. D **66**, 056005 (2002) [hep-ph/0205211].
- [457] V. A. Kostelecky and M. Mewes, Phys. Rev. D **69**, 016005 (2004) [hep-ph/0309025].
- [458] J. S. Diaz, V. A. Kostelecky and M. Mewes, Phys. Rev. D **80**, 076007 (2009) [arXiv:0908.1401 [hep-ph]].
- [459] A. de Gouvea and S. Shalgar, JCAP **1210**, 027 (2012) [arXiv:1207.0516 [astro-ph.HE]].
- [460] A. de Gouvea and S. Shalgar, JCAP **1304**, 018 (2013) [arXiv:1301.5637 [astro-ph.HE]].
- [461] B. Achkar, R. Aleksan, M. Avenier, G. Bagieu, J. Bouchez, R. Brissot, J. F. Cavaignac and J. Collot *et al.*, Phys. Lett. B **374**, 243 (1996).
- [462] *Improving Pressurized Water Reactor Performance Through Instrumentation: Application Case of Reducing Uncertainties on Thermal Power*, EPRI report prepared by Electricite de France, 2001; *Application of Orifice Plates for Measurement of Feedwater Flow*, EPRI report prepared by Electricite de France, 2001.
- [463] R. Sanchez *et al.*, Nuclear Engineering and Technology **42**, 474 (2010).
- [464] G. Marleau, A. Hebert and R. Roy, A User Guide for DRAGON. Report IGE-174 Rev. 5 (2000).

- [465] V. Kopeikin, L. Mikaelyan and V. Sinev, Phys. Atom. Nucl. **67**, 1892 (2004) [Yad. Fiz. **67**, 1916 (2004)] [hep-ph/0410100].
- [466] X. B. Ma, L. Z. Wang, Y. X. Chen, W. L. Zhong and F. P. An, arXiv:1405.6807 [nucl-ex].
- [467] V. I. Kopeikin, L. A. Mikaelyan and V. V. Sinev, Phys. Atom. Nucl. **64**, 849 (2001) [Yad. Fiz. **64**, 914 (2001)] [hep-ph/0110290].
- [468] V. N. Afanasev, V. V. Barmin, A. A. Burenkov, V. I. Demekhin, A. G. Dolgolenko, A. S. Gerasimov, V. S. Goryachev and Y. I. Povarov *et al.*, Phys. Atom. Nucl. **66**, 500 (2003) [Yad. Fiz. **66**, 527 (2003)].
- [469] V. Kopeikin, L. Mikaelyan and V. Sinev, Phys. Atom. Nucl. **69**, 185 (2006) [hep-ph/0412044].
- [470] F. P. An, X. C. Tian, L. Zhan and J. Cao, Chin. Phys. C **33**, 711 (2009).
- [471] A. C. Hayes, J. L. Friar, G. T. Garvey, G. Jungman, G. Jonkmans, Phys. Rev. Lett. **112**, 202501 (2014).
- [472] J. Allison, K. Amako, J. Apostolakis, H. Araujo, P. A. Dubois, M. Asai, G. Barrand and R. Capra *et al.*, IEEE Trans. Nucl. Sci. **53**, 270 (2006).
- [473] P. Antonioli, C. Ghetti, E. V. Korolkova, V. A. Kudryavtsev and G. Sartorelli, Astropart. Phys. **7**, 357 (1997) [hep-ph/9705408].
- [474] See the website: <http://www-nds.iaea.org/exfor/endl.htm>
- [475] W. Q. Jiang, S. D. Gu, J. Joseph, D. W. Liu, K. B. Luk, H. Steiner, Z. Wang and Q. Wu, Chin. Phys. C **36**, 235 (2012).
- [476] S. Jetter, D. Dwyer, W. Q. Jiang, D. W. Liu, Y. F. Wang, Z. M. Wang and L. J. Wen, Chin. Phys. C **36**, 733 (2012).
- [477] X. Guo *et al.* [Daya Bay Collaboration], hep-ex/0701029.
- [478] Y. Becherini, A. Margiotta, M. Sioli and M. Spurio, Astropart. Phys. **25**, 1 (2006) [hep-ph/0507228].
- [479] Triangular Universities Nuclear Laboratory (TUNL), the Nuclear Data Evaluation Group: <http://www.tunl.duke.edu/nucldata/>